Cloud Publications
International Journal of Advanced Remote Sensing and GIS
2019, Volume 8, Issue 1, pp. 2919-2932
ISSN 2320 – 0243, Crossref: 10.23953/cloud.ijarsg.400

Research Article

Estimation of Air Pollution Using Multi-Temporal Remote Sensing Technique for Dehradun District, Uttarakhand

Jyotsana Joshi, Kishor Chandra Kandpal, Neelam Rawat

Uttarakhand Space Application Centre, Dehradun, Uttarakhand, India

Correspondence should be addressed to *kandpalkishor128@gmail.com*

Publication Date: 16 January 2019

DOI: https://doi.org/10.23953/cloud.ijarsg.400

Abstract Air pollution is a major problem of many countries around the world. The main source of the air pollution due to growing urbanization, growth of the industry, vehicles etc. In this research produce an empirical model using Landsat 8 satellite data and ground PM 10 measurement for determination of particulate matter (PM 10) concentration in the atmosphere over Dehradun city, the capital of Uttarakhand . The research focus on air pollution determination using atmospheric reflectance (DOS method) and correlate to PM 10 ground measurement**.** The outcomes of this research showed that visible bands of Landsat 8 OLI were capable of calculating PM10 concentration to an acceptable level of accuracy.
Keywords *Air Pollution; AOT; DOS; PM10; Reflectance*

1. Introduction

Air pollution is a universally major issue to human being. It causes various health problems and effects on natural environment i.e. increase the level of temperature. Major industrialization, is the main source of air pollution and other cause of dispersion of air pollution, including emission from vehicle, weather condition, humidity, presence of building and thermal power plant. Air pollution consequently shows high spatial variability, even at short distances (Wijeratne et al., 2006). According to 2014 report of World Health Organization (WHO), 92% of the world population was living in places where WHO air quality guideline standards were not met. Outdoor air pollution in both cities and rural areas was estimated to have caused 3 million deaths worldwide in 2012.

Particulate matter (PM10) pollution consists of very small liquid and solid particles which diameter is less than 10 micrometer or less floating in the air. PM10 is a major component of air pollution that threatens both our health and our environment. (Masitah et al., 2007). Particles in this size range make up a large proportion of dust that can be drawn deep into the lungs. Larger particles tend to be trapped in the nose, mouth or throat. The study of particulate matter (PM) as air pollutant is important because of its effects on human health, atmospheric visibility, climate change, etc. (Leli et al., 2008). So mapping of air quality is important for the assessment of annual, seasonal changes and other environmental climate changes. Traditionally, two general approaches to mapping air pollution can be identified: spatial interpolation and air dispersion modeling (Elliott et al., 1996). The former approaches estimate the value of pollution concentration at un-sampled locations in an area of interest by

interpolating the measurements from the sampled stations (Masitah et al., 2007). Most of the air quality data that currently used are interpolated from the data collected from a limited number of measuring stations located mainly in cities or estimated by the numerical air dispersion models (Retalis et al., 2010).

Air pollutants can be measured from ground base stations with many different types of instruments. But these instruments are quite expensive and limited by the number of air pollutant station in each area. The limited number of the air pollutant stations and improper distributed not allowed a proper mapping of the air pollutants. Ground instruments are impractical if measurements are to be made over large areas or for continuous monitoring. So, they cannot provide a detail spatial distribution of the air pollutant over large cities.

This study focuses on the mapping of dispersion of air pollution using remote sensing techniques and ground station data. The basic method is a radiometric comparison of a satellite image recorded under polluted conditions, with a reference image acquired under less polluted condition. Ground station data were used to select a less polluted reference image. In remote sensing, different algorithms are used to estimate particulate matter (PM10), depending on the sensor and the spectral band (Sifakis and Deschamps, 1992; Sifakis et al., 1998; Retalis et al., 1999; Wald and Baleynaud, 1999; Ung et al., 2001). The relation between ground observations and estimates of aerosol optical thickness is described with linear regression providing the spatial distribution of air pollution. Therefore, in this study presented the potentiality of retrieving concentrations of particulate matter with diameters less than ten micrometer (PM10) in the atmosphere using the Landsat 8 satellite images over Dehradun. The main aim of the study is to finding a suitable empirical equation for the estimation of particulate matter using remote sensing technology and ground data.

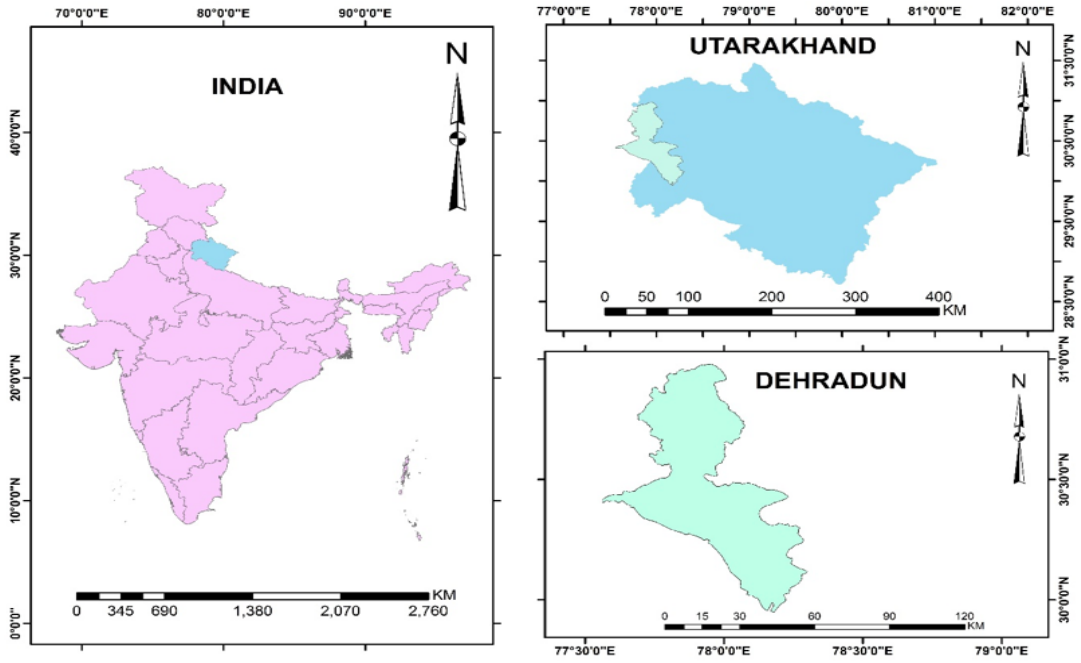

Figure 1: *Location map of study area*

Study Area

Dehradun district covers an area of 3,088 km^2 (1,192 sq mi). Geographical extension of Dehradun is between 78°00'E to 78°15'E longitudes and 30°15'north to 30°25'N latitudes. Dehradun is located in a synclinal valley within the Siwalik formation. Rocks under Siwalik formation were thrusted over the sediments of Indo-Gangetic Plain along the Himalayan Frontal Fault (Ori and Friend, 1984; Gupta, 1997). On the east, the Dehradun town is surrounded by the Song River, the Tons River on the west, the Himalaya ranges on the north and the south by Sal forests.

2. Materials and Methodology

The methodology process generally was divided into the four steps: data acquisition, pre-processing, data processing and validation of results. Arc GIS 10.4, ERDAS IMAGINE 14 and SPSS are used for the study.

Pre-processing

In the first step, the raw digital number (DN) values of Landsat imagery have been converted to radiance value. In the second step, the radiance value are converted to top of atmospheric reflectance (TOA).

Conversion to TOA Radiance

OLI and TIRS band data can be converted to TOA spectral radiance using the radiance rescaling factors provided in the metadata file:

$$L\lambda = ML*Qcal + AL \ldots (1)$$

Where:

Lλ = TOA spectral radiance [Watts/(m2 * srad * μm)]
ML = Band-specific multiplicative rescaling factor from the metadata
(RADIANCE_MULT_BAND_x, where x is the band number)
AL = Band-specific additive rescaling factor from the metadata
(RADIANCE_ADD_BAND_x, where x is the band number)
Qcal = Quantized and calibrated standard product pixel values (DN)

Conversion to TOA Reflectance

OLI band data can also be converted to TOA planetary reflectance using reflectance rescaling coefficients provided in the product metadata file (MTL file). The following equation is used to convert DN values to TOA reflectance for OLI data as follows:

$$\rho\lambda' = M\rho*Qcal + Ap \ldots (2)$$

Where:

ρλ' = TOA planetary reflectance, without correction for solar angle. Note that ρλ' does not contain a correction for the sun angle.

Mρ = Band-specific multiplicative rescaling factor from the metadata (REFLECTANCE_MULT_BAND_x, where x is the band number)
Aρ = Band-specific additive rescaling factor from the metadata (REFLECTANCE_ADD_BAND_x, where x is the band number)
Qcal = Quantized and calibrated standard product pixel values (DN)
TOA reflectance with a correction for the sun angle is then:

$$\rho\lambda = \rho\lambda'/\sin(\theta) \quad \ldots (3)$$

Where:

ρλ = TOA Planetary Reflectance (Unit less)
θ = Solar Elevation Angle (from the metadata, or calculated)

Atmospheric Correction

It is worth pointing out that Landsat 8 images are provided with band-specific rescaling factors that allow for the direct conversion from DN to TOA reflectance. However, the effects of the atmosphere (i.e. a disturbance on the reflectance that varies with the wavelength) should be considered in order to measure the reflectance at the ground. As described by Moran et al. (1992), the land surface reflectance (ρ) is:

$$\rho = \frac{\pi * (L\lambda - Lp) * d^2}{Tv * \{(ESUN\lambda * cos\theta * TZ)} \quad \ldots (4)$$

Where:

LP = path radiance
TV = atmospheric transmittance in the viewing direction
TZ = atmospheric transmittance in the illumination direction
Edown = downwelling diffuse irradiance
ESUNλ = mean solar exo-atmospheric irradiances
d = earth_sun distance (provided with Landsat 8 metadata)

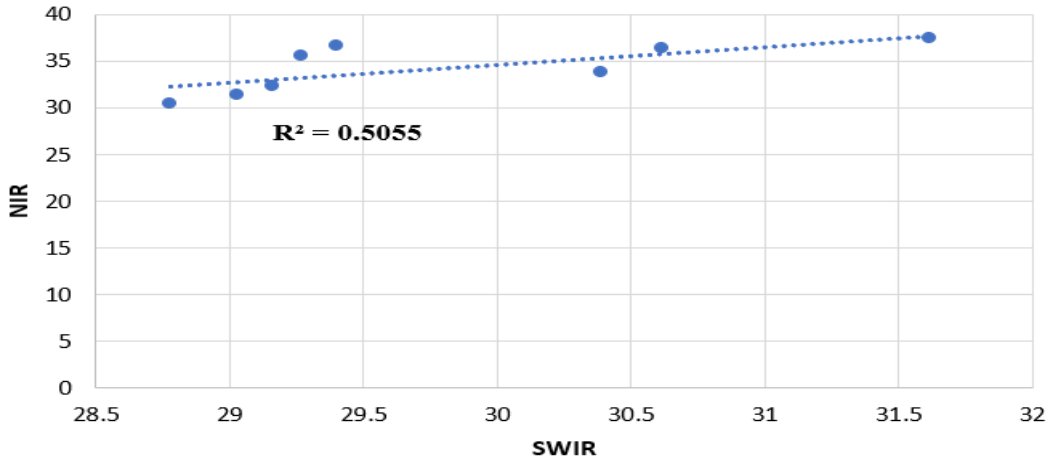

Figure 2: *Correlation between SWIR and NIR for DOS method*

Path Radiance (Using Dark object subtraction Method) DOS

This approach indicates lower Lp with increasing wavelength and negligible Lp in SWIR band. Correlation with SWIR band with NIR, Red, Green and Blue individually, and found that correlation as high as 0.50 for NIR band, 0.16 for Red band and 0.12 for Blue band. Then subtract minimum radiance value of NIR band from each visible band.

And the resulting land surface reflectance is given by:

$$\rho = \frac{\pi * (L\lambda - Lp) * d^2}{ESUN\lambda * \cos\theta sz} \quad \text{... (5)}$$

Atmospheric Reflectance

Atmospheric reflectance is calculated as:

AR = TOA – Surface Reflectance … (6)

Particulate matter (PM), also known as particle pollution, is a complex mixture of extremely small particles and liquid droplets that get into the air. Once inhaled, these particles can affect the heart and lungs and cause serious health effects.

Here in this Study PM10 is estimated by Multiple Regression Analysis, the result was extended to a three and four-band algorithm as:

A = e + e R1 + e R2 + e R3+ e R … (7)

Where:

A = Particle concentration (PM10)
Ratmi = Atmospheric reflectance, i = 0, 1 and 3 are the band number
e = algorithm coefficients

Regression Analysis and Mapping

Using linear regression, we established relations between processed image outputs (PM10) and ground data of PM10.

Linear Regression

Y = a + bX … (8)

Multiple Regression

Y = a + b1X1 + b2X2 + b3X3 +b3X4 … (9)

Where:

Y = the variable that you are trying to predict (dependent variable)
X = the variable that you are using to predict Y (independent variable)

a = the intercept
b = the slope

3. Results and Discussion

The digital numbers of the four visible bands namely blue, green, red and NIR of Landsat 8 OLI were extracted corresponding to the locations of ground PM10 measurements over Dehradun district. The Landsat visible band converted into Radiance, TOA and then surface reflectance using DOS method. The atmospheric reflectance calculated from the surface reflectance subtracted from TOA reflectance. The scatter plot of visible bands of atmospheric reflectance correlate to PM 10 ground measurements is shown in following figures.

Table 1: *Calculated PM10 Concentration from Satellite Image Data and PM10 Ground Measurement at Different Location of Dehradun District (2013)*

Ground station	pm10 concentration estimated from Imagery (µg/m³)	Monthly average pm10 concentration measured at ground station (µg/m³)
Clock tower	154.12	159
Raipur road	163.63	166
ISBT	183.74	182
Rishikesh	121.79	123

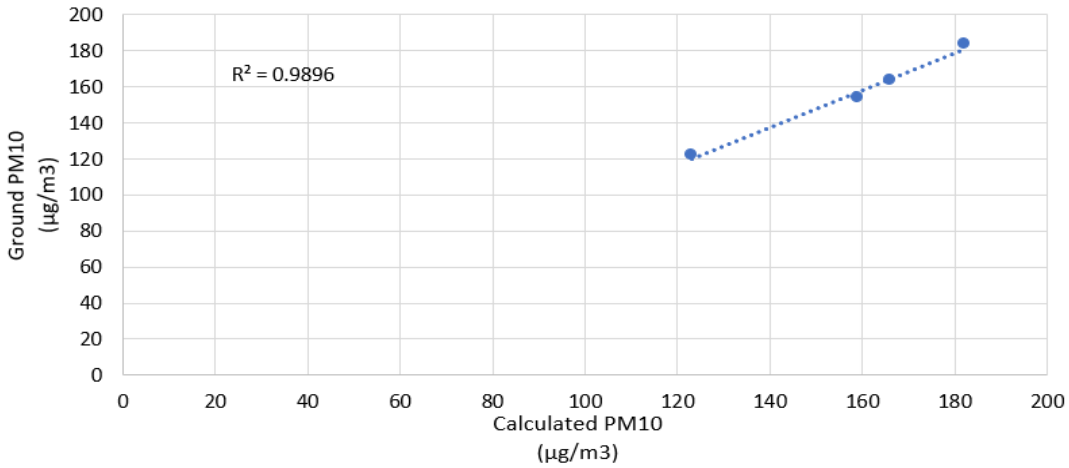

Figure 3: *Regression analysis between calculated PM10 and Ground PM10 (2013)*

Table 2: *Calculated PM10 concentration from satellite image data and PM10 ground measurement at different location of Dehradun District (2015)*

Ground station	PM10 concentration estimated from Imagery (µg/m3)	Monthly Average pm10 concentration measured at ground station (µg/m3)
Clock Tower	191.75	173
Raipur Road	188.67	159
ISBT	201.44	226
Rishikesh	174.32	156

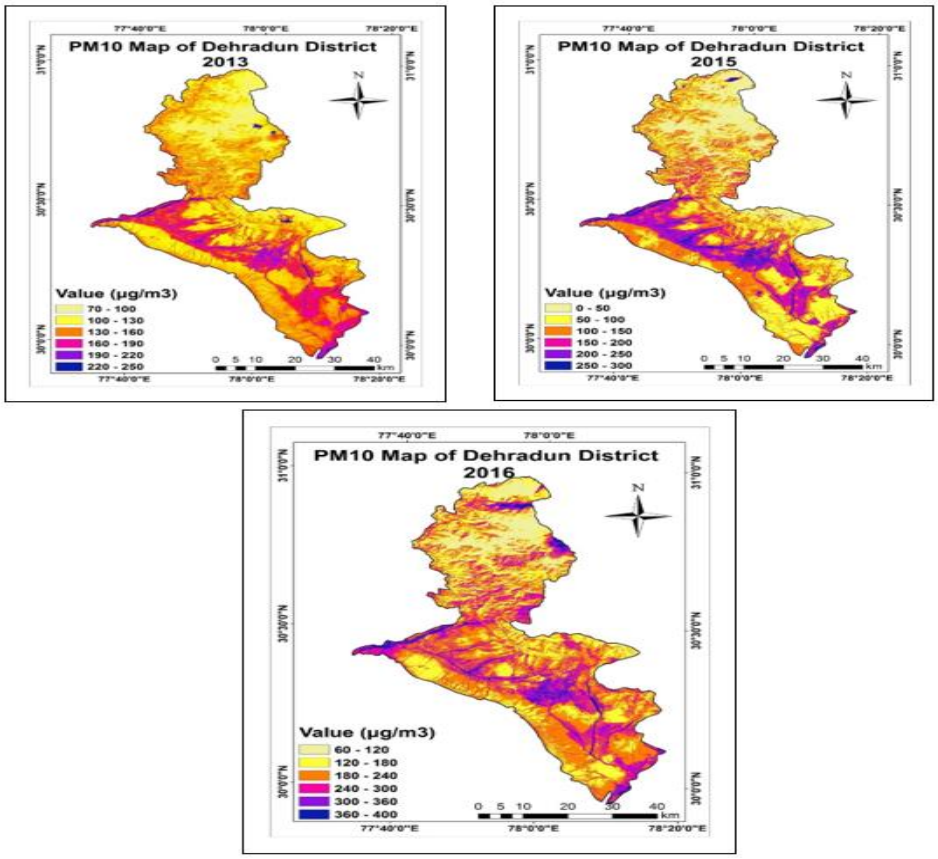

Figure 4: *PM10 Concentration Over Dehradun District (2013, 2015, 2016)*

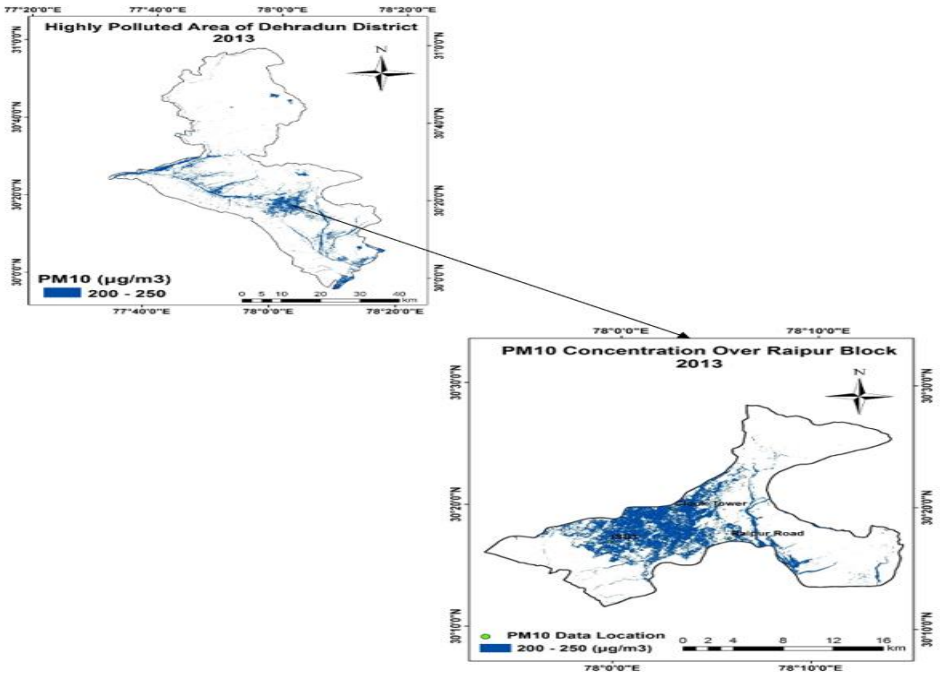

Figure 5: *Highly polluted area of Dehradun City (2013)*

In the Dehradun district, there are four PM 10 ground station i.e. Clock tower, ISBT, Risikesh and Raipur Road. The maximum concentration of calculated PM 10 was 201.44 µg/m³ at ISBT in Dehradun as calculated for May, 2013. It is observed that the minimum concentration of calculated PM 10 was 174.32 µg/m³ at Risikesh (Table 2). From Table 2, it can be observed that the concentration of PM 10 increased from 201.44 µg/m³ to 375.39 µg/m³ for 2016 and shifted from ISBT to Raipur road due to the urbanization at Raipur Road. The minimum concentration of PM 10 increased from 174.32 µg/m³ to 190.01 µg/m³ for 2016 at Rishikesh

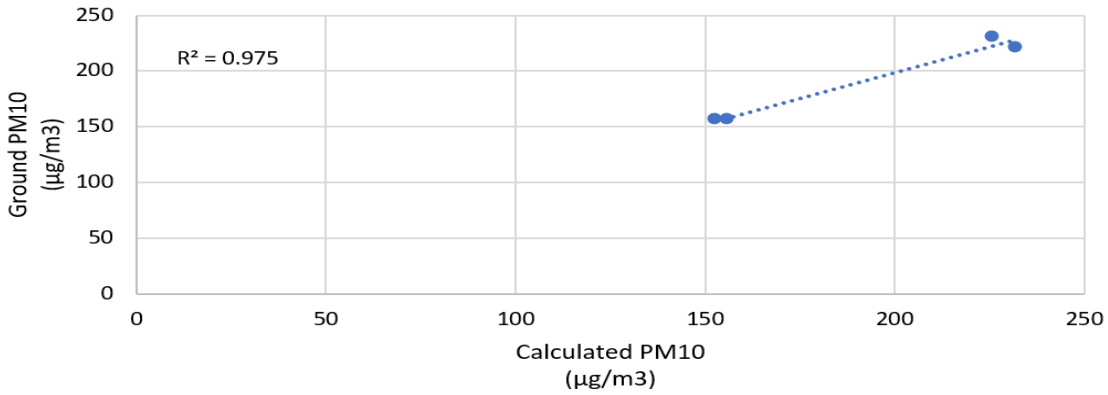

Figure 6: *Regression analysis between calculated PM10 and Ground PM10 (2015)*

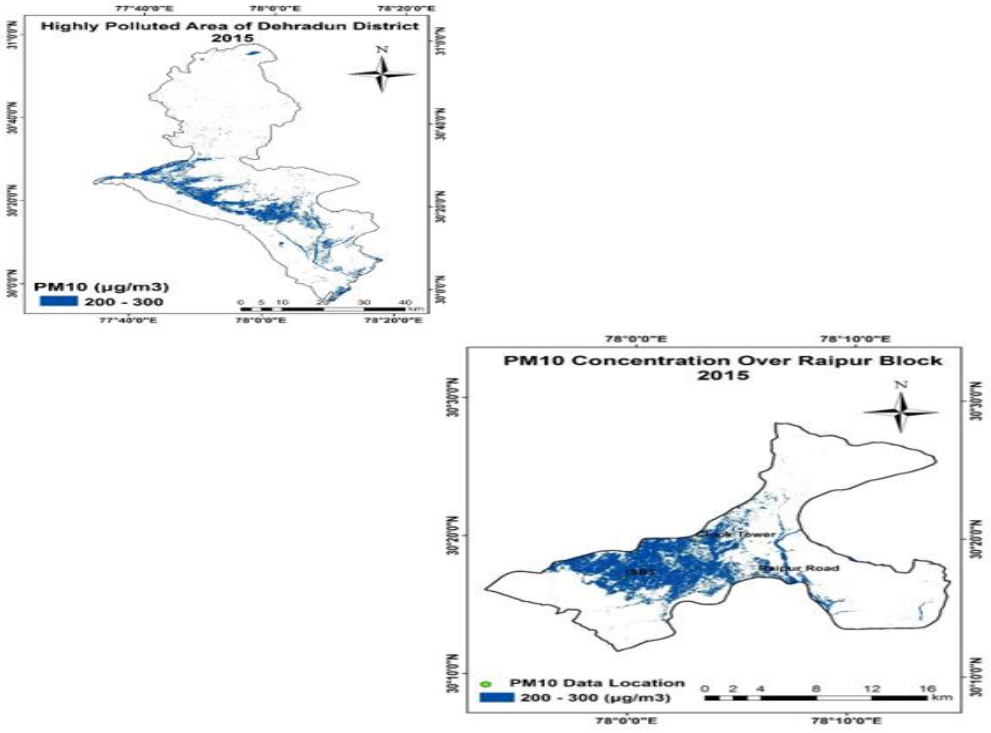

Figure 7: *Highly polluted area of Dehradun City (2015)*

Table 3: *Calculated PM10 concentration from satellite image data and PM10 ground measurement at different location of Dehradun District (2016)*

Ground station	pm10 concentration estimated from imagery (µg/m3)	Monthly average pm10 concentration measured at ground station (µg/m3)
Clock tower	206.48	209.79
Raipur road	375.39	377.76
ISBT	312.29	316.04
Rishikesh	190.01	197.13

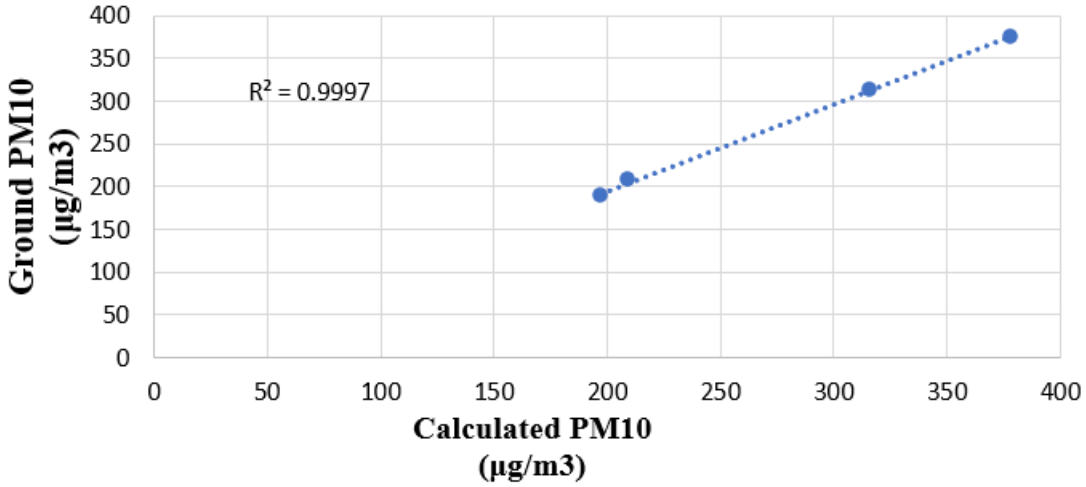

Figure 8: *Regression analysis between calculated PM10 and Ground PM10 (2016)*

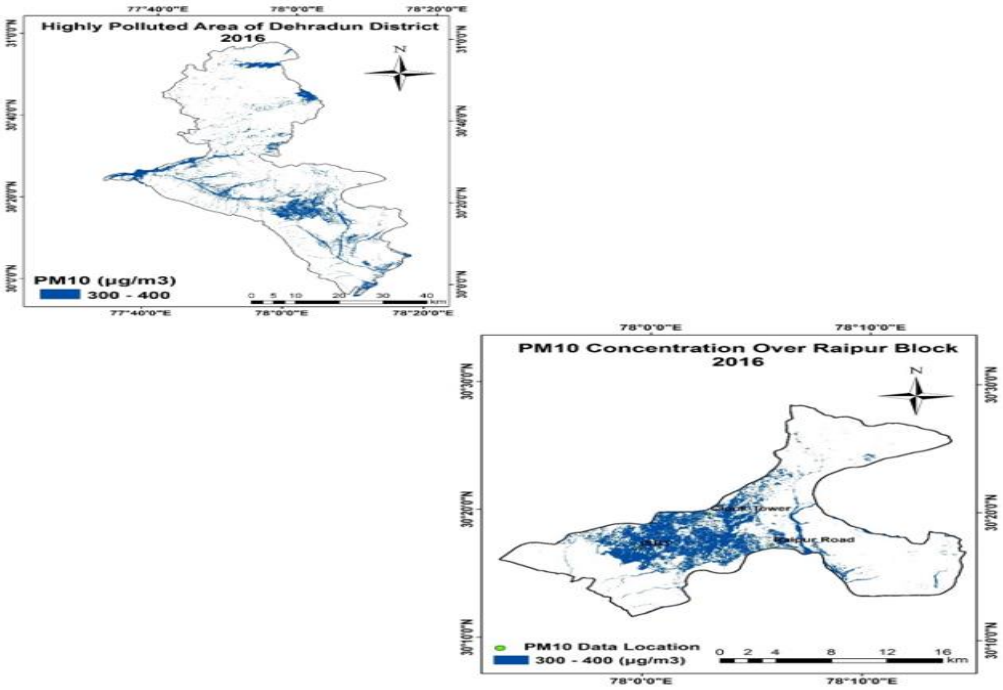

Figure 9: *Highly polluted area of Dehradun City (2016)*

The present paper highlighted the assessment of spatio-temporal pattern of PM 10 concentration during 2013, 2015 and 2016 over Dehradun -capital of the Uttarakhand and PM 10 changes during 3 years. The current study utilized Landsat data from 2013 to 2016 and validate with PM 10 ground station measurements. The atmospheric reflectance for blue, green and red bands were determined using equation (6), as shows in Figure (10-12). For the study, atmospheric reflectance values correlate with different bands, which is adjusted at the ground measurements due to lowest RMSE and highest R.

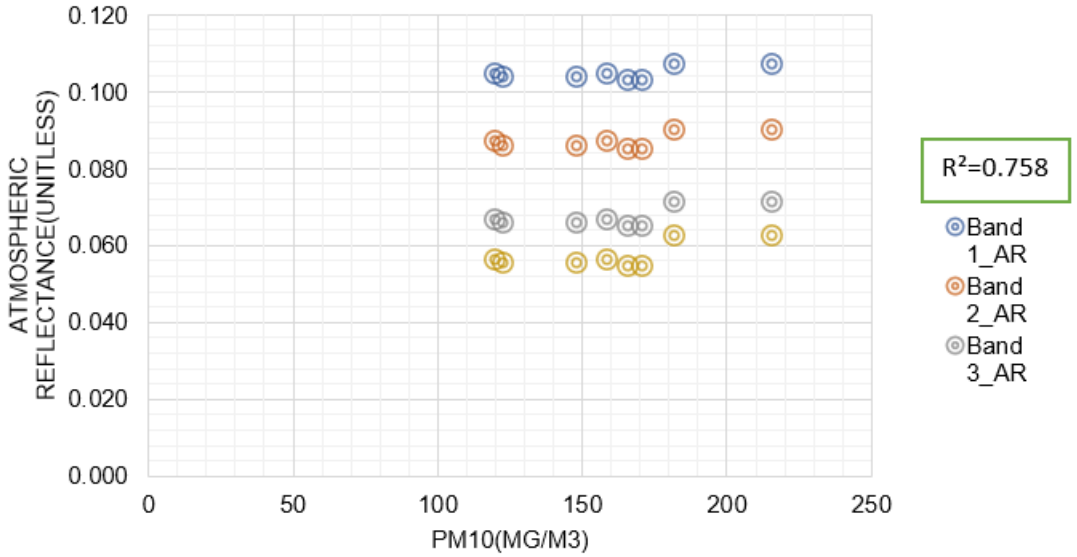

Figure 10: *Multiple regression between AR and PM10 estimated from ground (2013)*

Linear regression analysis is carried out to find the relationship between Atmospheric reflectance and ground PM 10 concentration. In the first part of analysis atmospheric reflectance of blue, green, red and NIR and ground PM10 concentration correlated separately. These resultant value of R^2 is less than 0.4. Therefore, Multiple linear regression analysis was used to develop a model for PM10 estimation, and the value of R^2=0.758 for 2013, R^2=0.531 for 2015 and R^2=0.841 for 2016.

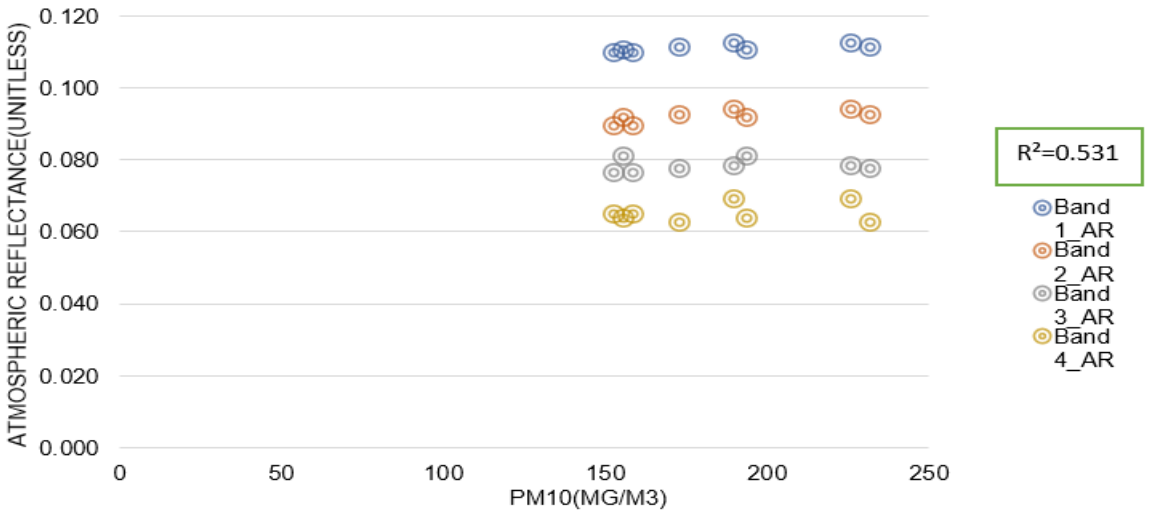

Figure 11: *Multiple regression between AR and PM10 estimated from ground (2015)*

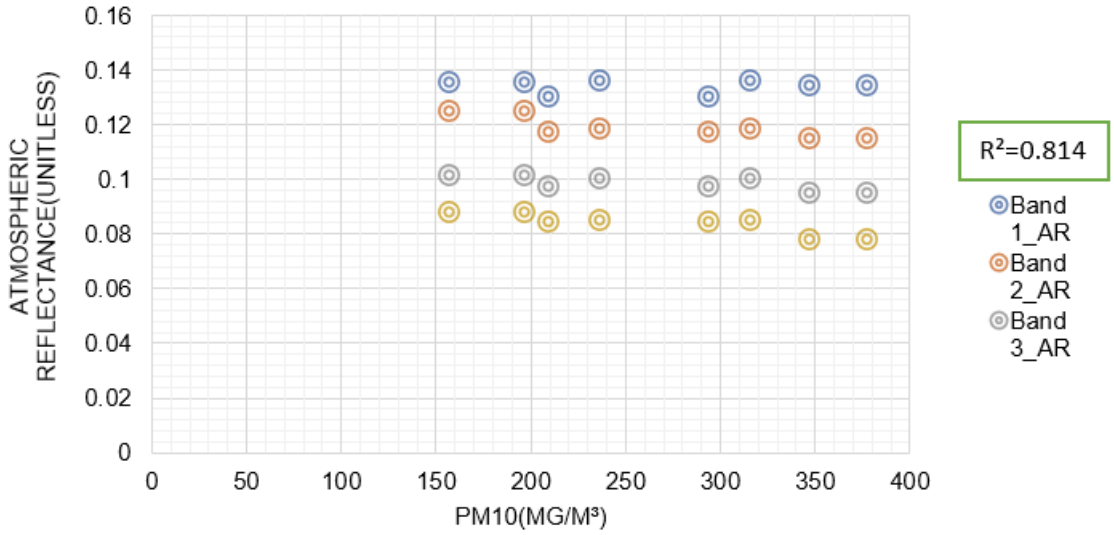

Figure 12: *Multiple regression between AR and PM10 estimated from ground (2016)*

Table 4: *Regression results (R) using different forms of algorithms. Calculated PM10 by algorithms, b1, b2, b3 and b4 are the reflectance values for band1, band2, band3 and band4 of Landsat 8 OLI*

S. No.	Algorithm	R^2
1.	PM10 = 0.00004b1 + 0.0986	0.02545
2.	PM10 = 0.00005b2 + 0.0787	0.366
3.	PM10 = 0.00007b3 + 0.0563	0.3875
4.	PM10 = 0.00009b4 + 0.0431	0.4014
5.	PM10 = -1069.36 + 5686.114b1 + 11564.33b2 – 3091.88b3 – 3090.33b4	0.9868
6.	PM10 = 0.00002b1 + 0.1063	0.7125
7.	PM10 = 0.00004b2 + 0.085	0.7133
8.	PM10 = -0.000006b3 + 0.063	0.018
9.	PM10 = 0.00001b4 + 0.0623	0.0461
10.	PM10 = 59.852 – 16563.4b1 + 25293.48b2 – 4615.48b3	0.5316
11.	PM10 = 0.00001b1 + 01305	0.1503
12.	PM10 = -0.00003b2 + 0.1284	0.4858
13.	PM10 = -0.00002b3 + 0.1031	0.3037
14.	PM10 = -0.00004b4 + 0.0940	0.06609
15.	PM10 = -2914.44 + 5152.015b1 + 7675.03b2 + 19199.64b3 – 3666.89b4	0.9615

A linear regression is used to create PM 10 algorithm based on highest value of R where the R=, for 2013, R= for 2015, and R= for 2016. The PM 10 algorithm is as below equation (5) for 2013, equation (10) for 2015 and equation (15) for 2016.

PM10 = -1069.36 + 5686.114b1 + 11564.33b2 – 3091.88b3 – 3090.33b4 (5)
PM10 = 59.852 – 16563.4b1 + 25293.48b2 – 4615.48b3s (10)
PM10 = -2914.44 + 5152.015b1 + 7675.03b2 + 19199.64b3 – 3666.89b4 (15)

Where PM 10 is the PM 10 concentration (γ g/m³), Ratm(γ 1), Ratm(γ 2), R(γ and R(γ are atmospheric reflectance of visible band.

Temporal Variation of PM10 Concentration

Below the graph shows the average monthly concentration for PM10, during the year 2013, the average PM10 recorded are 160.16 µg/m3, during the year 2015, the average PM10 recorded are 185.37 µg/m3 and in the year of 2016, the average PM10 recorded are 266.95 µg/m3 the result show that the average monthly PM10 concentration are increased during the year 2013, 2015, 2016.

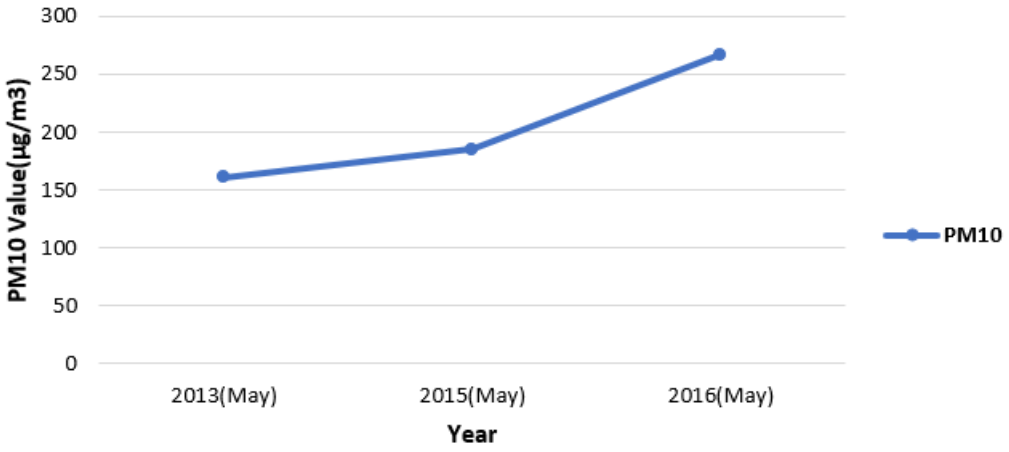

Figure 13: *Multi temporal graph of PM10*

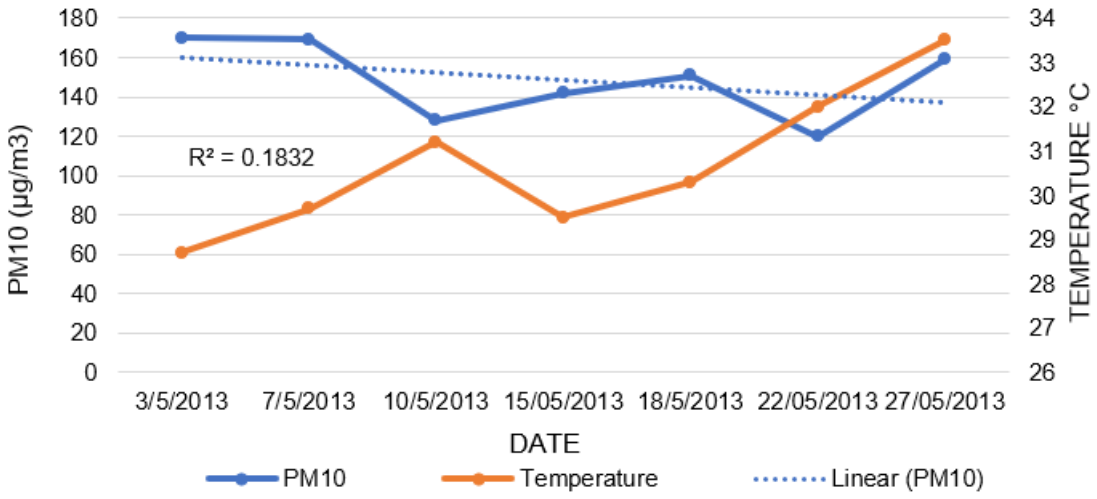

Figure 14: *The relationship graph between air temperature and PM10 (2013)*

The Relationship between Concentrations of Particulate Matter and Air Temperature

From the following figure, it can be observed that concentrations of PM10 had an obviously negative correlation with air temperature. As air temperature increased, concentration of particulate matter was significantly decreased. Because intense radiation heats city underlying surface. The lower atmosphere is not very stable and turbulent strengthens, which is advantages to the diffusion of

pollutants. Therefore, the probability of atmospheric pollution decreased with the increased of the air temperature in summer. While the temperature of surface low, the situation is contrary(Tian et. al 2014)

4. Conclusion

Remote Sensing and GIS based technique was used to estimate air pollution and identify the most polluted area of Dehradun district. The calculation of PM10 concentration using the visible bands reflectance value of Landat 8 imagery. The result show that the urban area of Dehradun district more polluted. This study also prove air pollution can be mapped using satellite data to provide a large coverage.

- The primary assumption about air pollutant particle, the solar irradiance did not reach earth surface, so the solar irradiance interact to atmospheric pollutants. Thus the atmospheric reflectance directly correlate to ground PM 10 measurements.
- In this present study, developed an algorithm to estimate the PM10 concentration over Dehradun District based on Landsat image data and ground monitoring stations data. Three years data has been used to validate the algorithm.
- The present study suggests that we can monitor PM10 concentration on large coverage, if we have selected or less ground PM10 stations.
- The result show that the average monthly PM10 concentration is increased during the year 2013, 2015, 2016.
- The major urban area of Dehradun district is doon valley and the highest PM10 concentration is found with in doon valley and is constantly increasing over the valley.

References

Bozyazi, E.G. 1998. *Analysis and mapping of air pollution: a GIS approach: A case study of Istanbul, Turkey*. MSc thesis, International Institute for Aerospace Survey and Earth Sciences (ITC), Enschede, The Netherlands.

Chakraborty, J., Schweitzer, L.A. and Forkenbrock, D.J. 1999. Using GIS to assess the environmental justice consequences of transportation system changes. *Transactions in GIS*, 3(3), pp.239–258.

Cheng, S. and Lam, K.C. 1997. *Climatic Impact on air pollution concentrations in Hong Kong. Department of Geography*. Occasional paper, The Chinese University of Hong Kong, Hong Kong.

Duk-Dong, L. and Dae-Sik, L. 2001. Environmental gas sensors. *IEEE Sensors Journal*, 1(3).

El Desouky, H.J., Moussa, K.F. and Hassona, H.H. 1998. Impact of automobile exhaust on roadside-soils and plants in Sharkiya Governorate. *Egyptian Journal of Soil Science*, 38(1-4), pp.137-151.

Hadjimitsis, D.G., Nisantzi, A., Themistocleous, K., Matsas, A. and Trigkas, V.P. 2010. *Satellite remote sensing, GIS and sun-photometers for monitoring PM10 in Cyprus: issues on public health*. Proceedings of SPIE - The International Society for Optical Engineering, 7826, 78262C.

Hadjimitsis, D.G., Clayton C.R.I. and Hope, V.S. 2004. An assessment of the effectiveness of atmospheric correction algorithms through the remote sensing of some reservoirs. *International Journal of Remote Sensing*, 25(18), pp.3651-3674.

van de, K.J. 2006. Statistical air quality mapping. Ph.d. thesis, Wageningen University, Wageningen, The Netherlands.

Lee, H.J., Liu, Y., Coull, B.A., Schwartz, J. and Koutrakis, P. 2011. A novel calibration approach of MODIS AOD data to predict PM2.5 concentrations. *Atmos. Chem. Phys.*, 11, pp.7991-8002.

McCubbin, D.R. and Delucchi, M.A. 1999. The health costs of motor vehicle related air pollution. *Journal of Transport Economics and Policy*, 33(3), pp.253-286.

Mishra. R.K., Pandey. J., Chaudhary. S.K., Khalkho A. and Singh. V.K. 2013. Estimation of air pollution concentration over Jharia coal field. *International Journal of Geomatics and Geosciences*, 4(1).

Nadzri, O., Mohd, Z.M.J. and Lim, H.S. 2010. Estimating particulate matter concentration over arid region using satellite remote sensing: a case study in Makkah, Saudi Arabia. Modern Applied Science, 4, pp.131-142.

Nhu Hung, N. and Van Anh, T. 2014. Estimation of Pm10 From AOT of satellite Landsat 8 image over Hanoi city. *International Symposium on Geoinformatics for Spatial Infrastructure Development in Earth and Allied Sciences*.

Nisantzi A., Hadjimitsis D.G. and Aexakis, D. 2011. *Estimating the relationship between aerosol optical thickness and PM10 using lidar and meteorological data in Limassol, Cyprus*. SPIE Remote Sensing.

Retalis, A., Hadjimitsis, D.G., Chrysoulakis, N., Michaelides, S. and Clayton, C.R.I. 2010. Comparison between visibility measurements obtained from satellites and ground. *Natural Hazards and Earth System Sciences Journal*, 10(3) pp.421-428.

Hameed Saleh, S.A. and Ghada H. 2014. Estimation of PM10 concentration using ground measurements landsat 8 OLI satellite image. *Geophysics & Remote Sensing*, 3, p.2.

Zhang Jin, T., Pouyat, R. and Zhang, J.T. 2000. Effects of urbanization on the concentrations of heavy metals in deciduous forest floor in a case study of New York City. *Scientia Silvae Sinicae*, 36(4), pp.42-45.

Cloud Publications
International Journal of Advanced Remote Sensing and GIS
2019, Volume 8, Issue 1, pp. 2889-2900
ISSN 2320 – 0243, Crossref: 10.23953/cloud.ijarsg.396

Research Article

Landsat Imagery Monitoring and Quantification of the Land Cover Changes in the Kan Watershed at Tiébissou (Center of Côte d'Ivoire)

Aimé Koudou[1]*, Cristian Constantin Stoleriu[2], Koffi Fernand Kouamé[3], Alin Mihu-Pintilie[4], Gheorghe Romanescu[2]

[1]Jean Lorougnon Guédé University of Daloa, Training and Research Unit of Environment, Department of Earth Sciences, BP 150 Daloa, Côte d'Ivoire
[2]Alexandru Ioan Cuza University of Iaşi, Faculty of Geography and Geology, Department of Geography, 20A Carol I Blvd., 700505, Iaşi, Romania
[3]Félix Houphouët-Boigny University of Cocody-Abidjan, Training and Research Unit of Earth Sciences and Mining Resources, University Research and Application Center in Remote Sensing (CURAT), Bd of the University, CURAT, 22 BP 801 Abidjan 22, Côte d'Ivoire
[4]Alexandru Ioan Cuza University of Iaşi, Interdisciplinary Research Department – Field Science, 54 Lascăr Catargi St., 700107, Iaşi, Romania

Correspondence should be addressed to **Aimé Koudou**, *kdaime@yahoo.fr*

Publication Date: 16 January 2019

DOI: https://doi.org/10.23953/cloud.ijarsg.396

Abstract The purpose of this study is to characterize and quantify the evolution and changes in land cover of the Kan watershed at Tiébissou between 1988 and 2015. It is based on the exploitation of Landsat 5 TM and Landsat 8 OLI images, submitted to a string of processing from ENVI 4.5, ARCGIS 10.0 and EXCEL 2010. Diachronic land cover analysis revealed six classes in the Kan watershed: water bodies, habitats, farming, dense forest, degraded forest and savannah. From 1988 to 2015, dense forest, habitats and farming grew respectively by 6.20%, 1.80% and 0.52% while savannah and degraded forest shrank by 6.83% and 1.62% respectively. Water bodies remained virtually stable. The largest changes occurred in the savannah (36.11%) while the least important changes were in the water bodies (0.20%). Degraded forest, dense forest, farming and habitats changed by 26.31%, 22.30%, 11.77% and 3.32% respectively. Dramatic changes have also occurred within each land cover classes at varying proportions.
Keywords *GIS; Kan watershed; Land cover; Progression; Regression; Remote sensing*

1. Introduction

The precious and vital natural resources for human survival, such as water, vegetation, are increasingly threatened by scarcity and disappearance for demographic, economic and climatic reasons.

In Côte d'Ivoire, land cover change has become unprecedented in recent decades. Vegetation cover is the perfect illustration of this change. The area of dense forest, which was 15 million hectares at the

beginning of the century and 12 million at Independence, was only 6 million hectares in 1975 and about 2.5 million hectares in 1990 (Aubreville, 1959; SODEFOR, 1996). The main offending agents in this case are agriculture and logging. Côte d'Ivoire is expected to lose all of its national forest cover by 2034 (Durrieu de Madron et al., 2015) if no action is taken to improve its management.

While some biophysical features of the territories are considered virtually stable on a human scale (geology, modeling, hydrographic network geometry, soil cover), others are likely to change more rapidly and significant changes may occur. These changes affect large areas in a few years. The most dramatic changes are of anthropogenic origin (land use, deforestation and exploitation of natural resources, expansion of urban agglomerations).

The Kan watershed is an agricultural area located in the center of Côte d'Ivoire, which experienced the long and severe drought of the 1970s. This drought has had a negative impact on natural resources in general, and more specifically on water resources, including water availability, soil productivity, food security, and in turn on human well-being. The palpable impacts of this drought were, among other things, the exposure of agricultural activities to the problem of inter-annual and inter-seasonal availability of water resources (surface and groundwater); the intermittence or even the complete drying up of the groundwater catchment works (wells), and the drastic decline of the regime of the small tributaries of the Kan stream, or even their fragmentation and almost total drying up during the exceptionally dry years. This last situation causes the limitation of the cultivable surfaces which are reduced for the most part to the zones of lowlands whose humidity drastically decreases. To better understand the changes to the surface condition of the Kan watershed, a follow-up study is needed. The purpose of this study is to characterize and quantify, from multidate images, evolution and changes in land cover between 1988 and 2015. The aim is to perform a diachronic analysis of land cover from 1988 to 2015 from Landsat images; to evaluate the evolution of different categories of land cover classes highlighted in the watershed, and to spatialize and quantify all of these changes.

The advent of space-based Earth observation techniques facilitates the mapping and monitoring of surface conditions in many previously inaccessible regions (Green et al., 1994; Mas, 2005; Shalaby and Tateishi, 2006; Jovanović et al., 2015; Rajasekhar et al., 2017; Boussaada-Maabdi et al., 2017). The possibility offered by remote sensing space to access an overview of large areas recurrently is therefore a major asset for the production of land cover maps.

2. Materials and Methods

2.1. Presentation of the Study Area

The study area is a part of the Kan watershed that represents a sub-watershed of the N'zi. It is an agricultural territory located in the center of Côte d'Ivoire between longitudes 4°01' and 5°24' west and latitudes 6°51' and 7°41' north (Figure 1). It covers an area of 2,086.31 square kilometers. The Kan watershed is part of the transition zone between the Southern Forest and the Northern Savannah. Its diet is of the equatorial type of attenuated transition or Baouléen climate characterized by a rainy season from March to October and a dry season from November to February. The average rainfall is between 1,000 and 1,200 millimeter and the average temperature is 30°C. Relief is slightly uneven with some plateaus whose average altitude varies between 200 and 300 meters. Geology is essentially granites and shales. Watershed soils are moderately and / or weakly desaturated ferralitic types with the addition of ferruginous tropical soils and clay or sand-humus or hydromorphic soils near streams and in shallows (Perraud, 1971). These soils are very conducive to agriculture which make the departments that make up the watershed (Tiébissou, Sakassou, south extreme of Bouaké and north-east of Yamoussoukro) a predominant area of agropastoral activities.

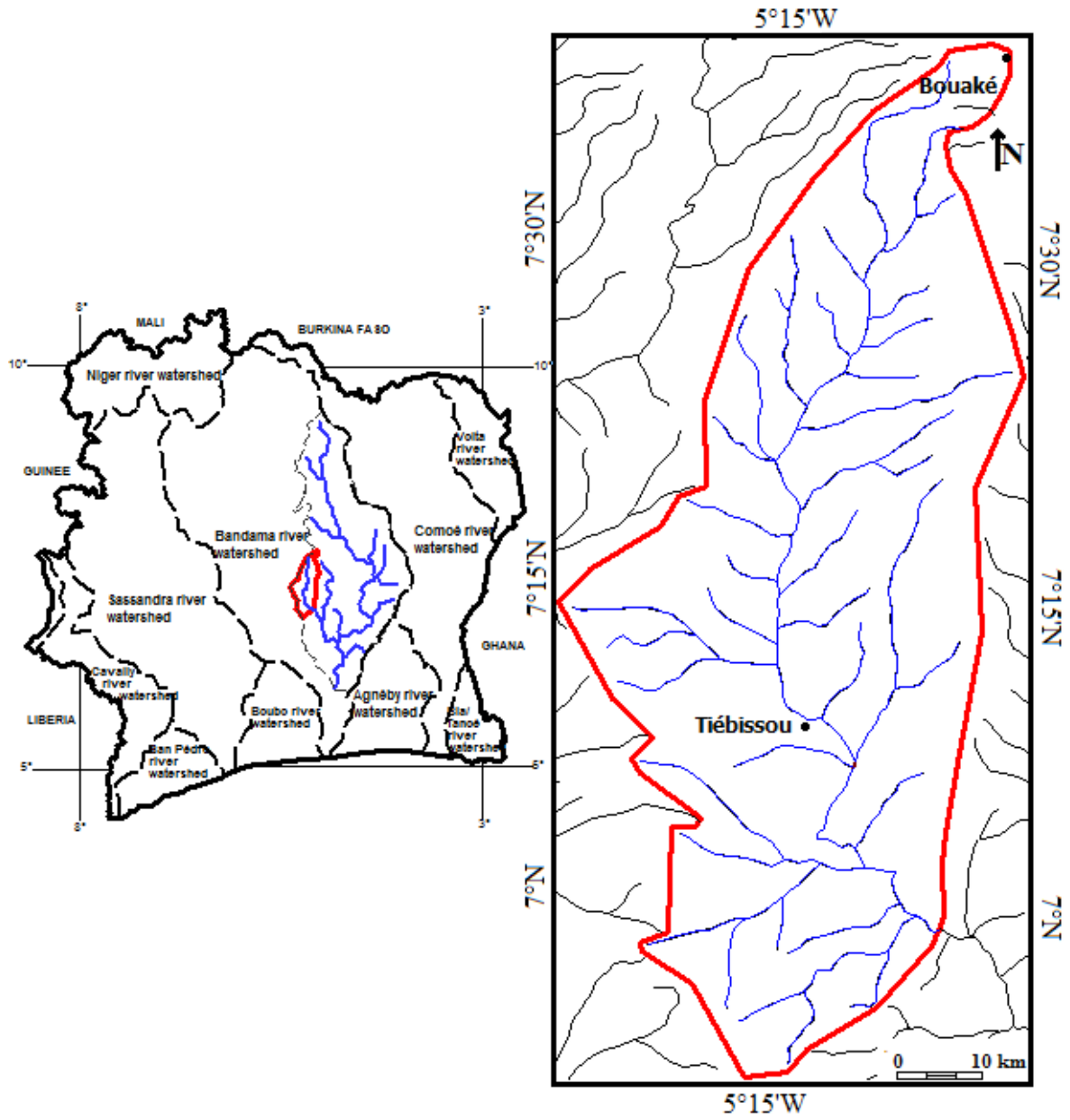

Figure 1: *Location of the Kan watershed*

2.2. Data and Software

The preferred sources of information used for mapping purposes to monitor dynamics of changes in the surface states of the natural environment are satellite images. They consist of Landsat 5 TM Scene 197-55 of December 23, 1988 and Landsat OLI Scene 197-55 of January 16, 2015 (Table 1). The choice of these images is dictated by the fact that they are a source of important information, downloadable for free on the NASA website (https://earthexplorer.usgs.gov/). Moreover, these images are adapted to the study of the evaluation of the occupation of the ground. The spatial resolution of these (30 meters) makes it possible to identify and characterize the different components of the landscape (Gracu, 2014).

Table 1: *Landsat Images of the study area*

Satellites	Sensors	Path	Row	Dates of acquisition
Landsat 5	TM	197	055	23/12/1988
Landsat 8	OLI	197	055	16/01/2015

These images are submitted to a string of appropriate processing from the software ENVI 4.5, ARCGIS 10.0 and EXCEL 2010.

2.3. Methods

The evolution of land cover classes and the detection of changes in the surface state of the Kan watershed are highlighted on the multidate satellite images through a string of treatments illustrated in Figure 2.

Orthorectified images of the study area taken in the dry, cloudless season are of acceptable radiometric quality. The preliminary treatment from the ENVI 4.5 software consisted of the extraction of the study area. The actual processing combined NDVI, PCA and color compositions to produce derived images for good spectral discrimination of different types of land cover in general, and in particular vegetation cover (N'Da, 2007). The development of the different classes of land occupation consisted in the creation of the training plots (ROIs) for the establishment of the land cover map based on the difference of spectral signatures of the objects on the ground. The method uses the maximum likelihood classification. This classification is evaluated by the various performance tests (kappa index, confusion matrix). A 3 × 3 median filter is applied to the cards to reduce intra-class heterogeneity by eliminating isolated pixels. The thematic validation to verify the credibility of the result consisted of a visual analysis by comparison between the resulting image of the classification and the basic image (color composition).

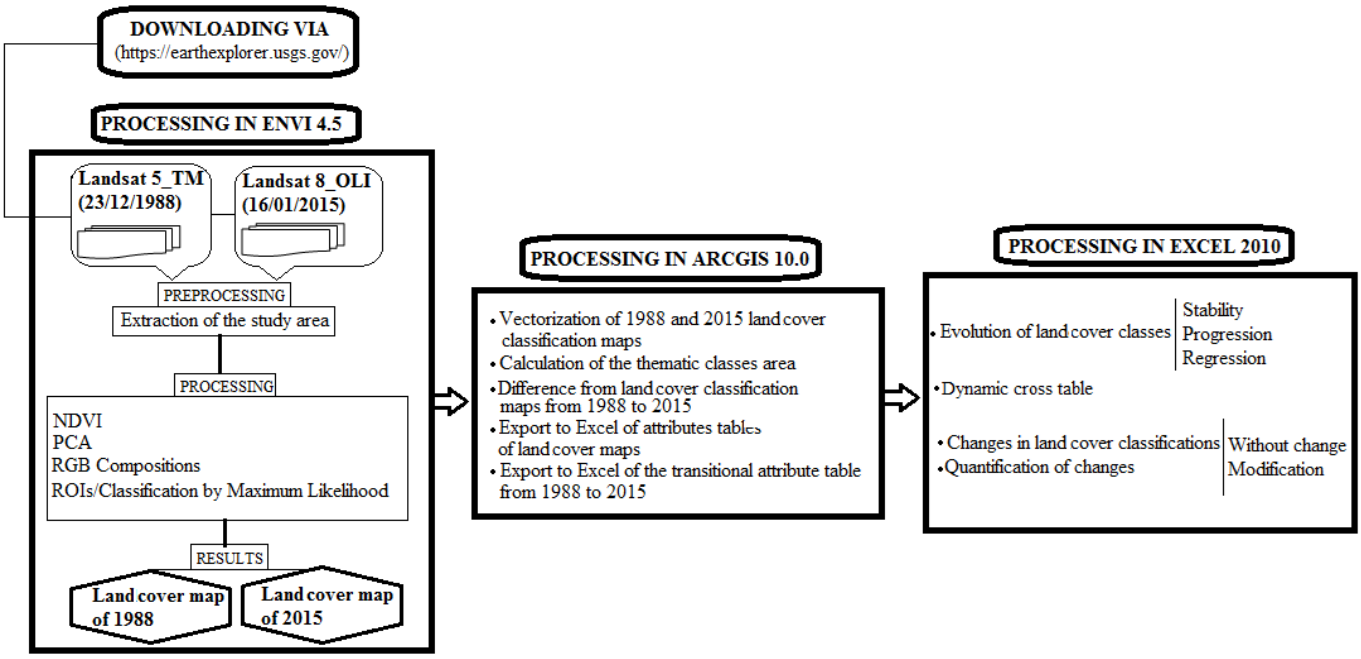

Figure 2: *Flow chart of satellite image processing*

The evolution of each land cover class is reflected in the relationship between the same class from 1988 to 2015. This relationship makes it possible to extract the "stable" or invariant areas characterized by values close to zero. "Regression" zones that indicate a loss of class surface and are characterized by a negative value. "Progression" zones of the class that translate a surface gain characterized by the positive value.

The changes in land cover are evidenced from the difference in land cover classification maps (Gupta et al., 1985) from 1988 to 2015 on ArcGIS 10.0. The resulting attribute table or transition attribute table that contains the number of pixels that have changed or not between the two dates is exported to Excel 2010 to highlight these different changes in land cover classes and to quantify them. Changes are characterized by a change or conversion of some or all of one class to another. Otherwise, the class remains stable or "unchanged".

3. Results and Discussion

3.1. Diachronic Analysis of Land Cover in the Years 1988 and 2015

The different colored compositions, the ACP and the NDVI made it possible to highlight six classes of occupation of the ground which are the water bodies, the habitats, the farming, the dense forest, the degraded forest and the savannah. Figures 3a and 3b show respectively the land cover maps from the supervised classification of the years 1988 and 2015.

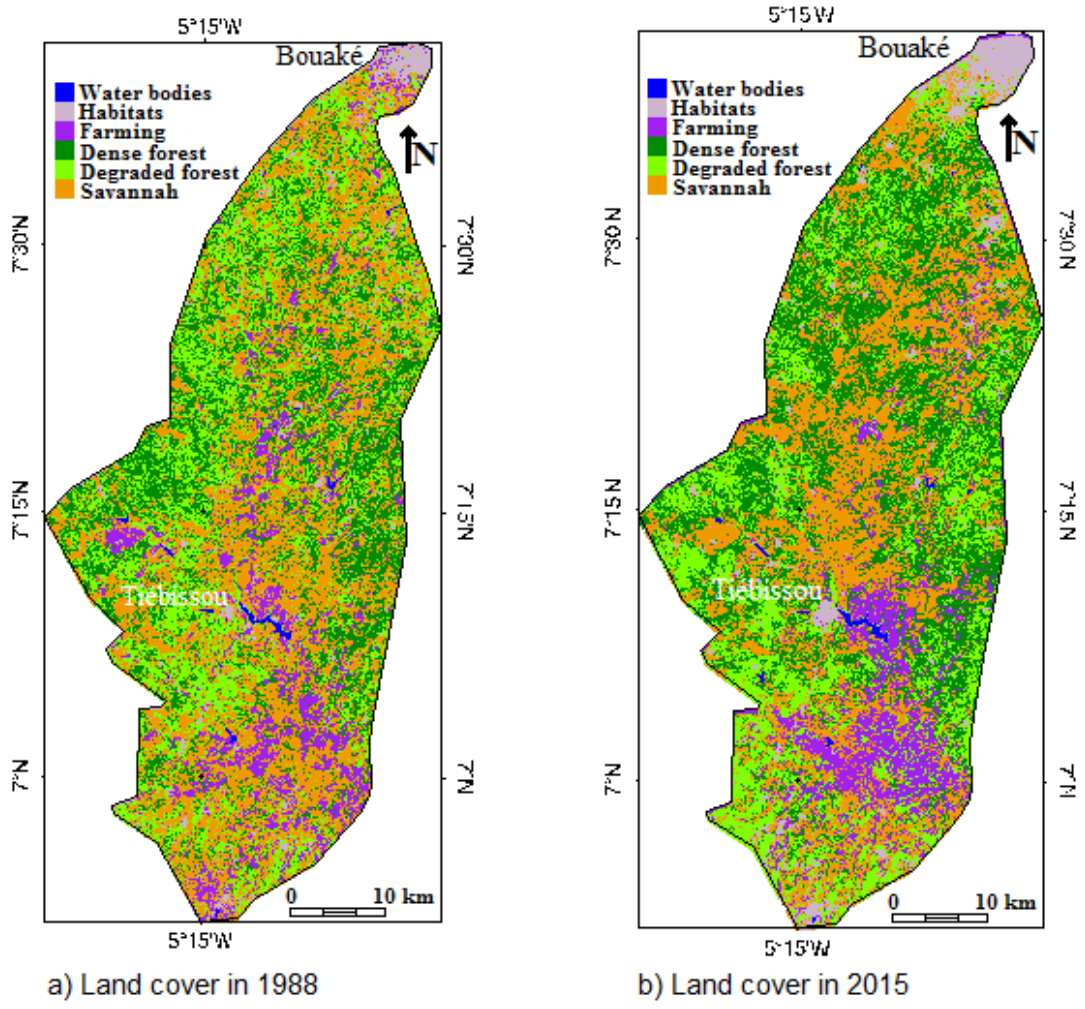

Figure 3: *Kan watershed land cover maps, 1988 (a) and 2015 (b)*

The spatio-temporal variation in the percentage of class sizes is shown in Figure 4.

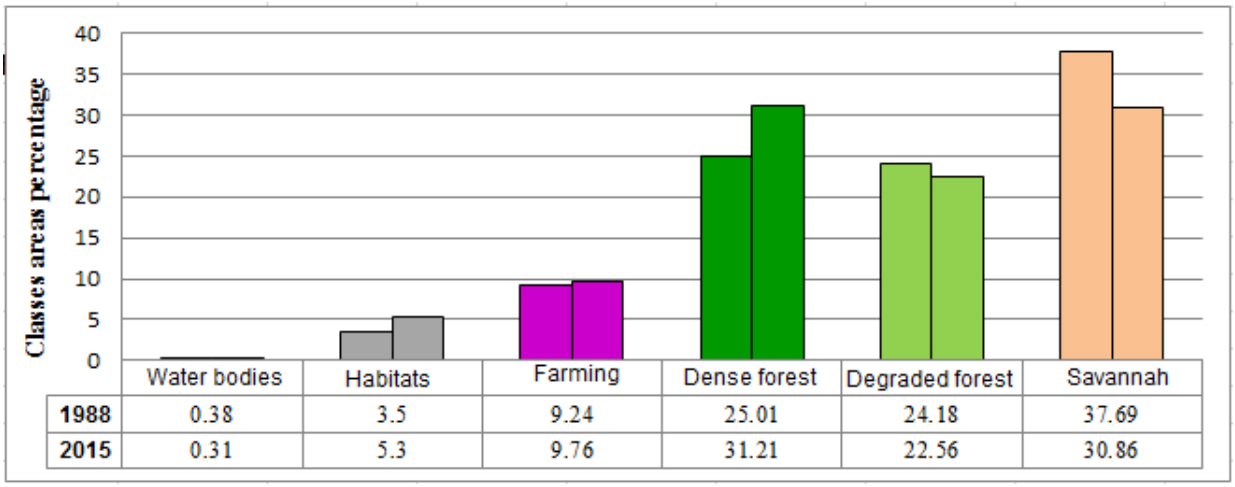

Figure 4: *Spatio-temporal variation in percentages of land cover classes sizes from 1988 to 2015*

The state of land cover in 1988 revealed a high proportion of savannah (37.69%) and a small proportion of water bodies (0.38%). The areas occupied by dense forest, degraded forest, farming and habitats vary respectively by 25.01%; 24.18%; 9.24% and 3.5%.

Compared with the year 1988, the highest proportion of land cover in 2015 is represented by dense forest (31.21%) and the lowest proportion (0.31%) is accounted for by water bodies. savannah, degraded forest, farming and habitats occupy respectively 30.86%, 22.56%, 9.76% and 5.3% of the total area of land cover in 2015.

3.2. Analysis of Changes in Land Cover from 1988 to 2015

Table 2 shows the evolution of land cover from 1988 to 2000.

Table 2: *Evolution of land cover in the Kan watershed from 1988 to 2015*

Years	Water bodies	Habitats	Farming	Dense forest	Degraded forest	Savannah
1988	0.38	3.50	9.24	25.01	24.18	37.69
2015	0.31	5.30	9.76	31.21	22.56	30.86
Evolution (1988-2015)	-0.07	1.80	0.52	6.20	-1.62	-6.83
Difference area	-1.34	37.53	10.77	129.39	-33.77	-142.58
Term	Regression	Progression	Progression	Progression	Regression	Regression

The Table 2 shows that land cover classes have evolved differently from 1988 to 2015. The savannah and degraded forest have strongly decreased (negative value of evolution) whereas the dense forest, the habitats and the farming have strongly progress (positive value of evolution). The water bodies remained practically stable (value of the regression statistically zero).

The evolution of land cover in the Kan watershed from 1988 to 2015 is illustrated in the graph (Figure 5).

The analysis of the evolution of land cover from 1988 to 2015 shows that the proportion of water bodies has hardly changed (around 0.07%). The latter has remained virtually stable. The dense forest,

habitats and farming grew with respective proportions of 6.20%, 1.80% and 0.52%. Savannah declined sharply (6.83%) from 1988 to 2015, compared to the degraded forest which declined slightly (1.62%).

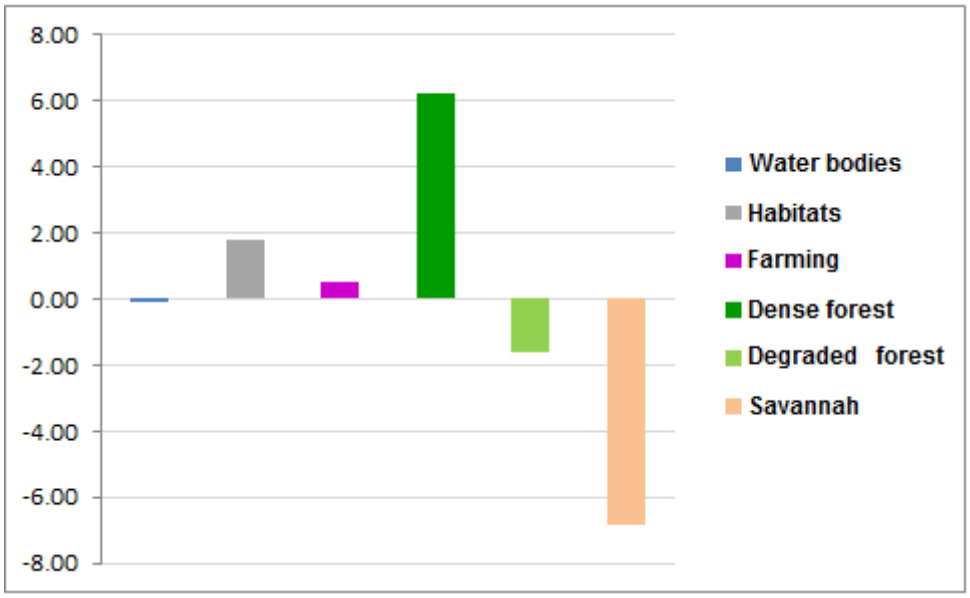

Figure 5: *Evolution of land cover from 1988 to 2015*

3.3. Detection of the Changes Made in the Different Classes of Land Cover from 1988 to 2015

This progression or regression of land cover classes has undoubtedly led to changes in the different classes presented in Table 3.

An analysis of Table 3 shows that all the land cover classes in the Kan watershed underwent more or less significant changes from 1988 to 2015. The total area of land cover is estimated at 1092.07 km² against 994.24 km² of the unmodified area, a percentage of 52.34% against 47.66%. The most important changes occurred at the savannah level with an area of 394.35 km², or 36.11%. The 394.35 km² of savannah have been converted to 40.40% in dense forest, 30.51% in farming, 20% in degraded forest, 9.05% in habitats and 0.04% in water bodies. The least significant changes affected the water bodies with an area of 2.18 km², or 0.20%. The classes of degraded forest, dense forest, farming and habitats changed with respective proportions of 26.31%, 22.30%, 11.77% and 3.32%.

The most dramatic changes in each land cover class (Table 3) are as follows:

- Farming: 70.95% of the area converted to savannah;
- Degraded forest: 67.03% of the area converted into dense forest;
- Dense forest: 65.74% of the area converted into degraded forest;
- Water bodies: 51.42% of the area converted into savannah;
- Habitats: 43.18% of the area transformed into savannah;
- Savannah: 40.40% of the area converted into dense forest.

Table 3: *Changes made in the different land cover classes from 1988 to 2015*

Land cover in 1988	Modified land cover classes from 1988 to 2015		Changes in each land cover class from 1988 to 2015		
	Modified areas (km²)	Percentage	Classes	Areas (km²)	%
Farming	128.52	11.77	Degraded forest	8.03	6.25
			Dense forest	14.34	11.16
			Habitats	14.68	11.42
			Water bodies	0.28	0.22
			Savannah	91.18	70.95
Degraded forest	287.31	26.31	Farming	6.09	2.12
			Dense forest	192.59	67.03
			Habitats	16.14	5.62
			Water bodies	0.18	0.06
			Savannah	72.31	25.17
Dense forest	243.50	22.30	Farming	4.79	1.97
			Degraded forest	160.08	65.74
			Habitats	6.98	2.87
			Water bodies	0.13	0.05
			Savannah	71.52	29.37
Habitats	36.21	3.32	Farming	7.94	21.93
			Degraded forest	6.24	17.22
			Dense forest	6.30	17.40
			Water bodies	0.10	0.27
			Savannah	15.64	43.18
Water bodies	2.18	0.20	Farming	0.15	6.89
			Degraded forest	0.32	14.60
			Dense forest	0.33	15.05
			Habitats	0.26	12.03
			Savannah	1.12	51.42
Savannah	394.35	36.11	Farming	120.32	30.51
			Degraded forest	78.88	20.00
			Dense forest	159.33	40.40
			Habitats	35.68	9.05
			Water bodies	0.14	0.04
Modified tatal area	1092.07	52.34			
Kan watershed area	2086.31	100			
Unmodified area	994.24	47.66			

3.4. Discussion

The technique of classification of the occupation of the ground implemented, the evolution of the classes and the various changes made in these classes deserve to be discussed. As long as the spectral characteristics of objects on the surface of the soil observed change over time, the comparison of multitemporal images makes it possible to detect the existence of possible changes

(Guarguet-Duport and Girel, 1995). In the present study, the results of the changes show some imperfections, notably confusions between certain classes whose characteristics are very close together during the classification. These include habitats modification, habitats conversion to farming, water bodies and savannah. Some modifications are probable since this dynamic take place over a period of 27 years. Nevertheless, a ground truth deserves to be undertaken. These confusions are also observed in the case of the transformation of degraded forest into dense forest and / or savannah and vice versa. The Landsat TM and OLI images, taken in the savannah zone and in the dry period, the vegetation is mostly herbaceous and tends to dry (without chlorophyllous activity) to mingle with bare soil. The few semi-deciduous dense forests and scattered crop plants in the savannah do not facilitate the discrimination of these classes. This same remark was made by N'Da et al., 2008; Aahda et al., 2008; Soro et al., 2013.

The maximum likelihood-supervised classification technique, however, remains relatively reliable (Brou, 2005, Koudou, 2013, Soro et al., 2014, Havyarimana, 2015, Koffi-Didia and Coulibaly, 2017) and is considered very reliable performing in the case of land cover map development (Kouassi, 2007). However, the single multispectral classification is ineffective in achieving an indisputable mapping of land cover from images. It is therefore necessary to use different image analysis procedures (spectral, textural and mathematical morphology) (Noyola-Medrano, 2006). The difficulty of certain land cover classes to be discriminated more particularly in the countries of sub-Saharan Africa was also highlighted by Kayembe et al. (2009).

Notwithstanding some confusions in some classes, these images have somehow been able to reveal the general trend of the dynamics of land cover in the Kan watershed. The strong progression of the dense forest and sharp regression of the savannah is in agreement with the results of Soro et al. (2014) in the center of Côte d'Ivoire.

The increase in the area of farming and habitats is attributable to population growth in this predominantly agricultural region where human pressure is constantly causing anthropisation of natural areas. As for the progress of the dense forest, it is due to the reforestation policy implemented by the Ivorian state and the introduction in this part of the territory of new cultural practices (rubber, etc.).

The even insignificant regression observed at the level of water bodies is to be attributed to the combined action of water withdrawals in the various dams or reservoirs for agricultural development and the evaporation of these plans of water. This situation causes the splitting up of rivers and even their almost complete drying up in very dry years. According to Soro et al. (2014), there is a food deficit or a decrease in surface runoff.

These multiple evolutions and changes in the land cover classes of the Kan watershed reflect a considerable impact of human activity (bushfires throughout the dry season, urban sprawl supported by population growth, agricultural development, etc.) on land cover.

4. Conclusion

The study of land cover dynamics of the Kan watershed using Landsat TM and OLI imagery allowed us to monitor changes in each land cover class and to quantify their evolution. From 1988 to 2015 in the Kan watershed, the classes of land cover of dense forest, habitats and farming grew by respectively 6.20%, 1.80% and 0.52%. The savannah and the degraded forest have regressed. The regression was strongly felt in savannah (6.83%) and dense forest (1.62%). The water bodies remained virtually stable. In addition, all land cover classes in the Kan watershed have undergone more or less significant changes during this period. The total modified area of the land cover classes is estimated at 1092.07 km² or 52.34%, compared to 994, 24 km² of the total unmodified area (47.66%). The most important changes occurred in the savannah (36.11%) while the least important changes

were in the water bodies (0.20%). Degraded forest, dense forest, farming and habitats changed with respective proportions of 26.31%, 22.30%, 11.77% and 3.32%.

Within each class, dramatic changes have occurred in different proportions:

- 70.95% of the farming were transformed into savannah;
- 67.03% of the degraded forest has been converted into dense forest;
- 65.74% of the dense forest has been converted into degraded forest;
- 51.42% of the water bodies were transformed into savannah;
- 43.18% of the habitats were transformed into savannah;
- and 40.40% of the savannah has been transformed into dense forest.

All these changes are due to the combined action of human activities supported by population growth and climate change.

The present study opens perspectives on the dynamics of the occupation of the soil in the years to come. It involves using predictive modeling, which is a projection technique on the future of a landscape, which takes into account all the socio-economic and biophysical factors that explain the changes observed in the occupation of soil in the future.

References

Aahd, A., Simonneaux, V., Sadik, E., Brahim, B. and Fathallah, S. 2009. Estimation des volumes d'eau pompés dans la nappe pour l'irrigation (plaine du Haouz, Marrakech, Maroc). Comparaison d'une méthode statistique et d'une méthode basée sur l'utilisation de la télédétection. *Revue des sciences de l'eau*, 22(1), pp.1-13.

Aubreville, A. 1959*. La flore forestière de la Côte d'Ivoire*. 2ème édition. Centre Technique Forestier Tropical, Nogent-Sur-Marne. Tome premier.

Boussaada-Maabdi, N., Bousnoubra-Kherici, H., Kherici, N. and Hammad, N. 2017. Mapping of land-cover from remotely sensed images in the valley of oued righ (algerian southeast). *Journal of Fundamental and Applied Sciences*, 9(2), pp.696-712.

Brou, Y.T. 2005. *Climat, mutations socio-économiques et paysages en Côte d'Ivoire*. Mémoire de synthèse des activités scientifiques présenté en vue de l'obtention de l'Habilitation à Diriger des Recherches, Université des Sciences et Techniques de Lille, France.

Durrieu de Madron, L., Gbalet P.E. and Balou, T. 2015. *Gestion durable des ressources forestières*. Rapport pour les Etats généraux de la forêt, de la faune et des ressources en eau.

Garguet-Duport, B. and Girel, J. 1995. Ecologie du paysage et télédétection des milieux alluviaux. *Revue d'Ecologie Alpine*, 3, pp.67-81.

Gracu, G. 2014. Using remote sensing imagery and GIS to identify land cover and land use within Ceahlău Massif (Romania). *Cinq Continents*, 4(10), pp.120-136.

Green, K., Kempka, D. and Lackey, L. 1994. Using remote sensing to detect and monitor land-cover and land-use change. *Photogrammetric Engineering & Remote Sensing*, 60(3), pp.331-337.

Gupta, D.N. and Munshi, M.K. 1985. Urban change detection and land-use mapping of Delhi. *International Journal of Remote Sensing*, 6(3-4), pp.529-534.

Havyarimana, F. 2015. *La contribution de l'instabilité sociopolitique dans l'anthropisation des paysages au Burundi: dynamique spatiale et biodiversité*. Thèse de Doctorat en Sciences Agronomiques et Ingénierie Biologique. Université Libre de Bruxelle.

Jovanović, D., Govedarica, M., Sabo, F., Bugarinović, Ž., Novović, O., Beker, T. and Lauter, M. 2015. Land cover change detection by using remote sensing – a case study of Zlatibor (Serbia). *Geographica Pannonica*, 19(4), pp.162-173.

Kayembe M.K.W., De, Maeyer, M. and Wolff, E. 2009. Cartographie de la croissance urbaine de Kinshasa (R.D. Congo) entre 1995 et 2005 par télédétection satellitaire à haute résolution. *Revue belge de géographie*, 3-4, pp.439-456.

Koffi-Didia, A.M. and Coulibaly, T.H. 2012. Analyse de la dynamique de l'occupation du sol dans le terroir Kiembara de 1986 à 2015 (Nord de la Côte d'Ivoire). *REGARDSUDS*, 1, pp.1-12.

Kouassi, A.M. 2007. *Caractérisation d'une modification éventuelle de la relation pluie-débit et ses impacts sur les ressources en eau en Afrique de l'Ouest : cas du bassin versant du N'zi (Bandama) en Côte d'Ivoire*. Thèse de Doctorat de l'Université de Cocody.

Koudou, A. 2013. *Conception d'outils d'aide à la décision pour la gestion intégrée des ressources en eau dans un contexte de variabilité climatique : application à la sélection des zones à potentialité aquifère et moins vulnérables à la pollution du bassin versant du N'zi*. Thèse Unique de Doctorat, Université Félix Houphouët-Boigny de Cocody.

Mas, J.F. 2005. Monitoring land-cover changes: a comparison of change detection techniques. *International Journal of Remote Sensing*, 20(1), pp.139-152.

N'DA, D.H. 2007. *Etude et suivi par télédétection et système d'informations géographiques d'une aire protégée soumise aux pressions anthropiques : Cas du Parc National de la Marahoué.* Thèse Unique de Doctorat, Université Félix Houphouët-Boigny d'Abidjan-Cocody.

N'Da, D.H, N'guessan, K.E. and Wadja, E.M. 2008. Apport de la télédétection au suivi de la déforestation dans le Parc National de la Marahoué (Côte d'Ivoire). *Revue Télédétection*, 6(3), pp.17-34.

Noyola-Medrano, M.C. 2006. *L'évolution morphologique actuelle du Champ Volcanique de la Sierra Chichinautzin (Mexique) à partir de l'analyse tomomorphométrique des cônes de scories et du changement de l'occupation du sol*. Thèse de Doctorat. Université Paris 7 Denis-Diderot.

Perraud, A. 1971. Les sols. In Le milieu naturel de la Côte d'Ivoire. Mémoires O.R.S.T.O.M., Paris, n°50, pp.269-390.

Rajasekhar, M., Sudarsana R., Siddi Raju, R. and Imran, B.U. 2017. Landuse and Landcover analysis using Remote Sensing and GIS: A case study in Uravakonda, Anantapur District, Andhra Pradesh, India. *International Research Journal of Engineering and Technology*, 4(09), pp.780-785.

Shalaby, A. and Tateishi, R. 2007. Remote sensing and GIS for mapping and monitoring land cover and land-use changes in the Northwestern coastal zone of Egypt. *Applied Geography,* 27, pp.28-41.

SODEFOR, 1996. *Plan d'aménagement de la forêt classée de Bouaflé*. Ministère de l'agriculture et des ressources animales. pp.3-61.

Soro, G., Ahoussi E.K., Kouadio, E.K., Soro, T.D., Oularé, S., Saley, M.B., Soro, N. and Biémi, J. 2014. Apport de la télédétection à la cartographie de l'évolution spatio-temporelle de la dynamique de l'occupation du sol dans la région des Lacs (Centre de la Côte d'Ivoire). *Afrique Science*, 10(3), pp.146-160.

Soro, T.D., Dje, K.B., Ahoussi K. E., Soro G., Kouassi, A.M., Kouadio, K.E., Oga, M.Y. and Soro, N. 2013. Hydroclimatologie et dynamique de l'occupation du sol du bassin versant du Haut Bandama à Tortiya (Nord de la Côte d'Ivoire). *VertigO - la revue électronique en sciences de l'environnement* [En ligne], 13(3) | décembre 2013, mis en ligne le 30 décembre 2013, consulté le 28 juillet 2017.

Cloud Publications
International Journal of Advanced Remote Sensing and GIS
2019, Volume 8, Issue 1, pp. 2901-2918
ISSN 2320 – 0243, Crossref: 10.23953/cloud.ijarsg.397

Case Study

Urban Solid Waste Management using Geographic Information Systems (GIS): A Case Study in Doha, Qatar

Perumal Balakrishnan[1*], Mohammed Harish[1], Mohammed Khalifa M.Z. Al-Kuwari[2]

[1]Department of Biological and Environmental Sciences, College of Arts & Sciences, Qatar University, Doha, Qatar
[2]Department of Humanities, College of Arts & Sciences, Qatar University, Doha, Qatar

Correspondence should be addressed to Perumal Balakrishnan, *drbala65@gmail.com*

Publication Date: 16 January 2019

DOI: https://doi.org/10.23953/cloud.ijarsg.397

Abstract Qatar is one of the rapidly developing countries in the world due to its surging economy. This has led to a boost in the population size and thus influencing the country's waste management system on a large scale. Management of waste is the foremost task of a country as it can lead to outspread of diseases, illness and can harm the environment if kept unmanaged. According to Qatar national vision 2030, the key role of Qatar is to plan and create solutions that are sustainable for management of waste. The major outflow of domestic waste in Qatar is from the homes, shops, hotels and restaurants. The method followed in Qatar for domestic waste disposal is collecting waste from the bins by the trucks, loaded in the transfer stations and then taken to landfills. This study is focused on the waste management in a small urban area of Qatar. Waste management in the sense, to make the waste collection sustainable by providing or reallocating the bins according to waste generation and population density utilizing GIS application. The results acquired after analysis shows that there is notable minimization or saving of time after re-distributing the bins.
Keywords *Buffer; GIS; Hotspot analysis; Network analysis; Qatar; Waste management*

1. Introduction

Qatar has been developing very fast in recent years and the country is continuing to grow. Solid waste management seems to be the most highly challenging task due to the high population growth, industrialization and urbanization. According to a report published by Ministry of Development Planning and Statistics (MDPS), 2017, Qatar Environment Day 2017, Qatar generates a per capita waste of 1.23 kg per day as of 2015. Qatar's production of domestic solid waste is more than 2.5 million tons per year. Solid portion of the waste mostly comprises of organic substances (~60 %) and the remaining portion comprises of the recyclables, which consists of paper, glass, plastics and metal (Zafar, 2016). Qatar, due to the lifestyle and continuously growing population has increasing amount of waste generation. Therefore, in order to cope up with the generated waste in a sustainable way, there needs to be a solution. The management of waste can be started from small scale, which then can be expanded to other areas. This research will enhance the idea about the waste management system in Qatar and how it can be managed in an efficient way using GIS. Qatar is one of the rapidly growing economies worldwide. Qatar needs to improve its waste management system to keep up the standard

level of living. One of the visions for Qatar 2030 is to create sustainable solutions for managing the solid waste. This study will provide information about the management of waste in urban areas, as there is a lack of research in those areas. This research also shows that there is a need for sustainability in managing waste as it makes the task more efficient, saving cost and time.

In any country, its population, geographical conditions, seasonality, and socio-cultural properties are the major components that effect the rate of production and composition of domestic solid waste (Akinci et al., 2012; Chandrappa et al., 2012; Khatib, 2011; Magrinho et al., 2006). As claimed by Khatib (2011), waste generation is dependent on the population growth of developed and developing countries, if the population growth increases, the waste generation tends to increase. The disposal of municipal waste from restaurants, hotels, and households, can create danger for public health and environment, if the wastes are not managed in a proper way. The economic status of the country determines the quantity of waste generated, however, the components of waste are almost similar to some degree among the countries. Research done by Chandrappa and Brown (2012), states that in low-income countries, the rate of waste generation is between 0.3-0.9 kg/capita/day, and in high-income countries, the rate of waste generation is between 1.4-2.0 kg/capita/day. Apart from the quantity of waste, the component that determines the generation rate of municipal solid waste (MSW) is the percentage composition of MSW constituents. In case of low-income countries, people's way of living produces organic waste that shows about 50% of the total MSW generated. And for the case of high-income countries, people's ways of living are a bit different, which is mostly ordering the food rather than cooking the food at home, and this will minimize the organic waste, which shows less than 30% and there might be an increase in inorganic materials like packaging materials (Khatib, 2011) that might increase the generation rate. The fundamental aspect of public health and environmental management is the management of solid waste. During the past times, solid waste generated were mostly natural and food waste. At those times, the problems with waste management were little, but due to the increase in population and rapid increase in urbanization and expansion in technology, the issues of managing solid waste became more problematic and as the generation of waste kept on increasing with the time passing on, the condition of solid waste management (SWM) got more daunting.

Management of waste includes the process of managing all the waste from its origin until the final scrapping. Waste generation can be from any sector of the society including industries and societies, and its management impacts households and health care. The management process of different wastes differs from country to country and place to place. The waste quantity can be differentiable in different sectors of a country. Where there are ongoing human activities, different sources contribute to the municipal or household wastes. Some studies have shown that the households generate much of the municipal waste (55%-80%) in the developing countries, and then comes the market or commercial outlets (10%-30%) having different quantities coming from the streets, industries and distinct establishments (Nabegu, 2010; Nagabooshnam, 2011; Okot-Okumu, 2012).

One of the significant administration issues in solid waste management is developing techniques for data interpretation (Tinmaz et al., 2006). The issue of waste is not only because of increased quantities but also largely because of inadequate management system. One of the largest oil producers globally is the kingdom of Saudi Arabia; yet, Management of solid waste in the country is done in the simplest way. The simplest way being the collection of waste and dumping it in open dumping ground (Ouda et al., 2013). After an increase in awareness of many problems faced due to the increased generation of about 14 Mt/year of MSW, the Government of Saudi made new rulings to aid the management of MSW in the early 2015.

A report "What a Waste: A Global Review of Solid Waste Management", published by the World Bank in 2012, conveyed numerical information associated with generation of waste, and demonstrated that the measure of waste produced had expanded from 0.64 kg/capita/day in 2002, with a population of

2.9 billion, to 1.2 kg/capita/day in 2012, with a population of 3 billion individuals. The increase in rate of waste generation was obviously the outcome of growing populace. The increasing amount of waste generation day by day is grasping the attention of the governments and stakeholders responsible for the country's waste management. Management of waste is a mandatory process to keep the environment tidy, which will help in minimizing the risk of negative effects that can deteriorate the health of all living beings.

1.2. Waste Management in Qatar and Gulf Co-Operation Council (GCC) Countries

Despite the fact that the Gulf co-operation council (GCC) countries are reviewed by their advanced development and richness, they do not have proper research with respect to the waste management and they utilize the extensive regions of deserts as landfills. The report published in 2008 by the Arab Forum for Environment and Development (Tolba et al., 2008) stated that GCC countries had the highest rate of construction waste followed by municipal waste, consisting mostly of organic materials. One of the main goals in Qatar national vision 2030 is to save the environment by promoting recycling and minimizing the generation of waste in all the public and private sectors. In any case, findings show that there is still much to improvement in the manage of solid waste in Qatar. Only few studies have been done in Qatar related to this topic, and this might be due to lack of information and methodologies to understand the issues identified with municipal solid waste generation. It is known from the previous studies that the quantity of waste generation depends on the population of the country. Qatar due to its rapid development of economy has seen an increase in rate of population and that contributes to multiplying the waste generation Table 1.

There are currently four waste transfer stations situated in South Doha, West Doha, Mesaimeer, and Dukhan, to which all the Qatar's urban waste from all its seven municipalities are brought. The wastes are then compacted from those transfer stations and transferred to the domestic solid waste management center or landfill situated in Mesaieed through transfer trailers. Q-Kleen is the private company under the administration of Ministry of municipality and environment that is in-charge for the transfer of waste from waste bins to transfer stations (Ahmad, 2016). As stated by the statistics for domestic solid waste generation 2013-2014, a sum of 7,569 tons of solid waste was generated out of which domestic waste comprised 2,700 tons. Domestic waste includes the waste from all sectors except for waste from hospitals and construction sites (Ahmad, 2016).

Table 1: *Daily generation of waste by type (metric ton/day)*

Year	Domestic waste	Construction waste	Bulky waste	Tires	Others	Total
2010	2,320	25,215	4,792	51	14	32,391
2011	2,234	26,219	4,798	59	16	33,325
2012	2,388	26,594	4,507	67	15	33,571
2013	2,550	25,629	4,922	70	28	33,197
2014	2,871	19,332	4,788	87	34	27,113
2015	3,002	11,716	5,614	125	594	21,051

Source: MDPS, 2017

According to one research (Ahmad, 2016) conducted for the quantification of domestic solid waste among 84 houses from different municipalities, it was revealed that the average quantity of waste was about 1.135 kg/capita/day. From the constituents of wastes, organic waste was found to be the most with 60.98%, and then plastics with 8.85%, followed by clean paper with 8.46%, and lastly ceramic scrap and glass with 6.10%. As of 2015, Qatar generates a per capita waste of 1.23 kg/day, according to MDPS (Figure 1).

Qatar is almost surrounded by water from all the sides except the southern part of the country that has a land border with the Kingdom of Saudi Arabia. As of 2016, Qatar has a population of about 2,545,603. Due to Qatar's fast-growing economy, population rates increased by 67.6% from 2010 to 2015. A small area in Qatar named Bin Mahmoud was used as a case study in this research. According to ministry of development planning and statistics, the population of Bin Mahmoud is 34,028, as of 2015. Bin Mahmoud falls under the Doha municipality and under zones 22 and 23.

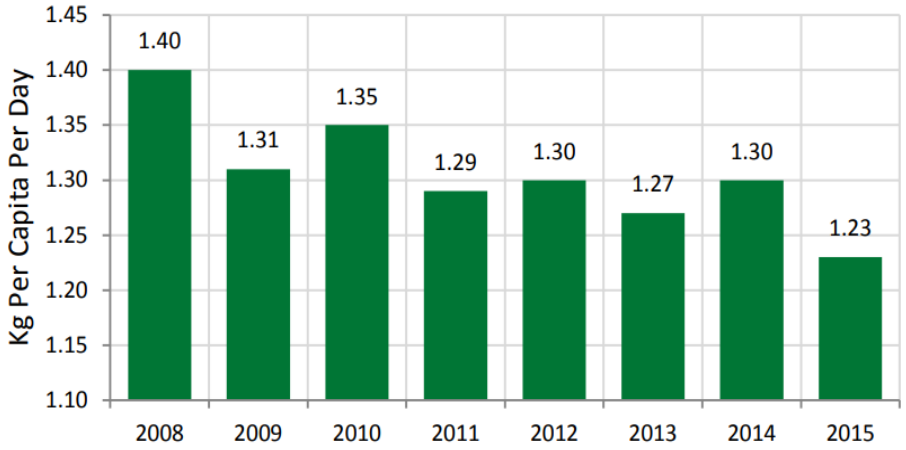

Figure 1: *Per capita domestic waste production (kg/per/day) (Source: MDPS, Qatar Environment Day 2017)*

We initiated this study to get a factual idea about the management of waste in Qatar's small residential/commercial area using GIS based application. In this study, GIS enabled us to get a realistic idea about the production and management of wastes in different locations of the study area and helped us in manipulating the data to perceive the mechanism of management of waste broadly. ArcGIS software was used to analyse the waste generation and capacity of bins allocated in each block of the study area. ArcGIS was also used to reallocate the bins according to proximity analysis and population density ensuring that all the places are covered. The objectives of the research were:

1. To review current solid waste management (SWM) practices including waste generation, location, type & size of waste bins.
2. To find and allocate new collection bins based on solid waste generation using GIS technique.
3. To solve the irregular distribution of bins and redistribute the waste bins of study area to complete the collection process at less cost and save time.
4. To find the optimal proximity distance for the collection bins by generating buffer zone.
5. To analyse the hotspots and cold spots of the waste bins in the study area.

Thus, the study was expected to help in analysing the present SWM collection issues and thus can be used as a decision-supporting tool for efficient collection and SWM in the study area.

2. Materials and Methods

Based on the proposals from the past studies, the objective was accomplished utilizing ArcGIS. The methodology of GIS techniques to be applied in the research area followed five phases:

1. Data collection
2. Development of GIS database
3. Analysis of present solid waste collection in the study area
4. The optimal allocation of collection bins for the proposed model based on road network, population density and;
5. Analysis of optimal proximity by creating buffer zone of the existing and proposed models.

2.1. Study Area

Qatar is a peninsula as it is mostly surrounded by water extending northwards covering an area of 11606.8 km^2 and shares a land border with the Kingdom of Saudi Arabia along the southern region. Qatar is divided in to 7 municipalities consisting of 94 zones, and 755 districts. The population of Qatar is about 2,545,603 as on February 28, 2016 (MDPS). Due to the exports of natural resources like petroleum and gas, Qatar has had a rapid developing economy, which aided in rapid increase in population rate. The study area is a residential area in Qatar, located in the country's east side covering an area of 1.8 km^2, known as "Bin Mahmoud". Bin Mahmoud area was chosen out of all the other areas in Qatar due to the reason that it is one of the oldest cities in Qatar, and contains all types of buildings, apartments, schools, mosques, open space, parks and other commercial outlets. Figure 2 presents the location of this area.

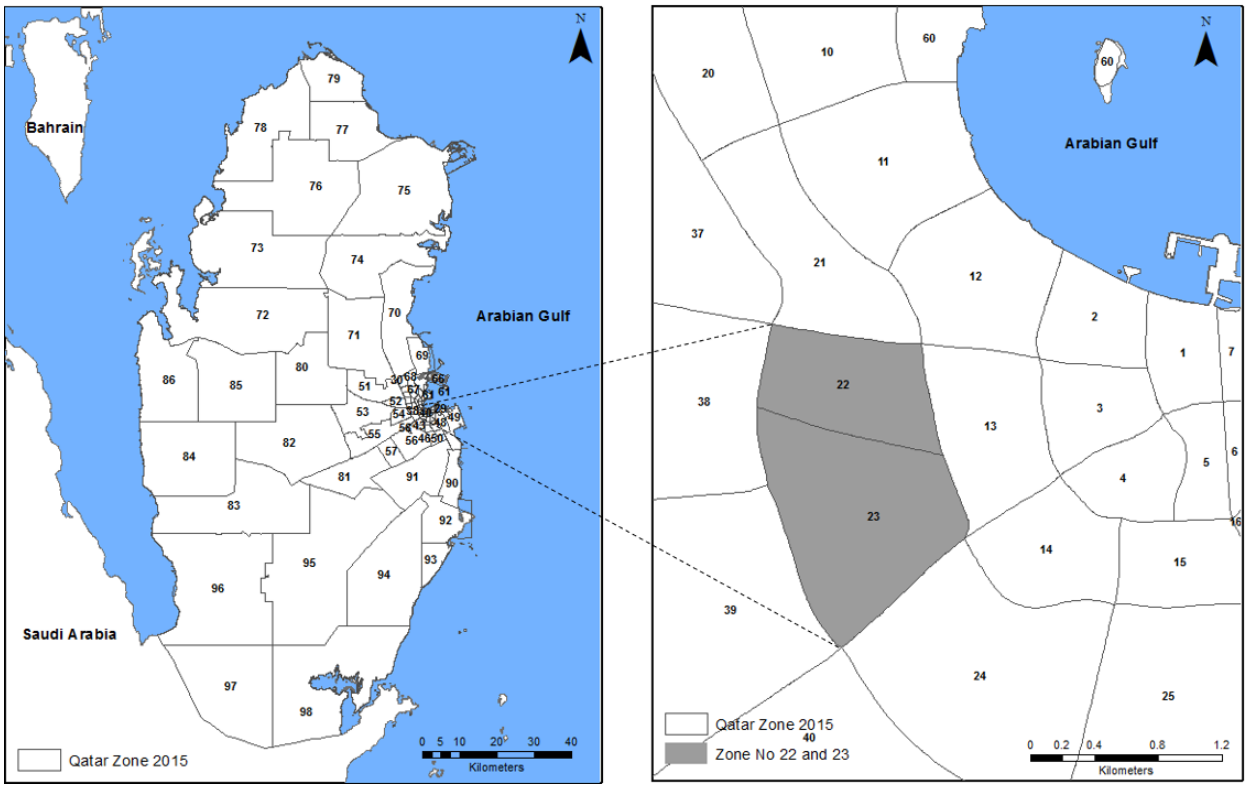

Figure 2: *Location of Bin-Mahmoud – Zones 22 and 23*

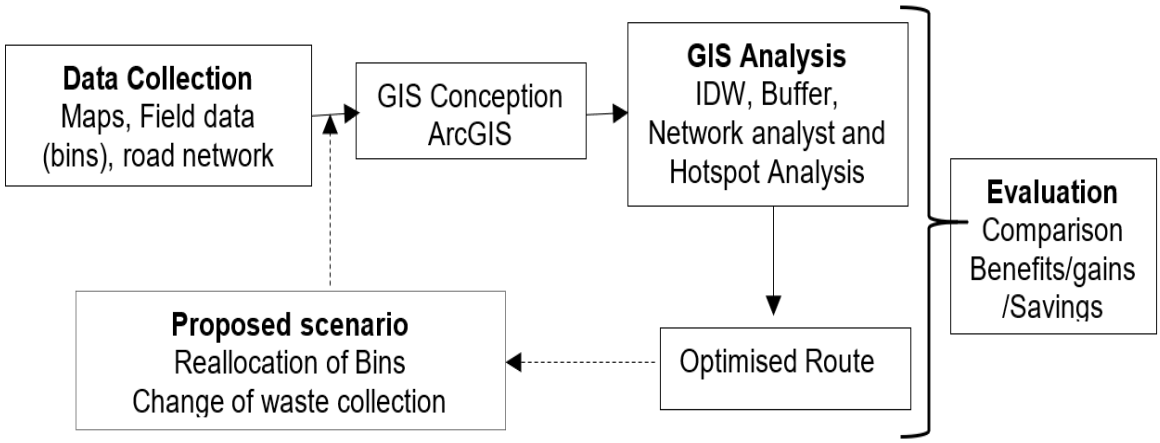

Figure 3: *Methodology and analysis steps*

2.2. Field Data Collection and Database Creation

The methodology includes the collection of data about the management of waste in Bin Mahmoud area of Qatar. The first step was going to the study area and noting down all the required data; location, number of bins and the capacity of each bin. This information collected was used in creating database for further analysis as shown in Figure 3.

Following are the ways in which the field-data collection was done:

- Locating the waste bins with GPS and marking on the map.
- Recording the number of waste bins in the study area.
- Monitoring the quantity of waste generated in different places.
- Creating a map that locates the bins and the distance between them.
- Recording how the waste is collected from the bins.
- Monitoring what type of vehicle and equipment are used for waste collection.
- Identifying if there are areas with the display of hoarding for the bins.
- Different numbers are allocated to the locations of bins to identify them easily.

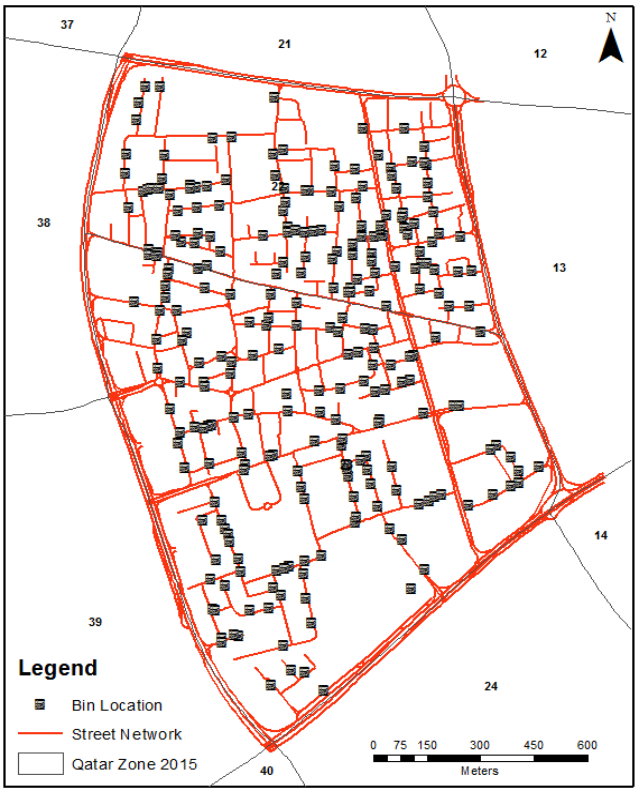

Figure 4: *Location of existing bins in Zones 22 and 23*

Primary data about the solid waste of the study area was collected through Global Positioning System (GPS) survey throughout the study area. The two hundred sixty bin locations were recorded with different bin types (Figure 4). The exact location of the solid waste bins, containers and illegal waste disposal sites was collected by using GPS device. Spatial data was generated using collected GPS data and Google Earth Images. An amount of secondary data about other relevant information associated with solid waste management like population, economic data, were collected from Government organizations. The different types and forms of information was converted into the GIS database. GIS software (ArcGIS 10.3) with its network analyst extension was used to recommend reallocation of waste bins, containers location, routes for collection and preparation of final maps.

2.3. Geostatistical Interpolation (Inverse Distance Weighted (IDW))

An interpolation model can be constructed and evaluated using the geostatistical analyst function. Selection made in one of the sites decides which options will be available in the next, and the way you manipulate the data aids in constructing a satisfactory model. The interpolation of inverse distance weighting evaluates the values that are not known by specifying the closest points, search distance, power setting and barriers (ESRI, 2015).

2.4. Buffer Analysis

A buffer zone can be defined as an area surrounding any mapped attribute, and that area is estimated in units of distance. It is utilized in the analysis of proximity (ESRI, 2015).

2.5. Hotspot Analysis

The hotspot analysis helps us to determine if the attribute is significant or not. It calculates the Getis-Ord Gi* statistic for each component in a dataset. This statistic results in z-scores, p-values and confidence level of bins which highlights high (hot spot) or low (cold spot) values clustering spatially. A statistically significant hotspot area is where the attributes have higher values with other high values surrounding them. A high value of z-score and low value of p-values means that the spatial cluster is formed of high values representing a hotspot area. A confidence level of 99 percent of statistical significance is given when the feature falls in the +/-3 bins. A confidence level of 95 percent of statistical significance is given when the feature falls in the +/-2 bins. A confidence level of 90 percent of statistical significance is given when the feature falls in the +/-1 bin. No confidence level is given when the feature falls in bin zero, as it is not statistically significant (ESRI, 2015).

2.6. Network Analysis

Network analysis in GIS aids in finding the efficient routes or creating routes to travel from one point location to another considering distance, time and cost on an existing attribute class or attribute layer. It helps in reducing the time and cost by determining the best course for travelling and reaching the destination (ESRI, 2015).

3. Results and Discussion

This section will discuss about the results obtained from all types of analysis and models created in ArcGIS software. The major findings in this research will demonstrate the need for bin allocations according to population density, waste generation, concentration of bins regardless of their capacity, and re-routing of collection trucks to reduce the time and cost.

3.1. Types of Bins

There were five types of bins found in the study area (Table 2).

Table 2: *Distribution of existing bins*

Type of bin	Number of bins
1100 Liter	364
360 Liter	9
240 Liter	38
18 Cubic Meters (18000 Liter)	1
7 Cubic Yard (5351 Liter)	6

The 1100-Liter bins were distributed the most around the area with other types of bins distributed in very less places. After creating the corrected new bin locations with corrected new bin capacities, the distribution of the type of bins and their numbers are listed in the Table 3.

Table 3: *Distribution of re-allocated bins*

Type of bin	Number of bins
1100 Liter	393
360 Liter	6
7 Cubic Yard	6

The 1100-liter bins were increased, and the 240-liter bins were removed. The larger bins were distributed in more places as they would consume less place by adding just one or two instead of four or five of the small bins and more over large bins can contain more waste. The 7 cubic yard waste drums were placed in places where they threw large materials like cupboards and house appliances.

3.2. Land Use Map - Zones 22 and 23

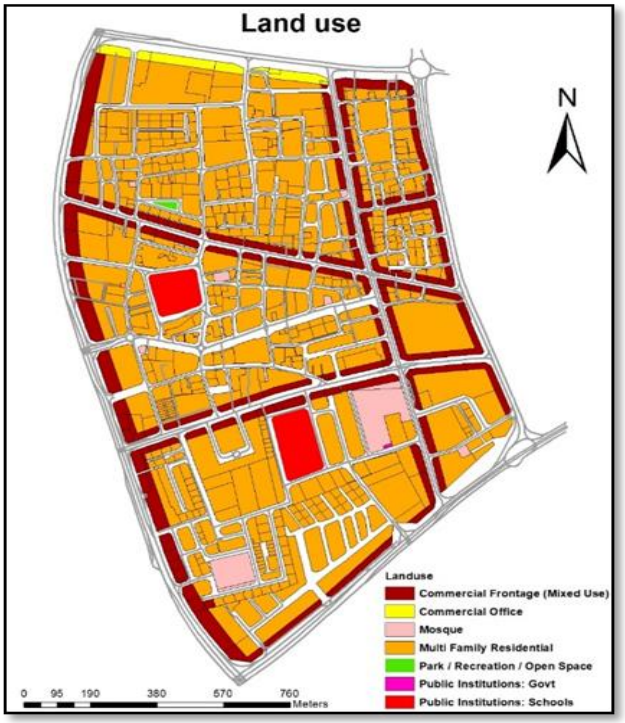

Figure 5: *Land use – Zones 22 and 23*

Seven types of land uses were present in Bin Mahmoud area (Figure 5). The data were collected from Qatar GISNet. Seven land uses included commercial frontage, commercial office, mosques, multifamily residential buildings, park/recreation/open space, and public institutions.

3.3. Block Level Population - Zones 22 and 23

The population map shows that the population is generally distributed between 133-313 people per block with highest population of 1011-1671 people in blocks of large apartment areas (Figure 6).

3.4. Existing Bin Location and Capacity

Existing bin capacities as distributed by the municipality are shown in Figure 7.

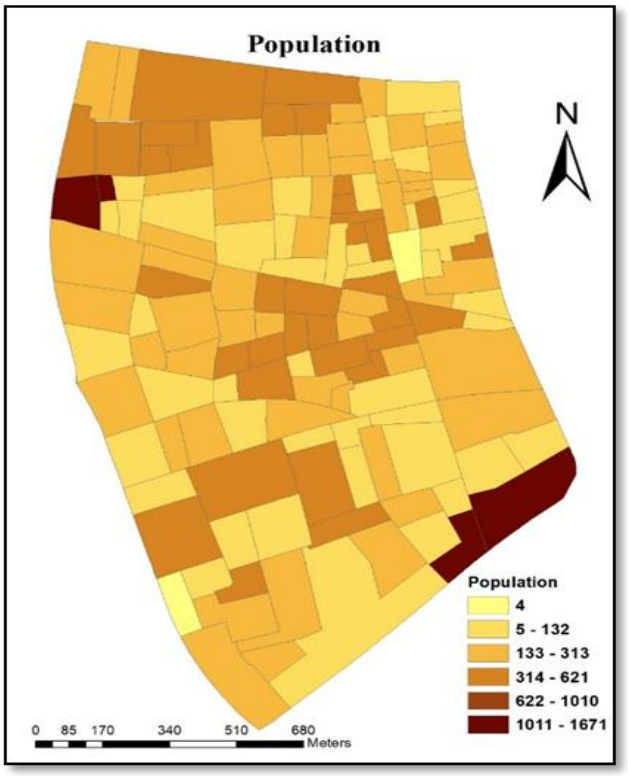

Figure 6: *Population 2015 – Zones 22 and 23*

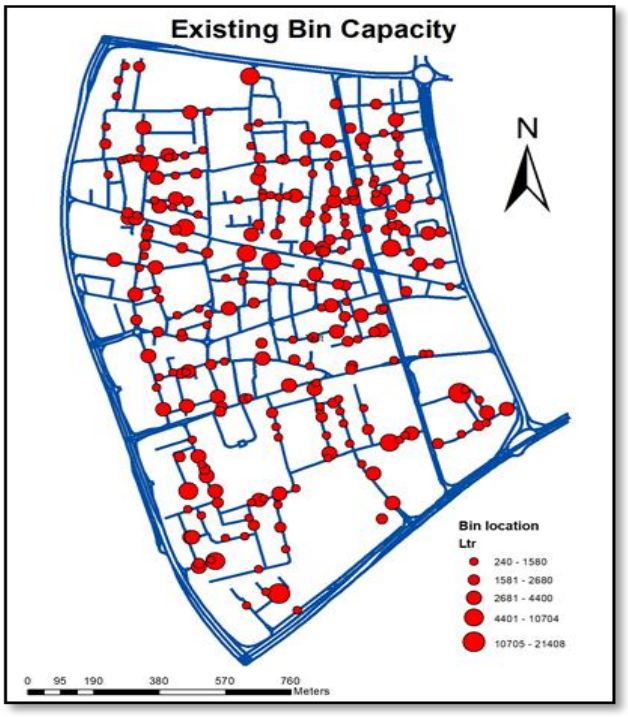

Figure 7: *Existing bin capacity in liters*

3.5. Waste Generation

Figure 8 was created for the waste generated per capita taken from Ministry of Development Planning and Statistics, which is 1.23 kg/person/day as of 2015. The highest generation of waste is from the areas with high population. Majority of the area produces a maximum of 300 kg/day with increasing waste generation of up to 2000 kg/day in areas of commercial outlets and high population living mostly in large apartments.

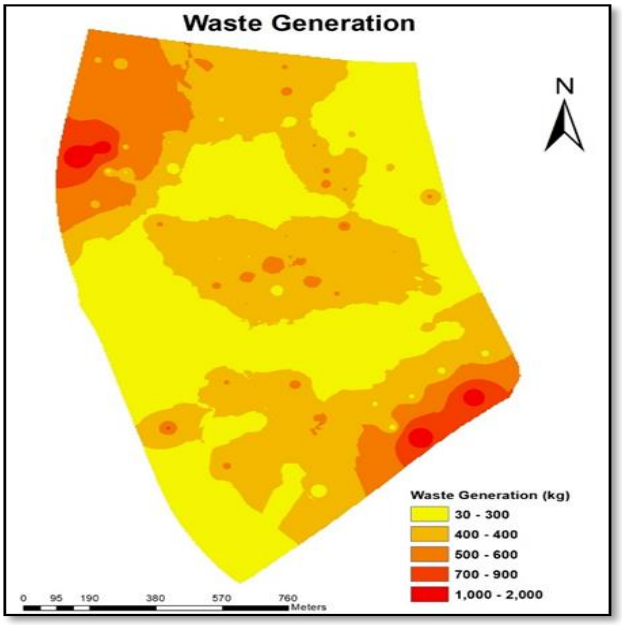

Figure 8: *Waste generation*

3.6. Re-allocation of Bin Location and Capacity

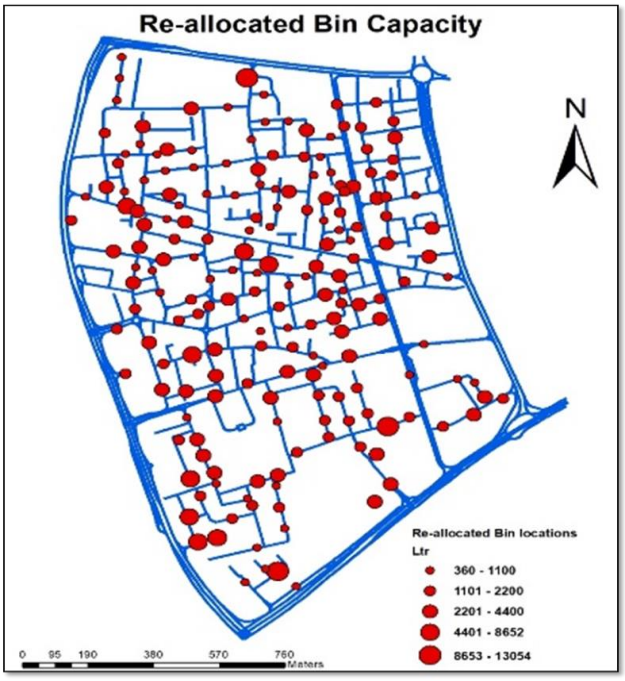

Figure 9: *Re-allocated bin capacities*

186 bin locations were allocated by suggesting different sizes of bins at different locations depending on the population and waste generations. Bin capacities were re-allocated and distributed depending on the population and waste generation after the analysis of the data using GIS (Figure 9).

3.7. Existing Bin Location - Buffer Zone

Figure 10: *Buffer zone map*

Figure 10 displays 50 m buffer from each of the bin locations. 50 m is the optimum distance for the residences. Some of the places were found to be vacant which were filled by adding or relocating the bins.

3.8. Re-allocation of Bin Location and its Buffer Zone

Figure 11 was created after the addition and reallocation of new bins according to the population distribution. Some of the vacant places that fell out of the buffer zone were covered by the buffer zone in this map, but still there were some more vacant places. These vacant places were found to be due to empty lands or empty apartments or the area was under construction.

Figure 11: *Re-allocated bin buffer zone map*

3.9. Hotspot Analysis for Existing Bin Location

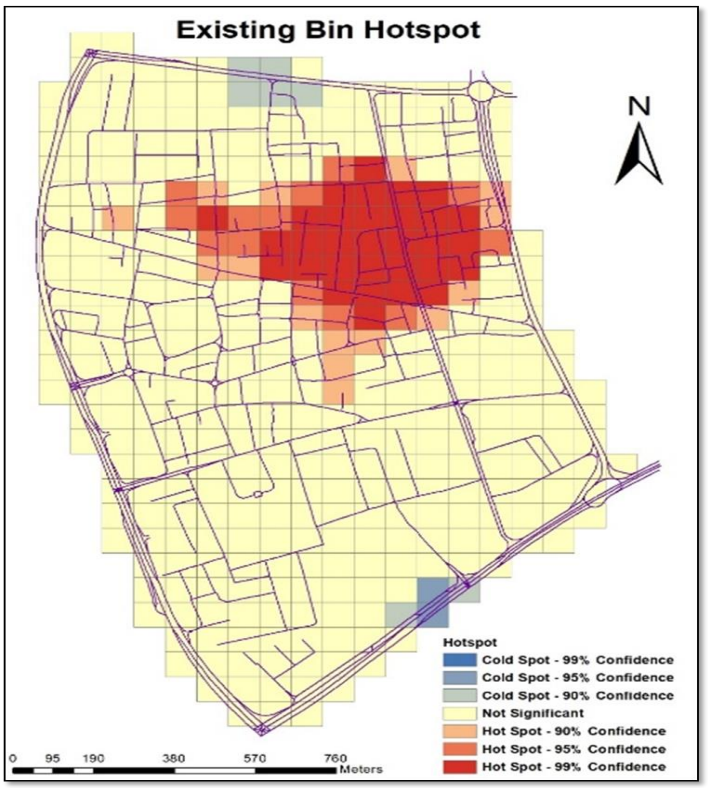

Figure 12: *Existing bin location - significance of hotspots*

It is well demonstrated in Figure 12 where the number of bins are concentrated more. These bins are the ones placed by the municipality. The red area in the map shows more concentration of bins, and it is classified into three categories of confidence level. The highest confidence level is 99%, which indicates the darkest red color, followed by lighter ones that are of confidence level 95% and 90%. The yellow area indicates that the bins in those areas are not of any significance. The areas that show the lowest significant values are the places that have very low number of bins and these form the cold spots.

3.10. Hotspot Analysis for Re-allocation of Bin Location

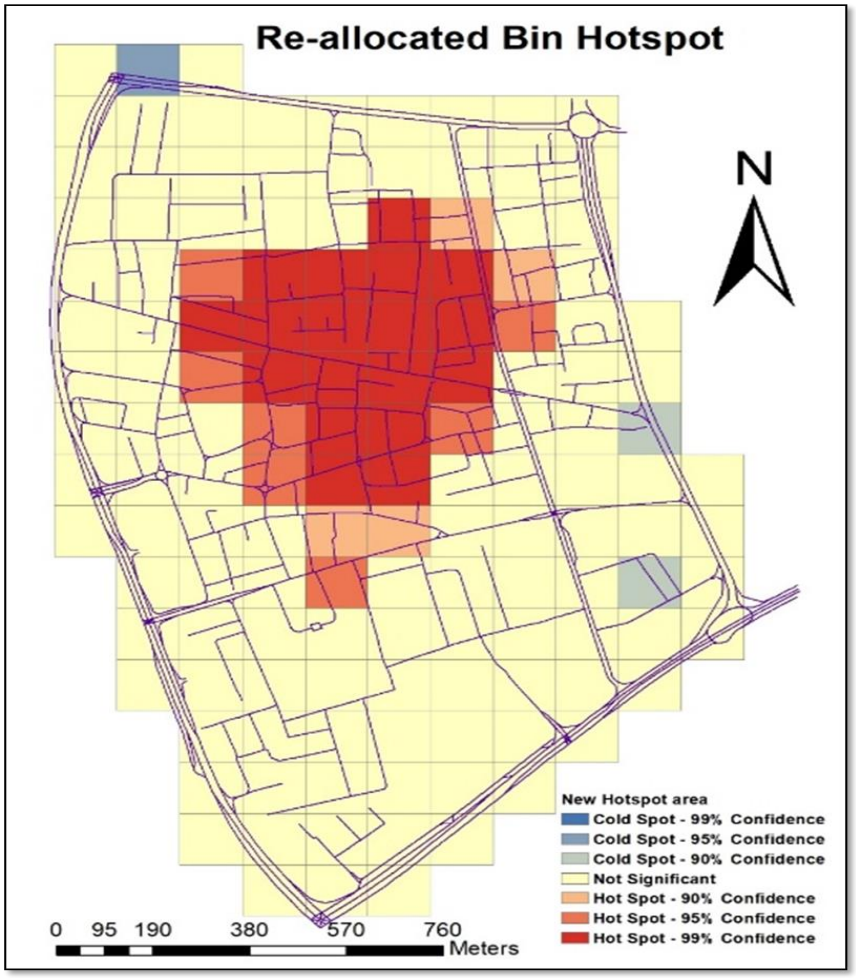

Figure 13: *Re-allocated bin location - significance of hotspots*

Figure 13 was created after new bin locations were added. As explained in the previous map the hotspot area is the area with more significant values or in other words more concentration of number of bins. Just the difference in this map is that the hotspot area has shifted a bit to the center of the map after relocation of the bins. Moreover, this is reasonable because of the high number of villas and small apartments in those areas. The tall buildings or apartments usually keep less number of bins with large capacity, so the hotspot does not fall in those areas. As for the cold spots, they have also shifted from the previous areas, due to the redistribution of bin locations in those areas.

3.11. Route Optimization for Existing Bin Location

The routing for the collection of existing bins from their locations were identified and interpolated using the network analyst. 219 stops were made for 260 bin locations. It is not that 260-bin locations only

had 260 bins; each bin location had one or more than one bins. The stops were made according to the hotspot of the bin locations. If there were bins nearby in one of the locations, only one stop was made for the convenience of collection (Figure 14).

Figure 14: *Route map for existing bin locations*

Zone 1- colored red as shown in the above figure 14 has 89 stops that has a routing distance of 6.5 miles and by following the speed limit given, it takes 20 minutes to cover that distance. Zone 1 also produces 20192 kg or about 20 tons of waste. The garbage truck collecting the garbage wastes can compact up to 20 tons. After checking the time, the waste trucks take at each stop, the average time taken was found out to be two minutes. The actual time taken to collect all the waste from Zone 1 is calculated by using the below formula:

Real time = (Number of stops* Time taken at each stops) + calculated time for Routing distance
Real time = (89*2) + 20 min = 198 minutes = 3.3 Hours.

Therefore, the total time taken to collect all the waste from zone 1 is 3.3 hours and it needs only one truck to complete the collection of waste.

Zone 2 - colored green has 65 stops that has a routing distance of 4.3 miles and takes 12 minutes to complete the route length. Zone 2 produces about 11891 kg or about 11.89 tons. So, the actual time taken to collect all the waste from zone 2 by stopping at all the stops is calculated as:

Real time= (65*2) + 12 min = 142 minutes = 2.37 Hours.

Therefore, it takes 2.37 hours to collect all the wastes from zone 2. Only one truck is enough to collect the waste from zone 2.

Zone 3 - colored yellow has 65 stops that has a routing distance of 4.7 miles and takes 13 minutes to complete the route length. Zone 3 produces 9772 Kg or about 9.7 tons of waste. So, the actual time taken to collect all the waste from zone 3 by stopping at all stops is calculated as:

Real time= (65*2) + 13 min = 143 minutes = 2.38 Hours.

Therefore, it takes 2.38 hours to collect all the wastes from zone 3. Only one truck is enough to collect the waste from zone 3.

To sum up, it took about 8.05 hours and a total of three trucks of 20 tons compacting capacity to collect the total waste of 41855 kg or about 41.85 tons generated from all the three zones.

3.12. New Route after Re-allocation of Bin Location

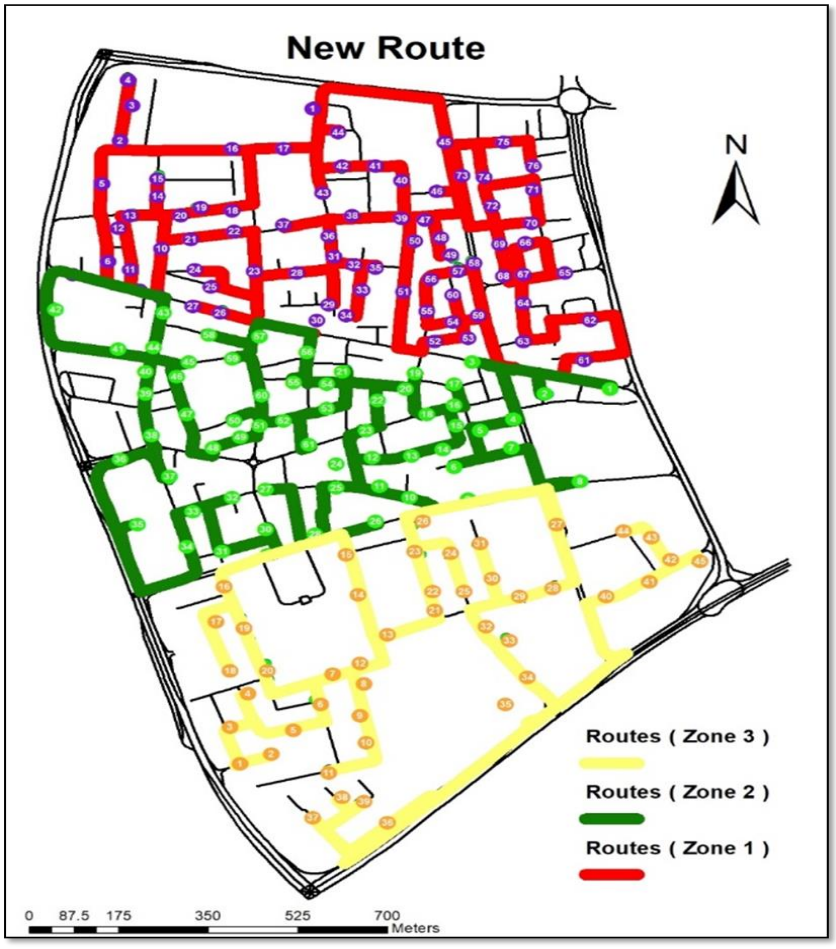

Figure 15: *Re-allocated bin locations - new routing map*

This new route was created after the new bin locations were added. There were 186 bin locations and 182 stops to be made. The stops and the number of bin locations are almost same due to the reason that the bin locations were added in such a way that it is not crowded in one place while the other place is empty. This has helped in reducing the time and cost.

The new route summary covers 17 miles and takes 49 minutes to complete the route length as derived from figure 15. There is an increase in distance due to the addition of bin location in places where no bins existed earlier. As per previous collection process, two minutes were taken into account for each stop. Therefore, in this new route for the new bin locations there are 182 stops in total. So, using the previous formula for calculation of real time taken after stopping at each location,

The real time = (182 * 2) + 49 minutes = 413 minutes or approximately 6.88 hours.

As one trucks has capacity to compact 20 tons, three trucks should be enough to collect all the wastes in the study area. Therefore, if the 6.88-hour job is divided in to three trucks, each truck will need different time in three different zones:

Zone 1: Time taken = (76*2) + 21 minutes = 173 minutes = 2.88 hours.

Zone 2: Time taken = (61*2) + 14 minutes = 136 minutes = 2.27 hours.

Zone 3: Time taken = (45*2) + 14 minutes = 104 minutes = 1.73 hours.

It is noticed that there is a huge reduction of time after redistributing the bins and rerouting, reducing the man power, saving cost and time. After new bin locations were created the collection time decreased from 483 minutes to 413 minutes, which saved around 1 hour and 10 minutes in total each day.

4. Conclusion

A short and brief description about management of solid waste and the advantages of using GIS in the process of managing this solid waste has started this case study. To use GIS in the process of solid waste management was the main aim of this case study. Through various field works in the study area and contextual findings, this research has shown the advantage of utilizing GIS in the fields related to solid waste management. Different case studies have shown that with GIS agencies and organizations running different waste management issues, it was possible to diminish the work stress, save time and reduce cost and enhance the serviceability.

The main approach used in this case study done in Qatar's Bin Mahmoud area was to use GIS to locate waste bins that are inappropriately placed and to relocate those waste bins and stabilize the amount of work done. Collection of the waste is the costliest part of waste management and is not an easy task. The main aim was to make the waste collection more efficient using GIS. The result was obtained by relocating the bins in such a way that they are distributed according to population and waste generation and in addition, optimizing the routes using GIS-based network analysis tool. The utilization of GIS can help in reducing the time and cost in a significant way.

The result obtained from this case study can help the municipality of Qatar in creating a more self-sufficient waste management strategy. This case study has proven that with GIS it is possible to reduce the workload and save time. As discussed in the previous section earlier the time taken to collect all the waste in the existing routes with its existing bin locations was 483 minutes and the new route made after re-allocating the bins needed only 413 minutes, reducing the time by 1 hour and 10 minutes from the existing collection time.

The utilization of GIS in the process of waste management in Qatar, starting from waste source to the dumping ground will help in analyzing, demonstrating, and solving all the complex problems. This will make the management system more efficient, which in turn will be saving a lot of time and cost and help also in making the management of waste sustainable in future.

This research project provides a general idea about the waste management in Qatar and about the Bin Mahmoud area's waste management in particular. The provided information in this case study could help in the future planning of waste management in Qatar.

References

Ahmad, F.I. 2016. Sustainable solutions for domestic solid waste management in Qatar. Master of Science in Engineering Management, Thesis, Qatar University, p.117.

Akinci, G., Guven, E.D. and Gok, G. 2012. Evaluation of waste management options and resource conservation potentials according to the waste characteristics and household income: A case study in Aegean Region, Turkey. *Resources, Conservation and Recycling*, 58, pp.114-124.

Chandrappa, R. and Brown, J. 2012. *Solid Waste Management: Principles and Practice*. Springer, p.414.

ESRI. 2015. *ArcGIS Desktop: Release 10.3.1*. Environmental Systems Research Institute, Redlands, CA.

Khatib, I.A. 2011: *Municipal Solid Waste Management in Developing Countries: Future Challenges and Possible Opportunities*. In: Kumar, S (ed) Integrated waste management - Volume II. pp.35-48.

Magrinho, A., Didelet, F. and Semião, V. 2006. Municipal solid waste disposal in Portugal. *Waste Management*, 26(12), pp.1477-1489.

Ministry of Development Planning and Statistics. Qatar Environment Day 2017. Availabel from: *https://www.mdps.gov.qa/en/statistics1/pages/topicslisting.aspx?parent=Environmental&child=EnvironmentalStatistics*

Nabegu, A.B. 2010. An analysis of municipal solid waste in Kano metropolis, Nigeria, *Journal of Human Ecology*, 31(2), pp.111-119.

Nagabooshnam, J.K. 2011. Solid waste generation and composition in Gaborone, Botswana, Potential for resource recovery, Master thesis, Energy and environmental engineering, Department of Management Engineering, Linkoping University, Sweden, p.67.

Okot-Okumu, J. 2012. Solid waste management in African cities – East Africa, Waste Management – An Integrated Vision. Available from: *https://www.intechopen.com/books/waste-management-an-integrated-vision/solid-waste-management-in-african-cities-east-africa*

Ouda, O., Cekirge, H. and Raza, S. 2013. An assessment of the potential contribution from waste-to-energy facilities to electricity demand in Saudi Arabia. *Energy Conversion and Management*, 75, pp.402-406.

Tinmaz, E. and Demir, I. 2006. Research on solid waste management systems: to improve existing situation in Corlu Town of Turkey. *Waste Management*, 26(3), pp.307-314.

Tolba, M.K. and Saab, N.W. 2008. *Arab environment future challenges. Technical Publications and Environment & Development magazine.* Available from: *http://www.afedonline.org/afedreport/Full%20English%20Report.pdf*

World Bank. 2012. What a waste: a global review of solid waste management. Available from: *https://openknowledge.worldbank.org/handle/10986/18027.*

Zafar, S. 2016. Solid Waste Management in Qatar. Available from: *https://www.ecomena.org/solid-waste-management-in-qatar/.*

Cloud Publications
International Journal of Advanced Remote Sensing and GIS
2019, Volume 8, Issue 1, pp. 2878-2888
ISSN 2320 – 0243, Crossref: 10.23953/cloud.ijarsg.395

Case Study

Environmental Sensitivity Index Mapping: A Case Study of PPMC Pipeline along Ugbomro Community and Environ, Delta State, Nigeria

Christopher Onosemuode[1], Okhae, S.E.[2], Gbemisola Okeowo[1]

[1]Federal University of Petroleum Resources, College of Science, Department of Environmental Management and Toxicology, Effurun, Delta State, Nigeria
[2]Ambrose Alli University, Faculty of Environmental Studies, Department of Geography and Environmental Management, Ekpoma-Edo State, Nigeria

Correspondence should be addressed to *onosemuode.chris@fupre.edu.ng*

Publication Date: 16 January 2019

DOI: https://doi.org/10.23953/cloud.ijarsg.395

Abstract Environmental Sensitivity Index (ESI) mapping provide a concise summary of coastal/inland resources that are at risk if an oil spill occurs nearby. Environmental sensitivity index (ESI) maps can be used for oil spill contingency planning, environment management planning and emergency response. To this end, the study attempts to establish the inland habitats and their sensitivity to oil spill along the 4.95km of the pipeline passing through Ugbomro community and as it relates to its environs. Ikonos image of the area obtained from Google Earth, were digitized manually and the land use/land cover map of the areas were derived using ArcGIS 10.1. The ESI classification and ranking was done for the inland habitat by considering the importance of indigenous flora/fauna species to rural livelihood, oil ecosystem interaction, and ease of clean up. The result suggests that built up area, water body and wetland having ESI ranking to be Very High and ESI classification of 5A, 5B and 5C respectively. Farmland ESI ranks High with ESI classification of 4, Semi natural vegetation has ESI ranking of Medium with ESI classification of 2 and bare surfaces had ESI ranking to be Low and ESI classified as 1. An emergency response zone and priority booming were proposed along the pipeline route as a means of curtailing the spread of oils to sensitive resources.
Keywords *ESI; Emergency; Oil spill; Pipeline; Risk; Zone*

1. Introduction

Crude oil remained one of the most sort after commodity which man cannot do without. Consequently, oil spills will continue to cause damaging effect on the environment because it is difficult to separate from oil exploration and exploitation (Aroh et al., 2010). In the Niger Delta, huge oil exploration and production are associated with frequent and rampant crude oil spills. The regular occurrence of oil spills in Niger Delta are results of deliberate act of vandalism of flowline, pipeline leakages, failures of oil facilities and overflow of process components. These caused considerable degradation of the environment, fundamental changes to social and environmental policies. Several barrels of oil have been spilled through oil pipeline into the environment due to lack of regular maintenance of pipelines (Nwilo and Badejo, 2010). Spilled oil is able to impair living things since its chemical constituents are

poisonous (Sojinu et al., 2010). The impacts of the oil spillages in the Niger Delta are numerous; such as adverse effect on the growth of plants due to widespread contamination of soil, pollution of water bodies (Batzias et al., 2011), impingement on organisms through internal exposure (ingestion and inhalation) and external exposure (skin and eye irritation) that causes infertility and cancer (Ordinioha and Brisibe, 2013).

Pipelines remain one of the most convenient and economical means of transporting crude oil across difficult terrain and over long distances from production facilities to distribution outlets (Alencar and De Almeida, 2010; Dey, 2010; Lins and de Almeida, 2012), though pipeline brings danger closer to homestead and farms (Phil-Eze and Okoro, 2009; Williams and Benson, 2010).

Oil pipeline spills can be caused by structural failure, operation error and third party damage (TPD) such as accidental rupture of pipelines (Achebe et al., 2012; Kandiyoti, 2012). Consequently, the present quest to increase production without addressing the animosity between host communities, government, and MOCs may further worsen existing problems of oil interdiction in oil-producing communities (Onuoha, 2008; Achudume, 2009). Despite global awareness of oil spill incidents, little attention is paid to onshore oil spills compared to offshore (Fingas, 2000; Reible, 2010; Chen and Denison, 2011). Most pipelines pass through various inland habitat and human settlements as is the case of the case of Ubgomro Community and Environ where the Federal University of Petroleum Resources is also situated. To this end, it is important to evaluate the proximity of human dwellings, sources of water, farms and other ecological habitat from sources of hazards (pipeline) (Shittu, 2014), with the specific objective of generating environmental sensitivity index classifications and maps of the ecosystem along the PPMC pipeline corridor across Ubgomo community and environ.

2. Materials and Methods

General Methodology

Developing ESI maps involves gathering spatial and non-spatial data to create strategic maps of sensitive resources (Human, Biological and Ecological feature) which are priority for response agencies involved in the emergency clean-up of oil spill in the environment. To accomplish the aim of this study the following procedure were employed; data acquisition, data manipulation, data analysis and presentation of the results (Figure 1).

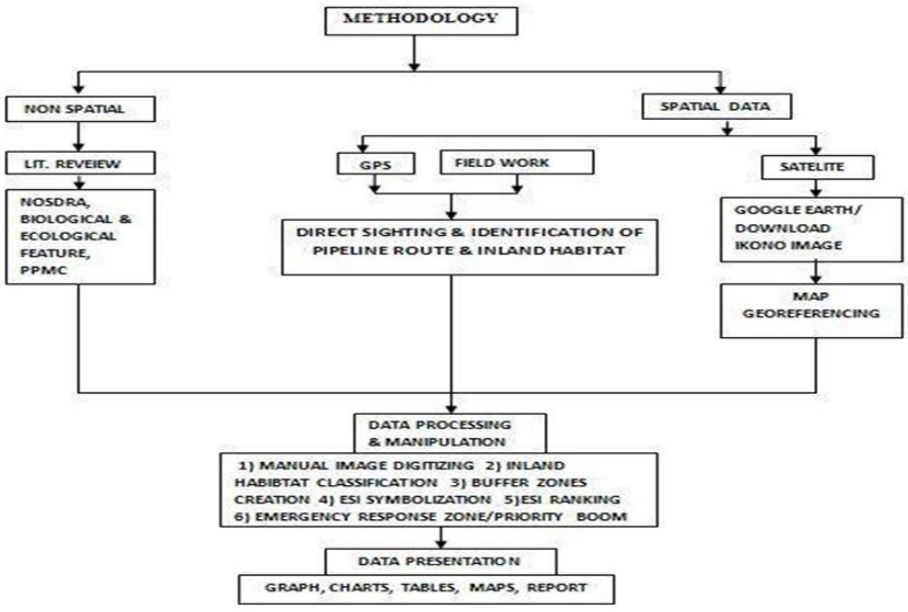

Figure 1: *Methodology flow chart*

Data Sources and Characteristics

Generating ESI maps requires interdisciplinary approach as such wide-ranging data and information are required on the biological and inland habitat types, image and data from agency responsible for oil spill emergency response as shown in Table 1 below.

Table 1: *Types of data, characteristics and sources*

Type of data	Resolution	Date	Source
Ikonos Image	0.25m	2015	Google Earth
Google Earth Pro	Eye altitude between 6.0 km-6.50 km.	2017	Data SIO, NOAA, U.S Navy, NGA, GEBCO, (c) 2017 Google Image, (c) 2017 Digital Globe
Literature on biological, ecological & marine (Fauna & Flora) resources	None	2015	Department of Biological Science University of Lagos, NOSDRA

Inland Habitat Classification

The study focused on inland habitat along PPMC pipeline in the study area. The google earth image of the study area were downloaded and georeferenced. Based on the prior knowledge of the area of study coupled with a brief examination of researches in the study area, a classification scheme for landuse/cover was developed for the study area (Table 2).

Table 2: *Land use/cover classification scheme adopted for the study*

S/N	Landuse/Cover Class
1	Built-Up Area
2	Wetland
3	Semi natural vegetation
4	Farmland
5	Bare surfaces
6	Water body

Categorization and ESI Ranking Classification of Inland Habitat

The main criteria considered to establish the degree of sensitivity to oil spill and other stress factor of an ecological class include its biological productivity, oil/ecology interaction and ease of clean up, and social, economic and human importance as posited by Fasona et al., 2011 was adopted in this study and shown in Table 3.

Table 3: *Land use/cover sensitivity ranking and classification*

Land use/cover Classes	Environmental Sensitivity Index (ESI) Rank	ESI class
Built Up Area	VH	5A
Water Body	VH	5B
Wetland	VH	5C
Farmland	H	4
Semi Natural Vegetation	M	2
Bare Surfaces	L	1

Buffering

Buffer zones of various standards were created along the PPMC pipelines corridor based on local standards prescribed by PPMC and international standards used in Gundlach E. et al., 2005 as shown in Table 4.

Table 4: *Buffer Standard Zones used and Sources*

S/N	Buffer zone	Source	Standards	Location
1	75m	PPMC	Local	Nigeria
2	250m	Gundlach et al., 2005	International	Turkey & Azerbaijan
3	500m	Gundlach et al., 2005	International	Turkey & Azerbaijan

Emergency Response Zones

Emergency response zones is usually strategically positioned at areas considered to be easily accessible; between area where the inland habitat features are likely to suffer great harm and where responders and equipment can easily be deployed within a short time after oil spill incident has been reported. The proposed emergency response zone along the study area is chosen by considering; i) the most delicate inland habitat features and ii) the proximity and accessibility of required responders and equipment deployment along the pipeline route.

3. Results and Discussion

This discussion the results of the of image processing, ecological classification of the inland habitat and its ESI ranking and the use of buffer standards, of 75m, 250m and 500m respectively for the establishment of the various habitat classes are presented.

Buffer Zones of the Land use/cover along PPMC Pipeline Corridor

The inland habitat classes were identified and represented in the land cover/use feature within the established buffer of 75m, 250m and 500m according to local and international standards (Figure 2).

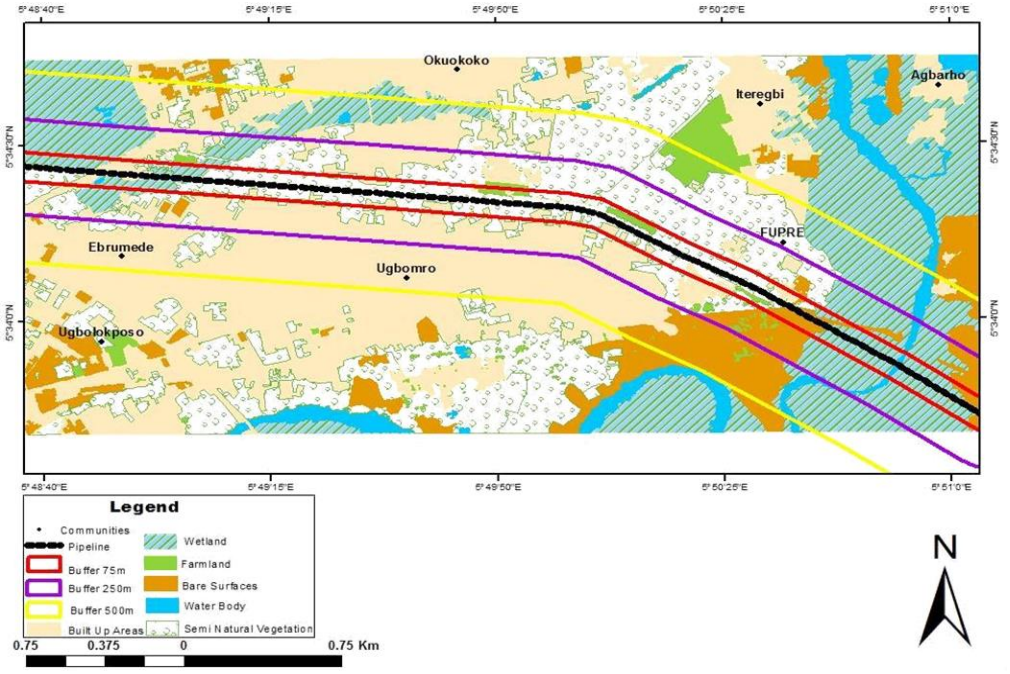

Figure 2: *Buffer zone standards along PPMC pipeline corridor*

Using the established buffer standards in Figure 1, Table 5 shows that bare surfaces occupy 6.56%, 6.83% and 8.32% of the land area respectively, built up areas occupy 11.36%, 26.68% and 35.08% respectively, farmlands is apportioned 2.42%, 1.73% and 1.67% respectively, semi natural vegetation has 53.81%, 39.68% and 29.57% respectively, water body within the specified buffer zones occupied 0.58%, 0.68% and 1.13% respectively and wetland has 25.26%, 24.48% and 24.22% respectively. The habitat that would be of most concern within the 75m buffer is the built up area of the presence of socio-economic and cultural activities that have direct relationship with the people and the impact increases for buffer zones of 250m and 500m, while this is closely followed by farmland that also has direct impact on the people of the study area but with a decreasing impact as the buffer zone increases.

Table 5: *Statistics of the land use/cover for the different buffer standards*

Buffer standards	Local buffer 75m		International Buffer 250m		International Buffer 500m	
Land use/Cover class	**Area (ha)**	**100%**	**Area (ha)**	**100%**	**Area (ha)**	**100%**
Bare Surfaces	4.87	6.56	16.64	6.83	39.41	8.32
Built Up Areas	8.44	11.36	64.96	26.68	166.1	35.08
Farmland	1.8	2.42	4.02	1.73	7.93	1.67
Semi Natural Vegetation	39.97	53.81	96.6	39.68	140.04	29.57
Water Body	0.43	0.58	1.66	0.68	5.35	1.13
Wetland	18.76	25.26	59.59	24.48	114.68	24.22
Total	74.28	100	243.46	100	473.52	100

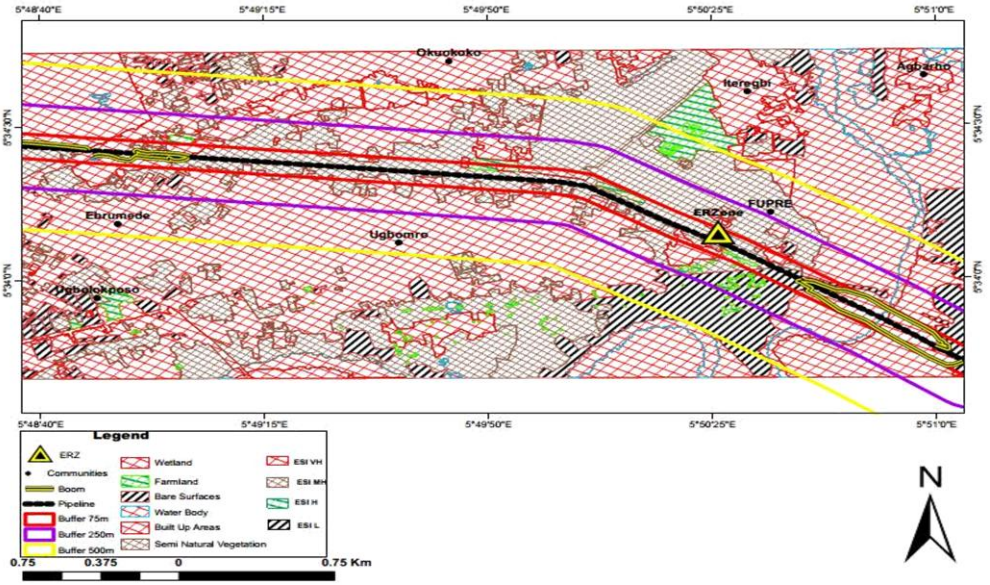

Figure 3: *Environmental sensitivity index map of study area*

Sensitivity Index Ranking and Classifications of the Land use/Cover

The Environmental Sensitivity Index map of the study area is shown in Figure 3, with built up area, water body and wetland having ESI ranking to be Very High and ESI classification of 5A, 5B and 5C respectively. Farmland ESI ranks High with ESI classification of 4, Semi natural vegetation has ESI ranking of Medium with ESI classification of 2 and bare surfaces had ESI ranking to be Low and ESI classified as 1. The details of each land use/cover are discussed in subsections below.

Built-Up Areas ESI Classification and Ranking for the Buffer Zones

The built-up area within the study area generally comprises of pockets of communities and other settlements within Uvwie Local Government Area. The Built-up area has environmental sensitivity index classification of 5A and ranks Very High (VH) for ESI (Table 6 and Figure 4). The very high SI is a result of the presence of the socio-economic and socio-cultural activities that present as a result of the presence of the Federal University of Petroleum Resources that is centred in the study area. When built up areas are impacted by oil it poses direct or indirect impact on the people and the flora and fauna. Oily sheens are formed on the soil surface and the oil can sticks to the walls of built up structures if the spill is heavy. Oil may come in contact with domestic material such as paper, broom and domestic waste which generates oily waste which must be properly managed to minimize pollution. When pipeline cuts across the communities they are at risk of accident that may lead to fire disaster and destroy lives, properties and means of livelihood. This very high SI ranking would therefore call for urgent attention and priority response in times of oil spill incident.

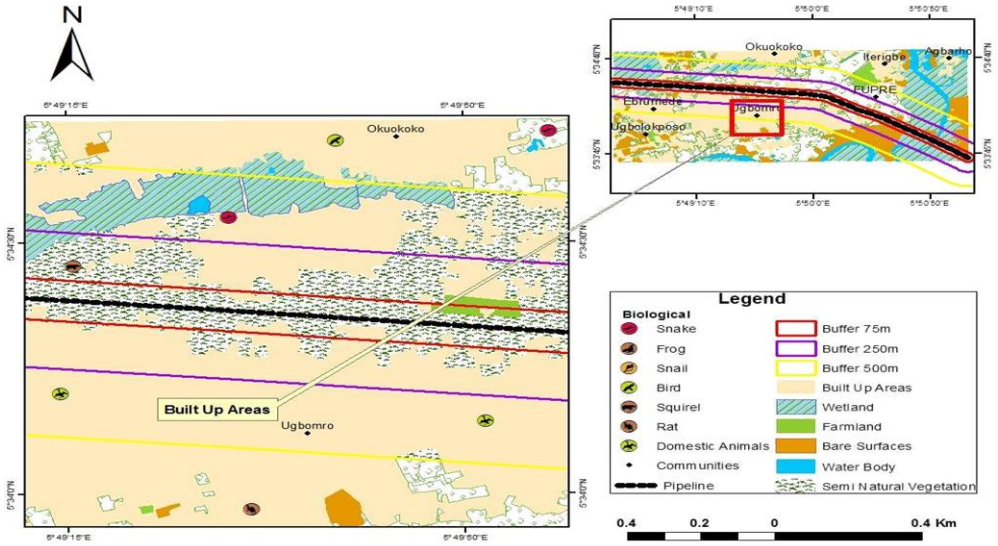

Figure 4: *Portion of built-up area along the pipeline corridor*

Table 6: *Land use/cover sensitivity ranking and classification*

Land use/cover classes	Environmental Sensitivity Index (ESI) Rank	ESI class
Built Up Area	VH	5A
Water Body	VH	5B
Wetland	VH	5C
Farmland	H	4D
Semi Natural Vegetation	M	2E
Bare Surfaces	L	1F

Water Body ESI Classification and Ranking for the Buffer Zones

The environmental sensitivity index classification of water body is 5B ranking Very High (VH) next to built-up area (Table 6 and Figure 5); this is because marine environment is very sensitive to oil. Marine spill maybe difficult to contain, recover and remediate. It contains floras and faunas that include aquatic plants, fishes, water birds (either breeding or migratory ones) and reptiles. Other varieties of species are water snail, frog, toad and water hyacinth. Oil tends to float and spreads on water because it is lighter. Depending on the nature of the oil spill and type of water body it is spilled on; when the spilled oil is acted upon by factors such as specific gravity, wind action and direction it

may result in processes such as dispersion, weathering, evaporation, oxidation, biodegradation and emulsification.

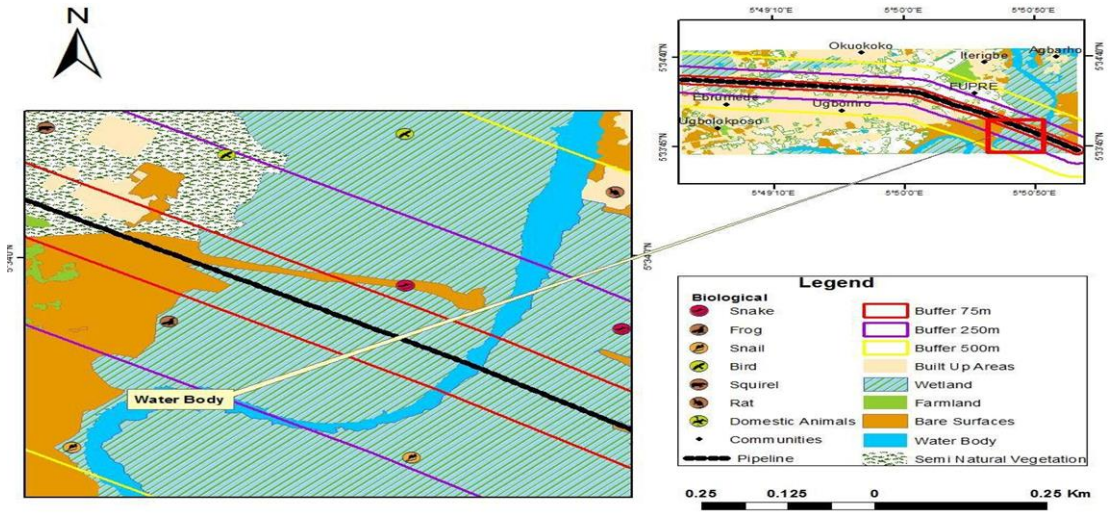

Figure 5: *Portion of water body along the pipeline corridor*

Wetland ESI Classification and Ranking for the Buffer Zones

Wetland in this study has environmental sensitivity index class of 5C and ranks Very High next to water body (Table 6 and Figure 6). The wetland is generally characterized by swampy and marsh/grass surfaces. They also comprise of biological lives such as crustacean, fishes, snapping shrimp, water snail, mudskipper and reptiles. Birds can be found here seasonally as they migrate for breeding and mating purpose and also supports another habitat around them. Oil spilled in this habitat usually persists for long as underlying wet soil below marsh and grasses restrict oil from flowing; leading to percolation of oil and seepage into the subsoil. As a result, hydrocarbons are deposited in the ground water aquifer. Grass covered with oil get sticky and soggy leaving residue over the surface when spillage is heavy.

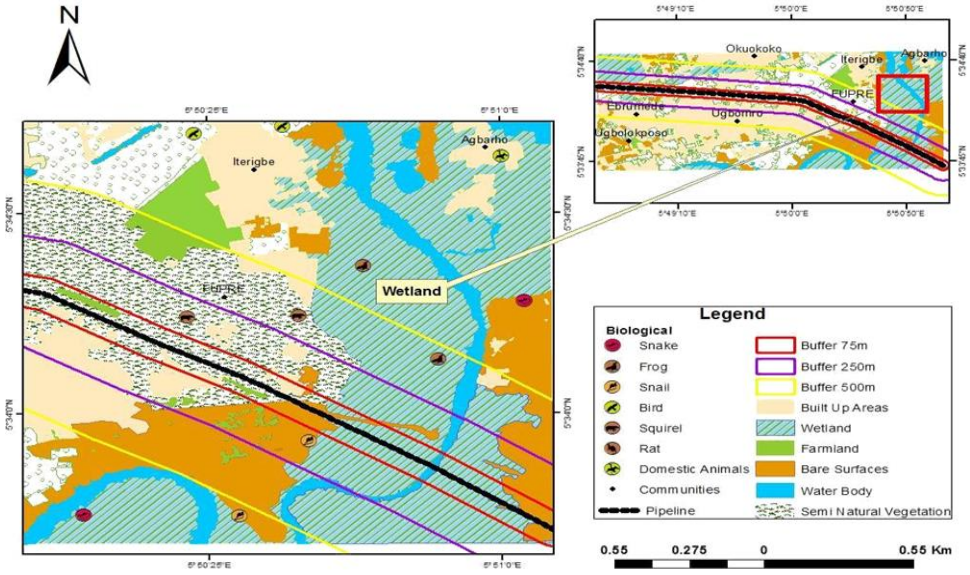

Figure 6: *Portion of wetland along the pipeline corridor*

Farmland ESI Classification and Ranking for the Buffer Zones

Farmland has ESI classification of 4D with High as ranking of its ESI (Table 6 and Figure 7). Farmland as used in this study describes area where agricultural activities are carried out for subsistence purposes. The biological lives found here are different flora species and fauna like snakes, ground squirrel, monitor lizard, and agama lizard. When farmland is polluted by oil the flora and fauna are affected as well as the ground water as oil seeps through soil. Plants may bioaccumulate residue of hydrocarbon in the soil; if they are ingested by human or animal it can have adverse health implications.

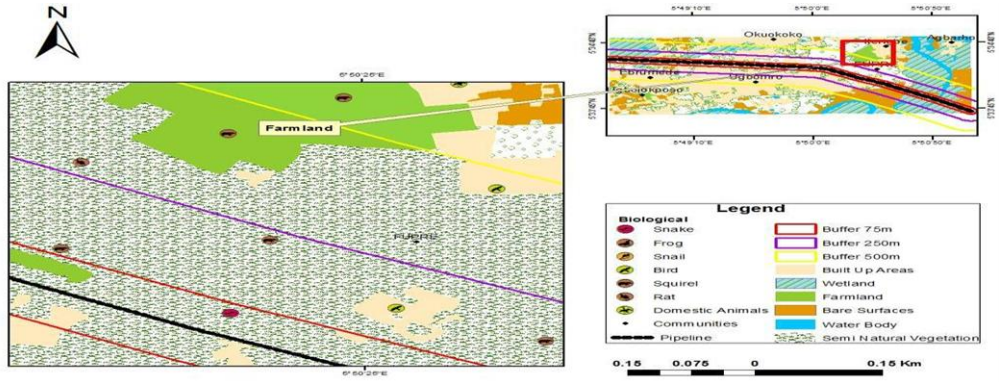

Figure 7: *Portion of farmland along the pipeline corridor*

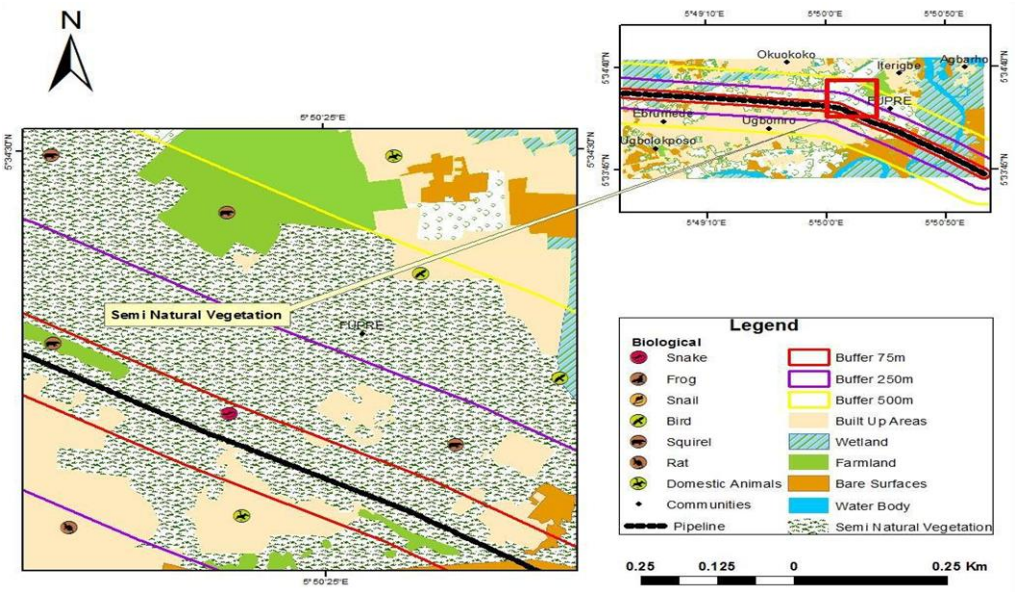

Figure 8: *Portion of semi natural vegetation along the pipeline corridor*

Semi Natural Vegetation ESI Classification and Ranking for the Buffer Zones

The feature semi natural vegetation is found mostly along the pipeline route south of Ugbomro, sparsely distributed between Ebrumede and Ugbolokposo communities and largely in FUPRE. The semi natural vegetation has ESI classification of 2E and is ranked Medium (Table 6 and Figure 8). Some floras found here include varieties of shrubs and grass species and faunas like rodent, Xerus sp (ground squirrel) and Rattus sp. (giant rat). Generally spilled oil travels slowly in this environment. Oil penetrates the topsoil and seep into the ground to infiltrate the soil leaving a slivery surface on the topmost soil layer.

Bare Surfaces ESI Classification and Ranking for the Buffer Zones

They are found at different section of the habitat. They have been exposed to human activities mostly in bid to reclaim land portions while some sections of it have been impacted by various natural components. Its ESI is ranked low (L) and its ESI classification is 1F (Table 6 and Figure 9). It would suffer the least impact in case of an oil spill. Generally, very few animals exist in this habitat some of them are lizard, cricket, small rodents and some other creeping insects. Oil tends to accumulate on topsoil and slowly seeps into the ground. Oil spill leaves stain on the soil surface as oil seeps into the soil and pollute micro biological species and ground water aquifer.

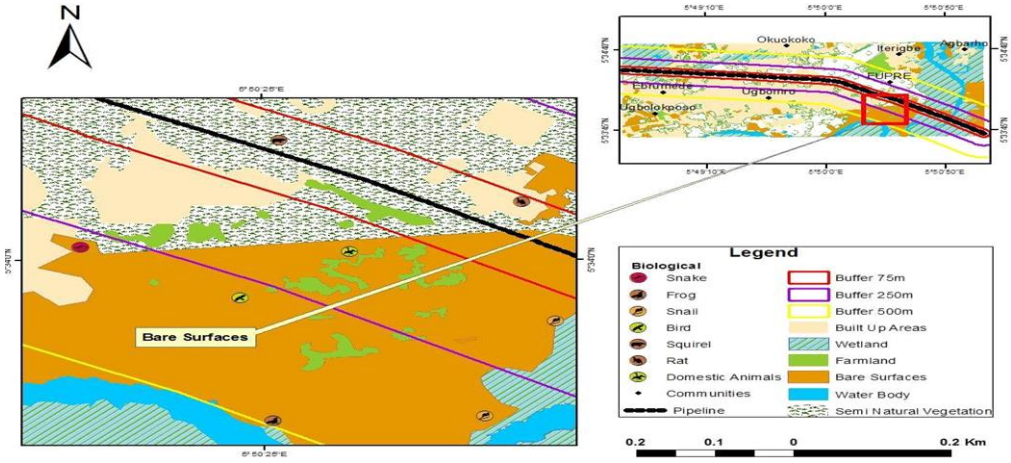

Figure 9: *Portion of bare surfaces along the pipeline corridor*

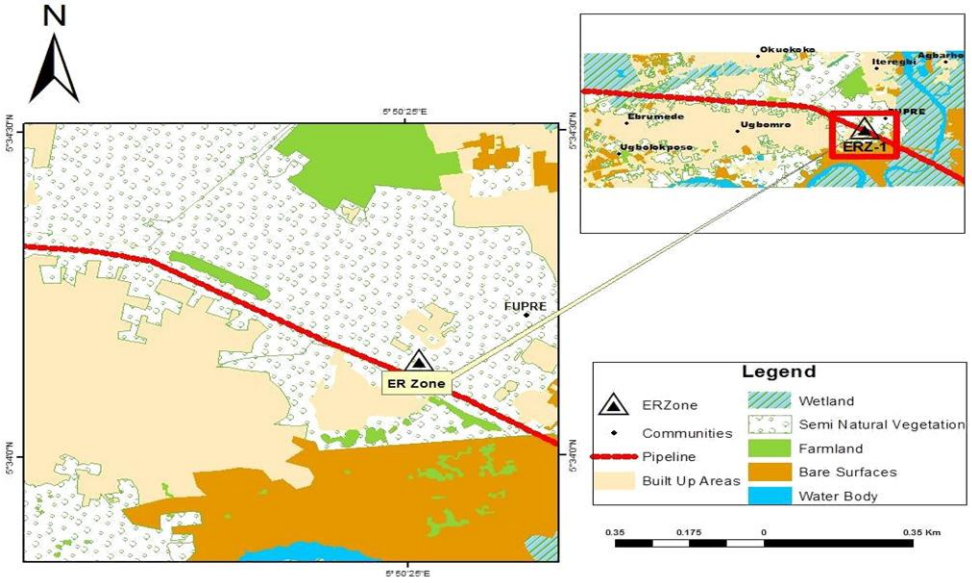

Figure 10: *Proposed emergency response zone along the pipeline corridor*

Emergency Response Zone (ERZ-1)

Emergency Response Zones (ERZ) is usually strategically positioned at areas considered to be easily accessible; between area where the inland habitat features are likely to suffer great harm and where responders and equipment such as hard booms, skimmers, storages and vehicles can easily be deployed within a short time after oil spill incident has been reported.

The emergency response zone (ERZ-1) has been proposed to be established along the PPMC pipeline corridor around the point at which the pipeline pass through the Federal University of Petroleum Resources, Delta which falls within the 500m buffer zone (Figure 10). The rationale being that the agency responsible for emergency response to oil spill and PPMC are some distant away and with the pipeline passing through the University, there is the danger of sabotage from student unrest anytime. To this end the institution can serve as ERZ to cater for emergency spills.

4. Conclusion

The PPMC pipeline safety can be evaluated as an individual risk, where the safety zone is set as the right-of-way. Thus, the surrounding ecosystem features that are endangered by oil spill can be pre-determined. The generation of buffer zone based on the standards encapsulates the endemic ecological resources that are susceptible to contaminants from pipeline oil spill, vandalism and ruptures due to mechanical or human errors along the study area. These ESI maps aids involved authorities and agencies responsible in managing this disaster in understanding what and where to respond to and the required equipment to use in managing the pipeline spill.

References

Achebe, C.H., Nneke, U.C. and Ansiji, O.E. 2012. *Analysis of oil pipeline failure in the oil and gas industries in the Niger Delta area of Nigeria*. Proceeding of the International MultiConference of Engineers and Computer Sciences, Hong Kong.

Achudume, A.C. 2009. Environmental health, development and economic empowerment of rural women In Nigeria. *Environment Development and Sustainability*, 11, pp.459-469.

Alencar, M.H. and de Almeida, A.T. 2010. Assigning priorities to actions in a pipeline transporting hydrogen based on a multicriteria decision model. *International Journal of Hydrogen Energy*, 35, pp.3610-3619.

Aroh, K.N., Ubong, I.U. and Eze, C.L. 2010. Oil spill incidents and pipeline vandalization in Nigeria Impact on public health and negation to attainment of Millennium development goal: the Ishiagu example. *Disaster Prevention and Management: An International Journal*, 191, pp.70-87.

Batzias, F.A., Siontorou, C.G. and Spanidis, P.M.P. 2011. Designing a realiable leak bio-detection system for natural gas pipeline. *Journal of Hazardous Materials*, 186, pp.35-58.

Chen, J. and Denison, M.S. 2011. The deepwater horizon oil spill: environmental fate of the oil and the toxicological effects on marine organisation. *The Journal of Young Investigators*, 21(6), pp.84-95.

Dey, P.K. 2010. Managing project risk using combined analytic hierarchy process and risk map. *Applied Soft Computing*, 10, pp.990-1000.

Fingas, M. 2000. *The Basics of Oil Spill Cleanup*. 2nd ed. Lewis Publishers, London, New York Washington DC.

Gundlach E.R., Cekirge M., Anul C., Orhan C. and Sutherland P. 2005. *Pipeline and coastal environmental sensitivity mapping for the BTC pipeline system in Turkey*. Proceedings of the 2005 International Oil Spill Conference.

Kandiyoti, R. 2012. *Pipelines Flowing oil and crude politics*. I.B.Tauris & Co Ltd., London. Lagos Journal of Geo-Information Sciences, 1(1).

Lins, P.H.C. and de Almeida, A.T. 2012. Multidimensional risk analysis of hydrogen pipelines. *International Journal of Hydrogen Energy*, 37, pp.13545-13554.

Nwilo, P.C. and Badejo, O.T. 2010. *Impacts and management of oil spill pollution along the Nigerian coastal areas*. In: Sutherlands, M. and Nichols, S. (Eds.), Administrating Marine Spaces: International Issues. A Publication of the international Federation of Surveyors (FIG).

Onuoha, F. 2008. Poverty, pipeline vandalisation/explosion and human security: integrating disaster management into poverty reduction in Nigeria. Available from: http://www.issafrica.org/uploads/16_2ONUOHA.PDF. Accessed 11/9/2017.

Ordinioha, B. and Brisibe, S. 2013. The human health implications of crude oil spills in the Niger delta, Nigeria: An interpretation of published studies. *Nigerian Medical Journal: Journal of the Nigeria Medical Association*, 54, p.10.

Phil-Eze, P.O. and Okoro, I.C. 2009. Sustainable biodiversity conservation in the Niger delta: a practical approach to conservation site selection. *Biodiversity Conservation*, 18, pp.1247-1257.

Reible, D. 2010. After the oil is no longer leaking. *Environmental Science and Technology*, 44, pp.5685-5686.

Shittu, W.J. 2014. Mapping oil spill human health risk in rivers state, Niger Delta, Nigeria: (Doctoral dissertation). Retrieved from University of Nottingham repository. Available from: http://eprints. nottingham.ac.uk/14115/1/Shittu_PhD_Thesis_%282014%29.pdf.

Sojinu, O.S.S., Wang, J., Sonibare, O.O. and Zeng, E.Y. 2010. Polycyclic aromatic hydrocarbons in sediments and soils from oil exploration areas of the Niger Delta, Nigeria. *Journal of Hazardous Materials*, 174, pp.641-647.

William, A.B. and Benson, N.U. 2010. Interseasonal hydrological characteristics and variability in surface water of tropical estuarine ecosystems within Niger delta. *Journal of Environmental Monitoring and Assessment*, 165(1-4), pp.399-406.

Cloud Publications
International Journal of Advanced Remote Sensing and GIS
2019, Volume 8, Issue 1, pp. 2933-2938
ISSN 2320 – 0243, Crossref: 10.23953/cloud.ijarsg.402

Research Article

Segmentation of High Resolution Worldview-2 Satellite Images

Shashidhar Sonnad[1]*, Lalitha Y. S.[2]

[1]Department of Electronics & Communication Engineering, APPA Institute of Engineering & Technology, Kalaburagi, Karnataka, India
[2]Department of Electronics & Communication Engineering, Don Bosco Institute of Technology, Bengaluru Karnataka, India

Correspondence should be addressed to *shashidharsonnad1@gmail.com*

Publication Date: 21 February 2019

DOI: https://doi.org/10.23953/cloud.ijarsg.402

Abstract This paper presents the segmentation technique used to segment the Worldview-2 high resolution satellite multispectral (MS) images. First the spectral features like Simple Ratio (SR), Normalized Difference Vegetation Index (NDVI), Soil Adjusted Vegetation Index (SAVI) and Modified Soil Adjusted Vegetation Index (MSAVI) are considered to extract the spectral features from the MS image. Next the MS image is segmented by using the over segmented k-means algorithm with novel initialization (OSKNI) method. The proposed method performs well in terms of User's accuracy (UA), Producer's accuracy (PA) and overall segmentation accuracy (OVA) compared to the existing k-means algorithm.

Keywords *Feature; Multispectral; Segmentation; Spectral*

1. Introduction

Image segmentation is the underlying process in majority of the applications of image processing like remote sensing, computer vision etc. Image segmentation is the process fall under region-based techniques of classifying remote sensing images before the classification of segments takes place (Banerjee et al., 2014; Paclı´ka et al., 2003). Image segmentation in RS images involves the extraction of texture or spectral features and clustering of the features extracted using the data clustering method. With respect to the remote sensing, segmentation is the way towards the outlining singular areas of homogeneous earth cover, while segmentation is the ensuring procedure of recognizing the depicted region as kinship to a particular earth cover (Johnson and Xie, 2011). This paper proposes an unsupervised clustering method of segmenting the RS images into the sectors of uniform areas using spectral features (Kumar et al., 2018). The spectral features considered in this paper are SR (Birth and McVey, 1968), NDVI (Rouse et al., 1973), SAVI (Huete, 1998) and MSAVI (Qi et al., 1994).

2. Materials and Methods

The Worldview-2 satellite images of Kalaburagi city (at geographical coordinates 17° 20′ 09″ N, 076° 50′ 15″ E) Karnataka, India are used to test the algorithm. The Worldview-2 image contains total 9 bands, panchromatic band is the first band with wavelength 450nm to 850nm and remaining 8 bands are multispectral bands covers total wavelength of 400nm to 1040nm. Three subset images

considered in this paper to test the k-means and proposed algorithm. The subset -1 consist of 3 clusters, cropland1 (non cultivated), tree and soil dug & field bands, represented by aquamarine, green and light yellow colours respectively in the ground truth image. The subset-2 image consist of 3 clusters, cropland1(non cultivated), cropland2 (cultivated), soldug & filed band, represented by aquamarine, dark green and light yellow colours respectively in the ground truth image. Subset-3 image consist of 3 clusters, crop land, trees, soil dug & field band represented by aquamarine, green, light yellow colours respectively.

2.1. Over Segmented k-means Algorithm with Novel Cluster Centre Initialization (OSKNI)

First over segment the data with k-number of clusters in to O and P clusters, using k-means algorithm, such that O=k+1 and P=k+2. And run the k-means algorithm, the initial cluster centre for O and P clusters is obtained by using the following steps.

1. Let A_1, A_2, A_3,….A_m are the set of information elements of O and P clusters, where m is the quantity of the data points.
2. Run k-means algorithm to produce O and P clusters.
3. The initial cluster centres for O and P clusters are found by using the Kaufman approach, steps 4 through 10 (Kaufman and Rousseeuw, 2005).
4. Select the principal sample the most halfway located sample.
5. For every new sample s_i run the following step
6. For every s_j find c_{ji} =max (Dj-d_{ji},0) where d_{ji}= ||s_i-s_j|| and D_j= min dp_j, where p is the chosen sample.
7. Calculate the scale of s_i using $\sum_j c_{ji}$.
8. Chose the new sample s_i which maximizes $\sum_j c_{ji}$.
9. If the selected centres are O then stop else continue step 5 through 8.
10. After forming clusters assign each sample to the cluster represented by nearest centre.
11. Now apply same procedure explained in step4 through 10 to find the initial cluster centre for P clusters.
12. Run k-means iterative algorithm on O and P clusters.
13. More than 99% of the pixel values unchanged between the present and previous clusters the k-means algorithm is stopped.
14. O and P over segmented clusters are fused using the procedure explained in the following subsection.

2.2. Fusion of O and P Clusters to Find Optimal Cluster Centre

The fusion decides the O x P clusters of occurrences, which are in fact the undistinguished occurrences. New k-beginning cluster mid pint for grouping the data sets in to k-portions originate from the average of the biggest groups of undistinguished occurrences. Along these lines the smallest groups are dropped, choosing just the k-largest clusters among O x P sets of undistinguished occurrences. In this way basic cluster centres are generated to implement the iterative k-means on data sets. Below equations explains the fusion process.

$$\bigsqcup_{o=1}^{O} UO = \bigsqcup_{p=1}^{P} VP = I \quad \dots (1)$$

Where O=k+1, P=O+1, I is the group of all occurrences in the data. UO is O clusters of first over segmentation. VP is P-clusters of second over segmentation (Ursani et al., 2007).

$$\forall_{o,p}, \exists Z_{o,p} = UO \cap VP \quad \dots (2)$$

Where, $Z_{o,p} \in Z$, ||Z||=O x P. By using the OSKNI clustering method the MS images under test are segmented. Figure 1, gives the process of spectral feature extraction from MS images and segmentation. Totally three times the k-means algorithm is applied on the datasets.

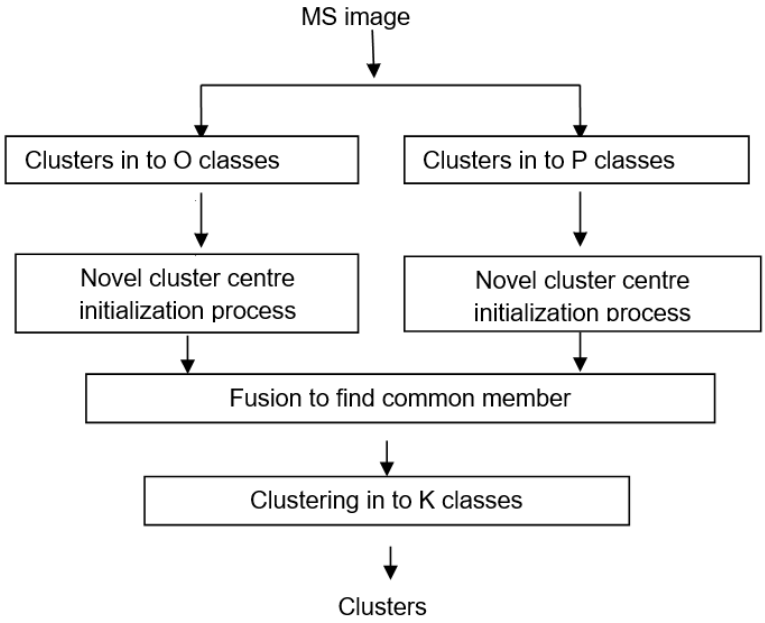

Figure 1: *Proposed segmentation method*

3. Results and Discussion

In this paper, we considered Worldview-2 images of Gulbarga district, 50 subset images of size 256 x256 are considered to test the proposed algorithm out of which three images results are presented in this paper. Segmentation results of k-means and proposed method of subset-1 (contains 3-classes), subset-2 (contains 3-classes) and subset-3 (contains 3-classes) are shown in Figure 2, 3 and 4 respectively. In Figure (a) of Figures 2, 3 and 4 shows the original MS images, Figure (b) in figures 2, 3, and 4, represent the ground truth. Figure (c) in Figures 2,3,and 4 represents the segmentation results of k-means algorithm, figure (d) in Figures, 2,3 and 4 represents the segmentation results of the proposed method.

It is observed from Figure 2 (c) that k-means algorithm is unable to differentiate the pixels belongs to class tree and field band & soil dug. Figure 2(d) shows the segmented result using the proposed method here the miss-clustered error due to k-means are reduced as we considered the common members of over segmented O and P clusters. From Figure 3 (c) is observed that k-means algorithm miss-clustered large number of pixels belongs to the class cropland-2 to the class field band & soil dug. From the proposed segmentation method shown in Figure 3 (d), it is clear that miss-clusters created by k-means are avoided between cropland-2 and field band & soil dug. Figure 4 (c) shows the segmentation result of subset-3using the k-means, it is observed from the figure that samples belongs to the trees are miss-clustered as field band & soil dug. Figure 4 (d) shows the segmentation result of the proposed method for subset-3 and it is observed that pixels belongs to all three classes are segmented properly.

Quantitative analysis of the existing k-means and proposed methods is carried out by using three parameters of the Kappa statistics namely, UA, PA and OVA. Figures (5) and (6) represents the results of parameter namely, user's accuracy, producers accuracy and over all accuracy for all three subsets-1, 2 and 3. From the quantitative analysis graphs it is shown that the k-means algorithm produces average PA of 51.07%, 80.83% and 53.92% for subset-1, 2 and 3 respectively and average

UA of 51.65%, 82.63 and 67.80 for subset-1, 2 and 3 respectively. On the other side proposed method segment the spectral subset images with higher accuracy compared to k-means algorithm. The average PA produced by OSKNI is 86.72%, 93.32% and 95.31 for subset-1, 2 and 3 respectively and average UA of 91.09%, 91.67% and 92.45 % for subset-1, 2 and 3 respectively. The overall accuracy produced by k-means is 76.63%, 88.10%, 78.94 for subset-1, 2 and 3 respectively while overall accuracy produced by OSKNI method is 97.45%, 97.01% and 96.98 % for subset-1, 2 and 3 respectively.

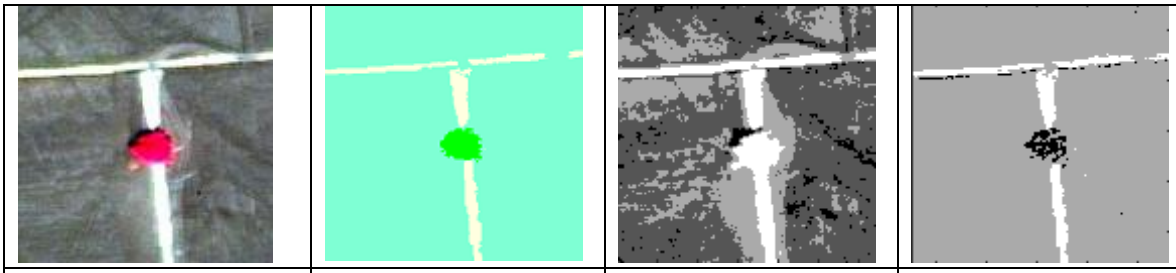

a. Original MS image with 3-clusters	b. Ground truth image	c. k-means result	d. Proposed method result

Figure 2.*Segmentation details of subset-1*

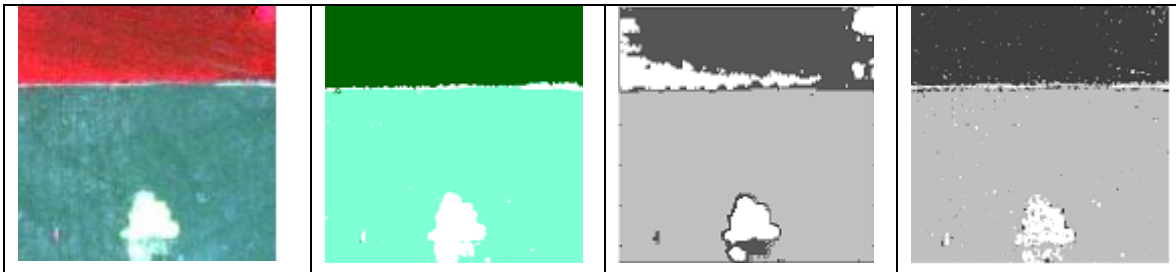

a. Original MS image class-7	b. Ground truth image	c. k-means result	d. Proposed method result

Figure 3.*Segmentation details of subset-2*

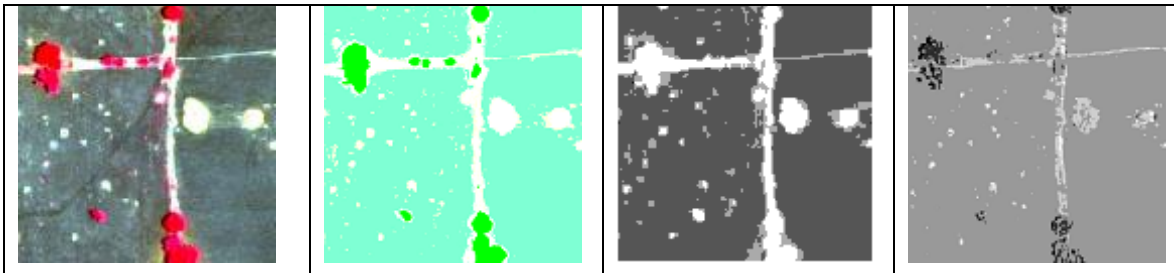

a. Original MS image class-4	b. Ground truth image	c. k-means result	d. Proposed method result

Figure 4.*Segmentation details of subset-3*

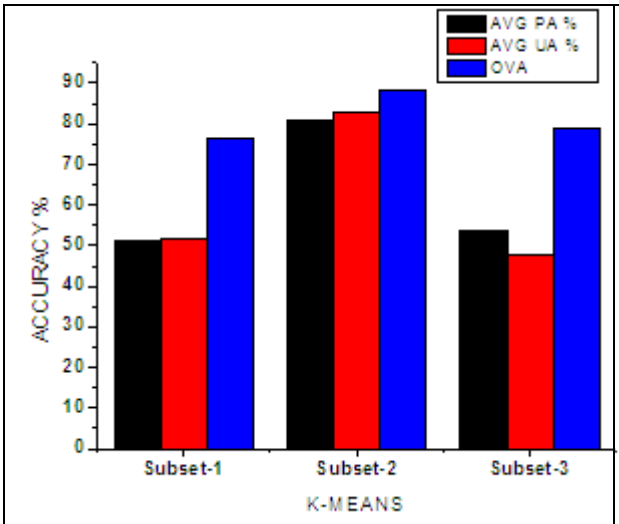

Figure 5. *PA, UA and OVA calculation for K-means method*

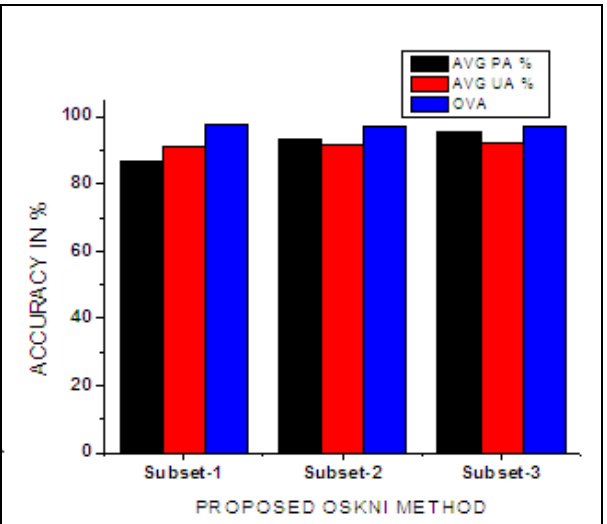

Figure 6. *PA, UA and OVA calculation for OSKNI method*

4. Conclusion

The k-means algorithm performance is depending on the initialization process. Unfortunately, k-means algorithm and many variants of the k-means algorithm proposed in the literature initialize the initial cluster centre by random sampling due to which the segmentation accuracy will decrease. Proposed over segmented k-means algorithm with novel cluster centre initialization (OSKNI) method utilizes the Kaufman initialization process to provide the good initialization for over segmented clusters O and P. Later the repetitive process of k-means is applied on the data set three times. The proposed method performs well in contrast with the k-means in terms of PA, UA and OVA presented in the previous section. In the future work the suitable post processing can be done to the results of the proposed method to improve the segmentation results further. In the future work different spectral features can also be considered to improve the segmentation results. The proposed method can also be compared with the other segmentation algorithm.

Acknowledgement

I thankful to Mr. Rajanna A Gourshetty Senior Project Scientist, Karnataka State Remote Sensing Application Centre, Kalaburagi for his kind support to generate the ground truth images and validating the ground truth images.

References

Banerjee, B., Varma, S., Buddhiraju, K.M. and Eeti, L.N. 2014. Unsupervised multi-spectral satellite image segmentation combining modified mean-shift and a new minimum spanning tree based clustering technique. *Journal of Selected Topics in Applied Earth Observations and Remote Sensing*, 7(3), pp.888-894.

Birth, G.S. and McVey, G. 1968. Measuring the color of growing turf with a reflectance spectroradiometer. *Agronomy Journal*, 60, pp.640-643.

Huete, A.R. 1998. A soil-adjusted vegetation index. *Remote Sensing of Environment*, 25, pp.295-309.

Johnson, B. and Xie, Z. 2011. Unsupervised image segmentation evaluation and refinement using a multi-scale approach. *Journal of Photogrammetry and Remote Sensing*, 66, pp.473-483.

Kaufman, L. and Rousseeuw, P.J. 2005. *Finding groups in data. An introduction to cluster analysis*. John. Inc., Canada.

Kumar, M., Garg, P.K. and Srivastav, S.K. 2018. A spectral structural approach for building extraction from satellite imageries. *International Journal of Advanced Remote Sensing and GIS*, 7(1), pp.2471-2477.

Paclı´ka, P., Duina, R.P.W. and van Kempenb, G.M.P. 2003. Segmentation of multi-spectral images using the combined classifier approach. *Image and Vision Computing*, 21, pp.473-482.

Qi, J., Chehbouni, A., Huete, A.R. and Kerr, Y.H. 1994. Modified Soil Adjusted Vegetation Index (MSAVI). *Remote Sensing of Environment*, 48, pp.119-126.

Rouse, J.W., Hase, R.H., Schell, J.A. and Deering, D.W. 1973. Monitoring vegetation systems in the great plain with ERTS. Proceedings of the third ERTS symposium, US Government Printing Office, NASA, Washington, DC, pp.309-317.

Ursani, A.A., Kpalma, K. and Joseph, R. 2007. *Over-segmentation of feature space for initialisation of K-means clustering*. Proceedings of the World Congress on Engineering and Computer Science, 2007, October 24-26, 2007, San Francisco, USA.

Cloud Publications
International Journal of Advanced Remote Sensing and GIS
2019, Volume 8, Issue 1, pp. 2955-2962
ISSN 2320 – 0243, Crossref: 10.23953/cloud.ijarsg.404

Research Article

Change Detection Analysis of Vamsadhara - Nagavali River Fluvial System, using Multi-Temporal Remote Sensing Data and GIS Techniques

Gara Raja Rao, Kollu Sai Satya Mounika, Mokka Jagannadha Rao

Department of Geology, Andhra University, Andhra Pradesh, India

Correspondence should be addressed to *satyamounikakollu@gmail.com*

Publication Date: 21 February 2019

DOI: https://doi.org/10.23953/cloud.ijarsg.404

Abstract Land use & Land cover change detection analysis has been carried out in the present study covering the Nagavali and Vamsadhara Fluvial system (18°40′N to 18°09′N latitude and 84°10′ E to 83°39′E longitude). Satellite images of Landsat-7 ETM+ (2000) Landsat ETM+ (2010) Landsat OLV-TIRS (2016) and 1975 SI Toposheets have been used to study the temporal changes in the land use and land cover by onscreen digitisation techniques in ARC GIS 10.1 software followed by image processing to obtain changes in various classes of land use during study period from 1975 to 2016. The classes include plantation, settlements, water bodies, coastal area, wetlands, agriculture land and area under river course of both rivers. The classes, which have shown an increased area from 1975 to 2016, include Agriculture (from 56.93 % to 63.95%) and Settlements (from 1.40% to 3.43%). The classes that have shown the decreasing trend of Land Use are Plantation (from 19.76% to 13.14%), water bodies (from 2.29% to 0.77%), Wetlands (from 0.72% to 0.57%). The area under river course of both the rivers has shown a decreasing trend. The analysis reveals that due to increased irrigation facility plantation, wetlands and water bodies have brought under agricultural use and this trend need to be arrested. The Plantation area for natural resource management furthermore declines the soil erosion in between the Vamsadhara and Nagavali river area.
Keywords *Change detection; Land cover; Land use; Rivers; Satellite imagery*

1. Introduction

The process of Land Use Land Cover Change is a dynamic phenomenon. Advances in observation and detection methods specially like remote sensing and geospatial techniques have led to the boost in Global, regional and local scale studies of LULC. The issue of land use / land cover changes has been given priority in many international and interdisciplinary researches such as remote sensing, political ecology and biogeography (Turner et al., 1995, Jensen, 2005; Turner et al., 2007). Knowledge of spatial land cover information is essential for proper management, planning and monitoring of natural resources (Zhu, 1997). It is considered necessary for many agricultural, Geological, Hydrological and Ecological models. Disaster management is another such discipline where its use is encountered. Land use and land cover analysis are important for many planning and management activities and considered as an essential element for physical modelling and understanding the earth as a system. Now-a-days land cover maps are prepared for planning and management purposes. Due

to synoptic view, map like format and repetitive coverage, satellite remote sensing imagery is a remarkable source for gathering quality data on land cover information on local, regional and global scale (Csaplovics, 1998; Foody, 2002). Multi-temporal satellite data are useful in assessing the relationship between natural and anthropogenic factors effect on land use / land cover change. To develop an action plan for land resource development, change detection analysis is very crucial in monitoring the changes.

Objective

The objective of the present study is to identify the temporal changes in the land use/land cover classes in the Vamsadhara and Nagavali fluvial system in the coastal tracts of the Srikakulam District, Andhra Pradesh for the period from 1975 to 2016.

Study Area

The region selected for the present study is Vamsadhara and Nagavali fluvial system in the coastal tracts of the Srikakulam District, Andhra Pradesh. It comprises an area of 2285 km^2 and lies between 18°40′N to 18°09′N latitude and 84°10′ E to 83°39′E longitude. The study area covers two major rivers of northern Andhra Pradesh namely Vamsadhara River and Nagavali River. Northern border of the study area is demarcated by Eastern Ghats and slope is decreasing from north to south. Vamsadhara and Nagavali rivers flow from North West to the South Eastern direction in Srikakulam district.

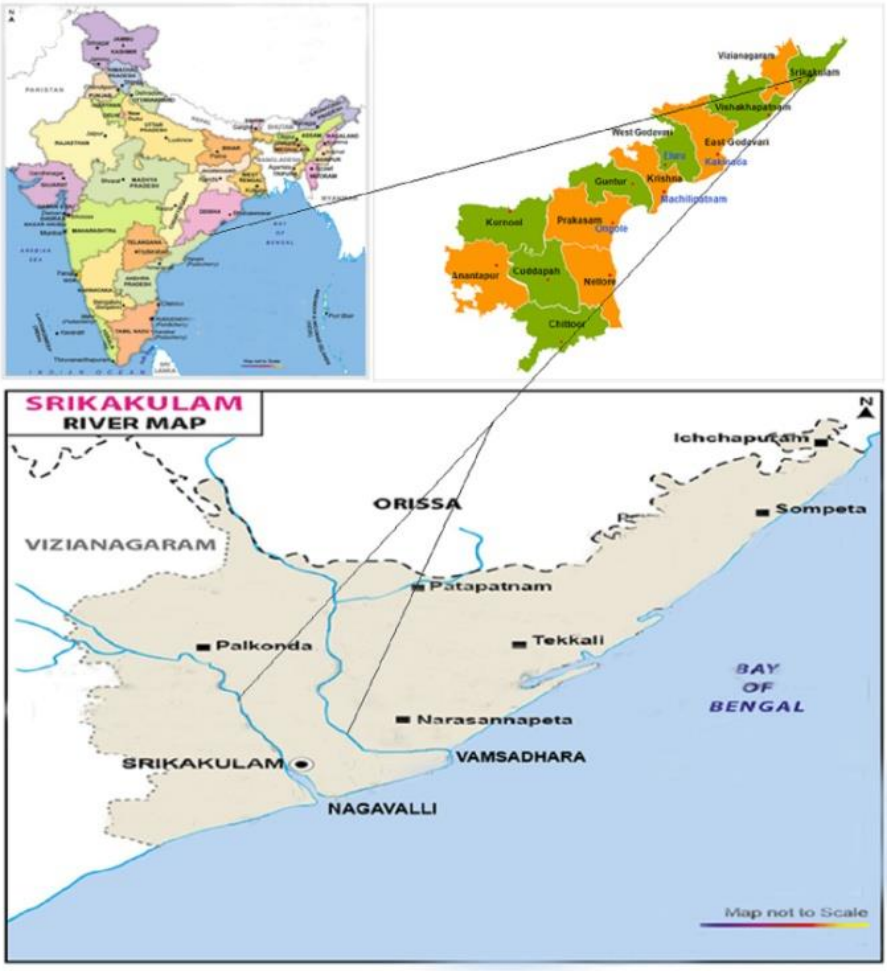

Figure 1: *Study area of Nagavali and Vamsadhara fluvial system*

Vamsadhara River originates in the border of Kalyansinghpur in Rayagada district and Thuamul Rampur in Kalahandi district of Odisha. Vamsadhara River flows for a length of 154 km in Orissa State and runs along the border of Orissa and Andhra Pradesh for a length of 29 km from Battili to Gotlabhadra and enters Andhra Pradesh at Gotlabhadra village. The river flows for a length of 82 km in Andhra Pradesh before emptying into the Bay of Bengal at Kalingapatnam in Srikakulam District of Andhra Pradesh. Vamsadhara is an important east flowing river between Mahanadi and Godavari. The river rises just south of the Belagad village in the undivided Phulbani district of Orissa at an elevation of about 600 m. The total length of the river is about 221 km, of which 125 km is in Orissa, 23 km is at the boundary between Orissa and Andhra Pradesh and 73 km is in Andhra Pradesh. Study area is shown in the following figure (Figure 1). The area between these two rivers forms present study area.

2. Materials and Methods

Time series satellite imagery was used to map the temporal trends spread in between Vamsadhara and Nagavali fluvial system. For this purpose, Topographic sheet 74 B/3, 65 N/16, 65 N/15, 65 N/14, and 65 N/11 were collected for the year (1975-76); Landsat-7 ETM+ (2000); Landsat-7 ETM+ (2010); Landsat OLI_TIRS image (2016) have been used for the present study and they are depicted in the Table 1. Satellite data of TM, ETM+, and OLI_TIRS is obtained from online Global Land Cover Facility (GLCF) website of USGS, USA for years 2000, 2010 and 2016 respectively. All the FCC (false color composite) images were geo-referenced by co-registering the selected ground control points that are prominently identified from the images as well as the Survey of India topographic maps of the area that are later brought to a common geographic coordinate system, which helped in comparing them with one another for estimating the areas and temporal changes in the land use/land cover that is shown in the following figure (Figure 2). The images enhanced through ALR technique has aided mapping of various land use/land cover features such as Plantation, Settlement, Water bodies, Coastal Area, Wetlands and Agriculture land through Onscreen-digitization in Arc GIS 9.3 Software.

Table 1: *Satellite imagery and characteristics*

2016 Landsat-8 (30Meter Resolution)			
	Date Acquired	**TARGET-WRS-PATH**	**TARGET-WES-ROW**
Coast side	2016-02-21	140	47
Up-Land side	2016-02-12	140	47
2010 Landsat-5 (30Meter Resolution)			
	Date Acquired	**TARGET-WRS-PATH**	**TARGET-WES-ROW**
Coast side	2010-01-19	140	47
Up-Land side	2010-01-26	141	46
2000 Landsat-ETM (30Meter Resolution)			
	Date Acquired	**TARGET-WRS-PATH**	**TARGET-WES-ROW**
Coast side	2000-03-20	140	47
Up-Land side	2000-04-12	141	46
TOPO SHEETS (74B/3, 65N/15, 65N/14, 65N/11) OF 1975-76			

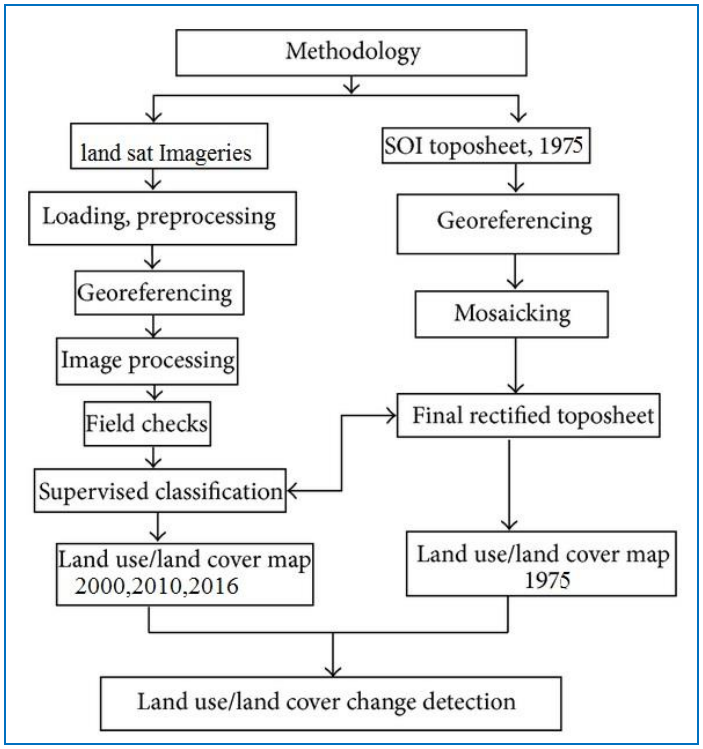

Figure 2: *Depicting the standard methodology for change detection studies*

3. Results and Discussion

Following Table 2, depict the land use / land cover changes from the year 1975 to 2016.

Table 2: *Land Use/ Land Cover data from 1975 to 2016 in Vamsadhara and Nagavali fluvial system*

Land Use/Land Cover Type	Area (km^2)			
	1975	**2000**	**2010**	**2016**
Agriculture	1301 (56.93)	1389.4 (60.80)	1414.31 (61.89)	1459.02 (63.85)
Settlement	32 (1.40)	60.20 (2.63)	63.20 (2.76)	78.56 (3.43)
Plantation	451.6 (19.76)	363.21 (15.89)	341.3 (14.93)	300.25 (13.14)
Water Bodies	52.48 (2.29)	30.39 (1.32)	27.15 (1.18)	17.56 (0.77)
Nagavali River	30.83 (1.34)	28.69 (1.25)	26.69 (1.16)	23.83 (1.04)
Vamsadhara River	33.0 (1.44)	31.15 (1.36)	30.15 (1.31)	26.17 (1.14)
Coastal Area	367.41 (16.07)	367.9 (16.10)	367.90 (16.10)	366.44 (16.03)
Wetlands	16.68 (0.72)	14.06 (0.61)	14.30 (0.62)	13.08 (0.57)
Total	**2285.0**	**2285.0**	**2285.0**	**2285.0**

This study has been undertaken to understand the land use and land cover changes in different land use classes namely agriculture, settlements, plantation, water bodies, Nagavali River, Vamsadhara River, coastal area and wetlands. The analysis results of the above process have been shown in Table 2. The data indicates that there are significant changes in the land use pattern among the classes studied. The classes such as agriculture and settlements have indicated an increased land usage whereas all the other classes have indicated the declining trend of land utilization. Details are discussed below. To have a better comprehension the output maps for all the four years namely 1975, 2000, 2010 and 2016 are presented (Figure 3 and Figure 4)

The land use and agriculture have shown an increasing trend where an area of 1301 sq km (56.93%) was under agriculture in the year 1975 which has increased to 1389.4 sq km (60.80%) during the year 2000. The area was further increased to 1414.31 sq km (61.89%) in the year 2010 and it recorded an area 1459.02 sq km (63.85%) in 2016. Thus, the class agriculture has shown a significant increase.

The area under settlements has shown an increasing trend, where an area of 32 sq km (1.40%) was under settlements in the year 1975 which has increased to 60.20 sq km (2.63%) during the year 2000. The area was further increased to 63.20 sq km (2.76%) in the year 2010 and it recorded an area of 78.56 sq km (3.43%) in 2016. In this way the class settlements have also shown a significant and consistent increase.

The area under plantation has shown a decreasing trend where an area of 451.6 sq km (19.76%) was under plantation in the year 1975 which has decreased to 363.21 sq km (15.89%) during the year 2000. The area has further decreased to 341.3 sq km (14.93%) in the year 2010 and it recorded an area of 300.25 sq km (13.14%) in 2016. Thus, the area under plantation indicated a decreasing trend.
The area under Water Bodies has shown a decreasing trend where Water bodies occupied an area of 52.48 sq km (2.29%) in the year 1975, which has decreased to 30.39 sq km (1.32%) during the year 2000. The area has further decreased to 27.15 sq km (1.18%) in the year 2010 and it recorded an area of 17.56 sq km (0.77%) in 2016. The trend indicated the area under water bodies are in decrease in the study area.

The area under Nagavali River has shown a decreasing trend where an area of 30.83 sq km (1.34%) was occupied by Nagavali River in the year 1975 which has decreased to 28.69 sq km (1.25%) during the year 2000. The area has further decreased to 26.69 sq km (1.16%) in the year 2010 and it recorded an area of 23.83 sq km (1.04%) in 2016. The results strongly suggest the area occupied by the Nagavali River course has been reduced significantly.

The area under Vamsadhara River has shown a decreasing trend where an area of 33.0 sq km (1.44%) was occupied by Vamsadhara River in the year 1975 which has decreased to 31.15 sq km (1.36%) during the year 2000. The area was further decreased to 30.15 sq km (1.31%) in the year 2010 and it recorded an area of 26.17 sq km (1.14%) in 2016. The area under Vamsadhara River has decreased significantly.

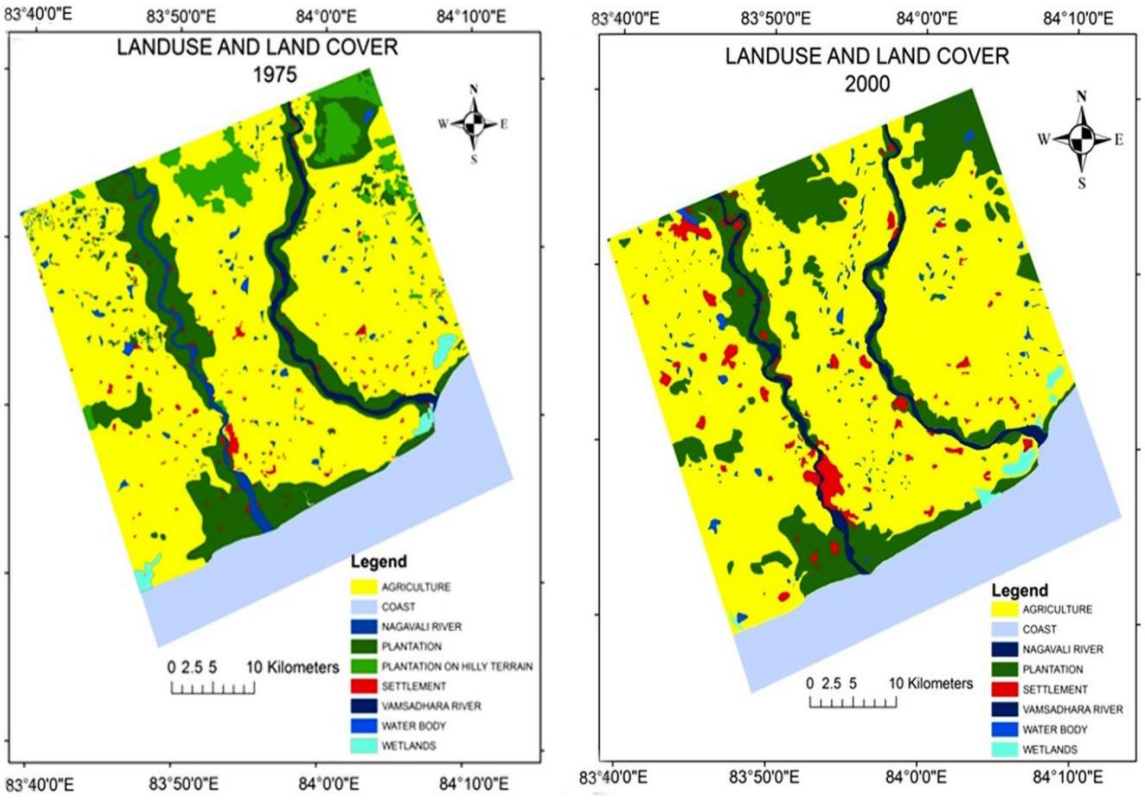

Figure 3: *The LULC changes during the years 1975 and 2000*

The area under Coastal area has shown a decreasing trend where an area of 367.41 sq km (16.07%) was occupied by Coastal area in the year 1975 which has decreased to 367.9 sq km (16.10%) during the year 2000. The area was stable and maintained 367.9 sq km (16.10%) in the year 2010 and it recorded an area of 366.44 sq km (16.03 %) in 2016. The area under coastal environment has come down slightly.

The area under wetlands has shown a decreasing trend where an area of 16.68 sq km (0.72%) was occupied by Coastal area in the year 1975 which has decreased to 14.06 sq km (0.61%) during the year 2000. The area was stable and maintained 14.30 sq km (0.62%) in the year 2010 and it recorded an area of 13.08 sq km (0.57%) in 2016. Thus, the class wet lands have registered a marginal decrease in the study period.

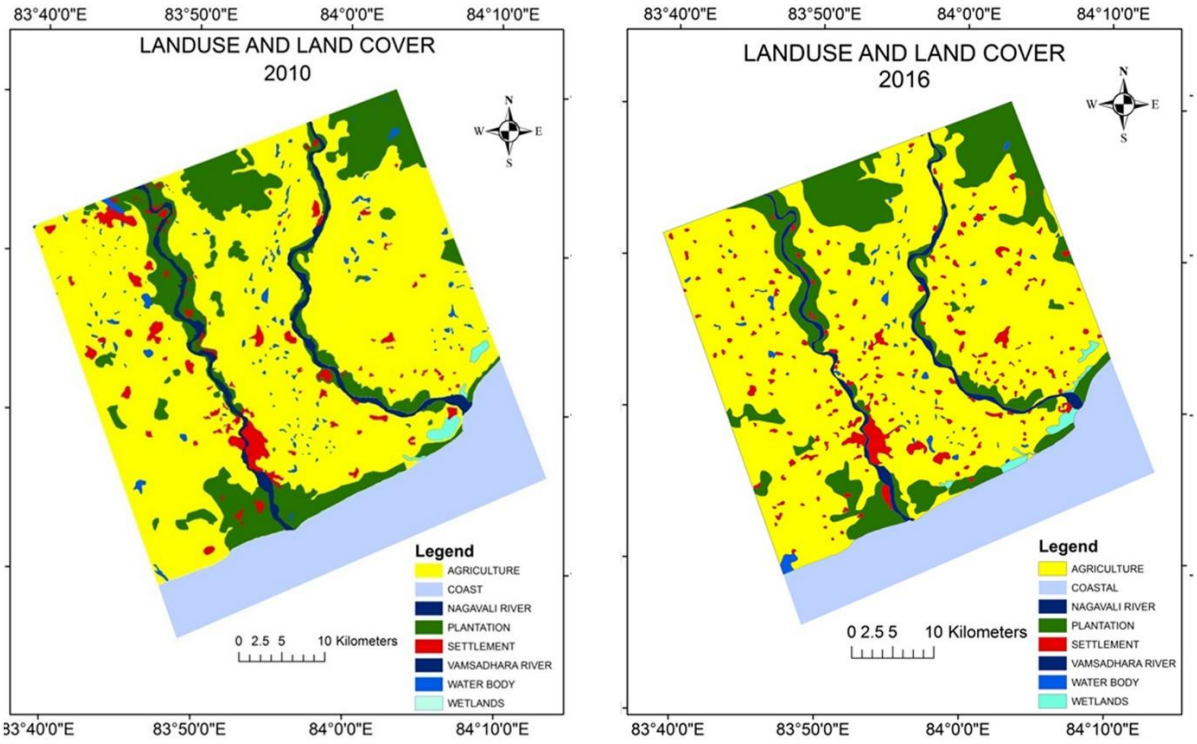

Figure 4: *The LULC changes during the years 2010 and 2016*

4. Conclusion

The present analysis reveals that due to deforestation and agricultural practices, forest area has rapidly declined in the study area, area under settlements has increased whereas the area under water bodies has decreased during the study period 1975 to 2016. It is estimated that almost all the decrease in dense forest area is because forestlands have been utilized for settlement, agriculture and related activities and the decrease may be due to human pressure on forests for firewood as well as grazing of cattle in the forested area, and urbanization. These activities also resulted; the risk of soil erosion.

According to the study of morphometric analysis (Panhalkar et al., 2012), it is recommended that in upper sub-basin of the two river systems, river needs to be given higher priority for soil conservation practices. In this study, Land use and Land cover changes from the year 1975-2016 are investigated for both the river systems together. The other parameters studies under land use and land cover changes namely river course, coastal area, and plantation also indicated a significant change and indicated a decreasing trend. This can be attributed to both the natural environmental changes as well as anthropogenic activities.

The results strongly suggest the study area is under increased human pressure on the natural environment and resources. Proper steps need to be taken under the environmental management to arrest further degradation of the land and water resources in the study area.

References

Anil, N.C., Sankar, G.J., Jagannadha Rao, M., Prasad, I. and Sailaja, U. 2011. Studies on Land Use/Land Cover and change detection from parts of South West Godavari District, AP - Using Remote Sensing and GIS Techniques. *The Journal of Indian Geophysical Union*, 15(4), pp.187-194.

Csaplovics, E. 1998. High Resolution space imagery for Regional Environmental Monitoring – Status quo and future trends. International Archives of Photogrammetry and Remote Sending, 32(7), pp.211-216.

Foody, G.M. 2002. Status of landcover classification accuracy assessment. *Remote Sensing for Environment*, 80, pp.185-201.

Greeshma, A.G., Jagannadha Rao, M., Karuna Karudu, T. and Mallikarjuna Rao, M. 2016. Distribution of benthic foraminiferal assemblages in Nagavali river estuary, Srikakulam, Andhra Pradesh. *Indian Journal of Geo-Marine Sciences*, 45(7), pp.875-881.

Jensen, J.R. 2005. *Introductory Digital Image Processing: A Remote Sensing Perspective*. Pearson Education, 3rd Ed.

Panhalkar, S.S., Mali, S.P. and Pawar, C.T. 2012. Morphometric Analysis and Watershed Development Prioritization of Hiranyakeshi Basin in Maharashtra, India. *International Journal of Environmental Sciences*, 3(1), pp.525-534.

Raja, R. 2018. Application of spatial technologies towards geological, morphological and slope based characterization of nagavali-vamsadhara river systems, east coast of India, with reference to gravity based flood mitigation. Andhra University, p.280.

Turner, B.L., Skole, D.L., Sanderson, S., Fischer, G., Fresco, L.O. and Leemans, R. 1995. *Land-Use and Land-Cover Change, Science/Research Plan*. IGBP Report No. 35/HDP Report No. 7, Stockholm, Sweden, and Geneva, Switzerland.

Turner, B.L., Lambin, E. and Reenberg, A. 2007. The emergence of land change science for global environmental change and sustainability. *Proceedings of National Academy of Sciences of the United States of America*, 104, pp.20666-20671.

Zhu, A.X. 1997. Measuring uncertainty in class assignment for natural resources map under fuzzy logic. *Photogrammetric Engineering and Remote Sensing*, 63(10), pp.1195-1202.

Cloud Publications
International Journal of Advanced Remote Sensing and GIS
2019, Volume 8, Issue 1, pp. 2963-2970
ISSN 2320 – 0243, Crossref: 10.23953/cloud.ijarsg.405

Research Article

Comparative Analysis of Different Methods of Leaf Area Index Estimation of Strawberry under Egyptian Condition

Abdelraouf M. Ali, Mohamed Aboelghar

National Authority for Remote Sensing and Space Sciences (NARSS), Al-Nozha El-Gedida, Cairo, Egypt

Correspondence should be addressed to *raouf.shoker@narss.sci.eg*

Publication Date: 5 March 2019

DOI: https://doi.org/10.23953/cloud.ijarsg.405

Abstract Leaf area index (LAI) is a factor for vegetative growth parameter. It is defined as leaf area per unit of ground area and could be used as a linkage between plant biophysical, biochemical and spectroscopic parameters. In this research, direct laboratory LAI measurements were tested versus different in situ field measurements for different parameters including LAI derived from LAI-2000 canopy analyzer and six hyperspectral vegetation indices (VIs) (normalized difference vegetation index (NDVI), chlorophyll index (CHI), photochemical reflectance index (PRI), triangular vegetation index (TVI), modified triangular vegetation index (MTVI)), that were generated from ASD-4 field spectroradiometer measurements. The objective is to calibrate the accuracy of LAI-2000 measurements and to examine hyperspectral vegetation indices as estimators of LAI through regression models. A strawberry cultivated area in the Nile delta of Egypt was selected as a study site. Linear regression models were used to calculate LAI through different variables with a high correlation coefficient (0.97, 0.93, 0.90, 0.90, 0.89 and 0.85) for $LA_{optical}$, PRI, TVI, NDVI, MTVI and Chl. Respectively. The correlation coefficient between actual and predicted models wasused for validation assessment, the higher accuracy for validation showed high accuracy of all generated models, however, PRI index MTVI, TVI, $LA_{optical}$, NDVI and Chl. Index showed relative higher accuracy 0.941, 0.927, 0.927, 0.906, 0.902 and 0.806 respectively. High similarity was found between optical and actual LAI. Generated models are valid during the maximumphase of vegetative growth of strawberry under local conditions of Egyptian Nile delta.

Keywords *Hyperspectral remotely sensed data; LAI; VIs*

1. Introduction

Healthy plant canopy visually appears green because of the significant high absorption of leaf pigments to red and blue spectra with a strong reflectance of green spectrum. Red edge district has a solid retention because of the leaf chlorophyll, nitrogen fixation, and reflection due to mesophyll cells in developing plants (Datt, 1998). Spectral reflectance at the near infrared region is an indication to the vegetation cover and biomass and could be presented as leaf area index (LAI) (Watson, 1947). First defined LAI as the total one-sided area of the canopy per unit ground surface area (Chen and Black, 1992) It is a one-sided area of leaves per unit ground area. It mirrors the biochemical and physiological processes of vegetation; therefore, it is considered a perfect indicator of crop growth and productivity.

Observing the dynamics of LAI is significant for a wide range of agricultural studies including crop monitoring and crop yield estimation (Fang et al., 2011).

The traditional approach of measuring (LAI) includes removal of leaves from the plant and derivation of their cumulative area instrumentally. This approach is destructive, time-consuming and very labor intensive. The rapid and non-destructive method of measuring LAI could be performed using canopy analyzers, such as LAI 2000 Plant Canopy Analyzer (Li-Cor, Lincoln, NE). This device measures optical interference of the canopy by comparing simultaneous measures of light interception above and below the plant canopy and converting this to LAI using standard equations. As this method depends on the spectroscopic parameters of the investigated plants, it is closely related to spectral reflectance measures Qi et al. (2000). Spectroscopic parameters and spectral reflectance characteristics could be represented in forms of broadband and narrowband remotely sensed data. Using broadband data with satellite imagery is powerful in crop mapping and crop acreage estimation; however, it results in loss of detail of vegetative spectral response (Broge and Leblanc, 2001). Spectral reflectance characteristics of plant canopy could be analyzed through hyperspectral data that provides numerous narrow bands at high-resolution (Sahoo et al., 2015).

Many studies have shown the effectiveness of hyperspectral data to improve LAI estimation (Pu et al., 2008; Verrelst et al., 2012; Duan et al., 2014). Hyperspectral data have been used for end-member extraction of mixed pixels Frank et al. (2009), atmospheric correction Perkins et al. (2012), improving the estimation of chlorophyll content and average leaf angle (Atzberger and Richter, 2012), spectroscopic identification of microorganisms (Aboelghar and Abdel Wahab, 2013) and for assessment of infected plants (Abdel Wahab et al., 2017).

Two main strategies have been addressed as methods to analyze the dynamic relation between LAI and spectral reflectance characteristics represented through hyperspectral data: 1) empirical relationship between vegetation indices (VIs) and biophysical parameter's (Xie et al., 2014) inversion of canopy radiative transfer models, such as the PROSAIL model (Jacquemoud et al., 2009). Estimation of (LAI) through empirical models could be applied in three main steps. The first step is the computation of spectral parameters that are significantly correlated with (LAI). This approach was used to estimate LAI of winter wheat (Xie et al., 2014) and to estimate (LAI) of rice at different growth stages under varying nitrogen rates Din et al. (2017).

In the current study, in situ hyperspectral remote sensing measurements in forms of Six hyperspectral vegetation indices (VIs): chlorophyll index (CHI), normalized difference vegetation index (NDVI), photochemical reflectance index (PRI), modified chlorophyll absorption ratio index (MCARI), triangular vegetation index (TVI), modified triangular vegetation index (MTVI) and test LAI-2000 canopy analyzer field measurements with LAI laboratory measurements for two seasons of strawberry were used to generate and validate empirical statistical regression models for LAI inversion in a case study in old strawberry cultivated lands in the Nile delta of Egypt.

2. Materials and Methods

2.1. Study Area and Sampling

The study site is located in El-Dair village, Egypt (latitude 30°22'10.56"N to 30°22'3.30"N, longitude 31°17'17.94"E to 31°17'16.53"E) with a total area of (933.8 m^2) (Figure 1). Investigated samples (strawberry canopy) were cultivated in forty-eight lines with eight meters length for each line. These lines with different treatments of fertilizers and plastic mulches cover all possible treatments of strawberry in Egyptian Nile delta. Three randomly selected samples from each line were considered in the study to establish the dataset for one hundred forty-four samples for each season and total of two hundred eighty-eight samples for the two seasons from which randomly selected two-hundred sixteen (216) measures were considered for modeling and seventy-two (72) measures were considered for

validation process. A GPS (Global Positioning System) was used to locate each measurement in the field.

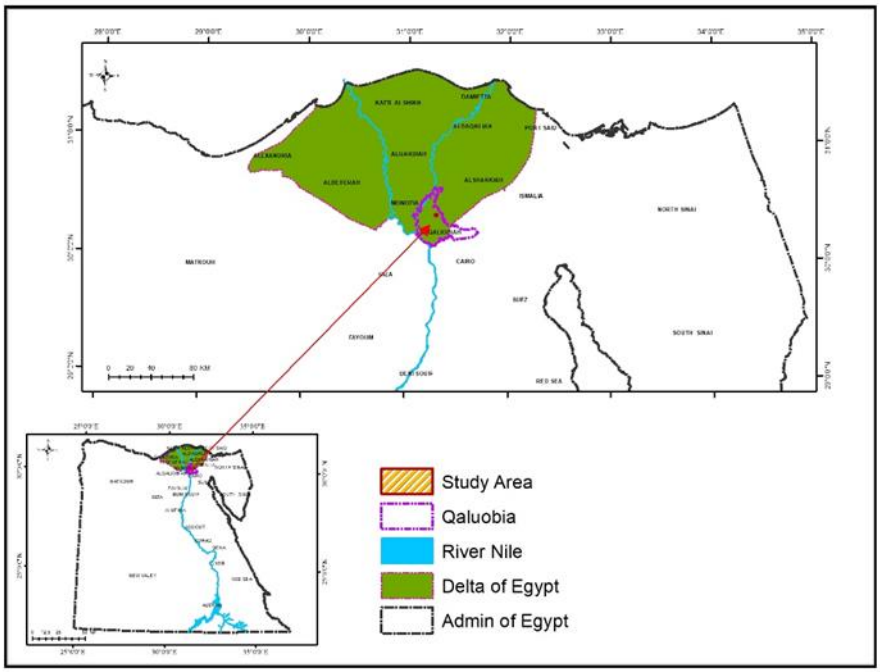

Figure 1: *Location map of the study area*

2.2. Canopy Spectral Reflectance

Measurements of Spectral reflectance were carried out through the day between the hours of 10:00 am and 24:00 pm under a clear and cloudless sky during Maximum vegetative crop growth through two seasons of 2015 and 2016. Canopy spectra were acquired with ASd-4 field spectroradiometer (an analytical spectral device (ASD, Boulder, CO, United States) that covers (350 - 2500 nm) spectral range (Pimstein et al., 2011). The radiometer sensor head was positioned 0.25 m above the canopy, with a nadir field of view. The reference panel ($Baso_4$) white panel was used to convert radiance from a Spectral acquired to derive the reflectance, which was used to calibrate the instrument at 5min intervals prior to each plot reflectance measurement Mahajan et al. (2014). The spectral data were exported to View Spec (ASD, Boulder, CO, United States) software and averaged for each treatment. For the analysis of the Field Spec measurements, six vegetation indices were calculated according to referenced and documented equations as shown in Table 1.

Table 1: *Used vegetation indices*

Vegetation index	Equation	Reference
NDVI	(pNIR - pred) / (pNIR + pred)	Rouse et al. (1974)
CARI	(r700 - r670) - 0.2 * (r700 - r550)	Kim et al. (1994)
PRI	(p531- p570)/(p531+ p570)	Gamon et al. (1997)
MCARI	[(P700-P670)-0.2(P700-P550)](P700/P670)	Daughtry et al. (2000)
TVI	0.5[120(p750-p550)-200(p670-p550)]	Broge and Leblanc (2001)
mTVI	1.2[1.2(p800−p550)-2.5(p670-p550)]	Haboudane et al. (2004)

2.3. LAI Measurements

At the same time as the spectra were acquired, LAI was taken using a Plant Canopy Analyzer (LAI-2000, Li-Cor, Inc., Lincoln, NE, United States) for all investigated samples. The LAI-2000 is amid the most widely used advanced canopy LAI analyzers for many crops. The protocol of using LAI-2000

device was applied with each measure of each sample during the two seasons. This device calculates LAI depending on radiation measurements made with a fish-eye optical sensor of a 148^{o} field of view. One Measurement was carried out above the canopy of the plant and 4 below the canopy are used to determine canopy light interception at 5 angles, LAI is calculated using a radioactive transfer model of in plant canopy. Measurements were made by positioning the optical sensor and pressing a button. The data were mechanically recorded into the control unit for storage and LAI calculations. Several below-canopy readings and the fish-eye view declare that LAI calculations are based on a large sample of the plant canopy. After collecting both above and below canopy measurements, the control unit performs all calculations and the results are available for immediate on-site-examination (LI-COR, Inc., 1992). Leaf samples from each point were collected and LAI was laboratory measured using a planimeter device. The planimetric approach was used for direct laboratory LAI measurements. This method is based on the principle of the correlation between the individual leaf area and the number of area units covered by that leaf in a horizontal plane. A leaf was horizontally fixed to a flat surface, its perimeter was measured with a planimeter, and its area was computed from this perimeter assessment. Planimeter consists of two identically perforated plates mounted in the top of an airtight drum, which is connected to a constant speed rotary pump. One plate, the specimen grid, is uncovered while the measuring grid is covered by an airtight slide. The pressure within the drum (the datum pressure) is noted before any leaves are mounted. Leaves are then mounted on the specimen plate and are held flat by suction pressure. When all leaves are mounted the pressure is brought back to the datum pressure by opening the slide which covers the measuring grid. The area of leaf is equal to the area of the exposed portion of the measuring plate. This area is recorded by a venire scale mounted on the slide.

2.4. Data Analysis

Laboratory measured LA_{Direct} was statistically correlated with each individual field measured factor. Working in this study could be divided into three parts: laboratory LAI measurements, in situ field measurements and regression analysis between laboratory LA_{Direct} versus optical $LA_{Optical}$ and between LA_{Actual} and each individual vegetation index. Modeling and validation should be process were carried out through cross-validation approach. In cross-validation approach, the data were divided into four subsets. For each modeling trial, seventy-two (72) measures were used as the validation set while the other subsets were put together to form a training set. Then, error estimation was averaged over the four trials to get the total effectiveness of the proposed model. In this approach, each measure was used twice, once in a validation set and ones in the training set.

3. Results and Discussion

Generally, the direct method is assumed to be the most correct for estimating LAI. This method serves as a reference for the performance of the indirect methods. In order to be able to use the indirect methods to determine the LAI, regression equations have been calculated between the results of the indirect and the direct method.

Regression analysis between laboratory measured LA_{Direct} as the dependent variable and each field measured factor as independent variable showed that all factors were highly correlated with laboratory measured LA_{Direct} as the correlation coefficient ranged from (0.85) to (0.97).This is clear evidence that spectral vegetation variables could be considered realistic indicators for canopy phonological, physiological and production parameters. The high statistical similarity between optical field measured $LA_{Optical}$ and laboratory LA_{Direct} is also an evidence for the high accuracy of the optical LAI measurements by LAI-2000 canopy analyzer. Similarly, (Mussche et al., 2001) reported high similarity between $LA_{Optical}$ and LA_{Direct} as long as no changes in the canopy structure are made (Jonckheere et al., 2005) also reported that no significant difference was found between LA_{Direct} and $LA_{Optical}$, however, correction for blue light scattering, clumping, and the non-leafy material is necessary when measuring LAI for tree cover.

All tested vegetation indices were highly correlated with LAI; however, the relatively high accuracy was found with PRI with (0.93) correlation coefficient. The generated models to retrieve LAI from spectral vegetation indices and the model that identify the correlation between LA_{Direct} and $LA_{Optical}$ along with the correlation coefficient for each generated model. Regression models between LA_{Direct} and each factor with the highest correlation coefficient were considered and shown in Table 2.

Validation process was applied using the correlation coefficient between LAI_{Actual} and $LAI_{Predicted}$. It was performed four times according to cross-validation approach and the average of the four trials was registered as shown in Figure 2.

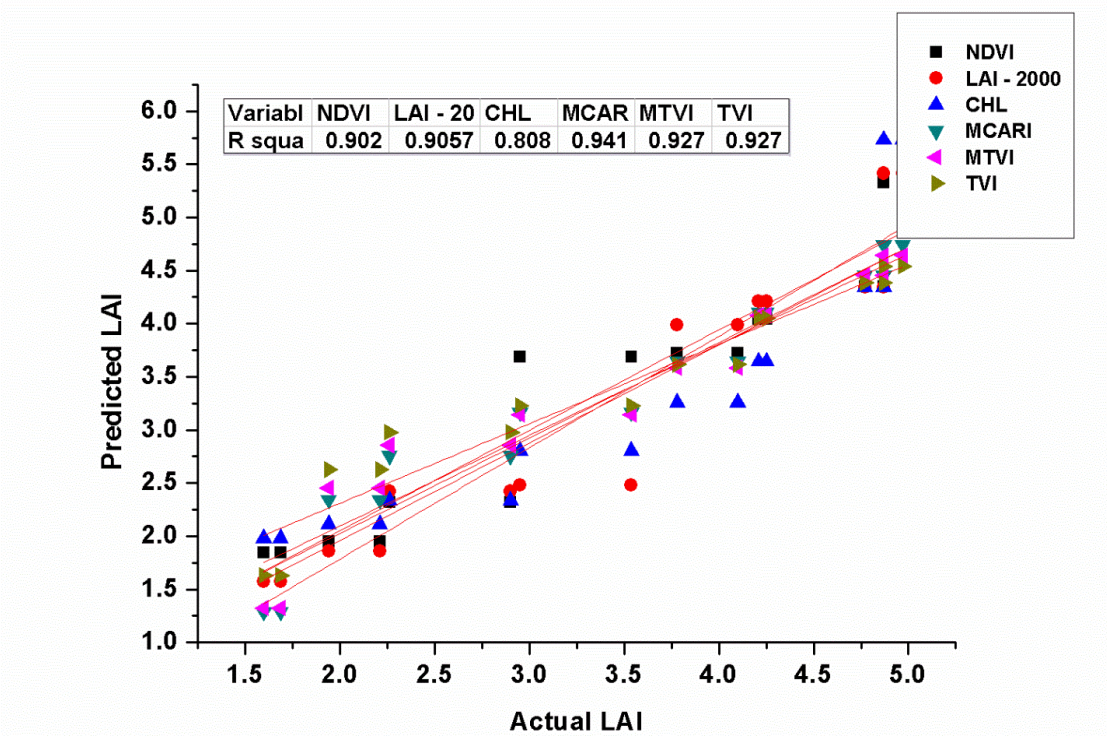

Figure 2: *Correlation coefficient between actual and predicted LAI through different generated models*

Table 2.*Regression analysis between the dependent variable (Laboratory measured LAI) and each field measured factor*

Independent variable	Slope	Intercept	R^2	SE	Model
$LAI_{Optical}$	0.53	3.19	0.97	0.02	$LAI_{lab} = 0.53LAI_{field} + 3.19$
NDVI	9.90	-3.53	0.90	0.67	$LAI_{lab} = 9.9NDVI - 3.53$
PRI	41.83	3.68	0.93	2.90	$LAI_{lab} = 41.83PRI + 3.68$
ChI	2.09	2.96	0.85	0.18	$LAI_{lab} = 2.09ChI + 2.96$
TVI	0.14	0.46	0.90	0.01	$LAI_{lab} = 0.14TVI + 0.46$
MTVI	5.81	0.20	0.89	0.42	$LAI_{lab} = 5.81MTVI + 0.2$

The direct method to estimate LAI quantifies the change of the needle area itself rather than measuring other variables that are influenced by canopy structure, e.g. radiation transmission and gap size, as in optical methods. At the same time, the direct methods to estimate LAI are more laborious and time-consuming than optical methods. Therefore, the main objectives of the current study were to propose a non-destructive method to estimate LAI and to compare optical and direct methods for LAI estimation of Strawberry plants. Basically, optical approach of LAI measurements depends on measuring light interception of a vegetation canopy. Comparative analysis was carried out between optical and direct LAI. Six regression models to retrieve LAI from spectral variables were generated with adequate accuracy ranged from (0.808) to (0.941). Generated models are site-specific limited to the conditions of observation including (site, crop phonology and meteorological conditions). These models could be applied regularly to predict LAI during the phase of the maximum vegetative growth. These regular monitoring of LAI could be the basis of early yield prediction system as canopy vigor is an accurate indicator for expected yield.

Our analysis is consistent with several studies that also compared optical non destructive LAI measures to direct destructive LAI estimates for different crops. Wihelm et al. (2000) found that the percentage of underestimation of LAI of Corn (Zea mays L.) was higher in case of direct methods than optical method. Oppositely, Hunt et al. (1999) found that the LAI 2000 overestimated LAI in soybean and the bean leaf beetle (C. trifurcate). They suggested that the optical instruments should overestimate LAI since instruments do not discriminate between leaf and stem; therefore, all plant parts are counted as leaf area in proportion to the amount of light they intercept. In contrast, destructive sampling measured only the area of leaf blades. We assume that the difference in the two trends of results is dependent on the differences between the crops being investigated. Grass stems (as the case of strawberry) are very thin and occupy a small area in proportion to total leaf area.

4. Conclusion

Six spectrally based regression models to retrieve LAI for strawberry cultivations in Egyptian Nile delta were generated in this study. All models showed high accuracy ranged from (0.808) to (0.941) as the correlation coefficient between actual and predicted LAI. Spectral variables were used in form of spectral vegetation indices. Among these (VIs), PRI showed a relatively higher accuracy than the rest of (VIs). The study confirmed the high accuracy of the optical field measured LAI as high correlation coefficient was found between LA_{Actual} and $LA_{Optical}$. Generated models are easy to be applied, however, they are site-specific models limited to the conditions of the observation. Proposed models could be used for early estimation of strawberry yield as vegetation health is an indicator for expected yield under the assumption of the absence of any up normal conditions (unexpected climatic conditions, epidemic infection etc.).

References

Abdel Wahab, H., Aboelghar, M., Ali, A. and Yones, M. 2017. Spectral and molecular studies on gray mold in strawberry. *Asian Journal of Plant Pathology*, 11, pp.167-173.

Aboelghar, M. and Abdel Wahab, H. 2013. Spectral footprint of Botrytis cinerea, a novel way for fungal characterization. *Advances in Bioscience and Biotechnology*, 4, pp.374-382.

Aboelghar, M., Arafat, S., Abo Yousef, M., El-Shirbeny, M., Naeem, S., Massoud, A. and Saleh, N. 2011. Using SPOT data and leaf area index for rice yield estimation in Egyptian Nile delta. Egyptian *Journal of Remote Sensing and Space Science*, 14(2), pp.81-89.

Atzberger, C. and Richter, K. 2012. Spatially constrained inversion of radiative transfer models for improved LAI mapping from future Sentinel-2 imagery. *Remote Sensing of Environment*, 120, pp.208-218

Broge, H. and Leblanc, E. 2001. Comparing prediction power and stability of broadband and hyperspectral vegetation indices for estimation of green leaf area index and canopy chlorophyll density. *Remote Sensing of Environment*, 76, pp.156-172.

Chen, J. and Black, T., 1992. Defining leaf area index for non-flat leaves. *Plant Cell & Environment*, 15(4), pp.421-429.

Datt, B. 1998. Remote sensing of chlorophyll a, chlorophyll b, chlorophyll a+b, and total carotenoid content in eucalyptus leaves. *Remote Sensing of Environment*, 66(2), pp.111-121.

Daughtry, C.S.T., Walthall, C.L., Kim, M.S., Brown de Colstoun, E. and McMurtrey III, J.E. 2000. Estimating corn leaf chlorophyll concentration from leaf and canopy reflectance. *Remote Sensing of Environment*, 74, pp.229-239.

Duan, S.B., Li, Z.L., Wu, H., Tang, B.H., Ma, L., Zhao, E. and Li, C. 2014. Inversion of the PROSAIL model to estimate leaf area index of maize, potato, and sunflower fields from unmanned aerial vehicle hyperspectraldata. *International Journal of Applied Earth Observation and Geoinformation*, 26, pp.12-20.

Fang, H., Liang, S. and Hoogenboom, G. 2011. Integration of MODIS LAI andvegetation index products with the CSM-CERES-Maize model for corn yield estimation. *International Journal of Remote Sensing*, 32(4), pp.1039-1065.

Franke, J., Roberts, D., Halligan, K. and Menz, G. 2009. Hierarchical Multiple Endmember Spectral Mixture Analysis (MESMA) of hyperspectral imagery for urban environments. *Remote Sensing for Environment*, 113, pp.1712-1723.

Gamon, J.A., Serrano, L. and Surfus, J.S. 1997. The photochemical reflectance index: an optical indicator of photosynthetic radiation use efficiency across species, functional types and nutrient levels. *Oecologia*, 112, pp.492-501.

Haboudane, D., Miller, J.R., Pattey, E., Zarco-Tejada, P.J. and Strachan, I.B. 2004. Hyperspectral vegetation indices and novel algorithms for predicting green LAI of crop canopies: modeling and validation in the context of precision agriculture. *Remote Sensing of Environment*, 90, pp.337-352.

Hunt, T.E., Haile, F.J., Hoback, W.W. and Higley, L.G. 1999. Indirect measurement of insect defoliation. *Environ. Entomol.*, 28, pp.1136-1139.

Jacquemoud, S., Verhoef, W., Baret, F., Bacour, C., Zarco-Tejada, P.J., Asner, G.P., Franc, C. and Ustin, S.L. 2009. PROSPECT + SAIL models: a review of use for vegetation characterization. *Remote Sensing of Environment*, 113, pp.56-66.

Jonckheere, I., Muys, B. and Coppin, P. 2005. Allometry and evaluation of in situ optical LAI determination in Scots pine: a case study in Belgium. *Tree Physiology*, 25, pp.723-732

Kim, M.S., Daughtry, C.S.T., Chappelle, E.W. and McMurtrey, J.E. 1994. *The use of high spectral resolution bands for estimating absorbed photosynthetically active radiation (Apar)*. In: Proceedings of the Sixth Symposium on Physical Measurements and Signatures in Remote Sensing, Val D'Isere, France. pp.299-306.

LI-COR. 1992. *LAI-2000 Plant Canopy Analyzer*. Instruction Manual. Lincoln, NE, USA.

Mairaj, D., Wen, Z., Rashid, M., Wang, S. and Zhihua S. 2017. Evaluating hyperspectral vegetation indices for leaf area estimation of *Oryzastiva* L. at diverse phenological stages. *Frontiers in Plant Science*, 8, p.820.

Mahajan, G.R., Sahoo, R.N., Pandey, R.N., Gupta, V.K. and Kumar, D. 2014. Using hyperspectral remote sensing techniques to monitor nitrogen, phosphorus, Sulphur, and potassium in wheat (Triticumaestivum L.). *Precision Agriculture*, 15(2), pp.227-240.

Mussche, S., Samson, R., Nachtergale, L., De Schrijver, A., Lemeur, R. and Lust, N. 2001. A comparison of optical and direct methods for monitoring the seasonal dynamics of leaf area index in deciduous forests. *Silva Fennica*, 35(4): 373-384.

Perkins, T., Adler-Golden, S., Matthew, M.W., Berk, A., Bernstein, L.S., Lee, J. and Fox, M. 2012. Speed and accuracy improvements in FLAASH atmospheric correction of hyperspectral imagery. *Optical Engineering*, 51(11), pp.111707-111711.

Pimstein, A., Karnieli, A., Bansal, S.K. and Bonfil, D.J. 2011. Exploring remotely sensed technologies for monitoring wheat potassium and phosphorus using field spectroscopy. *Field Crops Research*, 121(1), pp.125-135.

Pu, R., Gong, P. and Yu, Q. 2008. Comparative analysis of EO-1 ALI and hyperion, and Landsat ETM+ Data for mapping forest crown closure and leaf area index. *Sensors*, 8, pp.3744-3766.

Qi, J., Kerr, Y.H., Moran, M.S., Weltz, M., Huete, A.R., Sorooshian, S. and Bryant, R. 2000. Leaf area index estimates using remotely sensed data and BRDF models in a semiarid region. *Remote Sensing of Environment*, 73, pp.18-30.

Xie, Q., Huang, W., Dong L., Chen, P., Wu, C., Yang, G., Zhang, J., Huang, L. and Zhang, D. 2014. Leaf area index estimation using vegetation indices derived from airborne hyperspectral images in winter wheat. *IEEE Journal of Selected Topics in Applied Earth Observations and Remote Sensing*, 7(8), pp.3586-3594.

Rouse, J.W., Haas, R.H., Schell, J.A. and Deering, D.W. 1974. *Monitoring vegetation systems in the Great Plains with ERTS*. In: Freden, S.C., Mercanti, E.P. and Becker, M. (eds) Third Earth Resources Technology Satellite-1 Symposium. Technical Presentations, NASA SP-351, NASA, Washington, D.C. Volume I, pp.309-317.

Sahoo, R.N., Ray, S.S. and Manjunath, K.R. 2015. *Hyperspectral remote sensing of agriculture.* CRC Press, Boca Raton, FL.

Verrelst, J., Romijn, E. and Kooistra, L. 2012. Mapping vegetation density in a heterogeneous river floodplain ecosystem using paintable CHRIS/PROBA data. *Remote Sensing*, 4, p.2866-2889.

Watson, D.J. 1947. Comparative physiological studies in the growth of field crops. I. Variation in net assimilation rate and leaf area between species and varieties, and within and between years. *Annals of Botany*, 11, pp.41-76.

Wilhelm, W.W., Ruwe, K. and Schlemmer, M.R. 2000. Comparison of three leaf area index meters in a corn canopy. *Crop Sci.*, 40, pp.1179-1183.

Cloud Publications
International Journal of Advanced Remote Sensing and GIS
2019, Volume 8, Issue 1, pp. 2983-2996
ISSN 2320 – 0243, Crossref: 10.23953/cloud.ijarsg.409

Research Article

Remote Sensing of Watershed: Spectral Ratioing Study for Watershed Management

Deepa D. Naik and Vishal V. Somni

Department of Geography, Geoinformatics, Savitribai Phule Pune University, Pune

Correspondence should be addressed to Deepa D.Naik, *deepanaik.2009@gmail.com*

Publication Date: 13 April 2019

DOI: https://doi.org/10.23953/cloud.ijarsg.409

Abstract River catchments are basic hydrologic units and are important from the point of view of water budget management. There are longitudinal and seasonal variations in the catchment due spatio-temporal differences in terms of lithology, rainfall condition, intensity, land use land cover. Geospatial techniques and satellite data provide cost effective information about watershed. It is easy and profitable to use these techniques as data acquisition is easy, processing is fast Ratioing is one of the digital image processing technique useful to extract information about catchment characteristics and parameters for watershed development and planning. Indices give subtle tonal variations to identify the features spectrally. It de-emphasizes the effect of sun illumination, effect of topographic factors and highlights the region as per spectral properties of specific features. It enhances the quality of image to study the features in detail. These indices are also used to improve the accuracy of classification algorithms. For the current study Landsat-8 OLI used to study NDMI, EVI2, EBI, BSI, MNDWI and MODIS product MOD11A2 and MOD13A2 has used to study TCI, VCI and VHI indices. The study indicates that indices are one of the good techniques to extract spatially and temporally varying features. NDMI provides moisture condition information across watershed. EBAI and BSI highlights built up area and give idea about impervious surface. BSI gives information about bare soil where erosion mostly very common. EVI2 enhance the vegetation and MNDWI emphasize the waterbodies which seasonally varies. TCI, VCI and VHI useful to study drought conditions. The correlation between TCI and VHI, VCI and VHI studied to get information about drought. The above indices useful to study and extract several parameters to study runoff, erosion, sedimentation, ground water condition etc. Indices provide unidealistic information at various wavelengths. Repetitive coverage allows to monitoring dynamic features like water, vegetation, soil. Indices enhance the spectral information, increase the reparability of the classes of interest, and improve the quality of mapping. Such kind of technique's are beneficial for conservation and management of the earth resources for local government bodies to conserve the water and to reduce the intensity of the drought.
Keywords *Spectral ratioing; Watershed; land surface temperature; remote sensing; drought*

1. Introduction

Remote sensing of watershed plays vital role in water resource management. The country like India, where economy is mainly relying on the agriculture. In unfavorable condition farmers committed to suicide. Over exploitation of water resources, elongation of dry period, evapotranspiration and

decreasing rainfall are common problems and have impact on crop yields and agricultural sectors but also to forestry, tourism and environment sectors. Proper development and management of watershed leads to economic growth of that region and country ultimately. It furnishes information about the composition of the object. Spectral reflectance of any object changes with chemical and physical properties, structure of the object. These differences make it possible to identify different earth's materials by analyzing their spectral pattern. Watershed is hydrological unit and has enormous mixing of spectral reflectance within the region is common problem. Watershed in composed with so many features agriculture, forest, bare soil, impervious areas, urban features and water bodies. It is difficult to study all these features together with raw/ original image and all these objects have its unique importance in water resources and can be used as good indicators to study ground water recharge, runoff, erosion and sedimentation, to assess drought, flood. Studying each of the objects spectrally gives precise information about region and spectral correlation emphasized on condition of the objects and there inter-relationship with other features. Indices are good indicators of earth dynamic changes taken place beneath and on the earth surface. The changes one could not recognize with naked eyes those would be easily identified using spectrum. NDBI approach used to extract built-up areas of Lahore Pakistan (Bhatti and Tripathi, 2014). LAI calculations have been done with direct and indirect methods and discussed (Zheng and Moskal, 2009). Single band method used to extract open water information from multispectral image (XU HANQIU 2006). Comparative study between SPI, SWI and VHI for the period of pre-monsoon and monsoon seasons over Aravalli terrain (Bhuiyan, 2004). Comparative study TCI, VCI, VHI, TDVI and DSI in drought monitoring and yield impact for better understanding the differences and potential monitoring ability among these indices (Zhuo et al., 2016). TCI, VCI and VHI indices studied using MODIS data. compared TCI, VCI and VHI to obtain a better understanding about the differentiation between each index and their application for monitoring drought in East Java on El-Nino year of 2015 (Amalo et al., 2017). Studied relationship between water parameters and water indices of spectral images. Water parameters like pH, TDS, Alkalinity, Electrical conductivity, Cl, Na, SO_4, TH, etc. from 17 stations with two seasons using Landsat 8 OLI imageries has been analyzed (Mustafa et al., 2017). Water indices like NDWI, MNDWI, WRI, etc. were calculated with correlation and regression analysis. carried out extraction of built up area study using Landsat 8. The normalized difference built-up index (NDBI) has been useful for mapping urban built-up areas (Bhatti and Tripathi, 2014).

2. Study Area

The Krishna is fourth biggest river in terms of water inflows and river basin area in India. The Krishna River is almost 1400 km long. It is a major source of irrigation system for Maharashtra, Karnataka, Andhra Pradesh, and Telangana State. Figure 1 shows the location of the study region.

The Krishna basin extends over the same districts where total area covered is 258,948 sq. km, which is nearly 8% of the total geographical area of country. The extent of Krishna basin is between $73^{\circ}\ 17'\ to\ 81^{\circ}\ 9'E$ Longitude and $13^{\circ}\ 10'to\ 19^{\circ}\ 22'N$ Latitude. It is bounded by Balaghat range on the North, by the Eastern Ghats on the south and the east and by the Western Ghats in the west. Krishna River rises from Western Ghats near Jor Village of Satara district of Maharashtra at an altitude of 1337m just north to Mahabaleshwar. Its principal tributaries joining from right are the Ghatprabha, the Malprabha and the Tungabhadra whereas those joining from left are the Bhima, the Musi and the Munneruriver. The major part of basin is covered with agricultural land which approximately 75.86% of the total area and 4.07% of the basin is covered by water bodies. The basin spreads over 56 parliamentary constituencies (2009) comprising 23 of Andhra Pradesh, 18 of Karnataka and 15 of Maharashtra.

3. Data and Material

For this study, the following datasets and equations are utilized. Landsat-8 OLI image has been used for the present study where it has total 11 bands. Moderate Resolution Imaging Spectro-radiometer (MODIS) which is hyperspectral dataset. The product MOD11A2 and MOD13A2 has used to study TCI, VCI and VHI indices.

MOD13A2 is Terra Vegetation Indices 16-Day composite Level 3 Global 1 km product Sinusoidal Grid version 06. MOD11A2 is product of MODIS is Terra Land Surface Temperature / Emissivity, which is 8-days composite Level 3 product Sinusoidal Grid version 06.

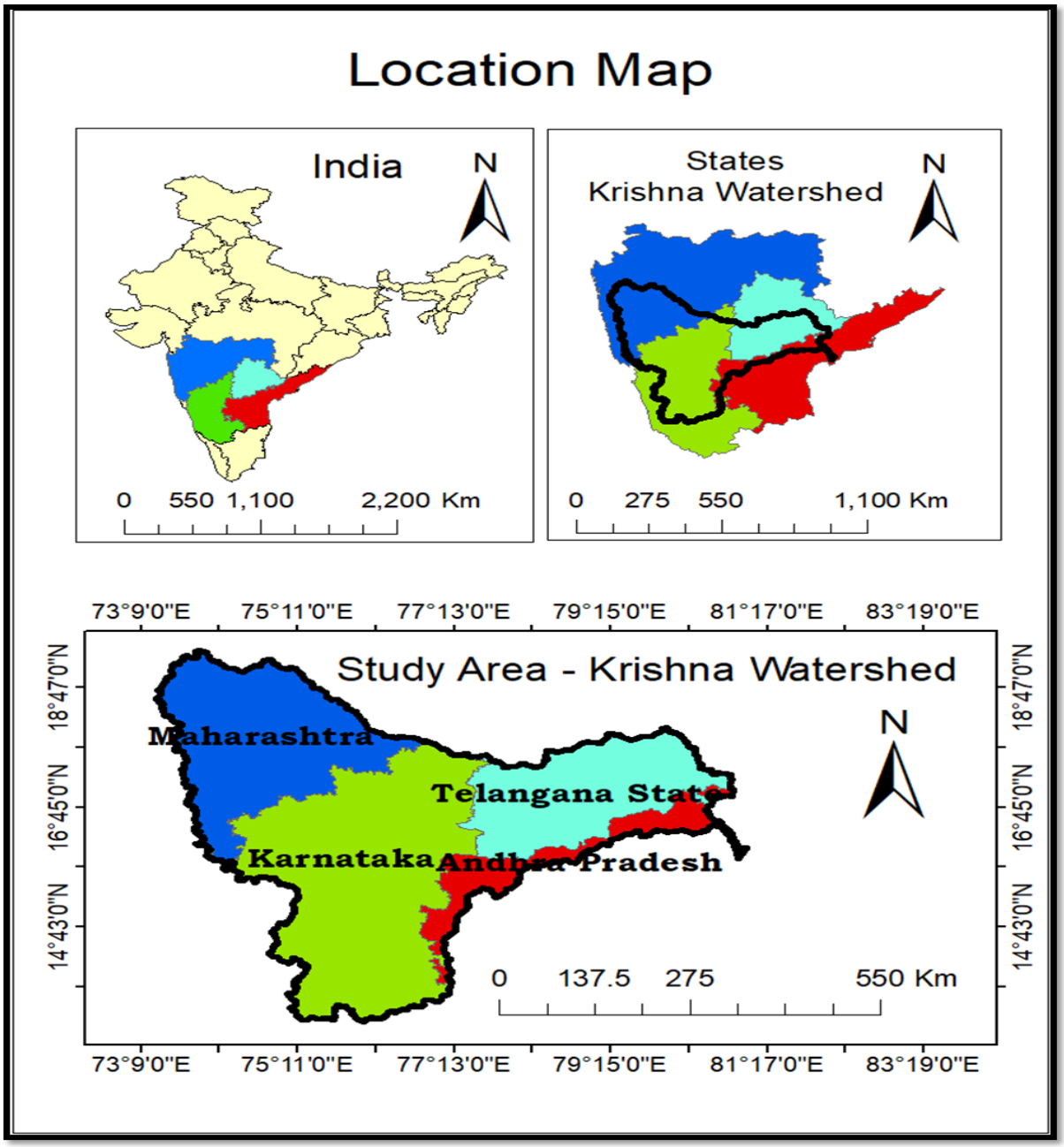

Figure 1: *Location map material and methods*

3.1. Use of Indices

Indices are Normalized Difference Moisture Index (NDMI) gives information about leaf moisture condition, which would be good indicators for forest studies like biomass estimation. Forest health study along with this gives some hints about ground water potential region as well as moisture is high there are chances of getting high ground water table. On other hand, it is also good for wet land identification.

Table 1: *Applied Indices and product information*

Sr. No.	Index Name	Formula	Product
1	Normalized difference moisture index (NDMI)	$NDMI = \frac{RED - NIR}{RED + NIR}$ Source: USGS Indices Guide	LANDSAT_8 OLI (Operational Land Imager)
2	Enhanced Vegetation Index_2 (EVI_2)	$EVI_2 = \frac{2.5 \times (NIR - RED)}{NIR + (2.4 \times RED) + 1}$ Source: Zhangyang Jiang, et al., 2007	LANDSAT_8 OLI (Operational Land Imager)
3	Enhanced Built-up Area Index (EBAI)	$EBAI = \frac{Ultra\ BLUE - BLUE}{Ultra\ BLUE + BLUE}$ *Self detected	LANDSAT_8 OLI (Operational Land Imager)
4	Bare Soil Index (BSI)	$BSI = \frac{(SWIR_1 + RED) - (NIR + BLUE)}{(SWIR_1 + RED) + (NIR + BLUE)}$ Source: Duy N B and Giang T T H, 2012	LANDSAT_8 OLI (Operational Land Imager)
5	Modified Normalized Difference Water Index (MNDWI)	$MNDWI = \frac{GREEN - SWIR_2}{GREEN + SWIR_2}$ Source: Mustafa T. Mustafa, et al., 2017	LANDSAT_8 OLI (Operational Land Imager)
6	Temperature Condition Index (TCI)	$TCI = 100 \times \frac{LST_{max} - LST_i}{LST_{max} - LST_{min}}$ Source: Amalo, 2017	MODIS – MOD11A2
7	Vegetation Condition Index (VCI)	$VCI = 100 \times \frac{NDVI_i - NDVI_{min}}{NDVI_{max} - NDVI_{min}}$ Source: Bhuiyan, 2004	MODIS – MOD13A2
8	Vegetation Health Index (VHI)	$VHI = 0.5 \times TCI + 0.5 \times VCI$ Source: Bhuiyan, 2004	MOD11A2 and MOD13A2

Enhanced Vegetation Index_2 (EVI_2) along with NDMI also use to study carbon sequestration, potential runoff areas and erosion zones. Wherever there is less moisture or less vegetation, in general runoff and erosion would be high. EVI_2 helpful in improving linearity with biophysical vegetation properties and in reducing saturation effects found in densely vegetated surfaces, commonly encountered in the Normalized Difference Vegetation Index (NDVI.) Lack of vegetation cover, less plants and less groundwater storage lead to emerge drought.

Bare soil index (BSI) used in identification and mapping of bare soil would be easy using indices for further land resource management and development planning. Bare soil is the region where erosion is severely observed and there would be loss of soil so with proper management practices. Such kind of losses can be identified using such bare soil index map in once glance. It is feasible to make out regions where management is required. Modified Normalized Difference Water Index (MNDWI) is useful to differentiate land and water. It is useful to delineate shoreline which is quite complex feature. MNDWI is helpful to extract water features as in this water get emphasized. For agriculture management, for cropping pattern study such kind of index is useful which highlight the water bodies. Enhanced Built-up Area Index (EBAI), it is useful to extract built-up region for settlement planning for rehabilitation in case of occurrence of any disasters like landslide and flood, this index is useful.

Temperature Condition Index (TCI): It is drought-monitoring index. TCI used to determine vegetation stress caused by temperature and excessive wetness (Singh et al., 2003). Mostly TCI shows the temperature and dryness of the vegetation cover. Lower TCI values represent high temperature and dry area and higher TCI values represents optimal condition (Ghaleb et al., 2015).

Vegetation Condition Index (VCI): Vegetation Condition Index rescales dynamics between 0 and 100 where it ranges extremely bad to optimum condition of moisture for vegetation (Kogan, 1995). VCI is useful to study vegetation stress due to temperature effect on crops and helps to study drought over an area.

Vegetation Health Index (VHI): VCI and TCI characterize respectively the moisture condition and thermal condition of vegetation while VHI represents overall vegetation health (Kogan, 2001). VHI computed by combining TCI values and VCI values together. During the calculation of VHI, an equal weight was assigned to both TCI and VCI since the moisture and temperature condition during the vegetation cycle is currently not known and thus is assumed that the share of weekly TCI and VCI is equal (Kogan, 2001). Lower the values of VHI, greater the intensity of drought whereas higher the VHI values, lesser the intensity of drought.

3.2. Calculation of Land Surface Temperature (LST)

Step 1. Conversion of Digital Number (DN) to Spectral Radiance (L):

$$L_\lambda = M_L Q_{cal} + A_L$$

Where,

L_λ = TOA spectral radiance (watt / (m2*srad*µm))

M_L = Band specific multiplicative rescaling factor from metadata

A_L = Band specific additive rescaling factor from metadata

Q_{cal} = Quantized and calibrated standard product pixel values (DN)

Step 2. Conversion of spectral radiance (L) to Top of Atmosphere Brightness Temperature (T):

$$T = \frac{K_2}{\ln(\frac{K_1}{L_\lambda} + 1)} - 273.15$$

Where,

T = Top of Atmosphere Brightness Temperature (K)

L_λ = TOA spectral radiance (watt / (m2*srad*µm))

K_1 = Band specific thermal conversion constant from the metadata

K_2 = Band specific thermal conversion constant from the metadata

Step 3. Land Surface Emissivity calculation:

$$e = 0.004 * PV + 0.986$$

Where,

PV = Proportion of Vegetation, which is calculated by the following formula,

$$PV = (NDVI - NDVI_{Min}/NDVI_{Max} - NDVI_{Min})^2$$

Where, NDVI is calculated by following formula,

$$NDVI = (NIR - RED) \ / \ (NIR + RED)$$

Step 4. Estimation of Land Surface Temperature (LST):

$$LST = \frac{T}{1} + w \times \left(\frac{T}{P}\right) \times ln(e)$$

Where,

LST = Land Surface Temperature (in Kelvin)

BT = At-satellite Brightness Temperature (in Kelvin)

w = Wavelength of emitted radiance (11.5 µm)

$P = h * c/s$ (1.438*10-2 mK)

Where,

h = Plank's constant (6.626*10-34Js)

c = Velocity of Light (3*108 m/s)

s = Boltzmann constant (1.38*10-23 J/K)

Calculate the LST for both the band 10 and band 11 in kelvin and 273.15 subtracted from both the raster files to get the temperature in °K. Finally, average of the two bands temperature is taken for study.

4. Results and Discussion

Enhanced Vegetation Index_2 (EVI_2)

Enhanced vegetation index, Modify the original values to more emphasize on vegetation patches within the region. Improvement over NDVI by optimizing the vegetation signal. It uses the blue reflectance region to correct for soil background signals and to reduce atmospheric influences, including aerosol scattering. In Figure 2, shades of green color indicate the vegetation distribution. Dark green show dense vegetation, light green color shows less dense vegetation cover such enhanced image would be useful to study minor vegetation changes.

Normalized Difference Moisture Index (NDMI)

It is useful to study moisture changes near infra-red (NIR) and Shortwave infra-red (SWIR), which is sensitive to the absorbance of leaf moisture (Figure 3). Dense forest in the image showing high moisture content as per density of vegetation moisture content keep on changing. Light green color shows less moisture and dark green color shows more moisture. Useful for various forestry applications like finding the forest type along with the probable identification of trees.

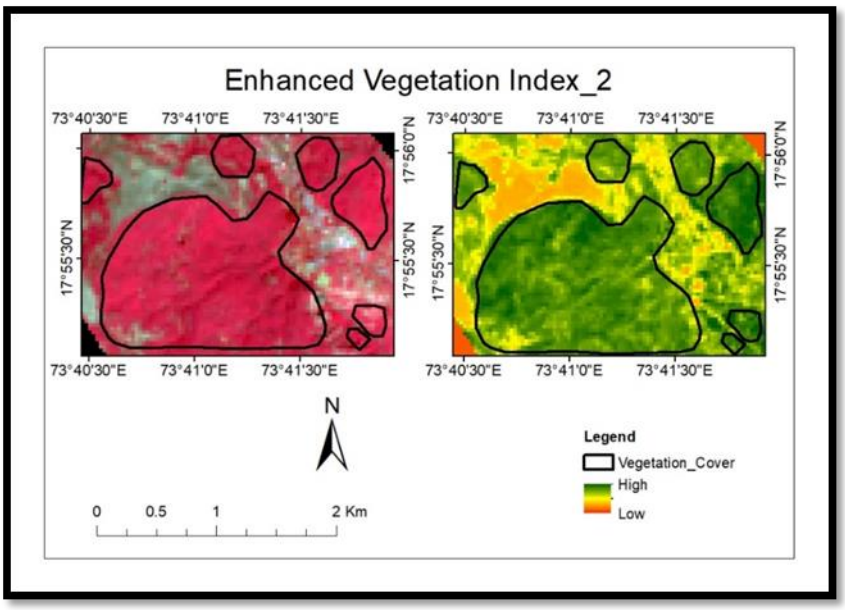

Figure 2: *Enhanced Vegetation Index_2 (EVI_2)*

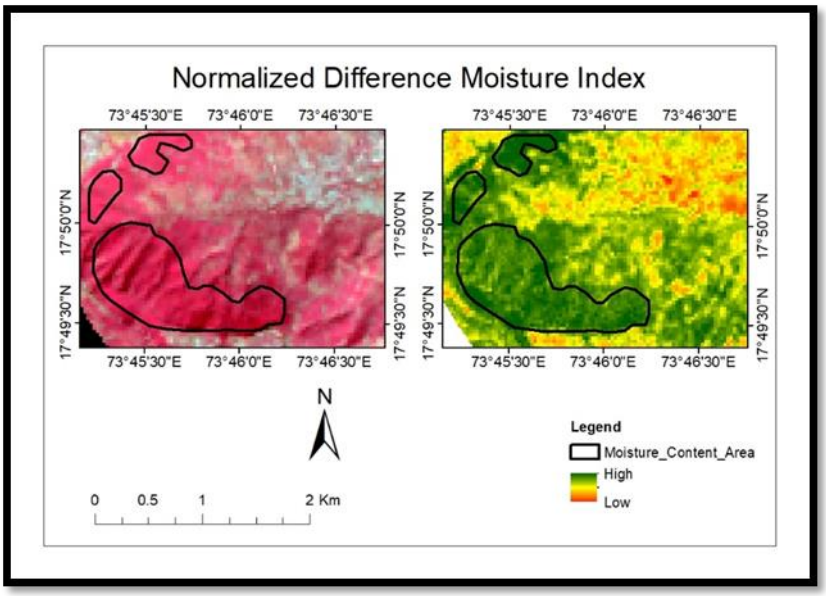

Figure 3: *Normalized Difference Moisture Index (NDMI)*

Bare Soil Index (BSI)

Monitoring bare soil region is important. Plays important role in ecosystem. These are the region where further development could be happened. On the other hand, these are the region known for soil erosion and runoff. Index is based on significant differences of spectral signature in the near infrared between the bare-soil and the backgrounds.

Figure 4 show dark brown to orange shade shows bare soil patches which can be easily delineate. Minor tonal variation also can easily observed.

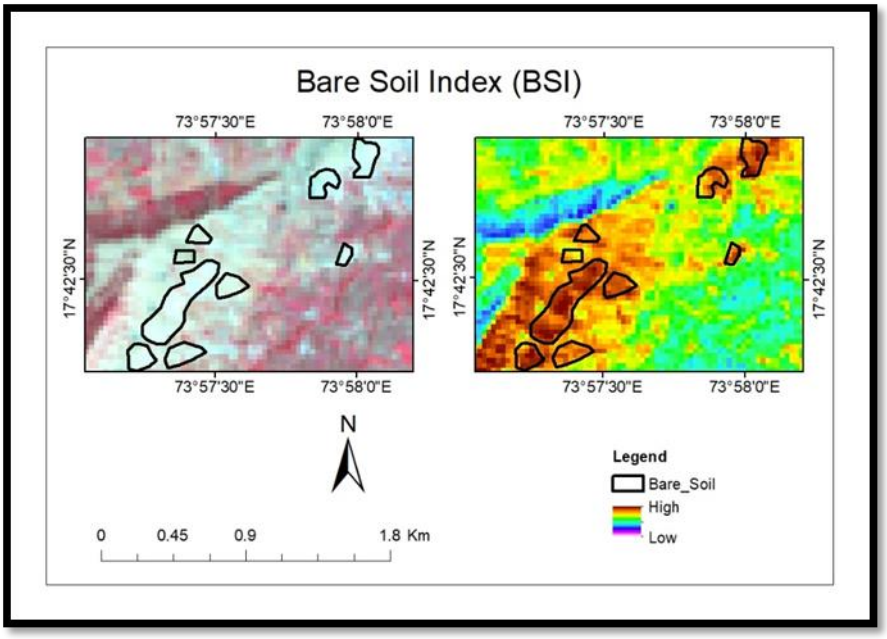

Figure 4: *Bare Soil Index (BSI)*

Modified Normalized Difference Water Index (MNDWI)

Substitution of a mid-infrared band. For the near infrared band used in the NDWI. It emphasizes water bodies. While suppressing and even removing built-up land noise as well as vegetation and soil noise. NDWI is sometimes over estimate as it mixed with soil, built up and vegetation. MNDWI highlight the water features. In case of raster edges cannot be easily delineated there would always mixing at the edges so such kind indices are useful to differentiate and highlight water bodies from surrounding features. In the Figure 5, mixing is easily observed at the edges so after applying index it would be easily noticeable.

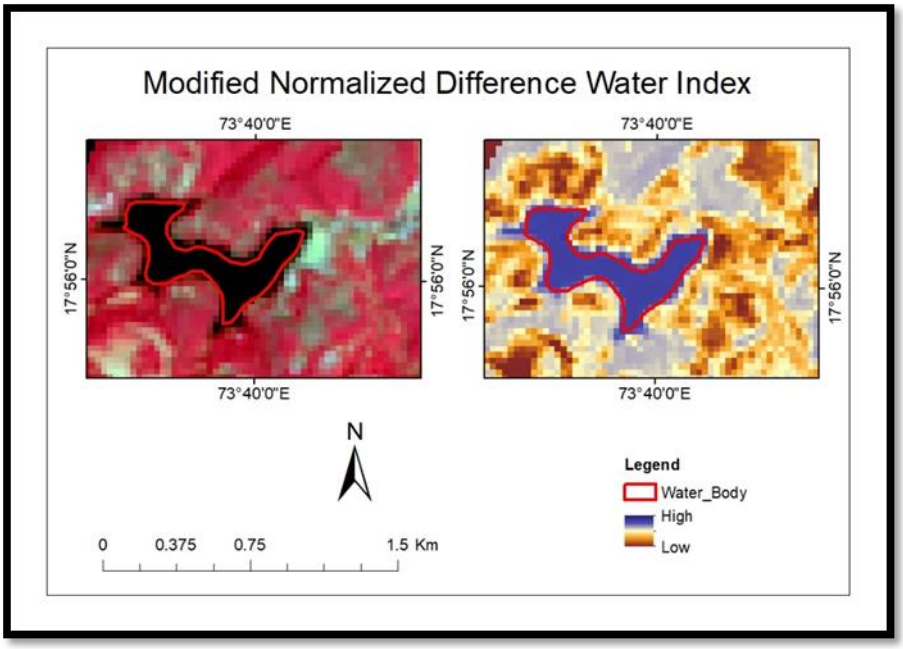

Figure 5: *Modified Normalized Difference Water Index (MNDWI)*

Enhanced Built-up Area Index (EBAI)

It is always difficult to identify built up area as it gets easily mixed with other background features like fallow and bare soil and vegetation however after applying this built up index. The built-up area is highlighted in Figure 6 white color which could be easily differentiate from the other background region.

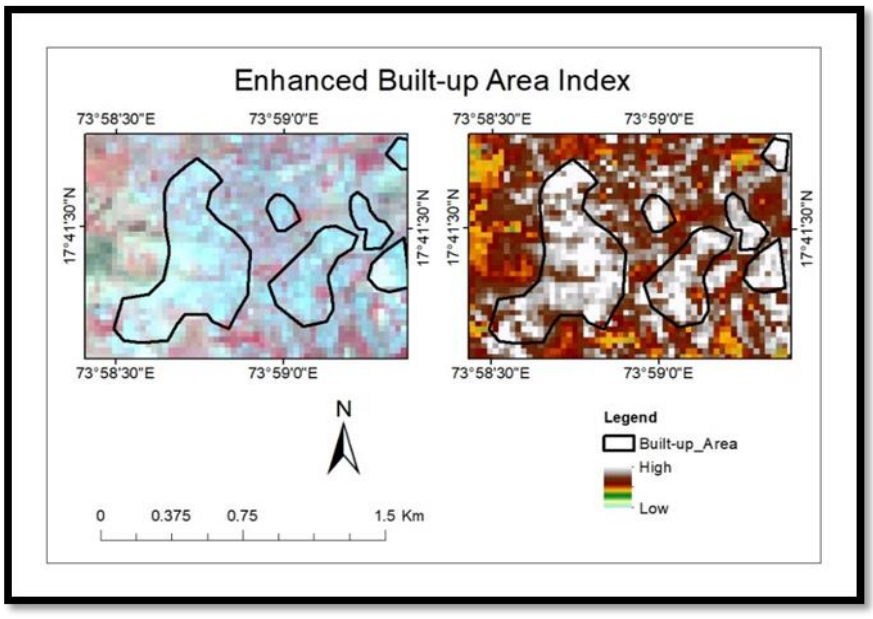

Figure 6: *Enhanced Built-up Area Index (EBAI)*

Temperature Condition Index (TCI)

Temperature Condition Index is one of the drought-monitoring indexes, which is generating by using MODIS product. Lower TCI values represent high temperature and dry area and higher TCI values represents optimal condition. TCI used to determine vegetation stress caused by temperature and excessive wetness (Singh et al., 2003). The present study tells about the temperature index variation from 0 to 100 in 3 years of 2014 to 2016. Spatial pattern of TCI shows the changes in vegetation condition due to temperature variation in the Figure 7. In 2014, almost everywhere in Krishna basin we can observe no drought area except the upper eastern part, which represents some part of Andhra Pradesh. Where as in December 2015, we can observe the extreme drought or extreme condition of temperature index increase near to the 0 which show extreme drought (Figure 7). In 2016, some part of upper Krishna basin is having no drought to moderate drought condition whereas southern part of Krishna basin is having moderate to severe drought condition.

Vegetation Condition Index (VCI)

Vegetation Condition Index is another drought monitoring index which is generated by using MODIS data. Vegetation Condition Index rescales dynamics between 0 and 100 where it ranges extremely bad to optimum condition of moisture for vegetation (Kogan, 1995). Vegetation index give us the result of the moisture content and vegetation stress. If moisture content is more then, the index shows the values towards 100 and vice versa. The Figure 8 show the changes in the VCI condition. As like TCI, spatial pattern of VCI also 2014 was the good period for vegetation condition than 2015 and 2016. The year 2015, show the values near to the 0 in upper Krishna basin. In 2016 as like TCI had shown the result in lower Krishna basin having less values show the less moisture condition and vegetation stress over that area.

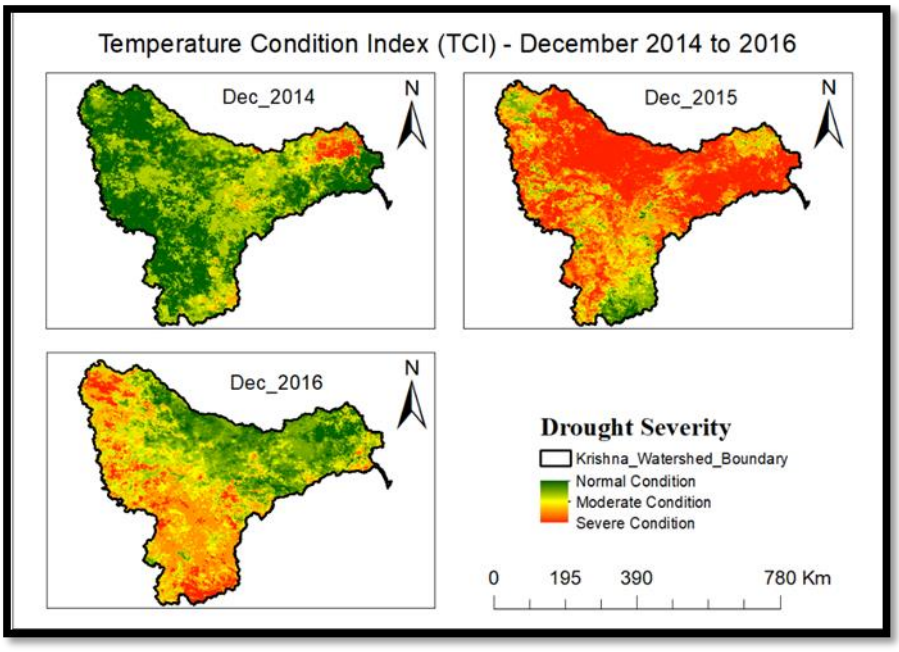

Figure 7: *Temperature Condition Index - Dec 2014-2016*

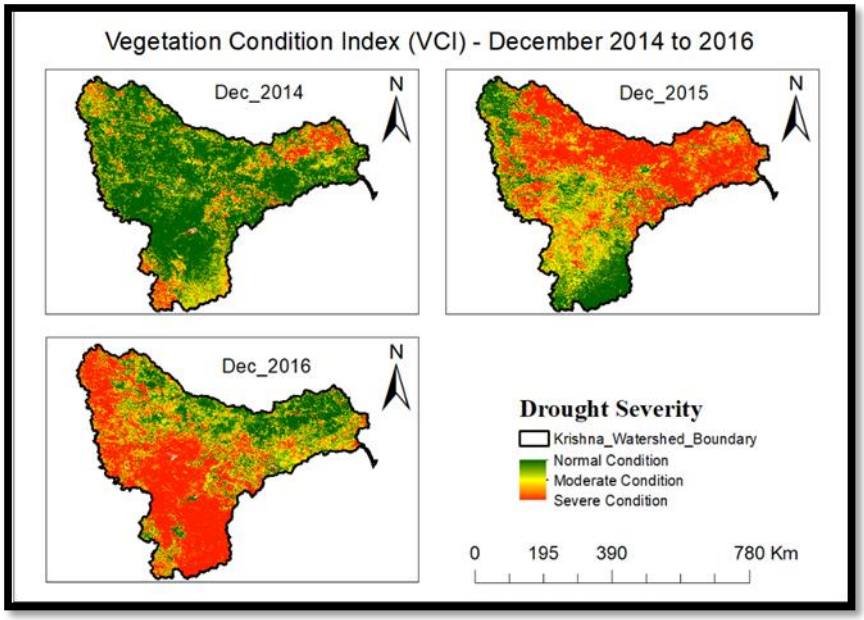

Figure 8: *Vegetation Condition Index (VCI) - Dec 2014-2016*

Vegetation Health Index (VHI)

VCI and TCI characterize respectively the moisture condition and thermal condition of vegetation while VHI represents overall vegetation health (Kogan, 2001). During the calculation of VHI, an equal weight was assigned to both TCI and VCI since the moisture and temperature condition. Range of VHI is from 0 to 100. The table below will tell us about the classification of drought in the values between 0 and 100.

Table 2: *VHI Drought Severity Classes*

Drought Classes	VHI
Extreme Drought	<10
Severe Drought	≥10 and <20
Moderate Drought	≥20 and <30
Mild Drought	≥30 and <40
No Drought	≥40

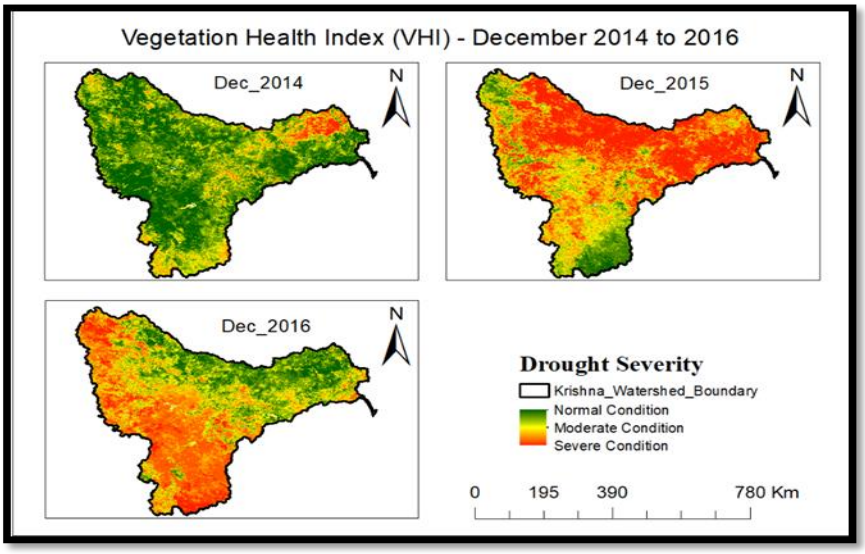

Figure 9: *Vegetation Health Index (VHI) - Dec 2014-2016*

The above map shows the vegetation health on the Krishna basin. In the 2014, no moderate condition has been observed as TCI and VCI also show the same result (Figure 9). In 2015, most of the part of Krishna basin suffer with severe to extreme drought which was classified in the Table 2. In 2016, lower Krishna basin has been observed with moderate to severe drought.

Correlation between TCI vs VHI and VCI vs VHI

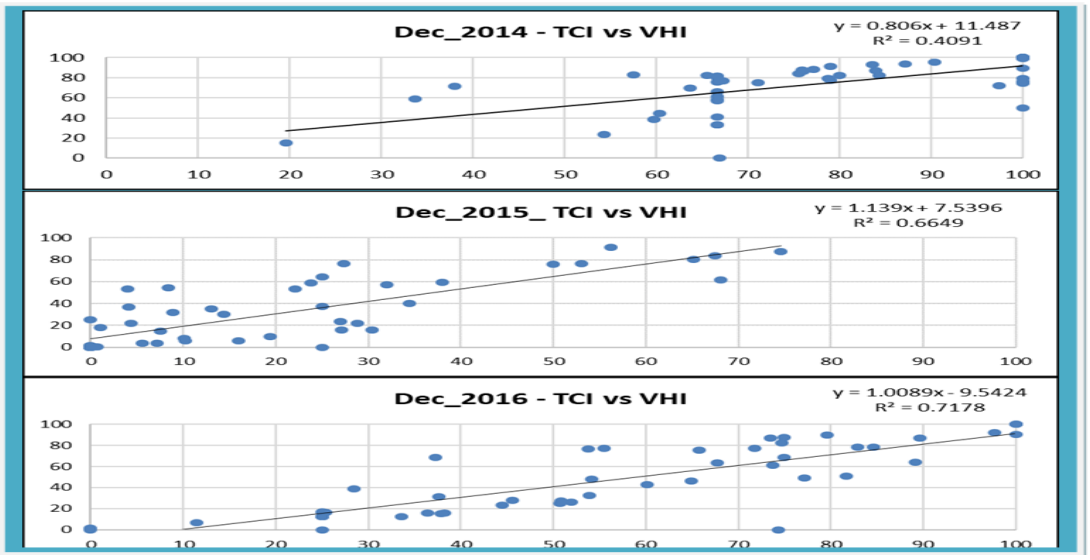

Figure 10: *Correlation Graph - TCI vs VHI - Dec 2014-2016*

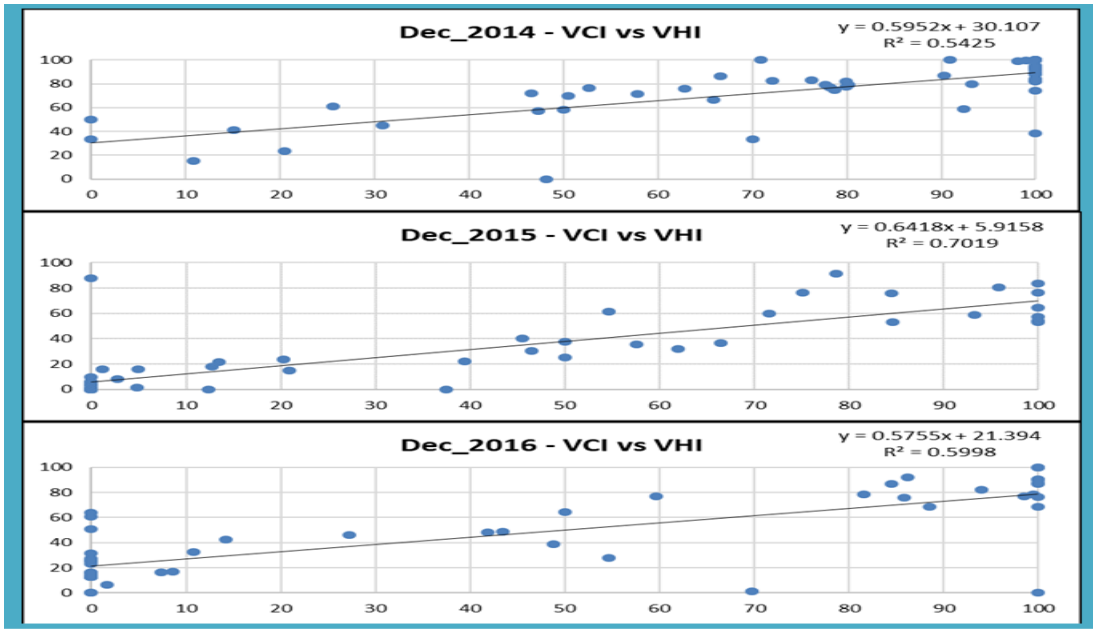

Figure 11: *Correlation Graph - VCI vs VHI - Dec 2014-2016*

The graph given above will tell us about the trend between the three indices (TCI vs VHI and VCI vs VHI). The relationship will show the correlation among the TCI vs VHI. In 2014 and 2015 VCI is strongly correlated with VHI and TCI has less correlation with VHI.

5. Conclusion

Band ratioing is precise technique to study complex and dynamic features in the watershed. Indices taken in this study are useful for various parameter extraction and can be used for watershed development and planning. Indices are good indicators normalized difference moisture index indicates leaf moisture condition and useful to predict ground water condition. Enhanced vegetation index 2 indicates the vegetation cover on the surface and can be correlated with ground water condition as lack of vegetation leads to depletion in ground water table. Bare soil index is useful for land resource management and planning as index emphasize bare soil region prominently and are good indicators of soil erosion and runoff. It is observed that modified normalized difference water index highlights water bodies and suppress and built-up land noise as well as vegetation and soil noise, modified the edges so one can easily separate land and water. Built up area as it get easily mixed with other background features can be easily identifiable after applying Enhanced built up area index. TCI, VCI and VHI are drought monitoring index. Temperature condition index shows changes in vegetation due to temperature condition. Vegetation condition index can be used to study vegetation stress. VCI and TCI depict respectively the moisture condition and thermal condition of vegetation while VHI provide overall vegetation health. TCI, VCI and VHI are good indicators of drought severity monitoring. There are many different mechanisms in the remote sensing by which, an object can be identified like linear and non-linear enhancement, Land surface temperature, spatial filter and band ratioing, classification. It furnishes information about the composition of the object. Remote sensing indices enhance contrast between features by dividing spectral reflectance bands. It is ratioing of two bands, which removes much of the effect of illumination in the analysis of spectral differences. Indices give subtle tonal variations to identify the features spectrally. It de-emphasizes the effect of sun illumination, effect of topographic factors and highlights the region as per spectral properties of specific features. It enhances the quality of image to study the features in detail. Watershed is a major contributor to raise the economic status of the specific region. It plays vital role in human development as well. Scientific observations of watershed with different aspects are major interest of study. For every aspect of

watershed management and development study like drought and flood monitoring, indices are effectively valuable.

References

Amalo, L.F., Hidayat, R. and Haris. 2017. Comparison between remote-sensing-based drought indices in East Java. *IOP Conference Series: Earth and Environmental Science*, 54(1), pp.1-7.

Bhatti, S.S. and Tripathi, N.K. 2014. Built-up area extraction using Landsat 8 OLI imagery. *GI Science & Remote Sensing*, 51(4), pp.445-467.

Bhuiyan, C. 2004. *Various drought indices for monitoring drought condition in Aravalli Terrain of India*. In: Proceedings of the XXth ISPRS Conference, Int. Soc. Photogrammetry and Remote Sensing, Istanbul.

Duy, N.B., Giang, T.T.H. and Son, T.S. 2012. *Study on vegetation indices selection and changing detection thresholds selection in Land cover change detection assessment using change vector analysis*. International Congress on Environmental Modelling and Software, Leipzig.

Ghaleb, F., Mario, M. and Sandra, A.N. 2015. Regional landsat-based drought monitoring from 1982 to 2014. *Climate*, 3, pp.563-577.

Hanqiu, X. 2006. Modification of normalized difference water index (NDWI) to enhance open water features in remotely sensed imagery. *International Journal of Remote Sensing*, 27(14), pp.3025-3303.

Jiang, Z., Huete, A.R., Kim, Y. and Didan, K. 2007. 2-Band enhanced vegetation index without a blue band and its application to AVHRR data. *Proceedings of SPIE – The International Society for Optical Engineering*, 6679, pp.667905_1-667905_9.

Kogan, F. 1995. Application of vegetation index and brightness temperature for drought detection. *Advance in Space Research*, 15(11), pp.91-100.

Kogan, F.N. 2001. Operational space technology for global vegetation assessment. *Bulletin of the American Meteorological Society*, 82(9), pp.1949-1964.

Mustafa, M.T., Hassoon, K.I., Hussian, H.M. and Abd, M.H. 2017. Using water indices (NDWI, MNDWI, NDMI, WRI and AWEI) to detect physical and chemical parameters by apply remote sensing and GIS techniques. *International Journal of Research – Granthalayah*, 5(10), pp.117-128.

Singh, R.P., Roy, S. and Kogan, F. 2003. Vegetation and temperature condition indices from NOAA AVHRR data for drought monitoring over India. *International Journal of Remote Sensing*, 24, pp.4393-4402.

Zheng, G. and Moskal, M.L. 2009. Retrieving Leaf Area index (LAI) using remote sensing: theories, methods and sensors. *Sensors*, 9(4), pp.2719-2745.

Zhuo, W., Huang, J., Zhang, X., Sun, H., Zhu, D., Su, W., Zhang C and Liu Z. 2016. *Comparison of five drought indices for agricultural drought monitoring and impacts on winter wheat yields analysis*. International Conference on Agro-Geoinformatics, pp.1-5.

Cloud Publications
International Journal of Advanced Remote Sensing and GIS
2019, Volume 8, Issue 1, pp. 2971-2982
ISSN 2320 – 0243, Crossref: 10.23953/cloud.ijarsg.408

Methodology Article

Google Earth, Google SketchUp and GIS Software; An Interoperable Workflow for Generating Elevation Data

José Gomes Santos[1], Kevin Bento[2], Joaquim Lourenço Txifunga[3]

[1]Department of Geography and Tourism - Faculty of Arts, University of Coimbra, Portugal; Center for Studies in Geography and Regional Planning - CEGOT, University of Coimbra, Coimbra, Portugal; Center of Applied Cartography, University of Brasília (UNB), Brasília, Brasil and Cartography Laboratory - GeoCart, Geography Department, Federal University of Rio de Janeiro (UFRJ), Rio de Janeiro, Brasil
[2]Department of Geography and Tourism - Faculty of Arts, University of Coimbra, Coimbra, Portugal
[3]Department of Geography and Tourism - Faculty of Arts, University of Coimbra, Coimbra, Portugal

Correspondence should be addressed to José Gomes Santos, *jgs@ci.uc.pt*

Publication Date: 11 April 2019

DOI: https://doi.org/10.23953/cloud.ijarsg.408

Abstract Data creation is often the only way for researchers to produce basic geospatial information for studies concerning river basins, slope morphodynamics, applied geomorphology and geology, urban and territorial planning, among others. This exercise results from an idea initially presented to students in a class context at the Geoinformatics Lab (Geography Department - University of Coimbra, Portugal). The main hypothesis (and goal) of this methodological essay was centered on the idea that it could be possible to develop an interoperable workflow where specific data processing tasks executed in Google SketchUp could produce elevation data that could be exported and geoprocessed with open source Geographical Information Systems (GFOSS) software. It starts with Google SketchUp (GS) graphical interface, with the selection of a satellite image referring to the study area – which can be anywhere on Earth's surface; subsequent processing steps lead to the production of elevation data at the selected scale and equidistance. This new data must be exported to GIS software in vector formats such as Autodesk Design Web format – DWG or Autodesk Drawing Exchange format – DXF. In this essay the option for the use of GIS Open Source Software (gvSIG and QGIS) was made. Correcting the original SHP by removing "data noise" that resulted from DXF file conversion permits the author to create new clean vector data in SHP format and, at a later stage, generate DEM data. This means that new elevation data becomes available, using simple but intuitive and interoperable procedures and techniques which configures a costless workflow.
Keywords *Contour lines; DEM; GFOSS; GIS; Google Earth; Google Sketchup; Interoperability*

1. Introduction

Geomorphometry is generally understood as a sub-branch of Geomorphology, whose object is related to the analysis and comparison of quantitative parameters (descriptive measures – attributes) related to the relief forms (objects) of the terrestrial surface. As referred by Hengl & MacMillan (2009) as cited in (Silveira and Silveira, 2015), DEM documents are widely used for providing continuous covering for large areas at a relative low cost. This automated digital computing provides measurements of surface shapes, context, patterns and texture, that can be used as substitutes for the criteria considered in

image or aerial photo interpretation. In the same work, the main argument for its use is the variety of procedures associated with measurements, dimensions and objects that can be derived by automated analysis of elevation data, applied to natural landscape mapping and modeling. This analysis permits the consistent extraction of several parameters or objects that can be considered as direct analogues of the criteria used by the manual interpreter to identify and delineate objects applied to several studies such as Hydrology, Pedology, Ecology, Geomorphology and Geology.

It is quite simple to identify and select for work some examples of standalone context tools (eg Arc2Earth, Contouring GE, among others) that help us to extract elevation data directly from Google Earth. However, not all of them are available for free, not all are up-to-date or not all offer the required accuracy and precision, or the required interoperability. This exercise reveals an original work flow that permits the production of contour lines related to any area of the globe (with the selected equidistance), by the implementation of specific tasks performed in a software suite that includes Google Sketch-up (GS) from which it becomes possible to export data in vector formats, namely DWG and DXF, and GIS software. From the moment the elevation data already converted to SHP format (open standard) enters the GIS environment some specific procedures must be carried out in order to correct errors and reduce uncertainty. In a later stage, it becomes possible to derive 3D information based on the production of a DEM. Depending on the user's objectives, the exercise could be completed and stopped at this stage, but he can also proceed and follow other directions, for example, the construction of derived raster maps (slope, slope exposure, contours, among others). Finally, it becomes also possible to produce new derived vector maps (SHP format) with elevation data in which the selected equidistance may be different from that initially used in the GS environment.

1.1. Terms and Concepts

The term “DEM” (an acronym for Digital Elevation Model) is often used (Hirt, 2006) as a generic term for Digital Surface Model (DSM) and Digital Terrain Model (DTM).[1] In fact, some definitions do not seem to distinguish the terms DEM and DSM, and it is also common to find some others that equals the terms DEM and DTM (Podobnikar, 2009), or consider DEM as subset of DTM that represents other morphological elements (Li et al., 2004). Other definitions can be found such as the one proposed by the USGS in the Glossary of the Landslide Hazard Program (USGS Glossary of USGS Landslide Hazard Program), which defines “DEM” as a regularly spaced GRID and “DTM” as a three-dimensional model (Triangulated Irregular Network – TIN). The DEM can be represented as a raster (a grid of squares, also known as a height map when representing elevation) or a vector-based TIN. In this case, TIN datasets are also referred to as a primary (measured) DEM, whereas the Raster DEM is referred to as a secondary (computed) DEM (Toppe, 1987). Other literature (Li et al., 2004) considers that DEM data could be acquired through techniques such as photogrammetry, lidar, ifSAR, land surveying, among others. In general terms, DEM is often used in GIS and is the most common basis for digital relief maps.

Although the DSM may be useful for landscape modeling, city modeling and visualization applications, the DTM is often required for flood or drainage modeling, Land-Use studies (Balenovic et al., 2015), Geology and other applications (UK Environment Agency, 2005). Recent research (Al-husban, 2017) showed that DEM could be considered as a computerized representation of Earth’s relief, and it is

[1]It should be stressed that most of the data providers like the United States Geological Survey (USGS), National Aeronautics and Space Administration (NASA), and European Space Agency (ESA), use the generic term "DEM". Instead, the Japan Aerospace Exploration Agency (JAXA) refers to ALOS World 3d, a 30-meter spatial resolution digital surface model, as a DSM. Although, the datasets captured with satellites, airplanes or other flying platforms, like Shuttle Radar Topography Mission (SRTM) and Advanced Spaceborne Thermal Emission and Reflection Radiometer - Global Digital Elevation Model (ASTER-GDEM), are originally considered as DSM data documents. The term DTM is often mentioned when it only includes surface data; it means that it does not take into account surface features like trees and buildings. It can thus be assumed that, in general terms, we should refer to DEM as a representation of the elevation of the Earth's surface above a certain datum, to DTM if the data represents the elevation of the surface with its features, and to DSM when the DEM includes the elevation of the terrain plus the natural and man-made features.

often used in Geosciences and Geostudies but also, in Architecture, Civil Engineering, and all issues related to Urban Studies and Territorial Planning. In this following, along with the present document, DEM will be used as a generic term for both DSM and DTM data documents.

One of the most common challenges that researchers and practitioners dealing with geospatial data are facing is data collection. There are three main sources of data for the construction of a DEM (Al-husban, 2017):

A. Field survey techniques, from the acquisition of precise points of latitude, longitude and elevation (x, y, z);

B. Topographic maps, from the derivation of contour lines, drainage, lakes and points of elevation;

C. Remote sensing, from the interpretation of aerial photographs or images acquired from satellites[2], especially for photogrammetry (stereoscopic methods), radars and, more recently, laser surveys.

The production of MDT data usually derives from line vector files that gather elevation data but it is also common to construct MDT files using interpolation processes executed on the basis of a cloud of points. In the year 2000, SRTM mission collected data over most of the land surface positioned between 60º N and 54º S (about 80% of all land on Earth) and allowed to generate a complete base of terrestrial digital topographic maps of high resolution, freely available now in two resolutions: 90 m and 30 m. In this case, the derivation of MDT data in GIS environment, with or without 3d visualization, obliges that the work must be done with raster files and in a later stage to convert them for vector formats. The United States National Aeronautics and Space Administration (NASA) Jet Propulsion Laboratory website (https://asterweb.jpl.nasa.gov/gdem.asp,) informs about the origins of ASTER GDEM mission stating that the Ministry of Economy, Trade and Industry (METI) of Japan and NASA jointly announced the release of the Advanced Spaceborne Thermal Emission and Reflection Radiometer (ASTER) Global Digital Elevation Model Version 2 (GDEM V2)[3] in October 17, 2011. ASTER GDEM coverage spans from 83º N to 83º S, encompassing 99% of the mass of the Earth. This represents another excellent geodata provider for spatial researches once it is generally accepted the idea that DEM data is often a very useful tool for landscape analysis.

Taking in line the considerable number of methodological options that allow the production of elevation data which will always depend on the available data, the access to it, as well as on the objectives of the user, especially in terms of application, the main purpose of this study is in the presentation of an interoperable methodology which is based on a set of applications that performs specific tasks leading to the derivation of MDT in any area of the globe, from the selection of a satellite image acquired and processed in GS software and geoprocessed in GIS environments.

2. Materials and Methods

This exercise requires the articulation between practices and tasks carried out in a two step process (two stages): Stage A) Google SketchUp environment and Stage B) GIS environment.

2.1. Google Sketch-up Environment

2.1.1. Study Area Selection, Data Acquisition and Preparation

In GS environment, the template selection "Urban Planning Meters" leads to the access of a graphical interface from which users can select the display mode of the image as well as the procedures that will

[2]Is quite common today the use of Unnamed Aerial Vehicles (UAV) for this propose.

[3]The first version of the ASTER-GDEM, released in June 2009, was generated using stereo-pair images collected by the ASTER instrument on board “Terra”.

allow the extraction of data from the Z coordinate. The execution of the following commands "File > Geo-location > add location" allows us to select the study area and the image to work and prepare it for the extraction of elevation data based on contour lines. In this essay the study area is located in the Central Region of Portugal (Figure 1), concretely, it is an area of the mountainous massif of the Serra da Estrela in which stands out the presence of a glacier valley - Glacier Valley of the River Zêzere. The command File> Geo-location> Show terrain, show us a 3D image (Figure 2A) and the use of tools "Orbit" and "Zoom" helps us to identify the volumes and the topography associated with the selected image. In order to extract elevation data from this satellite image it is necessary to draw a rectangle whose area completely involves the image to be selected (Figure 2B). The functionalities of the "show terrain" tool returns to 3D visualization of the ortho-image that we will now have to overlap the tangential to the base of the rectangle (Figure 2C)[4].

Figure 1: *The mountainous massif of the Serra da Estrela, Central Region of Portugal (image obtained from Google Earth, on the left); Selection of the satellite image to be rendered in GS environment (on the center).*

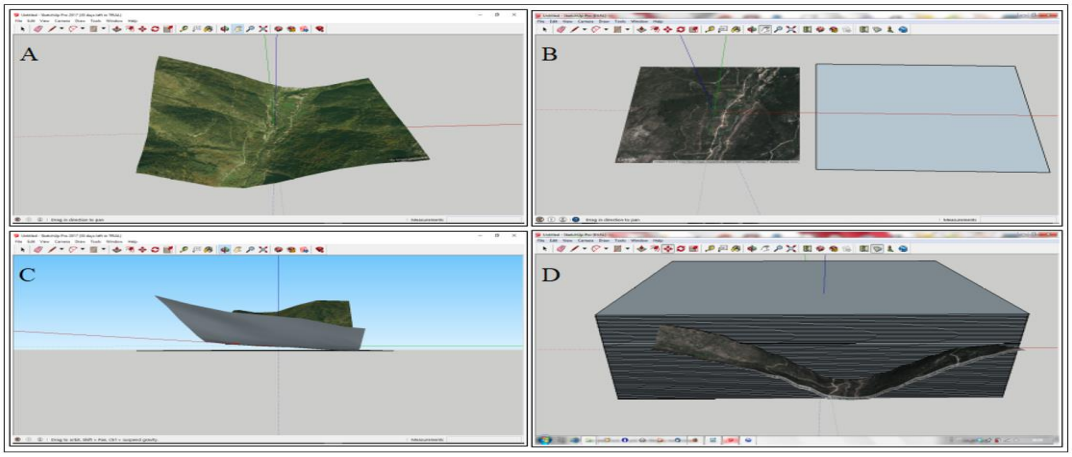

Figure 2: *Initial processing stage for the recording of contour lines in GS environment*

[4] At this stage it is important to identify the altitude of the lowest point of the ortho-image, and record its value. Google Earth was used to capture this basic information. On the other hand, the rectangle must be strictly tangent to the ortho-image in the contact with the base where its lowest point is located; it is not easy to execute this command in an absolutely strict way and, as such, already in the GIS environment, it will be necessary to resort to techniques of correction of deviations and inaccuracies of the elevation data, which are translated by the production of negative values of altitude that are going to be loaded to the vector file when exporting from the GS.

2.1.2. Box Model and Contour Lines Generation

In conceptual terms, the aim of this process is to create a “box module” with a layer-based architecture that, in its set, will intersect the ortho-image (Figure 2A). The first procedural task to generate the cutting layers consists on the use of the "Show Terrain" command, which allows us to view the ortho-image in a 3D perspective and informs about the altitude of the plans. By using the "Move" tool we have to create an over-raised copy of a rectangle (Figure 2B) whose area must completely involve the ortho-image. To raise this copy (new layer) that will have to be replicated as often as necessary in order to fill the “box module”, it is crucial to identify the execution status. For this purpose, the operator must verify if the cursor has a crosshair shape, and confirm if there is a graphic return defined by a "+" sign which must be accompanied by the information "on blue axis" (Z). The rectangle should be positioned tangentially to the lowest point of the ortho-image (Figure 2C), while in the lower right corner of the GS graphical interface, in "Distance / Lenght" it must be typed the distance (in meters) to which the new copy of the rectangle will be positioned above the original; that is, in practice, we are defining the equidistance value for the layers to be generated. The iteration of this procedure, by typing "40x", or "50x", or more, until the ortho-image is completely covered by the replicates of the rectangle leads to the generation of a volumetric layer-based module (Figure 2D).

After ensuring the uniqueness of this polyhedron through the "Make Group" command, with the "Move" tool selected, the sequence "Intersect faces> With Model" must be carried out. When removing the geometric model in order to permit the ortho-image to be seen, we verified that the contour lines corresponding to the altitude layers intersected by the model were recorded on the satellite image (Figure 3A). After deleting the geometric model by following the Window> Default Tray> Layers path and, deactivating the "Location Terrain" and "Location snapshot" layers, we obtain the 3D image of the generated contours (Figure 3B). To view this elevation data in the ortho-projection mode, we must select the commands View > Toolbars > Views > Top path (Figure 4).

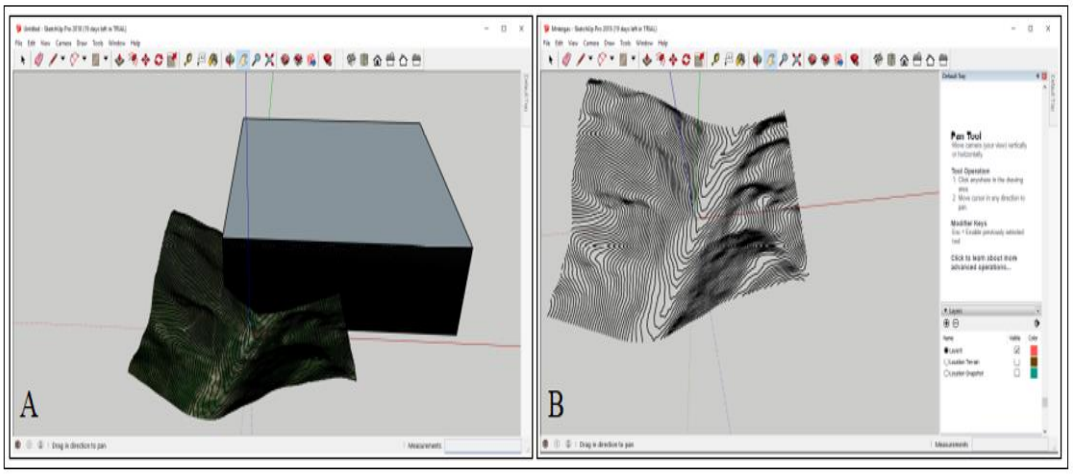

Figure 3: *Topographic surface engraved with the contour lines.*

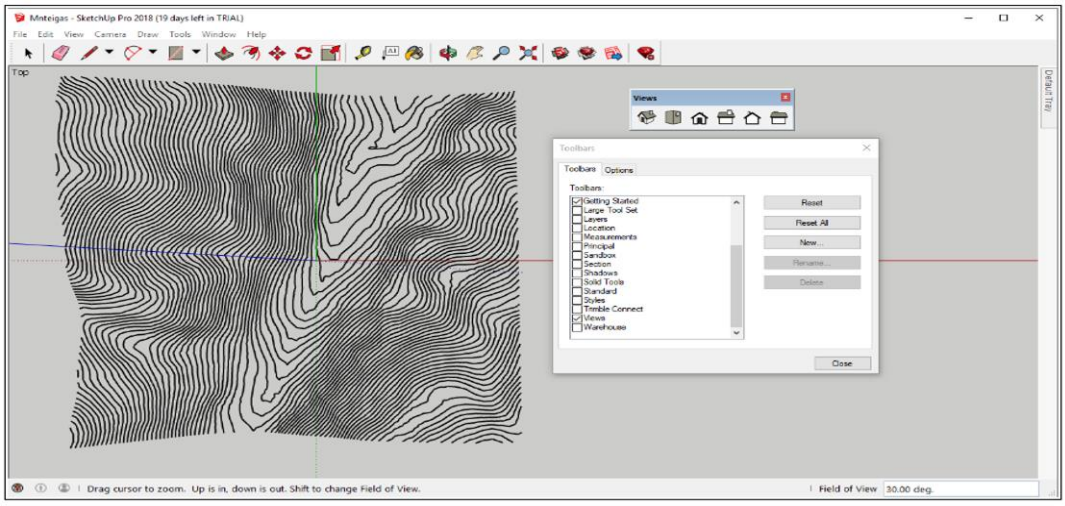

Figure 4: *Ortho-projection of the topographic surface engraved with the contour lines.*

The sequence of procedures and tasks performed in GS environment produced a set of elevation data and features that can be stored in vector formats which can be loaded in GIS software. Considering that GS does not allow to export data in SHP format, other options such as the DXF format are suitable because it can be loaded in GIS software and later converted to a first generation SHP, so-called because it involves raw data containing topographic, hypsometric and topological errors which need to be corrected or even removed from the SHP.

2.2. GIS environment - gvSIG and QGIS

The export of the vector data produced in the previous stage, in the GS environment, carries a lot of uncertainty and data noise, consequently, error as it was previously mentioned. It is therefore necessary to use a sequence of tasks and procedures for SHP correction. This geoprocessing stage was accomplished by using gvSIG and QGIS software (Free and Open Source Software). Once the conversion of the DXF file to SHP format has been performed, the observation and analysis of the SHP attribute table confronts us with the existence of four types of data that require attention:

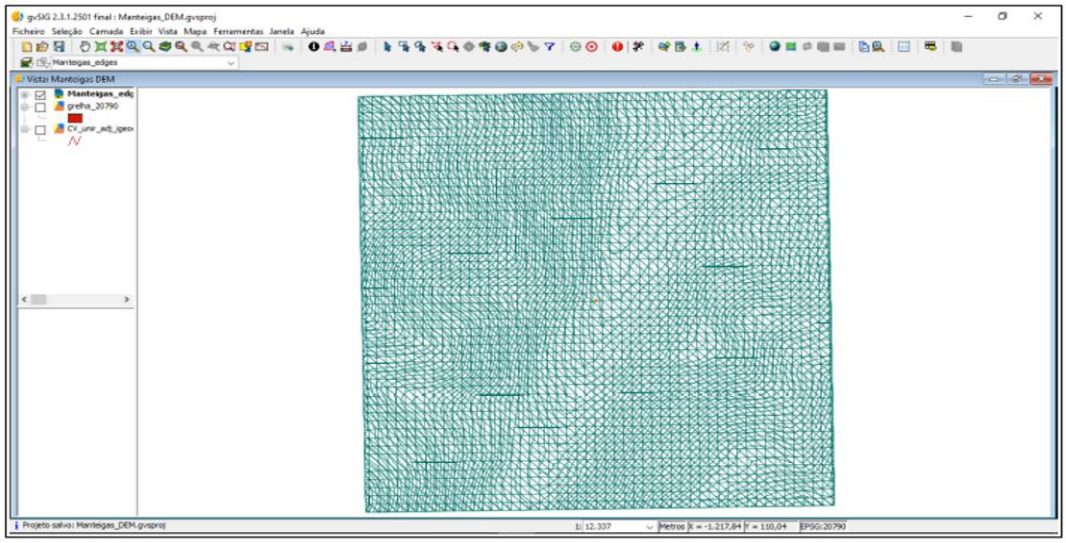

Figure 5: *Resulting DXF file, from the export process from GS to the gvSIG.*

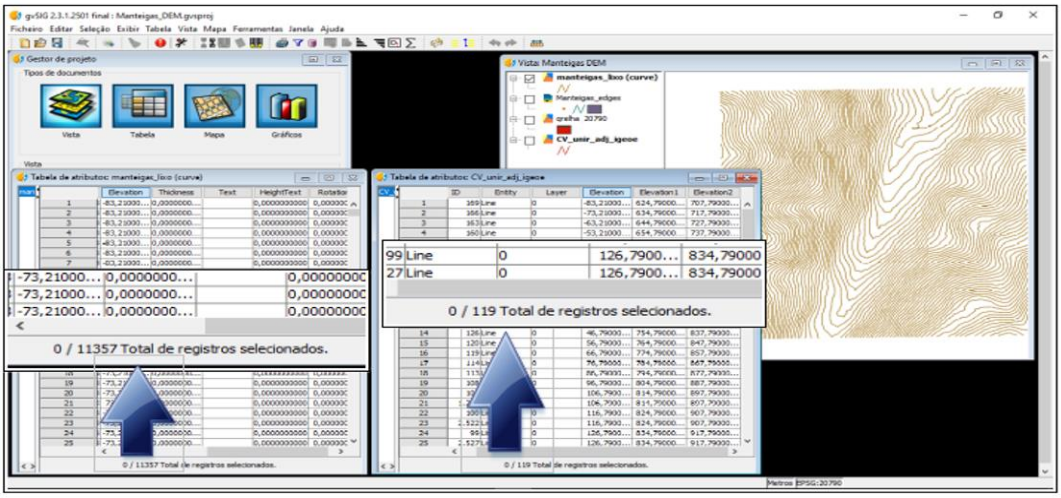

Figure 6: *Data resulting from the DXF - SHP conversion process, before and after the correction of the attribute values by running the merge of adjacent line features algorithm in gvSIG.*

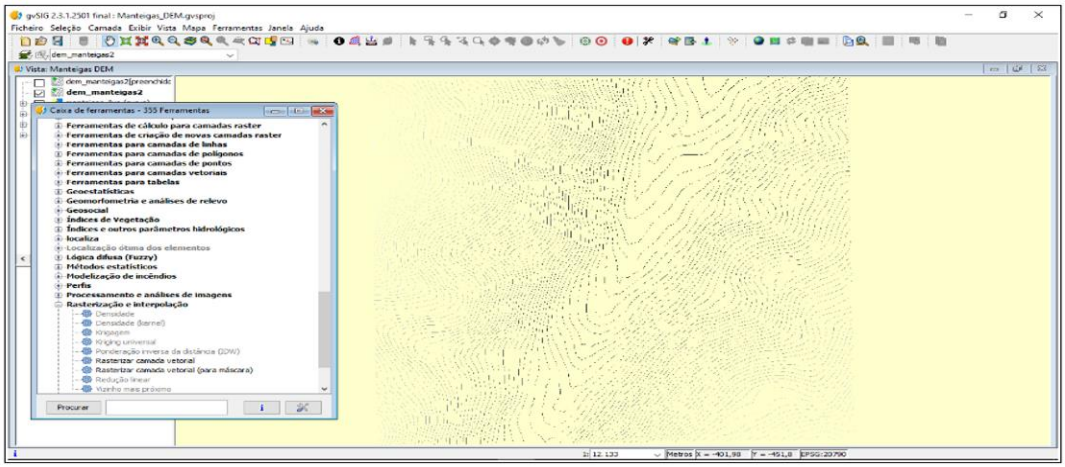

Figure 7: *Graphic result after the running process of "Rasterization and Interpolation" tool, gvSIG Sextante module.*

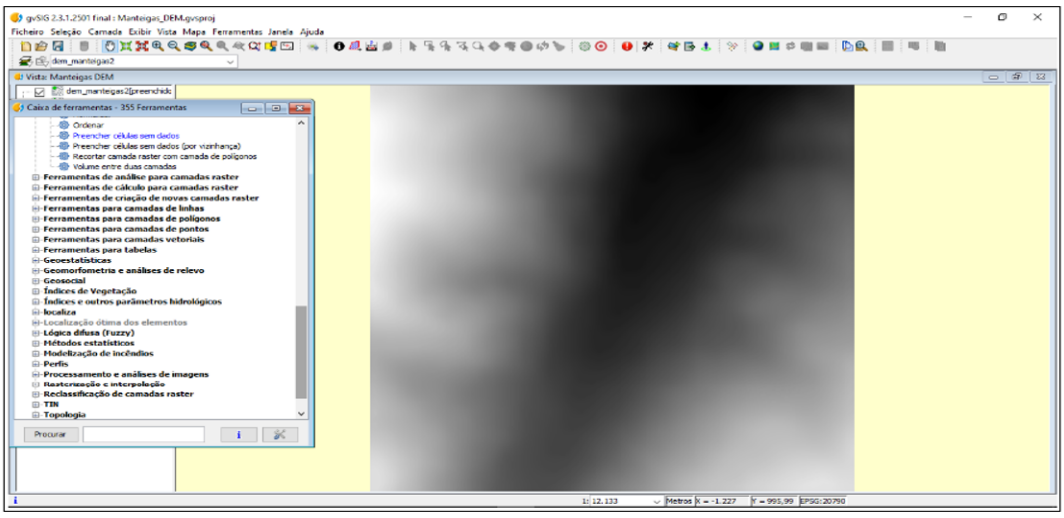

Figure 8: *DEM generated after the running of void filling process (pixel-resolution 10 m)*

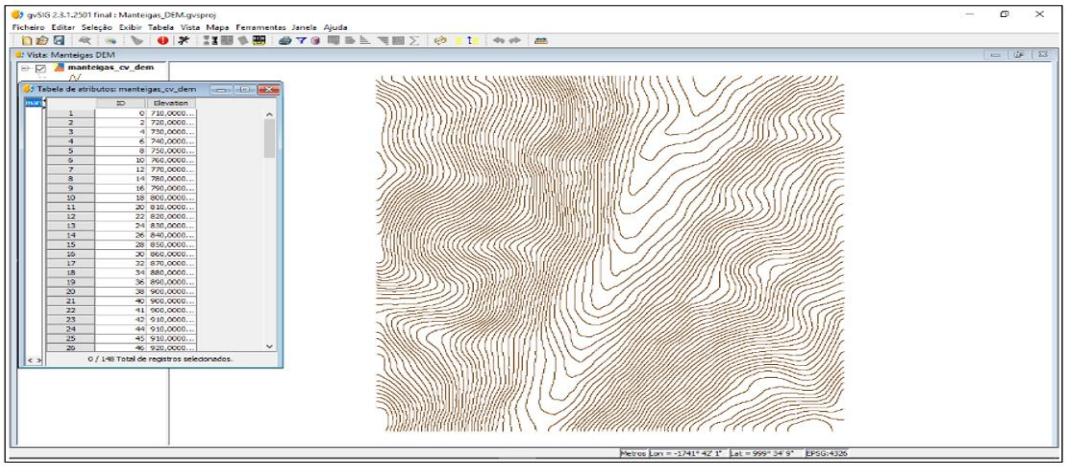

Figure 9: *Contour lines (in vector format and with records multiples of 10m), processed with the "Vectorise" algorithm (Sextant module).*

A. Data exported among with the contour lines, which have to be removed (Figure 5).

B. Adjacent entities within the same layer to merge together. Once the attribute containing the elevation data has been identified and selected by creating an appropriate query filter, the result is converted to SHP format. Each contour line must be represented by only one segment; however, an architecture defined by more than one feature resulted from the export process, which forces the use of the merge tool applied to the adjacent entities within the same layer to merge together. Figure 6 reveals the number of features before and after the execution of the algorithm "merge adj lines", available in the tool set for “Line Layers” (gvSIG sextant module). To perform this task, the wizard configuration does not accept more than one feature per contour line, so the "Options-Tolerance" field must be filled with the value "0", but the software replaces it immediately with the scientific notation "1.0E-4".

C. Negative elevation records, which are unreal regarding the geomorphology of the study area - it is a mountain area-, that require proper correction; the procedural significance of these records is associated to the positional adjustment of the rectangle (the first elevation layer) used for replicating in GS, in relation to the base level identified in the ortho-image. The correction of these data is carried out with the creation of a new field that is populated automatically using the Field Calculator tool. This can be seen as a two-step process that begins with the SUM of the original elevation records listed on the SHP attribute table, and the modular value of the smallest negative elevation record – which reflects the vertical shift of the rectangle to the base of the ortho-image.

D. Positive elevation records that represent the difference between the real and the lower elevation record of the ortho-image; to obtain the correct elevation data, in this attribute field, it is necessary to SUM the identified "lowest point value" with the ones obtained from the theoretical "zero level" which represent the reference to distinguish between positive and negative records, in other words, that are visible or invisible in the ortho-image. This second SUM can be realized in the field created in the task referred in 3), but the user can choose to create a new field using the Field Calculator, and to fulfil it with data resulting from the SUM of the records obtained in the process earlier described, with the minimum value of the real elevation identified and captured from Google Earth. However, the problem related to inaccurate elevation records generated in GS still is not solved. It is necessary to find a solution to obtain equidistant multiple values of 10m. There are some adequate procedures that can be performed in raster data model and DEM generation techniques. The use of the "rasterize vector layer" algorithm available on the "Rasterization and Interpolation" Sextant toolset, leads to generate a DEM using the contour line data as input (Figure 7). The resulting empty cells present in the DEM require the use of the "Fill" tool available in the "basic tools for raster layers”

toolset of Sextant (Figure 8). The generation of new vector contour lines (Figure 9), with the selected equidistance and records which are multiples of 10m, can be processed using the “Vectorise raster layers" algorithm available in the "Vectorization" toolset of Sextant.

3. Results

In previous stages of this work we have presented and described the main steps and the methodological procedures leading to the creation of a vector document in SHP format; and the techniques and the algorithms used to eliminate noise from input data in the GIS software, which had resulted from the conversion of data in DXF format to SHP, were also revealed. This methodological essay aimed at demonstrating that the combination of these techniques in a context of interoperability of data formats and software, makes it possible to derive new data that can serve as a new basis for more complex works. An example of it can be seen in Figure 10, which displays the result of the overlapping of contour lines in vector data model with the DEM rendered with hillshade effect (shaded relief). The user now has at his disposal derived elevation data, with desired detail and scale, which can serve as a basis for deriving new data, such as slope and slope exposure maps, and perform calculations to other complementary studies, such as the generation of river networks, basins and watersheds, stream order and other hydrologic data.

The visual comparison between the DEM derived from the GS-GIS performed in QGIS software (Figure 11A) and another DEM document built on the basis of the line vector files derived from the Portuguese Military Maps, sheets 213 and 224, 1:25000 (Figure 11B) reveals striking similarities. Attention is drawn to the high visual cartographic similarities shown in both cases and this perception is stressed with the statistical data when a comparison between both raster histograms is made. These results encourage the development of new studies that allow us to evaluate the degree of reliability of the data obtained, as well as to test, validate and improve the model presented in this methodological essay.

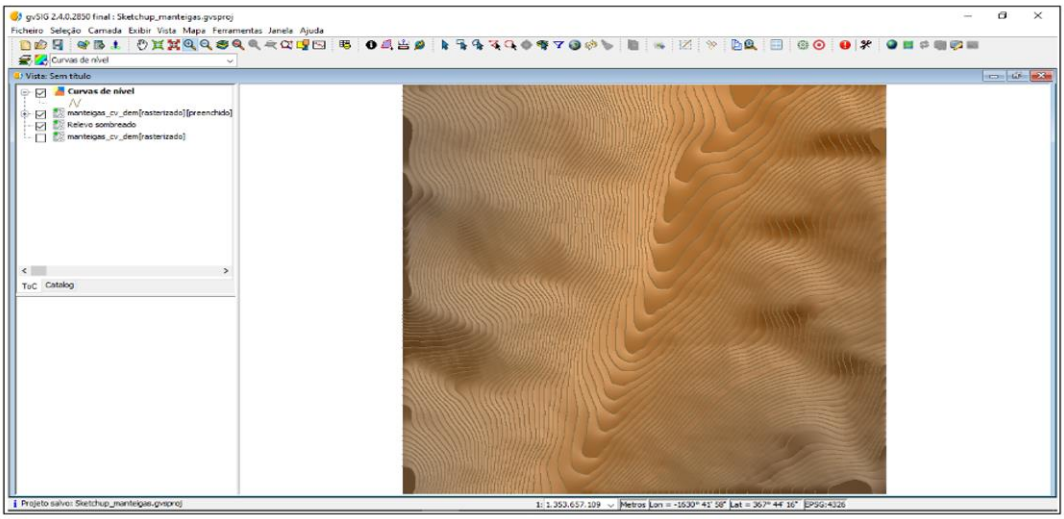

Figure 10: *Contour lines final layer (vector format, with 10m of equidistance) and DEM with shaded relief (raster format, 10m resolution pixel).*

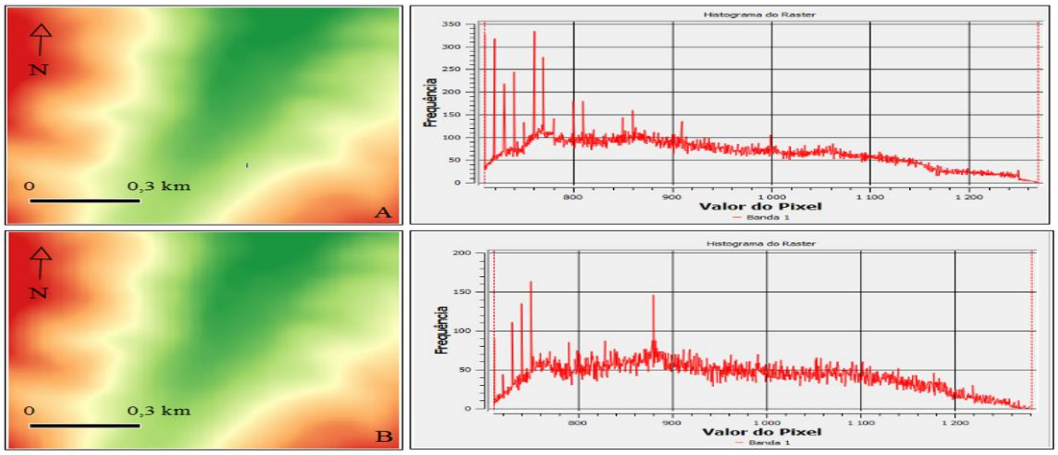

Figure 11: *DEM derived from GS-GIS conversion process and raster histogram for a sample of the study area (A), performed in QGIS software. DEM derived from line features, sheets 213 and 224 of the Portuguese Military Map, 1/25000 (B).*

4. Discussion

The lack, scarcity, high cost or simply conditioned access to geospatial data constitute barriers to research (academic and scientific) which sometimes can be overcome by the researchers themselves. Using autonomous strategies, one can produce basic data suitable for a subsequent integration into thematic complex work, and dispense themselves from the obligation to have recourse to institutional sources that do not always guarantee free and open access to geospatial data. As can be seen from the close-up of the figures presented, namely from Figures 10 and 11 which show the final results obtained, the methodology tested consists of a set of interoperable procedures that allows to obtain (and to produce) new elevation data from (and for) any place or region of the globe.

From the beginning of this methodological essay it was assumed that the main goal of this exercise was to provide alternative solutions, quick and virtually free of charge, for the generation of geospatial information using an interoperable combination of software. The use of this suite of applications involving Google Earth, Google SketchUp and GIS free and open source software (FOSS), namely, gvSIG and QGIS, conduced to the generation of vector and raster files containing elevation data with scale and equidistance selected by the operator. Once the required correcting tasks were performed in order to remove data noise resulting from the GS-GIS export process, the SHP data thus obtained can be integrated in researches under the most varied fields of knowledge and applications such as Hydrology, Geomorphology, Urban Planning, among others. Future works will discuss this methodology in the perspective of model validation based on the use of statistical methods and the comparison of the results obtained from various techniques used for the construction of DEM data.

5. Conclusion

A considerable number of sciences requires the use of basic elevation data for the characterization of the physical support of human activities, from the detailed urban studies to those involving tasks and activities related to land use and territory planning and management.

The implementation of a suite of interoperable solutions that allow the use of GIS software to match with other applications that render vector or raster information as, in this case, Google SketchUp, reflexes the creation of new elevation data which after undergoing processes such as error correction, uncertainty reducing and cartographic noise removal, shall be available to derive new data, with the guarantee of preservation of its integrity and reliability, so that it can integrate new chains of procedures related to various studies applied to diverse areas of Science and its applications, social and/or natural.

The generation of contour lines and DEM data are examples of a creative low-cost process, the importance of which is recognized in several domains of its application. The exercise here is intended to be an example of innovation in Geospatial teaching and research, an expedited solution which, based on an articulated procedural sequence, ensures a methodological work flow for the production of basic elevation data that allows researchers to overcome barriers placed at initial stages of most of the works, that invariably begins with the formulation of problems and equations for which they will have to find answers. "I do not have data – and now, what do I do?" This conception, which is sometimes more a matter of attitude than a real dilemma or a real problem, can cease to be an obstacle and have a deterrent effect on researchers decision-making process at crucial moments in the research process, if we think that the creation of geospatial data, with the required prudence, can be assured and performed by researchers and non professional users. This is a singular perspective of the Volunteered Geographic Information paradigm, where data users can be also data producers and providers.

Acknowledgement

This work was supported by the European Regional Development Funds, through the COMPETE 2020 – Operational Programme 'Competitiveness and Internationalization', under Grant POCI-01-0145 - FEDER-006891; and by National Funds through the Portuguese Foundation for Science and Technology (FCT) under Grant UID/GEO/04084/2013.

Co-financed

References

Al-husban, Y. 2017. Comparison of accuracy of two global DEMs and the extracted DEM from the topographic map of the Tafilah Governorate. *Journal of Earth Science and Engineering*, 7, pp.230-241.

Balenovic, I., Marjanovic, H., Vuletić, D., Paladinić, E., Sever, M. and Indir, K. 2015. Quality assessment of high density digital surface model over different land cover classes. *Periodicum Biologorum*, 117(nº 4), pp.459-470.

Hirt, C. 2016. *Digital terrain models*. In Encyclopedia of Geodesy, Switzerland. Springer International Publishing, Switzerland. Available from: *https://www.researchgate.net/publication/278683672_Digital_Terrain_Models*.

Li, Z., Zhu, Q. and Gold, C. 2004. *Digital Terrain Modeling: Principles and Methodology*. 1st Edition, CRC Press, Boca Raton, Florida, USA, p.318.

Podobnikar, T. 2009. Methods for visual quality assessment of a digital terrain model. *Surveys and Perspectives Integrating Environment and Society*, 2(n°2).

Silveira, R. and Silveira, C. 2015. Análise comparativa entre modelos digitais de elevação com distintas características de processamento e aquisição, Bol. Geogr., Maringá. *Número Especial*, 33, pp.106-121.

Toppe, R. 1987. *Terrain models - A tool for natural hazard mapping*. In Avalanche Formation, Movement and Effects. Proceedings of the Davos Symposium, Davos, Switzerland, September, 1986, International Association of Hydrological Sciences Publ., Wallingford, UK, 1987. pp.629-638.

UK Environment Agency, 2005. *Appendix A – Glossary and Acronyms*. Severn Tidal Tributaries Catchment Flood Management Plan – Scoping Stage. Available from: *https://web.archive.org/web/20070710054700/http://www.environmentagency.gov.uk/commondata/acrobat/app_a_1243533.pdf.*

USGS Glossary of USGS Landslide Hazard Program. Available from: *https://landslides.usgs.gov/learn/glossary.php.*

Cloud Publications
International Journal of Advanced Remote Sensing and GIS
2019, Volume 8, Issue 1, pp. 2997-3010
ISSN 2320 – 0243, Crossref: 10.23953/cloud.ijarsg.415

Research Article

GIS Application for Assessment and Mapping of Irrigation Water Quality in Piedmont Plain of Jalgaon District, Maharashtra, India

Nitin S. Ghope, Kailas P. Dandge, Sopan T. Ingle and Vishaishwar M. Rokade

School of Environmental and Earth Sciences, Kavayitri Bahinabai Chaudhari North Maharashtra University, Jalgaon, Maharashtra, India.

Correspondence should be addressed to Nitin S. Ghope, *ghope.nitin7@gmail.com*

Publication Date: 13 June 2019

DOI: https://doi.org/10.23953/cloud.ijarsg.415

Abstract The irrigation water quality and related hazards to crop yield is frequently a complex phenomenon that comprises the major effect of physico-chemical parameters. In the present investigation, an attempt has made to assess the groundwater quality and geo-spatial disparity of irrigation water quality index for agricultural purpose in piedmont zone of Jalgaon district. The Irrigation Water Quality Index (IWQI) was computed by Meireles Irrigation Water Quality Index technique. In the present study, ground water samples were collected from thirty-six different locations of piedmont plain of Jalgaon district. Samples were analysed in the laboratory for various quality parameters such as, Electrical Conductivity (EC), Sodium (Na) Bicarbonate (HCO3), Chloride (Cl), Magnesium (Mg), Calcium (Ca) using standard methods and Sodium Absorption Ratio (SAR) was calculated using standard equation. The correlation among the irrigation water quality parameters was calculated statistically. The present investigation's revealed that, the computed values of Irrigation Water Quality Index (IWQI) exhibits that, 77.78 % sample location (3/4 area) was moderately restricted and 22.22% sample location (1/4) was highly restricted for irrigation use in the piedmont region. The results of geo-spatial distribution of IWQI show's that, the major restrictions were observed at Pal village from northern part whereas minor restriction were found at all remaining part of the study area. The overall trends of increasing restrictions were observed from western to eastern part of piedmont plain of Jalgaon district. Hence, the above results revealed that, intensive agriculture by over use of inorganic fertiliser, pesticides, high depth water, polluted drain water and improper irrigation practices was posed a serious threat to groundwater quality in agricultural areas of piedmont plain of Jalgaon district.
Keywords *Geo-spatial techniques; Irrigation; IWQI; Piedmont plain*

1. Introduction

Agriculture is the main occupation of the people in India as well as Maharashtra and study region, which is subject to uncertainty of rainfall; irrigation plays a vital role in developing the agricultural economy (District Gazetteer, 1962). Central Water Commission (CWC) has estimated as 139.9 Mha, the ultimate irrigation potential of India, these irrigation potentials from major and medium irrigation projects is assessed as 58.47 Mha. Irrigation potential created in our country from major and medium irrigation plans, which stood at 9.7 Mha in 1951, has increased to 47.97 Mha in 2016 (CWC, 2017). The Central Ground Water Board (CGWB) has examined ground water resources area out of which

1635.84 sq. km. is under command and 9742.99 sq. km. is non-command out of total geographical area 11378.83 sq. km. (CGWA, 2013). Irrigated agriculture is totally dependent on suitable water supply of applicable water quality (Islam, 2009). Groundwater is regularly used for domestic, industrial and irrigation purpose in the global world. The groundwater represents the second source for the freshwater in the piedmont region that is origin from the terrestrial surface water bodies (Rabeiy, 2017). Irrigation water quality is associated to its influences on soils and crop productivity and its cultivation. The concern that water will be an infrequent natural resource in the modern era. World Health Organisation and Water Resource Ministry has been motivated the emerging countries into the appraisal of the water qualities at sources of water in current ages (Kannel et al., 2007). Irrigation water quality is assessed by the total volumes of soluble elements and the types of present element inside the irrigation water. Irrigation waters whether derived from the natural sources as springs then blowing from minor tributaries of main rivers or pumped from dug wells, tube wells and bore wells, contain significant amounts of chemical matters in solution that may decrease crop yield and decline soil fertility (Ayers and Westcot, 1985). Groundwater is one of the most useful water resources on the Earth, which is applied for essential uses such as drinking, agriculture and industry, etc. (Chitsaz and Azarnivand, 2016). Numerous studies were carried out to measure the geochemical properties of groundwater (Sujatha and Reddy, 2003); (Laluraj, Gopinath and Dineshkumar, 2005); (Subramani, Elango and Damodarasamy, 2005); (Ravikumar and Somashekar 2012). Water quality plays a vital role in encouraging agricultural production and normal of human health (Tiwari et al., 2017).

Geographical Information System (GIS) is an effective and powerful tool for mapping, monitoring, modelling and assessing water quality, detecting environmental change, determining water availability, preventing flooding and managing water resources on a local or regional scale (May et al., 2013). Spatial analysis extension tool of ArcGIS 10.2 permits statistical interpolation techniques of the irrigation groundwater quality parameters at unknown fields from known fields values to generate a continuous surface which helps us to study the spatial variation of irrigation water quality index of the piedmont region (Shabbir and Ahmad, 2015). Geographical Information System (GIS) assist to assess, mapping and monitoring of irrigation water quality in agriculture sector and has significant role in the agricultural practices and management of natural water resources (Srinivas et al., 2013).

Ground water quality parameters for assessment of probable precipitation of salts, induction to salinity and sodicity by irrigation activities are used to classify groundwater for irrigation purpose (Tiwari et al., 2017). The classification of groundwater quality that considers the interface of both salinity and soil sodicity with the toxicity risk (Meireles et al., 2010). The main approach of this study is to assess and mapping of Irrigation Water Quality Index (IWQI) by Meireles method, that interpreted restriction of groundwater quality for irrigation in various soil and plants.

2. Study Region

The present work was conducted in Northern part of Jalgaon district in Khandesh region; which is known as Piedmont plain in Earth Science. Piedmont plain of Jalgaon district was selected for the present investigation which has been originating in eastern part of Khandesh region in between Satpuda mountain and Aner - Tapi river in Jalgaon district of Maharashtra. The area coverage of the study region is 2118 sq. km. Geographically, the UTM geographic location is lined between 21° 00′ 40″ to 21° 23′ 44″ N latitude and 75° 02′ 51″ to 76° 02′ 39″ E longitude (Figure 1). The topographic elevation or altitude of the catchment is ranging from 45 to 1062 m. According to (Govt. of Maharashtra 2011), the total geographical area of the piedmont plain has recorded 2,118 sq. km (18.00%) out of total geographical region of the district is (11,765 sq. km.). The surrounded natural boundaries have been demarked by Tapi River at eastern and southern side, western boundary has marked by Aner River and Satpuda Mountain has covered northern part of the piedmont plain region (Govt. of Maharashtra, 1962). The climate of the study area is classified as hot summer and dry throughout the year. According to meteorological view, this area falls in the tropical region, the mean daily maximum temperature reaches 42.5^0 C. In the past decade, the average rainfall in the last

decade has been fallen 75 to 80 cm per year in the region (TERI, 2014). The piedmont area consists of alluvial plain of Tapti valley. Geologically, most of the part of study region is covered by Deccan traps excluding alluvium land on northern sides of Tapi River. Central Ground Water Board has taken up several studies in the district and compiled the report on Hydrogeology of the district. Ground water exploration in the district has been taken up in different phases since 1957-58. According to, Geological Survey of India (GSI), the ground water exploration has been done in alluvial and hard rock areas occupied by Deccan Trap Basalt. These trap rocks are the result of outpouring of enormous magma flows which had extend over hundreds of kilometer of western, central and southern India to appearance a major part of the Deccan plateau at the end of Mesozoic era (CGWA, 2013).

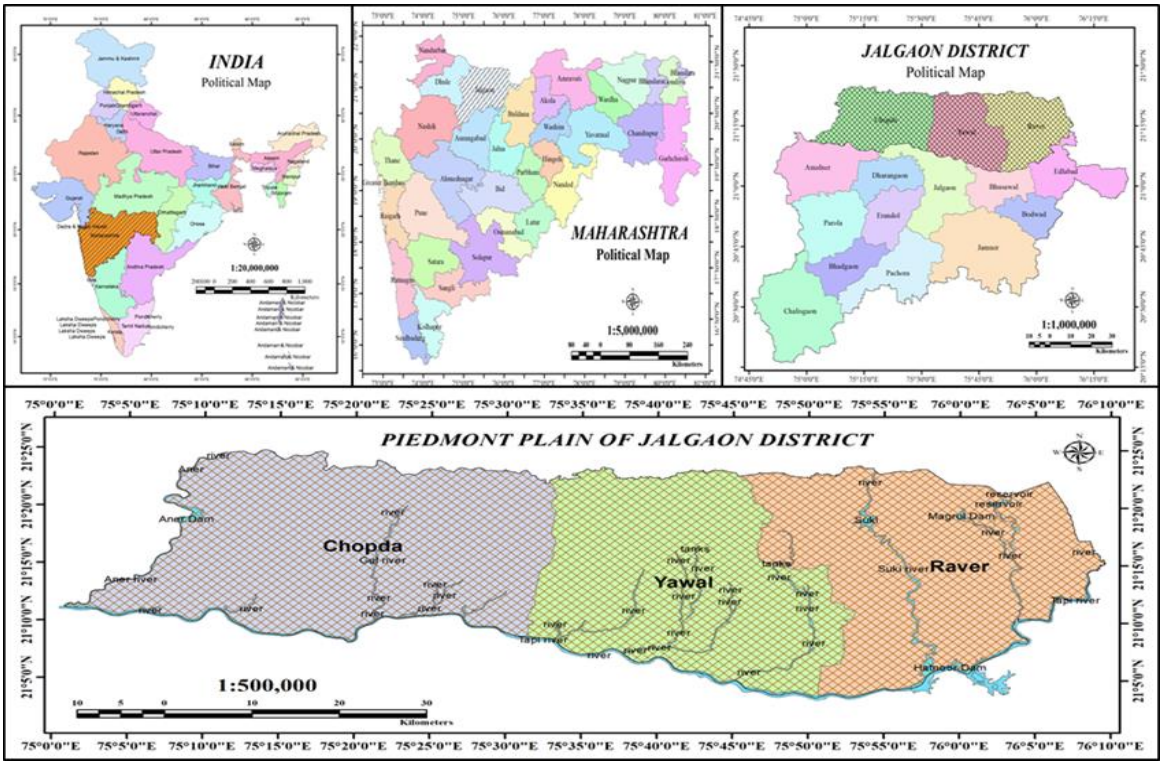

Figure 1: *Location of Piedmont Plain of Jalgaon District*

3. Materials and Methodology

In the present investigation, 36 sampling locations were selected by using systematic sampling techniques for groundwater sample from piedmont plain of Jalgaon district. The samples were collected in one litre polyethylene cans which were pre-rinsed and washed in the laboratory using proportionate distilled water and hydrochloric acid and before filling the sample it is washed thoroughly with representative sample. Global Positioning System (Garmin Ertex - 20) was used for recording and mentioned geographical coordinates of sampling locations shown in Table - 5. The scientific standards methods were applied for water sampling, handling, transporting, storing and laboratory analysis (APHA 1998). The collected samples were analysed for various water quality parameters like Electrical Conductivity (EC), Sodium (Na) Bicarbonate (HCO_3), Chloride (Cl), Magnesium (Mg), Calcium (Ca), whereas Sodium Absorption Ratio (SAR) was calculated by equation 1 (Wilcox, 1948).

$$SAR = \frac{Na}{\frac{\sqrt{Ca + Mg}}{2}} \qquad \text{Eq. – 1}$$

The main objective of present investigations is to know Irrigation Water Quality Index (IWQI) for the classification of groundwater quality zone in the piedmont plain area of Jalgaon district. Groundwater

quality parameters were used in this inspection; such as, Electrical Conductivity (EC), Sodium Absorption Ratio (SAR), major cations include Sodium (Na) and major anions include Chloride (Cl) and Bicarbonate (HCO_3) (Meireles et al., 2010). Digital electrical conductivity meter was used for determination of conductivity and UV Spectrophotometer (UV) was used for anions, titration method was used to determine for bicarbonate, and other calculation methods were used to analyzed the water quality variables (APHA, 1998). These various water quality parameters were calculated and classified to determine the suitability of irrigation groundwater quality based on the recommendation of (Ayers and Westcot, 1985), (Todd, 1980). The examined irrigation water quality index (IWQI) by using Meireles techniques (Meireles et al., 2010). The Inverse Distance Weighted (IDW) method used for presenting geo-spatial distribution of supporting parameters and groundwater quality index (Srinivas et al., 2013). Groundwater quality parameters were analysed by *Karl's Pearson`s* coefficient of correlation techniques for standardization of data in SPSS (Alberto et al., 2001). Geo-spatial distribution of irrigation water quality index (IWQI) were displayed variation pattern by using interpolation techniques from Geo-statistical analyst tools of ArcGIS 10.2 software (Xiao et al., 2016).

3.1. Irrigation Water Quality Index (IWQI)

The application of degraded water quality in irrigation has been the main cause for the decline in the quality of soil and the agricultural crops (Ayers and Westcot, 1985). The concept of indices to represent gradations in water quality was first proposed by (Horton, 1965) then the WQI was modified by Brown and co-authors (Brown et al., 1972). Similarly, Meireles were prepared a water quality index for irrigation purpose by using water quality parameters (Meireles et al., 2010); such as mention in (Table 1). It is known as Irrigation Water Quality Index (IWQI). Several methods of calculation have been put into exercise to current a precise assessment of water quality (Zahedi, 2017; Al-mussawi, 2016; Abbasnia et al., 2018 and Gidey, 2018) were investigated IWQI by similar techniques and presented outcomes by GIS-integrated technique on the base of the combination of the five different classes of irrigation water quality parameters (Meireles et al., 2010).

Table 1: *Irrigation water quality index characteristics* (Maireles et al., 2010)

IWQI	Water use restrictions	Recommendation	
		Soil	Plant
85 ≤100	**No restriction (NR)**	May be used for most of soils with low probability of causing salinity and sodicity problems, being recommended leaching within irrigation practices, except for in soils with extremely low permeability.	No toxicity risk for most plants
70 ≤85	**Low restriction (LR)**	Recommended for use in irrigated soils with light texture or moderate permeability, being recommended salt leaching. Soil sodicity in heavy texture soils may occur, being recommended to avoid its use in soils with high clay levels 2:1.	Avoid salt sensitive plants
55 ≤70	**Moderate restriction (MR)**	May be used in soils with moderate to high permeability values, being suggested moderate leaching of salts.	Plants with moderate tolerance to salts may be grown
40 ≤55	**High restriction (HR)**	May be used in soils with high permeability without compact layers. High frequency irrigation schedule should be	Should be used for irrigation of plants with moderate to high tolerance to salts with special salinity

		adopted for water with EC above 2.000 dS/m-1 and SAR above 7.0.	control practices, except water with low Na, Cl and HCO3 values
0 ≤40	**Severe restriction (SR)**	Should be avoided its use for irrigation under normal conditions. In special cases, may be used occasionally. Water with low salt levels and high SAR require gypsum application. In high saline content water soils must have high permeability, and excess water should be applied to avoid salt accumulation.	Only plants with high salt tolerance, except for waters with extremely low values of Na, Cl and HCO3.

3.2. Computation of Irrigation Water Quality Index (IWQI)

The irrigation water quality index (IWQI) proposed in this study was formulated in two stages. In the first stage, parameters that contribute to most variability in irrigation water quality was recognized using Principal Components and Factor Analysis (PC/FA) as defined in SPSS (Alberto et al., 2001). In the second stage, a meaning of quality measurement values (q_i) and aggregation weights (w_i) was established.

Table 2: *Weight for the IWQI parameters* (Maireles et al., 2010)

Parameters	Wi
Electrical Conductivity (EC)	0.211
Sodium (Na)	0.204
Bicarbonate (HCO3)	0.202
Chloride (Cl)	0.194
Sodium Absorption Ration (SAR)	0.189
Total	1.0000

Values of (qi) was assessed based on each parameter value, according to irrigation water quality parameters projected by the University of California Committee of Consultants - UCCC and by the criteria recognized by (Ayers and Westcot, 1985), shown in (Table 3).

Table 3: *Parameter limiting values for quality measurement (qi) calculation* (Ayers and Westcot, 1994)

qi	EC	SAR	Na	Cl	HCO3
	µS/cm	meq/l	meq/l	meq/l	meq/l
85 - 100	200 - 750	2 ≤ SAR < 3	2 ≤ Na < 3	1 ≤ Cl < 4	1 ≤ HNO3 < 1.5
60 - 85	750 - 1500	3 ≤ SAR < 6	3 ≤ Na < 6	4 ≤ Cl < 7	1.5 ≤ HNO3 < 4.5
35 - 60	1500 - 3000	6 ≤ SAR < 12	6 ≤ Na < 9	7 ≤ Cl < 10	4.5 ≤ HNO3 < 8.5
00 - 35	EC < 200 OR EC ≥ 3000	SAR < 2 OR SAR ≥ 12	Na < 2 OR Na ≥ 9	Cl < 1 OR CL ≥ 10	HNO3 < 1 OR HNO3 ≥ 8.5

Irrigation water quality parameters were represented by a non-dimensional number; the higher the value, the better the quality water. Values of qi were calculated using the equation 2, based on the tolerance limits shown in (Table 3) and water quality results determined in laboratory:

$$q_i = qi_{max} - \left\{ \frac{(X_{ij} - X_{inf}) * q_{iamp}}{X_{amp}} \right\} \qquad \text{Eq.- 2}$$

Where;

qi_{max} = The maximum value of qi for the class;
X_{ij} = The observed value for the parameter;
X_{inf} = The corresponding value to the lower limit of the class to which the parameter belongs;
q_{iamp} = The class amplitude;
X_{amp} = The class amplitude to which the parameter belongs.

In order; to evaluate x_{amp}, of the last class of each parameter, the upper limit was the highest value determined in the physical-chemical and chemical analysis of the water samples. Each parameter weight used in the WQI was obtained from the PC/FA, by the sum of all factors multiplied by the explain ability of each parameter. Then w_i values were normalized such that their sum equals one, according to equation 3.

$$w_i = \frac{\sum_{j=1}^{k} F_j A_{ij}}{\sum_{j=1}^{k} \sum_{j=1}^{n} F_j A_{ij}} \qquad \text{Eq. - 3}$$

Where;

w_i = The weight of the parameter for the WQI;
F = Component 1 auto value;
Aij = the explain ability of parameter i by factor j;
i = the number of physical, chemical and chemical parameters selected by the model, ranging from 1 to n;
j = The number of factors selected in the model, varying from 1 to k.

The water quality index was calculated as:

$$IWQI = \sum_{i=1}^{n} qiwi \qquad \text{Eq. - 4}$$

Where;

WQI is dimensionless parameter ranging from 0 to 100;
q_i = is the quality of the i^{th} parameter, a number from 0 to 100, function of its concentration or measurement;
w_i = is the normalized weight of the i^{th} parameter, function of its importance in explaining the global variability in water quality.

4. Results and Discussion

Sodium (Na)

Irrigation water containing large amounts of sodium is of special concern due to sodium's effects on the soil and poses a sodium hazard.

Irrigation water covering major volumes of sodium is of special relation due to sodium's effects on the soil particles and arises a sodium hazard in the agriculture field (Fipps, 2003). Saline irrigation waters chief in sodium salts limit the potential harvesting of agricultural crops directly impacting physiological functions of plants and indirectly reducing the soil properties (Rengasamy, 1987). Irrigation water has high sodium (Na) content can bring about a displacement of exchangeable cations calcium and magnesium from the clay minerals of the soil, followed by the replacement of the cations by sodium. Sodium saturated soil peptizes and loses permeability, so that their fertility and decline suitability for

cultivation (Matthess, 1982). The investigated sodium (Na) values of all the ground water samples are showed in Table 4 and the results displayed by geo-spatial map [Figure 2 (a)]. The measured sodium of all water samples ranges from 1.461 to 8.596 meq/l and the average sodium value is 3.439. The upper allowable limit of sodium is less or equal to 9 meq/l for irrigation purpose (Ayers and Westcot, 1985).

Table 4: *Simple statistical investigation of groundwater quality parameters*

Parameter	Min	Max	Arithmetic mean	Median	Mode	Quartile deviation	Standard deviation
Na	1.461	8.596	3.439	3.024	#N/A	1.002	1.536
EC	276.100	1355.000	713.278	767.150	#N/A	195.338	262.802
Cl	0.336	7.952	2.643	2.434	2.912	0.931	1.837
HCO3	0.058	0.452	0.251	0.248	0.252	0.037	0.083
SAR	0.884	4.452	1.852	1.475	#N/A	0.498	0.866
IWQI	43.229	66.655	58.280	58.577	#N/A	3.700	6.091

Note: All concentration is noted in meq/l except EC, EC = (µS/cm), # - Not Applicable.

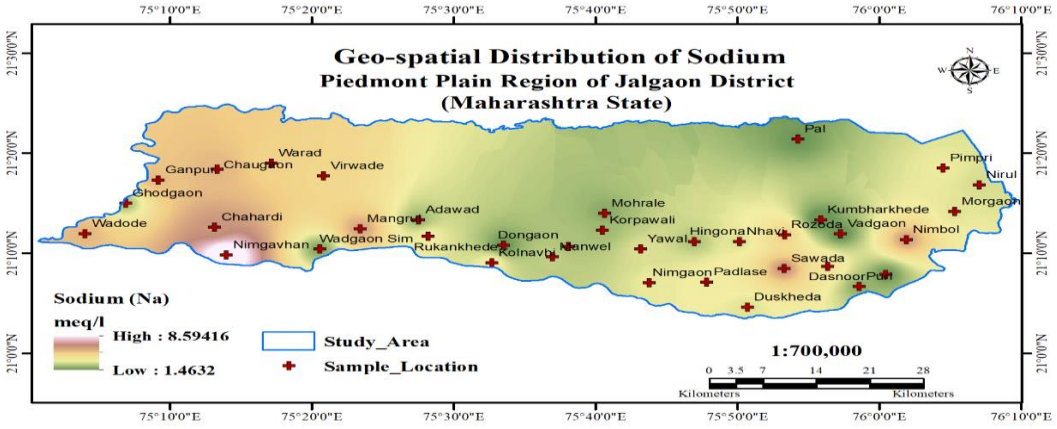

Figure 2(a): – *Geo-spatial distribuation of Sodium.*

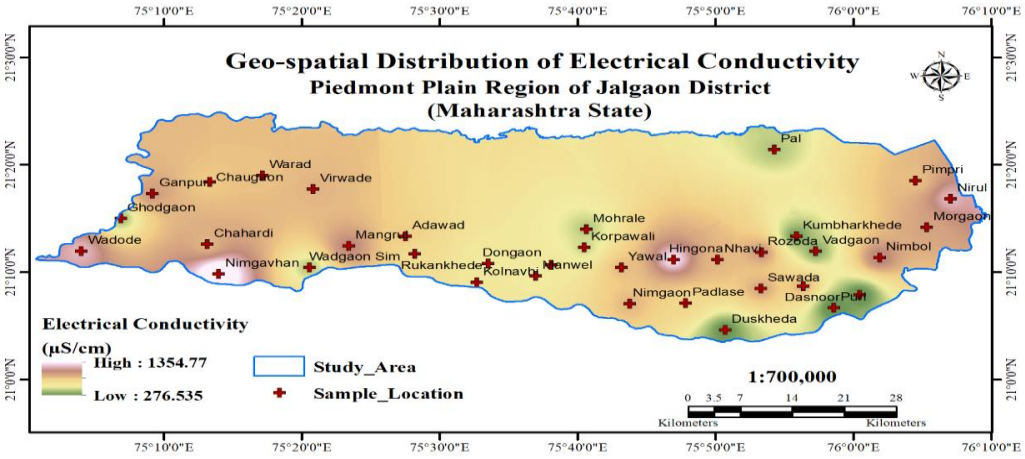

Figure 2(b): *Geo-spatial distribuation of Electrical Conductivity*

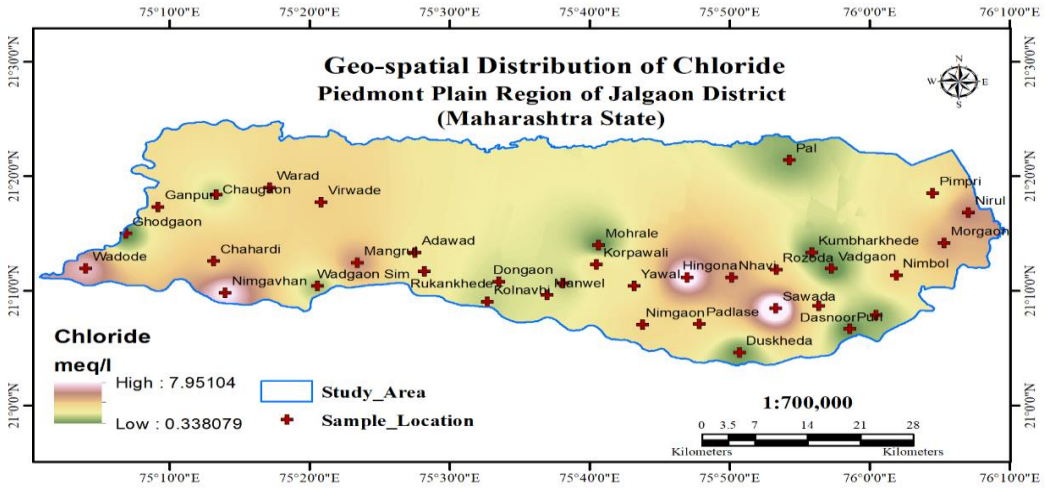

Figure 2(c): *Geo-spatial distribuation of Chloride.*

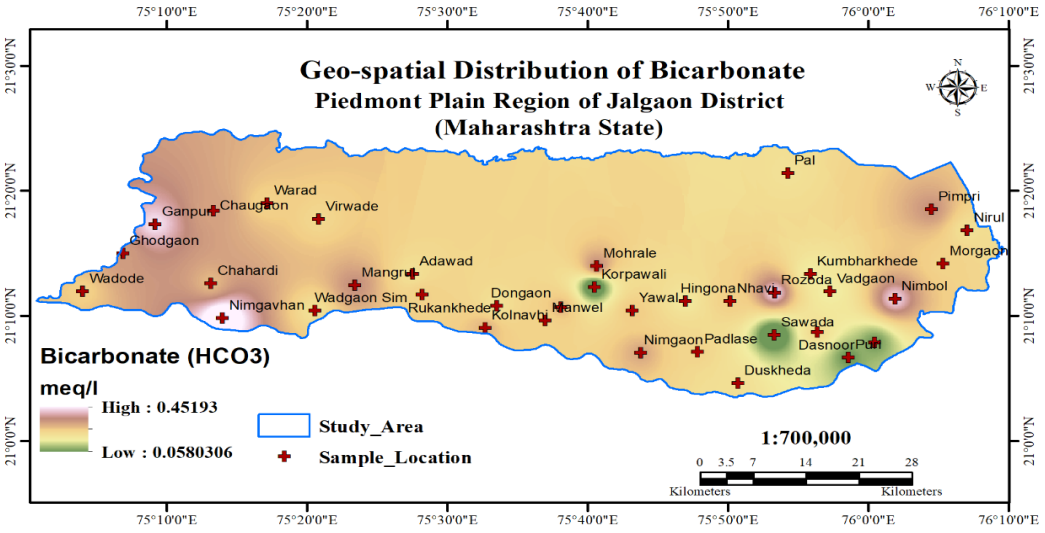

Figure 2(d): *Geo-spatial distribuation of Bicarbonate.*

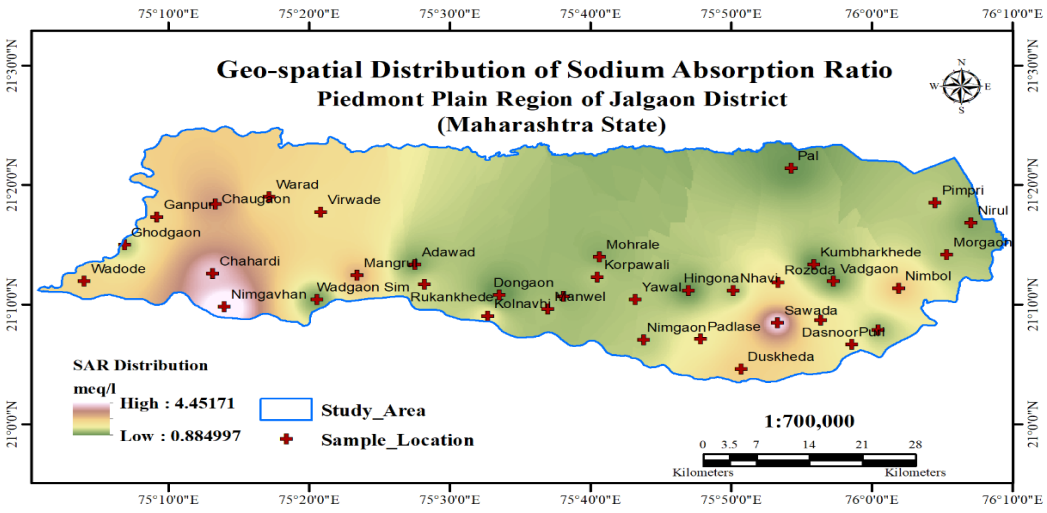

Figure 2(e): *Geo-spatial distribuation of Sodium Absorption Ratio.*

Electrical Conductivity (EC)

Electrical conductivity is the capability of any medium water to carry an electric current. The occurrence of dissolved solids such as calcium, chloride, and magnesium etc. in water samples transfer the electric current through water. According to, (Ayers and Westcot, 1985), the maximum allowable level of conductivity is 3000 μS/cm. The investigated electrical conductivity values of all the ground water samples are mentioned in table 4 and the results displayed by geo-spatial map [Figure 2 (b)]. The measured electrical conductivity of all water samples ranges between from 276.5 μS/cm to 1355.0 μS/cm and the average electrical conductivity value is 713.278 μS/cm. The present study revealed that, electrical conductivity at all corner of the piedmont plain region is under desirable limits.

Chloride (Cl)

Higher level of chlorides in water can cause problems (Subramani et al., 2005). The content of chloride ions in irrigation water increases with the increase of EC and sodium ions. Many plants are sensitive to high chloride concentrations and sometimes to high levels of Na in their leaf's (Miller and Donahue 1995). In present study area, the chloride content in water samples varies from 0.336 to 7.952 meq/l (Table 4) and its geo-spatial distribution map is shown as per [Figure 2 (c)]. The result of the study was revealed that, observed chloride values were within standards limit which conclude that, the water is appropriate for irrigation in agricultural activity as far as chloride is concerned.

Bicarbonate (HCO_3)

Alkalinity is a calculate of the volume of water to nullify a mixed acid. Existence the major element of alkalinity, carbonate and bicarbonate ions are normally accountable for high pH values of water (Simsek and Gunduz, 2007). Bicarbonates (HCO_3) encourage calcium precipitation in the form of calcium carbonate (lime) during dry season, resulting in a higher SAR in water (Gupta et al., 1985). The observed concentrations for Bicarbonates (Table 4) varies between 0.058 and 0.452 meq/l with an average value of 0.251 meq/l and geo-spatial variation of bicarbonate is shown [Figure 2 (d)]. All the groundwater samples were exhibit suitability for irrigation in piedmont plain region (Ayers and Westcot, 1985).

Sodium Absorption Ratio (SAR)

A high sodium ion in irrigation water disturbs the hydraulic conductivity (permeability) of soil and makes water infiltration difficulties (Lenntech, 2016). SAR and EC communally can be used to estimate irrigation water quality (Vasanthavigar et al., 2010). The water quality features that effect the standard rate of infiltration of water are the salinity and the comparative absorptions of sodium, magnesium and calcium ions in water that is known as the Sodium Adsorption Ratio (Simsek and Gunduz 2007). The SAR value of irrigation water measures the relative amounts of sodium (Na) to calcium (Ca) and magnesium (Mg) and is computed by above equation - 1. According to (Ayers and Westcot, 1985) table 3 shows that the standard requirement of mentioned parameters with its standard limits for defining quality of individual parameters. The calculated values of SAR in groundwater samples of the study area were observed between 0.884 to 4.452 meq/l with average value of 1.852 meq/l. The calculated SAR distribution were shown through the geo-spatial mapping [Figure 2 (e)]. All the groundwater samples were fit for irrigation in study region as far as SAR is concerned.

Irrigation Water Quality Index (IWQI)

ArcGIS 10.2 version with Geostatistical Analyst Tools Extension was used to make a spatial distribution map of the Irrigation Water Quality Index (IWQI) by weighted overlay model used the combination of five thematic water quality maps (Na, EC, Cl, HCO_3 and SAR). Calculated IWQI values are generally categorised into five types, such as No Restriction (NR), Low Restriction (LR), Moderate

Restriction (MR), High Restriction (HR) and Severe Restriction (SR) water uses for agricultural and detailed explanation about restriction and recommendation of water has given in table 1 for soil and plant (Meireles et al., 2010). Table 5 shows that, the geo-spatial distribution and categories of irrigation water quality index (IWQI) in piedmont region. The geo-spatial distribution of several Hydro-chemical parameters can be effectively mapped by applying GIS techniques (Srinivas et al., 2013). The result of geo-spatial distribution of IWQI showed that 77.78% sample location was moderately restricted, and 22.22% sample location was highly restricted for irrigation use. Hence, based on above analysis about 1/4 of the total area coverage was found with highly restriction and 3/4 of the area coverage were recorded with moderately restricted for irrigation use with respect to IWQI. Such type of waters will be harm to soil quality and agricultural yield loss (Gidey, 2018). In Figure 3 shown that the Geo-spatial distribution of Irrigation Water Quality Index in piedmont plain of eastern Khandesh area.

Table 5: *Geographical location and categories of irrigation Water Quality Index (IWQI) by maireles*

Sample No.	Latitude (m)	Longitude (m)	Altitude (m)	Depth (ft)	Sample Location	IWQIM	Category
1	21.233166667	75.677500000	275	200	Mohrale	55.72	MR
2	21.250027778	75.114694444	186	160	Ghodgaon	53.51	HR
3	21.197444444	75.888555556	247	220	Rozoda	65.32	MR
4	21.077166667	75.844944444	217	300	Duskheda	62.49	MR
5	21.117916667	75.729944444	208	350	Nimgaon	59.01	MR
6	21.195166667	75.470055556	189	240	Rukhankhede	52.52	HR
7	21.177888889	75.634555556	222	120	Sakali	58.84	MR
8	21.160638889	75.616361111	211	150	Manwel	56.69	MR
9	21.207527778	75.390222222	193	240	Mangrul	62.93	MR
10	21.186000000	75.835694444	237	240	Nhavi	61.98	MR
11	21.189361111	76.031444444	242	255	Nimbol	58.31	MR
12	21.111555556	75.976305556	231	70	Puri	59.85	MR
13	21.308416667	76.074666667	289	290	Pimpri	63.00	MR
14	21.280527778	76.117388889	259	150	Nirul	57.95	MR
15	21.173555556	75.719972222	224	200	Yaval	62.88	MR
16	21.205277778	75.674888889	244	150	Korpawali	56.95	MR
17	21.210222222	75.219444444	181	210	Chahardi	56.47	MR
18	21.288666667	75.152916667	202	180	Ganpur	62.77	MR
19	21.173833333	75.342666667	182	160	Wadgaon Sim	66.66	MR
20	21.235944444	76.088611111	243	120	Morgaon	64.78	MR
21	21.141166667	75.888194444	225	250	Sawada	57.60	MR
22	21.222472222	75.458638889	204	230	Adawad	64.28	MR
23	21.199551111	75.954468333	237	265	Vadgaon	45.55	HR
24	21.222512778	75.930954167	243	275	Kumbharkhede	47.44	HR
25	21.145416667	75.939111111	239	230	Dasnoor	57.89	MR
26	21.199388889	75.066861111	165	140	Wadode	63.56	MR
27	21.131333333	76.007444444	231	115	Dhamodi	60.03	MR
28	21.316666667	75.286138889	256	310	Warad	65.54	MR
29	21.163777778	75.233055556	176	180	Nimgavhan	50.65	HR
30	21.186500000	75.782583333	239	220	Hingona	55.03	MR
31	21.295722222	75.347416667	245	200	Virwade	65.14	MR
32	21.306805556	75.222083333	242	270	Chaugaon	66.50	MR
33	21.118691389	75.796996111	217	170	Padalse	50.60	HR
34	21.150777778	75.545194444	201	250	Kolnhavi	56.83	MR
35	21.356527778	75.904527778	398	450	Pal	43.23	HR
36	21.180194444	75.558527778	199	200	Dongaon	49.59	HR

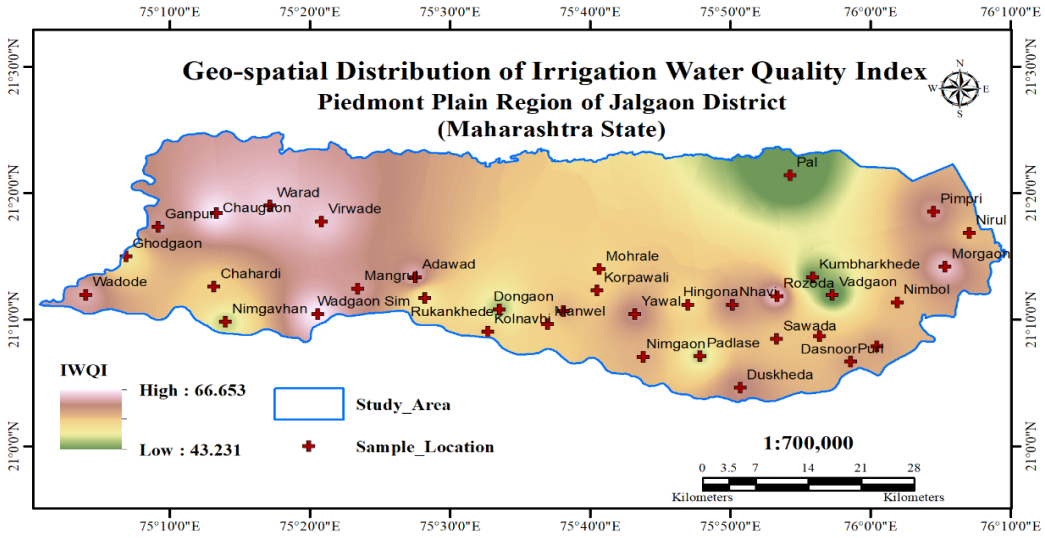

Figure 3: *Geo-spatial distribution of Irrigation Water Quality Index*

Statistical Investigation

The SPSS (version 17), a statistical software package were used for computing inter parameters relationships and chief element study of the database (Tiwari et al., 2017). Statistical investigation is an essential method used to process large volumes of quantitative data and expressing normal tendencies (Wang et al., 2013). This investigation attempts to establish the nature of the relationship among the water quality parameters and IWQI (Alberto et al., 2001). The computed simple statistic and correlation matrix of the 6 measured parameters is mentioned in Table 4 & 6.

Table 6: *Karl's Pearson Correlation*

N = 36		Na	EC	Cl	HCO_3	SAR	IWQI
Na		1	0.735**	0.635**	0.512**	0.923**	0.235
	Sig. (2-tailed)		0.000	0.000	0.001	0.000	0.167
EC		0.735**	1	0.835**	0.495**	0.481**	0.250
	Sig. (2-tailed)	0.000		0.000	0.002	0.003	0.141
Cl		0.635**	0.835**	1	0.036	0.518**	0.174
	Sig. (2-tailed)	0.000	0.000		0.833	0.001	0.310
HCO3		0.512**	0.495**	0.036	1	0.279	0.131
	Sig. (2-tailed)	0.001	0.002	0.833		0.099	0.445
SAR		0.923**	0.481**	0.518**	0.279	1	0.174
	Sig. (2-tailed)	0.000	0.003	0.001	0.099		0.309
IWQI		0.235	0.250	0.174	0.131	0.174	1
	Sig. (2-tailed)	0.167	0.141	0.310	0.445	0.309	
** Correlation is significant at the 0.01 level (2-tailed).							

5. Conclusion

In the present investigation, the data of thirty-six groundwater samples was generated using standard methods for testing Meireles Irrigation Water Quality Index (MIWQI) model. The present study revealed that, the values observed for Electrical Conductivity (EC), Sodium (Na) Bicarbonate (HCO3), Chloride (Cl), Magnesium (Mg), Calcium (Ca) and Sodium Absorption Ratio (SAR) were found well below prescribed limits for irrigation water. The computed values of Irrigation Water Quality Index (IWQI) exhibits that, ¾ part of study area has found moderately restricted and ¼ part of study region

has recorded highly restricted for soil and growing plants based on IWQI. The results of geo-spatial distribution of IWQI showed that, the major restrictions were observed at Pal village from Northern part whereas minor restriction were found at all remaining part of the study area. The overall trends of increasing restrictions were observed from western to eastern part of piedmont plain of Jalgaon district. Hence, the above results conclude that, intensive agriculture by over use of inorganic fertiliser; pesticides, high depth water, polluted drain water and improper irrigation practices were posed a serious threat to groundwater quality in agricultural areas of piedmont plain of Jalgaon district.

References

Abbasnia, A., Radfard, M., Mahvi, A.H., Nabizadeh, R., Yousefi, M., Soleimani, H. and Alimohammadi, M. 2018. Groundwater quality assessment for irrigation purposes based on irrigation water quality index and its zoning with GIS in the villages of Chabahar, Sistan and Baluchistan, Iran. *Data in Brief*, 19, pp.623-31.

Al-mussawi, W. 2016. *Determining irrigation water quality index for evaluation groundwater quality of Green-Belt Zone, Karbala, Iraq*. 4th International Congress on Civil Engineering, Architecture & Urban Development, pp.1-13.

Alberto, W.D., María del Pilar, D., María Valeria, A. and María de los Ángeles, B. 2001. Pattern recognition techniques for the evaluation of spatial and temporal variations in water quality. A Case Study: Suquía River Basin (Córdoba–Argentina). *Water Research*, 35(12), pp.2881-94.

Lenore S. Clesceri, Arnold E. Greenberg, Andrew D. Eaton (1998). *Standard Methods for Examination of Water and Wastewater*. *American Public Health Association (APHA)*. https://doi.org/ISBN 9780875532356 Available from: Reference Book

Ayers, R.S. and Westcot, D.W. 1985. *Water Quality for Agriculture*. FAO Irrigation and Drainage Paper 29 Rev.1. Available from: *http://www.fao.org/3/T0234E/T0234E00.html*.

Brown, R.M., McClelland, N.I., Deininger, R.A. and O'Connor, M.F. 1972. A Water Quality Index - Crashing the Psychological Barrier. *Indicators of Environmental Quality*. Available from: DOI: *10.1016/b978-0-08-017005-3.50067-0*

CGWA. 2013. Ground Water Information of Jalgaon District (Maharashtra). Available from : *http://cgwb.gov.in/District_Profile/Maharashtra/Jalgaon.pdf*

CWC. 2017. Annual Report (2016-17). Available from: *http://cwc.gov.in/annual-reports-english*

Fipps, G. 2003. Irrigation water quality standards and salinity management strategies. *Texas A&M Agrilife Extension*, 4(03), pp.1-18.

Gidey, A. 2018. Geospatial distribution modeling and determining suitability of groundwater quality for irrigation purpose using geospatial methods and Water Quality Index (WQI) in Northern Ethiopia. *Applied Water Science*, 8(3), p.82.

Govt. of Maharashtra. 1962. Jalgaon District Gazetteers. Available from: *https://gazetteers.maharashtra.gov.in/cultural.maharashtra.gov.in/english/gazetteer/gazetteerlist.html*

Govt. of Maharashtra. 2011. Jalgaon District Census Handbook. Directorate of Census Operations, Maharashtra Ministry of Home Affairs, Exchange Building, 2nd Floor, Sir Shivasagar Ram Gulam Marg, Mumbai – 400001. Series-2 (Part XII - A), pp.1-1060.

Horton, R.K. 1965. An index number system for rating water quality. *Journal of Water Pollution Control Federation*, 37(3), pp.300-6.

Islam, M.S. and Shamsad, S.Z.K.M. 2009. Assessment of irrigation water quality of Bogra district in Bangladesh. *Bangladesh Journal of Agricultural Research*, 34(4), pp.507-608.

Kannel, P.R., Lee, S., Lee, Y.S., Kanel, S.R. and Khan, S.P. 2007. Application of water quality indices and dissolved oxygen as indicators for river water classification and urban impact assessment. *Environmental Monitoring and Assessment*, 132(1-3), pp.93-110.

Laluraj, C.M., Gopinath, G. and Dineshkumar, P.K. 2005. Groundwater chemistry of shallow aquifers in the coastal zones of Cochin, India. *Applied Ecology and Environmental Research*, 3(1), pp.133-9.

Lenntech. 2016. *Irrigation Water Quality*. Available from: *https://www.lenntech.com/applications/irrigation/quality/irrigation-water-quality.htm.*

Matthess, G. 1982. *The Properties of Ground Water*. John Wiley and Sons, New York, USA.

Balathandayutham, K., Valliammai, A., Kavitha, B. and Mayilswami, C. 2013. Remote Sensing and GIS Application for Groundwater Quality Mapping in Palar sub basin, Tamilnadu, India. *International Journal of Advanced Life Sciences*, 6(3), pp.210-15.

Meireles, A.C.M., Andrade, E.M.D., Chaves, L.C.G., Frischkorn, H. and Crisostomo, L.A. 2010. A new proposal of the classification of irrigation water. *Revista Ciência Agronômica*, 41(3), pp.349-57.

Miller, R.W. and Donahue, R.L. 1995. *Soils in Our Environment*. 11th ed. Pearson/Prentice Hall, USA.

Rabeiy, R.E. 2017. Assessment and modeling of groundwater quality using WQI and GIS in Upper Egypt Area. *Environmental Science and Pollution Research*, pp.1-10.

Ravikumar, P. and Somashekar, R.K. 2012. Assessment and modelling of groundwater quality data and evaluation of their corrosiveness and scaling potential using environmetric methods in Bangalore South Taluk, Karnataka State, India. Water Resources, 39(4), pp.446-73.

Rengasamy, P. 1987. Importance of calcium in irrigation with saline-sodic water - a viewpoint. *Agricultural Water Management*, 12(3), pp.207-19.

Shabbir, R. and Ahmad, S.S. 2015. Use of geographic information system and water quality index to assess groundwater quality in Rawalpindi and Islamabad. *Arabian Journal for Science and Engineering*, 40(7), pp.2033-47.

Simsek, C. and Gunduz, O. 2007. IWQ index: a GIS-integrated technique to assess irrigation water quality. *Environmental Monitoring and Assessment*, 128(1-3), pp.277-300.

Srinivas, Y., Oliver, D.H., Raj, A.S. and Chandrasekar, N. 2013. Evaluation of groundwater quality in and around Nagercoil town, Tamilnadu, India: an integrated geochemical and GIS approach. *Applied Water Science*, 3(3), pp.631-51.

Subramani, T., Elango, L. and Damodarasamy, S.R. 2005. Groundwater quality and its suitability for drinking and agricultural use in Chithar River Basin, Tamil Nadu, India. *Environmental Geology*, 47(8), pp.1099-110.

Sujatha, D. and Reddy, B.R. 2003. Quality characterization of groundwater in the south-eastern part of the Ranga Reddy district, Andhra Pradesh, India. *Environmental Geology*, 44(5), pp.579-586.

TERI. 2014. Assessing Climate Change Vulnerability and Adaptation Strategies for Maharashtra: Maharashtra State Adaptation Action Plan on Climate Change (MSAAPC).

Tiwari, A.K., Singh, A.K., Singh, A.K. and Singh, M.P. 2017. Hydrogeochemical analysis and evaluation of surface water quality of Pratapgarh district, Uttar Pradesh, India. *Applied Water Science*, 7(4), pp.1609-23.

Todd, K.T. 1980. *Groundwater Hydrology*. 3rd ed. John Wiley & Sons, Inc., USA.

Vasanthavigar, M., Srinivasamoorthy, K., Vijayaragavan, K., Ganthi, R.R., Chidambaram, S., Anandhan, P., Manivannan, R. and Vasudevan, S. 2010. Application of water quality index for groundwater quality assessment: Thirumanimuttar sub-basin, Tamilnadu, India. *Environmental Monitoring and Assessment*, 171(1-4), pp.595-609.

Wang, Y., Wang, P., Bai, Y., Tian, Z., Li, J., Shao, X., Mustavich, L.F. and Li, B.L. 2013. Assessment of surface water quality via multivariate statistical techniques: a case study of the Songhua River Harbin region, China. *Journal of Hydro-environment Research*, 7(1), pp.30-40.

Wilcox, L.V. 1948. *The quality of water for irrigation use*. US Department of Agriculture Technology Bulletin 962, Washington DC.

Xiao, Y., Gu, X., Yin, S., Shao, J., Cui, Y., Zhang, Q. and Niu, Y. 2016. Geostatistical interpolation model selection based on ArcGIS and spatio-temporal variability analysis of groundwater level in piedmont plains, Northwest China. *SpringerPlus*, 5(1), p.425.

Zahedi, S. 2017. Modification of expected conflicts between drinking water quality index and irrigation water quality index in water quality ranking of shared extraction wells using multi criteria decision making techniques. *Ecological Indicators*, 83, pp.368-79.

Cloud Publications
International Journal of Advanced Remote Sensing and GIS
2019, Volume 8, Issue 1, pp. 2939-2954
ISSN 2320 – 0243, Crossref: 10.23953/cloud.ijarsg.403

Research Article

Morphometric Analysis of Mun River Basin, Thailand: A Geographical Information System Approach

K. Swetha[1], G. Jayachandra Reddy[2]

[1]Department of Geography, College of Sciences, Sri Venkateswara University, Tirupati – 517502, India
[2]Director, UGC CSEAPS, College of Arts, Sri Venkateswara University, Tirupati – 517502, India

Publication Date: 21 February 2019

Correspondence should be addressed to *sskswetha22@gmail.com, jayachandrareddy.g@gmail.com*

DOI: https://doi.org/10.23953/cloud.ijarsg.403

Abstract The aim of present study is to investigate morphometric analysis of Mun river basin in Thailand. The drainage parameters performed such as linear, aerial and relief aspects of 23 sub watersheds in the concentrated area. The analysis shows that watershed conatins 6611 drainage segments and stream order from I to VII. From that 5275 segments are comes under I order stream, 1025 are II order, 235 are in III order, 57 are IV order, 16 are in V order, 2 and 1 segments are comes under VI and VII order, respectively. The total stream length of Mun river basin is 40353.8 km. The majority of basin contains the bifurcation ratio value is >5. This indicates that geologically hard rock terrain, less infiltration and high flash flood. This analysis helps to better understanding the management and planning activities in study area .
Keywords *Arc GIS; Morphometry; Linear aspect; Aerial aspect and Relief aspect*

1. Introduction

It is a tool for measuring Morphometric, mathematical analysis of the configuration of the earth's surface, form, and dimensions of its landforms (Clarke,1966). This examination provides a quantitative explanation of the basin geometry to grab initial slope or inequalities within the rock hardness, structural controls, recent geologic process and geomorphic history of the basin (Strahler, 1964). The current investigation deals with the fluvialmorphometry, which includes the consideration of linear, aerial and relief aspects of the Sub-watersheds. The study area has been divided into 23 sub-watersheds. GIS techniques are used for assessing various terrain and morphometric parameters of the watershed, as they provide a flexible environment and a powerful tool for the manipulation and analysis of abstraction data significantly for the feature identification and also the extraction of knowledge for higher understanding.

1.1. The Study Area

Mun river basin is located between 15°19′14″N latitude and 105°30′29″E longitude, 15°19′14″N latitude and 105°30′29″E longitude. The river begins in the Khao Yai National Park area of the Sankamphaeng Range, near Nakhon Ratchasima in the northeast (Isan) of Thailand. It flows east through the Khorat Plateau in southernIsan (Buriram, Surin and Sisaketprovinces) for 750 kilometres, until it joins the

Mekong at Khong Chiam in Ubon Ratchathani. The Mun River's main tributary is the Chi River, which joins it in Kanthararom district of Sisaket province. For the present study, as a preparatory work of Thailand Toposheet numbers ND 47-4, ND-8, ND 48-1, ND 48-2, ND 48-3, ND 48-5, ND 48-6, ND 48-7, NE 47-12, NE 47-16, NE 48-9, NE 48-10, NE 48-13 and NE 48-14 with the scale of 1:250,000 were used for preparing base map. Area of the basin is 116226 km² (Figure 1).

In 1994, The National Economic and Social Development Board (NESDB) commissioned a study on water availability in all of Thailand's river basins. The studies were based on the Royal Irrigation Department's (RID) classification of river basins in Thailand, which divides the country into 25 river basins. This classification, however, is based on both hydrological and administrative boundaries and as Alford (1994) pointed out, on the eight natural basins which are totally within Thailand. With the Chi river emptying in to the Mun river near Ubon Ratchathani, some 100 km upstream of the confluence with the Mekong river, the two river systems are split by RIDs classification, though the river system that lies within Thai territory would actually be the Mun basin with its largest tributary as the Chi river. As the largest tributary to the Mekong river and the very core of regional planning effort we will consider the Mun basin (in Alford's sense), denoted here as the Chi-Mun river basin.

2. Materials and Methods

The general purpose of this analysis of watershed, from a Survey of India, toposheet on 1:2,50,000 scale have been used for preparation maps like base map and drainage network map of the watershed and demarcate the 23 sub-watershed in the concentrated area based on the elevation, slope and outlet points. The numbers were given in the Figure 2. The watersheds have been digitized through the ArcGIS Software 10.1 and calculated the stream orders, which was proposed by Strahler (1952). The various Quantitative morphometric analysis was carried out in 23 micro-watersheds separately for assessing their linear, areal and relief aspects.

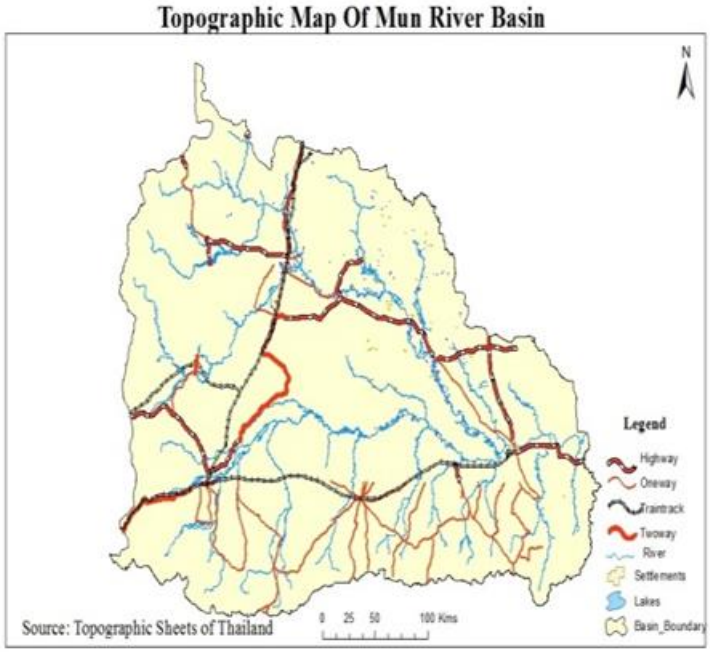

Figure 1: *Study area*

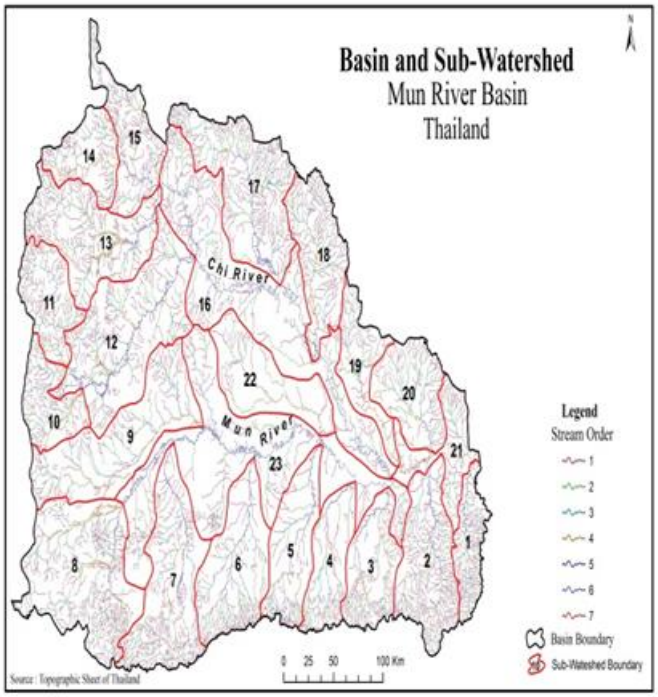

Figure 2: *Sub-watershed and steam orders*

Table 1: *Methodology adopted for computations of morphometric parameters*

Morphometric Parameters	Formula	Reference
I. Linear Aspects		
Stream Order	Hierarchical rank of streams	Strahler (1952)
Bifurcation Ratio (Rb)	Rb=Nu/Nu+1 Nu=Total no. of stream segments of order "u' Nu+1= Number of segments of the next higher order	Schumm (1956)
Mean Bifurcation Ratio (Rbm)	Rbm= Average of Bifurcation ratios of all orders	Strahler (1957)
Stream Length (Lu)	Length of the stream (Km)	Horton (1945)
Mean Stream Length (Lsm)	Lsm=Lu/Nu Lu=Total stream length of order 'u' Lu-1=Total stream length of its next lower order	Horton (1945)
Stream Length Ratio (Rl)	Rl= Lu/Lu-1 Lu=Total stream length of the order 'u' Lu-1=Total stream length of its next lower order	Horton (1945)
II. Areal Aspect		
Drainage Density (Dd)	Dd=Lu/A Lu=Total stream length of all orders (Km) A=Area of the Basin (Km^2)	Horton (1945)
Texture Ratio (Rt)	T=Nu/P Nu=Total no. of streams of all orders P=Perimeter(Km)	Smith (1950)
Stream Frequency (Fs)	Fs= Nu/A Nu= Total no. of streams of all orders A=Area of the Basin (Km^2)	Horton (1945)
Form Factor (Ff)	$Ff=A/Lb^2$ A=Area of the Basin (Km^2)	Horton (1932)

	Lb^2= Square of the basin length (m)	
Elongation Ratio (Re)	Re=2√(A/Pi)/Lb A= Area of the Basin (Km^2), Pi=3.14 Lb=Basin length (m)	Schumm (1956)
Circularity Ratio (Rc)	Rc=4*Pi *A/P^2 A= Area of the Basin (Km^2), Pi=3.14 P^2 =Square of the perimeter (Km)	Miller (1953)
Length of Overland Flow (Lg)	Lg=1/D*2 Lg=Length of overland flow Dd=Drainage density	Horton (1945)
III. Relief Aspects		
Relative Relief (R) (or) Basin Relief (Bh)	R = H-h H=Maximum height (m) h=Minimum height (m)	Strahler (1952)
Relief Ratio (Rh)	Rh= R/Lb R= Relative relief (m) Lb= Basin length (m)	Schumm (1956)

The morphometric analysis of a drainage basin and its drainage network can be better achieved through the latest technologies like GIS, since conventional measurement of these parameters is laborious and cumbersome. The methodology adopted for the computation of morphometric parameters given in Table 1.

3. Results and Discussion

In the present study, the morphometric parameters such as linear, areal and relief aspects for the delineated sub-watersheds are calculated based on formulas suggested by various workers and the results are discussed below.

Linear Aspects

Linear aspects of the basin are related to the channel patterns of the drainage network wherein the topological characteristics of the stream segment in terms of open links of the network, which consists of all of the segment of stream of a particular river, is reduced to the level of graphs, where stream junctions act as points (nodes) and streams, which connect the points (junctions) become links or lines wherein the numbers in all segments are counted, their hierarchical orders are determined, the length of all stream segments are measured and their different interrelationship are studied. The nature of flow paths in in terms of sinuosity is equally important in the study of linear aspects of the drainage basins. Thus, the linear aspect includes the discussion and analysis of stream order (μ), stream number (nμ), bifurcation ratio (Rb), stream lengths (Lμ), length ratio (R^L), length of overland flow (L^g), sinuosity indices etc.

Stream Order

The designation of stream orders in the first step in drainage basin analysis based on a hierarchic ranking of streams. In the present study, ranking of streams has been carried out basin on the method proposed by Strahler (1964). According to him “each finger-tip channel is designated as segment of 1st order. At the junction of any two 1st order segments, a channel of 2nd order is produced and extends down to the point, where it joins another 2nd order segments whereupon a segment of 3rd results and so forth”. These streams may have additional stream segments of lower orders than their own order

and thus these do not affect the classification (Figure 1). It may be mentioned that the hierarchical order increases only when two stream segments of equal meet and form a junction. The order does not increase if a lower order stream segment meets a stream segment of high order.

The entire basin consists 6611 segments of river in the range of stream order I to VII. Out of which 5275 segments are comes under I order stream, 1025 are II order, 235 are in III order, 57 are IV order, 16 are in V order, 2 and 1 segments are comes under VI and VII order respectively.

Taking into sub watershed individually seven and eight sub-watershed consist above 500 stream segments, 2,12,16,17 and 23 sub watersheds are consist above 400 stream segments, 6 and 13 sub-watersheds are consist above 300 stream segments, 1,3,4,5,9,15 and 18 sub watersheds are consist above 200 stream segments, 10,11,14,19,20, and sub-watersheds are consist of above 100 stream segments and 22 sub watershed is consist below 100 stream segments. The sub-watersheds with higher no of stream segments are characterized by bigger watershed area.

Table 2: *Stream order and stream length of mun river basin*

Sub-Watersheds	***Number of Streams (Nu)***								***Stream Length in Km (Lu)***							
	I	**II**	**III**	**IV**	**V**	**VI**	**VII**	**Total**	**I**	**II**	**III**	**IV**	**V**	**VI**	**VII**	**Total**
1	186	42	9	2	1	-	-	239	718.5	229.2	109.5	20	105.9	-	-	1183.1
2	369	72	15	3	1	-	-	460	1442.2	385.3	180.6	126.1	160.8	-	-	2295.0
3	170	35	8	3	1	-	-	217	698.8	216.2	94	149.8	107.2	-	-	1266.3
4	164	29	6	2	1	-	-	202	443	179.1	185	69.1	84.4	-	-	960.6
5	218	26	8	3	1	-	-	256	489.8	168.4	113.6	102.4	171.1	-	-	1045.3
6	232	50	14	4	1	-	-	301	739.4	358.4	245.6	40.6	156.7	-	-	1540.7
7	401	75	20	4	1	-	-	501	1370.2	384.3	288.4	196.5	199.6	-	-	2439.0
8	427	102	25	5	3	-	-	562	1620.5	622	254.1	493.2	334.6	-	-	3324.4
9	169	36	8	2	-	-	-	215	927	326.3	263.5	267.1	-	-	-	1783.9
10	108	32	5	2	-	-	-	147	580.6	241.1	122.1	122.2	-	-	-	1066.0
11	151	35	6	1	-	-	-	193	752.7	265	137.7	120.4	-	-	-	1275.8
12	359	65	16	4	1	-	-	445	1393.3	534.5	288.5	137.5	428.3	-	-	2782.1
13	256	59	11	2	1	-	-	329	1303.5	443.3	160.5	370.7	105.8	-	-	2383.8
14	118	31	8	3	-	-	-	160	619.5	177.2	100.8	139.8	-	-	-	1037.3
15	202	47	8	5	2	-	-	264	828.3	226	151.9	117.9	179.9	-	-	1504.0
16	394	50	11	1	-	1	-	457	1619.3	450.8	219.7	33.7	-	775	-	3098.5
17	395	81	17	4	1	-	-	498	1555.6	587.5	307.2	40.7	276	-	-	2767.0
18	246	44	6	2	1	-	-	299	1062.7	374.6	124.7	160.5	49.5	-	-	1772.0
19	89	12	13	1	-	-	-	115	435.3	135.1	118.2	182.8	-	-	-	871.4
20	120	29	9	3	1	-	-	162	626.3	301.2	172.9	241.6	36.9	-	-	1378.9
21	110	23	2	-	-	-	1	136	533.9	196.2	79.1	-	-	-	118.1	927.3
22	43	12	2	1	-	-	-	58	355.4	184.1	26.5	165.4	-	-	-	731.4
23	354	40	8	3	1	1	-	407	1218.8	361	239.7	216.1	295.1	589.3	-	2920.0

Stream Length

The numbers of streams of various orders in watershed are counted and their lengths from mouth to drainage divided are measured with the help of GIS software's, (Table 2) the stream length (Lu) has been computed based on the law proposed by Horton (1945) for all the 23 sub watersheds (Table 1). Generally, the total length stream segments are maximum in first order streams and decreases as the stream order increases.

The total stream length of Mun river basin is about 40353.8 km of which first order stream length is about 21334.6 km. The second order stream length is 7346.8 km. The third order stream length is 3983.8 km. The fourth order stream length is 3514.1 km. The fifth order stream length is 2691.8 km. The sixth order stream length is 1364.3 km. and the seventh order stream length is 118.1 km.

The large sub-watershed such as, sub watershed 8, 16, 23, 12 and 17 are compressing the total stream lengths of 3324.4, 3098.5, 2920, 2782.1 and 2767 km are respectively. Obviously, the lesser total stream length is observed in the watershed of lesser area. Higher of I order stream segments are notably observed in sub watershed 8, 16, 17, 2, 12, 7,13, 23 and 18. Whereas in II order, the stream lengths are higher in sub watershed such as, Sub watershed 8, 17, 12, 16 and 13. Generally, the total length of stream segments is maximum in first order streams and decreases as the stream order increases.

Mean Stream Length

According to Strahler (1964), the mean stream length is a characteristics property related to the drainage network and is associated surface. The mean stream length (Lsm) has been calculated by dividing the total stream length of order 'u' and number of stream length of order 'u' (Table 1) it is noted from (Table 3) that Lsm varies from 4.08 to 12.61 and Lsm of any given order is greater than that of the higher order, this might be due variations in slope and topography.

Stream Length Ratio

Stream length ratio (RL) may be defined as the ratio of the mean stream length of the one order to the next lower order of stream segment (Table 1) Horton's law (1945) of stream length states that stream length segments of each of the successive orders of a basin tends to approximate a direct geometric series with streams length increasing towards higher of streams.

Table 3: *Mean stream length and stream length ratio of various sub-watersheds*

	Mean stream length in km (Lsm)								***Stream length ratio (RI)***						
S.No.	I	II	III	IV	V	VI	VII	Lsm	II/I	III/II	IV/III	V/IV	VI/V	VII/VI	Average
1	718.5	229.2	109.5	20	105.9	0	0	4.95	0.31	0.47	0.18	5.29	0	0	1.04
2	1442.2	385.3	180.6	126.1	160.8	0	0	4.98	0.26	0.46	0.69	1.27	0	0	0.44
3	698.8	216.2	94	149.8	107.2	0	0	5.83	0.3	0.43	1.59	0.71	0	0	0.5
4	443	179.1	185	69.1	84.4	0	0	4.75	0.4	1.03	0.37	1.22	0	0	0.5
5	489.8	168.4	113.6	102.4	171.1	0	0	4.08	0.34	0.67	0.9	1.67	0	0	0.59
6	739.4	358.4	245.6	40.6	156.7	0	0	5.11	0.48	0.68	0.16	3.85	0	0	0.86
7	1370.2	384.3	288.4	196.5	199.6	0	0	4.86	0.28	0.75	0.68	1.01	0	0	0.45
8	1620.5	622	254.1	493.2	334.6	0	0	5.91	0.38	0.4	1.94	0.67	0	0	0.56

9	927	326.3	263.5	267.1	0	0	0	8.29	0.35	0.8	1.01	0	0	0	0.36
10	580.6	241.1	122.1	122.2	0	0	0	7.25	0.41	0.5	1	0	0	0	0.31
11	752.7	265	137.7	120.4	0	0	0	6.61	0.35	0.51	0.87	0	0	0	0.28
12	1393.3	534.5	288.5	137.5	428.3	0	0	6.25	0.38	0.53	0.47	3.11	0	0	0.74
13	1303.5	443.3	160.5	370.7	105.8	0	0	7.24	0.34	0.36	2.3	0.28	0	0	0.54
14	619.5	177.2	100.8	139.8	0	0	0	6.48	0.28	0.56	1.38	0	0	0	0.37
15	828.3	226	151.9	117.9	179.9	0	0	5.69	0.27	0.67	0.77	1.52	0	0	0.53
16	1619.3	450.8	219.7	33.7	0	775	0	6.78	0.27	0.48	0.15	0	22.99	0	3.98
17	1555.6	587.5	307.2	40.7	276	0	0	5.55	0.37	0.52	0.13	6.78	0	0	1.3
18	1062.7	374.6	124.7	160.5	49.5	0	0	5.92	0.35	0.33	1.28	0.3	0	0	0.37
19	435.3	135.1	118.2	182.8	0	0	0	7.57	0.31	0.87	1.54	0	0	0	0.45
20	626.3	301.2	172.9	241.6	36.9	0	0	8.51	0.48	0.57	1.39	0.15	0	0	0.43
21	533.9	196.2	79.1	0	0	0	118.1	6.81	0.36	0.4		0	0	1.49	0.45
22	355.4	184.1	26.5	165.4	0	0	0	12.61	0.51	0.14	6.24	0	0	0	1.14
23	1218.8	361	239.7	216.1	295.1	589.3	0	7.17	0.29	0.66	0.9	1.36	1.99	0	0.86

Bifurcation and Mean Bifurcation Ratio (Rb and Rbm)

The term bifurcation ratio (Rb) may be defined as the ratio of the number of stream segments of given order to the number of segments of the next higher order (Schumm, 1956). Strahler (1957) demonstrated that bifurcation ratio shows a small range of variation for different environmental except where the powerful geological control dominates.

Table 4: *Bifurcation ratio of various sub watersheds of Mun river basin*

	Number of streams (Nu)								Bifurcation Ratio (Rb)								
S.No.	I	II	III	IV	V	VI	VII	Total	RB1	RB2	RB3	RB4	RB5	RB6	Rbm	S.No.	I
1	186	42	9	2	1	-	-	239	4.42	4.66	4.5	2	0	0	2.60	1	186
2	369	72	15	3	1	-	-	460	5.12	4.8	5	3	0	0	2.99	2	369
3	170	35	8	3	1	-	-	217	4.85	4.37	2.66	3	0	0	2.48	3	170
4	164	29	6	2	1	-	-	202	5.65	4.83	3	2	0	0	2.58	4	164
5	218	26	8	3	1	-	-	256	8.38	3.25	2.66	3	0	0	2.88	5	218
6	232	50	14	4	1	-	-	301	4.64	3.57	3.5	4	0	0	2.62	6	232
7	401	75	20	4	1	-	-	501	5.34	3.75	5	4	0	0	3.02	7	401
8	427	102	25	5	3	-	-	562	4.18	4.8	5	1.66	0	0	2.61	8	427
9	169	36	8	2	-	-	-	215	4.69	4.5	4	0	0	0	2.20	9	169
10	108	32	5	2	-	-	-	147	3.37	6.4	2.5	0	0	0	2.05	10	108
11	151	35	6	1	-	-	-	193	4.31	5.83	6	0	0	0	2.69	11	151
12	359	65	16	4	1	-	-	445	5.52	4.06	4	4	0	0	2.93	12	359
13	256	59	11	2	1	-	-	329	4.33	5.36	5.5	2	0	0	2.87	13	256
14	118	31	8	3	-	-	-	160	3.8	3.87	2.66	0	0	0	2.40	14	118
15	202	47	8	5	2	-	-	264	4.29	5.87	1.6	2	0	0	2.29	15	202
16	394	50	11	1	-	1	-	457	7.88	4.54	11	0	1	0	4.07	16	394
17	395	81	17	4	1	-	-	498	4.87	4.76	4.25	4	0	0	2.98	17	395
18	246	44	6	2	1	-	-	299	5.59	7.33	3	2	0	0	2.99	18	246
19	89	12	13	1	-	-	-	115	7.41	0.92	1	0	0	0	1.56	19	89
20	120	29	9	3	1	-	-	162	4.13	3.22	3	3	0	0	2.23	20	120
21	110	23	2	-	-	-	1	136	4.78	11.5	0	0	0	2	3.05	21	110

22	43	12	2	1	-	-	-	58	3.58	6	2	0	0	0	1.93	22	43
23	354	40	8	3	1	1	-	407	8.85	5	2.66	3	1	0	3.42	23	354
Ave.									5.21	4.92	3.67	1.85	0.09	0.09	2.67	Ave.	

The mean bifurcation ratio (Rbm) may be defined as the average of bifurcation ratio of all orders (Strahler, 1957). The Mun river basin the higher mean bifurcation ratio has been observed for the sub watershed 11, 15 and 21.

Mean bifurcation shows stable trends in a region of uniform geological structure and lithologies but they show variable trends over varying geological structures, (Sing et al., 1984) have remarked that “geological structure and associated lithologies do not cause significant variations in bifurcation ratios and this observation holds parity with the conclusions of (Miller, 1953)”.

Horton (1945) classified the mean bifurcation ratio into two classes: 0 to 2 flat or rolling basin; 3 to 4 mountainous or hilly regions.

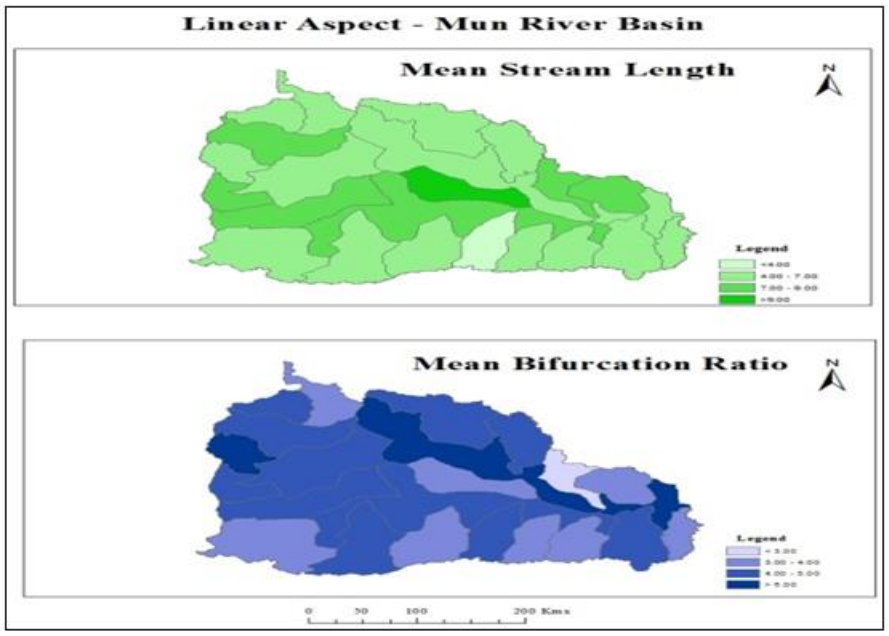

Figure 3: *Linear aspect – mun river basin*

“Mean bifurcation ratios register very small variation from region to region irrespective of structural control” (Savindra Sing et al., 1894). Fallowing strahler it may be postulated that mean bifurcation ratios show small variation from one region to another and such variations may be ascribed to chance variations.

The Mean bifurcation ratio (Rbm) of entire basin have identified as 2.67 whereas the Mean bifurcation ratio (Rbm) values of the 23 sub watersheds have varied between 1.56 to 4.07 notably the average basins bifurcation ratio of each stream order doesn’t possess any greater variations. Table 4 reveals sub watershed 3, 9, 10, 14, 15, 19, 20 and 22 are identified with the mean bifurcation ratio values of less than 2.5 and these sub watersheds are observed with the soil types of Palaviduthi or Aeolian or Vyologam, geological these sub watersheds are identified with either silliminate or recent alluvium.

Areal Aspect

The areal aspect of the drainage basin include the study of basin perimeter, geometry of closed links i.e. basin shape, law of basin area, law of allometric growth, stream frequency, drainage density, drainage texture, form factor, elongation ratio, and circularity ratio etc.

Basin Area

Basin area is very important Morphometric attribute as it is related to the spatial distribution of a number of significant attributes such as drainage density, stream frequency, drainage texture, slopes absolute and relative reliefs, dissection index etc. The drainage area is delineated on the basis of water divides and the areas of all stream segments of each order. All of the ground surface, which directly feeds the first order basins. The area of second order stream segments include the area of first order segments plus the areas of inter-basins, which are triangular patches of ground surfaces contributing directly to the second order segments. The same principle works for all the increasing successive order segments (Sing and Srivasava, 1974). Thus, the basin area becomes automatically cumulative from the first order to the successive higher orders. For the present study area of the sub watersheds is 116226 km² notably sub watershed 23, 16, 12, 8, 9 and 7 sub watersheds are the highest basin respectively (12316, 11148, 8322, 8172, 6871, and 6246 km²) (Table 5).

Table 5: *Basin area, Perimeter, Basin length of the Mun river basin*

No. of Sub.	Area (sqkms)	Perimiter (kms)	Length (kms)
1	2075	290.968	103.54
2	4838	354.407	122.05
3	3339	261.936	89.96
4	3016	268.839	103.17
5	3731	306.896	115.15
6	5088	319.568	122.8
7	6246	447.671	140.39
8	8172	468.675	125.92
9	6871	477.351	175.96
10	2598	270.126	95.86
11	2952	257.71	85.44
12	8322	495.377	159.22
13	5851	436.979	140.1
14	2657	238.967	85.45
15	3403	364.021	121.07
16	11148	873.762	309.54
17	6503	446.477	159.12
18	4029	349.418	116.18
19	2643	348.328	125.81
20	3565	258.527	78.35
21	2620	406.497	87.71
22	4242	330.375	135.72
23	12316	1141.32	365.48

Basin Shape

The geometry of basin shape is a paramount significance as it helps in the description and comparison of different forms of the drainage basins and it is also related to the functioning of the units of the basins and its genesis. On the average 3 sub-categories of basin shapes have been recognized viz. (i) circular, (ii) elongated, and (iii) indented.

Basin Length

Length in a straight line from the mouth of a stream to the farthest point on the drainage dived of its basin. The study area has total length of 3163.99 km and the 23 and 16 sub watersheds are the high basin length.

Form Factor (Rf)

According to Horton (1932), form factor (Rf) may be defined as the ratio of basin area to square of the basin length. With the reference to the Table 6 it is observed than form factor of the entire Mun river basin is 0.29. The sub watersheds are 2, 3, 6, 7, 8, 12, 14, 20 and 21 have observed the form factor value above 0.3 implies that the sub watersheds are relatively circular in shape, whereas the remaining watersheds have observed with less than 0.3 are comes under elongated in shape. Particularly sub watershed 23 have registered with the lowest value (0.09) and highly elongated. The elongated basin with low form factor indicates that the watershed will have flatter peak of flow for longer duration. Flood flows of such elongated basins are easier to manage of the circular basin.

Elongation Ratio (Re)

Schumm (1956) defined elongation ratio (Re) as the ratio between the diameter of the circle of the same area as the drainage basin and the maximum length of the basin. In general the values of elongation ratio vary from 0.6 to 1.0 over a wide variety of climatic and geological types. Values close to 1.0 are typical of regions of very low relief, whereas values in the range 0.6 to 0.8 are usually associated with high relief and steep ground slope (Strahler, 1964).
These values can be grouped in to 3 categories namely:
i) Circular (>0.9)
ii) Oval (0.8 to 0.9)
iii) Less elongated (<0.7)

Elongation ratio of the sub watershed of the study area varies from (0.34 to 0.72) (Table 6). The lowest elongation ratio (0.32) in case of sub watershed 8 is indicates high relief (2236 m) and steep slope and less elongated in shape. Most of the study area covers the less elongated in shape. Especially the sub watershed IX and X are no relief or flat surface and sub watershed 21 and 22 are the circular in shape with low relief (191 and 253) and shape. A circular basin is more efficient in the discharge of runoff than an elongated basin (Sing, 1997).

Circularity Ratio (Rc)

The circularity ratio was proposed by Miller (1953) as comparison of the basin area with the area of the circular having the same perimeter. The circularity ratio is influenced by the length and frequency of streams, geological structure, landuse/landcover, climate relief and slope of the basin. In this study circularity value varies between 0.03 to 0.67 (Table 6). High circularity ratio values more than 0.4 have

observed for the sub watershed 2, 3, 4, 5, 6, 8, 10, 11, 12, 14, 17, 18, 20 and 22 sub watersheds, and one can said it is more or less circular and notably characterised by the drainage density between 0.15 to 0.35 km/sq km.

The remaining watersheds are observed with the circularity value between 0.3 to 0.4 and it can be said the sub watersheds are elongated in shape, and the drainage density are in this area are observed with either lower density 3.5 to 10.5. Soil, geomorphology, land use and geological formation of this area implies no direct relationship with the variations in the circularity ratio. Notably there is a close relationship between number of stream and circularity ratio, the higher circularity ratio values are usually associated lower number of stream segments and vice versa.

Drainage Density (d)

Drainage density refers total stream lengths per unit area. Horton (1945) defines drainage density as ratio of total length of all stream segments in a given drainage basin to the total area of the basin.

The drainage density can classified into five categories (Savindra Sing, 1978).

i) Extremely low drainage density (0 – 0.25 km)
ii) Low drainage density (0.25 km – 0.35 km)
iii) Moderate drainage density (0.35 km – 0.4 km)
iv) High drainage density (0.4 km – 0.45 km)
v) Very high drainage density (above 0.45 km)

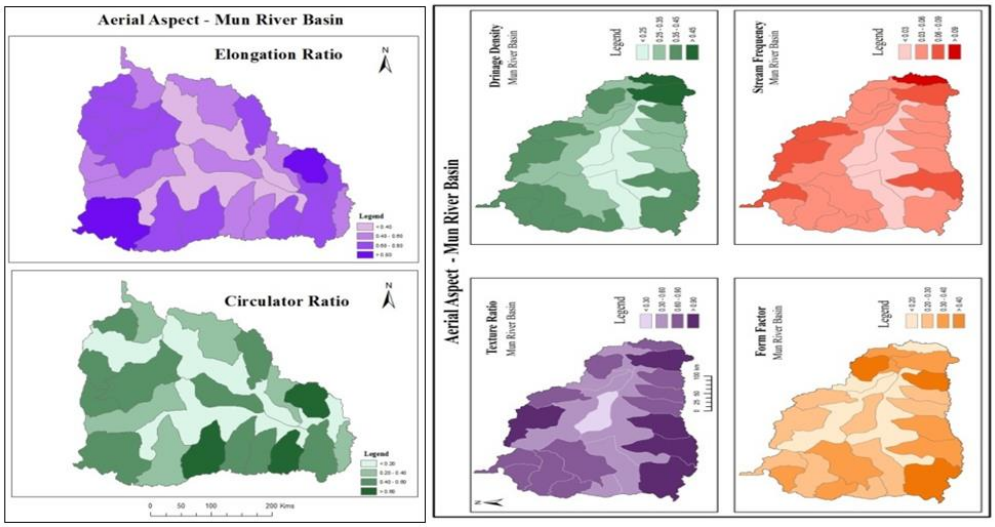

Figure 4: *Aerial aspect – mun river basin*

According to Nag (1998) low drainage density generally results in area of highly resistant (or) permeable sub soil material, and low relief. High drainage density is the result of weak (or) impermeable sub surface material and mountainous relief. Low drainage density leads to coarse drainage texture while high density leads to fine drainage texture.

The low drainage density of the study area are varies from (0.17 to 0.25) indicating low drainage density with low relief ratio of 67m, 162m and 0m respectively coarse drainage texture. Whereas the sub watershed 4, 5, 6, 12, 16, 19 and 21 sub watersheds indicating moderate drainage density (0.25 to 0.35) with high relief 529m, 729m, 2020m, 400m, 938m, 460m, 414m, and 365m respectively and it has the coarse to related coarse drainage texture.

Stream Frequency (Fs)

Stream frequency or drainage frequency is the measure of number of stream per unit area (Horton, 1932). The general categories of the stream frequency are:

- Poor (0.01 to 0.03)
- Moderate (0.03 to 0.06)
- High (0.06 to 0.09)
- Very high (above 0.09)

Sub-watershed 1 comes under the very high stream frequency, sub-watershed 3, 4, 5, 6, 8, 10, 11, 12, 13, 14, 16, 19, 20 and 21 are comes under the moderate stream frequency, sub-watershed 2, 7, 15, 17 and 18 are comes under the high stream frequency and the remaining 9, 22 and 23 sub watersheds are comes under the poor stream frequency.

Drainage Texture (Rt)

According to Horton (1945) drainage texture is the total number of stream segments of all orders per perimeter of that area. It is the one of the important concept of geomorphology which means that the relative spacing of drainage lines. Drainage lines are numerous over impermeable areas than permeable areas.

Smith (1950) has classified drainage density in to five deferent textures.

- The drainage density less than 2 indicates very coarse
- The drainage density between 2 to 4 is coarse
- The drainage density between 4 to 6 is moderate
- The drainage density between 6 to 8 is fine
- The drainage density is greater than 8 is very fine

In the present study the drainage density is less than 2, it indicates very coarse drainage texture.

Length of Overland Flow (Lg)

The length of overland flow, considered as a dominant hydrologic and morphometric factor is the mean horizontal length of flow path from the divided to the stream in a first order basin and is a measure of stream spacing and degree of dissection and approximately one half the reciprocal of the drainage density (Brice, 1964). It is the length of water before it gets concentrated into definite stream channels (Horton, 1945).

The Figure reveals that the length of overland flow is less in, Sub watershed 1, 2, 10, 11, 15, 17 and 18 sub watersheds, as drainage density is high in these sub watersheds, when comparing remaining sub watersheds. The computed value of length of overland flow for all sub watersheds varies from 0.87 to 2.94.

Table 6: *Areal aspects of various sub-watersheds of mun river basin*

S.No.	Area of Basin in sq.km (A)	Length of Basin in km (Lb)	Perimeter in km (P)	Drainage Density in km (Dd)	Texture Ratio (Rt)	Stream Frequency (Fs)	Form Factor Ratio (Ff)	Elongation Ratio (Re)	Circulatory Ratio (Rc)	Length of Overland flow (Lg)
1	2075	103.5	290.9	0.57	0.82	0.11	0.19	0.49	0.3	0.87
2	4838	122	354.4	0.47	1.29	0.09	0.32	0.64	0.48	1.06
3	3339	89.9	261.9	0.37	0.82	0.06	0.41	0.72	0.61	1.35
4	3016	103.1	268.8	0.31	0.75	0.06	0.28	0.6	0.52	1.61
5	3731	115.1	306.8	0.28	0.83	0.06	0.28	0.59	0.49	1.78
6	5088	122.8	319.5	0.3	0.94	0.05	0.33	0.65	0.62	1.66
7	6246	140.3	447.6	0.39	1.11	0.08	0.31	0.63	0.39	1.28
8	8172	125.9	468.6	0.4	1.19	0.06	0.51	0.81	0.46	1.25
9	6871	175.9	477.3	0.25	0.45	0.03	0.22	0.53	0.37	2
10	2598	95.8	270.1	0.41	0.54	0.05	0.28	0.6	0.44	1.21
11	2952	85.4	257.7	0.43	0.74	0.06	0.4	0.71	0.55	1.16
12	8322	159.2	495.3	0.33	0.89	0.05	0.32	0.64	0.42	1.51
13	5851	140.1	436.9	0.4	0.75	0.05	0.29	0.61	0.03	1.25
14	2657	85.4	238.9	0.39	0.66	0.06	0.36	0.68	0.58	1.28
15	3403	121	364	0.44	0.72	0.07	0.23	0.54	0.32	1.13
16	11148	309.5	873.7	0.27	0.52	0.04	0.11	0.38	0.18	1.85
17	6503	159.1	446.4	0.42	1.11	0.07	0.25	0.57	0.4	1.19
18	4029	116.1	349.4	0.43	0.85	0.07	0.29	0.61	0.41	1.16
19	2643	125.8	348.3	0.32	0.33	0.04	0.16	0.46	0.27	1.56
20	3565	78.3	258.5	0.38	0.62	0.04	0.58	0.86	0.67	1.31
21	2620	87.7	406.4	0.35	0.33	0.05	0.34	0.65	0.19	1.42
22	4242	135.7	330.3	0.17	0.17	0.01	0.23	0.54	0.48	2.94
23	12316	365.4	1141.3	0.23	0.35	0.03	0.09	0.34	0.11	2.17
Average	5053.26	137.52	409.26	0.36	0.72	0.05	0.29	0.6	0.4	1.47

Relief Aspects

The relief aspects of the drainage basins are related to the study of three dimensional features of the basin involving area, volume and altitude of vertical dimensions of land forms wherein different morphometric methods are used to analysis the terrain characteristics, which are the result of basin process. Thus, this aspect includes the analysis of the relationships between area and altitude (hypsometric analysis), altitude and slope angle (clinographic analysis), average ground slope, relative relief, relief ratio, dissection index, profiles of terrains and the rivers. The stream elevation can be estimated from the contour crossings on the topographic sheets. The total drop in elevation from the source to the mouth can be found for the elevation from the source to the mouth for the tributaries and the horizontal distances can be measured along the channel using a map measures.

Relative Relief

Relative relief also termed as “amplitude available relief” or “local relief” is defining as the difference in height between the highest and the lowest points (height) in a unit area. Relative relief is very important morphometric variable which is used for the overall assessment of morphological characteristics of terrain and degree of dissection (Glock, 1932).

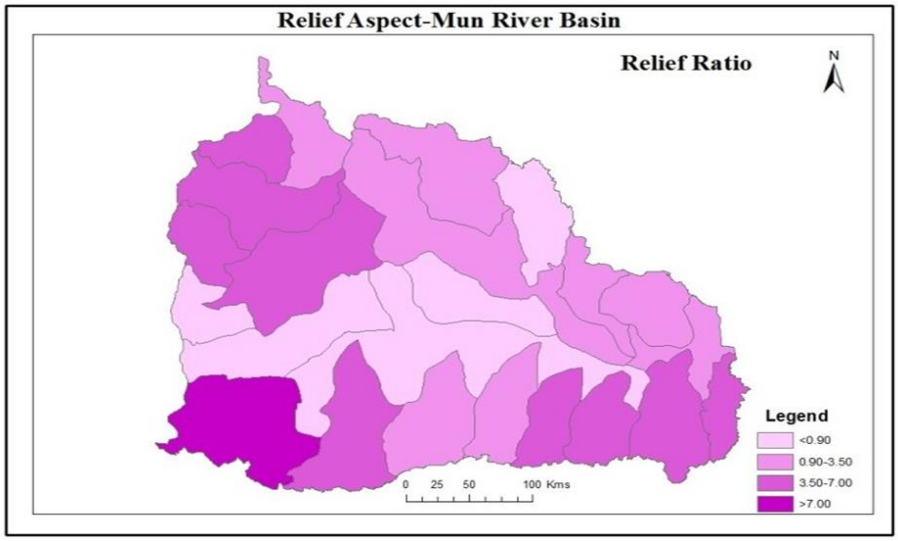

Figure 5: *Relief aspect – mun river basin*

Table 7: *Relief aspect of various sub-watersheds in mun river basin*

No. of Sub-Watersheds	Maximum Height (H)	Minimum Height (h)	Relative Relief (R)	Relief Ratio (Rr)
1	591	150	441	4.26
2	756	120	636	5.21
3	698	129	569	6.32
4	561	134	427	4.14
5	439	127	312	2.71
6	440	139	301	2.45
7	890	161	729	5.19
8	2236	216	2020	16.04
9	0	0	0	0
10	0	0	0	0
11	1340	940	400	4.68
12	1250	223	1027	6.45
13	1250	312	938	6.69
14	1310	850	460	5.38
15	650	236	414	3.42
16	565	123	442	1.42
17	557	192	365	2.29
18	492	388	104	0.89
19	370	128	242	1.92
20	280	135	145	1.85
21	259	128	131	1.49
22	191	124	67	0.49
23	293	131	162	0.44

The relative relief of sub watersheds of the study area varies from 0m to 2020m. Notably the extremely low relative relief (<160m) of the study area of sub watershed 9, 10, 18, 20, 21 and 22, moderately low relative relief of the study area is sub watershed 5, 6, 19 and 23, low relative relief 1, 3, 4, 11, 14, 15, 16 and 17. The remaining sub watershed 2, 7, 13 and 8, 12 are moderately high and high relative relief.

Relief Ratio

The relief ratio of maximum relief to horizontal distance among the longest dimension of the basin parallel to the principle drainage line is termed as relief ratio (Schumm, 1956). According to him there is direct relationship between the relief and channel gradient, there is also a correlation between hydrological characteristics and the relief ratio of a drainage basin.

The relief ratio normally increases with decreasing area and size of sub watersheds of a drainage basin (Gottschalk, 1964). Notably sub watershed 9, 10, 18, 22 and 23 are the larger sub watersheds observed with lower relief ratio of less than 0.90 respectively. Sub watershed 8 is the lower observed with higher relief ratio (above 7.00).

4. Conclusion

In over all, the mun river basin contains the 23 sub-watersheds, 6611 drainage segments and contains I to VII stream orders. In that 5275 segments are comes under I order stream, 1025 are II order, 235 are in III order, 57 are IV order, 16 are in V order, 2 and 1 segments are comes under VI and VII order, respectively. The total stream length of Mum river basin is 40353.8 km. The majority of basin contains the bifurcation ratio value is >5. This indicates that geologically mountanious terrain, less infiltration and high flash flood. This analysis helps to better understanding the management and planning activities in study area.

Acknowledgment

I deem it a great privilege to express my most sincere and heartiest thanks and profound sense of gratitude to my internal guide Dr. G. Jayachandra Reddy Associate Professor, Centre for Southeast Asia & Pacific Studies (Geography), Sri Venkateswara University, Tirupati, for his guidance and supervision in the Dissertation work and having permitted me to choose the dissertation topic of my choice. His inspiration and suggestion, as well as his co-operation has been an attribute in the completion of this dissertation. I cannot but consider myself lucky to have worked under guidelines of knowledge of hunger, excellence pursuing and over helpful personality A. Jegan Kumar, Asst. Professor, Department of Geography, Bharathidasan University, Tiruchirapalli, for taken me as a trainee under his supervision, as well as his valuable guidance, sound, fruitful advise encouragement, and co-operation at all stages.

References

Clarke, J.I. 1966. *Morphometry from Maps - Essays in Geomorphology*. Elsevier Publishing Company, New York, pp.235-274.

Horton, R.E. 1932. Drainage basin characteristics. *Transactions - American Geophysical Union*, 13, pp.350-361.

Horton, R.E. 1945. Erosional development of streams and their drainage basins: hydrophysical approach to quantitative morphology. *Geological Society of America Bulletin*, 56, pp.275-370.

Miller, V.C. 1953. *A quantitative geomorphic study of drainage basin characteristics in the clinch Mountain Area, Virginia and Tennessee*. Proj. NR 389-402, Tech Rep 3, Columbia University, Department of Geology, ONR, New York.

Nag, S.K. 1998. Morphometric analysis using remote sensing techniques in the chaka sub-basin, Purulia District, West Bengal. *Journal of the Indian Society of Remote Sensing*, 26(1&2), pp.69-76.

Nag, S.K. and Chakraborty, S 2003. Influence of rock types and structures in the development of drainage network in hard rock area. *Journal of the Indian Society of Remote Sensing*, 31(1), pp.25-35.

Schumn, S.A. 1956. Evolution of drainage systems and slopes in badlands at perth amboy. *Geological Society of America Bulletin*, 67, pp.597-646.

Singh, S. and Singh, M.C. 1997. Morphometric analysis of kanhar river basin. *National Geographical Journal of India*, 43, pp.31-43.

Smith, K.G. 1950. Standards for grading textures of erosional topography. *American Journal of Science*, 248, pp.655-668.

Strahler, A.N. 1952. Dynamic basis of geomorphology. *Geological Society of America Bulletin*, 63, pp.923-938.

Strahler, A.N. 1957. Quantitative analysis of watershed geomorphology. *Transactions - American Geophysical Union*, 38, pp.913-920.

Strahler, A.N. 1964. *Quantitative Geomorphology of Drainage Basins and Channel Networks*. Edited by Chow, V.T. Handbook of Applied Hydrology, McGraw Hill Book Company, New York.

Cloud Publications
International Journal of Advanced Remote Sensing and GIS
2019, Volume 8, Issue 1, pp. 3030-3046
ISSN 2320 – 0243, Crossref: 10.23953/cloud.ijarsg.417

Research Article

Spatial Distribution Analysis of Surface Water Quality Index Using Remote Sensing and GIS: A Case Study of Erandol (Maharashtra, India)

Ganpat B. More, Kailas P. Dandge and Sanjaykumar R. Thorat

School of Environmental and Earth Sciences,Kavayitri Bahinabai Chaudhari North Maharashtra University, Jalgaon, Maharashtra, India.

Correspondence should be addressed to Ganpat B. More, *moreganpat05@gmail.com*

Publication Date: 6 July 2019

DOI: https://doi.org/10.23953/cloud.ijarsg.417

Abstract Surface water is one of the essential natural resource which support the eco-system to provide a suitable habitat to many living organisms. Monitoring of surface water gives a valuable information to evaluate the water quality problems. The objective of the present study is to evaluate status of surface water quality using drinking water quality index method and spatial distribution techniques using GIS and satellite images of Erandol area (Maharashtra, India). The integrated water samples were collected from different locations and analyzed for 13 physico-chemical characteristics which were compared with the BIS permissible limits. The WQI were calculated by using standard methods of CCMEWQI and WAWQI. The geospatial tools like high resolution multispectral remote sensing data (RESOURCESAT-2, LISS IV), GIS software, and GPS were used to perform the spatial distribution analysis using different water quality parameters. The CCMEWQI and WAWQI method indicated that the both 74% of water samples were found to be in good water quality whereas 22% and 16% of fair to poor water quality respectively. The remaining samples exhibit marginal to very poor water quality. As per WAWQI, 5% of samples found to be unsuitable for drinking and fish culture purpose during monsoon, winter and summer season. The decline in water quality was due to various anthropogenic activities including discharge of untreated sewage, enrichment of water sources through surface runoff and traditional methods of irrigation, and overuse of pesticides and inorganic fertilizer.
Keywords *Remote sensing and GIS; Spatial distribution; Surface water; Water quality index*

1. Introduction

Water is the very essential component for the growth of human, agriculture, and industry (Gupta et al., 2017). In the last decades, the industrial development and urbanization are the big causes for deteriorating rural and urban water quality and ultimately its effect on to the aquatic environment (Simsek and Gunduz, 2007). Deterioration and shortage of water are both affecting the water reservoirs, it results in decreasing of ecological functions (Sherrard and Erskine, 1991). The national and international agencies such as WHO, CPCB, BIS, ICMRI has stated that the water quality is about 70% in India is polluted due to discharge of industrial and domestic wastewater in to the natural stream and because of these pollutions the water quality is too poor for the consumption (Ramakrishnaiah et al., 2009; Jindal and Sharma, 2011). The excess amount of presence of fluorides is led to 66 million

peoples in 22 states at risk and over 10 million peoples at risk due to the arsenic in the 06 states of India (Nickson et al., 2007). Hence, proper water quality assessment is very important to the utilization of surface water for domestics as well as flourishing aquatic life (Li et al., 2009). Assessment of water quality by using various scientific methods for the physicochemical and biological parameters has been reported in the different international kinds of literature (Avvannavar and Shrihari, 2008; Shin et al., 2014; Satyanarayanan et al., 2007).

The water quality index was initially proposed by (Horton, 1965). Since many agencies responsible for water supply are strongly suggested to this index. The several scientists proposed various procedures for the calculating water quality index (Štambuk-Giljanović, 1999; Zagatto et al., 1998). Water quality index was proposed to generate a converted complicated data in the form of single value for the easily usable by the community. Numerous water quality index guideline are used in worldwide are National Sanitation Foundation Water Quality Index (NSFWQI), Canadian Council of Ministers of the Environment Water Quality Index (CCMEWQI), British Columbia Water Quality Index (BCWQI), Oregon Water Quality Index (OWQI) Weighted Arithmetic Water Quality index (WAWQI) for the assessment of Water Quality Index (Brown et al., 1970; BCMOELP, 1965; CCME, 2001, Cude, 2001). To determine the complications associated with management of data and retrieving the success and failure of working approaches to making a better water quality, the water quality index appears to be an effective and competent index. In general, there are two steps which are followed in the water quality index, first one is the conversion of the selected water quality data into the sub-index values and second is the combination of these values for the water quality index value.

Remote sensing and GIS are effective tool for the mapping of groundwater as well as surface water quality and it's important for monitoring the environmental changes. The GIS technology has been utilized for the classification of water quality based on the correlation of characteristics, land use and land cover pattern, and water quality parameters of reservoirs (Chandra et al., 2017). GIS database has been used by various scientists in order to the preparation of geospatial maps of water quality index considering concentrations values of different water quality parameters. Many researchers utilized GIS Technology for locating suitable zones of surface water for domestic as well as irrigation purpose. (Cecchi et al., 2007; Huang et al., 2012; Munafò et al., 2005) investigated GIS-based spatial distribution characteristics of Fe, Cu and Mn in the surface water and their effects on to the wetland vegetation of pearl river estuary in China by using ordinary Kriging method of ArcGIS Geostatistical Analyst.

In the investigation of surface water quality, remote sensing and GIS is frequently utilized for suitable analysis, managing recorded data, vulnerability assessment of surface water contamination and assessment of integrated surface water quality models with geospatial data for developing spatial decision support system. (Hussain et al., 2016; Wang et al., 2008) investigated GIS-based integrated pollution index study of surface water quality of urban, suburban and rural areas in Shanghai from the period of 1982 to 2005. (Singh et al., 2018) have studied the level of contamination of surface water near to the mine site of Jharia coalfield, Jharkhand, with the help of a modified water quality index. surface water quality map is very important for the evaluation of safe water for drinking and irrigation purpose and as well as indicating precaution of potential environmental health problems.

The present study was aimed to investigate surface water quality and provide spatial distribution zone maps of the surface water quality index by using physico-chemical parameters such as pH (units), Conductivity (µS/cm), Total Dissolved Solid (mg L^{-1}), Nitrate-Nitrogen (mg L^{-1}), Total Hardness (mg L^{-1}), Chloride (mg L^{-1}), Calcium (mg L^{-1}), Sodium (mg L^{-1}), Potassium (mg L^{-1}), Fluorides (mg L^{-1}), Alkalinity (mg L^{-1}), Sulphate (mg L^{-1}) and MPN (MPN/100 ml) levels. The water quality index status, as well as the spatial distribution zone map, were analyzed by the water quality index method applied to 19 different locations of the study area. The approaches utilized for calculating the WQI was Canadian Council of Ministers of the Environment Water Quality Index (CCMEWQI) and Weighted Arithmetic Water Quality Index (WAWQI). The geospatial tools like ArcGIS 10.2, RESOURCESAT-2, LISS-IV,

IDW interpolation and GPS were used to generate the spatial distribution map of surface water for the Erandol (Maharashtra, India).

2. Study Methodology

2.1. Study Area

Erandol is located on the bank of Anjani river. It is a small-town (Taluka) in Jalgaon district of Maharashtra state, India (Figure 1). It is bounded, Jalgaon Taluka towards East, Parola Taluka towards west, Dharangaon Taluka towards north and Pachora Taluka towards the south. It is also known as Ekchakranagri due to its history as well as the mythological background. It is situated on 20°55′N 75°20′E / 20.92°N 75.33°E and It has an average elevation of 227 meters (744 feet) above the sea level. As per the Census 2011, Erandol Taluka of Jalgaon district has a total population of 166,521. Out of which 86,304 are males while 80,217 are females. In 2011 there were total 35,227 families residing in Erandol Taluka. The Average Sex Ratio of Erandol Taluka is 929. As per Census 2011 out of the total population, 18.7% of people live in Urban areas while 81.3% lives in the Rural areas. The average literacy rate in urban areas is 76.7% while that in the rural areas is 73.5%. Also, the Sex Ratio of Urban areas in Erandol Taluka is 942 while that of Rural areas is 927. Geographically Erandol is Situated at Tapi Valley of the Deccan Plate, between the Satpuda Hills and Ajanta Hills.

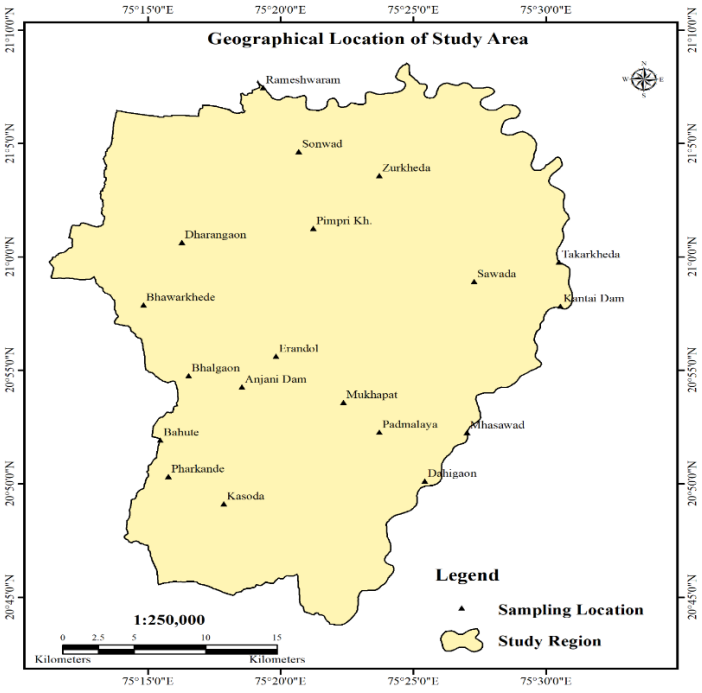

Figure 1: *Study area showing sampling locations in Erandol (Maharashtra, India)*

3. Materials and Methods

3.1. Collection of Sample and Analysis

The surface water samples were collected in acid washed and precleaned plastic container from 19 different locations as per standard methods (IS: 2498, 1966 – Part-I) during monsoon, winter season in the year 2016, and for summer season in the year 2017 (S1 to S19) (Table 1). The sampling locations were obtained with the help of global positioning system (GPS) receiver. The physicochemical and biological analysis was carried out for thirteen parameters as per the standard methods given by (Snyder 1961) for different parameters like pH (units), Electric Conductivity (µS/cm), Total Dissolved

Solid (mg L^{-1}), Nitrate-Nitrogen (mg L^{-1}), Total Hardness (mg L^{-1}), Chloride (mg L^{-1}), Calcium (mg L^{-1}), Sodium (mg L^{-1}), Potassium (mg L^{-1}), Fluorides (mg L^{-1}), Alkalinity (mg L^{-1}), Sulphate (mg L^{-1}) and MPN (MPN/100 ml). All analysis was carried out in triplicate form and the mean value was taken.

Table 1: *Sampling locations of surface water*

Sample ID	Village	Latitude	Longitude	Source
S1	Pimpri Kh.	21.0202	75.3538	River
S2	Dharangaon	21.0099	75.2712	Nalla
S3	Rameshwaram	21.1427	75.3170	River
S4	Sonwad	21.0765	75.3447	River
S5	Zurkhed	21.0590	75.3952	River
S6	Sawada	20.9812	75.4547	Lake
S7	Mhasawad	20.8701	75.4503	River
S8	Dahigaon	20.8345	75.4238	Dam
S9	Kasoda	20.8178	75.2974	Lake
S10	Pharkande	20.8379	75.2627	River
S11	Bahute	20.8604	75.2302	Dam
S12	Bhalgaon	20.9120	75.2754	Dam
S13	Erandol	20.9263	75.3303	River
S14	Anjani Dam	20.9037	75.3088	Dam
S15	Bhawarkhede	20.9640	75.2470	Dam
S16	Mukhapat	20.8923	75.3726	Dam
S17	Padmalaya	20.8704	75.3952	Lake
S18	Kantai Dam	20.9631	75.5089	Dam
S19	Takarkheda	20.9953	75.5081	River

3.2. Water Quality Index

There are different methods were reported by researchers for calculations of WQI to compare the physico-chemical and biological parameters are (Canadian Council of Ministers of the Environment (CCME, 2005; Bhargava, 1983 a, b, c; Steinhart et al., 1982; Horton, 1965; Brown et al., 1972; Cude, 2001; Maciunas and Deininger, 1976). For the present investigation, among the above methods the Canadian Council of Ministers of the Environment Water Quality Index (CCMEWQI) and Weighted Arithmetic Water Quality Index (WAWQI) were adopted for the calculations of WQI.

3.3. Canadian Council of Ministers of the Environment Water Quality Index (CCMEWQI)

CCMEWQI has introduced by Canadian Council of Ministers of the Environment (CCME). For the calculation of CCMEWQI, there are three factors to be consider i.e. Scope, Frequency and Amplitude. This equation is the modified form of the mathematical expression proposed by British Columbia Ministry of Environment, Lands and Parks and Alberta Environment. There should be sampling of four variables in four times for the calculation of CCMEWQI. The agency Canadian Council of Ministers of the Environment has considered eight parameters but we have used twelve parameters with their importance in water quality i.e. pH (units), Conductivity (µS/cm), Total Dissolved Solid (mg L^{-1}), Nitrate-Nitrogen (mg L^{-1}), Total Hardness (mg L^{-1}), Chloride (mg L^{-1}), Calcium (mg L^{-1}), Sodium (mg L^{-1}), Potassium (mg L^{-1}), Fluorides (mg L^{-1}), Alkalinity (mg L^{-1}) and Sulphate (mg L^{-1}) for the calculation of CCMEWQI. There are three factors with different mathematical equations are as follows:

1. Scope: F_1 denotes the percentage of variables that do not meet their objectives at least once during the time period under consideration (“failed variables”), relative to the total number of variables measured:

$$F_1 = \left(\frac{No.of\ failed\ variables}{Total\ no.of\ variables}\right) \times 100 \quad (1)$$

2. Frequency: F_2 denotes the percentage of individual tests that do not meet the objectives (failed tests):

$$F_2 = \left(\frac{No.of\ failed\ tests}{Total\ no.of\ tests}\right) \times 100 \quad (2)$$

3. Amplitude: F_3 denotes the amount by which failed test values don't meet their objectives. F_3 is calculated by three steps as follows:

i. a) When the test value must not exceed the objective:

$$Excursion_i = \left(\frac{Failed\ test\ value_{\ i}}{Objective_{\ j}}\right) - 1 \quad (3)$$

b) For the cases in which the test value must not fall below the objective:

$$Excursion_{\ i} = \left(\frac{Objective_j}{Failed\ test\ value_{\ i}}\right) - 1 \quad (4)$$

ii. The collective amount by which individual tests are out of compliance is calculated by summing the excursions of individual tests from their objectives and dividing by the total number of tests (both those meeting objectives and those not meeting objectives). This variable, referred to as the normalized sum of excursions, or nse, is calculated as:

$$nse = \frac{\sum_{i=1}^{n} Excursion_i}{number\ of\ tests} \quad (5)$$

iii. F_3 is calculated by an asymptotic function that scales the normalized sum of the excursions from objectives(nse) to getting a range between 0 and 100.

$$F_3 = \left(\frac{nse}{0.01nse+0.01}\right) \quad (6)$$

Once the factors F_1, F_2 and F_3 has been calculated, the index himself can be calculated by summing the three aspects as if they were vectors. The sum of the squares of each factor is therefore equal to the square of the index. This approach treats the index as a three-dimensional space defined by each factor along one axis. With this model, the index changes in direct proportion to changes in all three factors:

$$\text{CCMEWQI} = 100 - \left(\frac{\sqrt{{F_1}^2+{F_2}^2+{F_3}^2}}{1.732}\right) \quad (7)$$

The divisor 1.732 normalizes the resultant values to a range between 0 and 100, where 0 represents the "worst" water quality and 100 represents the "best" water quality. Once the CCME WQI value has been determined, water quality is ranked by relating it to one of the categories are shown in Table 2.

Table 2: *Range, status and ecological status of the CCMEWQI method (CCME, 2005)*

WQI	Water quality status (WQS)	Ecological status
95–100	Excellent	Water quality is protected with virtual absence of threat or impairment; conditions very close natural or pristine levels.
80–94	Good	Water quality is protected with only minor degree of threat or impairment; conditions rarely depart from natural or desirable levels.
65–79	Fair	Water quality is usually protected but occasionally threatened or impaired; conditions sometimes depart from natural or desirable level.

45–64	Marginal	Water quality is frequently threatened or impaired; conditions often depart from natural or desirable levels.
0–44	Poor	Water quality is almost always threatened or impaired; conditions usually depart from natural or desirable levels.

3.4. Weighted Arithmetic Water Quality index (WAWQI)

Weighted Arithmetic WQI has proposed by Horton (1965). A set of thirteen most commonly used water quality parameters namely pH (units), Conductivity (µS/cm), Total Dissolved Solid (mg L^{-1}), Nitrate-Nitrogen (mg L^{-1}), Total Hardness (mg L^{-1}), Chloride (mg L^{-1}), Calcium (mg L^{-1}), Sodium (mg L^{-1}), Potassium (mg L^{-1}), Fluorides (mg L^{-1}), Alkalinity (mg L^{-1}), Sulphate (mg L^{-1}) and MPN (MPN/100ml) for the calculation of WAWQI given by the following equations:

Step 1: In the first step, unit weight (W_i) for various parameters is inversely proportional to the recommended standard (*S standard*) for the corresponding parameter. W_i values were calculated by using the following formula.

$$W_i = k\sum \frac{1}{S_{standard}} \quad (8)$$

The constant of proportionality *K* in the above equation can be determined from the following equation:

$$K = \frac{1}{\sum \frac{1}{S_1} + \frac{1}{S_2} + \cdots \frac{1}{S_n}} \quad (9)$$

Step 2: Calculate quality rating scale (Q_i) of i^{th} parameter for a total of n water quality parameters is calculated by using this equation:

$$Q_i = \left(\frac{Q_{actual} - Q_{ideal}}{S_{standard} - Q_{ideal}}\right) \quad (10)$$

Step 3: Finally, the overall WQI was calculated by aggregating the quality rating with the unit weight linearly using the following equation:

$$WAWQI = \frac{\sum_{i=1}^{i=n} Q_i W_i}{\sum W_i} \quad (11)$$

Where,
W_i = unit weight for each water quality parameter;
K = proportionality constant;
Q_i = the quality rating scale for each parameter;
Q_{actual} = estimated concentration of i^{th} parameter in the analyzed water;
Q_{ideal} = the ideal value of this parameter in pure water,
Q_{ideal} = 0 (except pH = 7.0 and DO = 14.6 mg L^{-1});
$S_{standard}$ = recommended standard value of i^{th} parameter;
n = number of water quality parameters.

In this study, the WQI was considered for human consumption or uses, and the maximum permissible WQI for the drinking water was taken as 100 score. Rating scale proposed was in the range of 0–100 and grading were proposed as a below (Table 3).

Table 3: *Range, status and possible usage of WAWQI method (Horton, 1965)*

WQI	Water quality status (WQS)	Possible usage
0–25	Excellent	Drinking, irrigation and industrial
26–50	Good	Drinking, irrigation and industrial
51–75	Poor	Irrigation and industrial
76–100	Very poor	Irrigation
Above 100	Unsuitable for drinking and fish culture	Proper treatment required before use

3.5. Geographic Information System (GIS) Analysis

The base map of Erandol area was digitized from different data products includes survey of India toposheet no. 460/8 on scale 1:2,00,000 has utilized for interpretation as well as base map preparation. The land use and urban settlement map was taken from IRS-P6 LISS IV data of 2015. The longitude and latitude of predetermined locations was taken by using GARMIN 12-Channel GPS. To determine spatial distribution of surfacewater quality index, contour maps and identification of district boundaries were generated by using ArcGIS 10.2 software. The spatial modelling for surfacewater quality index has been done by using Inverse distance weighted (IDW) interpolation technique. The CCMEWQI and WAWQI map was prepared by subtracting individual point data and then designed in GIS.

3.6. Concept of IDW Interpolation Method

IDW interpolation regulates amounts by consuming a sequential biased grouping points of sample sets. The function of inverse distance has its weight cells. Additionally, a lesser amount of importance in the calculation of the output value when input point is from the output cell position. The series of input values utilized to interpolate have limitations when IDW used output value for a cell. Since the IDW remains average of weighted distance, the average neither larger than highest nor smaller than the lowest input. Hence, it is not possible to generate points or valleys uncertainty these excesses have not previously stood experimented. Likewise, for the reason of an average, the surface of output will cannot permit from sample points. The adequately condensed sampling to signify the indigenous dissimilarity gives superlative outcomes from IDW. Hence, IDW method is perfect for investigation through water quality data from several sampling points compactly blowout. Uncertainty the sampling of input points is thin, the outcomes might not be effectively signifying the chosen surface.

4. Results and Discussion

4.1. Water Quality Parameters

For calculating WQI, the prime essential component is the results of physicochemical parameters of various water bodies (Bora and Goswami, 2016). The seasonal variations of physicochemical parameters of selected sampling sites during Monsoon, Winter and Summer season is tabulated in Table 4. pH is generally identifying the alkalinity and acidity of water. From the Table 4, it was observed that the average pH value for Monsoon, Winter and Summer season were 10.42, 10.68 and 10.55 which is above the standards given by WHO, ICMR, BIS and CPCB. It happens due to the presence of carbonates and bicarbonates in the soil. The high alkalinity was present in the water samples because of presence of bicarbonate ions, which is due to free CO_2 combines with water to form carbonic acid (Azeez et al., 2000).

The Alkalinity is a capacity to neutralize acids from water. The major components of alkalinity in water are hydroxide, carbonates and bicarbonates. In most of the cases alkalinity is caused due to free CO_2. In the present investigation, the average alkalinity values found during Monsoon, Winter and Summer

season were 122.35, 122.16 and 100 mg L^{-1} respectively. The alkalinity has exceeding prescribed limit at the sampling sites S9 as per BIS standards.

Electrical conductivity is a numerical expression of the ability of a water sample to carry an electric current and varies with the number and types of ions in the solution contain. EC was measured using a digital conductivity meter and the results were denotes in microsiemen/centimeter. In the study area, average EC values were ranged between 490.54, 441.73 and 395.92 µS/cm during Monsoon, Winter and Summer season respectively. In the sites S1, S2, S3, S4, S5, S9, S10, S13 and S14 have high EC value in the Monsoon, Winter and Summer season exceeding to ICMR standard of 300 µS/cm.

Total Hardness (TH) is the concentration of multivalent metallic cations in solution. It is because of the presence of mainly two cations responsible for hardness of water are calcium and magnesium. The average concentration of hardness was found to be in the range of 103.1, 92.7 and 81 mg L^{-1} during Monsoon, Winter and Summer season respectively. The highest value was at S4, S9 and S10 during Monsoon, Winter and Summer season, which were within the desirable BIS limit of 500 mg L^{-1}.

TDS is sum of the cations and anions concentration expressed in mg L^{-1} and BIS desirable limit is 500 mg L^{-1}. The high amount of TDS is occurred due to the sewage discharges and anthropogenic activities near to the water body (Jindal and Sharma, 2011). The average concentration of TDS present in water samples range of 429.29, 391.51 and 324.15 mg L^{-1} during the season of Monsoon, Winter and Summer. The high value of TDS found in sites S2, S3, S4, S5, S9 and S10 during Monsoon, sites S2, S4, S5, S9 and S10 during Winter and sites S4, S5 and S10 during Summer season respectively.

Calcium is naturally present in water body. One of the main reasons of occurrence of calcium in water is its natural occurrence in the earth crust. In water calcium is generally present as Ca^{2+}. In general, River contains 1-2 mg L^{-1} calcium but in lime stone areas calcium present as high as 100 mg L^{-1}. The average concentration calcium of the different water sites in study region during Monsoon, Winter and Summer was found to be 28.02, 25.99 and 22.02 mg L^{-1}. All the values of calcium in sites S1 to S19 was observed below the desirable limit to BIS of 75 mg L^{-1}.

Sodium (Na) ranks 6^{th} among the elements in order of abundance and is present in most natural waters. In surface waters, Na concentration may be less than 1 mg L^{-1} or may exceed 300 mg L^{-1} depending upon the geographical area. During Monsoon, Winter and Summer season, the average Na values observed to be 81.05, 74.96 and 67.06 mg L^{-1}. Sites S2, S4, S5, S9, S10 and S13 observed high concentrations in all seasons and site S4 exceeded desirable limit cited by BIS, i.e., 200 mg L^{-1}.

Potassium (K) is naturally occurring element, however concentrations remain quite lower compared to Na, Ca and Mg and its abundance and constitutes 2.4% by weight of the earth crust. The average K concentration for the water samples in study region during Monsoon, Winter and Summer season were 23.55, 21.09 and 16.94 mg L^{-1}. In the sites S4, S5, S9, S10 and S13 observed quietly high concentrations of mean K values prescribed by BIS of 200 mg L^{-1} during all the seasons.

Chlorides concentrations in water are directly proportional to mineral content of water surface and ground waters have considerable amount of chlorides than upland and mountain supplies. The sources being the leaching from various rocks, surface run-off from inorganic fertilizers and faecal matter containing high quantity of chlorides along with nitrogenous wastes. The mean concentration of chlorides in all the samples taken from locations in study area observed 6.29, 5.23 and 3.40 mg L^{-1} during Monsoon, Winter and Summer season respectively. The all values of chlorides concentration were well within prescribed limits of BIS of 250 mg L^{-1}.

Nitrate-Nitrogen (NO_3-N) occurs in trace quantities in surface water but may attain high levels in some groundwater. It is an important nutrient for plants and causes eutrophication if receiving high amount in

water bodies. The mean concentration of NO_3-N in all water samples in study region during Monsoon 2.41 mg L^{-1}, Winter 1.97 mg L^{-1} and Summer 0.83 mg L^{-1} respectively. All the values were well within the permissible limits of BIS.

Sulphate (SO_4) is one of the major anions present in natural water. It has its intense effect on human body when present in excessive amount. In the study area, average concentration of SO_4 during Monsoon, Winter and Summer season is 104.11, 90.25 and 87.67 mg L^{-1}. The SO_4 of surfacewater of the study area is given Table 4 and it is found that site S10 has exceeding SO_4 values during all seasons as per BIS prescribed limit i.e., 200 mg L^{-1}. Also, sites S3, S5, S6, S7, S9, S13, S14, S16, S18 and S19 present high values but below permissible limit of SO_4 during all seasons.

Fluorides is an active component presents in both simple and complex forms. It has commonly present in groundwater than surfacewater. It was found that, when fluorides present approximately >1 mg L^{-1} causes mottled enamel commonly called as dental fluorosis (CPCB, 2008). The main sources of fluorides in ground water is different fluorides bearing rocks but, due to industrial activities i.e., phosphate fertilizer and aluminum processing it occurs in surfacewater. The mean values of fluorides present in study during Monsoon 0.20 mg L^{-1}, Winter 0.21 mg L^{-1} and Summer 0.17 mg L^{-1} respectively. All the values of fluorides from sampling sites were well within the desirable limit i.e., 1 mg L^{-1} as prescribed by BIS.

The "Most Probable Number" (MPN) method is useful to estimate the concentration of viable microorganisms in a water sample. In the present investigation, it was found that all the water sampling sites were exceeding the prescribed limits during all seasons. It is due to various activities such as vehicle washing, cloth washing, bathing etc. The mean values of “most probable number" (MPN) were observed during Monsoon 3 MPN/100ml, Winter 3 MPN/100ml and Summer 4 MPN/100 ml respectively.

Table 4: *Surface water quality data*

Location	Season	pH	EC	Alkalinity	TH	TDS	Ca	Na	K	Chlorides	NO_3-N	SO_4	F	MPN
		(units)	(µS/cm)	----------	----------	----------	----------	----------	mg L^{-1}	----------	----------	----------	----------	MPN/100ml
Pimpri Kh (S1)	M	9.55	325	63	71	432	16	34.6	7	4.3	0.1324	45.3	0.045	2
	W	10.46	280	82	63	325	18.4	39.7	9	3.33	0.1935	67.8	0.0435	4
	S	11.11	272.5	75	60	271	17.7	44.9	11	2.2	0.3913	89.3	0.0572	2
Dharangaon (S2)	M	9.8	1026	132	87	567	19.36	96.25	26	6.7	0.7621	79.54	0.0045	3
	W	10.01	789	146	79	535	27.65	104.2	31.54	6.2	0.5945	98.65	0.0015	3
	S	10.48	628.3	150	66	484	37.3	127.5	34.7	4.6	0.3143	111.5	0.0008	4
Rameshwaram (S3)	M	8.2	523	64	73	503	19.7	38.5	6.9	3.1	0.7325	105.6	0.145	2
	W	8.9	495	69	69	389	16.8	45.8	6.5	2.8	0.4536	96.2	0.256	1
	S	9.48	320.3	75	54	197	12.6	47.3	5.1	1.92	0.1404	87.3	0.216	2
Sonwad (S4)	M	10.1	864	125	296	968	42	231	45	10.67	1.0153	165	0.0246	3
	W	10.36	693	168	269	893	34	197	39	10.2	0.9354	146	0.0368	2
	S	10.43	608.2	175	230	810	37	168.4	34.8	9.52	0.8203	120.8	0.0254	2
Zurkhed (S5)	M	10.65	954	169	108	798	67.9	167.2	75.25	9.78	1.2687	168.65	0.1247	1
	W	10.89	769	185	96	693	58.7	156.1	69.76	7.98	1.0654	1.745	0.0836	0
	S	11.35	766.6	125	72	594	57.2	118.1	55.4	6.12	0.7245	119.08	0.0981	3
Sawada (S6)	M	9.89	187.2	87	63	168	22.45	45.3	7.45	4.36	1.358	98.23	0.237	2
	W	10.15	198.1	82	56	149	19.58	41.7	7.76	2.89	1.267	89.65	0.1461	4
	S	10.18	165.1	50	40	110	13.6	36.7	6.4	1.04	0.4903	72.6	0.1139	2
Mhasawad (S7)	M	10.23	268.5	87.4	57.9	278.6	21.6	61.3	23.7	3.45	1.34	78.6	0.1324	2
	W	10.54	245.6	81.5	59.4	265.7	18.9	59.7	18.6	2.98	1.25	69.1	0.1645	4
	S	10.1	222.7	60	48	188	18.1	45.2	11.6	1.6	0.5416	65.9	0.1768	3
Dahigaon (S8)	M	10.54	255.7	67.4	67	164	16.24	43.21	7.65	1.6	0.857	87.65	0.646	1
	W	10.98	247	56.7	48	162	13.8	37.8	6.89	1.9	0.832	82.47	0.734	3
	S	10	207.4	50	46	133	12.7	36.5	5.8	1.28	0.3143	63.03	0.4017	2
Kasoda (S9)	M	11.45	689	710	210	564	39.8	136.7	45.6	6.75	1.25	96.7	0.476	3
	W	11.75	645	703	178	501	37.1	129.6	38.7	4.96	1.65	94.3	0.376	2
	S	11.35	598.7	515	191	485	35.7	121.2	35.8	4.52	1.3997	85.5	0.2412	2
Pharkande (S10)	M	10.7	1978	162	219	1831	34	187	38	27.6	4.213	256.1	0.0214	2
	W	10.9	1925	157	206	1723	30	182	23	22.4	3.7632	241	0.0235	0
	S	10.1	1787	120	172	1350	23.4	168.1	19.2	16.76	1.3264	206.8	0.0123	4
Bahute (S11)	M	11.23	267	68	87	245	18.7	54.32	8.1	2.4	0.7354	77.14	0.5641	4
	W	11.14	251	57	79	240	18.9	41.16	8.4	1.9	0.5432	75.25	0.5321	3
	S	11.36	241.4	55	76	186	16.1	36.2	7.9	1.6	0.3399	71.6	0.4909	4

Bhalgaon (S12)	M	10.42	235	59	54	176	15.6	41.7	9.1	1.76	0.1012	69.8	0.3154	2
	W	10.65	213	57	56	171	14.8	40.3	9.5	1.35	0.1245	67.5	0.2647	4
	S	10.73	196.8	50	46	163	14.2	37.6	7.8	1.52	0.0634	63.4	0.2261	3
Erandol (S13)	M	11.41	422	78	69	367	35.7	97.6	39.4	3.93	2.74	89.74	0.0423	4
	W	11.25	415	73	67	374	34.2	96.1	34.1	3.7	2.65	78.65	0.0256	2
	S	11.32	399.1	70	64	331	27.3	77.2	26.9	3.28	0.4903	77.8	0.0146	2
Anjani Dam (S14)	M	10.1	325	78	67	231	36.4	59.4	10.7	4.65	9.54	97.6	0.0823	2
	W	10.25	301	71	63	206	31.7	48.1	10.2	3.12	8.6	96.2	0.0147	2
	S	9.92	273.9	60	54	196	14.4	40.2	7.3	1.92	5.8955	80.9	0.088	4
Bhawarkhede (S15)	M	11.4	204	78	89	189	24	57	14	4.6	2.45	86	0.1034	1
	W	11.7	167	68	81	167	20.6	48	16	3.8	2.04	79	0.5687	1
	S	11.26	181.9	65	70	158	15.7	35.8	9.3	1.28	0.3913	63.2	0.4415	2
Mukhapat (S16)	M	9.86	183	64	96	167	34	46	9.7	4.6	2.7	96	0.0832	1
	W	10.2	181	60	90	154	39	37	8.1	4.9	2.1	83	0.0945	2
	S	9.78	158.5	55	78	126	13.8	29.7	6.5	1.2	0.1639	68.7	0.0622	2
Padmalaya (S17)	M	11.5	226	98	69	149	34	37	42	6.76	7.68	76	0.6127	3
	W	11.7	236	84	53	161	28	32	38	7.1	4.36	69	0.6412	1
	S	11.16	176.9	60	44	130	23.1	29.5	21.3	1.28	0.5416	61.4	0.4017	2
Kantai Dam (S18)	M	10.74	164	59	79	125	19	39	17.3	6.41	2.6512	98	0.0146	4
	W	11.01	141	52	68	114	17.6	36	15.2	4.32	2.1278	82	0.0354	2
	S	10.28	118.6	40	66	90	14.7	28.8	8.4	1.04	0.6208	71.5	0.0423	3
Takarkheda (S19)	M	10.35	224	76	97	234	16	67	14.6	6.14	4.36	106.5	0.1463	2
	W	10.14	201.3	69	81	216	14.2	52	10.5	3.6	3.01	97.4	0.1325	4
	S	10.22	198.6	50	62	157	13.9	45.4	6.7	2	0.8482	85.6	0.1278	3

4.2. Water Quality Index (WQI)

WQI analysis for twelve water quality parameters of Erandol area from sites S1-S19 was charted in Table 5.

Table 5: *CCMEWQI and WAWQI of surface water Samples from S1 to S19*

Location	CCMEWQI	Water Quality Status (CCMEWQI)	WAWQI	Water Quality Status (WAWQI)
Pimpri Kh (S1)	93.1956	Good	33.2855	Good
Dharangaon (S2)	80.6774	Good	52.5671	Poor
Rameshwaram (S3)	83.4862	Good	36.4620	Good
Sonwad (S4)	68.1077	Fair	71.5653	Poor
Zurkhed (S5)	79.5546	Fair	64.6968	Poor
Sawada (S6)	93.1944	Good	29.6206	Good
Mhasawad (S7)	93.1941	Good	32.5324	Good
Dahigaon (S8)	93.1938	Good	32.8327	Good
Kasoda (S9)	68.8706	Fair	77.3862	Very Poor
Pharkande (S10)	64.2472	Marginal	100.514	Unsuitable for drinking and fish culture
Bahute (S11)	93.1921	Good	36.0984	Good
Bhalgaon (S12)	93.1936	Good	29.8148	Good
Erandol (S13)	93.1918	Good	41.6337	Good
Anjani Dam (S14)	93.1944	Good	34.5845	Good
Bhawarkhede (S15)	93.1944	Good	34.4504	Good
Mukhapat (S16)	93.1946	Good	30.5403	Good
Padmalaya (S17)	93.1914	Good	36.6354	Good
Kantai Dam (S18)	93.1935	Good	27.7104	Good
Takarkheda (S19)	93.1942	Good	32.2380	Good

In the study area, the values for spatial distribution map of Canadian Council of Ministers of the Environment Water Quality Index (CCMEWQI) shows five classes of water quality i.e., excellent: sky blue colour, good: blue colour, fair: light blue colour, marginal: light pink colour and poor: pink colour. The CCMEWQI values from study area suggested that the water quality of major part falls under good category i.e. 74%, fair category i.e. 22% and minor parts falls under marginal category i.e. 4% during all seasons (Table 6).

Table 6: *Percent distribution of CCMEWQI*

CCMEWQI	Water quality status (WQS)	Present percentage of surface water sample
95–100	Excellent	0%
80–94	Good	74%
65–79	Fair	22%
45–64	Marginal	4%
0–44	Poor	0%

There are no parts falls under the excellent and poor category. The sampling sites S1, S2, S3, S6, S7, S8, S11, S12, S13, S14, S15, S16, S17, S18 and S19 were falls under good category, sites S4, S5 and S9 were falls under fair category and site S10 were fall under marginal category. There are no major seasonal variations appears during this investigation. The spatial distribution map for CCMEWQI undoubtedly shows that the northern and south western region of the study area has marginal water quality index during all seasons (Figure 2).

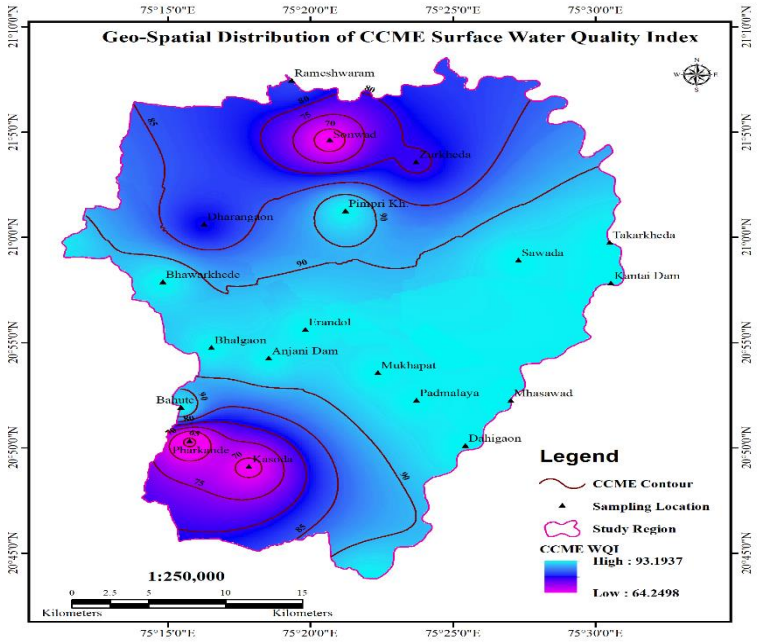

Figure 2: *Spatial distribution of CCMEWQI Index in study area*

The values for Weighted Arithmetic Water Quality index (WAWQI) map also shows five classes of water quality viz. excellent: dark orange colour, good: light orange and yellow colour, poor: green colour, very poor: sky blue colour and unsuitable for drinking and fish culture: blue colour. The WAWQI percentage values from study area shows excellent: 0%, good: 74%, poor: 16%, very poor: 5% and unsuitable for drinking and fish culture: 5% respectively Table 7. The major part of the study area falls in the good category during all seasons and there are no major seasonal variations in the study area. The mean values of WAWQI are tabulated in Table 5. Sites S1, S3, S6, S7, S8, S11, S12, S13, S14, S15, S16, S17, S18 and S19 were falls in good category while sites S2, S4 and S5 falls under poor category, sites S9 falls in very poor category and S10 falls under unsuitable for drinking and fish culture respectively. Again, as discussed in CCMEWQI results the spatial distribution map shows that the northern and south western region of study area has falls under very poor and unsuitable for drinking and fish culture category (Figure 3).

Table 7: *Percent distribution of WAWQI*

WAWQI	Water quality status (WQS)	Present % of surface water sample
0–25	Excellent	0%
26–50	Good	74%
51–75	Poor	16%
76–100	Very poor	5%
Above 100	Unsuitable for drinking and fish culture	5%

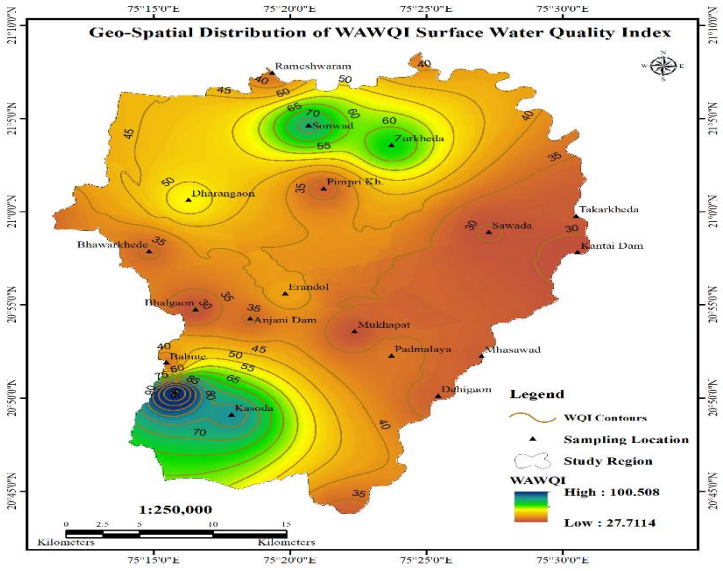

Figure 3: *Spatial distribution of WAWQI index in study area*

5. Conclusion

The present study indicated that the GIS techniques and WQI methods could provide valuable information for assessment of water quality. The spatial distribution of water quality index in the study area was carried out by using GIS techniques and remote sensing data. The GIS technology have magnificently proved its ability in surfacewater quality index mapping of Erandol area. A total 19 surfacewater samples were collected during Monsoon, Winter and Summer season and analyzed for thirteen different physico-chemical parameters. The pH values during Monsoon, Winter and Summer season were found higher than the prescribed permissible limit which indicates that surface water of study area was alkaline in nature. The Alkalinity at sampling site S9 was found to be higher as per BIS standards during all seasons. It is due to the higher concentration of carbonates and bicarbonates. A total fifty percent EC values from all sampling sites were found to be exceeding permissible limit as per ICMR standards during Monsoon, Winter and Summer seasons. The values of TH in study area were found to be lower during all seasons but, in the S4, S9 and S10 site it was near to the permissible limit. The major cations, sodium values during all season were found to be higher but, all values were found below the permissible limit except S4 site. The major anions, Sulphate values in sampling location S10 exceeded the permissible limit during Monsoon, Winter and Summer season. The "most probable number" (MPN) concentration was found to be higher in all location due to dumping of domestic wastewater, washing of animals and other domestic activities etc. A GIS technology utilizes for spatial analysis and IDW interpolation technique has been demonstrated an important tool to represents the WQI in the study area. The spatial distribution map for CCME WQI and WAWQI was also generated by using GIS and IDW techniques for well distinguished water potability over space. Based on CCMEWQI and WAWQI methods the major part of the study area falls under good condition during Monsoon, Winter and Summer season. The both CCMEWQI and WAWQI methods are very useful and effective tool to recapitulate and account on the monitoring data to the administrative authority to know the status of surfacewater quality and people also have opportunity to better use in future. In the study area the overall high values of CCMEWQI occurs in middle, east and west region during Monsoon, Winter and Summer season. There was no significant variation observed in CCMEWQI during Monsoon, Winter and Summer season. The WAWQI values occurs higher in south western and north region of study area during Monsoon, Winter and Summer season. The results of both methods i.e. CCMEWQI and WAWQI showed significant equality. On the basis of CCMEWQI and WAWQI it is concluded that most of the sampling locations were exhibit good water but in the south western and north region i.e. S4, S5, S9 and S10 indicating the deteriorated water quality.

Acknowledgement

The authors are thankful to Shri. G. H. Raisoni Foundation, Jalgaon and DST-SERB, New Delhi for providing all the financial assistance to carry out this work. The authors are also gratefully acknowledged the support provided by the Director, School of Environmental and Earth Sciences, Kavayitri Bahinabai Chaudhari North Maharashtra University, Jalgaon.

References

Avvannavar, S.M. and Shrihari, S. 2008. Evaluation of water quality index for drinking purposes for river Netravathi, Mangalore, South India. *Environmental Monitoring and Assessment*, 143(1-3), pp.279-290.

Azeez, P.A., Nadarajan, N.R. and Mittel, D.D. 2000. The impact of monsoonal wetland on groundwater chemistry. *Pollut Res.*, 19(2), pp.249-255.

BCMOELP. 1965. The British Columbia Water Quality Index, Water Quality Branch, Environmental Protection Department, British Columbia Ministry of Environment, Lands Parks, Victoria.

Bhargava, D.S. 1983a. A light penetration model for the Rivers Ganga and Yamuna. *Int. J. Dev. Technol. (England)*, 1(3), pp.199-205.

Bhargava, D.S. 1983b. Most rapid BOD assimilation in Ganga and Yamuna Rivers. *J. Environ. Eng. Am. Soc. Civ. Eng.*, 109(1), pp.174-188.

Bhargava, D.S. 1983c. Use of water quality index for river classification and zoning of Ganga River. *Environ. Pollut. Ser. B (England)*, 6(1), pp.51-67.

BIS. 2012. *Indian Standards Specification for Drinking Water, B.S. 10500*. Government of India, New Delhi.

Bora, M. and Goswami, D.C. 2016. Water quality assessment in terms of water quality index (WQI): case study of the Kolong River, Assam, India. *Applied Water Science*, 7(6), pp.3125-3135.

Brown, R.M. and McClelland, N.I. 1972. *A water quality index-crashing the psychological barrier*. In Indicators of Environmental Quality, pp.173-182.

Canadian Council of Minister of the Environment (CCME). 2001. Canadian water quality guidelines for the protection of aquatic life: CCME Water Quality Index 1.0, Technical report, Winnipeg MB, Canada.

Cecchi, G. and Munafò, M. 2007. Estimating river pollution from diffuse sources in the Viterbo province using the potential non-point pollution index. *Annali dell'Istituto Superiore di Sanita*, 43(3), pp.295-301.

Chandra, D.S. and Asadi, S. 2017. Estimation of water quality index by weighted arithmetic water quality index method: a model study. *International Journal of Civil Engineering and Technology*, 8(4), pp.1215-1222.

CPCB. 2008. Guideline for water quality management. Central Pollution Control Board, Parivesh Bhawan.

Cude, C.G. 2001. Oregon water quality index: A tool for evaluating water quality management effectiveness. *Journal of the American Water Resources Association*, 37(1), pp.125-137.

Gupta, N., Pandey, P. and Hussain, J. 2017. Effect of physicochemical and biological parameters on the quality of river water of Narmada, Madhya Pradesh, India. *Water Science*, 31(1), pp.11-23.

Horton, R.K. 1965. An index number system for rating water quality. *J. Water Pollut. Control Fed.*, 37(3), pp.300-306.

Huang, L. and Bai, J. 2012. Spatial Distribution of Fe, Cu, Mn in the surface water system and their effects on wetland vegetation in the Pearl River Estuary of China. *Clean - Soil, Air, Water*, 40(10), pp.1085-1092.

Hussain, R. and Khan, A. 2016. Clinico-hematological and biochemical studies on naturally infected camels with trypanosomiasis. *Pakistan Journal of Zoology*, 48(2), pp.311-316.

ICMR (Council of Medical Research). 1975. *Manual of Standards of Quality for Drinking Water Supplies, Indian*. Special Report No. 44, p.27.

Jindal, R. and Sharma, C. 2011. Studies on water quality of Sutlej River around Ludhiana with reference to physicochemical parameters. *In Environmental Monitoring and Assessment*, 174, pp.417-425.

Li, Z. and Fang, Y. 2009. Temporal and spatial characteristics of surface water quality by an improved universal pollution index in red soil hilly region of South China: A case study in Liuyanghe River watershed. *Environmental Geology*, 58(1), pp.101-107.

Maciunas, J. and Deininger, R.A. 1976. A comparison of several indexes quality. *Water Environment Federation*, 48(5), pp.954-958.

Munafò, M. and Cecchi, G. 2005. River pollution from non-point sources: A new simplified method of assessment. *Journal of Environmental Management*, 77(2), pp.93-98.

Nickson, R. and Sengupta, C. 2007. Current knowledge on the distribution of arsenic in groundwater in five states of India. *Journal of Environmental Science and Health - Part A Toxic/Hazardous Substances and Environmental Engineering*, 42(12), pp.1707-1718.

Ramakrishnaiah, C.R. and Sadashivaiah, C. 2009. Assessment of water quality index for the groundwater in Tumkur taluk, Karnataka state, India. *Journal of Chemistry*, 6(2), pp.523-530.

Satyanarayanan, M. and Balaram, V. 2007. Assessment of groundwater quality in a structurally deformed granitic terrain in Hyderabad, India. *Environmental Monitoring and Assessment*, 131(1–3), pp.117-127.

Sherrard, J. J. and Erskine, W.D. 1991. Complex response of a sand-bed stream to upstream impoundment. *Regulated Rivers: Research & Management*, 6(1), pp.53-70.

Shin, J.J. and Mellano, C. 2014. Treatment of glenoid chondral defect using micronized allogeneic cartilage matrix implantation. *Arthroscopy Techniques*, 3(4), pp.e519-e522.

Simsek, C. and Gunduz, O. 2007. IWQ Index: A GIS-integrated technique to assess irrigation water quality. *Environmental Monitoring and Assessment*, 128(1–3), pp.277-300.

Singh, P.K. and Panigrahy, B.P. 2018. Evaluation of the surface water quality index of jharia coal mining region and its management of surface water resources. *Environmental Pollution*, pp.429-437.

Snyder, R.G. 1961. Vibrational spectra of crystalline n-paraffins. II. Intermolecular effects. *Journal of Molecular Spectroscopy*, 7(1-6), pp.116-144.

Štambuk-Giljanović, N. 1991. Water quality evaluation by index in Dalmatia. *Water Research*, 33(16), pp.3423-3440.

Steinhart, C.E. and Schierow, L.J. 1982. Environmental quality index for the great lakes. *Water Resour. Bull.*, 18 (6), pp.1025-1031.

Wang, J. and Da, L. 2008. Temporal variations of surface water quality in urban, suburban and rural areas during rapid urbanization in Shanghai, China. *Environmental Pollution*, 152(2), pp.387-393.

Zagatto, P.A. and Lorenzetti, M.L. 1998. Proposal for a new water quality index. SIL Proceedings, 26(5), pp.2449-2451.

Cloud Publications
International Journal of Advanced Remote Sensing and GIS
2019, Volume 8, Issue 1, pp. 3096-3105
ISSN 2320 – 0243, Crossref: 10.23953/cloud.ijarsg.424

Research Article

2D Flood Simulation and Development of Flood Hazard Map by using Hydraulic Model

Srinivasa Rao G.[1], Tushar Surwase[2], Asiya Begum[2], Mruthyunjaya Reddy K.[3], Jagadeeswara Rao P.[4]

[1]ISRO Headquarter, Bangalore
[2]Disaster Management Support Division, National Remote Sensing Centre/ ISRO, Hyderabad
[3]Programme Planning and Evaluation Group (PPEG), National Remote Sensing Centre/ ISRO, Hyderabad
[4]Andhra University College of Engineering (AUCOE) Visakhapatnam

Correspondence should be addressed to Tushar Surwase, *tusharsurwase@ymail.com*

Publication Date: 5 August 2019

DOI: https://doi.org/10.23953/cloud.ijarsg.424

Abstract A flood is an overtopping of water from channel banks which submerges land which is usually dry. In India, floods in Godavari and Sabari River are observed several times but 2006 flood was one of the severe events which affected Khammam district extensively. The present paper demonstrates the analysis of severe flood of Khammam using hydraulic modeling. For this purpose HEC-RAS 2D a Hydraulic model was used to simulate the behavior of study area which covers part of Godavari River and Sabari River in Telangana and Andhra Pradesh states. Model provides detail temporal simulated parameters like depth of water, water elevation with respect to M.S.L and Velocity of flowing water. SRTM 30m posting, river discharge data, LULC for assigning Roughness coefficient was used as input to the model. HEC-RAS Simulated flood results were validated with remotely sensed Radarsat satellite observations. Performance of HEC-RAS model was evaluated according to the criteria of measure of fitting raster cells with satellite data. Validation results showed that performance of HEC-RAS model is very effective and can be used by hydrologist or water resources engineers for planning and development.
Keywords *Flood inundation simulation; Godavari; RADARSAT; Sabari; SRTM*

1. Introduction

Floods are one of the major natural disasters affecting the South-Asian region. India and Bangladesh are two from eight South-Asian countries which are reported to be worst affected countries in the world, accounting to be 1/5th of global death count due to floods (Agarwal and Sunita, 1991). In India, nearly 40 million of land is prone to floods. Floods are frequent phenomena in the country occurring during monsoon season (June-October), which affects to crop lands, infrastructure as well as lives. Repetitive flood inundation is threatening human life and property which indeed requires effective flood risk assessment (Matgen et al., 2007). Prediction of flood inundation is not straightforward since the flood inundation extent is highly dependent on topography and it changes with time. Flood prediction is a very complex process in both spatial and temporal contexts whereas the Conventional engineering methods is time consuming. Application of the hydraulic numerical modelling for flood analysis and flood plain management is a strategic and essential tool for an integrated flood plain management

(Cheung, 2003; Chang, 2000). Flood risk assessment and management are fundamental steps for identifying prone risk areas, current hazards, and reducing them in future flood events (Ranzi, 2011). To propose measures on flood management it needs basic understanding of flood analysis. There are two approaches of understanding, first is, *in situ* flood observations (Hagen and Lu, 2011) but *in situ* observation are not available all the time, so another one is observing flood by Remote sensing satellite data (Haq et al., 2012; Chormanski et al., 2011) but it still limits us to know the temporal behavior in flood event. So, in order to develop flood hazard and risk zone maps and to know the temporal behaviour of flood event it is essential to simulate the flood inundation by numerical models. The studies of Flood inundation modelling using hydrodynamic models approach for designing river engineering and irrigation schemes and mapping flood risks has been carried out by various researchers worldwide (Werner, 2004; Bates et al., 2005; Patro et al., 2009). There are various numerical models like HEC-RAS (Hydrologic Engineering Corporation- River Analysis System) developed by US Army of Corps of Engineers, MIKE developed by Danish Hydraulic Institute, Denmark (DHI, 1997). SOBEK developed at the Delft Hydraulics, Delft have been developed for floodplain delineation and flow simulation to delineate the floodplain zones and calculate the associated risk. All these models have capability to solve 1D and 2D equations. For present study HEC-RAS model is used to simulate flood inundation for study area. HEC-RAS releases new version 5.0 Beta with 2D capability which is a great innovation for futuristic flood studies (MoyaQuiroga et al., 2015). The study goal is to analyze the 2006 flood event of part of Godavari and Sabari river north eastern part of Telangana.

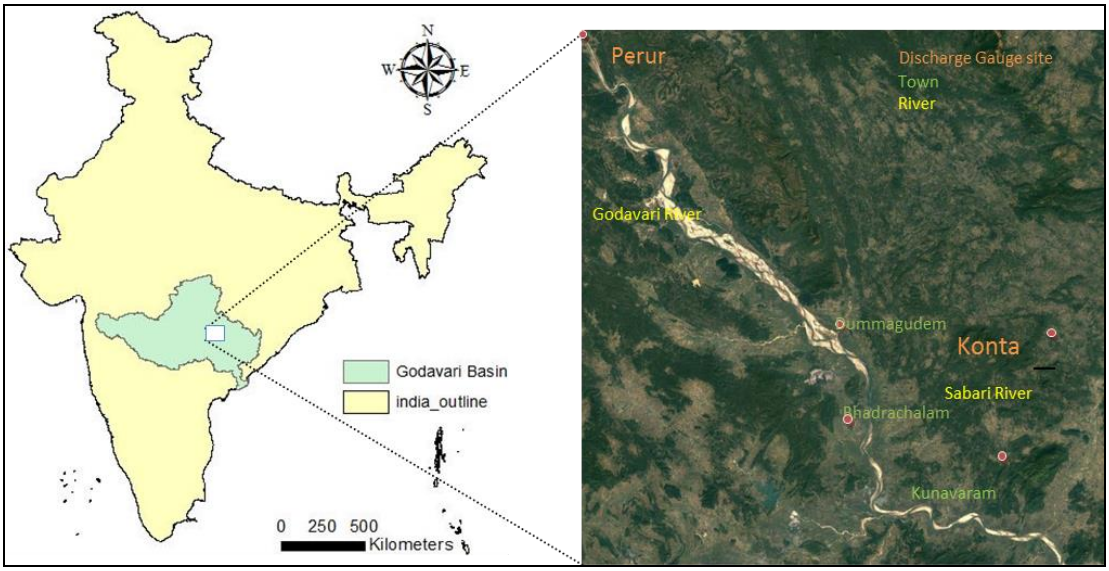

Figure 1: *Study area along with discharge gauge site*

2. Study Area

Figure 1 depicts the Godavari River stretched from Perur to Kunavaram and Sabari River stretched from Konta in Chattisgarh to Kunavaram in Andhra Pradesh state (2006). The origin of Godavari River is Brahmagiri Mountain (Western Ghats) in Nashik District; Maharashtra River flows from West to east and falls into Bay of Bengal 93 km south of Rajahmundry. The river Sabari is a tributary of River Godavari It merges in river Godavari at Kunavaram, about 40-km from Bhadrachalam town. The Godavari basin is bounded, on east by Eastern Ghats and on the West by the Western Ghats on the North by the Satmala Hills, the Ajanta Range and the Mahadeo Hills on the South. Sabari River is 280 mm/km. The study area lies in between latitudes 18^0 38' and 18^0 25' and longitudes 80^0 12' and 80^0 26'. The type of soil observed in the study area are Red sandy loams, clay loams, Alluvial, Sandy Alluvial, Deltaic Alluvial,

Coastal sandy loams, Heavy clays and Saline soils (Shodhganga Chapter IV). These soils are low pervious in nature generating more runoff on surface and hence favouring Inundation. The study area of Godavari river stretch is about 186.6 km and Sabari river stretch is about 37.07 km. In Khammam district Mandals (small town) like Kunavaram, Vararamachandrapuram and Kukunuru.

Velerupadu and Boorugumpadu were badly affected and V. R. Puram, Chintoor and some part of Kunavaram were affected by Sabari River. Flood affects crops, Pakka buildings and 60 villages where flood water last for eight days. In East Godavari district, mandals like Katrenikona, Mummidivaram, Inavalli are submerged in Godavari water and near about 40 villages and about 2000 victims were severely affected (Sewa Bharati, 2006).

3. Data Used

Spatial Hydraulic modeling requires data of two type's Geographical data and Hydraulic data. Geographical data such as Digital Elevation Mode (DEM) which gives a description of elevation of an area, for the study area SRTM (Shuttle Radar Topographic Mission from USGS) of grid cell size 30 m (1 arc-second) was used. Hydraulic data deals with the time series Discharge data of Godavari River at Perur gauge station and for Sabari River at Konta gauge station. Discharge data at an interval of 12 hrs were obtained for flood event from Central water commission (CWC) Hyderabad. For the Perur and Konta gauge station Daily discharge data is available from 2000. Land Use Land Cover (LULC) of 1:250000 scales derived from Advanced Wide Field Sensor (AWiFS) data of 56 m grid size were used in order to assign manning 'n' roughness coefficient. The study simulates flood event from 04 Aug 2006 12.00 hours to 10 Aug 2006 24.00 hours. This time stamp was selected because the study area was severely affected by flood.

4. Methodology

4.1. DEM Preprocessing

SRTM 30 m DEM is used and clipped to study area extent. DEM Preprocessing is required if DEM contains null values if any. These null values can be filled by fill and sink hydrology tool. In order generate geometric statistics; the projection of DEM should be in projected coordinate system, for present study area WGS_1984 _UTM_Zone 44N Projection was used, where WGS_1984 is a Datum.

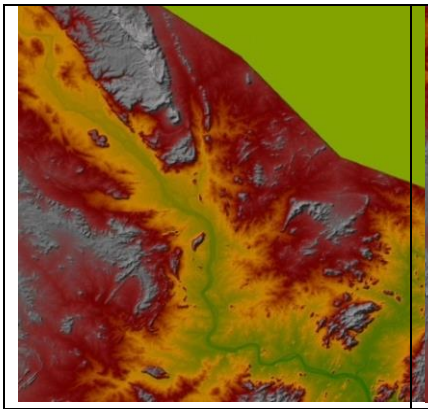

Figure 2: *Created terrain*

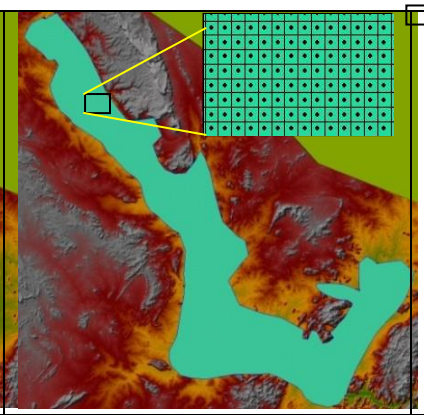

Figure 3: *Terrain with cells*

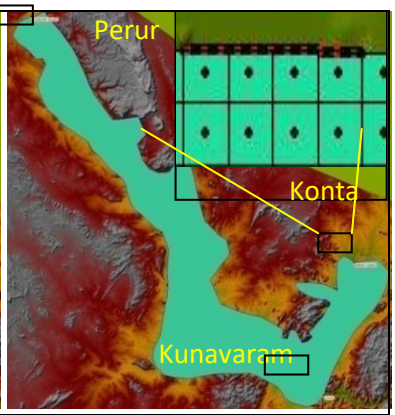

Figure 4: *Boundary condition*

4.2. HEC-RAS Model Setup

The projected DEM is basic input to hydraulic modeling. Model converts DEM into terrain in the form of Triangular Irregular Network (TIN) file. TIN file is a vector representation of DEM Figure 2 shows terrain created from DEM. Further, study area was defined by 2D closed polygon. The 2D polygon

area covers probable areas that are liable to inundate. This area can be defined by two methods in order to minimize optimization of 2D Mesh cells. First method is to define 2D polygon area based on previous floods extend observed by satellite. Another method is to define polygon by digitizing the 2D polygon boundary connecting higher elevated areas like hills and mountains. For present study, second method was adopted as high elevated hills are surrounding to the study area. After Defining 2D Polygon area computational cells area generated. The cells are rectangular in shape and at boundary it may be rectangular or polygon up to 8 sides. Cell size was kept to be 30 m in order to enclose DEM cell size. Figure 3 shows 2D polygon with computational cells, these cells are also called as Mesh.

Further, three boundary condition assigned to study area. Two inflow hydrograph boundary condition and one normal depth boundary condition. Inflow hydrograph one at Perur gauge site on Godavari River and one at Konta gauge site on Sabari River. Figure 4 shows the assigned boundary condition to study area. Similarly Inflow hydrograph at Perur and Konta gauge site for the event obtained from CWCis shown in Figure 5. The normal depth 0.00032 slope was assigned according to the topographic conditions of the study area.

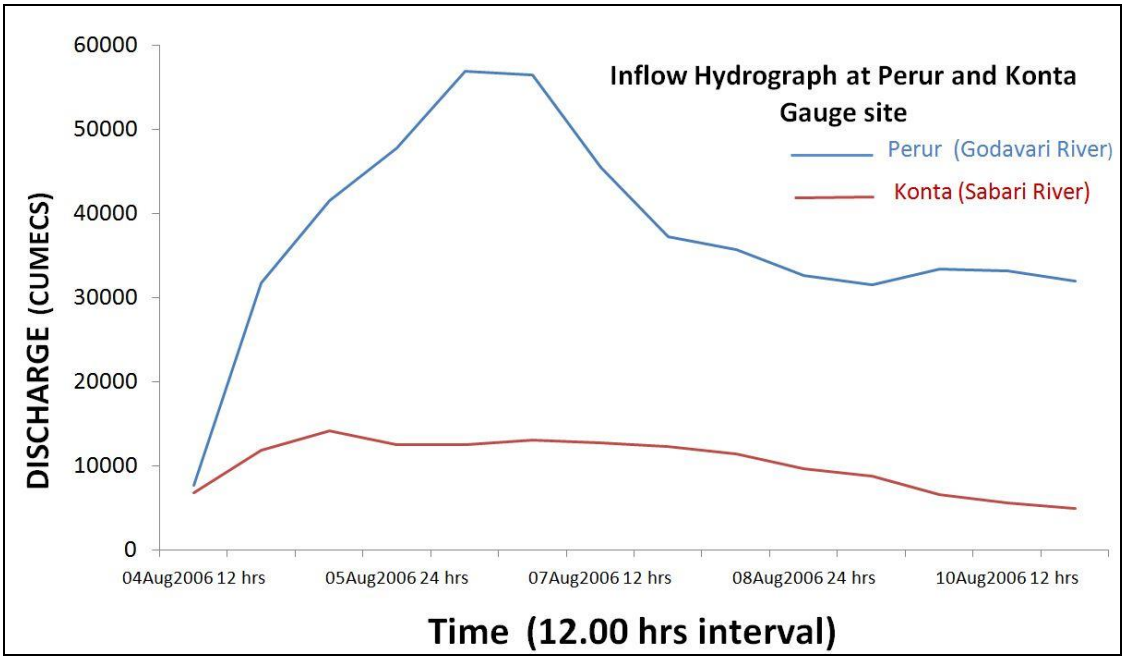

Figure 5: *Hydrograph at Perur and Konta Gauge site on Godavari and Sabari River respectively*

4.3. HEC-RAS Simulations

HEC-RAS 2D 5.0.1 beta version has capability to solve two equations such as Diffusion wave and full momentum equation. Diffusion wave considers parameters such as Gravity, Friction and Pressure. Whereas Full momentum equation considers parameter like Gravity, Friction, Pressure, Acceleration, Turbulent eddy viscosity, Corollis effect. Both equations are derived from Continuity equation. For present study, Full momentum equation was used to simulate the flood event as all parameters are considered. The full momentum equation (1 and 2) as shown below for two directional specific flows p and q.

$$\frac{\partial p}{\partial t}+\frac{\partial}{\partial x}\frac{(p^2)}{(h)}+\frac{\partial}{\partial y}\frac{(pq)}{(h)}=-n^2pg\frac{\sqrt{(p^2+q^2}}{h^2}-gh\frac{\partial s}{\partial x}+pf+\frac{\partial}{\rho\partial x}(h\tau_{xx})+\frac{\partial}{\rho\partial y}(h\tau_{xy})\ldots 1$$

$$\frac{\partial q}{\partial t}+\frac{\partial}{\partial x}\frac{(q^2)}{(h)}+\frac{\partial}{\partial y}\frac{(pq)}{(h)}=-n^2qg\frac{\sqrt{(p^2+q^2}}{h^2}-gh\frac{\partial s}{\partial y}+qf+\frac{\partial}{\rho\partial y}(h\tau_{yy})+\frac{\partial}{\rho\partial x}(h\tau_{xy})\ldots 2$$

Where,

p and q are the specific flow in the x and y directions (m^2/sec), n is the manning's resistance, s is the surface elevation in (meters), h is the water depth (meters), g is gravitational acceleration (m/sec^2), ρ is the density of water (kg/m^3), τ_{xx}, τ_{yy}, τ_{xy} are the components of effective shear stress and f is the Corollis(/sec).

4.4. Model Performance

Model Performance has been evaluated based on measures of fit F_1 and F_2 (MoyaQuiroga et al., 2015; Horrit et al., 2007; Di Baldasarre et al., 2009). It depends on the simulated raster cells that are fitted with the satellite image. It gives the degree of accuracy of the model, F_1 ranging from 0 to 1 and F_2ranging from -1 to 1. The equation of F_1 and F_2 is given in the equation 3 and 4 respectively.

$$F_1=\frac{A}{A+B+C}\ldots 3$$

$$F_2=\frac{A-B}{A+B+C}\ldots 4$$

Where, A is correctly predicted cells, B is Over-predicted cells and C is under predicted cells. The value closer towards 1 indicates model performance is better.

4.5. Flood Hazard Map

The flood Hazard was developed for the study area according to the simulated flood depth in inundated areas. The hazard classification was assigned according to the Japan ministry of land infrastructure and transport (MLIT) shown in Table 1.

Table 1: *Flood hazard classification according to MLIT*

Flood hazard	Depth (meters)	Hazard
H1	<0.5	Very low
H2	0.5-1	Low
H3	1-2	Medium
H4	2-5	High
H5	>5	Extreme

There are five flood hazard classifications H_1, H_2, H_3, H_4 and H_5 according to depth of inundation. H_1 hazard (depth less than 0.5 meter) is entitled to be very low as people can evacuate easily on their feet. H_2 hazard (depth 0.5-1 meter) is entitled to be very low, in this zone, evacuation becomes difficult for adults and infants, animals may get exposed to hazard. H_3 hazard (depth 1-2 meters) is a medium zone, where people may get drowned but they will be safe in their homes having plinth level to be 0.6 to 1 meter. H_4 hazard (depth 2-5 meters) is entitled to high hazard zone where all people in this zone are not safe in their homes but at the most they may be safe on their roofs. H_5 hazard (depth greater than 5 meters) is an extreme hazard zone where people are not safe even on their roofs.

5. Results and Discussion

The HEC-RAS model results are in two decimal floating point raster stored in tiff file format. The simulated results are in the form of flood inundation with depth, velocity, water surface elevation with

respect to time. Results for desired date and time can be achieved within the simulated period such as 04 Aug 2006 12.00 hours to 10 Aug 2006 24.00 hours at one hour time interval. For present study, simulated results for 07 Aug 2006 at 08.00 hours was taken into consideration for validating with RADARSAT satellite image acquired on same date and time Figure 6 shows the RADARSAT image and its derived flood extent.

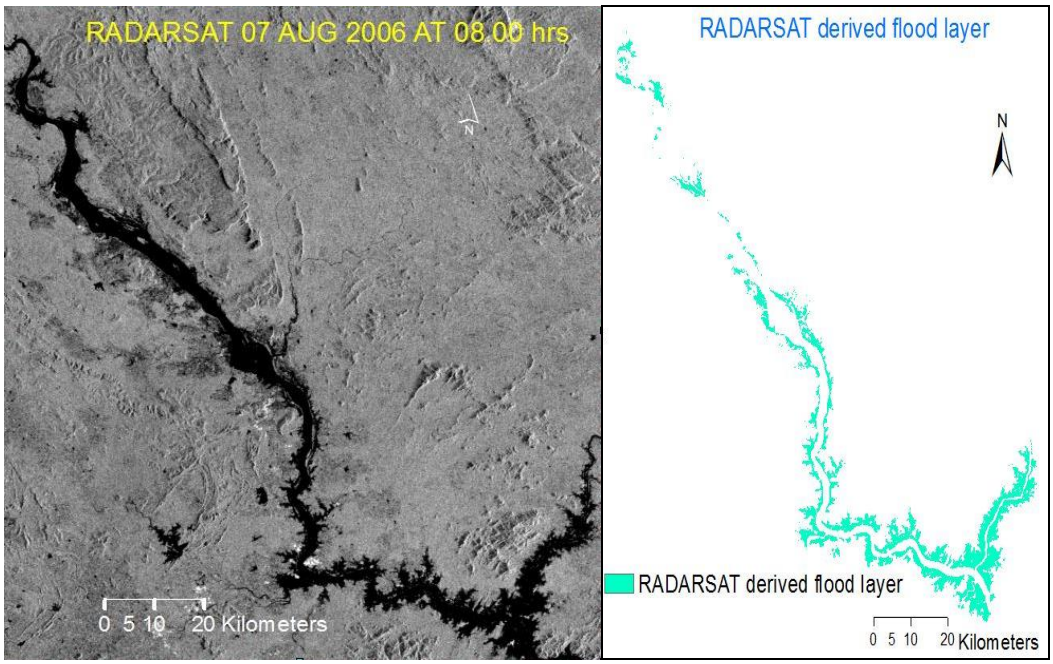

Figure 6: *Radarsat image during flood event and its derived flood extent on the right*

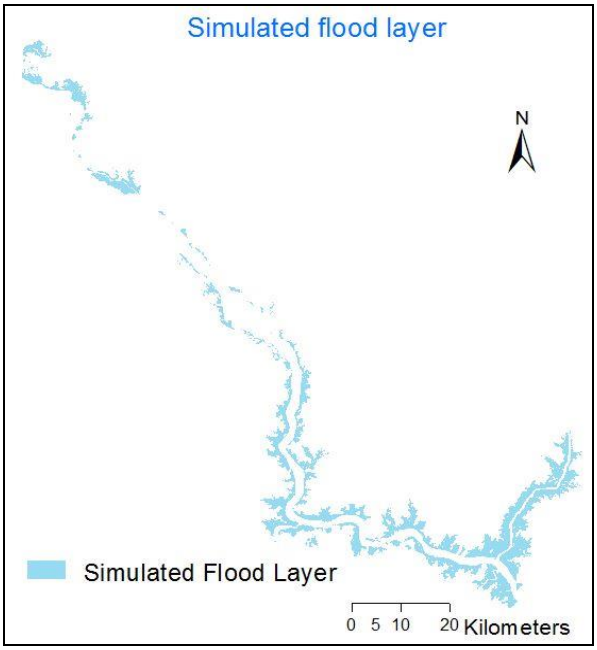

Figure 7: *Simulated flood inundation layer*

The evaluated measures of fit F_1 and F_2 by using the GIS tools like Arc-GIS and ERDAS shown in Table 2.

Table 2: *HEC-RAS model performance based on measures of fit*

Sr No.	Correctly predicted cells A	Over predicted cells B	Under predicted cells C	F1 A/ (A+B+C)	F2 (A-B)/ (A+B+C)	Flood observed (FO)	Flood simulated (FS)	FS/FO
1.	142331	42476	49527	0.61	0.43	45272	43579.74	0.96

Since F_1 and F_2 are closer to 1 indicates the accuracy of model performance which tends to be better and the ratio of flood simulated to flood observed is 0.96 this means 96 percent of inundated area is matched. The Figure 8 shows the variation of inundation with respect to time.

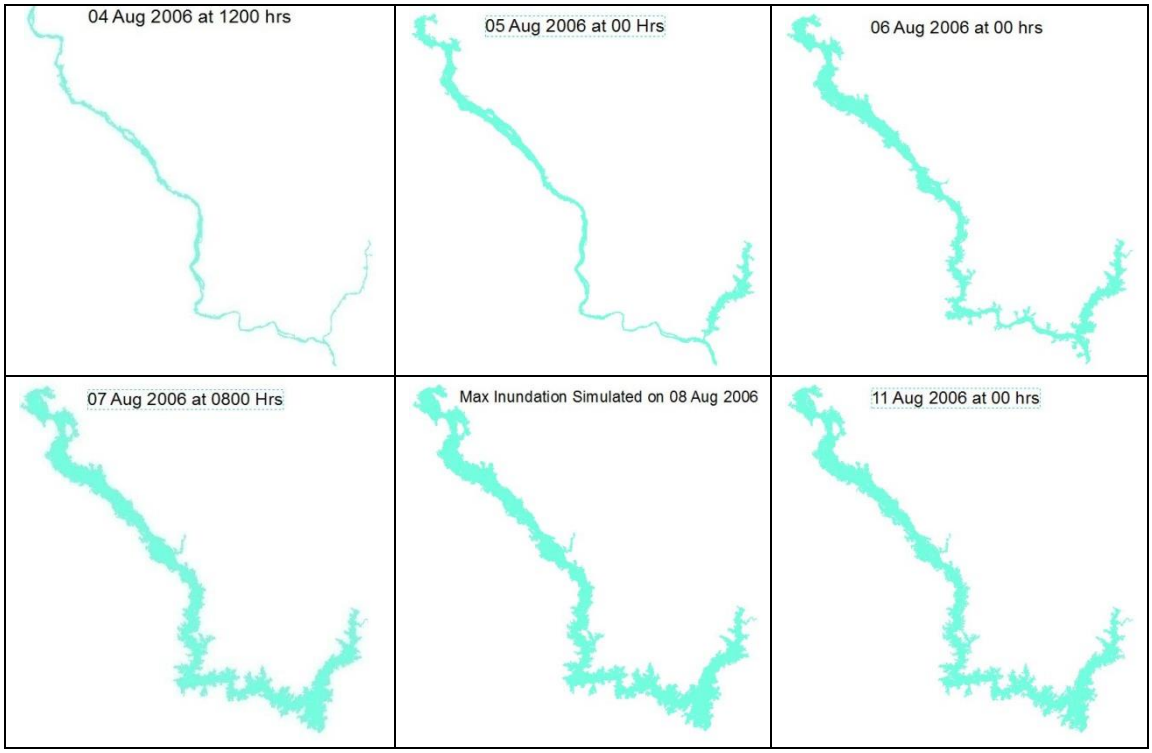

Figure 8: *Variation of flood Inundation with respect to time and discharge (Figure 5)*

The flood hazard Map was developed by considering the extreme inundation (maximum depth) simulated by the model. The hazard classification was done based on Japan ministry of land infrastructure and transport (MLIT) shown in Table 1. Figure 9 shows the flood hazard map for study area.

The depth is classified into five classes from H_1 to H_5 shown in Figure 9. Many villages on east and west side of Sabari river and north and south side of Godavari river got affected. Total of 301 villages affected for study area out of which 36 villages are of extreme category. The villages falling in extreme category are Chidumurum, Chatti, Kummur, Bojaraigudem, Jallagudem, Markandeyulapeta, Tallagudem, Regulapadu, Abhicherla, Kuturgutta, Kuturu, Muluru, Bhagvanpuram, Repaka, Peddarukur, Ravigudem, Chinnaruku, Gundugudem, Chintharajupalle, Waddegudem, S. Kothagudem on the either side of Sabari River and Rekapalle, Pocharam, Pochavaram, Kukunoor, Tipurapendamedu, Gommuru, Morampalle, Nagineprolu, Dantenam, Tekulagudem, Peddagollagudem, Ramachandrapuram forest, Thathakur, Dacharam and Tirumalapuram are on Either side of Godavari River river. Same villages are also in the H_3 and H_4 hazard zone category.

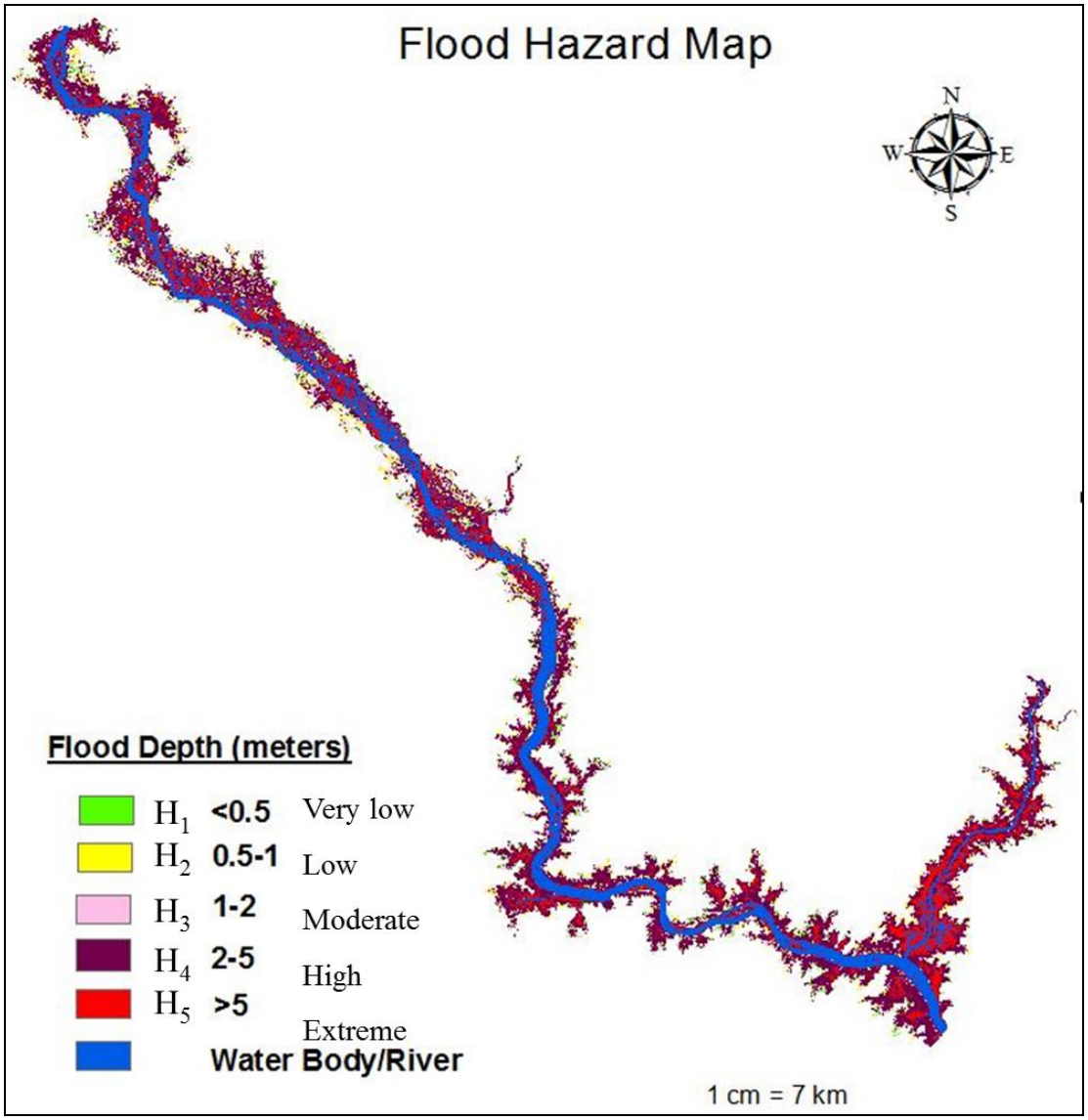

Figure 9: *Flood hazard map from maximum simulated depth*

6. Conclusion

The HEC-RAS model performance shows better performance when compared to RADARSAT satellite image. Inundation increases with increases in discharge values as shown in Figure 2. The villages falling in extreme category $H_5$are Chidumurum, Chatti, Kummur, Bojaraigudem, Jallagudem, Markandeyulapeta, Tallagudem, Regulapadu, Abhicherla, Kuturgutta, Kuturu, Muluru, Bhagvanpuram, Repaka, Peddarukur, Ravigudem, Chinnaruku, Gundugudem, Chintharajupalle, Waddegudem, S. Kothagudem on the either side of Sabari River and Rekapalle, Pocharam, Pochavaram, Kukunoor, Tipurapendamedu, Gommuru, Morampalle, Nagineprolu, Dantenam, Tekulagudem, Peddagollagudem, Ramachandrapuram forest, Thathakur, Dacharam and Tirumalapuram are on Either side of Godavari River are most vulnerable villages as depth simulated in some part of this villages are greater than 5 meters so people from this villages an event occasion are suggest to move towards higher elevation such that away from river towards northeast if village are on northern side of bank of Godavari river and move towards southeast if village are on southern side of bank of Godavari river. For Sabari river, villages lying on East side of are suggest to move towards east direction and villages lying on west side of Sabari river are suggested to move towards to the west side away from river.

List of Abbreviations

DEM – Digital Elevation Model; CWC – Central Water Commission; MLIT – Ministry of Land Infrastructure and Transport (Japan); AWiFS – Advanced Wide Field Sensor; LULC – Land Use Land Cover

Acknowledgements

The authors would like to thank United States Army Corps of Engineers (USACE) for making the HEC-RAS freely available. The authors would also like to extent their thanks to NRSC Disaster management team for their continuous support throughout the study.

References

Agarwal, A. and Sunita, N. 1991. *Floods, floodplains and environmental myths*. State of Indian environment: A citizen report, Centre for Science and Environment, New Delhi.

Chormanski, J., Okruszko, T., Ignar, S., Batelaan, O., Rebel, K.T. and Wassen, M.J. 2011. Flood mapping with remote sensing and hydrochemistry: a new method to distinguish the origin of flood water during floods. *Ecol Eng.*, 37(9), pp.1334-49.

Cheung, K.F., Phadke, A.C., Wei, Y., Rojas, R., Douyere, Y.J.M., Martino, C.D., Nakazaki, E. 2003. Modeling of storm-induced coastal flooding for emergency management. *Ocean Engineering,* 30(11), pp.1353–1386.

Chang, T.J., Hsu, M.H., Teng, W.H., and Huang, C.J. 2000. A GIS-Assisted Distributed Watershed Model for Simulating Flooding and Inundation. *Journal of the American Water Resources Association,* 36(5), pp.975–988.

Di Baldasarre, G., Schumann, G. and Bates, P. 2009. A technique for the calibration of hydraulic models using uncertain satellite observations of flood extent. *J Hydrol.*, 367, pp.276-82.

Hagen, E. and Lu, X. 2011. Let us create flood hazard maps for developing countries. *Nat Hazards*, 58, pp.841-3.

Haq, M., Akhtar, M., Muhammad, S., Paras, S. and Rahmatullah, J. 2012. Techniques of remote sensing and GIS for flood monitoring and damage assessment: a case study of Sindh province, Pakistan. *Egypt J Rem Sens Space Sci.*, 15(2), pp.135-41.

Horrit, M., Di Baldasarre, G., Bates, P. and Brath, A. 2007. Comparing the performance of a 2-Dfinite element and a 2-D finite volume model of floodplain inundation using air borne SAR imagery. *Hydrol Process*, 21, pp.2745-59.

Matgen, P., Schumann, G., Henry, J.B., Hoffman, C. and Pfister, L. 2007. Integration of SAR derived river inundation areas, high precision topographic data and a river flow model towards near real time flood management. *International Journal of Applied Earth Observation and Geo-information*, 9, pp.247-263.

MLIT. 2005. *Flood hazard mapping manual in Japan*. Ministry of Land Infrastructure and Transportation. p.87.

Moya Quiroga, V., Kure, S., Udo, K. and Mano, A. 2016. Application of 2D numerical simulation for the analysis of the February 2014 Bolivian Amazonia flood: Application of the new HEC-RAS version 5. RIBAGUA Elsevier, 3(1), pp.25-33.

Patro, S., Chatterjee, C., Mohanty, S., SinghN., R., Raghuwanshi, S. 2009. Flood inundation modeling using MIKE FLOOD and remote sensing data. *Journal of the Indian Society of Remote Sensing*, 37, p.107. *https://doi.org/10.1007/s12524-009-0002-1*

Ranzi, R., Mazzoleni, M., Milanesi, L. and Pilotti, M. 2011. Critical review of non-structural measures for water-related risks. In: KULTUrisk. UNESCO-IHE, Delft, The Netherlands. p.42.

Sewa Bharati. 2006. The Godavari Flood Disaster- August, Andhra Pradesh *http://www.sewabharathi.com/?m=1*

Shodhganga Chapter IV.
http://shodhganga.inflibnet.ac.in/jspui/bitstream/10603/152603/11/09_chapter%204.pdf

Werner M. 2004. A comparison of flood extent modelling approaches through constraining uncertainties on gauge data. *Hydrology and Earth System Sciences* 8(6), pp.1141-1152.

Cloud Publications
International Journal of Advanced Remote Sensing and GIS
2019, Volume 8, Issue 1, pp. 3106-3113
ISSN 2320 – 0243, Crossref: 10.23953/cloud.ijarsg.431

Research Article

Monitoring Land Use Land Cover Change for Dehradun District of Uttarakhand from 2009-2019

Apeksha Agarwal[1], Krishna Kumar Soni[2], MSS Rawat[1]

[1]Department of Geography, HNB Garhwal (A Central) University, Srinagar Garhwal, Uttarakhand- 264174, India
[2]Department of Geography, Gujarat University, Ahmedabad-380009, Gujarat, India

Correspondence should be addressed to Apeksha Agarwal, *apeksha.ag@gmail.com*

Publication Date: 6 September 2019

DOI: https://doi.org/10.23953/cloud.ijarsg.431

Abstract Land cover indicates the physical land type on the earths surface in the form of waterbodies, vegetation etc. whereas land use refers to the human adjustments with the land. Human has been modifying the land as a resource to fulfill their own needs since time immemorial but recently changes in land use land cover is unprecedented at local, regional as well as at the world level. These changes builds an enormous pressure on the surrounding environment and leading to climate change and loss of biodiversity. Thus, an attempt has been made to detect changes in land use land cover classes in Dehradun district of Uttarakhand state. The study has been carried out for 10 years (2009-2019) through remote sensing approach using satellite imageries of LANDSAT-5 "TM" for March 2009 and LANDSAT-8 "OLI" & "TIRS" sensor for April 2019. Methodology based on supervised classification has been applied using maximum likelihood in QGIS. The current analysis resulted that the district Dehradun has experienced land use land cover changes rapidly, as the area occupied by vegetation was about 46 percent during 2009 has decreased to 28 percent in 2019. About 27.54 percent area covered by vegetation gets turned into agriculture, 4.60 percent area into urban/ built-up and 6 percent into barren land. Agriculture and Urban/ Built-up area has increased immensely. Other land use land cover classes such as waterbody and barren land has also undergone changes. Monitoring and mediating the consequences of LULC classes has therefore become a major priority of researchers and policymakers around the world.
Keywords *Change detection; Dehradun district; Land conversion matrix; Land use land cover*

1. Introduction

Human relies on land as a resource for the fulfillment of there own needs thus land is an important natural resource from the developmental point of view. Basically land use and land cover are completely different terminologies but sometimes used interchangeably (Dimyati et al., 1996). Land cover indicates the physical land type on the earths surface in the form of waterbodies, vegetation etc. whereas land use refers to the human adjustments with the land. The land use land cover pattern of a region is an outcome of natural and socio-economic factors prevailing and their utilization by man over the time and space. Industrialization and other factors has recently encouraged the concentration of maximum populations in the urban areas (urbanization) and due to which giving way to depopulation

of their rural counterparts, along with the intensification of agriculture and abandonment of the marginal lands.

Thus, land use land cover change detection is very essential for better understanding of the landscape dynamics during a given period of time (Kiefer Lillesand, 1987; Zhang, 2011) and to asses additions as well as the losses. Land use land cover change is an accelerating process worldwide which are mainly driven by the anthropogenic activities, which in turn changes the ecosystem (Ruiz-Luna and Berlanga-Robles, 2003; Turner and Ruscher, 2004).

The need of digital classification of land use land cover is necessary for the extraction of accurate results and thus lead to better understanding of relationships among human and various natural phenomenon and finally helps in decision making processes (Jokar Arsanjani et al., 2013; Pontius and Malanson, 2005).

Use of Geospatial technology has become important in the field of land use land cover mapping of a region as it gives a detailed information about the land features in very less time with better accuracy (Selcuk et al., 2003). Introduction of satellite imageries with very high resolution and advancement in GIS technology has given way for more consistent monitoring of changes in land use land cover classes over the earth.

Through this study an attempt has been made to map the status of land use land cover of Dehradun district of Uttarakhand for two time periods i.e. 2009 and 2019 and also to detect the changes that has been taken place during the last ten years using geospatial techniques.

2. Materials and Methods

2.1. Study Area

Dehradun district is one the 13 districts of the state Uttarakhand, also the capital of the state lies in the same district. As of 2011 Census, it is the second most populous District, encompassing an area of 3074.40 sq. km., extending in between 29^0 57' 56.44" North to 31^0 1' 127.13" North Latitudes and 77^0 38' 19.57" East to 78^0 14' 24.53" East Longitudes (Figure 1). It has an area of 3088 sq. km. with the population size of 1696694. The district comprises of 7 tehsils, 6 developmental blocks and 767 villages. Few places of national importance are present in the district such as Forest Research Institute, Indian Millitary Academy, Lal Bahadur Shastri National Academy of Administration and Survey of India. Temperate climate is found in most of the places in the district with the elevation of 288 m to 3096 m.

2.2. Database and Methodology

A research methodology is the theme of any research work; it defines the way through which conclusion for the problem can be taken out. Generally, it includes the very first step to the end result (Figure 2). Collection of data for the present work is of secondary in nature. Toposheet from Survey of India, Remote Sensing Satellite Imageries acquired from US Geological Survey has been used.

The base map of the district has been prepared with the help of SOI Toposheet and freely available maps of the concerned area. The base map of the district has been digitized and proper attribute data has been inputted in the QGIS environment.

High resolution remote sensing satellite data of LANDSAT-5 with 7 spectral bands of March 31, 2009 and LANDSAT-8 with 9 spectral bands of April 28, 2019 has been used for identification, classification and change detection of land use land cover classes for the period from 2009 to 2019.

The main tools used for processing, analysis and interpretation are QGIS (Free Source Software) and MS-Excel.

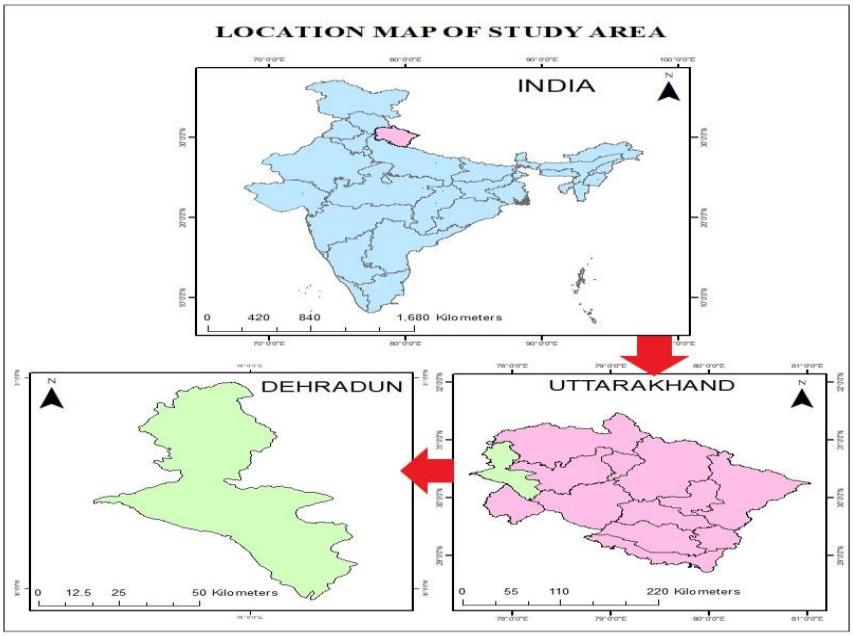

Figure 1: *Study area: Dehradun district*

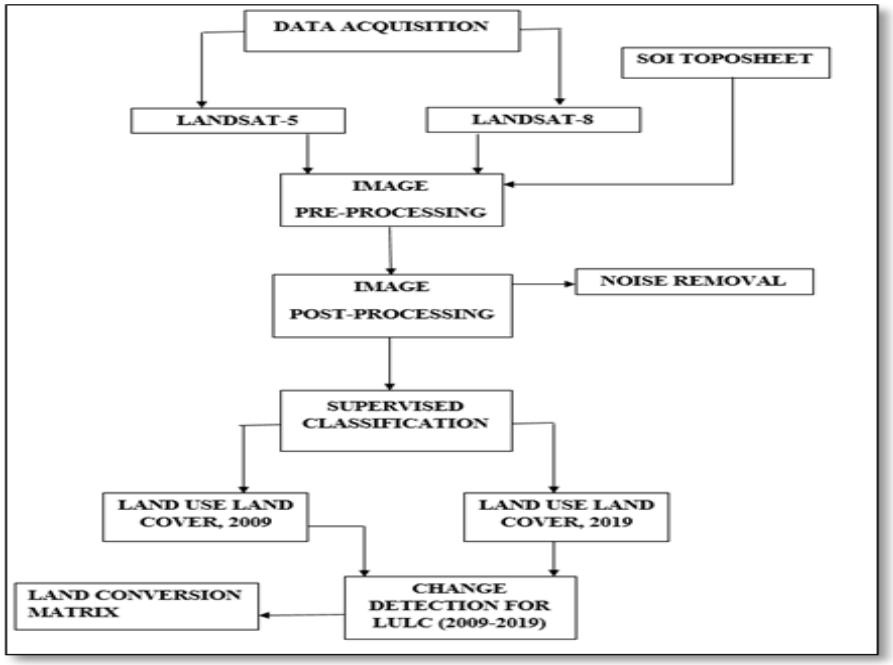

Figure 2: *Methodology chart*

2.2.1. Land Use Land Cover Classification

A number of methods has already been invented for land use land cover classifications, which are known as unsupervised and supervised classification. Land use classification can be carried out based on the relative spectral similarity among the pixels may be either by an unsupervised method in group cases, or by a supervised method based on similarity of cases of predefined classes that have been characterized spectrally. In the present study supervised method of classification with maximum likelihood algorithm has been applied in QGIS so as to get the higher accuracy in classification.

Majorly five land use land cover classes have been identified: Urban/ Built-up, Agriculture, Barren, Vegetation and Waterbody.

2.2.2. Change Detection of Land Use Land Cover and its Analysis

To find out changes in land use land cover classes, post-classification detection method has been applied. Change information has been extracted by comparing pixels of the same class and thus the interpretation of the change has been done.

Classified image pairs of two years i.e. 2009 and 2019 and compared using cross-tabulation in order to determine qualitative and quantitative aspects of the changes for the period of 10 years from 2009 to 2019. A change matrix or land conversion matrix has been produced using QGIS software. All the tabulations related to the gains and losses among the land use land cover classes between 2009 and 2019 has been done using MS-Excel.

3. Results and Discussion

The final results obtained through the analysis of multi-temporal satellite imageries are diagrammatically illustrated in Figure 3 (a) (b), 4 (a) (b) and data has been shown in Table 1 and 2. Figure 3 (a) (b) and 4 (a) (b) depicts land use land cover classification for the year 2009 and 2019. Table 1 and 2 shows changes in different land use land cover classes over the span of 10 years. A brief account of these results is discussed in the successive paragraphs.

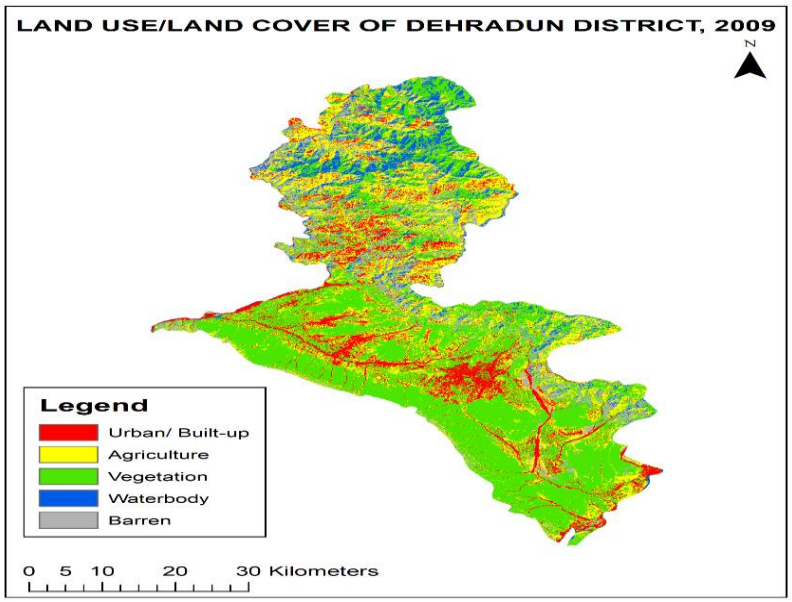

Figure 3 (a): *Land Use Land Cover, 2009 (based on Landsat Satellite Imagery)*

3.1. Land Use Land Cover Classification 2009-2019

The spatial distribution pattern of five land use land cover classes in Dehradun district for the year 2009 has been shown in Figure 3 (a) while Figure 4 (a) depicts for the year 2019. Figure 3 (b) reveals that in 2009 out of the total area 46.56 percent (1431.71 km^2) was under vegetation which is highest among all. 22.88 percent (703.60 km^2) was under agriculture, 12.53 percent (385.40 km^2) under urban/built-up, 11.54 percent (353.89 km^2) under barren land and 6.49 percent (199.81 km^2) was under waterbody. During 2019 as illustrated in Figure 4 (b), the area under different five land use land cover categories was found about 28.49 percent (876.15 km^2) under vegetation, 36.92 percent (1135.19 km^2) under agriculture land, 18.39 percent (564.65 km^2) under urban/built-up, 13.43 percent (413.11 km^2) under barren land and only 2.77 percent (85.27%) was under waterbody.

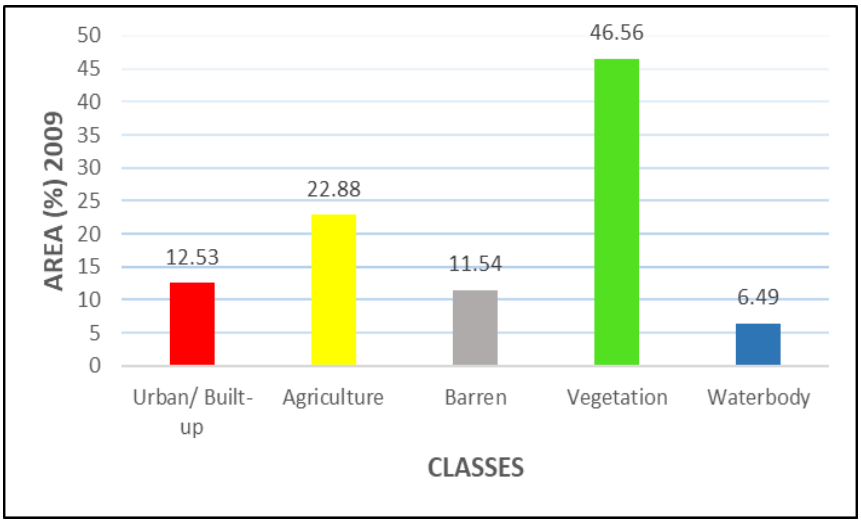

Figure 3 (b): *Area under five land use land cover classes, 2009*

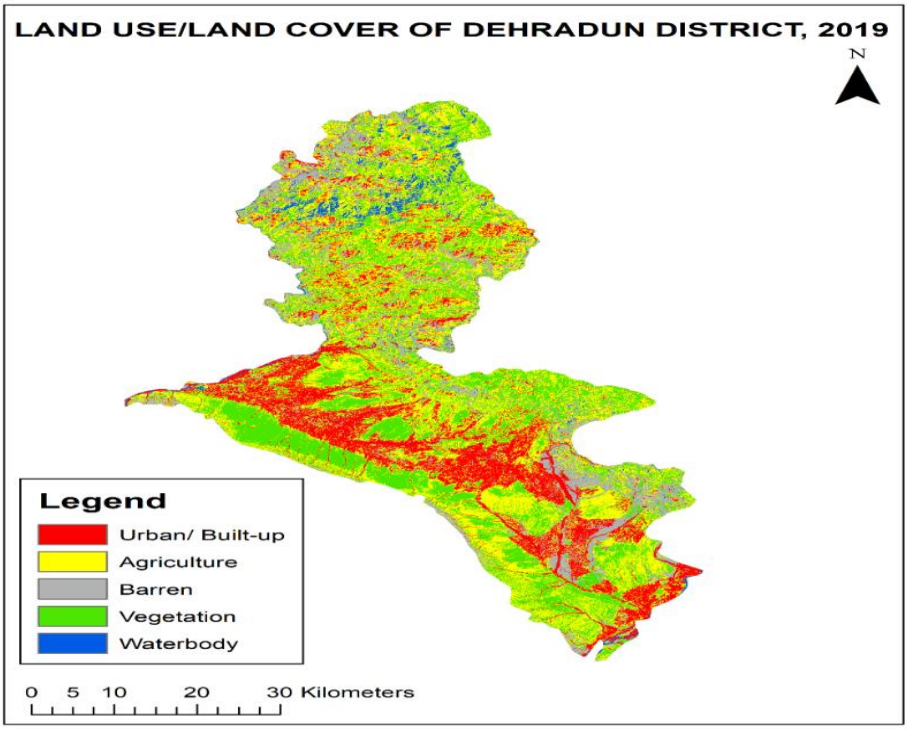

Figure 4 (a): *Land use land cover, 2019 (based on Landsat Satellite Imagery)*

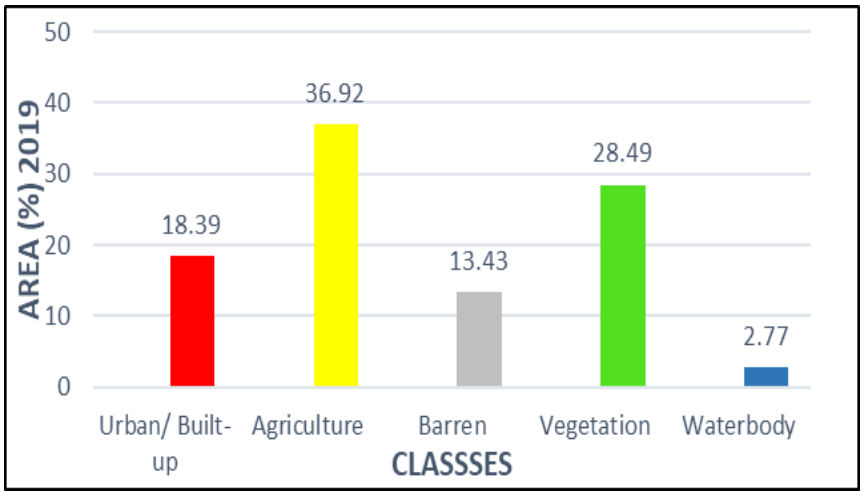

Figure 4 (b): *Area under five land use land cover classes, 2019*

3.2. Land Use Land Cover Changes 2009-2019

Table 1 and 2 data reveals that various changes of +ve and –ve nature has occurred in five land use land cover classes pattern in Dehradun district during last one decade i.e 2009 to 2019. Out of all the five land use land cover classes, the area covered by class agriculture has immensely increased from 703.60 km^2 to 1135.19 km^2 from 2009 to 2019 accounting for 14.04 percent of the area. The area under urban/ built up reach from 385.40 km^2 to 564.65 km^2 from 2009 to 2019 which leads to 5.86 percent of the area. The Barren land class has also been slightly increased from 353.89 km^2 in 2009 to 413.11 km^2 in 2019 contributing for 1.89 percent of area. The two classes of land use land cover have shown negative values in the study region. Vegetation has immensely decreased from 1431.71 km^2 to 876.15 km^2 from 2009 to 2019 accounting for 18.07 percent of area. Also there is a slight decrease in the length of waterbodies from 199.81 km^2 to 85.27 km^2 from 2009 to 2019 accounting for 3.72 percent of area (Table 1).

Table 1: *Change in area (sq. km.) among land use land cover classes from 2009-2019*

Class	2009		2019		Change (2009-2019)	
	Area in (sq. km.)	Area in (%)	Area in (sq. km.)	Area in (%)	Area in (sq. km.)	Area in (%)
Urban/ Built up	385.40	12.53	564.65	18.39	179.25	5.86
Agriculture	703.60	22.88	1135.19	36.92	431.59	14.04
Vegetation	1431.71	46.56	876.15	28.49	-555.56	-18.07
Waterbody	199.81	6.49	85.27	2.77	-114.54	-3.72
Barren	353.89	11.54	413.11	13.43	59.22	1.89
Total	3074.40	100	3074.40	100	0.00	0.00

Source: Calculated by Authors

Table 2: *Land conversion matrix (in %) for five land use land cover classes from 2009-2019*

LULC Classes (2009-2019)	Urban/ Built-up	Agriculture	Vegetation	Waterbody	Barren
Urban/ Built up	74	21.85	4.60	0.71	2.29
Agriculture	8	51.49	27.54	14.52	18.42
Vegetation	0.71	9.95	62	34.04	35.04
Waterbody	0	0.04	0	42.88	0.89
Barren	17	16.67	6.00	8.04	43.36
Class total	100	100	100	100	100

Source: Calculated by Authors

To understand how different land use land cover classes has changed into other uses over 10 years, a land conversion matrix (Table 2) has been prepared based on the percentage which in turn explains that:

- Vegetation covered area of about 27.54 percent has turned into agriculture, 4.60 percent area under urban/ built up and 6 percent area under barren land;
- Agriculture area of about 21.85 percent has turned into urban/ built up, 16.67 percent into barren land and 9.95 percent area into vegetation;
- Barren land area of about 35.04 percent has turned into vegetation, 18.42 percent into agriculture, 2.29 percent area into urban/ built up;
- Under urban/ built up class, 17 percent of the area has been turned into barren land and 8 percent of area into agriculture;
- About 34.04 percent area of waterbody has been turned into vegetation, 14.52 percent into agriculture, 8.04 percent into barren land and 0.71 percent into urban/ built up.

4. Conclusion

The work has been carried out for Dehradun district in the state of Uttarakhand advocates that multi-temporal land use land cover classifications derived from high resolution satellite data provides suitable data to assess past as well as present changes in land use land cover classes.

The changes in land use land cover classes has been rapid. Urbanization has found to be among the major drivers of change, as the statistics of the change shows a drastic increase in the urban/ built-up area from 12.53 percent in 2009 to 18.39 percent in 2019. Also agriculture area has increased from 22.88 percent to 36.92 percent and barren land area from 11.54 percent to 13.43 percent. Vegetation cover in the study area has immensely reduced from 46.56 percent in 2009 to 28.49 percent in 2019. Thus the results shows that there is a drastic increase of urban/ built-up area and agriculture area whereas reduction in green cover and waterbody area within the concerned district. As the rapid growth of the cities in Dehradun district as expected to progress, it can be expected that further urbanization will probably impact the overall vegetation cover in the .

The present work itself explains that how important is the applicability of Geospatial Technology, it helps to analyze the lengthy temporal as well as spatial datasets with faster results in a more accurate manner which is in another way not at all possible with the use of conventional mapping techniques.

Acknowledgement

This paper constitutes a part of mini project done during DST-NRDMS sponsored Summer Training Programme. Moreover, we acknowledge the supply of LANDSAT data by the US Geological Survey.

References

Abdelhamid, A. 2006. *Urban development and planning in the occupied palestinian territories: impacts on urban form*. The Conference on Nordic and International Urban Morphology: Distinctive and Common Themes, Stockholm, Sweden.

Anderson, J.R. 1976. *A land use and land cover classification system for use with remote sensor data. U.S*. Government Printing Office. p.964.

Chauhan, H.B. and Nayak, S. 2005. Land use/land cover changes near Hazira Region, Gujarat using remote sensing satellite data. *J. Indian Soc. Remote Sens.*, 33, pp.413-420.

Government of India (2011). Primary Census Abstract for Slum, Office of the Registrar General & Census Commissioner, India.

Dimyati, M., Mizuno, K. and Kitamura, T. 1996. An analysis of land use/cover change using the combination of MSS Landsat and land use map: a case study in Yogyakarta, Indonesia. *Inter. J. Rem. Sen.*, 17, pp.931-944.

Epstein, J., Payne, K. and Kramer, E. 2002. Techniques for mapping suburban sprawl. *Photogrammetric Engineering & Remote Sensing*, 63(9), pp.913-918.

Jokar Arsanjani, J., Helbich, M., Kainz, W. and Darvishi Boloorani, A. 2013. Integration of logistic regression, Markov chain and cellular automata models to simulate urban expansion. *International Journal of Applied Earth Observation and Geoinformation*, 21, pp.265-275.

Kiefer Lillesand, T. 1987. *Remote sensing and image interpretation*. 5th ed. John Wiley & Sons, New York. p.721.

Pontius, G.R. and Malanson, J. 2005. Comparison of the structure and accuracy of two land change models. *International Journal of Geographical Information Science*, 19(2), pp.243-265.

Rawat, J.S., Kumar, M. and Biswas, V. 2013. An integrated approach of remote sensing and GIS for land use/cover change detection: a case study of Bhimtal Tourist Town (India). *Bulletin of Environmental and Scientific Research*, 2(23), pp.1-6.

Ruiz-Luna, A. and Berlanga-Robles, C.A. 2003. Land use, land cover changes and costal lagoon surface reduction associated with urban growth in northwest Mexico. *Land. Ecol.*, 18, pp.159-171.

Selcuk, R., Nisanci, R., Uzun, B., Yalcin, A., Inan, H. and Yomralioglu, T. 2003. Monitoring land-use changes by GIS and remote sensing techniques: case study of Trabzon. Available from: *http://w.fig.net/resources/proceedings/fig_proceedings/morocco/proceedings/TS18/TS18_6_reis_el_al.pdf*

Shrestha, D.P. and Zinck, J.A. 2001. Land use classification in mountainous areas integration of image processing digital elevation data and field knowledge. *International Institute for Aerospace Survey and Earth Sciences*, 3(1), pp.78-85.

Turner, M.G. and Ruscher, C.L. 2004. Change in landscape patterns in Georgia. *USA Land. Ecol.*, 1 (4), pp.251-421.

Yu-Pin, L., Nien-Ming, H., Pei-Jung, W., Chen-Fa, W. and Peter, H.V. 2007. Impacts of land use change scenarios on hydrology and land use patterns in the Wu-Tu watershed in Northern Taiwan. *Landscape and Urban Planning*, 80(1 and 2), pp.111-126.

Zhang, R., Tang, C., Ma, S., Yuan, H., Gao, L. and Fan, W. 2011. Using Markov chains to analyze changes in wetland trends in arid Yinchuan Plain, China. *Mathematical and Computer Modelling*, 54(3), pp.924-930.

Zubair, A.O. 2006. *Change detection in land use and land cover using remote sensing data and GIS, A case study of Ilorin and its environs in Kwara State*. M.Sc. Thesis, Department of Geography, University of Ibadan.

Cloud Publications
International Journal of Advanced Remote Sensing and GIS
2019, Volume 8, Issue 1, pp. 3011-3029
ISSN 2320 – 0243, Crossref: 10.23953/cloud.ijarsg.416

Research Article

Predictive Land Use Change under Business-As-Usual and Afforestation Scenarios in the Vea Catchment, West Africa

Isaac Larbi*[1], Gerald Forkuor[2], Fabien C.C. Hountondji[3], Wilson Agyei Agyare[4], Daouda Mama[5]

[1]Climate Change and Water Resources, West African Science Service Centre on Climate Change and Adapted Land Use (WASCAL), Université d'Abomey -Calavi, Cotonou, 03, Benin.
[2]Remote Sensing Unit, WASCAL Competence Center, Ouagadougou, Burkina Faso.
[3]Faculté d'Agronomie, Université Parakou, Benin.
[4]Department of Agricultural Engineering, Kwame Nkrumah University of Science and Technology, Kumasi, Ghana.
[5]Institut National de l'Eau, Université d'Abomey-Calavi, Cotonou, 03, Benin.

Correspondence should be addressed to Isaac Larbi, *larbi.i@edu.wascal.org*

Publication Date: 6 July 2019

DOI: https://doi.org/10.23953/cloud.ijarsg.416

Abstract This study aimed to assess the historical Land use/land cover (LULC) changes and project the future (2025) LULC pattern in the Vea catchment based on Business as Usual (BAU) and afforestation scenarios of land use. Landsat Imagery of 1990, 2001, 2011 and 2016 were classified at overall accuracy assessment of 82%, 86%, 85% and 88% respectively. Major transitions were modeled using the Multi-layer Perceptron Neural Network algorithm, and the future scenarios maps of LULC were projected based on the Markov chain after validation of the Land Change Modeler. The results indicate the conversion of forest/mixed vegetation (23.1%) and grassland (76.9%) to cropland as the dominant LULC conversion from 1990 to 2016. An increase in cropland, built-up areas, and water bodies were observed while grassland and forest/ mixed vegetation decreased over the last 27 years. The 2025 LULC simulation indicates continuous expansion of cropland at the expense of forest/mixed vegetation which is projected to decrease by 4.5% in 2025 for the BAU scenario. Under afforestation scenario, where forest/mixed vegetation and grassland are expected to increase, cropland is projected to decrease by 20% in 2025. These findings set a reference ground for sustainable land use governance through responsible planning and management of land and water resources by considering trade-offs between cropland expansion and ecosystems' preservation in the Vea catchment.

Keywords *Cropland; Land change modeler; land use/land cover change; Vea catchment*

1. Introduction

In the past decades, research has revealed unprecedented rates of land use/land cover (LULC) change which can be attributed to many factors including but not limited to overgrazing and rapid socio-economic development (WRC, 2008; Gyasi et al., 2011). These changes are responsible for the increasing land degradation and declining soil productivity (Braimoh and Vlek, 2004; Biro et al., 2013). According to the World Atlas of Desertification (WAD), over 75% of the Earth's land area is already degraded, and about 90% could become degraded by 2050 (Cherlet et al., 2018). Globally, Africa

accounts for 65% of the total extensive cropland degradation of the world (Thiombiano and Tourino-Soto, 2007) and the situation is not different in the White Volta Basin (WVB) where the Vea catchment in Ghana is located.

In the WVB, the issue of LULC change has been addressed by several studies (Daudze, 2004; Mahe et al., 2005; Abagale et al., 2009; Agyemang, 2009; Gyasi et al. 2011, Batuuwie, 2015). For example, Abagale et al. (2009) showed that the Nasia basin within the WVB has undergone considerable LULC change between 2000 and 2008 with a loss of 10% closed savannah, a decrease of 3.2% in open savannah woodland and an increase in built up areas from 2.7% to 11.4%. Similar observation was also made by the study of Baatuuwie (2015) that observed a decrease in the forest/dense woodland areas and an increase in settlement and cropland (46.5% to 49.2%) between 1990 and 2015 when they used a multidimensional approach to assess land degradation at Nawuni (a sub-basin within the WVB). However, these studies on LULC change in the WVB have been conducted on a scale which may ignore or over-simplify landscape features due to the coarse resolution of the underlying data (e.g. 250 m MODIS). Consequently, spatial details at local (watershed) scale are missing. Understanding spatial patterns of LULC at local scale is important for local level management and decision making, which is normally not possible with coarse regional scale products. By using a higher spatial resolution (30m) satellite image, this study seeks to provide future LULC information which will be relevant for improving land management at the Vea catchment due to the findings of earlier research reporting continuous degradation.

In the Vea catchment, there are limited studies on LULC changes as well as projection of the future LULC specific to the catchment. Apart from broader scale studies (Daudze, 2004; Mahe et al., 2005; Batuuwie, 2015) covering the WVB, only Forkuor (2014) studied LULC changes in the catchment and revealed that the catchment is dominated by agricultural land, which occupied about 52% of the Vea catchment. Little effort has been made in projecting future LULC patterns which is essential for: (1) devising effective national land use plans and policies for sustainable development and (2) improving water and land management for effective implementation of the sustainable development goals (eg., SDG 15), in the context of climate change and climate variability. As LULC data are essential input to a number of biophysical and economic models, knowledge of future LULC patterns will be necessary in knowing the plausible state of our natural resources (e.g., water, land) in the future and devise appropriate strategies to avert calamity. The most widely used technique in obtaining this information is through the analysis of remotely sensed data in conjunction with ground data (Braimoh and Vlek, 2004; Daudze, 2004).

This study assessed the historical (1990 to 2016) LULC changes and projects the future (2025) LULC patterns in the Vea catchment based on Business-as Usual (BAU) and afforestation scenarios. The study provides the basis for understanding the past, present and future LULC patterns, and information to decision makers for sustainable land management in the Vea catchment.

2. Materials and Methods

2.1. Study Area

The study area is the Vea catchment located between latitudes 10°30'- 11°08' N and longitudes 0^{o} 59'- 0^{o} 45'W (Figure 1). The Vea catchment is a sub-catchment of the White Volta Basin (WVB) with an area of about 308 km^2 and covers mainly the Bongo and Bolgatanga districts in the Upper East Region of Ghana with a small portion in the south-central part of Burkina Faso. The climate of the catchment is controlled by the movement of the Inter-Tropical Discontinuity (ITD) over the West African region (Obuobie, 2008). Located in a semi-arid agro-climatic zone, the catchment crosses three agro-ecological zones: the Savanna and Guinea Savanna zones in Ghana, and north Sudanian Savanna zone in Burkina Faso (Forkuor, 2014). The catchment is characterized by a uni-modal rainfall regime from May to October with a mean annual rainfall of about 956 mm which normally peaks in August (Larbi et al., 2018). The temperature is uniformly high with a mean annual value of 28.9^{o}C and

potential evapotranspiration exceeds monthly rainfall for most part of the year, except the three wettest months of July, August and September (Limantol et al., 2016). The catchment is characterized by fairly low relief with elevation ranging between 89 m and 317 m (Figure 1) whereas the LULC is mainly dominated by cropland followed by grassland interspersed with shrubs and trees. Agriculture, which includes the cultivation of annual crops such as *Vigna unguiculata* (cowpea), *Oryza sativa* (rice), *Sorghum bicolor*, (sorghum) *Pennisetum glaucum* (millet), and *Arachis hypogaea* (groundnuts), is the main activity of the people in the catchment.

2.2. Landsat Data Processing

2.2.1. Landsat Images

The 30m resolution Landsat Images for the years 1990, 2001, 2011 and 2016 (Table 1) covering a period of 27 years, were downloaded for two scenes based on availability and seasonal compatibility from the United States Geological Survey (USGS) GLOVIS website (USGS, 2017). A cloud cover criterion of less than 10% was used. In all cases, end of growing/harvest season (October and November) images were used to reduce the confusion between natural vegetation and agricultural lands, and to minimize interference due to cloud cover (Ruelland et al., 2008; Zoungrana et al., 2015).

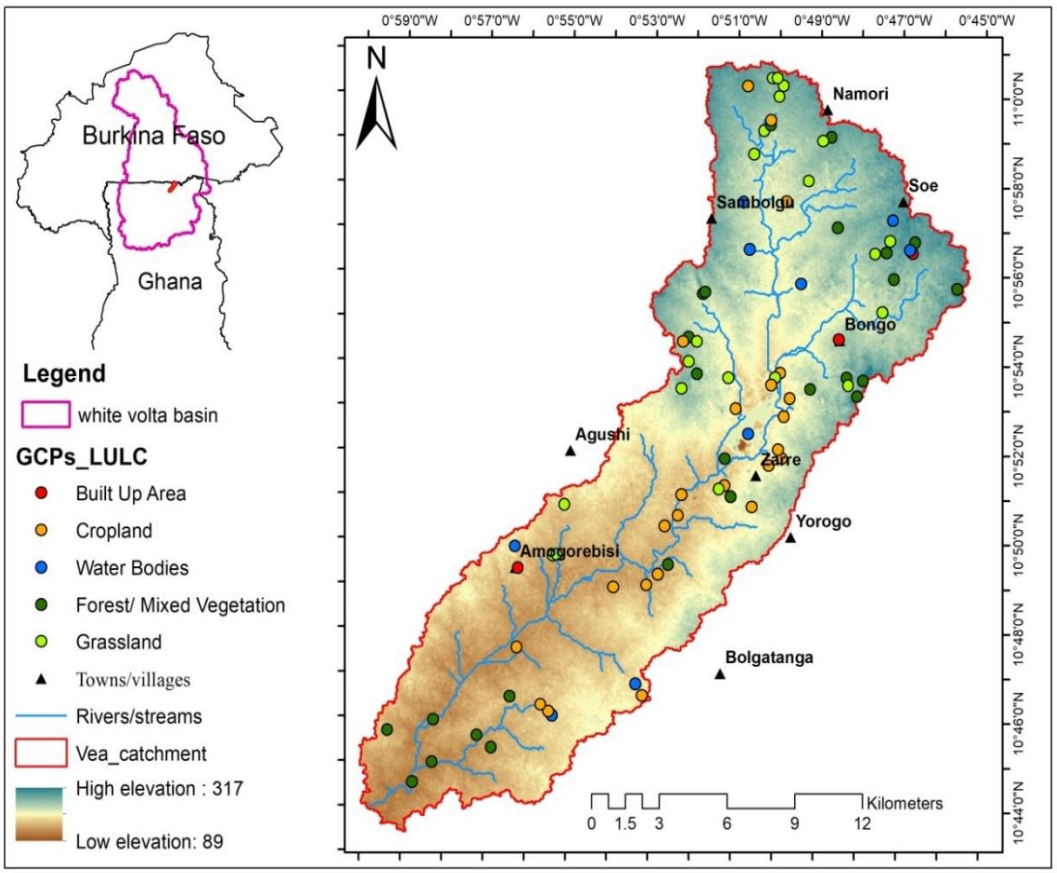

Figure 1: *DEM map of Vea catchment with LULC ground truth data*

Table 1: *General characteristics of landsat images*

Date of acquisition	Platform (sensor)	Scene path and row (p, r)	No. of bands
2016-10-24	Landsat 8 (OLI /TIRS)	p194r052; p194r053	11
2011-10-24	Landsat 7(ETM+)	p194r052; p194r053	8
2001-10-27	Landsat 7(ETM+)	p194r052; p194r053	8
1990-11-02	Landsat 4/5(TM)	p194r052; p194r053	7

OLI: Operational Land Imager; ETM+: Enhanced thematic mapper, Thematic Mapper (TM); Bands used: 5, 4, 3 and 2.

2.2.2. Reference Data

Reference data used for the classification and accuracy assessment were obtained from high-resolution images of Google Earth, previous 2013 LULC map of the Vea catchment (Forkuor, 2014) and a field campaign using Global Positioning Systems (GPS). The google earth imagery is provided by digital globe and SPOT satellite over the study area with resolution between 10 m to 1.5 m. These datasets were collected to serve as a basis for image classification and accuracy assessment. The field campaign was conducted within the same dry season (January to March 2017) for best correlation between the 2016 Landsat image and the ground features. In all, a total of 250 reference points from both 2017 field campaign (150 points) and Google Earth Image (100 points) of the year 2016 were collected. Sixty percent of the collected data were used for training and the remaining for validation. With the help of a handheld GPS device, a total of 150 polygons were created for five LULC types during the field survey. The polygons were created from 30 m X 30 m plots of a particular LULC type (eg. Cropland). Two hundred reference points from 2011 Google Earth Image and previous 2013 LULC map of the catchment were used for the classification (58 points) and validation (142 points) of the 2011 image. The year 2001 Landsat image was classified (65 points) and validated (135 points) based on 200 points selected from Google Earth Image. Also, 215 points were collected for the year 1990 of which 56 were used for classification and 159 points for validation. The samples were picked from areas that remained unchanged after loading the samples of the year 2001 on the 1990 Landsat image.

2.3. Mapping and Accuracy Assessment

2.3.1. Image Classification

The LULC maps were produced based on the methodology outlined in Figure 2 by considering five LULC classes (Table 2) based on previous studies in the study area and the LULC classification scheme of the study by Forkuor (2014). A supervised image classification based on maximum likelihood algorithm - a statistical decision criterion that assigns pixels to the class of the highest probability was performed (Chander et al., 2009; Ahmad, 2012). The Landsat images of 1990, 2001, 2011 and 2016 were classified based on training data obtained from both onscreen digitization of various LULC classes and part of the reference data collected for the various LULC classes.

Table 2: *Land use/land cover classification scheme modified from Forkuor (2014)*

LULC categories	Description
Water body	Areas permanently covered with standing or moving water such as inland waters, waterlogged areas, wetlands, dams, dugouts and streams.
Grassland	Mainly the mixture of grasses and shrubs with or without scattered trees (<10 trees per hectare) and areas covered with only grasses.
Built-up areas	Areas of human settlements, roads, artificial surfaces etc.
Cropland	Areas used for crop cultivation (irrigated and rain-fed agriculture), harvested agricultural land and bare soil.

Mixed vegetation/ Forest	Areas with dense trees usually over 5 m tall, riparian vegetation, shrubs and trees.

2.3.2. Accuracy Assessment

The aim of accuracy assessment is to quantitatively determine how effectively pixels were grouped into the correct feature classes in the area under investigation. Accuracy assessment of the classified image of the year 1990, 2001, 2011 and 2016 were performed using reference data. An error or confusion matrix which is one of the most widely used accuracy assessment method (Congalton and Green, 2009) was generated for all the LULC classes. The error of omission or producer's accuracy, error of commission or user's accuracy, overall accuracy and the Kappa value were determined for each classified LULC map.

2.4. Scenarios Development

Developing scenarios of future LULC conditions is important for a variety of research themes, including hydrologic change and water availability (Wilk and Hughes, 2002). In developing countries such as Ghana, due to the complex land tenure systems, land use change is a relatively uncontrolled process compared to developed countries. In this study, two different LULC change scenarios, i.e., Business-as-usual (BAU) and afforestation scenarios (Table 3) were considered. The afforestation scenario was created by altering the probability matrices for cropland, grassland and forest/mixed vegetation produced from the Markov chain analysis by limiting the probability that grassland and forest/mixed vegetation would be converted to cropland.

Table 3: *Land use/land cover change scenarios*

Scenarios type	Description
Business- -as-usual	The future 2025 LULC map is produced based on the historical trend of LULC transitions (expansion in cropland at the expense of natural vegetation) from 1990 to 2016.
Afforestation	Increase in natural vegetation (forest/mixed vegetation and grassland) by 15% in the future 2025 by limiting the expansion of cropland.

2.5. Change analysis and modelling

2.5.1. Post Classification Change Analysis using the Land Change Modeler

Diverse modelling tools have been applied to analyse LULC dynamics over the past years with each tool producing different degrees of accuracy (Wu and Webster, 2004). Embedded in IDRISI software are various land use modelling tools such as the Land Change Modeller (LCM), Cellular Automata (CA), CA_Markov, GEOMOD, and STCHOICE which are commonly used (Eastman, 2006). For short-term projections, mostly ten years or less, LCM has been noted to provide good projection accuracy in LULC change analysis (Roy et al., 2014). Moreover, compared to other models that project LULC change based on supervised classifications, the LCM produces more accurate output due to the robust nature of the Multi-layer perceptron (MLP) neural network used in LCM (Vega et al., 2012). These reasons guided the choice of the LCM to project the LULC changes in the Vea catchment for the 2025 horizon.

The LULC change analysis and the scenarios maps for the Vea catchment were produced in the LCM using the following procedure: change analysis, transition potential modelling, model validation and change projection (Figure 3). The model evaluates LULC change between two sets of images of different dates, same legend, and spatial characteristics, and presents the change results in graph and map forms (Megahed et al., 2015). In this study, the LULC changes for the four time periods (1990 to

2001, 2001 to 2011, 2011 to 2016 and 1990 to 2016) were performed by post-classification comparison technique, a widely used approach for LULC change detection (Mahmoud et al., 2016). The LULC change analysis was performed using the change detection module in the LCM which provides information on; gains and losses of each LULC class, the net change which is the difference between the gains and losses of each class, contributors to the net change experienced by each class, and the transition of areas among each LULC class that has occurred between two different dates (Eastman, 2006).

2.5.2. Transition Potentials Modelling using the Multi-layer Perceptron Neural Network

The LULC maps of the year ($2001t_1$ – $2011t_2$ and $1990t_1$ – $2016t_2$) were used as inputs to produce the transitions. The change analysis module was used to identify the most dominant transitions (grassland to cropland, forest/mixed vegetation to cropland and forest/mixed vegetation to grassland) which were used to create transition potential maps required for modelling by setting a threshold of 1000 hectares. The likelihood of transformation from other classes to cropland (Evidence likelihood image) was created using the change maps. The LCM employs logistic regression, SimWeight and Multi-Layer Perceptron (MLP) neural network as modelling algorithms to model transition variables. The MLP neural network was employed in this study to produce the transition potential maps. The MLP is extensively enhanced and requires no user intervention, with the ability to model several transitions at a time, and also capable of modelling non-linear relationships (Eastman, 2006). The MLP neural network operates as a feedforward artificial neural network (ANN) model with uni-directional data flow through hidden layers in between (Nazzal et al., 2008). The neural network training is based on a supervised training algorithm which is a common method of training ANN. The transition potential maps for the LULC changes were produced with MLP accuracy rate (85%) which is within the acceptable range (Eastman, 2006).

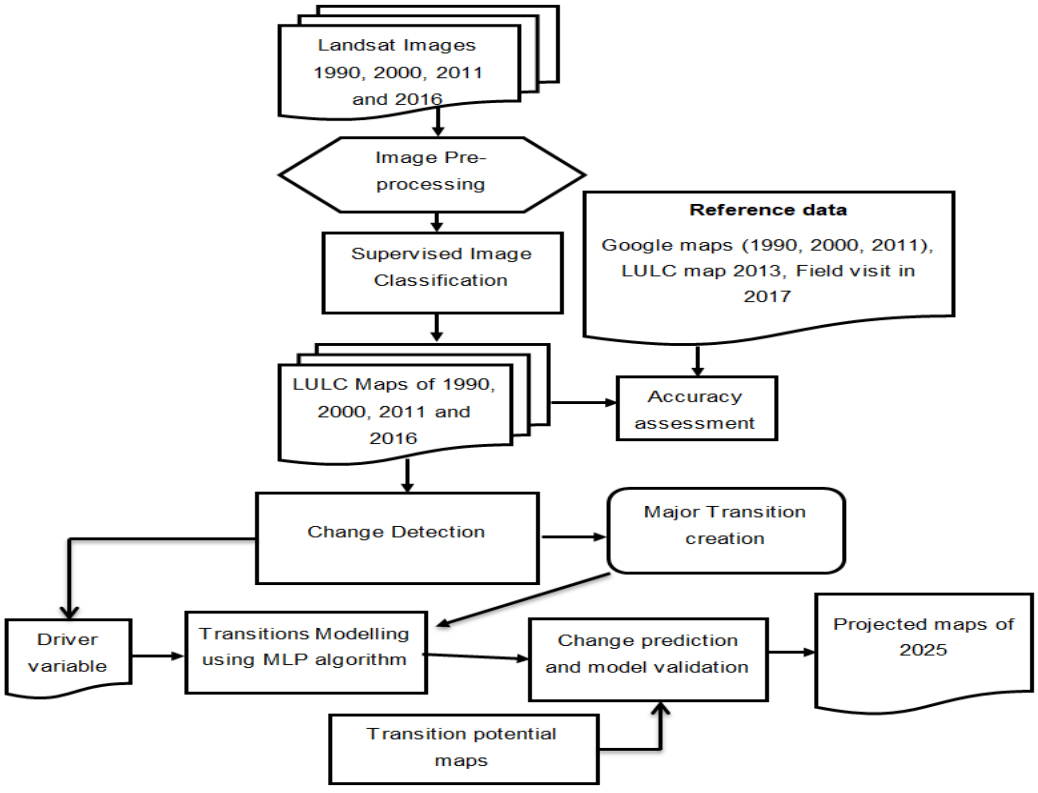

Figure 2: *Flowchart of LULC mapping, change analysis and modelling*

2.5.3. LCM Validation and Change Projection

The LCM model projective power was assessed using the Cramer's V by modelling the transitions from 1990-2001 using the transition sub model after setting the driver variable (Evidence likelihood variable) which is obtained from the historical changes between 1990 and 2001), to produce the transition potentials required to project the 2011 LULC map using the Markov chain. The Markov chain calculates how much land transition from one class to another from time t_o to t_1 in each transition based on the historical rate of LULC changes (Eastman, 2006; Olmendo et al., 2015). To validate the LCM, the statistical approach which examines the agreement between a pair of maps that show any categorical variable, and can have any number of categories was used (Pontius and Chen, 2008). The output of the simulated 2011 map was compared with the real or classified map of 2011 using the validation module to evaluate the accuracy of the model through the application of Kappa Index (Pontius, 2000; Langley et al., 2001) which includes; overall accuracy of simulation run (K_{no}) and the level of agreement of location ($K_{location}$). The Kappa value ranges from -1 which indicates no agreement to 1 which indicates perfect agreement (Pontius, 2000). This is done to ascertain the quality of the projected map and the actual LULC map. Comparison between changes indicated by the real map to the change shown by the simulated map over the validation period was made. After validation and assessment of the model, the LCM was used to project the future LULC scenarios maps for the year 2025 based on the same driving variable and the historical LULC change between 1990 and 2016 by going through the procedure defined in Figure 2.

3. Results

3.1. Accuracy Statistics and LULC Change Analysis

The accuracy assessment results of the classified LULC maps indicate overall classification accuracies of 82% (1990), 86% (2001), 85% (2011), 88% (2016) and Kappa statistics above 0.8 (Table 4a - 4d).

Table 4: *Accuracy statistics of the classified land use/land cover maps*

(a) Year 1990; Overall accuracy = 82.3%; Kappa = 0.8

LULC	Reference image					Reference totals	User accuracy (%)	Producer accuracy (%)
	1	2	3	4	5			
Cropland	31	5	3	0	0	39	79.5	77.5
Grassland	4	30	6	0	0	40	75.0	75.0
Forest/mixed vegetation	3	5	32	0	0	40	80.0	78.0
Built-up Areas	2	0	0	28	0	30	93.3	100.0
Water bodies	0	0	0	0	10	10	100.0	100.0
Classified total	40	40	41	28	10	159		

(b) Year 2001; Overall accuracy = 85.9%; Kappa = 0.84

LULC	Reference image					Reference total	User accuracy (%)	Producer accuracy (%)
	1	2	3	4	5			
Cropland	30	3	1	0	0	34	88.2	78.9
Grassland	4	27	3	1	0	35	77.1	81.8
Forest/mixed vegetation	1	3	26	0	0	30	86.7	86.7
Built-up Areas	3	0	0	22	0	25	88.0	95.7
Water bodies	0	0	0	0	11	11	100.0	100.0
Classified total	38	33	30	23	11	135		

(c) Year 2011; Overall accuracy = 84.5%; Kappa = 0.82

LULC	Reference image					Reference total	User accuracy (%)	Producer accuracy (%)
	1	2	3	4	5			
Cropland	31	4	3	1	0	39	79.5	83.8
Grassland	3	24	5	0	0	32	75.0	77.4
Forest/mixed vegetation	1	3	30	0	0	34	88.2	78.9
Built-up areas	2	0	0	23	0	25	92.0	95.8
Water bodies	0	0	0	0	12	12	100.0	100.0
Classified total	37	31	38	24	12	142		

(d) Year 2016; Overall accuracy = 88%; Kappa = 0.86

LULC	Reference image					Reference total	User accuracy (%)	Producer accuracy (%)
	1	2	3	4	5			
Cropland	26	2	1	0	0	29	89.7	83.9
Grassland	3	22	1	0	0	26	84.6	81.5
Forest/mixed vegetation	1	2	20	0	0	23	87.0	90.9
Built up areas	1	1	0	14	0	16	87.5	100.0
Water bodies	0	0	0	0	6	6	100.0	100.0
Classified total	31	27	22	14	6	100		

The LULC classification results of the year 1990, 2001, 2011, 2016 and the area under each LULC type are shown in Figure 3 and Table 5 respectively. Cropland was found to be dominant in the LULC maps of the year 2001 (40.62%), 2011 (54.09%) and 2016 map (56.64%) with the southern part of the catchment mostly dominated by natural vegetation (forest/mixed vegetation and grassland) as shown in Figure 4. The changes in LULC from 1990 to 2001, 2001 to 2011, 2011 to 2016 and 1990 to 2016 in terms of the net change of the LULC classes which were analyzed by the LCM are shown in Figure 4 and Table 5. The most dominant LULC change was the conversions of grassland to cropland, followed by the conversion of forest/mixed vegetation to cropland within the last 27 years. Between 1990 and 2001, cropland increased by 22.87% followed by built-up areas (22.46%) while grassland decreased by 25%. Between 2001 and 2011, cropland continued to increase by 24.9% together with built- up areas (25.3%) while grassland and forest/mixed vegetation decreased by 34.6% and 20.7% respectively. During the last five years (2011 to 2016), built-up areas continued to increase by 39.14%, followed by water bodies (12.87%) and cropland areas (4.50%), while grassland and forest/mixed vegetation decreased further (Table 6). Between 1990 and 2016, forest/mixed vegetation and grassland decreased by 20.8% and 44.9% respectively, while cropland, water bodies and built-up areasshowed an increase. The results of the rate of change (Table 6) of the LULC types showed that built- up areas, cropland and water bodies increased at an annual rate of 0.04, 3.0 and 0.01 km^2 respectively while grassland and forest/mixed vegetation cover decreased at an annual rate of 2.6 and 0.45 km^2 respectively within the last 27 years.

Table 5: *LULC classification statistics with area in km^2 (%) from 1990 to 2016*

LULC Class	1990	2001	2011	2016	Area coverage (%)			
					1990	2001	2011	2016
Cropland	96.53	125.15	166.64	174.50	31.33	40.62	54.09	56.64
Grassland	150.33	120.26	89.38	82.72	48.80	39.04	29.01	26.85
Built-up areas	0.69	0.89	1.02	1.67	0.22	0.29	0.33	0.54
Water bodies	4.56	5.35	4.27	4.90	1.48	1.74	1.39	1.59
Forest/mixed veg.	55.96	56.42	46.76	44.28	18.17	18.31	15.18	14.37

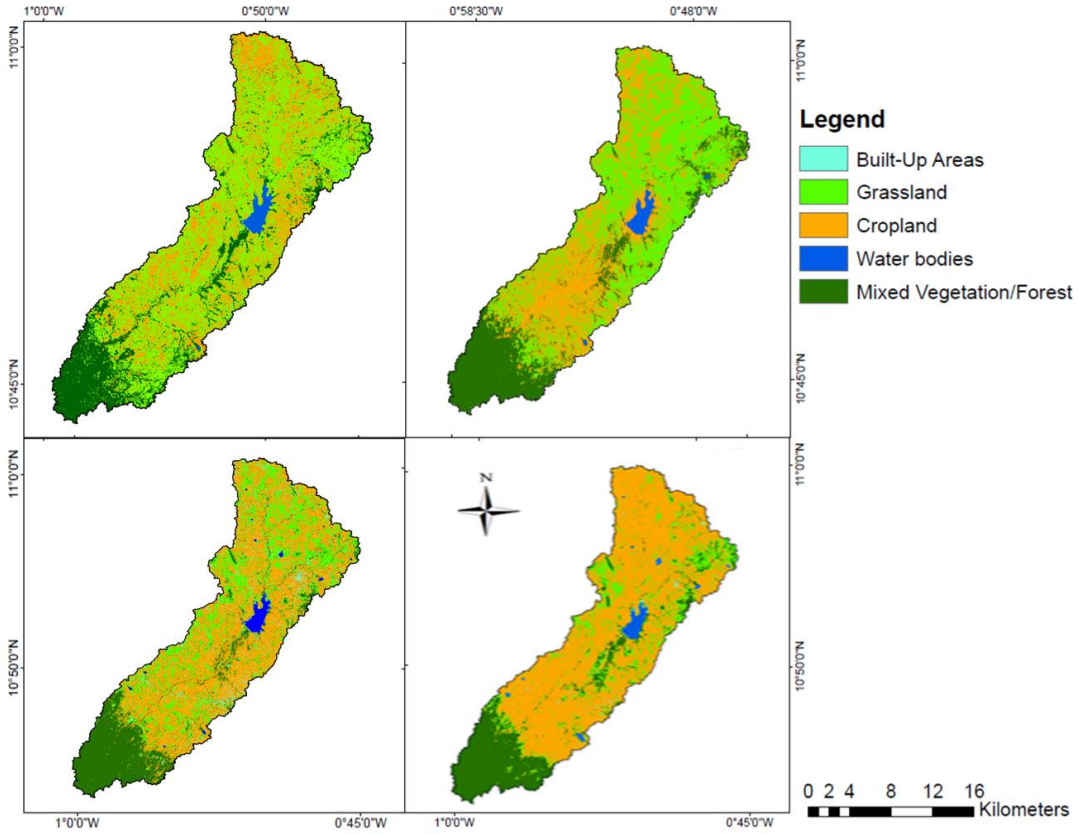

Figure 3: *Spatial distribution of land use/cover maps of the Vea catchment for 1990, 2001, 2011 and 2016*

Table 6: *Change statistics and rate of change of LULC type from 1990 to 2016*

LULC Class	Area change (km^2)				Rate of change (km^2) per year			
	1990-2001	2001-2011	2011-2016	1990-2016	1990-2001	2001-2011	2011-2016	1990-2016
Cropland	2862 (22.8%)	4149 (24.9%)	786 (4.5%)	7797 (80.7%)	2.60	4.15	1.57	3.00
Grassland	-3007 (-25%)	-3088 (-34.6%)	-666 (-8.1%)	-6761 (-44.9%)	-2.73	-3.09	-1.33	-2.60
Built-up areas	20 (22.4%)	13 (25.3%)	66 (39.1%)	98 (58.6%)	1.8	0.01	0.13	0.04
Water bodies	79 (14.7%)	-108 (-12.3%)	63 (12.8%)	34 (6.9%)	0.07	-0.11	0.13	0.01
Forest/mixed vegetation	45 (0.8%)	-966 (-20.7%)	-248 (-5.6%)	-1168 (-20.8%)	0.04	-0.97	-0.50	-0.45

NB: Percentage change in LULC type is found in the bracket.

3.2. Contributors to the Changes in Land Use/Land Cover

In order to observe the transformations from all other LULC classes to cropland, charts of contributors (LULC types which are converted to other LULC type) to cropland area dynamic over the 27 year period expressed in hectares were produced (Figure 4). The main contributing factor to the expansion in cropland within the last 27 years was grassland followed by forest/mixed vegetation. From 1990 to 2001, grassland contributed about (20%) to the increase in cropland followed by forest/mixed vegetation (14%). Similar observations were made from the year 2001 to 2011, and 2011 to 2016,

where grassland and forest/mixed vegetation were the main contributors to the increase in cropland in the Vea catchment.

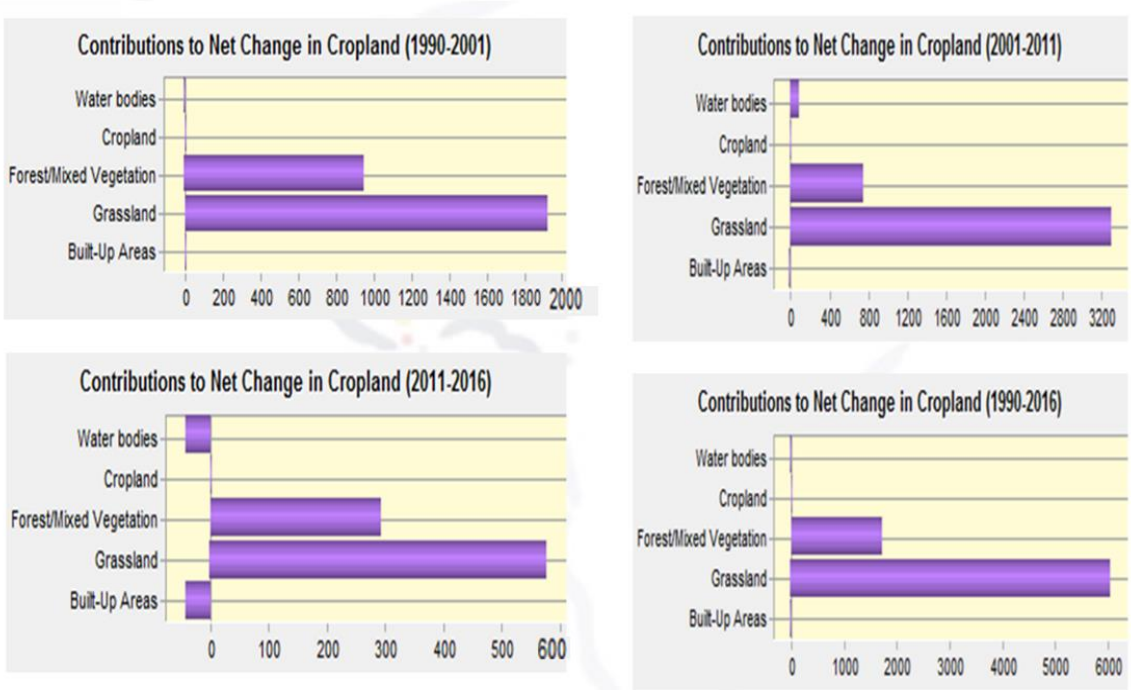

Figure 4: *Contribution to net change in cropland (in hectares) by forest/mixed vegetation and grassland for 1990-2001, 2001-2011, 2011-2016 and 1990-2016*

3.3. Model Validation

The results of the overall Cramer's V test of projective power of the LCM as presented in Table 7 indicate Cramer's V value greater than 0.4. Comparison of the modelled and classified LULC maps of 2011 (Figure 5 and Table 8) showed minor differences between the simulated and actual maps. In the simulated map (Figure 5), the area for cropland was a little underestimated while grassland was a little overestimated especially in the northern part of the catchment. The statistical validation of the simulated change in 2011 and the corresponding error is shown in Table 8. A simulated change of 29.22 km^2 of cropland which is less than the actual change of 41.49 km^2 was observed with an error of 7.3%. The Kappa value which is related to the location and quantity of the image was observed to be high when the modelled and classified LULC maps were compared. The overall accuracy of simulation run (K_{no}) and the level of agreement of location ($K_{location}$) values were found to be 80.47% and 78.35% respectively. This indicates that the LCM was capable of projecting the 2011 LULC map by simulating the historical changes that occurred from the year 1990 to 2001, hence is capable of projecting a reasonable result for the year 2025. Between 1990 and 2016, the contribution from grassland and forest/mixed vegetation to cropland were 76.9% and 23.1% respectively.

Table 7: *Cramer's V test for each LULC*

Evidence likelihood variable	Overall Cramer's V	Water bodies	Cropland	Forest/mixed vegetation	Grassland	Built-up areas
(1990-2001)	0.5549	0.2155	0.9042	0.6393	0.3351	0.0577
(1990-2016)	0.4668	0.2726	0.6180	0.2334	0.0474	0.00

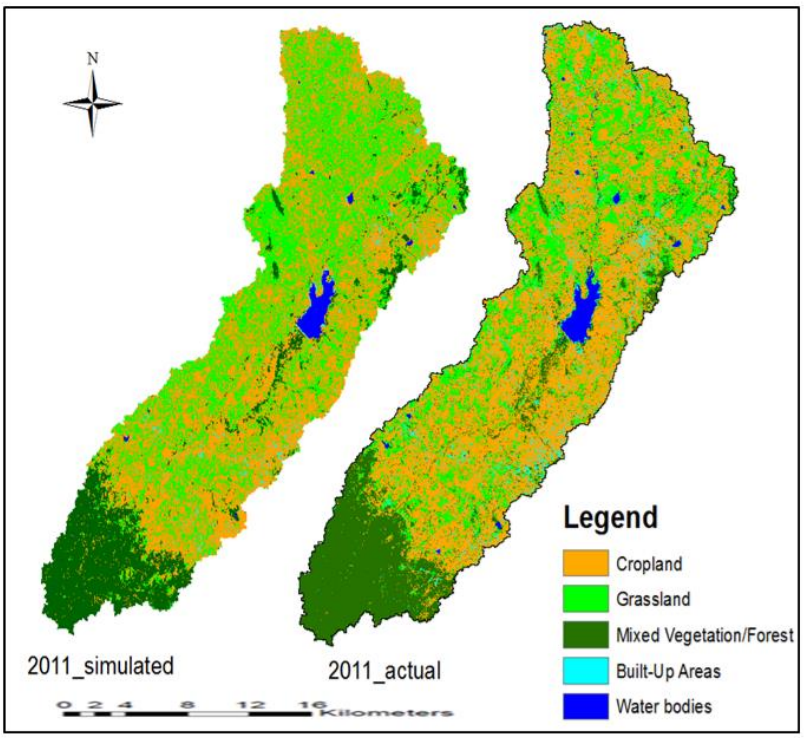

Figure 5: *Simulated and actual LULC maps of 2011*

Table 8: *Comparison between actual and simulated LULC area statistics (in km^2) for the year 2011*

LULC Class	2001	Area coverage (km^2)		Simulated-Actual or error (km^2)
		Actual 2011	Simulated 2011	
Cropland	125.15	166.64 (41.49)	154.43(29.28)	-12.21(7.3%)
Grassland	120.26	89.38(-30.88)	97.97(-22.29)	8.59(9.6%)
Built-up areas	0.89	1.02 (0.13)	0.95(0.06)	-0.07 (6.7%)
Water bodies	5.35	4.27 (-1.08)	4.35(-1.0)	0.08 (1.9%)
Forest/mixed veg.	56.42	46.76 (-9.66)	50.42(-6.0)	3.66 (7.8%)

NB: Values in the bracket indicate simulated change and actual change in km^2 during the validation period.

3.4. Simulation of LULC Changes

The outputs from the Markov chain projection of the future 2025 LULC maps for the two LULC change scenarios are shown in Figure 6. In BAU scenario, as shown in Table 9, there is an evidence of potential increase in cropland at the expense of natural vegetation (grassland and forest/mixed vegetation) from 56.6% in 2016 to 57.5% in 2025. Grassland is projected to increase from 26.8% to 28.5% which can be attributed to the projected decrease in forest/mixed vegetation from 14.4% to 11.8% by the year 2025. There were no changes in water bodies and built-up areas due to the fact that the model considered the major transitions that occurred over the past years. In the case of afforestation scenario, which considers limitation in cropland expansion by promoting vegetation growth while ensuring food security, there would be a potential increase in forest/mixed vegetation from 14.4% in 2016 to 15.3% in 2025. Grassland is projected to increase from 26.85% in 2016 to 31.3% in 2025, while cropland decreased from 56.6% to 51.3% by 2025.

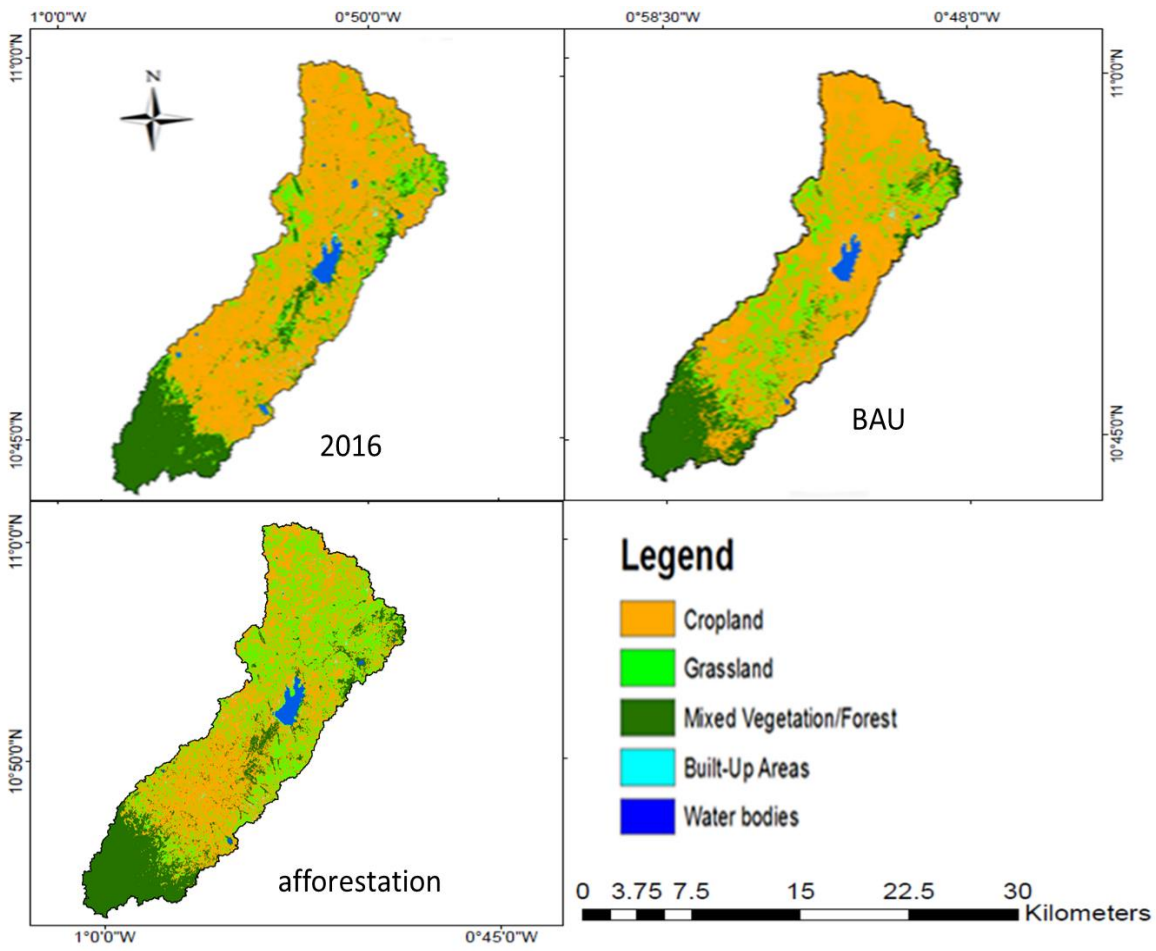

Figure 6: *LULC maps for the year 2016 and for the two 2025 scenarios (BAU and afforestation)*

Table 9: *Projected LULC area statistics (in km^2) for the year 2025 relative to baseline (2016)*

LULC Class	Baseline 2016	Future 2025 scenarios	
		BAU	afforestation
Cropland	174.50 (56.6%)	177.04 (57.5%)	155.5 (51.3%)
Grassland	82.72 (26.8%)	88.06 (28.5%)	94.55 (31.3%)
Built-up areas	1.67 (0.5%)	1.67 (0.5%)	1.02 (0.5%)
Water bodies	4.90 (1.6%)	4.90 (1.6%)	4.90 (1.6%)
Forest/mixed vegetation	44.28 (14.4%)	36.40 (11.8%)	46.66 (15.3%)

4. Discussion

4.1. Classification Accuracy, LCM Model Projection and Validation

This study assessed the changes in LULC over period 27 years and modelled the changes to produce the future 2025 scenario maps of LULC conditions in the Vea catchment using the LCM. The accuracy of the LULC classification observed in this study can be attributed to the heterogeneity of the study area and the likely confusion between grassland and cropland due to the mono-temporal data used. This is in line with the observation made by Zoungrana et al. (2015) that the confusion between natural vegetation and agricultural lands are minimized when late-season images (eg. October images) are classified. However, Forkuor (2014) noted that the heterogeneity of the Vea catchment whereby grasses and trees are intermixed with harvested croplands can be seen as a major contributing factor to the spectral confusion between grassland and cropland. In terms of the model projection accuracy,

an overall Crammer's V value of 0.55 (1990-2001) and MLP neural network accuracy rate of 85% were achieved and according to Eastman (2006), a Cramer's V value above 0.4 and accuracy rate of about 80% is acceptable in modelling.

The model validation results based on the comparison between the actual and simulated 2011 LULC map obtained from this study can be attributed to the nature of the model. It was noticed that the simulation in our study shows less change than the actual change (Table 8) during the validation period (2001-2011). Also, some LULC changes were not relatively well simulated by the model during the validation period which according to Olmendo et al. (2015) can be attributed to the acceleration of changes that occurs in the reference year which does not show during calibration period. According to Robertson and Swinton (2005), if the changes during the calibration interval which in this case 1990-2001 are not stationary with the changes during the validation interval (2001-2011) as shown in Table 6, then an extrapolation from the calibration interval to the validation interval will probably have systematic errors which will affects the accuracy of projection. Moreover, the differences between the simulated and actual LULC maps and the reported Kappa statistics can be attributed to the fact that Land changes involve complex processes that are shaped by dynamic, non-linear human-nature interactions, which can be difficult for the available variable and algorithm to capture (Perez-Vega et al., 2012; Kolb et al., 2013).

4.2. Spatio-Temporal Analysis of Historical LULC Changes

The historical LULC change analysis indicated a loss of vegetation in the southern part of the Vea catchment in the year 1990 which can be attributed to deforestation (cutting down of trees for charcoal production and timber) and agricultural expansion. Between 1990 and 2016, forest/mixed vegetation area which consist of forest, riparian vegetation, shrubs and closed woodland were found to have decreased due to cropland expansion over the past 27 years. However, in 2001, there was an increase in vegetation at the southern part of the catchment and this can be attributed to measures such as the enforcement of the forest protection laws put in place to protect the area and the creation of forest reserves. The observed decrease in natural vegetation is similar to the results obtained by Daudze (2004), who found a decrease in woodland and mixed vegetation in the same region from 1986 to 2000 due to an increase in agricultural area and bare land. The LULC change dynamics mainly the conversion of natural vegetation to cropland observed over the last 27 years have also been reported by other studies such as Braimoh and Vlek (2004); Mahe et al. (2005) in the same region. These changes in LULC can be attributed to human activities such as farming in this region. Farming in this region is characterized by low inputs i.e little or no amendment, continuous cropping, with farms usually expanded and scattered across the landscape to increase yield (Boateng, 2013). Apart from farming activities, overgrazing by cattle, firewood or charcoal production are all contributory factors to the loss of natural vegetation in this region (Gyasi et al., 2011; Agyemang, 2007).

The revealed expansion in cropland over the past 27 years confirms the results obtained by studies such as Forkuor (2014); Boateng (2013); Ruelland et al. (2010); Brinkmann et al. (2012) in similar regions. For example, a study by Baatuuwie (2015) found an increase in settlement/cropland from 46.1% to 49.2% between 1990 and 2013 at the Nawuni basin, for which Vea is a sub-catchment. Similarly, Awotwi et al. (2014) also observed an expansion in agricultural land from 1990 to 2006 as a result of clearing of savannah and grassland in the White Volta basin where the Vea catchment is located. The expansion in cropland in the Vea catchment can be attributed to numerous factors such as; increase in socio-economic activities of the area and construction of a number of small dams together with the Vea dam over the last 27 years for irrigation, which as a result has increased the cultivation of crops such as cereals (maize and rice) and legumes in the area. In terms of built-up areas, an increase from 0.22% (1990) to 0.54% (2016) was noticed, which is a sign of an increase in population and socio-economic development at the catchment. Although the number of dams increased between the year 2001 and 2011, the decrease in water bodies from 1.74% to 1.39% is possibly due to severe siltation of the Vea dam during that period. Also, Conventional tillage and

continuous cropping and grazing practiced by the majority of farmers along the steep slope upstream of the Vea dam induces erosion and hence siltation of the reservoir (Baatuuwie, 2015). Between 2011 and 2016, the water body increased from 1.39% to 1.59% and this can be attributed to the increase in mean annual rainfall of the Vea catchment over the period observed by the study of Larbi et al. (2018).

4.3. Relevance of Results to achieving National and International Goals

The results obtained in this study, though at local scale, are essential for (1) the formulation and implementation of national developmental policies (e.g., the Ghana Shared Growth and Development Agenda II - GSGDA II) (FAO, 2017); (2) attainment of United Nation's sustainable development goals (SDGs) and (3) input to biophysical and economic models for decision making.

The GSGDA II outlines the policies and strategies to be adopted by the Government of Ghana (GoG) to combat the negative effects of climate change on socio-ecological systems. Ghana has a local government structure which permit local scale implementation of national policies through local government institutions (e.g. metropolitan, municipal and district assemblies - MMDAs) and ministries (e.g. Food and Agriculture; Environment, Science, Technology and Innovation; lands and forestry). As the Vea catchment forms a substantial part of two local government divisions, i.e. Bongo district and Bolgatanga Municipal, results obtained can contribute to achieving local scale objectives/targets in land use planning and climate change adaption. Due to the country's abundant endowment of natural resources, the GSGDA II identifies the following, amongst others, as some of the broad areas for policy intervention in a bid to develop the country and attain economic prosperity: (1) natural resource management and minerals extraction, (2) biodiversity management, (3) protected areas/forest management and (4) land management and restoration of degraded forests. In this regard, the objectives and results of this study, especially the projected patterns of LULC, will enable the relevant national authorities to formulate future-relevant natural resource policies needed for the sustainable use of resources and achievement of economic prosperity. For example, based on the results presented in section 3.4, the scenario selected by decision makers will be key to determining which land management policies should be pursued to ensure environmental sustainability and food security.

On one hand, pursuit of results of BAU scenario, which projected further increase in cropland area, will mean the promotion of agricultural management practices/policies that reduce GHG emissions, such that the projected increase in cropland area will not necessarily lead to increasing GHG emission and subsequent negative climate change repercussions. Previous studies in Ghana have shown how cropland expansion, coupled with unsustainable agricultural practices increase CO_2 emissions (Asumadu-Sarkodie and Owusu, 2016). On the other hand, selection of results of afforestation scenario, which projected an increase in natural/semi-natural vegetation, will mean the formulation and promotion of sustainable agricultural intensification and modernization programs. Chartres and Noble (2015) observed that a reduction in cropland area will not lead to food insecurity even if GHG emissions are significantly reduced through afforestation. Food demand is bound to increase in the near future due to the continuous rise in population. This requires the formulation and promotion of policies that will increase agricultural productivity while maintaining ecological integrity (Robertson and Swinton, 2005). In addition to considering results of the two scenarios separately, policy makers also have the option of considering different aspects of the two in formulating appropriate national policies.

Apart from its usefulness for formulating and implementing national policies and programs, the results of this study can contribute to assess and monitor progress towards attaining SDGs (e.g., 2, 6, 13, 15). In the case of SDG 15 (life on earth), for example, information on historical, present and future patterns of LULC are essential data for the derivation of indicators needed to monitor relevant targets. The continuous reduction of forest land in the study area (past and future) as found by this research is important information for the derivation of indicators 15.1.1 and 15.2.1 (FAO, 2017), which can be used to access the progress a country is making towards achieving SDG 15. Specifically, comparison of calculated indicators (e.g. Forest area as a proportion of total land area) based on the projected

LULC (up to 2025) and the present state (e.g. 2016), can assist policy makers to formulate appropriate forest management policies that will ensure the attainment of the targets by 2030. Similarly, using results of this study in biophysical models will generate results that will help in achieving other SDGs. For example, previous studies have showed that LULC changes affect the quality and quantity of surface runoff and therefore availability of water resources. Using a physically-based hydrological simulation model and land use scenarios, Yira et al. (2017) found that land use changes such as cropland expansion and savanna degradation increases peak discharge and alters the flood risk of populations. The future LULC patterns projected by this study, when used as input to such simulation models, can provide useful insights into future changes in water availability and an appreciation of whether or not SDG 6 can be achieved. Climate change related risks such as floods and droughts, which have been found to be increasing in recent years (Sylla et al., 2015), can also be minimized when appropriate measures are taken based on results of such simulations.

5. Conclusion

This study analyzed the historical (1990-2016) LULC changes in the Vea catchment and used the Land Change Modeler to project LULC up to 2025 LULC based on two scenarios. The outputs from Maximum likelihood classification of the Landsat images show an expansion in cropland at the expense of natural vegetation (forest/ mixed vegetation and grassland) for the period under consideration. The study also found out that cropland expansion over the past years in the catchment will become the main feature of LULC change especially in forest/mixed vegetation areas under BAU scenario. However, the area covered with vegetation showed an increase in the future under the afforestation scenario. The study demonstrated the ability of the LCM in projecting the future LULC condition of the study area with accuracy above 80% minimum acceptable degree of accuracy without considering exogenous factors (eg. socio-economic data, land policy and biophysical factors). The study recommends in future integration of these factors if possible and the application of other land use change models to improve the accuracy of the future projection. The future LULC condition under BAU scenario calls for the need to make a reasonable land use plan with an emphasis on controlling cropland expanding into forested and water bodies areas in the catchment. Furthermore, Sustainable Agriculture Land Management (SALM) practices must be adopted to intensify production without necessarily converting the remaining land cover of the catchment. The outcome of this study is promising for West Africa where information on historical, present and future patterns of LULC is essential for the mitigation and adaptation strategies in the context of climate change. Results of this study will contribute to devising effective land use plans and policies for climate change adaption, support progress monitoring and attainment of UN SDGs and improve climate, water and land simulation models for effective decision making.

Acknowledgments

This paper was extracted from a Doctoral research study undertaken at Universite D'Abomey Calavi, Benin. My sincere appreciation goes to the Federal Ministry of Education and Research (BMBF) and West African Science Centre on Climate Change and Adapted Land Use (WASCAL; *www.wascal.org*) for providing the scholarship and financial support for this programme. My sincere appreciation also goes to Prof. Anne Verhoef of University of Reading, UK for initial review of the document.

Funding

This work which is part of a doctoral study has been funded by the German Federal Ministry of Education and Research (BMBF) through West Africa Science Centre of Climate change and Adapted Land use (WASCAL).

Conflicts of Interest

The authors declare no conflict of interest.

References

Abagale, F.K., Kyei-Baffour, N. and Ofori, E. 2009. Degradation of the Nasia river basin in the Northern Ghana. *Ghana Journal of Development Studies*, pp.154-174.

Agyemang, I. 2009. *Assessment of environmental degradation in Northern Ghana: A GIS based participatory approach*. PhD dissertation, University of Leeds.

Ahmad, A. 2012. Analysis of maximum likelihood classification on multispectral data. *Applied Mathematical Sciences*, 6, pp.6425-6436.

Alcamo, J. and Henrichs, T. 2008. *Towards guidelines for environmental scenario analysis*. J. Alcamo, editor. pp.13-35. Environmental futures: the practice of environmental scenario analysis.Elsevier, Amsterdam, the Netherlands. Available from: http://dx.doi.org/10.1016/S1574-101X (08)00402-X.

Asumadu-Sarkodie, S. and Owusu, P.A. 2016. The relationship between carbon dioxide and agriculture in Ghana: A comparison of VECM and ARDL model. *Environmental Science and Pollution Research*, 23(11), pp.10968-10982.

Awotwi, A., Yeboah, F. and Kumi, M. 2014. Assessing the impact of land cover and climate changes on water balance component in White Volta Basin. *Water and Environment Journal*, pp.1747-6585.

Bansode, S. and Patil, K. 2016. Water balance assessment using Q-SWAT. International Journal of Engineering Research, 20, pp.515-518.

Baatuuwie, B.N. 2015. *Multi-dimensional approach for evaluating land degradation in the savanna belt of the white volta basin*. PhD dissertation, KNUST, Ghana.

Biro, K., Pradhan, B. Buchroithner, M. and Makeschin, F. 2013. Land use / land cover change analysis and its impact on soil properties in the northern part of Gadarif Region, Sudan. *Land Degradation and Development*, 24, pp.90-102.

Boateng, P.K. 2013. Agricultural production, land-use/cover change and the desertification debate in the West African Savannah: an adapted political ecology approach. *J. Arts Hum.*, 2, pp.21-35.

Braimoh, A.K. and Vlek, P.L.G. 2004. Land-cover change analyses in the Volta Basin of Ghana. *Earth Interactions*, 8, p.21.

Brinkmann, K., Schumacher, J., Dittrich, A., Kadaore, I. and Buerkert, A. 2012. Analysis of landscape transformation processes in and around four West African cities over the last 50 years. *Landscape and Urban Planning*, 105, pp.94-105.

Chartres, C.J. and Noble, A. 2015. Sustainable intensification: overcoming land and water constraints on food production. *Food Security*, 7(2), pp.235-245.

Cherlet, M., Hutchinson, C., Reynolds, J., Hill, J., Sommer, S. and von Maltitz, G. 2018. *World Atlas of Desertification.* Publication Office of the European Union, Luxembourg.

Clark Labs. 2009. *The land change modeler for ecological sustainability*. IDRISI Focus Paper, Clark University, Worcester, MA. Available from: http://www.clarklabs.org/applications/upload/Land-Change-Modeler-IDRISI-Focus-Paper-pdf.

Congalton, R.G. and Green, K. 2009. *Assessing the accuracy of remotely sensed data*. Principles and Practices. 2nd ed., CRC Press Inc., London.

Daudze, K.E.S. 2004. *Land use and land cover study of the savannah ecosystem in the upper west region using remote sensing*. PhD dissertation, CuvillierVerlag Gottingen, Germany

Eastman, R.J. 2006. *IDRISI Andes, guide to GIS and image processing*. Clark University, Worcester, pp.87-131.

Food and FAO. 2017. Keeping an Eye on Sustainable Development Goals (SDG) 15. Rome, Italy. *http://www.fao.org/3/a-i7334e.pdf*.

Forkuor, G. 2014. *Agricultural Land Use Mapping in West Africa Using Multi-sensor Satellite Imagery*. PhD dissertation, Julius-Maximilians-Universität, Würzburg.

Gyasi, A.E., Kranjac-Berisavljevic, G. and Oduro, W. 2011. Sustainable land management for mitigating land degradation: lessons from the slam project experience in Ghana. Accessed in May 2017.

Lizuka, K., Johnson, B.A., Onishi, A., Magcale-Macandog, D.B., Endo, I. and Bragais, M. 2017. Modeling future urban sprawl and landscape change in the Laguna de Bay Area, Philippines. *Land*, 6, p.26.

Kolb, M., Mas, J.F. and Galicia, L. 2013. Evaluating drivers of land-use change and transition potential models in a complex landscape in Southern Mexico. *Int. J. Geogr. Inf. Sci.*, 27(9), p.1804e1827.

Langley, S.K., Cheshire, H.M. and Humes, K.S. 2001. A. Comparison of single data and multitemporal satellite image classification in semi-arid grassland. *J. Arid Environ*., 49, pp.401-410.

Larbi, I., Hountondji, F.C.C, Annor, T., Agyare, W.A., Gathenya, J.M. and Amuzu, J. Spatio-temporal trend analysis of rainfall and temperature extremes in the vea catchment, Ghana. Climate, 6, pp.1-17.

Limantol, A.M., Keith, B.E., Azabre, B.A. and Lennartz, B. 2016. Farmers' Perception and Adaptation Practice to Climate Variability and Change: A Case Study of the Vea Catchment in Ghana. *Springer Plus*, 5, p.830.

Mahe G., Paturel, J.E., Servat, E., Conway, D. and Dezetter, A. 2005. The impact of landuse change on soil water holding capacity and river flow modeling in the Nakambe River, Burkina Faso. *J. Hydol.*, 300, pp.33-43.

Mahmoud, I. M., Duker, A.A., Conrad, C. Thiel, M. and Shaba, A.H. 2016. Analysis of settlement expansions and urban growth modeling using geoinformation for assessing potential impact of urbanization on climate in Abuja City, Nigeria. *Remote Sensing*, 8(3), p.220.

Megahed, Y., Cabral, P., Silva, .J and Caetano, M. 2015. Land Cover Mapping Analysis and Urban Growth Modelling Using Remote Sensing Techniques in Greater Cairo Region - Egypt. *International Journal of Geo-Information*, 4, pp.1750-1769.

Nazzal, J.M., El-Emary, I.M. and Najim, S.A. 2008. Multilayer perceptron neural network (MLPs) for analyzing the properties of Jordan oil shale*. World Appl. Sci. J.*, 5, pp.546-552.

Obuobie, E. 2008. *Estimation of groundwater recharge in the context of future climate change in the White Volta River Basin*. PhD dissertation, Rheinische Friedrich Wilhelms Universität, Bonn/Germany.

Olmedo, M.T.C., Paegelow, M. and Mas, J.F. 2013. Interest in intermediate soft-classified maps in land change model validation: suitability versus transition potential. *Int. J. Geogr. Inf. Sci*., 27, pp.2343-2361.

Olmedo, M.T.C., Pontius Jr., R.G., Paegelow, M. and Mas, J.M. 2015. Comparison of simulation models in terms of quantity and allocation of land change. *Environ. Model. Softw.*, 69, pp.214-221.

Perez-Vega, A., Mas, J.F. and Ligmann-Zielinska, A. 2012. Comparing two approaches to land use/cover change modeling and their implications for the assessment of biodiversity loss in a deciduous tropical forest. *Environ. Model. Softw.,* 29 (1), p.11e23.

Pontius, G.R. 2000. Quantification error versus location error in comparison of categorical maps. *Photogramm. Eng. Remote Sensing*, 66, pp.1011-1016.

Pontius, R.G. and Chen, H. 2008. *Land change modeling with GEOMOD*. Available from: *http://planet.botany.uwc.ac.za/nisl/computing/IDRISI_andes/Documentation/Land%20Change%20Modeling%20with%20GEOMOD.pdf.*

Robertson, G.P. and Swinton, S.M. 2005. Reconciling agricultural productivity and environmental integrity: a grand challenge for agriculture. *Frontiers in Ecology and the Environment*, 3(1), pp.38-46.

Roy, H.G., Dennis, M.F. and Emsellem, K. 2014. *Predicting land cover change in Mediterranean catchment at different time scales*. Springer International Publisher, Guimareas, Portugal.

Ruelland, D., Dezetter, A., Puech, C. and Ardoin - Bardin, S. 2008. Long - term monitoring of land cover changes based on landsat imagery to improve hydrological modelling In West Africa. *International Journal of Remote Sensing*, 29, pp.3533-3551.

Ruelland, D., Levavasseur, F. and Tribotté, A. 2010. Patterns and dynamics of land-cover changes since the 1960s over three experimental areas in Mali. *International Journal of Applied Earth Observation and Geoinformation*, 12, pp.S11-S17.

Sylla, M.B., Giorgi, F., Pal, J.S., Gibba, P., Kebe, I. and Nikiema, M. 2015. Projected changes in the annual cycle of high-intensity precipitation events over West Africa for the late twenty-first century. *J. Clim*., 28, pp.6475-6488.

Tewolde, M.G. and Cabral, P. 2011. Urban sprawl analysis and modeling in Asmara, Eritrea. *Remote Sens.*, 3, pp.2148-2165.

Thiombiano, L. and Tourino-Soto, I. 2007. *Status and trends in land degradation in Africa*. In Environmental Science and Engineering (Subseries: Environmental Science). Berlin, Heidelb. pp.39-53.

US Geological Survey Earth Resources Observation and Science Center (EROS), USGS, Sioux Falls, SD, USA. 2017. Available online: http://earthexplorer.usgs.gov/.

Varun, N.M, Rai, P.K. and Mohan, K. 2014. Prediction of land use changes based on land change modeler (LCM) using remote sensing: a case study of Muzaffarpur (Bihar), India. *J. Geogr. Inst. Cvijic*, 64(1), pp.111-127.

Vega, P.A, Mas, J.F. and Zielinska, A.L. 2012. Comparing two approaches to land use cover change modeling and their implications for the assessment of biodiversity loss in a deciduous tropical forest. *Environmental Model Software*, 29, pp.11-23.

Water Resources Commission. 2008. *White Volta River Basin - Integrated Water Resources Management Plan*, Ghana

Wilk, J. and Hughes, D.A. 2002. Simulating the impacts of land-use and climate change on water resource availability for a large South Indian catchment. *Hydrol. Sci. Journal*, 47(1), pp.19-30.

Wu, F. and Webster, C.J. (2004). Simulating artificial cities in a GIS Environment: urban growth under alternative regulation regimes. *International Journal of Geographical Information Science*, 14(7), pp.625-648.

Yasmine, M., Pedro, C., Joel, S. and Mário, C. 2015. Land cover mapping analysis and urban growth modelling using remote sensing techniques in Greater Cairo Region - Egypt. *International Journal of Geographical Information Science*, 4, pp.1750-1769.

Yira, Y., Diekkrüger, B., Steup, G. and Bossa, A.Y. 2017. Modeling land use change impacts on water resources in a tropical West African catchment (Dano, Burkina Faso). *J. Hydrol.*, 537, pp.187-199.

Zoungrana, B.J.B., Conrad, C., Amekudzi, L.K., Thiel, M. and Da, E.D. 2015. Land use/cover response to rainfall variability: a comparing analysis between NDVI and EVI in the Southwest of Burkina Faso. *Climate*, 3, pp.63-77.

Cloud Publications
International Journal of Advanced Remote Sensing and GIS
2019, Volume 8, Issue 1, pp. 3114-3125
ISSN 2320 – 0243, Crossref: 10.23953/cloud.ijarsg.432

Research Article

Development of Flow Duration Curves and Eco-Flow Metrics for the Tawi River Basin - (Jammu, India)

Yaggesh Sharma[1], Ashish Aggarwal[1], Jaspal Singh[2]

[1]Petroleum & Earth Sciences Department, University of Petroleum & Energy Studies (UPES), Energy Acres Building, Bidholi, Dehradun- 248007, Uttarakhand, India
[2]Ground Water cell, Agriculture Department, Roopnagar-140001, Punjab, India

Correspondence should be addressed to Yaggesh Sharma, *yaggeshsharma24@gmail.com*

Publication Date: 21 September 2019

DOI: https://doi.org/10.23953/cloud.ijarsg.432

Abstract A Flow duration Curve (FDC) and eco-metrics are one of the principal techniques employed to study the changes in flow regimes and flow discharge in any river basin. Stream flows vary widely over a year and this variability can be assessed by using FDC's which is a curve plotting stream flows (Q) on the vertical axis and the percent of time the flow is equalled or exceeds (P) a critical discharge threshold on the horizontal axis for a particular river basin. Flow Duration curves (FDCs) are imperative instruments which are fundamental for water asset distribution and administration, which can further be analysed to get a great deal of hydrological data to understand the impact of climate changes on water asset frameworks. Results got from the flow duration curves are required by hydrologists and specialists associated with various water asset ventures such as assessing the hydropower capabilities of a waterway, stream health, surge control examines such as recurrence outlines, runoff estimations, figuring the dregs stack and broken down solids of a stream, and contrasting the adjacent catchments. Apart from these classical uses, the FDCs can also be used to survey the health status of the streams in terms of its ecological status. The present study has been undertaken with an objective to identify the ecological health status of the Tawi River, based on eco-flow metrics. Eco-surplus and eco-deficit are known as the indicators of Hydrologic Alteration (IHA) and are used to study intra and inter annual variations in river flows. The daily stream flow data at Gulab Singh Bridge, Jammu from the Hydrological Data Centre of the Central Water Commission (CWC), Jammu has been used to develop the Flow Duration Curve (FDCs) for the different periods like daily, monthly, annual etc. Finally, 10- daily time series have been used to identify the ecosurplus and the ecodeficit years and their respective magnitudes. Further, an eco-flow metric for the Tawi River was prepared for the 30 years daily discharge data from the period 1977 to 2007. The results of the study conclude that Tawi River is an ecosurplus river, in most of the years of the study period. The ecology of Tawi River is at par for the study period except for the years 1999 and 2000. Although the ecology is under sustaining conditions, but the metric has been falling in course of time, which can be a signal of ecological deterioration in the future.

Keywords *Flow duration curve (FDC); Ecosurplus; Ecodeficit; River ecology; Tawi river*

1. Introduction

Changes in stream administration, stream health and waterway releases are usually seen in a substantial number of streams worldwide as a result of natural and environmental changes. However, the qualities and the results occurring from such changes are not completely comprehended. River discharge or stream flow is the most important part of the hydrological cycle for its very close connection to water assets. River flow characteristics such as flow discharge and duration, and eco-statistics are critical parts to understand the ecological integrity, processes and changes taking place in these river ecosystems. Many earlier studies have suggested that climatic changes would deeply influence the water cycle resulting in expansion of extreme climatic events worldwide. The resulting climatic variations will significantly modify the regional river discharges and seasonal flow regimes. Escalated human activities such as modified land use patterns, artificial water intake, and construction of dams and reservoirs, have also directly impacted the stream flow and altered the natural river flow regimes for the past few decades.

Changes in river and stream discharges and flow regimes have been analysed by an ever-increasing number of analysts in various parts around the world. To date many researchers and scientists worldwide, have developed methods to relate flow statistics to ecological health in order to quantify and characterize the effects of hydrologic modifications on river ecosystem integrity. To assess the impact of flow statistics on ecosystem integrity various indicators or hydrological metrics have already been developed. The indicators of Hydrologic Alteration (IHA) which were developed by Richter, Baumgartner, Powell, and Braun (1996) are one of the most widely used metrics to assess the changes on flow regimes due to different flow regulations. Eco-deficit and eco-surplus can be calculated for any time period and indicates the overall loss or gain in stream flows due to flow regulation imposed during that period (Vogel et al., 2007). Based on the previous studies such as the Detailed analysis of Flow regimes changes in the Upper Yangtze river by Gao et al. (2012), Assessment of environmental flow requirements in Damodar river basin using flow duration indices by Mitra et al. (2018), Design flow duration curves for environmental flows estimation in Damodar river basin, India, by Verma et al. (2017); the present study is carried out to understand and analyze the basic concept of FDCs and study the changes in the eco-flow metrics of respective water bodies, to provide a meaningful insight into the flow characteristics of streams and contrasting the contiguous catchments in terms of their ecological integrity. Therefore, the study has been undertaken considering three broad objectives (a) Development of flow duration curves for the flow regimes in the Tawi River basin using the available data for the period 1989 to 2000 (b) Identification of 25th and 75th dependable years and (c) Examining and quantifying the changes in flow regime in the Tawi River basin Based on the eco-flow metrics (ecosurplus and ecodeficit).

2. Literature

2.1. Flow Duration Curve

The Flow Duration Curve is a cumulative frequency curve that demonstrates the percent of time amid which indicated releases equalled or surpassed a critical discharge threshold in a given period. They demonstrate how the flow is distributed during a time period (calculated usually once a year).The vertical axis shows the flow, and the horizontal axis gives the probability percentage of flow magnitude that exceeds or equals the given threshold. For example, the FDC demonstrates the level of flow that charges for at least 50% of the year (known as Q50). The flow exceeding 95% of the year (Q95) is often a characteristic value for minimum river flow (Ian Bostan, 2013). The FDC is a medium to study the flow characteristics of rivers and streams and to make inter and intra comparisons for different basins.

An example of flow duration curve of a river for natural and regulated flow is shown in the Figure 1 below.

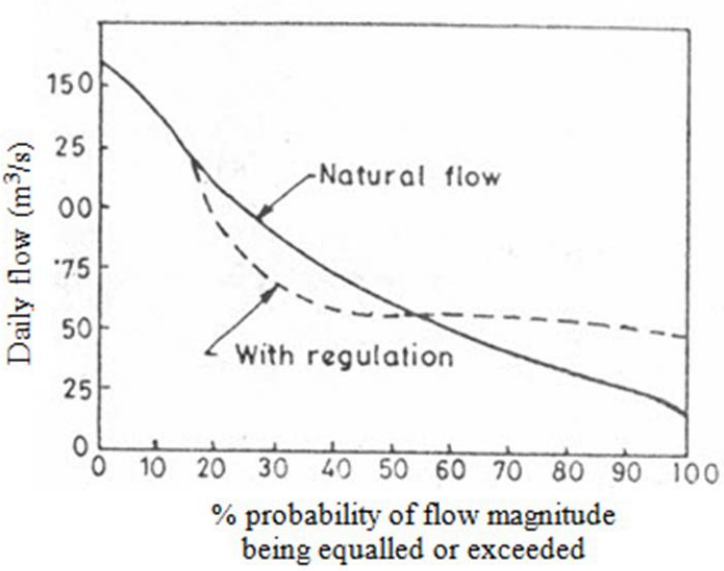

Figure 1: *Flow duration curve of a river for natural flow and regulated flow* (Source: Subramanya, 2009)

To create a Flow Duration Curve, daily, weekly, or monthly flows are organized by magnitude for a given period of time, and the percent of time during which the stream equalled or surpassed the predetermined threshold is derived. The plotted curve indicates discharge versus the percent of time amid which they equalled or surpassed a specific threshold subsequently represents an average for the considered period as opposed to the flow distribution within a single year (Searcy, 1959).

2.2. An Ideal FDC

An FDC plots Q (discharge) as a function of its corresponding exceedance probability:

$$P_p = \frac{m}{(N+1)} \times 100\% \ldots \text{(Weibull plotting formula)}$$

Where, Pp = Percentage probability (the probability that a given flow magnitude will be equalled or exceeded (% of time); m = Order number or Rank of the discharge with 1 being the largest possible value; N = Number of data points used in the listing

The ordinate Q, at any percentage probability P_p, represents the magnitude of flow in an average year that can be expected to be equalled or exceeded P_p percent of time and is termed as P_p% dependable flow. In a perennial river Q100=100% dependable flow whereas for an intermittent or ephemeral river, the streamflow is zero for a finite part of a year and therefore Q100 is equal to zero (Subramanya, 2009). The plot between discharge Q and Pp is the flow duration curve.

2.3. Eco Flow Metrics

Eco-surplus and eco-deficit are amongst the various other Indicators of Hydrologic Alteration (IHA) and are used to examine intra and inter annual variations in flows and can reveal significant changes if present in the streamflow time series. The eco-surplus and eco-deficit measurements depend on the 25^{th} and 75^{th} percentile flow duration curves (FDCs). FDCs are developed from stream flow data over a period of interest and give a measure of the percentage of time that stream flow equalled or exceeded a given value. The range from the 25^{th} to 75^{th} percentiles could be considered as the normal flow range for the river ecosystem. If the annual or seasonal FDC for a given year is below the 25^{th} percentile FDC, the area between the 25^{th} percentile FDC and the annual or seasonal FDC is defined as Eco-deficit. This value represents the amount of water insufficiency or how bad is the state of river

ecology. On the other hand, if the annual or seasonal FDC of a given year is located above the 75th percentile FDC, the area between the 75th percentile FDC and the annual or seasonal FDC is called Eco-surplus, and indicates the goodness level of the river ecosystem The values of the eco-surplus and eco-deficit are divided by the annual mean or seasonal mean flow amount to quantify the fractions of eco-surplus and eco-deficit, respectively (Gao et al., 2012). These fractions of Eco-surplus and Eco-deficit are termed as the Eco-flow Metrics. Figure 2 below shows a general definition of eco-surplus and eco-deficit areas derived from a FDC.

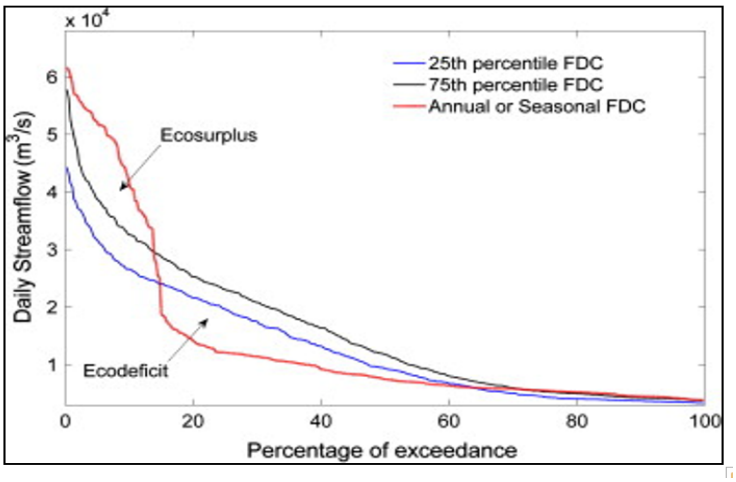

Figure 2: *General definition of eco-surplus and eco-deficit in a flow duration curve* (Source: Gao et al., 2012)

3. Study Area

3.1. General Topography

The Tawi River basin is a small part of Western Himalayas and is contained between 32°35' to 33°35' North Latitude & 75°45' to 75°45' East Longitude. At the upper part the basin is narrow and elongated; it broadens down along lower part. The upper portion of the basin is characterized by rugged mountainous topography, whereas lower basin consists of low hills and a gradational plain. The average height of basin is about 2200 meter above mean sea level. The basin ground elevation varies from 400 meter to 4000 meter above mean ocean level. Figure 3 below shows the location map of Tawi river basin.

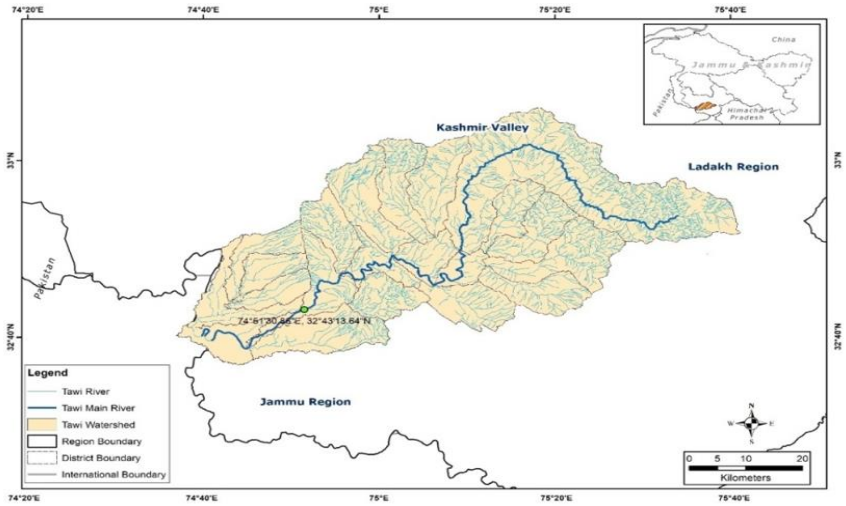

Figure 3: *Location map of the study area*

The slope of the basin is from east to west in the upper part and NE to SW in the lower part. The river, at its upper scopes is nourished by liquefying of snow and ice of Kali-Kundi Glacier at its origin and by rain. In the lower part, the catchment is dominatingly rain nourished. A little region of around 200 square meters is snow bound. The upper part of the basin is covered by hard granite intrusive rocks and the lower part by loose and soft Siwalik rocks. The Tawi river basin falls mostly within the districts of Jammu, Udhampur, and small portion of Doda districts. In the present study, the area of about 1885sqkm.upto Jamrnu has been considered.

3.2. Climate

In the Tawi Basin, July and August are for the most part the wettest months with around 55% rainfall and November is the month with least rainfall with around 2-3% of aggregate rainfall. Tawi encounters substantial floods in July and August. Monsoon begins from first July with heavy thunder showers that lasts up to mid-September. The North-Eastern catchment area comprising of Bhaderwah and adjoining area have extra tropical mountain type climate. The mountain type climate has wide variation in temperature and rainfall depending upon the location and direction of the land features. In this area winter is very severe and influence of South-West monsoon is negligible. Central territory consists of Udhampur district where again climate is of mountain type but has sufficient influence of monsoon. The South-Western zone consisting of Jammu district has a warm climate with strong monsoon influence, and can be described as similar to tropical climate during certain parts of the year. The River Tawi is snow fed at its origin from the Kali-Kundi glacier. The Kali-Kundi and Seoj-Dhar start experiencing snowfall in November. Snow is very deep and in some years it continues till May.

3.3. Water Resources

The Tawi River is gifted with enormous water resource potential for irrigation, domestic water supply and power generation. A study on assessment of water availability has been done by the NIH regional centre (NIH Report CS-86). The stream is of around 141 km length up to the point where it enters Pakistan, from its origin at Himalayan Kali-Kundi glacier. It has nine major tributaries carrying 4.3 lakhs cusec water release of Tawi in September 1988 at Jammu, with minimum discharge around 300-400 cusecs. Low water flow is experienced during the long stretch of October, November and December. But there are also occasional rises of water level during winters because of downpours and during early summers due to snow melting from the seasonal snow cover in the upper catchment.

3.4. River Profile

From origin to outfall the long section of Tawi River exhibits wide degree of variations. The variations in Slopes along different river reaches are as follows:

R.L 4000m-1600m = Steep gradient of 1:10:42. (R.L represents the River Length)
R.L. 1600m-900m = Slight changes in slopes
Below 800m = Slope is decreasing

However, variation is not linear. The gradient changes from very steep at upper part to concave and flat in the lower courses. The reason may be because there is degradation in the upper stages and aggradation in the lower stages. Based on field investigations it has been reported that flood plains, meander, meander core and other depositional landforms are formed at the lower course of the river. There are all indicative of non regime nature of the river.

4. Data and Methodology

In order to achieve the project objectives, the data used and the methodologies adopted in the current study have been described in subsequent sections:

4.1. Data

FDCs and eco-flow metrics assessment requires huge amount of flow data. The data used in the present study is the daily river discharge data of the Tawi River from the year 1977 to 2007.This data was collected from the Hydrological Data Centre of the Central Water Commission in Jammu, (*www.cwc.nic.in*). Since the accuracy of the collected data used for this project is not known, the outcomes given here might be thought to be indicative.

4.2. Methodology

In the present investigation, Indicators of hydrologic alteration (IHA) namely Ecosurplus and Ecodeficit were examined to study the changes in river ecology. Yearly eco-surplus and eco-deficit values were computed utilizing daily stream flow data.

Annual, monthly and daily FDCs were built for the available stream flow data for the period (1977-2007). These FDCs were utilized to check the status of river ecology. Based on the 30 years of annual, monthly and daily FDC's, the 25^{th} percentile FDC and the 75^{th} percentile FDC were calculated. But the obtained 25^{th} and 75^{th} percentile years were not that accurate, and the results obtained were not satisfactory for the said time stamps. Therefore, to get the desired 25^{th} and 75^{th} percentile years, we opted for the 10 daily averaged FDC for the 30-year daily data.

The 25^{th} and the 75^{th} percentile FDCs relating to the 10-daily (Ten days cumulative flow in a month) stream flow data were then used as the upper and the lower limits of the river ecology to justify its ecological status. The range from the 25^{th} to 75^{th} percentile was considered as the normal range for the river ecology. If the 10-daily averaged FDC of a given year are located below the 25^{th} percentile FDC, the area between the 25^{th} percentile FDC and 10-daily averaged FDC is defined as Eco-deficit, which represented the bad state of river ecology. Conversely, if the 10-daily averaged FDC of a given year is located above the 75^{th} percentile FDC, the area between the 75^{th} percentile FDC and the 10-daily average FDC is termed Eco-surplus and represented the level of goodness of the river ecosystem.

Later, the eco-values of all the years and the 10-daily average discharge data for the 25^{th} and the 75^{th} percentile years were averaged individually. All the positive averaged eco-values were divided by the sum of the averaged 25^{th} percentile year and the maximum positive averaged eco-value. Similarly, all the negative averaged eco-values were divided by the sum of the averaged 75^{th} percentile year and the minimum negative averaged eco-value. These fractions of eco-values were termed as Eco-flow metrics.

5. Results and Discussion

5.1. FDCs for Different Periods (Annual, Monthly, Daily & 10 Daily)

The method described in section 4 was used to develop daily, weekly and annual FDCs for the given period of data showing the flow discharge vs the percentage of time. Figure 4, 5 and 6 below show the daily, weekly and annual FDC's for the Tawi river basin.

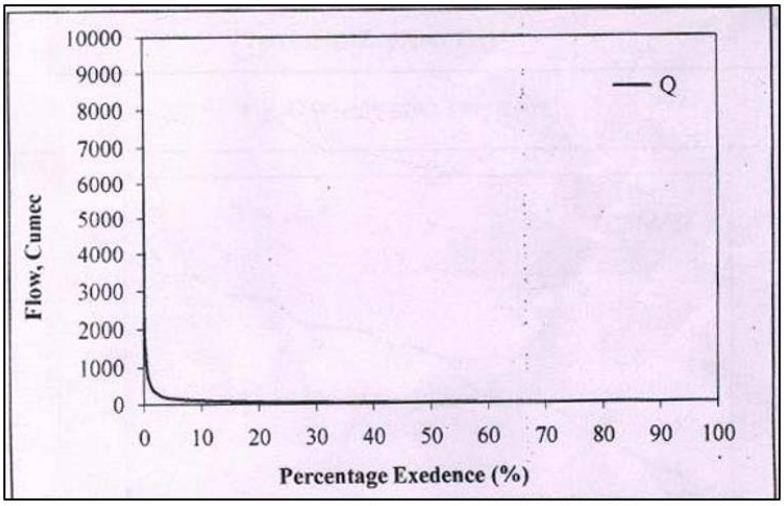

Figure 4: *Daily average FDC showing the discharge values from (1977-2007)*

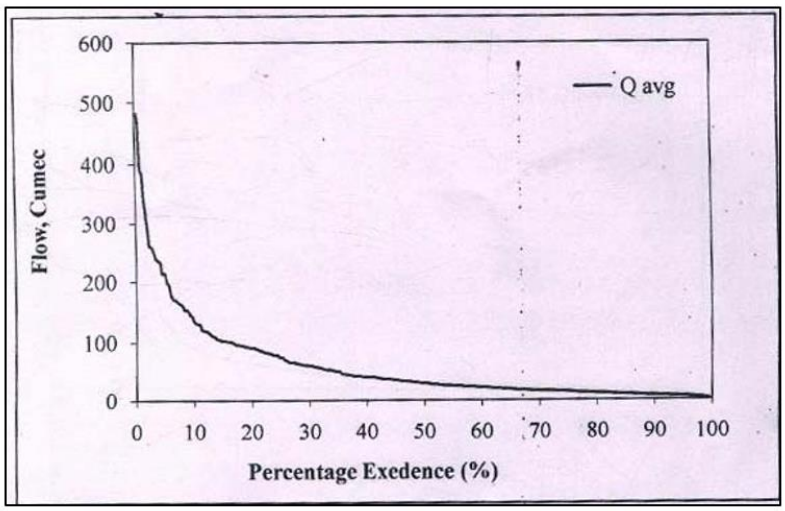

Figure 5: *Weekly averaged FDC (1977-2007)*

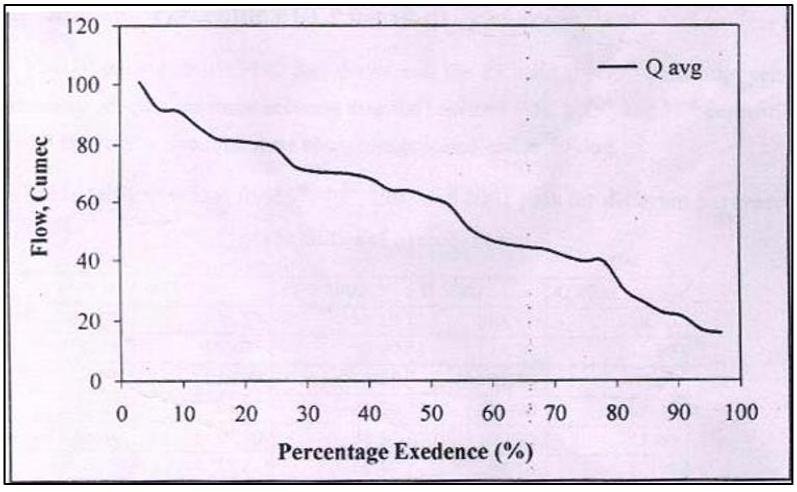

Figure 6: *Yearly FDC (1977-2007)*

5.2. 25th and 75th Percentile FDCs for 10-daily average data:

The 25th and the 75th percentile years were obtained, but these years were not so accurate and the results obtained were not satisfactory. Therefore, 10 daily averaged FDC was chosen, and the 25th and 75th percentile years were then obtained. Figure 7 below shows the 10-daily average FDC for the Tawi basin.

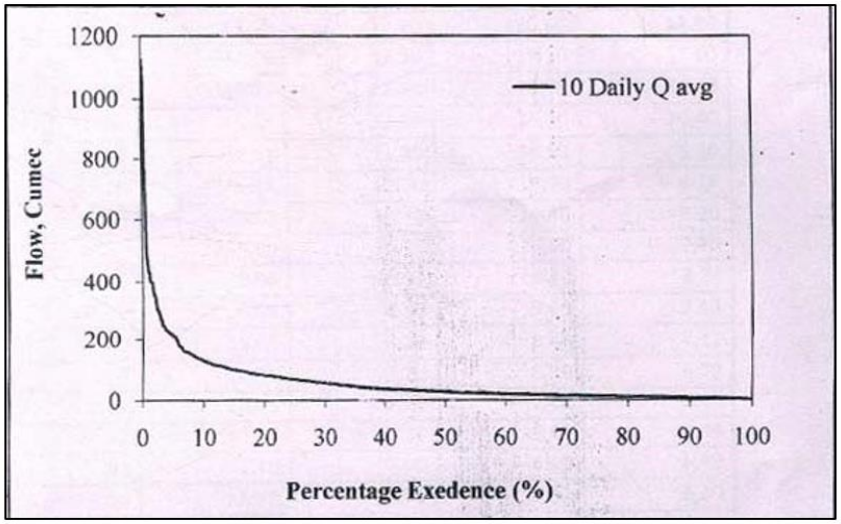

Figure 7: *10-daily average FDC (1977-2007)*

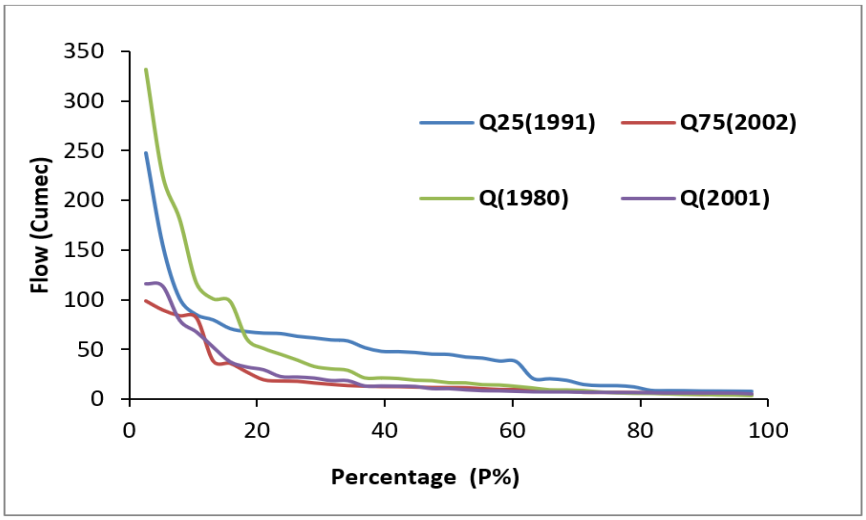

Figure 8: *25th and 75th percentile FDC (1977-2007)*

Figure 8 below shows the 25th and 75th percentile years for 10-daily averaged FDC. During the study period 1977-2007, Q25 was achieved in the year 1991 and Q75 was achieved in the year 2002. Q1980 shows the discharge curve when the value was nearest to Q25, which suggests that there was a major drawdown in water flow between 1980 and 1991, which had resulted into lesser Q values between 1980 and 1991. Q75 was achieved in 2002 and the nearest year where the value was close to Q75 was 2001. The range from the 25th to 75th percentile was considered as the normal range for the river ecology.

Table 1 below, shows the Flow values for 25th, 75th percentile probabilities of exceedance for 1991 and 2002, and also shows the discharge values at the nearest years 1980 and 2001.

Table 1: *Flow values for 25th, 75th percentile probabilities of exceedance for 1991 and 2002*

p%	Q25Percentile (1991)	Q75 percentile (2002)	Q 1980	Q 2001
2.63	248.10	99.10	331.60	115.70
5.26	155.33	90.00	224.90	113.30
7.89	101.59	84.20	181.40	79.20
10.53	85.14	82.20	116.70	67.30
13.16	79.90	38.60	100.90	52.00
15.79	71.21	36.40	98.60	37.40
18.42	68.11	27.60	60.60	32.10
21.05	66.59	19.80	51.10	29.30
23.68	66.14	18.60	45.30	22.50
26.32	63.40	18.30	39.40	22.00
28.95	61.77	16.60	33.00	21.00
31.58	59.76	15.20	30.60	18.50
34.21	58.73	14.00	29.10	18.40
36.84	52.02	13.40	21.50	13.09
39.47	48.24	13.00	21.50	13.09
42.11	47.96	12.90	20.90	12.90
44.74	47.09	12.50	19.20	12.60
47.37	45.47	12.10	18.70	10.40
50.00	45.13	12.00	16.70	10.40
52.63	42.55	11.90	16.50	9.20
55.26	41.45	10.90	14.70	8.35
57.89	38.52	10.10	14.40	8.20
60.53	38.00	10.10	13.00	7.70
63.16	20.94	10.00	11.40	7.23
65.79	20.64	8.80	9.50	7.13
68.42	19.05	8.50	9.40	7.11
71.05	14.88	7.20	8.80	6.79
73.68	13.75	7.20	7.40	6.70
76.32	13.70	7.20	6.50	6.49
78.95	12.46	7.00	6.00	6.46
81.58	8.96	6.70	5.90	6.20
84.21	8.69	5.90	5.50	6.02
86.84	8.62	5.70	4.90	6.01
89.47	8.30	5.00	4.90	5.98
92.11	8.24	4.80	4.30	5.97
94.74	8.13	4.80	4.20	5.86
97.37	8.00	4.80	3.70	5.10
Average	**48.83**	**20.89**	**43.77**	**22.39**

5.3. Ecosurplus and Ecodeficit Flows

The obtained 25th and the 75th percentile years were used for determining the ecosurplus and the ecodeficit flow. The Figure 9 below shows the Eco-deficit areas where the discharge value is less than 25th percentile value and the Eco-surplus areas where the discharge values is greater than 75th percentile value. The area between the 25th and 75th percentile values is the area with normal flow.

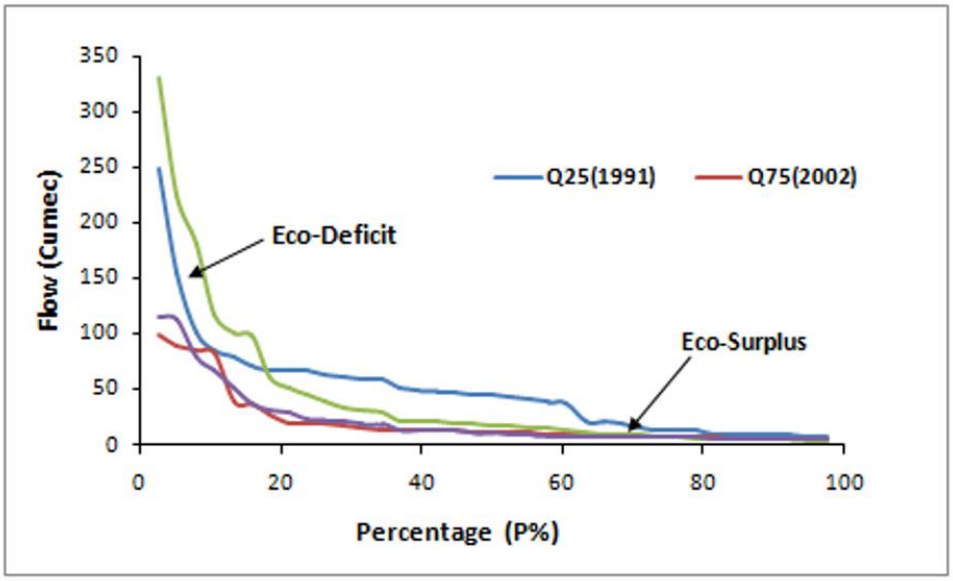

Figure 9: *Eco-surplus and eco-deficit areas for the study period*

5.4. Eco-Flow Metric

The eco-surplus and the eco-deficit flow data obtained was further used to create an Eco-flow Metric for the given data period. The Ecoflow Metrics provides a clear indication of the flow type which tells us about the river ecology. Table 2 below shows the eco-flow metrics calculated for each year during the study period 1977 to 2007.

Table 2: *The eco-values and the eco-flow metric values for each year (1977-2007)*

Year	Eco values	Eco flow metric
1977	51.34	0.47
1978	25.49	0.23
1979	29.17	0.27
1980	8.29	0.08
1981	35.02	0.32
1982	16.80	0.15
1983	24.41	0.22
1984	5.73	0.05
1985	4.84	0.04
1986	5.02	0.05
1987	1.75	0.02
1988	60.48	0.55
1989	-1.80	-6.12
1990	35.67	0.33
1991	48.83	0.45
1992	17.99	0.16
1993	22.46	0.21
1994	35.06	032
1995	23.10	O.21
1996	37.95	0.35
1997	12.56	0.11
1998	-0.14	-0.01
1999	-6.23	-0.43
2000	-5.12	-0.35
2001	-1.11	-0.08
2002	20.89	0.19

2003	17.63	0.16
2004	36.57	0.33
2005	37.08	0.34
2006	5.33	005
2007	-0.86	-006

Figure 10 below shows a graphical representation of the eco flow metrics for the study period as calculated from Table 2. The figure clearly shows that Tawi River is an ecosurplus river, in most of the years of the study period and that the ecology of Tawi River is at par except for the years of 1999 and 2000 where the eco flow metrics are falling down and suggest some extreme changes in the flow regime during those years.

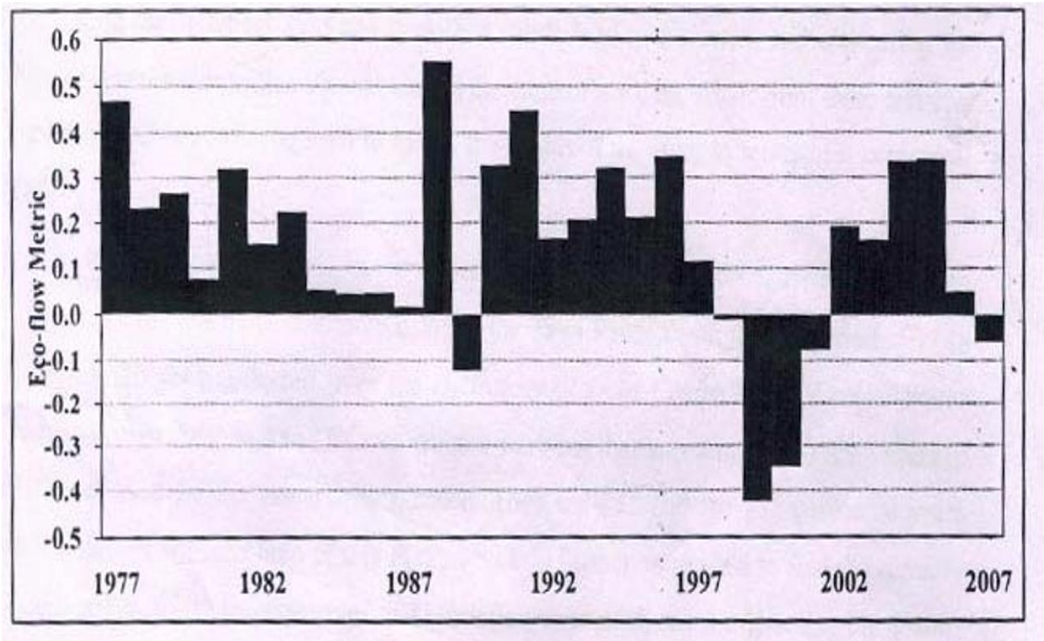

Figure 10: *Eco-flow metrics for the study period*

The results indicate that although the ecology of Tawi basin is under sustaining condition but the metric has been falling in due course of time, which can be a signal of ecological deterioration in the future.

4. Conclusion

Changes in the flow regime of the Tawi River Basin were analyzed based on recordings of daily river discharge data during the period from 1977 to 2007. Eco-surplus and eco-deficit areas were identified based on the Flow duration curves which showed the spatial and temporal changes in the Tawi river flow during the study period. Eco-metrics were derived and plotted for the entire period which indicated that the metrics in the river basin has been gradually falling down over the years suggesting ecological deterioration in the area. The eco flow metrics were quite low for the years of 1999 and 2000, which suggest some hydrologic extremes during those years. Thus Flow duration curves coupled with eco flow metrics provide a good framework to study the flow regimes in a river basin and its impact on the ecological health in the catchment. Our results indicate that although the ecology of Tawi basin is under sustaining condition but the metric has been falling in due course of time, which can be a signal of ecological deterioration in the future.

References

Bostan, I., Gheorghe, A.V., Dulgheru, V., Sobor, I., Bostan, V. and Sochirean, A. 2013. *Resilient energy systems*. Renewables: wind, solar, hydro. Springer Netherlands, p.517.

Gao B., Yang D. and Zhao T.H. 2012. Changes in the eco-flow metrics of the Upper Yangtze River from 1961 to 2008. *Journal of Hydrology*, 448-449, pp.30-38.

Hydrological Data Centre of the Central Water Commission in Jammu, for daily stream flow data. Available from: *www.cwc.nic.in*.

Mitra, S. and Singh, A. 2018. Assessment of environmental flow requirements of Damodar river basins by using flow duration indices method – a case study. *International Journal of Hydrology*, 2(3).

Technical report of National Institute of Hydrology, Roorkee, India. 1991-1992. *Water availability studies of river Tawi*. Report No. CS-86.

Richter, B.D., Baumgartner, J.V., Powell, J. and Braun, D.P. 1996. A method for assessing hydrologic alteration within ecosystems. *Conservation Biology*, 10(4), pp.1163-1174.

Searcy, J.K. 1959. *Manual of Hydrology: Part 2*. Low-Flow Techniques Flow-Duration Curves. USGS WSP 1542 - A US Government Printing Office, Washington DC, USA.

Subramanya, K. 2009. *Engineering Hydrology*. Tata McGraw Hill, Third Edition.

Verma, R.K, Murthy, S., Verma, S. and Mishra, S. 2017. Design flow duration curves for environmental flows estimation in Damodar river basin, India. Applied Water Science, 7(3), pp.1282-1293.

Vogel, R.M., Sieber, J., Archfield, S.A., Smith, M.P., Apse, C.D. and Huber-Lee, A. 2007. Relations among storage, yield and instream flow. *Water Resources Research*, 43, p.W05403.

Cloud Publications
International Journal of Advanced Remote Sensing and GIS
2019, Volume 8, Issue 1, pp. 3156-3169
ISSN 2320 – 0243, Crossref: 10.23953/cloud.ijarsg.441

Research Article

Spatio-temporal Variation in Landuse/cover Dynamics in Shahzad River Basin Uttar Pradesh, India: A Geospatial Approach

Tanzeel Khatoon, Akram Javed

Department of Geology, Aligarh Muslim University, Aligarh, India

Correspondence should be addressed to Tanzeel Khatoon, *tanzeelsiddiqui@outlook.com*

Publication Date: 22 November 2019

DOI: https://doi.org/10.23953/cloud.ijarsg.441

Abstract Landuse/cover is an important component that reflects the interaction between environment and human activities. Landuse/cover pattern is an outcome of natural and socio-economic factors and their utilization by man in space and time. The present study makes an attempt to monitor landcover dynamics in Shahzad river basin, a rainfed basin in Lalitpur district of Uttar Pradesh (India) using remote sensing and GIS technique. Digital Elevation Model (DEM) was prepared using Shuttle Radar Topography Mission (SRTM) data, the lowest and highest elevations encountered in the basin are 280 m and 495 m above MSL respectively. The higher elevations are encountered in southern most parts of the basin whereas lower elevations are found in the north. The general slope is from south to north, as defined by the course of the Shahzad river. Two data set viz. IRS-P6 LISS III data of 2005 and IRS-P6 LISS III of 2015 have been analyzed through visual interpretation technique. Visual interpretation technique was used to identify the various landuse/cover categories. Landuse/cover maps of 2005 and 2015 derived from satellite data were digitized in Arc GIS environment. Editing and topology building was carried out using Arc GIS 10 and area under each category of landuse/cover was computed in km2 as well as in percentage. An attempt was made to estimate and quantify the overall change as well as transitional change in landuse/cover classes over a decade. A comparison of 2005 and 2015 data analysis suggests that the area of water body has significantly increased from 19.53 km^2 in 2005 to 34.85 km^2 in 2015, i.e. 15.32 km^2 (1.39%), the area of uncultivated land has decreased from 352.81 km^2 (32.61%) in 2005 to 337.80 km^2 (30.7%) in 2015, showing 15.01 km^2 (1.91%) decrease. The area of cultivated land has increased from 464.78 km^2 (42.76%) to 473.06 km^2 (43%), i.e. 8.28 km^2 (0.24%). However, vegetation in the watershed has reduced, i.e. under open forest and dense forest has reduced by 11.37 km^2 (1.04%) and 13.27 km^2 (1.21%) respectively during 2005-2015. Open scrub, stone quarry, built-up land, exposed rock and wasteland have also reported change in their respective areas. Open scrub has slightly increased from 73.63 km^2 (6.69%) to 76.23 km^2 (6.93%), whereas stone quarry has increased from 1.78 km^2 (0.16%) to 3.53 km^2 (0.32%), which suggests expansion in quarrying activity. Change matrix analysis indicates that cultivated land, uncultivated land, open scrub and wasteland are the most unstable categories which have interchanged into different landuse/cover during 2005-2015. Moreover it also indicates, cultivated land (38.42 ha), uncultivated land (51 ha) and open scrub (59.64 ha) has been converted into settlement area.

Keywords *Landuse/land cover; Change matrix; Accuracy assessment*

1. Introduction

Land use and land cover (LULC) are terminologically different terms but are often used interchangeably. Land cover refers to the physical characteristics of the earth including area captured under vegetation, water, soil, landforms, topography etc. whereas landuse refers to the pattern in which land resources have been utilized by the humans. Different driving forces acting upon the surface of earth lead to the formation or modification of land use/cover categories. The land use/cover pattern of a region is an outcome of natural and socio-economic factors and their utilization by man in time and space (Rawat and Kumar, 2015). Hence, assessing the land use/ cover and their dynamic nature is not only important for estimating the area of a land used under different categories but in turn helps in evaluating the potential of natural resources, watershed management, socio-economic planning and other development sectors.

Since land use/cover are paired complementary to each other thus change in land use affects the land cover and vice versa. Change in land cover does not primarily indicate deterioration of land but it may be driven by the anthropogenic activities and can also be triggered by natural processes there by affecting the biospheric and climatic cycle. Since natural resources are dynamic in nature, thus land use/cover changes are important elements for monitoring, evaluating, protecting and planning for earth resources (Rawat et al., 2013). LULC classification and change detection is one of the most reliable methods to monitor the land dynamics. Change detection of LULC is generally carried out using multi-temporal data sets to assess changes in the landscape witnessed in the country, especially at watershed or basin level to provide more accurate information about landuse/cover dynamics for proper management and conservation of natural resources (Gibson and Power, 2000).

Remote sensing and GIS have emerged as one of the most powerful tools for classifying, mapping, monitoring, evaluating and assessing the natural resources in less time, with low cost and better accuracy. Satellite image pixcels can be classified in LULC categories either by automatic extraction or by visual interpretation method (Meinel and Neubert, 2000). Automatic classification is based on extrapolating the celebrated patches of homogeneous color and texture on the satellite image, thereby providing a meaningful categorization of LULC (Dronova et al., 2011; Chen et al., 2012). Further the pixel-based analysis may lead to the ‘salt-and-pepper’ effect in mapping heterogeneous landscapes (Zhang et al., 2014). It is difficult to determine the accuracy of the result produced by the automatic classification, even sometimes it fails to recognize difference in “use” of given surface land (Fallati et al., 2017). On the other hand, visual interpretation is a slow and tiresome method as compared to the automatic supervised classification but can be rationally used when analyst is familiar with the field and research area is comparatively small. Visual interpretation has advantage over automatic classification since the former can identify dynamic changes more accurately and hence represents the process of landuse/cover change more effectively. Therefore this interpretation technique is frequently used in practical approach like in rural development, smart city project, flood mapping etc. (Zhang et al., 2014). Vector layer in form of polygons are used to divide the image into the parcels, these parcels are classified into desired classes, thus avoids inter-class spectral variation (Apline et al., 1999; Apline and Smith, 2008).

In the recent past the advancement of research has led to more emphasis on development at watershed level, as the traits and allocation of natural resources depends upon the natural boundary. Many workers consider watershed as a basic unit for the identification, estimation, development and prioritization of natural resources. Adinarayana et al. (1995) used integrated approach to prioritize watershed on the basis of sediment yield index in Western Ghats, Rahaman et al. (2015) prioritized sub watershed on morphometric basis using Fuzzy Analytical Hierarchy Process in Kallar watershed, Welde (2016) conducted the study on prioritization of watershed for land and water management in Tekeze dam, Ethiopia. Watershed, besides being a naturally occurring hydrological unit also carries a unique socio-ecological aspect which plays an important role in determining the ecological, food and social security and provision of life support services to local communities. Several attempts have been

made in the recent past to quantify the change detection by applying remote sensing and GIS techniques. Kibret et al. (2016) carried out a study in South Central Ethiopia, to assess the LULC changes during four decades using multi temporal satellite data. Fallati et al. (2017) have carried out LULC analysis in the Republic of Maldives using remote-sensing data through visual interpretation technique in conjunction with socioeconomic data.

The present study makes an attempt to assess the LULC changes and probable causes leading to the changes in the Shahzad watershed, Lalitpur district, Bundelkhand, India from 2005 to 2015. The region of Bundelkhand have complex geological and physiographical landscape varying from Bundelkhand Plains, Bundelkhand upland and vindhyan Plateaus. The study area has remained socio-economically backward with moderate drought frequency but high intensity, and faces the metrological drought. Hence, monitoring the resources and assessing the cause of changes become a prime focus especially in the agricultural dominant watershed. The major objectives of the study are to (i) identify and delineate different LULC categories under the area for 2005 and 2015 (ii) Verify the accuracy of the data in order to get more reliable and accurate results (iii) quantify the amount of overall change in LULC categories both in area and percentage as well as to monitor the LULC transformation from one category to another and (iv) ascertain the possible causes of change. Several studies have been carried out throughout the globe on the change detection analysis by using remote sensing data (Palaniyandi and Nagarathinam, 1997; Rogan and Chen, 2004; Güler et al., 2007; Chunxiao et al., 2008; Song et al., 2009; Prakasam, 2010; Nagarajan and Poongothai, 2011; Liu et al., 2012 and Garai and Narayana, 2018).

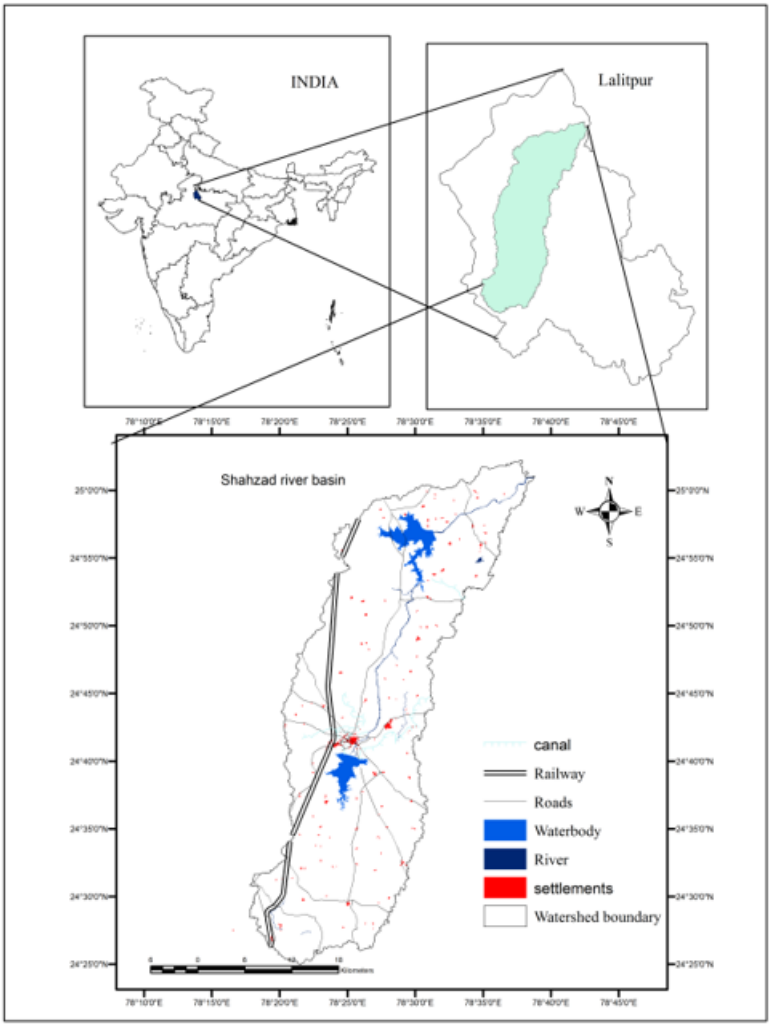

Figure 1: *Location map of Shahzad basin*

Study Area

The Shahzad river basin is located in Lalitpur district of Bundelkhand region in Uttar Pradesh (India) and bounded by 24° 25' N to 25° 03'N latitudes and 78° 17' E to 78° 39' E longitudes with a geographical area of about 1100 km^2. Shahzad river (a tributary of Jamini river) flows from south to north through the center of the watershed bifurcating it into East and West. The basin experiences sub-humid climate with average annual rainfall of 806 mm. Topography is represented by plains, pleateau, hills and ridges where elevation values range from 280m to 495m above mean sea level. Geologically, the area is dominated by Bundelkhand Granatoid Complex (BGC) comprising of gneisses, schist and granites which are underlained by arechean formation. North East-South West (NE-SW) trending quartz reefs and basic dykes traverse the BGC. Thick pile of quaternary sediments of older alluvium comprising of Banda alluvium overlies on the BGC formation. Sandstone of Kaimur group (Upper Vindhyan) is exposed in the south (GSI, 2008). The basin is mainly drained by Shahzad river and its tributaries. The dendritic to sub-dendritic drainage pattern dominates the watershed, however there are variation in drainage pattern at local level, where main river divides the entire watershed into eastern and western halves. Two reservoirs namely Shahzad reservoir and Govindsagar reservoir are the characteristics feature in the north and south respectively.

The watershed is mainly defined agricultural land where the main landuse is cultivation which is by and large rainfed, however irrigation from ground water at places is through tube wells. Major crops grown in the area are Sorghum, Pigeon pea, Black gram, Green gram, Barley, Mustard etc. Over exploitation of ground water has not only resulted in lowering of water level but has also caused failure of wells.

2. Materials and Methods

Data Base Preparation

IRS P6 LISS III false color composite (FCC) of 2005 and 2015 February, with band combination 2,3,4 and spatial resolution of 23.5m were used for landuse/cover mapping and classification (Figure 2). The data for same month has been used to reduce the reflectance conflict and seasonal variation for the classification of landuse/cover. The satellite data pertaining to study area was obtained from National Remote Sensing Centre (NRSC), Hyderabad. The data set were imported to ERDAS imagine version 14 to extract the desired form of image used for classification purpose. The layer stack option in raster tool box was used to generate standard false color composite (FCC). Image was geo-referenced and was projected in Universal Transverse Mercator (UTM) projection, taking World Geodetic System (WGS84) as the datum. The study area lies in UTM Zone 44 N. The georeferenced boundary of Shahzad watershed as Area of Interest (AOI) was superimposed on satellite image to subset the image and to extract the study area.

Landuse/Cover Delineation and Analysis

Visual interpretation technique was followed for change detection of land use/cover using ArcGIS 10 software, since the authors are familiar with the area being classified. Interpretation keys were developed on the basis of field knowledge and literature. To enable storage of data associated with each LULC, a data base structure was created prior to visual interpretation of IRS FCC images. Based on spectral characteristics of landuse/cover classes, the interpretation keys were developed (Table 1) and on-screen digitization for various landuse/cover classes was created in form of polygons with unique ids. Ground truthing was carried in key areas to verify the spectral signature. Twelve landuse/cover classes were identified in the study area viz. (i) cultivated land (ii) uncultivated land (iii) dense forest (iv) open forest (v) open scrub (vi) waterbody (vii) dry waterbody (viii) exposed rock (ix) stone quarry (x) industrial land (xi) built up land and (xii) wasteland.

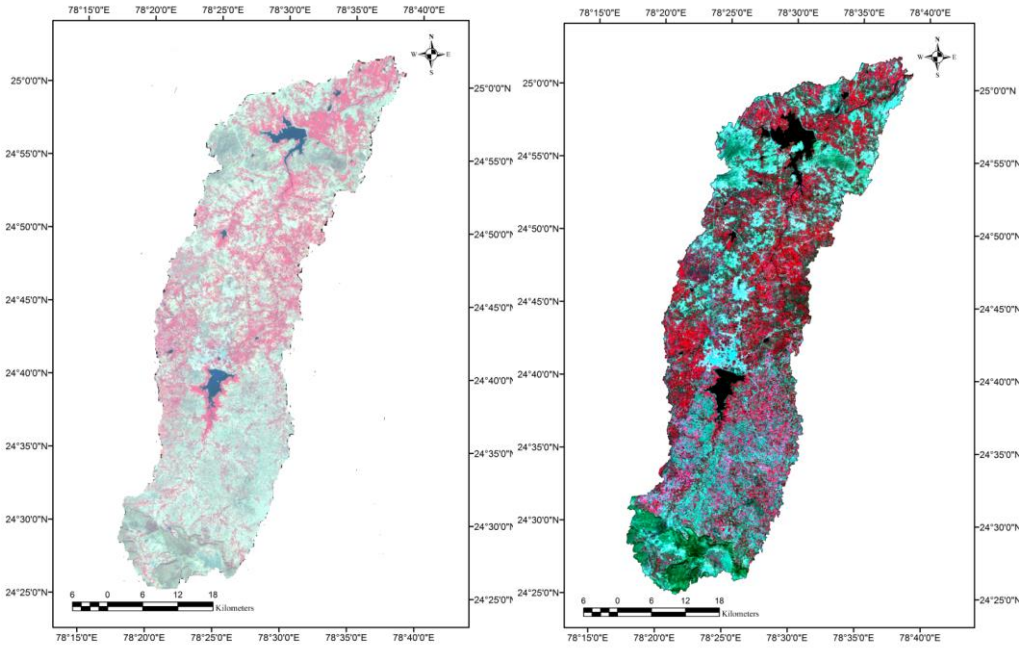

(a) **(b)**

Figure 2: *Satellite images (a) IRS P6 LISS III (2010), (b) IRS R2 LISS III (2015)*

Table 1: *Spectral characteristic of landuse/cover classes*

Landuse/cover class	Image characteristics	Topography	Relief/slope
Cultivated land	Pinkish to bright red color, Coarse texture, irregular pattern and regular to sub-regular shape	Plain	Very low to gentle
Uncultivated land	Bluish green to brownish green tone, smooth texture, contiguous pattern and irregular in shape	Plain	Very low to gentle
Dense forest	Dark greenish tone, woolly texture, contiguous to non-contiguous pattern and irregular shape	High relief/ plateau slope	Moderate to steep
Open forest	Greenish tone, medium texture, contiguous to non-contiguous generally found within the protected or reserved forest	High relief/ rugged	Gentle to moderate
Open scrub	Light greenish tone with medium to smooth texture, scattered and irregular in shape	Rugged/plain	Gentle to moderate
Waterbody	dark blue to black in color, smooth texture, irregular shape with defined boundary	Depressed to plain	Low to very gentle slope
Dry waterbody	Light cyan color, smooth texture irregular shape associated along the boundaries of waterbody	Depressed to plain	Low to very gentle slope
Exposed rock	Bright tone, rough texture, bold topography, isolated hillocks and plateau generally devoid of vegetation	Rugged	Moderate to steep slope
Industrial land	Bright tone, smooth texture, regular to sub-regular shape	Plain	Very gentle slope
Stone quarry	Milky to light cyan tone, rough texture, depressed pit filled with water, scattered and irregular in shape	Rugged/ subdued	Moderate to gentle
Settlement	Bright cyan tone, coarse texture, semi-circular pattern and irregular shape	Plain	Low to very gentle slope
Wasteland	Bright cyan tone, smooth texture, non-contiguous, scattered pattern and irregular shape	Plain/rugged	Low to very gentle slope

Accuracy Assessment

An accuracy assessment was carried out after the LULC mapping was accomplished. Landuse/cover result of 2015 was validated by ground observation and recorded GPS values, transect walk, group discussion and interview, as well as Google earth imagery. Validation and training data set for 2005 landuse/cover result were Google image, topographic map and group discussion and interview conducted during field visits in 2014 and 2015. 500 sample points for each year were selected throughout the study area. Sample were randomly selected based on areal extend of each category. To further increase the accuracy, some sample points were taken at transitional boundary of two different LULC classes, dam boundary and intersection of cultural classes like road, river, railways etc. Confusion matrix (contingency table) for 2005 and 2015 was created using the observed and the classified landuse/cover map of each class for accuracy assessment. Accuracy parameter viz. producer's accuracy (a measure of omission error), user's accuracy (a measure of commission error), overall accuracy and kappa statistics were estimated (Thakkar et al., 2017). Producer's accuracy is a ratio of number of correctly classified pixels to the number of training pixels (the column total) used in particular category whereas User's accuracy is obtained by dividing the number of correctly classified pixel by total number of pixel in that category (the row total). The overall accuracy is computed by dividing the number of correctly classified pixel by total number of reference pixel. Kappa analysis is a discrete multivariate technique used in accuracy assessments (Jensen 1996). Kappa analysis yields a Khat statistic (an estimate of Kappa) that is a measure of agreement or accuracy (Congalton 1991).

$$\hat{k} = \frac{N\sum_{i=1}^{r} xii - \sum_{i=1}^{r}(xi+ . x+i)}{N^2 - \sum_{i=1}^{r}(xi+ . x+1)}$$

Where,

r = number of rows in the error matrix
x_{ii} = number of observation in row i and column i (on the major diagonal)
x_{i+} = total of observations in row i (shown as marginal total to right of the matrix)
x_{+1} = total of observation in column i (shows as marginal total at bottom of the matrix)
N = total number of observation included in matrix

Landuse/Cover Change Detection and Analysis

Post classification technique was applied to the generated temporal landuse/cover maps to perform the landuse/cover change detection. Vector layer of 2005 and 2015 were overlaid to produce change information inform of "from" to "to" classes. Cross tabulation of two different decadal data of classified image were compared to determine the qualitative and quantitative aspect of the change for the period 2005-2015. Change matrix was produced in GIS environment. Quantitative areal data of the overall landuse/cover changes as well as gains and losses in each category between 2005 and 2015 were then compiled.

3. Results and Discussion

Landuse/Cover Status

Landuse/cover derived through 2005 IRS data suggests that, the basin occupies an area of about 464.78 km^2 (42.10%) under cultivated land and 352.81 km^2 (31.92%) area under uncultivated land. Open scrub occupies an area of 73.63 km^2 (6.69%), which is wide spread throughout the whole basin. Open forest though present as patches throughout the basin has an area of 24.99 km^2 (2.27%), whereas dense forest occupies an area of 65.07 km^2 (5.91%) and is confined to southern and north-western parts of the basin. The exposed rock terrain is largely confined to the southern part of the basin and occupies an area of 0.56 km^2 (0.05%). Although the settlements/built-up land are present throughout the basin, but are largely confined to the central part of the basin in and around Lalitpur

town and occupies an area of about 15.06 km^2 (1.36%). Wasteland occupies an area of 77.64 km^2 (7.05%) and is found in the northern and western parts, and is associated with the open scrub, cultivated and uncultivated lands. The other land use/land cover category viz; industrial land and stone quarry occupy areas of about 3.87 km^2 (0.31%) and 1.78 km^2 (0.16%) respectively. The quarrying activity is reported from southern part of the Shahzad watershed, where sandstone is being mined for use as a building stone. Figure 3 (a) presents land use/land cover map derived from LISS III FCC data of 2005.

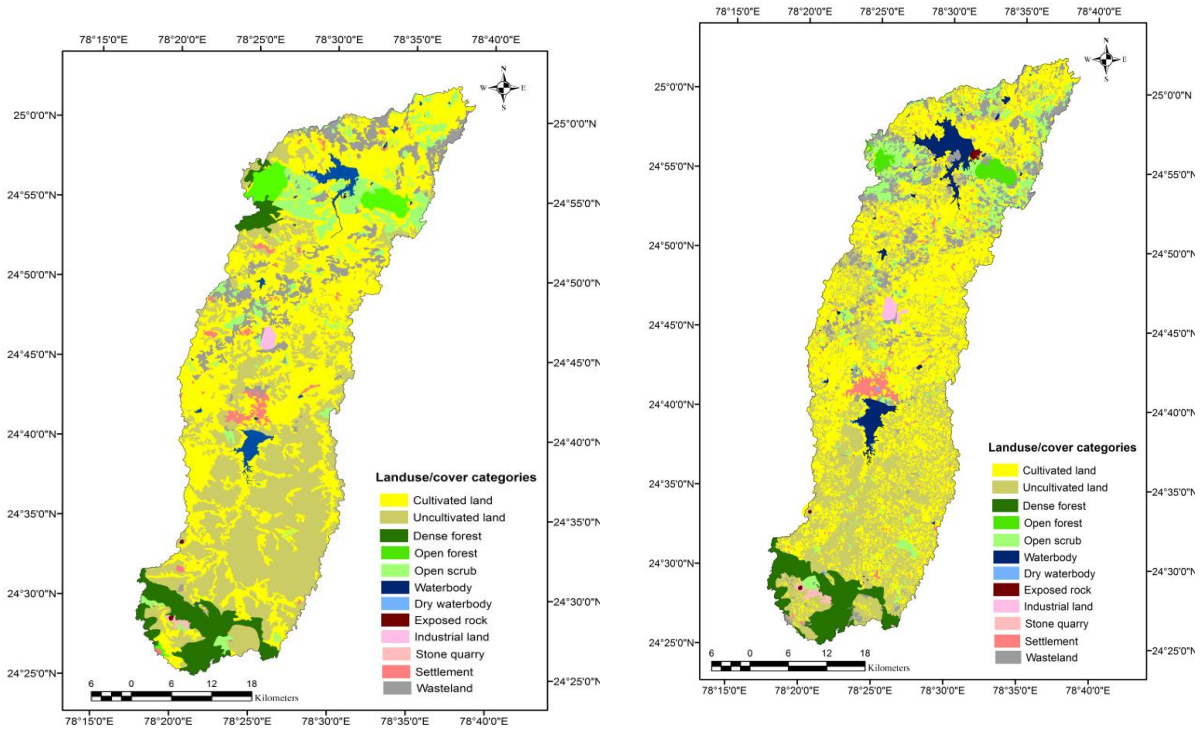

Figure 3: *Landuse/cover of Shazad watershed (a) 2005 (b) 2015*

Landuse/cover analysis of 2015 IRS data suggests that in Shahzad basin cultivated land covers an area of 473.65 km^2 (43.00%), whereas 337.80 km^2 (30.70%) area is occupied by uncultivated land. The other dominant LULC categories are wasteland and open scrub with areas of 83.53 km^2 (7.59%) and 76.23 km^2 (6.93%) respectively. Natural vegetative cover i.e. dense forest covers 51.80 km^2 (4.70%) area whereas open forest occupies 13.62 km^2 (1.23%) area. Though the area under waterbody has increased to 34.85 km^2 (3.16%) but an increase in area of about 2.07 km^2 (0.18%) is also observed in dry waterbody, compared to 2005. The other land use/land cover categories viz; industrial land and stone quarry, occupy areas of about 4.69 km^2 and 3.53 km^2 respectively. Table 2 presents details of area and extent of change under each category of LULC in the Shahzad watershed during 2005-2015. Figure 3 (b) presents LULC map derived from 2015 IRS FCC data.

Table 2: *Landuse/cover statistics (2005-2015) of Shahzad watershed*

Landuse/cover category	2005		2015		Change 2005-2015	
	Area (km^2)	Area (%)	Area (km^2)	Area (%)	Area (km^2)	Area (%)
Cultivated land	464.78	42.10	473.06	43.00	8.25	0.9
Uncultivated land	352.81	31.07	337.80	30.70	-15.01	-1.37
Dense forest	65.07	5.91	51.80	4.70	-13.27	-1.21
Open forest	24.99	2.27	13.62	1.23	-11.37	-1.04
Open scrub	73.63	6.69	76.23	6.93	2.6	0.24
Wasteland	77.64	7.05	83.53	7.59	5.89	0.54
Waterbody	19.53	1.77	34.85	3.16	15.32	1.39
Dry waterbody	0.32	0.02	2.07	0.18	1.75	0.16
Exposed rock	0.56	0.05	1.52	0.13	0.96	0.08
Industrial land	3.87	0.31	4.69	0.47	0.82	0.16
Stone quarry	1.78	0.16	3.53	0.32	1.75	0.16
Settlement	15.06	1.36	16.71	1.51	1.65	0.15
Total	1100	100	1100	100	75.67	7.4

Accuracy Assessment

Accuracy assessment is an important factor in classification. One of the most commonly followed method is the preparation of a classification error matrix (confusion matrix/contingency table). Error matrices compare, on a category-by-category basis, the relationship between known reference data (ground truth) and the corresponding result of a classification (Lillesand et al., 2004).

The error matrix shows the overall accuracy of 83.2% and 84.6% followed by Kappa coefficient of 0.80 and 0.82 in classified images of 2005 and 2015 respectively. Both producer and user accuracy of individual classes ranges from 65.21% to 96.11% and 71.42% to 100% in 2005 (Table 3) whereas for 2015, producer and user accuracies turned out to be 71.42% to 100% and 73.33% to 96.07%, respectively (Table 4).

Table 3: *Error matrix for LULC map derived using FCC data of 2005*

	Reference data 2005														
Lulc classes	**Cl**	**Ucl**	**Df**	**Of**	**Os**	**Wb**	**Dwb**	**Er**	**Il**	**Sq**	**Stlmnt**	**Wl**	**Total**	**PA (%)**	**UA (%)**
Cl	99		7	4	2								112	96.11	88.39
Ucl		69					1		2		5	7	84	93.24	82.14
Df	2		15	4	2								23	65.21	65.21
Of			1	32	4							1	38	76.19	84.21
Os				2	58					1	2	6	69	77.33	84.05
Wb	2					16							18	94.11	88.88
Dwb						1	3						4	75	75
Er								6				1	7	75	85.71
Il									6				6	75	100
Sq		1								5		1	7	83.33	71.42
Stlmnt		2			3						51	4	60	79.68	85
Wl		2			6			2			6	56	72	73.68	77.77
Total	103	74	23	42	75	17	4	8	8	6	64	76	500		
	overall accuracy			83.2%						kappa coefficient			0.80		

PA - Producers accuracy; UA - User accuracy.

Table 4: *Error matrix for LULC map derived using FCC data of 2015*

	Reference data 2015														
Lulc classes	**Cl**	**Ucl**	**Df**	**Of**	**Os**	**Wb**	**Dwb**	**Er**	**Il**	**Sq**	**Stlmnt**	**Wl**	**Total**	**PA (%)**	**UA (%)**
Cl	88	1	7	4							2		102	96.70	86.27
Ucl	1	75			12						7	3	98	88.23	76.53
Df			33	5									38	80.48	86.84
Of				42	3								45	79.24	93.33
Os		6	1	2	50								62	72.46	80.64
Wb	2					11	2				3		15	91.66	73.33
Dwb						1	5						6	71.42	83.33
Er								4				1	5	66.66	80
Il									6			2	8	100	75
Sq										3		1	4	100	75
Stlmnt		3									47	2	52	79.66	90.38
Wl					4			2				59	65	86.76	90.76
Total	91	85	41	53	69	12	7	6	6	3	59	68	500		
Overall accuracy			84.6%									kappa coefficient		0.82	

PA - Producers accuracy; UA - User accuracy.
Cl - Cultivated land; Ucl - Uncultivated land; Df - Dense forest; Of - Open forest; Os - Open scrub; Wb - Water body; Dwb - Dry water body; Er - Exposed rock; Il - Industrial land; Sq - Stone quarry; Stlmnt -Settlement; Wl - Waste land.

Landuse/Cover Change

A comparative analysis of the 2005 and 2015 land use/land cover suggests significant changes in the Shahzad basin. Amongst the notable changes are, a substantial decrease in uncultivated land from 352.81 km^2 in 2005 to 337.80 km^2 in 2015, showing 15.01 km^2 (1.37%) reduction in area with respect to 2005. The area under dense forest has reduced from 65.07 km^2 in 2005 to 51.80 km^2 in 2015, i.e. 13.27 km^2 (1.21%) fall in its aerial extent with respect to 2005. The area under open forest has also decreased from 24.99 km^2 in 2005 to 13.62 km^2 in 2015, which is 11.37 km^2 (1.04%). The area under cultivated land has increased from 464.78 km^2 in 2005 to 473.06 km^2 in 2015, an increase of 8.25 km^2 (0.9%). Area under wasteland has marginally, increased from 77.64 km^2 in 2005 to 83.53 km^2 in 2015, showing 5.89 km^2 (0.54%) in its areal extent. The area under open scrub has gone up from 73.63 km^2 (6.69%) in 2005 to 76.23 km^2 in 2015, showing a small increase of 2.6 km^2 in its extent. The area under dry waterbody has increased from 0.32 km^2 to 2.07 km^2. However, the area under water body has increased from 19.53 km^2 (1.77%) in 2005 to 34.85 km^2 in 2015, which is 15.32 km^2 (1.39%). The area under settlement/built-up land has increased from 15.06 km^2 (1.36%) in 2005 to 16.71 km^2 (1.51%) in 2015. The area under stone quarry has expanded from 2.29 km^2 in 2005 to 3.53 km^2 in 2015. Area under Industrial land area has increased from 3.87 km^2 in 2005 to 4.69 km^2 in 2015 suggesting some development and industrial expansion. Exposed rock has increased from 0.56 km^2 in 2005 to 1.52 km^2 in 2015 due to the fact that vegetative cover over it has been removed/ degraded and the underlying rock is exposed. Figures 4 and 5 show the changes in major LULC categories during 2005-2015.

Change Detection

Change detection matrix (Table 5) was prepared to understand the land cover dynamics under various categories. Major LULC changes occurred during the decade (2005-2015) are listed below:

(i) An area of about 8.41 km^2 of dense forest has been converted into open scrub, 5.01 km^2 area under wasteland, 2.24 km^2, 1.64 km^2, 0.67 km^2 and 0.32 km^2 area into uncultivated land, stone quarry, cultivated land and open forest respectively whereas 46.63 km^2 is still under dense forest.
(ii) An area about 18.90 km^2 under open scrub has been converted into cultivated land, 13.33 km^2 area into uncultivated land, 18.06 km^2 into waste land, 1.97 km^2 under dense forest, 1.27 km^2 into industrial

land, 1.21 km^2 under waterbody, 1.10 km^2 under exposed rock and 0.59 under settlement whereas 17.98 km^2 area of open scrub has remained unchanged.

(iii) An area of about 27.79 km^2 under wasteland has been converted into agricultural land (15.71 km^2 area into cultivated land and 12.08 km^2 area into uncultivated land), 15.08 km^2 area into open scrub whereas 34.16 km^2 area still remain under wasteland.

(iv) An area of about 6.78 km^2 open forest has been converted into open scrub, 4.02 km^2 area into wasteland whereas 12.93 km^2 remained under open forest category.

(v) An area of about 205.14 km^2 uncultivated land remained in same category during 2005-2015 whereas 118.68 km^2 has been converted into cultivated land, 10.47 km^2 into open scrub and 15.13 km^2 into wasteland.

(vi) An area of about 104.01 km^2 cultivated land has been converted into uncultivated land, 14.03 km^2 area into waterbody, 17.29 km^2 into open scrub, 7.10 km^2 into wasteland, 1.72 km^2 into dry waterbody, 1.06 km^2 into dense forest, and 0.38 km^2 into settlement.

Table 5: *Landuse/cover matrix showing land encroachment (in hectare) of Shahzad basin during 2005-2015*

2005/2015	Cl	Uc Ucl	Df	Of	Os	Wb	Dwb	Er	Il	Sq	Stlmnt	Wl	2005
Cl	**31873.23**	10401.34	106.77	5.48	1729.51	1403.91	172.14	4.81	26.19	6.11	38.42	710.04	46478
Ucl	11868.53	**20514.61**	180.26	22.30	1047.98	49.43	0.39	0.83		32.09	51	1513.53	35281
Df	67.81	224.67	**4663.09**	32.21	841.77		1.05	0.09		164.83	10.29	501.87	6507.71
Of	52.44	33.27	35.09	**1293.32**	678.23						4.49	402.13	2499
Os	1890.67	1333.17	197.99	8.67	**1798.86**	121.94		110.23	1.27	34.08	59.64	1806.44	7363
Wb	31.93	2.49	0.26		8.37	**1871.72**	34.11	0.16		1.66	1.14	1.88	1953.74
Dwb						32.05							32.05
Er	7.09	4.19			4.19	1.90		**34.43**		4.47			56.29
Il									387				387
Sq	2.23	57.73			5.76			2.24		**109.98**		0.34	178.30
Stlmnt											**1506**		1506
Wl	1571.03	1208.50	1.31		1508.29	4.43	0.01		53.65			**3416.74**	7764
	47365	33780	5184.80	1362	7623	3485.40	207.71	152.81	468.12	353.25	1671	8353	110006.11

Cl - Cultivated land; Ucl - Uncultivated land; Df - Dense forest; Of - Open forest; Os - Open scrub; Wb - Water body; Dwb - Dry water body; Er - Exposed rock; Il - Industrial land; Sq - Stone quarry; Stlmnt -Settlement; Wl - Waste land. No change transition types = bold.

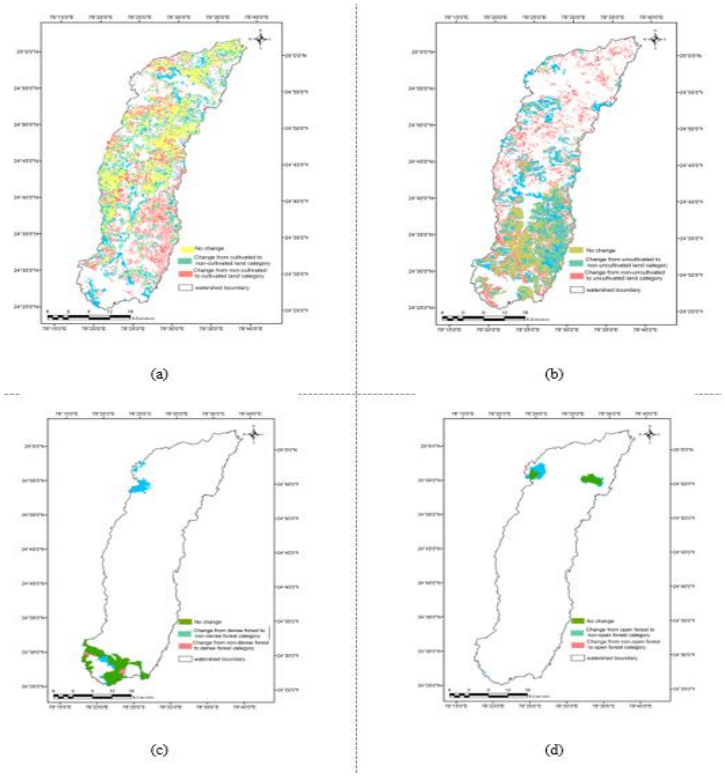

Figure 4: *Landse/cover change in different categories during last decade (2005-2015) in Shahzad basin (a) Cultivated land (b) uncultivated land (c) Dense forest and (d) Open fores*

t

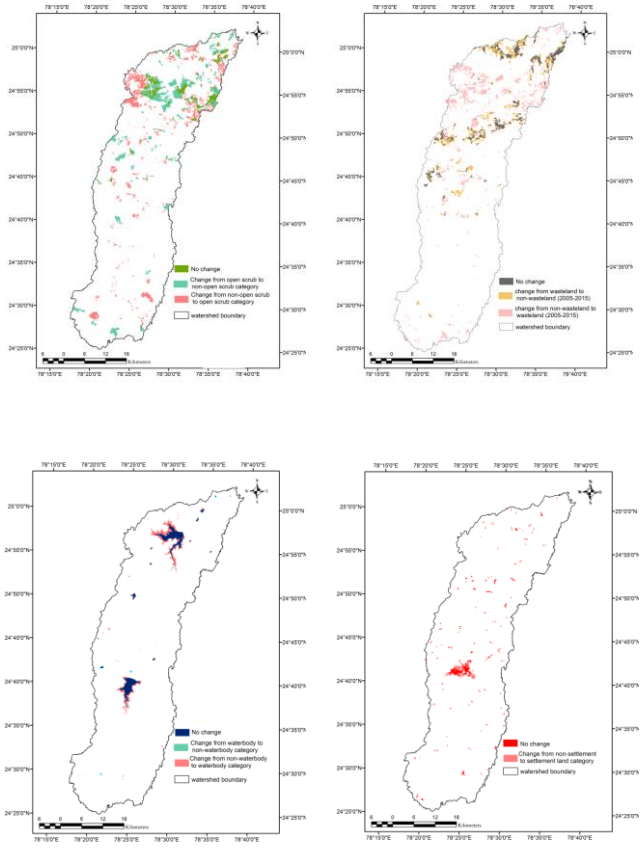

Figure 5: *Landse/cover change in different categories during last decade (2005-2015) in Shahzad basin (a) Open scrub (b) Wasteland (c) waterbody and (d) Built-up land*

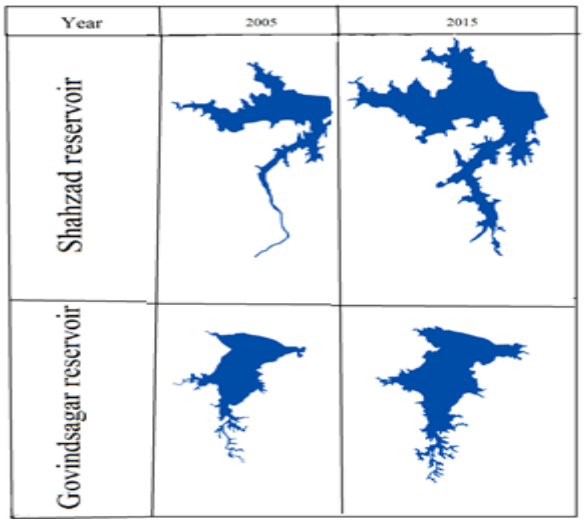

Figure 6: *Water spread in major reservoir during 2005 and 2015*

Surface Water and Landuse Pattern

Agriculture in Shahzad basin is rainfed and depends upon the rainfall but it has been observed that area around the surface water body especially environ dams have shown positive change over the decade. Figure 6 shows the water spread in the reservoir during 2005 and 2015 which has resulted into conversion of uncultivated lands into cultivated land thereby indicating good irrigation facilities and water availability.

4. Conclusion

Multi temporal satellite imagery and GIS application have proved to be cost effective and accurate method to quantify the spatial and temporal phenomenon of LULC dynamics which would have not been possible with the conventional mapping. From the study it is concluded that LULC is dynamic in nature, thus interconversion of one LULC class to another at different part of the watershed in same time period is frequent depending upon the local variation like water availability, geology, livestock stress etc. e.g. in some part of the study area, 15.08 km^2 wasteland has converted into open scrub whereas in other part 18.06 km^2 open scrub has converted to wasteland. Study area is primarily agriculture dominated watershed thus, both cultivated and uncultivated land are of paramount importance. Cultivated land has increased by 8.25 km^2 due to conversion of uncultivated land and open scrub into cropland due to increase in irrigation facility over the decade. The Dense forest has reduce in its areal decreased by 13.27 km^2 due to conversion and degradation in open forest, whereas open forest has been converted into open scrub and waste land due to natural and anthropogenic factors. Other dominated category is open scrub which has increased by 2.6 km^2 since wasteland, open forest and dense forest has been converted into open scrub. Areal extent of dry waterbody has increased due to decline rainfall and utilization of surface water but overall extent of waterbody has also increased as water from Rajghat reservoir (built on the Betwa river) fed to Govindsagar reservoir for irrigation purpose. Settlement has increased due to expansion of Lalitpur town over a decade. The present study highlights the capacity of remote sensing coupled with GIS in analyzing the change dynamics of LULC. A study like this will open a new spectrum for planning, managing and utilizing the available natural and land resource at watershed level.

References

Adinarayana, J., Krishna, N.R. and Rao, K.G. 1995. An Integrated Approach for Prioritisation of Watersheds. *Journal of Environmental Management*, 44(4), pp.375–384.

Aplin, P. and Smith, G.M. 2008. Advances in object-based image classification. the international archives of the photogrammetry. *Remote Sensing and Spatial Information Sciences*, 37, pp.725–728.

Aplin, P., Atkinson, P.M. and Curran, P.J. 1999. Fine spatial resolution simulated satellite sensor imagery for land cover mapping in the United Kingdom. *Remote Sensing of Environment*, 68(3), pp.206–216.

Chen, X., Chen, J., Shi, Y. and Yamaguchi, Y. 2012. An automated approach for updating land cover maps based on integrated change detection and classification methods. *ISPRS Journal of Photogrammetry and Remote Sensing*, 71, pp.86–95.

Chunxiao, Z., Zhiming, L. and Nan, Z. 2008. Using remote sensing and GIS to investigate Landuse dynamic change in Western Plain of Jilin Province. *The International Archives of the Photogrammetry, Remote Sensing and Spatial Information Sciences*, XXXVII, pp.1685–1690.

Congalton, R.G. 1991. A review of assessing the accuracy of classifications of remotely sensed data. *Remote Sensing of Environment*, 37, pp.35-46.

Dronova, I., Gong, P. and Wang, L. 2011. Object-based analysis and change detection of major wetland cover types and their classification uncertainty during the low water period at Poyang Lake, China. *Remote Sensing of Environment*, 115(12), pp.3220–3236.

Fallati, L., Savini, A., Sterlacchini, S. and Galli, P. 2017. Land use and land cover (LULC) of the Republic of the Maldives: first national map and LULC change analysis using remote-sensing data. *Environmental Monitoring and Assessment*, 189(8).

Garai, D. and Narayana, A.C. 2018. Land use / land cover changes in the mining area of Godavari coal fields of southern India. *The Egyptian Journal of Remote Sensing and Space Sciences*, 21(3), pp.375-381.

Gibson, P. and Power, C. 2000. *Introductory Remote Sensing: Digital Image Processing and Applications*. Routledge, London.

Güler, M., Yomralıoğlu, T. and Reis, S. 2007. Using landsat data to determine landuse/land cover changes in Samsun, Turkey. *Environmental Monitoring Assessment*,127, pp.155-167.

Jensen, J.R. 1996. *Introductory digital image processing: a remote sensing perspective*. 2nd Edition, Prentice Hall, Inc., Upper Saddle River, NJ.

Kibret, K.S., Marohn, C. and Cadisch, G. 2016. Assessment of land use and land cover change in South Central Ethiopia during four decades based on integrated analysis of multi-temporal images and geospatial vector data. *Remote Sensing Applications: Society and Environment*, 3, pp.1–19.

Lillesand, T.M., Kiefer, R.W. and Chipman, J.W. 2004. *Remote sensing and Image Interpretation*, 5th edition. John Wiley & Sons.

Liu Y., Pei Z., Wu Q., Guo L., Zhao H. and Chen X. 2012. *Land use/land cover classification based on multi-resolution remote sensing data*. In: Li D., Chen Y. (eds), Computer and Computing Technologies in Agriculture V. CCTA 2011. IFIP Advances in Information and Communication Technology, Vol. 369., Springer, Berlin, Heidelberg

Meinel, G. and Neubert, M. 2000. A comparison of segmentation programs for high resolution remote sensing data. *Spring*, 35(Part B), pp.1097–1105.

Nagarajan, N. and Poongothai, S. 2011. Identification of land use and land cover changes using remote sensing and GIS. *IACSIT International Journal of Engineering and Technology*, 3(5), pp.570–576.

Palaniyandi, M. and Nagarathinam, V. 1997. Land use/land cover mapping and change detection using space borne data. *Journal of Indian Society of Remote Sensing*, 25, p.27.

Prakasam, C. 2010. Land use and land cover change detection through remote sensing approach: A case study of Kodaikanal taluk, Tamil nadu. *International Journal of Geomatics and Geosciences*, 1(2), pp.150–158.

Abdul Rahaman S, Abdul Ajeez S, Aruchamy S, et al. 2015. Prioritization of sub watershed based on morphometric characteristics using fuzzy analytical hierarchy process and geographical information system – A Study of Kallar Watershed, Tamil Nadu. *Aquatic Procedia*, 4, pp.1322–1330.

Rawat, J.S. and Kumar, M. 2015. Monitoring land use/cover change using remote sensing and GIS techniques: A case study of Hawalbagh block, district Almora, Uttarakhand, India. *The Egyptian Journal of Remote Sensing and Space Science*, 18(1), pp.77–84.

Rawat, J.S., Biswas, V. and Kumar, M. 2013. Changes in land use/cover using geospatial techniques: A case study of Ramnagar town area, district Nainital, Uttarakhand, India. *Egyptian Journal of Remote Sensing and Space Science*, 16(1), pp.111–117.

Rogan, J. and Chen, D. 2004. Remote sensing technology for mapping and monitoring land-cover and land-use change. *Progress in Planning*, 61, pp.301–325.

Song, X., Yang, G., Yan, C., Duan, H., Liu, G. and Zhu, Y. 2009. Driving forces behind land use and cover change in the Qinghai-Tibetan Plateau : a case study of the source region of the Yellow River, Qinghai Province, China. *Environmental Earth Science*, 59, p.793.

Thakkar, A.K., Desai, V.R., Patel, A. and Potdar, M.B. 2017. Post-classification corrections in improving the classification of land use/land cover of arid region using RS and GIS: The case of Arjuni watershed, Gujarat, India. *Egyptian Journal of Remote Sensing and Space Science*, 20(1), pp.79–89.

Welde, K. 2016. International Soil and Water Conservation Research Identi fi cation and prioritization of subwatersheds for land and water management in Tekeze dam watershed, Northern Ethiopia. *International Soil and Water Conservation Research*, 4(1), pp.30–38.

Zhang, C., Cooper, H., Selch, D., Meng, X., Qiu, F., Myint, S.W. and Xie, Z. 2014. Mapping urban land cover types using object-based multiple endmember spectral mixture analysis. *Remote Sensing Letters*, 5(6), pp.521–529.

Cloud Publications
International Journal of Advanced Remote Sensing and GIS
2019, Volume 8, Issue 1, pp. 3047-3056
ISSN 2320 – 0243, Crossref: 10.23953/cloud.ijarsg.419

Research Article

Detection of Residential Buildings to Estimate Population in Lebanon using GeoEye Images

Kamel Allaw[1], Jocelyne Adjizian Gerard[1], Makram Chehayeb[2], Nada Badaro Saliba[1]

[1]CREEMO, Geography Department, Saint Joseph University, Beirut, Lebanon.
[2]Surveying Department, Islamic University of Lebanon, Lebanon.

Correspondence should be addressed to Makram Chehayeb, *makram.ch92@gmail.com*

Publication Date: 18 July 2019

DOI: https://doi.org/10.23953/cloud.ijarsg.419

Abstract Scholars in urban planning and Geography are increasingly interested in grasping demographic information using Remote Sensing data. The accurate detection of residential buildings from satellite images seems to be essential in this domain. This paper has a dual purpose: It aims firstly at developing an automatized method for residential buildings extraction, then, evaluating the relationship between residential building characteristics (number, area, and volume) and demographic data. To do so, a dual phasic methodology is proposed. During the first phase, the extraction of residential buildings has been done using a transformation into HSI representation where the buildings corresponds to the higher values of band I. After that, the image has been transformed into vector and the forms of the buildings have been adjusted using convex hull tool in ArcGIS. The identification of residential buildings has been done using statistical data. The volumes of buildings has been calculated using MATLAB script. During the second phase, a multivariate regression has been established and a strong relationship (R^2=0.87) has been found between the volume of buildings and the population data.

Keywords *Building detection; Convex hull; High resolution satellite image; HIS; Population; Supervised classification*

1. Introduction

Building detection is the subject of many studies in the field of Remote Sensing due to the wide range of applications that become available thanks to the generated data. In the scientific literature, several approaches were adopted which differ according to the type of adopted method and the used data. A semi-automated approach has been adopted by Rüther et al. (2002) using an active contour model and the dynamic programming optimization technique. As well, Koç et al. (2005) who developed an approach using high resolution images, by applying classification, and using the digital surface model (DSM) and object extraction techniques. An automated approach has been adopted by Guo et al. (2002) who used high resolution IKONOS satellite images and adopted a snake-based approach for 2D building outlines' extraction from, airborne laser scanning system has been used to capture height data. Moreover, a pair of aptical and synthetic aperture radar (SAR) images have been used by Tupin et al. (2003) to automatically extract building outlines. They first used SAR image to extract partially potential building footprints, then, they used the optical one to detect shapes based the extracted lines

In addition, Jin X. and Davis C.H. (2005) have automatically extracted buildings from high resolution satellite imagery using contextual, structural, and spectral information. This approach is characterized by three different extraction strategies: A shape analysis differential morphological profile (DMP) has been used to generate and verify building hypotheses, shadows modeling to generate relevant information in order to determine the characteristics (position and size) of adjacent buildings and spectral information has been used to detect small bright buildings which cannot be detected based on contextual and structural information. The major disadvantage of this approach is its inability to detect ceiling roof buildings where only 70% of the buildings are successfully detected. Furthermore, GÜDÜCÜ (2008) proposed a method for limit extraction based on color segmentation and using high resolution satellite images. Lee et al. (2003) proposed a new method based on Supervised classification and Hough transformation and using Ikonos images to accurately detect building roofs. Koç D. and Türker M. (2005) developed an approach using high resolution images, by applying classification, and using the digital surface model (DSM) and object extraction techniques. In addition, Inglada, J. (2007) proposed a new method for man-made objects' detection based on support vector machines classification (SVM) and using high resolution optical remote sensing imagery. In this method, the original bands of SPOT 5 satellite images have been used for SVM learning and the extra bands (such as NDVI, nDSM and other texture measures) were used to find building patches. The additional bands increased the accuracy of the method by 10%. Salar Ghaffarian, Saman Ghaffarian (2014), applied an approach to detect buildings by collecting field data to make a supervised classification where pixels are classified into four classes, and applying morphological operations. Some methods based on classification are proposed for detecting and extracting buildings from remote sensing images this, by indicating a set of training sample to take several classes for supervised classification and using high resolution satellite images.

The previously presented methods might be accurate in structured urban areas. However, those methods are not compatible with unorganized areas where finding a pattern seems to be difficult. For that, it is essential to find a method to be accurate and useful for unorganized areas. In this context, Lebanon, as the majority of third world countries, witnessed a rapid and uncontrolled urban sprawl as a result of the corruption and the limited planning regulations (CDR, 2005). As a result, the establishment of plans to handle this situation faces huge challenges since it is difficult to obtain the required data related to constructed areas and its population data. For that, this situation imposes the elaboration of precise methods to provide researchers and specialists in urban planning with the necessary information about the built-up and population characteristics. Consequently, the aim of this study to design and test an appropriate method for building detection and population estimation.

2. Case Study

The Lebanese Republic, occupying an area of 10452 km^2, is located in western Asia on the eastern shore of the Mediterranean Sea between latitudes 33° and 35° N and longitudes 35° and 37° E (Figure 1). It borders the Sea in the west, Syria in the north and east, and Occupied Palestine in the south. In order to extract the necessary data for this study, a sample of 30 villages (e.g. unorganized areas) have been chosen. Those municipalities are arbitrarily chosen and geographically well distributed through the country.

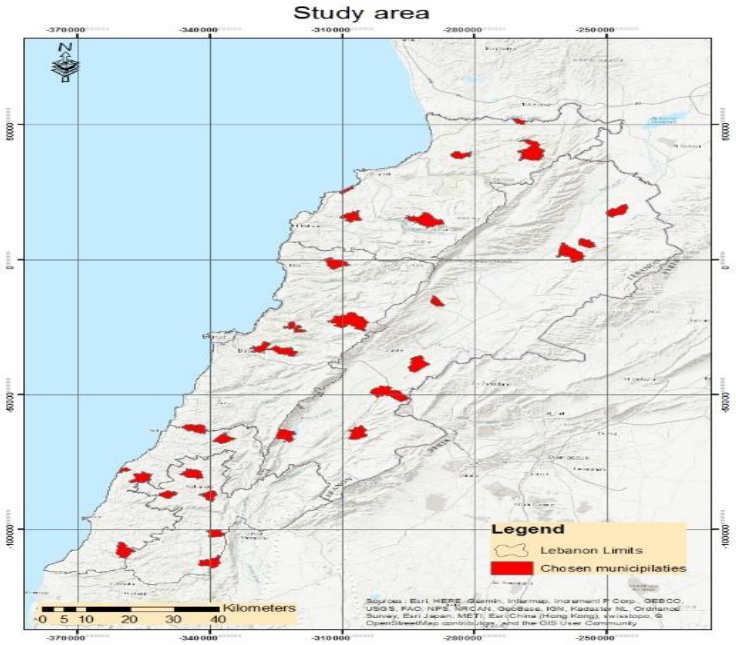

Figure 1: *Distribution of the selected municipalities on Lebanon map*

3. Methodology and Data

3.1. Building Detection

To extract the buildings from the Geo-eye satellite image, three steps have been followed. First, a conversion from RGB color space to HSI color model has been done using “RGB to HIS tool” in ERDAS Imagine Software. It is important to note that the HSI color model represents each color with three components: hue (H), saturation (S), intensity (I) (Figure 2).

The Hue component (H) describes the color itself in the form of an angle between 0 and 360 degrees, the Saturation component measures the degree of purity of a color, that is, the amount of gray added to the color. The range of the S component is [0, 1]. The Intensity is the degree of brightening or darkening of a color. The range is between [0, 1] where 0 means black, 1 means white. The essential advantage of the HSI model is to distinctly separate the information of brightness, from the hue and saturation. The advantage of this model for image processing and color compositions is that it improves the visual quality of an image since.

After that, the converted HSI image can be displayed on 'ARCMAP', according to the three components H, S, and I. To determine the values corresponding to buildings, the same satellite image has been represented according to each of the three bands (H, S, I) (Figure 3). By visual interpretation, it’s easy to distinguish the color of the interval representing the buildings and the other elements which took the same I value (rocky land, roads ...). As a result, the buildings correspond to the highest values of Band I. Then, the image shown according to I band, has been converted into vector data (shape file), so that we can eliminate all elements that are non-buildings such as rocky terrain, some road portion... By this conversion, all polygons of negligible area have been eliminated (e.g. the polygons which have a surface less than 10 m^2).

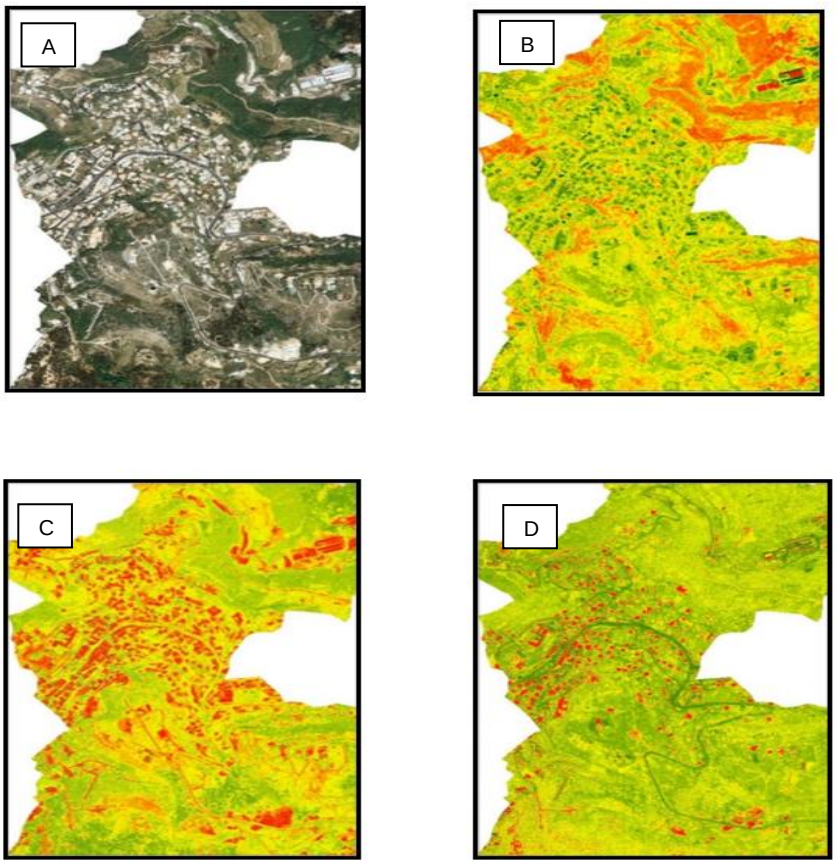

Figure 2: *a) Satellite imagery represented Bikfaya, b) Displayed image according to the band H, c) Displayed image according to the band I, d) Displayed image according to the band S*

Figure 3: *Polygons represented the building in Bikfaya*

3.2. Generation of Polygons Representing Buildings

In the field of geometry, convex polygons are those whose diagonals are always internal and whose internal angles do not exceed the radian pi or 180 degrees. Another way to determine if a polygon is convex is to draw segments between two points of the figure, whatever its position, if these segments are always internal, it will be a convex polygon.

'Convex Hull' is the smallest polygon that completely surrounds a set of points. This method is used to adjust the shape of the polygons that represent the buildings in all the selected municipalities. By generating these convex polygons, we can clearly distinguish all the detected buildings, and then calculate their surfaces. Because of some errors due to the existence of other objects with similar values of buildings such as roads and land, certain building areas are affected, since the polygons generated represent a larger area than the real one, which is manually adjusted as much as possible before calculating the areas of buildings (Figure 4).

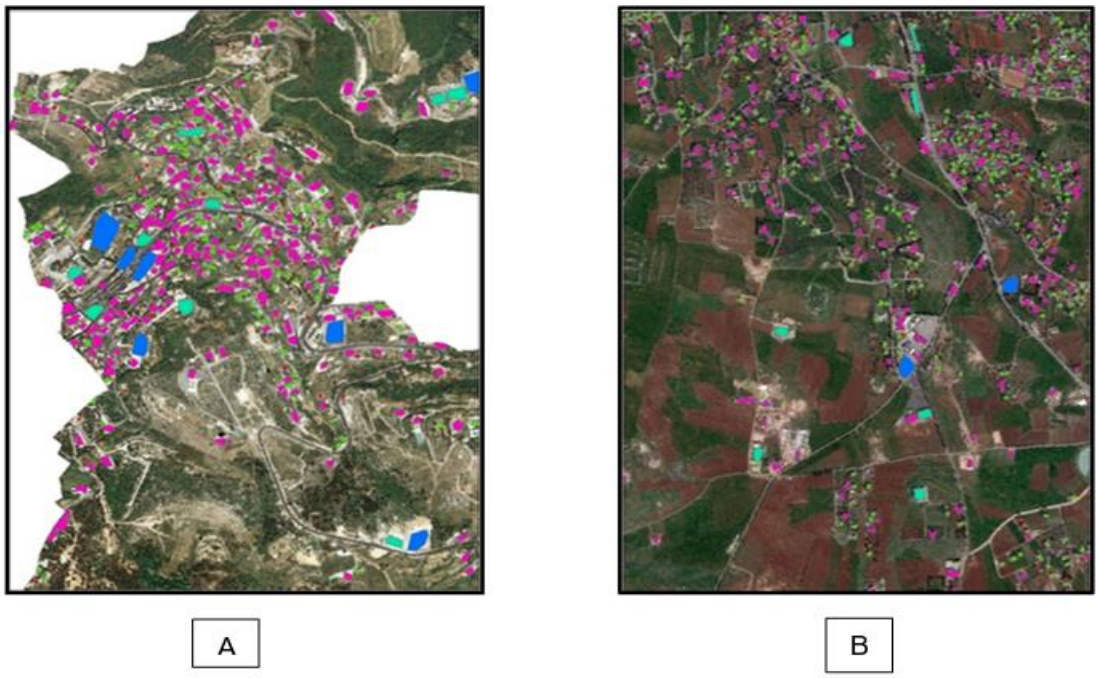

Figure 4: *Application of convex Hull in a) Bikfaya, b) Nabatieh ElFaouka*

3.3. Identification of Residential Buildings

In order to identify the residential buildings, the area has been considered as a key identifier. In fact, the area of residential buildings in Lebanon is usually between 80 and 130 m^2 (Table 1). In practice, the areas of generated polygons have been divided into three categories: buildings with small areas, large areas' buildings and residential buildings. As a result, all polygons with surface less than 30 m^2 have been eliminated because they do not represent residential buildings. Moreover, buildings with an area between 30 and 230 m^2 have been considered as residential buildings because this interval include the majority of residential buildings' areas. As well, the polygons whose surfaces vary between 230 and 1000 m^2, have been classified as residential buildings since they may represent one or two residential buildings. As a result, polygons whose areas are greater than 1000 m^2 have been eliminated because they don't represent residential buildings.

Table 1: *Housing distribution following the surface of the residential building in Lebanon (The central administration of statistics in Lebanon)*

Residential building area	Lebanon 2014 %
Less than 30 m^2	0.9
30 – 80 m^2	14.1
80 – 130 m^2	41.9
130 – 180 m^2	21.3
180 – 230 m^2	14.8
More than 230 m^2	5.8
Unknown	1.1
Sum	100

3.4. Buildings' Areas

The areas of buildings can be calculated by multiplying the average area of buildings in each municipality by the number of buildings previously calculated. This calculation method may reduce the error resulting from the detection of buildings or residential buildings identification.

3.5. Buildings' Volumes

The volume of buildings can be calculated by multiplying the mean area of buildings in each municipality with the number of buildings and the corresponding mean height.

$$Built - up\ volume = Mean\ area * number\ of\ buildings * mean\ height$$

So, in order to determine the buildings' volumes, it is necessary to know the height of buildings. Thus, we have applied the following method. Since we are using an RGB image and based on the hue range of the image, the green areas have been detected and selected. Then, this RGB image has been transformed into "L-A-B" format and green areas has been made as luminescent as possible to get rid of them in the thresholding procedure. Using Otsu's method, a multi-threshold image function has been used to divide the image into four categories: highly bright, bright, dark and highly dark where highly dark area is the most probable area to represent the buildings' shadow. After that, a binary image has been generated and the areas which don't represent a building's shadow are removed (Otsu, 1979). At this point, the shadow's areas are located on the image and the buildings' heights are determined using the following method: There is a relation between the azimuth of the sun, the dimension of shadow and the height of building, consequently, since the azimuth of sun is known (almanac data) and the dimension of shadow is known (form the already generated image), the building height can be calculated. At the end, the areas and heights of buildings are calculated; the volume can be calculated by multiplying them together.

3.6. Population Data

The population data relative to the chosen villages are determined by visiting each municipality and count the number of unit residence and we got the mean number of family size, so by multiplying the mean number of family size with number of residential unit we get the population in each municipality.

4. Results

4.1. The Volume of Buildings

Using the previously described method, the number of residential buildings (Table 2), the areas of residential buildings and their volumes have been calculated for each municipality (Table 3).

Table 2: *Distribution the number of the buildings according to the intervals of surfaces*

Municipality	Number of buildings between 30-230 m^2	Number of buildings between 230-1000 m^2	Total number
Aabba	973	107	1080
Aain Baalbek	810	193	1003
Aakkar El-Aatiqa	466	443	909
Aaytanit	21	33	54
Amioun	307	349	656
Babliyé	420	120	540
Baskinta	586	238	824
Beit Chabab	600	213	813
Beit Meri	459	621	1080
Bikfaya	183	257	440
Blida	398	219	617
Bqerzla	167	66	233
Deir Ez-Zahrani	538	404	942
Dibbabiyé	173	14	187
Ehden	428	476	904
Jbal El-Botm	299	118	417
Jebaa	34	12	46
Joun	352	137	489
Khirbet Rouha	316	286	602
Laboué	1193	245	1438
Majdel Aanjar	658	608	1266
Markaba	289	144	433
Michmich Jbayl	190	74	264
Nabatieh El-Faouka	751	353	1104
Qaa Baalbek	678	166	844
Qalamoun	349	219	568
Ras El Matn	40	311	351
Roum	161	90	251
Saksakiyé	887	155	1042
Terbol Zahlé	281	252	533

Table 3: *The areas and volumes of buildings for each municipality*

Municipality	Total number of building	Mean surface (m^2)	Buildings surface (m^2)	Building volume (m^3)	Population
Aabba	1080	144	155520	544320	5000
Aain Baalbek	1003	171	171513	600295.5	8000
Aakkar El-Aatiqa	909	265	240885	963540	15500
Aaytanit	54	203	10962	43848	800
Amioun	656	280	183680	642880	6800
Babliyé	540	185	99900	349650	4000
Baskinta	824	204	168096	588336	7500
Beit Chabab	813	178	144714	578856	16000
Beit Meri	1080	288	311040	1244160	15500
Bikfaya	440	298	131120	458920	7000
Blida	617	240	148080	518280	4500
Bqerzla	233	197	45901	137703	1500
Deir Ez-Zahrani	942	241	227022	908088	15000
Dibbabiyé	187	140	26180	78540	880
Ehden	904	310	280240	1120960	16500
Jbal El-Botm	417	199	82983	248949	1350
Jebaa	46	203	9338	28014	500
Joun	489	198	96822	338877	4800

Khirbet Rouha	602	251	151102	528857	10000
Laboué	1438	165	237270	949080	17000
Majdel Aanjar	1266	263	332958	1331832	17000
Markaba	433	219	94827	331894.5	6500
Michmich Jbayl	264	208	54912	192192	2000
Nabatieh El-Faouka	1104	210	231840	927360	17500
Qaa Baalbek	844	175	147700	516950	6000
Qalamoun	568	225	127800	511200	16000
Ras El Matn	351	198	69498	277992	7500
Roum	251	226	56726	170178	1800
Saksakiyé	1042	161	167762	587167	7000
Terbol Zahlé	533	261	139113	486895.5	6000

4.2. Relationship between Buildings and Population

After detection of residential buildings and after we determine the number of building, the area of residential buildings and the volume of buildings, a regression model was created based on census 2013 population data and independent variables for residential building number (Figure 5), area (Figure 6) and volume (Figure 7). The result shows a strong relation with r-squared 0.87.

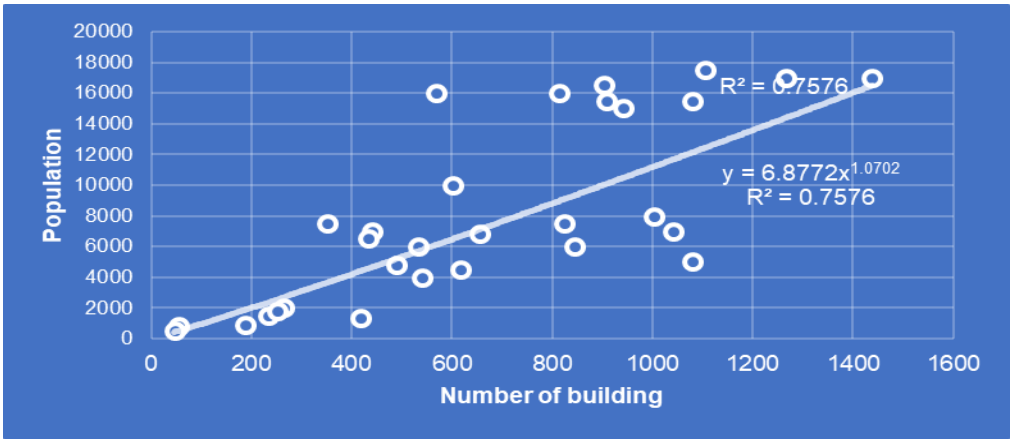

Figure 5: *The relationship between the number of buildings and population data*

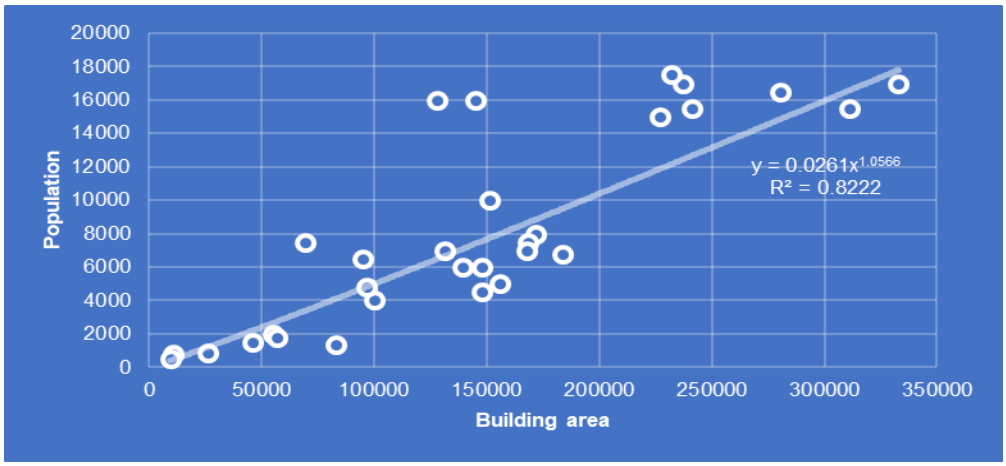

Figure 6: *The relationship between building areas and population data*

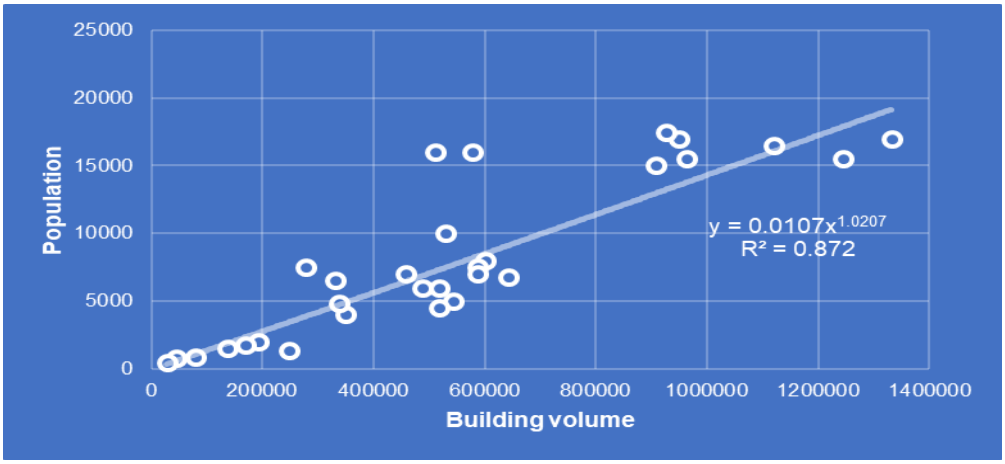

Figure 7: *The relationship between building volumes and population data*

5. Discussion

The results of this study have been shown a strong relationship between the characteristics of buildings (number, area and volume) and the population data.

To verify the result, a municipality where the numbers of residential and non-residential buildings are known has been chosen. After applying the method used to identify the residential building, the results are summarized in the following confusion matrix (Table 4).

Table 4: *Confusion matrix of residential building detection accuracy*

		Actual situation	
		Residential building	Non-residential building
Predicted	Residential building	901	31
	Non-residential building	116	161

$$Sensitivity = \frac{TP}{TP + FN} = \frac{901}{901 + 116} = 0.8859$$

$$Specificity = \frac{TN}{TN + FP} = \frac{161}{161 + 31} = 0.8385$$

The results show that 88.59% of the residential buildings and 83.85% of non-residential buildings were correctly identified.

As a result, the validation of the results and the analysis of error have proved that the margin of error is acceptable. Consequently, the established mathematical relationship can be considered as a valid method to estimate the population data from remote sensing data.

However, this study was limited by the difficulty to identify mixed-use buildings.

6. Conclusion

The combination of remotely sensed data and GIS tools was helpful and efficient in building detection and population estimation. In fact, the detection of residential buildings using HSI transformation and "Convex Hull" tool and based on statistical information seemed to be accurate and effortless. Moreover, the estimation of buildings' height is a reliable method for buildings' volume calculation

taking into consideration the amount of information that might ensure. Furthermore, the established mathematical relationship between buildings' volume and population allow planners to accurately estimate population using building volumes. At the end, this method might be applied in a variety of situations such as unorganized urban areas and rural areas in order to grasp the necessary information for planners before the establishment of plans or as a monitoring tool for urban sprawl and growth.

References

Council for development and Reconstruction. 2005. National physical master plan of the Lebanese territory. Available from: *http://www.cdr.gov.lb/study/sdatl/English/NPMPLT.PDF*.

Ghaffarian, S. and Ghaffarian, S. 2014. *Automatic building detection based on supervised classification using high resolution google earth images*. ISPRS Technical Commission III Symposium, 5 – 7 September 2014, Zurich, Switzerland.

Güdücü, H.V. 2008. Building detection from satellite images using shadow and color information. Available from *http://citeseerx.ist.psu.edu/viewdoc/download?doi=10.1.1.632.5114&rep=rep1&type=pdf.*

Guo, T. and Yasuoka, Y. 2002. *Snake-based approach for building extraction from high-resolution satellite images and height data in urban areas*. Proceedings of 23rd Asian Conference on Remote Sensing.

Inglada, J. 2007. Automatic recognition of man-made objects in high resolution optical remote sensing images by SVM classification of geometric image features. *Journal of Photogrammetry and Remote Sensing*, 62(3), pp.236-248.

Jin, X. and Davis, C.H. 2005. Automated building extraction from high-resolution satellite imagery in urban areas using structural, contextual, and spectral information. *Journal on Applied Signal Processing*, 14, pp.2196-2206.

Koç, D. and Türker, M. 2005. *Automatic building detection from high resolution satellite images*. International Conference on Recent Advances in Space Technologies. RAST2005, pp.617-622.

Lari, Z. and Ebadi, H. 2007. *Automated building from high-resolution satellite imagery using spectral and structural information based on artificial neural networks*. Conference on Information Extraction from SAR and Optical Data, with Emphasis on Developing Countries.

Lee, D.S., Shan, J. and Bethel, J.S. 2003. Class-guided building extraction from Ikonos imagery. *Photogrammetric Engineering and Remote Sensing*, 69(2), pp.143-150.

Rüther, H., Martine, H.M. and Mtalo, E.G. 2002. Application of snakes and dynamic programming optimization technique in modeling of buildings in informal settlement areas. *Journal of Photogrammetry and Remote Sensing*, 56, pp.269-282.

Tupin, F. and Roux, M. 2003. Detection of building outlines based on the fusion of SAR and optical features. *Journal of Photogrammetry and Remote Sensing*, 58, pp.71-82.

UN Habitat. 2010. *Lebanon – Urban Issues, United Nations Human Settlements*. Available from: *https://unhabitat.org/lebanon/lebanon-urban-issues/.*

Unsalan, C. and Boyer, K.L. 2005. A system to detect houses and residential street networks in multispectral satellite images. *Computer Vision and Image Understanding*, 98, pp.423-461.

Cloud Publications
International Journal of Advanced Remote Sensing and GIS
2019, Volume 8, Issue 1, pp. 3057-3072
ISSN 2320 – 0243, Crossref: 10.23953/cloud.ijarsg.420

Research Article

Extraction and Analysis of Feature Layers from Airborne LiDAR Point Clouds in Downtown Urban Landscapes

Fahmy F.F. Asal

Civil Engineering Department, Faculty of Engineering, Menoufia University, Shebin El-Kom, Egypt.

Correspondence should be addressed to Fahmy F.F. Asal, *fahmy_asal@hotmail.com*

Publication Date: 18 July 2019

DOI: https://doi.org/10.23953/cloud.ijarsg.420

Abstract Light Detection And Ranging (LiDAR) is a well-established active remote sensing technology that can provide accurate digital elevation measurements for the ground surface and non-ground features such as vegetations, trees, roads and buildings etc. Extraction of non-ground features from airborne LiDAR measurements has been a main objective for researches in the past twenty years. This study aimed at exploring the different methods for extraction of non-ground features from airborne LiDAR point clouds for creation of reliable feature layers that can be employed in a wide range of engineering and environmental applications. Also, undertaking comparative study for the application of Gaussian low pass filter, focal analysis mean filter and DTM slope-based filter on airborne LiDAR Digital Surface Models (DSMs) of varying window sizes in extraction of reliable feature layers have been a main objective of this study. Airborne LiDAR dataset captured over the downtown of the City of Vaihingen in Germany has been exploited in the study. Visual analysis of the extracted feature layers has shown that Gaussian low pass filter of 3x3 window size has removed a small range of non-ground features heights while detailed and structured feature layer has been obtained using window size of 21x21. Additionally, the focal analysis mean filter has achieved better removal of non-ground features compared to Gaussian low pass filter at similar window sizes where better representation of the downtown landscape has been obtained using window size of 21x21 and larger. On the other hand, visual analysis has not shown clear differences between the feature layers extracted using DTM slope-based filter due to changing the filter window sizes. Statistical analysis has indicated that the ranges of elevations in the feature layers from the different examined filters have increased with increasing the filter window size till 15x15. Also, the standard deviations of the feature layers have increased due to increasing the window sizes of Gaussian low pass and focal analysis mean filters, however increasing the window size of the DTM slope-based filter has produced slight increases in the standard deviation. Additionally, increasing the window size of Gaussian low pass and the focal analysis mean filters has produced feature layers of skewness approaching to zero with window size of 21x21. This has referred to feature layers of symmetrical Gaussian normal distribution curves. Moreover, dramatic decreases have occurred in the feature layer kurtosis due to increases in the filter window sizes till window sizes of 21x21 in the cases of Gaussian low pass and focal analysis mean filters which referred to more consistent and outlier free feature layers.

Keywords *Airborne laser scanning; DSM/DEM/DTM; DTM slope-based filter; Feature extraction; Focal analysis mean filtering; Gaussian low pass filtering*

1. Introduction

Three-Dimensional (3D) modeling has been gaining importance in a wide range of applications including tourism, telematics, civil protection, real estate management, and financial management (Tomljenovic et al., 2015). El-Garouani et al. (2014) carried out a research that investigated the requirements of high-resolution surface models in simulation of urban modeling where Digital Surface Models (DSMs) were created from aerial image stereo pairs using the image matching techniques. Also, they were investigating the different methods of creating 3D city structures in addition to reviewing possible methods for involvement of the extracted features and 3D models from the digital elevation data in various GIS applications such as natural disasters and telecommunications planning. Airborne Laser Scanning (ALS) namely; airborne LiDAR is an active remote sensing technology that can provide massive 3D data capture known as point clouds can be used in creation of high-quality Digital Surface Models (DSMs). Also, valuable products such as Digital Elevation Models (DEM) of the extracted man-made features such as buildings, power lines, roads in addition to and natural features including vegetation mask, single trees, vertical tree structures constitute standard outputs from airborne LiDAR point clouds (Büyüksalih and Gazioğlu, 2019; Tomljenovic et al., 2015). Non-ground features can be extracted from the DSMs leaving a ground surface model that is usually known as a Digital Terrain Model (DTM). In urban environment separation of non-ground surface features from ground surface points can provide a valuable combination of two datasets that can widen their applications. For example, detailed ground surface elevations can be important for predicting flood inundation and potential effects of sea level rise, however detailed models of man-made objects known as feature layers can be very important for property owners, planning authorities and insurance companies (Büyüksalih and Gazioğlu, 2019; Priestnall et al., 2001). Also, Feature layers can be employed in creation of surface roughness maps necessary for flood and hydrodynamic modelling since researchers defined the surface roughness as the standard deviation of the extracted residual surface models known as feature layers (Grohmann et al., 2011 & 2009).

Airborne LiDAR has been a very effective and prolific technology that can be exploited in mapping and modeling of various types of landscapes due to its capability of providing highly accurate measurements of the landscape features with exploitation of single pulse, multiple pulses or full waveform. Many newer approaches use full-waveform measurements since they can save a much better source of information. Three-dimensional coordinates of the laser beam reflections, the intensity and the pulse width can be extracted by a waveform decomposition, which fits a series of Gaussian pulses to the waveform. Since multiple reflections can be detected from the full waveform and overlapping pulse reflections can be distinguished higher point density can be achieved compared to the conventional discreet returns (Tomljenovic et al., 2015). Also, Airborne LiDAR is emerging into a wide range of applications, in ecology, forestry, geomorphology, seismology, environmental research due to its capability to produce three-dimensional point data with high spatial resolution and high accuracy (Jawaka et al., 2014). Additionally, LiDAR data have been used intensively in terrain surface modelling since LiDAR sensors can record distances between the sensor and targets that is called the range data in addition to the strength of the backscattered energy reflected from the targets and known as the intensity data. Moreover, LiDAR sensors use the near-infrared spectrum range of high separability in the reflected energy from different targets allowing LiDAR intensity data to be exploited in land-cover classification (Mahadi et al., 2018; Shaker and El-Ashmawy, 2012). Thus, Airborne LIDAR is gaining increasing importance in recent years as it also, can provide topographic information with dense point cloud data as well as all detailed surface models that can be used in a wide range of disciplines including cartography, construction, city planning, forestry, energy, hydrology, geology, transportation, telecommunications, security, disaster, aviation and infrastructure (Büyüksalih and Gazioğlu, 2019). Furthermore, Airborne LiDAR can provide laser-based measurements of the distance between an aircraft, the platform carrying the system, and the ground to deliver 3D point clouds as a representation of the scanned surface of high spatial density. This can be in the range from under 1 point per square meter (ppsm) and above (Heinzel and Ginzler, 2019). Additionally, airborne LIDAR uses transmitted properties of scattered light for detecting intended targets that allows its potential uses for spatial planning and management including mangrove monitoring (Mahadi et al., 2018). In addition,

the superiority of ALS systems basing on LiDAR technology has been determined by the fact that the signal can penetrate small gaps in vegetation and semi-transparent objects on the earth's surface to provide additional information about physical properties of the scanned object (Tomljenovic et al., 2015). Moreover, ALS technology has many characteristics that provide its superiority over the other remote sensing technologies including: 1) High-speed data capture for extended areas with each data point of 3D positional coordinates in addition to signal backscatter information including signal intensity and echo width for full-waveform ALS systems. 2) High degree of spatial coverage and accurate spatial data that can easily be collected. 3) Elevation data are directly measured through the range measurements of the laser pulse. 4) Multiple returns per one laser pulse from the ALS data can be used as a great source of information in vegetated areas in forestry applications. 5) ALS multiple returns can provide insight into the vertical forest structure and complexity (Tomljenovic et al., 2015; Sithole, 2001).

Sevgen (2019) stated that Airborne LiDAR data have been increasingly used for classification of urban landscapes for urban planning, mapping, and change detection monitoring. He classified airborne LiDAR data of a complex urban area from Bergama District, İzmir, Turkey into four classes; buildings, trees, asphalt road, and ground using an algorithm called Random Forest (RF) supervised classification method. He also, used ground truth data collected from the studied area to select training data and validate the results since buildings were very close to each other and trees sometimes cover the rooftops of buildings. Finally, he acknowledged that the most challenging part of his study was to generate ground truth in a complex area; however, he recommended obtaining results of an overall accuracy of 70.20%. Wang et al. (2019) reviewed the potential of using LiDAR data in improving the accuracy of urban tree species classification. They reviewed the different studies that utilized LiDAR data in urban tree species mapping, with great emphasis on the studies where LiDAR data was fused with optical imagery, through classification accuracy comparison, general workflow extraction and discussion and summarizing of LiDAR data contributions. They recommended that combining LiDAR data in urban tree species identification could achieve better classification accuracy and improve the classification accuracy on finer and larger species levels while aiming to maintain the classification costs. Vosselman and Maas 2001 stated that for production of DTMs from Airborne LiDAR measurements many points were measured on vegetation, buildings and other objects above the ground surface that required to be removed from the dataset. This can be done by filtering the data since several algorithms were developed through making assumptions on the spatial distribution of the points in the terrain and verifying these assumptions on the points to be classified as ground points or not. However, the filtering process becomes difficult when the objects to be removed such as buildings are similar in shapes to objects that comprise parts of the terrain such as dikes (Vosselman and Maas, 2001).

Perko et al. (2015) proposed a simple filtering approach that can be applied on the DSMs in order to extract DTMs with focus on robustness and computational efficiency to filter DSMs extracted from satellite stereo images. They acknowledged that their approach represented an evolution of an existing DTM generation method as it included integration of multi-directional processing as well as slope dependent filtering. They acknowledge that their DTM generation workflow was fully automatic and required no user interaction. Finally, they recommended that qualitative and quantitative evaluations of the created DTMs with respect to reference LiDAR data showed effectiveness of their algorithm. Jawaka et al. (2014) exploited what was called Canopy Height Model (CHM)-based workflow for individual tree crown delineation and 3D feature extraction in addition to building feature delineation from high-density LiDAR point cloud data in an urban landscape. In addition, they evaluated the accuracy through exploitation of very high-resolution panchromatic (PAN) (spatial) and 8-band (multispectral) WorldView-2 (WV-2) imagery. Their workflow included creation of DSM from LiDAR point cloud, generation of a hill-shade image and an intensity image, generation of bare earth DTM and extraction of trees and buildings. They recommended that overestimation of trees and buildings were due to the incorrect filtering of the point clouds. Additionally, they acknowledged that LiDAR-based 3D feature extraction supplemented by high resolution satellite data should have potential to be used for understanding and characterization of urban features.

Uzar and Yastikli (2013) presented an automatic building extraction approach using LiDAR data and aerial photographs from a multi-sensor system positioned at the same platform. The approach consisted of segmentation, analysis and classification steps based on object-based image analysis using chessboard, contrast split and multi-resolution segmentation methods. They used the scale, shape, completeness, brightness and statistical parameters in determining threshold values for classification in the analysis. Also, they used the intensity images created from LiDAR data and morphological operations in improving the accuracy of the building class. Finally, they recommended that the approach achieved an overall accuracy of about 93% for the target class in suburban neighborhood in addition to completeness of 96.73% and correctness of 95.02% where the analyses were performed by comparing the automatically extracted buildings with reference data. Liu et al., 2013 stated that researchers extensively applied Locally Excitatory Globally Inhibitory Oscillator Networks (LEGION) for segmentation where these networks are neural oscillator networks based on biological frameworks. They developed a modified LEGION segmentation to extract buildings from high-quality DSMs where the extraction is implemented without assumptions on the underlying structures in the DSM and without prior knowledge of the number of regions. In addition, they used grey level co-occurrence matrix homogeneity to measure DSM height texture of complex information DSM in urban landscape. Then they used homogeneity to distinguish buildings from trees. Moreover, they proposed a least square solution with perpendicular constraints for determining regularized rectilinear building boundaries in addition to proposing arc line fitting for the buildings. Hui et al. (2019) presented a threshold-free filtering algorithm based on what they called expectation–maximization and on the assumption that point clouds are seen as a mixture of Gaussian models. They used mixed Gaussian model for partitioning of point clouds for separation of ground points and non-ground points from the point clouds with the application of the expectation–maximization to realize the separation which calculates the maximum likelihood estimates of the mixture parameters.

Tomljenovic et al. (2015) carried out an overview of building extraction approaches applied to Airborne Laser Scanning data through examining elements used in original publications, such as data set area, accuracy measures, reference data for accuracy assessment, and the use of auxiliary data. They stated that the analysis revealed trends and challenges with showing remaining deficiencies such as inconsistent accuracy assessment measures and limitations of independent reference data sources for accuracy assessment. However, they recommended that despite deficiencies, ALS data constituted a valuable source of spatial information for building extraction. In addition, they recommended that taking into account the short civilian history of ALS it can be concluded that ALS has been well established in the scientific community and seemed to become indispensable in many fields. Sithole (2001) described the modifications made to slope based filter for removal of above ground features and explained the slope-based filter assuming that ground slopes do not rise above a certain threshold while features of slopes above this threshold do not belong to the ground surface. Such assumptions limited the use of the filter to terrain with gentle slopes where making modifications to the filter is necessary. So, the filter was modified allowing a varied threshold depending on the ground slope where with the use of the modified filter the number of ground points in steep terrain not filtered off was reduced. Li et al. (2019) explored pavement distress identification using low-altitude Unmanned Aerial Vehicle LiDAR (UAV LiDAR) and Random Forest Classification (RFC) for a section of an asphalt road in the suburb of Shihezi City in Xinjiang Province of China. They carried out spectral and spatial feature analysis of pavement distress of 48 multidimensional and multiscale features extracted based on point cloud elevations and reflection intensities. Then, they extracted the pavement distresses from the dataset by utilizing the RFC method and acknowledged that the overall accuracy of the distress identification was 92.3%, and the kappa coefficient was 0.902. Also, they recommended that their method achieved an overall accuracy of 95.86% with the use of validation dataset.

Shaker and El-Ashmawy (2012) carried out a research aimed at investigation and evaluation of the use of LiDAR data only (range and intensity data) in extracting land cover information. They combined different bands generated from LiDAR data including normal heights, intensity texture, surfaces slopes, and Principal Component Analysis PCA) with the original data for studying the influence of including

these layers on the classification accuracy. Also, they used the maximum likelihood classifier to conduct classification process for LiDAR data and considered it as one of the best classification techniques. Additionally, they selected a study area of an urban district in Burnaby, British Colombia, Canada, to test the different band combinations to extract four information classes namely; buildings, roads and parking areas, trees, and low vegetation areas that can be grass areas. Finally, they recommended that an overall accuracy of more than 70% that can be achieved using the intensity data and other auxiliary data generated from the range and intensity data. Mahadi et al. (2018) carried out a research that aimed at mapping the mangrove coverage and canopy height using airborne LiDAR data at mangrove areas of Sangkulirang district, East Kutai, East Borneo. They used corrected point cloud LiDAR data and classified it into seven classes namely; ground, mangroves, non mangroves, water, vehicle, low point and isolated point. Also, they used ground class as the data source for DTM while they used mangrove as the data source for DSM. Then, they created a Canopy Height Model (CHM) through the subtraction operation (DSM – DTM) where the CHM represented the height of mangroves canopy from land. At the end, they recommended that mangrove distribution had an area of 64.07 km^2 and the height of mangrove canopy was dominated by about 10-30 meters while the maximum height reached 54.04 meters. Feng et al. (2019) stated that urban land-use mapping is a challenging remote sensing activity; however with the availability of diverse remote sensors, integration of multisource data can provide an opportunity for improving urban land-use classification accuracy. They presented a paper that proposed a modified two-branch convolutional neural network for the adaptive fusion of Hyper-Spectral Imagery (HSI) and LiDAR data. Their model consisted of HSI branch and LiDAR branch sharing the same network structure for reduction of the time cost of network design. Also, they utilized a residual block in each branch to extract hierarchical, parallel and multiscale features. In addition, they proposed an adaptive-feature fusion module for integration of HSI and LiDAR features basing on Squeeze-and-Excitation Networks. Moreover, they acknowledged that their two-branch network showed good performance with an overall accuracy of 92% and stated that compared with single-source data, introduction of multisource data improved the accuracy by at least 8%. Finally, they recommended that their proposed network can effectively extract and fuse features for a better urban land-use mapping accuracy.

This study aimed at exploring the different methods for extraction of non-ground features from Airborne LiDAR point clouds for creation of feature layers that can be utilized in a wide range of engineering and environmental applications. The study also, aimed at applying a comparative study of the application of three different filtering techniques namely; Gaussian low pass filter, focal analysis mean filter, and DTM slope-based filter on airborne LiDAR DSM in downtown urban landscape at varying filter window sizes for extraction of reliable and accurate feature layers. In addition, evaluating the effects of the sizes of user defined windows of Gaussian low pass filter, focal analysis mean filter and DTM slope-based filter on the characteristics of the extracted feature layers has been a main objective of the analysis.

2. Materials and Methods

A sample of LiDAR data of the ISPRS WG III/4 Test Project on Urban Classification and 3D Building Reconstruction has been provided by ISPRS WG III/4 and the German Association of Photogrammetry and Remote Sensing (DGPF) (Cramer, 2010). The test data were captured over the City center of Vaihingen in Germany that constitute the downtown of the City on 21 August 2008 by Leica Geosystems using a Leica ALS50 system of 45° field of view and average flying height of 500 meters above ground. The whole airborne laser scanning data set of DGPF comprised 10 strips with average strip overlap of 30% and median point density of 6.7 points /m^2. However, point density varied considerably over the whole block depending on the overlap but in areas covered by only one strip the mean point density was about 4.0 points/m^2 (Rottensteiner et al., 2013). In this study, the file Vaihingen _Strip_09.las has been exploited for extraction and analysis of different quality feature layers through filtering of airborne LiDAR DSM in urban downtown landscapes. In Figure 1, Vaihingen_Strip_09.las test data file represented a complete Airborne laser scanning (ALS) strip that formed a trapezoidal of 1448 meters in length (height) and 495 meters in width at one of the bases and 451 meters in width at the opposite base. Thus, this

ALS strip covered an area of about 684904 of square meters. The sample data consisted of 3,675,745 LiDAR data measurements giving LiDAR point cloud density of 5.368 points per one square meter (pts/m^2). This means that one LiDAR measurement was recorded for every 0.186 square meters in average. The statistical analysis of the dataset has given a minimum elevation of 152.243 meters and a maximum elevation of 348.092 meters producing a range of elevations of 195.849 meters. Additionally, the mean elevation of the dataset is 275.4267 meters, the median is 273.394 meters and the standard deviation is 19.555 meters.

A Digital Surface Model (DSM), Figure 2 has been created from Vaihingen_Strip_09.las LiDAR data file using version 6.4 of SAGA (System for Automated Geoscientific Analyses), an open source GIS software. The Inverse Distance Weighting (IDW) interpolation method with a power of four and grid resolution of half a meter have been used as the interpolation parameters. The generated DSM in Figure 2 has been subjected to filtering operations with Gaussian low pass filter and focal analysis mean filter for extraction of non-ground objects and creation of feature layers in the downtown urban landscape. Filtering of LiDAR DSM have been performed using different window sizes of 3x3, 5x5, 7x7, 9x9, 11x11, 15x15, 21x21, 25x25, 31x31, 35x35 and 41x41 under SAGA 6.4 open source GIS software and Surfer 15 commercial software packages. The generated DTMs from Gaussian low pass filter and focal analysis mean filter of varying window sizes have been algebraically subtracted from the original LiDAR DSM producing different quality feature layers. The extracted feature layers have been subjected to visual and statistical analysis in order to assess the efficiency of the filtering algorithms with different window sizes in creation of reliable feature layers. Also, the original LiDAR DSM have been subjected to filtering operations using DTM slope-based filter under SAGA 6.4 using the same user defined window sizes mentioned above. However, in each filtering operation of LiDAR DSM with DTM slope-based filter the DSM is separated into two models directly; a bare earth model representing a DTM and a removed object model representing a feature layer. The removed object models resulting from the application of the DTM slope-based filter of varying window sizes and representing feature layers have been analyzed visually and statistically and compared with the feature layers extracted from the other two filtering algorithms.

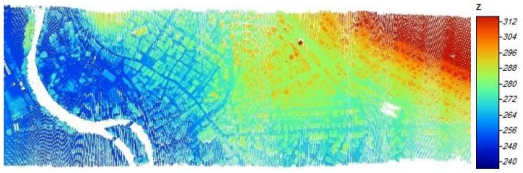

Figure 1: *Point cloud airborne LiDAR dataset created from the data file Vaihingen_Strip_09.las.*

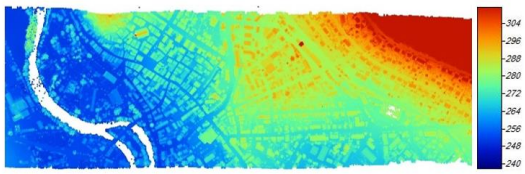

Figure 2: *DSM created from the point cloud airborne LiDAR dataset of the file Vaihingen_Strip_09.las.*

3. Results and Discussion

3.1. Extraction of Feature Layers Using Gaussian Low Pass Filter of Varying Window Sizes

Low pass filtering is a spatial filtering process based on using low pass filters designed to emphasize low spatial frequency features and deemphasize high spatial frequency features of an image in a spatial domain (Lillsand and Kiefer, 2000; Jensen, 2000). Low frequency information of an image represents the background patterns of the image. The output from low pass filtering of a digital image is an image of much of details in the original image have been smoothed or removed. Thus, low pass filtering can be identified as a process of smoothing or blurring a digital image (Jensen, 2005; Mather, 1999). Gaussian low pass filter is a smoothing filter that is used to blur or soften data and remove details and noise from DSMs and raster images. The amount of smoothing is determined by the standard deviation where for higher standard deviations a larger search radius is required (Ringeler, 2003; Abdalla & Elmahal, 2015; Hui et al., 2019). Gaussian low pass filter has been performed on the LiDAR DSM, Figure 2 with varying

window sizes for removal of non-ground features resulting in different quality DTMs that can be utilized in extraction of feature layers. Each one of the created DTMs from Gaussian low pass filter of varying window sizes has been algebraically subtracted from the airborne LiDAR DSM, Figure 2 giving feature layers of different qualities. The resulting feature layers from the subtraction operations have been analyzed visually and statistically in order assess the effects of the filter window size on the characteristics of the extracted feature layers.

Figure 3: *Feature Layer extracted from LiDAR DSM using Gaussian low pass filter of 3x3 window size*

Figure 4: *Feature Layer extracted from LiDAR DSM using Gaussian low pass filter of 7x7 window size*

Figure 5: *Feature Layer extracted from LiDAR DSM using Gaussian low pass filter of 11x11 window size*

Figure 6: *Feature Layer extracted from LiDAR DSM using Gaussian low pass filter of 21x21 window size*

Figures from 3 to 8 depict feature layers extracted from Airborne LiDAR DSM through the application of Gaussian low pass filter using varying window sizes as 3x3, 7x7, 11x11, 21x21, 31x31 and 41x41 respectively. Figure 3 depicts a feature layer produced through application of Gaussian low pass filter with 3x3 window size on the LiDAR DSM. Such feature layer is structured showing most of the details of the downtown landscapes with streets and buildings have been clear. However, the legend in Figure 3 have recorded a range that is between -0.6 and +0.6. This means that Gaussian filter with window size of 3x3 has attenuated a small range of high frequencies since the heights of the downtown features have to be higher than that. With increasing the window size of the filter to 7x7 clearer improvements can be observed where more structured and detailed feature layer has been recorded in Figure 4. However, the legend has recorded heights from -1.6 and 1.6 which has been still less than that expected heights for downtown landscapes. Figure 5 depicts a feature layer of a wider range of heights (-2.4 to 2.4) with clearer representation of the rooftops of the building in blue color tones, however, parts of the downtown landscape still being missed out due to application of Gaussian low pass filter of 11x11 window sizes. Much better representation of the downtown landscapes has been obtained from the application of Gaussian low pass filter of bigger window sizes as shown in Figure 6 which has been obtained due to application of filter window size of 21x21 where more structured feature layer with increasing in the blue color tones representing the rooftops of the buildings and wider ranges of feature heights (-3.2 to 3.2) have been obtained. More increases in the filter window size have not produced much changes of the feature layer 2D views as shown in Figure 7 and 8 which are feature layers resulting from the application of Gaussian filter of window sizes of 31x31 and 41x41 respectively. However, increasing the filter window sizes has increased the ranges of the elevations in the feature layers to be closer to the actual heights of buildings in the downtown landscapes.

Figure 7: *Feature Layer extracted from LiDAR DSM using low pass Gaussian filter of 31x31 window size*

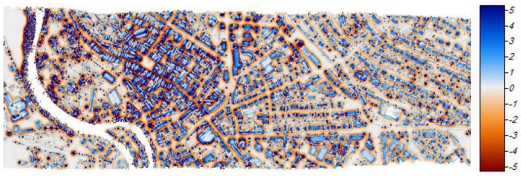

Figure 8: *Feature Layer extracted from LiDAR DSM using low pass Gaussian filter of 41x41 window size*

Table 1 depicts the statistical analysis results of the feature layers extracted from LiDAR DSM through the application of Gaussian low pass filter of varying window sizes of 3x3, 7x7, 11x11, 15x15, 21x21, 25x25, 31x31, 35x35 and 41x41. Form table 1 the minimum heights are in negative values that could be due to spikes resulting from the subtraction operation of the created DTMs from the original DSM, however the absolute minimum height has increased with increasing the window size of the Gaussian low pass filter. Also, the maximum heights in the feature layer and ranges of heights in the feature layer have increased with increasing the filter window sizes. The same can be said on the standard deviation of the feature layer which have increased with increasing the filter window size referring to better extraction of the features of downtown landscape. Also, increasing the filter window size has improved the skewness and kurtosis statistical properties of the created feature layers where increasing the filter window size has provided feature layers of skewness and kurtosis values approaching to zero which means feature layers of more symmetrical Gaussian normal distribution curves in addition more consistent feature layers free from outliers can be obtained from the application of larger window size Gaussian low pass filter.

Table 1: *Statistical analysis results of the feature layers extracted from LiDAR DSM through the application of Gaussian low pass filter of varying window sizes*

Gaussian low pass filter window size	Feature layer from filter 3x3	Feature layer from filter 5x5	Feature layer from filter 7x7	Feature layer from filter 11x11	Feature layer from filter 15x15	Feature layer from filter 21x21	Feature layer from filter 25x25	Feature layer from filter 31x31	Feature layer from filter 35x35	Feature layer from filter 41x41
	-	-	-	-	-	-	-	-	-	-
Min. (m)	22.955	51.576	57.768	61.174	61.939	61.345	60.752	60.138	59.545	58.741
Max. (m)	8.643	19.857	21.093	22.468	27.024	28.799	29.399	29.780	30.218	32.827
Mean (m)	0.000	0.000	0.000	0.000	-0.002	-0.004	-0.005	-0.006	-0.007	-0.008
Median (m)	-0.001	-0.003	-0.005	-0.011	-0.033	-0.085	-0.133	-0.187	-0.244	-0.328
Range (m)	31.598	71.433	78.861	83.642	88.963	90.144	90.151	89.919	89.763	91.568
Standard Deviation (m)	0.324	0.780	0.954	1.218	1.568	1.885	2.078	2.256	2.420	2.640
Skewness (m)	-1.993	-1.793	-1.431	-0.798	-0.285	-0.018	0.099	0.189	0.262	0.351
Kurtosis (m)	83.249	66.253	48.422	26.757	13.780	9.037	7.498	6.539	5.905	5.293

3.2. Extraction of Feature Layers Using Focal Analysis Mean Filter of Varying Window Sizes

Focal analysis mean filter has been recommended by some authors as a method for smoothing of the DSMs and attenuation of the high frequencies (e.g. Priestnall et al., 2001; Sharma et al., 2010). In this study, focal analysis mean filter has been performed on airborne LiDAR DSM, Figure 2 with varying window sizes for extraction of non-ground features and depicting them in a separate feature layer through creation of a DTM. The created DTMs from focal analysis mean filtering of the LiDAR DSM at varying window sizes have been algebraically subtracted from the original DSM, Figure 2 for extraction of feature layers of varying qualities. The extracted feature layers have been subjected to visual and statistical analysis in order to assess the effects of changing the window size of the focal analysis mean filter on the characteristics of that feature layers.

Figures from 9 to 14 depict feature layers extracted from focal analysis mean filtering of Airborne LiDAR DSM, Figure 2 with window sizes of 3x3, 7x7, 11x11, 21x21, 31x31 and 41x41 respectively. Similar to the feature layer extracted using 3x3 Gaussian low pass filter the feature layer from 3x3 window size, Figure 9 is structured showing all the details of the downtown landscapes including streets and buildings. However, the legend in figure 9 is of higher range (from -1.2 to +1.2) compared to that in Figure 3 that has been between -0.6 and +0.6. This means that focal analysis filter 3x3 has achieved better removal of the non-ground features compared to Gaussian low pass filter with similar window size. With increasing the window size of the filter to 7x7 more structured and more detailed feature layer has been obtained in Figure 10. This has been clear in the wider representation of the color tones and representation of the rooftops of the buildings in blue color tones referring to higher elevation features. Also, the range of the heights in the feature layer has been between -2.0 and 2.0, however it has been still less than the expected heights for the downtown landscapes. Figure 11 depicts a feature layer of wider range of heights (-2.4 to 2.4) with clearer representation of the rooftops of the building in blue color tones, however, parts of the downtown landscape have been missed out with the application of focal analysis mean filter of 11x11 window size. Better representation of the downtown landscapes has been obtained from the application of focal analysis mean filter of bigger window sizes that has been clear in Figure 12 obtained from the application of filter window size of 21x21 where more structured feature layer with increases in blue color tones representing the rooftops of the buildings and wider ranges of feature heights (-4 to 4) have been recorded in the legend. More increases in the filter window size have produced considerable changes of the feature layer as shown in Figure 13 and 14 which represent feature layers resulting from the application of filter of window sizes of 31x31 and 41x41 respectively. In Figure 13 and 14 the blue color tones have increased and become darker referring to higher urban features. Also, wider ranges of feature heights have been represented in Figure 13 and 14 as -5 to +5 and -6 to +6 respectively.

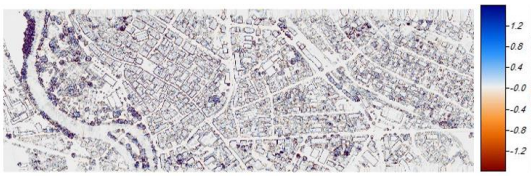

Figure 9: *Feature Layer extracted from LiDAR DSM using focal analysis mean filter of 3x3 window size*

Figure 10: *Feature Layer extracted from LiDAR DSM using focal analysis mean filter of 7x7 window size*

Figure 11: *Feature Layer extracted from LiDAR DSM using focal analysis mean filter of 11x11 window size*

Figure 12: *Feature Layer extracted from LiDAR DSM using focal analysis mean filter of 21x21 window size*

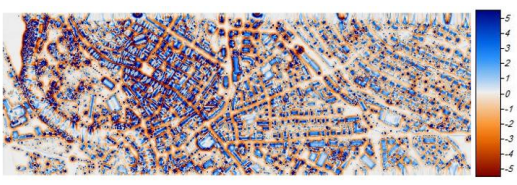

Figure 13: *Feature Layer extracted from LiDAR DSM using focal analysis mean filter of 31x31 window size*

Figure 14: *Feature Layer extracted from LiDAR DSM using focal analysis mean filter of 41x41 window size*

Table 2: *Statistical analysis results of the feature layers extracted from LiDAR DSM due to application of focal analysis mean filter of varying window sizes*

Focal analysis mean filter window size	Feature layer from filter 3x3	Feature layer from filter 5x5	Feature layer from filter 7x7	Feature layer from filter 11x11	Feature layer from filter 15x15	Feature layer from filter 21x21	Feature layer from filter 25x25	Feature layer from filter 31x31	Feature layer from filter 35x35	Feature layer from filter 41x41
Min. (m)	-59.240	-65.592	-67.295	-67.996	-67.562	-66.085	-65.134	-64.096	-63.705	-70.759
Max. (m)	21.328	18.535	23.286	27.872	29.039	29.931	30.214	32.733	34.112	35.463
Mean (m)	0.000	0.000	0.000	0.000	0.000	0.001	0.001	0.002	0.003	0.005
Median (m)	-0.001	-0.004	-0.007	-0.018	-0.042	-0.114	-0.176	-0.276	-0.341	-0.430
Range (m)	80.568	84.127	90.581	95.869	96.600	96.016	95.347	96.829	97.817	106.222
Standard Deviation (m)	0.795	0.976	1.145	1.468	1.771	2.185	2.430	2.752	2.938	3.178
Skewness (m)	-1.855	-1.437	-0.961	-0.413	-0.168	-0.026	0.000	-0.012	-0.036	-0.081
Kurtosis (m)	83.733	51.952	34.028	17.280	11.890	10.349	10.830	12.428	13.752	15.819

Table 2*: depicts the statistical analysis results of the feature layers extracted from LiDAR DSM through application* of focal analysis mean filter of varying window sizes of 3x3, 7x7, 11x11, 15x15, 21x21, 25x25, 31x31, 35x35 and 41x41. Form Table 2 the minimum heights have been in negative values that can be due to outliers resulting from the subtraction of the created DTM from the original DSM, however the minimum heights of the feature layers have decreased with increasing the window size of the focal analysis mean filter. Also, the maximum heights in the feature layer and consequently the ranges of heights in the feature layers have increased with increasing the filter window sizes. The same can be said on the standard deviation of the feature layer which have increased with increasing the filter window size referring to better extraction of high features in downtown landscape due to increasing the filter window sizes. Also, increasing the filter window sizes has left noticeable decreases on the absolute values of the skewness and kurtosis which refers to improvements in the statistical properties of the extracted feature layers. This means feature layers of more symmetrical Gaussian normal distribution curves and more consistent feature layers free from outliers can be obtained from the application of the focal analysis mean filter with larger window sizes.

3.3. Extraction of Feature Layers Using DTM Slope-Based Filter of Varying Window Sizes

DTM slope-based filter is a grid filtering approach that works under the open source GIS software namely; SAGA (System for Automated Scientific Analysis). This filtering approach can be used to filter a DSM to classify the grid cells into a bare earth layer and a removed object layer where these layers can be also known as DTM layer and non-ground feature layer respectively. Such filtering approach has been basing on the concepts described by Vosselman (2000) assuming that a big elevation difference between two neighboring grid cells is unlikely to be caused by a steep slope in the terrain (Wichmann, 2010; Vosselman, 2000). Thus, the probability that the higher elevation value grid cell could be a ground point decreases if the distance between the two grid cells decreases. In addition, the filter defines the acceptable height difference between the two grid cells as a function of the distance between them. Then, the grid cell is classified as ground if there is no other grid cell within the filter search radius such that the height difference between these grid cells is larger than the allowed maximum height difference at the distance between these grid cells. Moreover, an approximate ground surface slope variable is used to modify the filter function to match the overall slope in the whole DSM area. Furthermore, a confidence interval could be applied for omission of blunders (Wichmann, 2010; Sithole, 2001; Sithole & Vosselman, 2003).

Figure 15: *Feature layer extracted from LiDAR DSM with the use of DTM slope-based filter of 3x3 window size*

Figure 16: *Feature layer extracted from LiDAR DSM with the use of DTM slope-based filter of 7x7 window size*

Figure 17: *Feature layer extracted from LiDAR DSM with the use of DTM slope-based filter of 11x11 window size*

Figure 18: *Feature layer extracted from LiDAR DSM with the use of DTM slope-based filter of 21x21 window size*

Figure 19: *Feature layer extracted from LiDAR DSM with the use of DTM slope-based filter of 3x31 window size*

Figure 20: *Feature layer extracted from LiDAR DSM with the use of DTM slope-based filter of 41x41 window size*

Figures from 15 to 20 depict removed object models that represent feature layers produced directly from the application of the DTM slope-based filter on airborne LiDAR DSM, Figure 2 with window sizes of 3x3, 7x7, 11x11, 21x21, 31x31 and 41x41 respectively. As shown in the Figures from 15 to 20 the DTM slope-based filter has extracted non- ground objects to create feature layers that has been very detailed with keeping the actual elevations of the different features. This has been very different from the cases of the Gaussian low pass filter and the focal analysis mean filter where subtraction operations have been necessary to separate the feature layer from the DSM with the use of the filtered out DTM. Two-dimensional visual analysis of the feature layers, Figures from 15 to 20 has been unable to show distinguishable differences between the obtained feature layers since they show similar color tone distribution, very close textures and almost the same patterns. Even the accompanied legend with the extracted feature layers depict the same ranges of elevations and the same elevation values.

Table 3 depicts the statistical analysis results of the feature layer extracted from airborne LiDAR DSM using DTM slope-based filter of varying window sizes. The statistical analysis of the feature layers has shown clear changes in the minimum elevations of the feature layers which decrease due to increasing the filter window sizes referring to better extraction of the non-ground features. This has not been the case with the maximum elevations in the feature layers which have been kept unchanged with increasing the DTM slope-based filter window sizes. The values of the minimum and maximum elevations have been reflected on the ranges of elevations, since the range of elevations in the feature layer is calculated as the algebraic difference between the maximum elevation and the minimum elevation. Thus, the ranges of elevations in the feature layers have increased with increasing the window sizes of the DTM slope-based filter. Also, the standard deviations of the extracted feature layers have increased with increasing the filter window sizes. On the other hand, increasing the

window sizes of the DTM slope-based filter has resulted in decreases in the skewness and kurtosis of the feature layers and consequently improvements of the statistical properties of the feature layers. Thus, the feature layers obtained from bigger window sizes have been of more symmetrical Gaussian normal distribution curves and of more consistent elevations and free from outliers.

Table 3: *Statistical analysis results of the removed object models namely; non-ground feature layers extracted from airborne LiDAR DSM using DTM slope-based filter of varying window sizes*

DTM Slope based filter window size	Feature layer from filter 3x3	Feature layer from filter 5x5	Feature layer from filter 7x7	Feature layer from filter 11x11	Feature layer from filter 15x15	Feature layer from filter 21x21	Feature layer from filter 25x25	Feature layer from filter 31x31	Feature layer from filter 35x35	Feature layer from filter 41x41
Min. (m)	243.163	242.102	242.102	242.102	223.487	223.487	223.487	223.487	223.487	223.487
Max. (m)	347.968	347.968	347.968	347.968	347.968	347.968	347.968	347.968	347.968	347.968
Mean (m)	276.778	276.937	277.032	277.173	277.256	277.298	277.290	277.267	277.253	277.239
Median (m)	275.105	275.278	275.385	275.543	275.631	275.683	275.686	275.666	275.651	275.641
Range (m)	104.804	105.866	105.866	105.866	124.480	124.480	124.480	124.480	124.480	124.480
Standard Deviation (m)	17.836	17.911	17.945	17.972	17.984	17.981	17.962	17.941	17.936	17.929
Skewness (m)	1.013	0.999	0.992	0.983	0.979	0.978	0.979	0.981	0.983	0.985
Kurtosis (m)	4.290	4.237	4.213	4.184	4.173	4.173	4.180	4.191	4.197	4.203

3.4. Comparative Analysis of the Feature Layer Extracted with the Use of Different Filtering Approaches

Figures from 21 to 24 depict charts of the statistical analysis of the feature layers extracted from airborne LiDAR DSM through the application of the three filtering approaches; Gaussian low pass filter, focal analysis mean filter and DTM slope-based filter with varying sizes. Figure 21 depicts the relationship between the ranges of elevations in the feature layers extracted from LiDAR DSM using the different filtering techniques and the filter window sizes. From that Figure the ranges of elevations in the feature layers from the three filtering approaches have increased with increasing the window size till window size of 15x15 where the ranges of elevations have recorded slight changes with more increases in the window sizes. The situation is a bit different when studying the standard deviation of the extracted feature layers from the different filtering approaches against the filter window size, see Figure 22. Thus, the standard deviations of the extracted feature layers have increased with relatively high rates due to increasing the window sizes of Gaussian low pass and focal analysis mean filters, however increasing the window sizes of DEM slope-based filter have produced increases in the standard deviation of the extracted feature layers but at very small rates. Figure 23 depicts the relationship between the skewness of the extracted feature layers from the three different filtering techniques against the filter window sizes. In this Figure, increasing the window size of Gaussian low pass filter and the focal analysis mean filter have resulted in increases in the skewness values letting them approaching to zero till window size of 21x21. This means that the feature layer from Gaussian low pass and focal analysis mean filter of window size of 21x21 have been almost of symmetrical Gaussian normal distribution curves. However, in the case of the feature layers produced from the application of the DTM slope-based filter the skewness property of the extracted feature layer has decreased towards the zero-value due to increasing the window sizes but with very small rates.

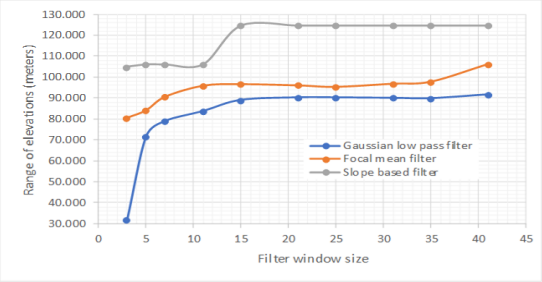

Figure 21: *The relationship between the ranges of elevations in the feature layers and the filter window size*

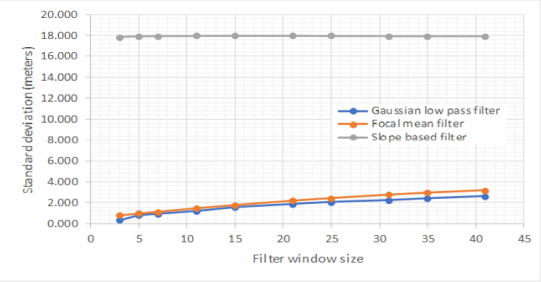

Figure 22: *The relationship between the standard deviations of elevations in the feature layers and the filter window size*

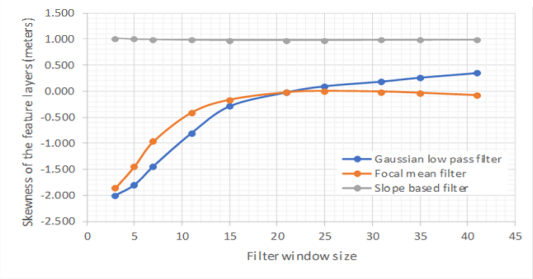

Figure 23: *The relationship between the skewness of the feature layers and the filter window size*

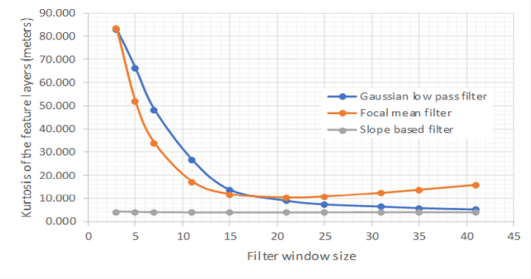

Figure 24: *The relationship between the kurtosis of the feature layers and the filter window size*

Figure 24 represents the relationship between the kurtosis of the produced feature layers and the filter window sizes. From Figure 24 it can be seen that increasing the window sizes of the Gaussian low pass filter and the focal analysis mean filter have produced decreases in the Kurtosis of the extracted feature layers. These decreases in the kurtosis values have been dramatic till window size of 21x21 in the cases of the Gaussian low pass filter and focal analysis mean filter while it has been very small in the feature layers extracted using these two filtering approaches with larger window sizes. The situation is different in the case of the feature layer extracted using the DTM slope-based filter since increasing the filter window size have produced decreases and consequently improvements in the kurtosis of the extracted feature layers but the rate of decreases has been very slight. In general, it can be recommended that applications of the three filtering approaches with increases in the window sizes have produced better removal of noise and outliers giving more consistent feature layers.

4. Conclusion

Extraction and analysis of feature layers from airborne LiDAR measurements has been an important application of airborne LiDAR point clouds in mapping and modelling of the environment. This study has concerned with exploring the different methods for extraction of the non-ground features from Airborne LiDAR measurements in order to create reliable feature layers that can be utilized in a wide range of engineering and environmental. The study also, aimed at applying a comparative study of the application of three main filtering techniques namely; Gaussian low pass filter, focal analysis mean filter, and DTM slope-based filter on airborne LiDAR DSMs in downtown urban landscapes at varying filter window sizes for extraction of reliable accurate feature layers. A dataset of airborne LiDAR measurements of the ISPRS WG III/4 test project on urban classification and 3D building reconstruction that was captured over the downtown of Vaihingen in Germany on 21 August 2008 by Leica Geosystems has been exploited in this research. Visual analysis has shown that Gaussian low pass filter with window size of 3x3 has attenuated a small range of the LiDAR DSM high frequencies however with increasing the window size of the filter to 7x7 clearer improvements have been observed where more structured and detailed feature layer has been obtained. However, much detailed and structured feature layer has been obtained from window size of 21x21 that has been interpreted in

increasing of the amounts of the blue color tones representing the rooftops of the buildings and wider ranges of feature heights. Focal analysis mean filter has achieved better removal of the non-ground features compared to Gaussian low pass filter of similar window size. Also, much better representation of the downtown landscapes has been obtained from the application of focal analysis mean filter of window size of 21x21 and larger where more structured feature layer with increases in blue color tones representing the rooftops of the buildings and wider ranges of feature heights have been obtained. DTM slope-based filter has extracted feature layers that have been different from those extracted by Gaussian low pass filter and focal analysis mean filter since varying the window size of the DTM slope-based filter have not left noticeable effects on the produced feature layers.

Statistical analysis of the feature layers from different filtering approaches has indicated that the ranges of elevations in the feature layers from the three filtering approaches have increased with increasing the window size till window size of 15x15 where slight changes in the ranges have occurred with more increases in the window sizes. Also, the standard deviations of the extracted feature layers have increased with considerable rates due to increasing the window sizes of the Gaussian low pass and focal analysis mean filters, however increasing the filter window size has produced increases on the standard deviation of the extracted feature layers from DTM slope-based filter but with very small rates. Additionally, increasing the window size of Gaussian low pass filter and the focal analysis mean filter have produced skewness of absolute values approaching to zero till window size of 21x21 which refers to improvements in the statistical properties of the feature layers. However, in the case of the feature layers produced from the application of the DTM slope-based filter the skewness of the extracted feature layer has decreased towards the zero-value due to increasing the window sizes but with very small rates which means that the feature layer from DTM slope-based filter have not been of Ideal symmetrical Gaussian normal distribution curves. Moreover, dramatic decreases in the kurtosis of the feature layers have occurred due to decreases in the window sizes of the filter till window size of 21x21 in the cases of Gaussian low pass filter and focal analysis mean filter while decreases in kurtosis have been very mild due to more increases in the filter window sizes. However, increasing the window size of the DTM-slope based filter have produced slight decreases in the kurtosis of the extracted feature layers. In general, it can be recommended that application of the three filters with increases in the window sizes has produced more consistent feature layers with less noise and less outliers. The outcomes from exploitation of the extracted feature layers in different applications could help extraction of the optimum feature layer from airborne LiDAR measurements.

Acknowledgements

The Vaihingen data set was provided by the German Society for Photogrammetry, Remote Sensing and Geoinformation (DGPF) [Cramer, 2010]: *http://www.ifp.uni-stuttgart.de/dgpf/DKEP-Allg.html.*

References

Abdalla, A. and Elmahal, A.El. 2015. Augmentation of vertical accuracy of digital elevation models using gaussian linear convolution filter. *International Conference on Computing, Control, Networking, Electronics and Embedded Systems Engineering*, Sudan.

Büyüksalih, İ. and Gazioğlu, C. 2019. New Approach in Integrated Basin Modelling: Melen Airborne LiDAR. *International Journal of Environment and Geoinformatics (IJEGEO),* 6(1), pp. 22-32.

Cramer, M. 2010. The DGPF test on digital aerial camera evaluation – overview and test design. *Photogrammetrie – Fernerkundung – Geoinformation*, 2, pp.73-82.

El-Garouani, A., Alobeid, A. and El Garouani, S. 2014. Digital surface model based on aerial image stereo pairs for 3D building. *International Journal of Sustainable Built Environment*, 3, pp.119-126.

Feng, Q., Zhu, D., Yang, J. and Li, B. 2019 Multisource Hyperspectral and LiDAR Data Fusion for Urban Land-Use Mapping based on a Modified Two-Branch Convolutional Neural Network. *ISPRS Int. J. Geo-Inf.*, 8, p.28.

Grohmann, H., Smith, M.J., C.H., Riccomini, C., 2011. Multi-scale Analysis of Topographic Surface Roughness in the Midland Valley, Scotland. *IEEE Transactions on Geoscience and Remote Sensing*, 49, pp.1200-1213.

Grohmann, H., Smith, M.J., C.H. and Riccomini, C. 2009. Surface roughness of topography: a multi-scale analysis of landform elements in Midland Valley, Scotland. *Proceedings of Geomorphometry*, Zurich, Switzerland.

Heinzel, J. and Ginzler, C. 2019. A single-tree processing framework using terrestrial laser scanning data for detecting forest regeneration. *Remote Sens.*, 11, p.60.

Hui, Z., Li, D., Jin, S., Ziggah, Y.Y., Wang, L., Hu, Y. 2019. Automatic DTM extraction from airborne lidar based on expectation- maximization. *Optics and Laser Technology*, 112, pp.43–55.

Jawaka, S.D., Panditraob, S.N. and Luisa, A.J. 2014. Airborne LiDAR and high-resolution satellite data for rapid 3d feature extraction. *The International Archives of the Photogrammetry, Remote Sensing and Spatial Information Sciences*, Volume XL-8, 2014 ISPRS Technical Commission VIII Symposium, Hyderabad, India.

Jensen, J. 2005. *Introductory digital image processing – a remote sensing perspective*. Third Edition. Pearson Prentice Hall, Upper Saddle River, New Jersey, USA.

Jensen, J. 2000. *Remote sensing of the environment: an earth resource perspective*. Pearson Prentice Hall, Upper Saddle River, New Jersey.

Li, Z., Cheng, C., Kwan, M.P., Tong, X., and Tian, S. 2019. Identifying asphalt pavement distress Using UAV LiDAR point cloud data and random forest classification. *ISPRS Int. J. Geo-Inf.*, 8, p.39.

Lillesand, T.M. and Kiefer, R.W. 2000. *Remote Sensing and Image Interpretation*. Fourth Edition, John Wiley & Sons, Inc.

Liu, C., Li, J., Zhang, S. and Ding, L. 2012. A point clouds filtering algorithm based on grid partition and moving least squares. *Procedia Engineering*, 28, pp.476-482.

Liu, C., Shi, B., Yang, X., Li, N. and Wu, H. 2013. Automatic buildings extraction from LiDAR data in urban area by neural oscillator network of visual cortex. *IEEE Journal of Selected Topics in Applied Earth Observations and Remote Sensing*, 6(4), pp.2008-2019.

Mahadi, A.T., Sirega, V.P. and Nursugi. 2018. Mapping of mangrove coverage and canopy height using LiDAR data at Sangkulirang District, East Kutai, East Borneo. *IOP Conf. Ser.: Earth Environ. Sci*.

Mather, P.M. 1999. *Computer processing of remotely-sensed images: an introduction*. Second Edition, John Wiley & Sons Ltd., Baffins Lane, Chichester, West Sussex P019 1UD, England.

Perko, R., Raggam, H., Gutjahr, K.H. and Schardt, M. 2015. Advanced DTM generation from very high-resolution satellite stereo images. *ISPRS Annals of the Photogrammetry, Remote Sensing and Spatial Information Sciences*, Volume II-3/W4, PIA15+HRIGI15 – Joint ISPRS conference, Munich, Germany.

Priestnall, G., Jaafar, J. and Duncan, A. 2001. Extracting urban features from LiDAR digital surface models. *Computers, Environment and Urban Systems*, 24, pp.65-78.

Ringeler, A. 2003. *Module Gaussian Filter. SAGA-GIS Module Library Documentation (v2.2.5).* Available from: *http://www.saga-gis.org/saga_tool_doc/2.2.5/grid_filter_1.html*.

Rottensteiner, F., Sohn, G, Gerke, M. and Wegner, J.D. 2013. ISPRS *Test Project on Urban Classification and 3D Building Reconstruction*. ISPRS - Commission III - Photogrammetric Computer Vision and Image Analysis, Working Group III / 4 - 3D Scene Analysis. Available from: *http://www.commission3.isprs.org/wg4/.*

Sevgen, S. C. 2019. Airborne lidar data classification in complex urban area using random forest: a case study of Bergama, Turkey. *International Journal of Engineering and Geosciences*; 4(1), pp.045-051.

Shaker, A. and El-Ashmawy, N. 2012. Land cover information extraction using LiDAR data. *International Archives of the Photogrammetry, Remote Sensing and Spatial Information Sciences*, Volume XXXIX-B7, 2012, XXII ISPRS Congress, Melbourne, Australia.

Sharma, M., Paige, G.B. and Miller, S.N. 2010. DEM development from ground-based LiDAR data: a method to remove non-surface objects. *Remote Sens.,* 2, pp.2629-2642.

Sithole, G. 2001. Filtering of laser altimetry data using a slope adaptive filter. *International Achieves of Photogrammetry and Remote Sensing,* Volume XXXIV-3/W4 Annapolis, 2001.

Sithole, G. and Vosselman, G. 2003. *Report: ISPRS Comparison of Filters*. ISPRS Commission III, Working Group 3 & Department of Geodesy, Faculty of Civil Engineering and Geosciences Delft University of Technology the Netherlands.

Tomljenovic, I., Höfle, B., Tiede, D. and Blaschke, T. 2015. Building extraction from airborne laser scanning data: an analysis of the state of the art. *Remote Sens*., 7, pp.3826-3862.

Uzar, M. and Yastikli, N. 2013. Automatic building extraction using LiDAR and aerial photographs. *Bol. Ciênc. Geod*., sec. Artigos, Curitiba, 19(2), pp.153-171.

Vosselman, G. 2000. Slope based filtering of laser altimetry data. *IAPRS, Vol. XXXIII, Part B3*, Amsterdam, The Netherlands. pp.935-942.

Vosselman, G. and Maas, H.G. 2001. Adjustment and filtering of raw laser altimetry data. *Proceedings of OEEPE Workshop on Airborne Laserscanning and Interferometric SAR for Detailed Digital Terrain Models*.

Wang, K., Wang, T. and Liu, X. 2019. A review: individual tree species classification using integrated airborne LiDAR and optical imagery with a focus on the urban environment. *Forests*, 10, p.1.

Wichmann, V. 2010. *Module DTM Filter (slope-based). SAGA-GIS Module Library Documentation (v2.2.5).* Available from*: http://www.saga-gis.org/saga_tool_doc/2.2.5/grid_filter_7.html*.

Cloud Publications
International Journal of Advanced Remote Sensing and GIS
2019, Volume 8, Issue 1, pp. 3073-3095
ISSN 2320 – 0243, Crossref: 10.23953/cloud.ijarsg.422

Research Article

Impact of the Accuracy of Land Cover Data sets on the Accuracy of Land Cover Change Scenarios in the Mono River Basin, Togo, West Africa

Djan'na H. Koubodana[1, 2, 3], Bernd Diekkrüger[2], Kristian Näschen[2], Julien Adounkpe[1], Kossi Atchonouglo[3]

[1]West Africa Science Service Centre on Climate change and Adapted Land Use, WASCAL-Climate Change and Water Resources, University of Abomey Calavi, 03 BP 526 Cotonou, Benin
[2]Department of Geography, University of Bonn, Meckenheimer Allee 166, 53115 Bonn, Germany
[3]Faculty of Sciences, University of Lomé, Po. Box 1515 Lomé, Togo

Correspondence should be addressed to Djan'na H. Koubodana, *koubo2014@gmail.com*

Publication Date: 2 August 2019

DOI: https://doi.org/10.23953/cloud.ijarsg.422

Abstract Knowledge about land use and land cover (LULC) dynamics is of high importance for a number of environmental studies including the development of water resources, land degradation and food security. Often, available global or regional data sets are used for impact studies, although they have not been validated for the area of interest. Validation is especially required if data are used to set up a land change model predicting future changes for management purposes. Therefore, three different LULC maps of the Mono River Basin in Togo were evaluated in this study. The analyzed maps were obtained from three sources: CILSS (2 km resolution), ESA (300 m), and Globeland (30m) datasets. Validation was performed using 1,000 reference points in the watershed derived from satellite images. The results reveal CILSS as the most accurate data set with a Kappa coefficient of 68% and an overall accuracy of 83%. CILSS data shows a decrease of savanna and forest whereas an increase of cropland over the period 1975 to 2013. The increase of cropland area of 30.97% from 1975 to 2013 can be related to the increase in population and their food demand, while the losses of forest area and the decrease of savanna are further amplified by using wood as energy sources and the lack of forest management. The three datasets were used to simulate future LULC changes using the Terrset Land Change Modeler. The validation of the model using CILSS data for 2013 showed a quality of 50.94%, it is only 40.04% for ESA and 20.13% for Globeland30. CILSS data was utilized to simulate the LULC distribution for the years 2020 and 2027 because of its satisfactory performances. The results show that a high spatial resolution is not a guarantee of high quality. The results of this study can be used for impact studies and to develop management strategies for mitigating negative effects of land use and land cover change.
Keywords *Land cover maps; Land cover scenario; Land Change Modeler (LCM); transition probabilities*

1. Introduction

Land use and land cover (LULC) change in West Africa is mostly caused by population growth, although locally other drivers may be of importance (Atsri et al., 2018). With increasing population

demand for food, energy, and water is also increasing (Lambin et al., 2003), which causes land use and land cover changes (LULCC). West Africa is a region facing severe LULCC, particularly in the Republic of Togo (TG) and the Republic of Benin (BN), which are experiencing an environmental and social decline resulting in increasing subsistence farming. This causes an acceleration of the degradation of the natural resources and the increase of agricultural area due to rapid population and economic growth (Koglo et al., 2018).

Land use refers to "man's activities on land which are directly related to the land," while land cover is "the vegetation and artificial constructions covering the land surface" (Anderson et al., 1976). LULCC in West African countries are driven by natural and anthropogenic factors. The anthropogenic factors are mainly related to demographic growth (Brink and Eva, 2009), while the natural factors are linked to climate variability and climate change (Koubodana, 2015; Oguntunde et al., 2006). LULCC influence hydrological processes as agricultural intensification results in increased surface runoff, reduced groundwater recharge, and transfer of pollutants (Veldkamp and Lambin, 2001). Knowledge about LULC dynamics at the watershed scale is indispensable for water and land resource management (Eisfelder et al., 2012; Wisser et al., 2010).

LULC products from remote sensing are often the input for environmental modeling and analysis. This is the case in hydrologic modeling and trend analysis (Wisser et al., 2010), biomass and energy modeling (Eisfelder et al., 2012), population density modeling (Sutton, 1997) as well as risk and hazard analysis (Herbst et al., 2006; Mishra et al., 2014).

In many studies, LULC assessment has been performed with data available from the U.S Geological Survey (USGS). These products are developed on a large, often global scale and applying them to the local scale without any validation can significantly affect the model results and future scenario development (Pontius and Neeti, 2010; Sun and Robinson, 2018). In the present study, the impact of the LULC data sets accuracy on future scenarios in the Mono River Basin (MRB) was investigated.

For LULCC analysis and future scenario prediction, a number of models have been developed like the GEOMOD, the Cellular Automata (CA) and STCHOICE (Arsanjani et al., 2013) and applied in a number of studies (Herbst et al., 2006; Mishra et al., 2014). A comparison of four statistical approaches of these models (Markov chain, logistic regression, generalized additive models, and survival analysis) was done by Sun and Robinson (2018) to detect their ability to quantify LULC changes and to perform prediction. The results show that the generalized additive model performs better for overall accuracy and is best for LULC validation and modeling. For example, Pontius and Neeti (2010); Pontius and Spencer. (2005) analyzed the uncertainty of future LULC scenarios and discussed techniques to quantify the meaningful differences between future scenarios using the GEOMOD model. However, each land cover modeling approach was developed with different strengths, weaknesses, and applications (Mas et al., 2014). A number of studies on LULCC used computation of transition potentials, the spatial trend change analysis and land cover change prediction using the Land Change Modeler (LCM), a tool in the TerrSet Geospatial Monitoring and Modeling System integrated in the IDRISI software (Du et al., 2012; Eastman, 2006). This LCM software provides a robust set of tools for change analysis and spatial trend analysis utilizing different variables as drivers for future scenarios computation (Eastman, 2006; Mishra and Singh, 2010). Generally, LULC data are required for the analysis of the past, but also for developing LULC scenarios (Rounsevell et al., 2006). Thus, validated data are used to analyze the drivers of change in the past and to project them for the future (Pontius et al., 2001).

The methodology described by Olofsson et al. (2013); Pontius and Malanson (2014) to detect or to compare LULCC often used in the generation of LULC maps can also be applied for evaluating the results of different scenarios. Peixoto et al. (2006); Stehman. (2009) have described the method of spatial accuracy assessment by sampling approach and have proposed this method as appropriate for land cover accuracy assessment. The analysis of Pontius and Millones (2011) discussed the

limitations of comparing two maps using the Kappa coefficient and proposed a new methodology for comparison namely “quantify disagreement and allocation disagreement”. Nevertheless, the Kappa coefficient is still considered as a vital tool for accuracy assessment measurement in a number of studies (Biondini and Kandus, 2006; Milad et al., 2017; Ren et al., 2018; Sitthi et al., 2016).

This study analyzes LULCC in the MRB from 1975 to 2013 using different data sources and simulates potential future LULC distributions. The main objective of this study is therefore to assess the accuracy of past and future land cover changes in the MRB using different data sets. The specifics objectives are: (i) to analyze the past LULCC in the MRB using three different data products, (ii) to project future LULC considering population growth as the main driver and (iii) to determine how the choice of the data set will influence projected future LULC accuracy.

2. Materials and Methods

2.1. Study area

The study area is the Mono River Basin (MRB) in West Africa. The study area was selected for LULCC change analysis because of huge environmental problems like flooding downstream of the Nangbéto dam, soil erosion and dam-siltation caused by agricultural intensification, and cutting of trees, all exacerbated by the non-existence of any cooperative communal structure and reduced livelihood opportunities (SAWES, 2011). The MRB is the second largest river in Togo, and shared with the Republic of Benin. The basin is located between 06°16’ and 9°20’North latitude and 0° 42’and 1° 40' East longitude (Figure 1). At the outlet at Athiémé, the basin covers an area of 22,014 km^2 with 88% of its area in Togo and the 12% in Benin (PCCP, 2008). The MRB is 309 km long, has its source in the Alédjo Mountains (Amoussou, 2010) in the north of Benin and drains into the Atlantic Ocean via ”la bouche du roi”. The elevation of the basin ranges from 12 to 948 meters (http://srtm.csi.cgiar.org/). The biggest dam on the river is at Nangbéto and produces 20% of the total hydroelectricity used by Togo and Benin.

The watershed area encompasses two climate zones. In the south, from 6° to 8°N, two rainy seasons and two dry seasons exist with rainfall between 1200 and 1500 mm/year in the mountainous area of the southwest and 800 to 1000 mm/year in the coastal zone.

The natural vegetation is mainly savanna and is composed of the bush and tree savanna, gallery forests, and grassland. The relief is generally flat, except for the mountainous regions of the West and the Northwest. In the lower part of the basin, there are very narrow coastal sedimentary island, often covered by alluvial deposits.

In 2011, the MRB was populated by about 5.1 million inhabitants (FAO, 2012; PCCP, 2008; SAWES, 2011). The main socioeconomic activities are agriculture, trade, fisheries and livestock husbandry (Amoussou, 2010). According to FAO (http://worldpopulationreview.com/countries/togo- population), the population in Togo has tripled since 1975 and is still increasing (Table 1).

Table 1: *Past and future scenarios of population (millions of inhabitants) in Togo from 1975 to 2050*

Year (T)	1975	2000	2010	2015	2020	2025	2030	2035	2040	2045	2050
Population (P)	2.40	4.90	6.50	7.40	8.34	9.41	10.5	11.66	12.86	14.08	15.29
Growth rate (K)	-	2.86	2.83	2.59	2.39	2.41	2.19	2.10	1.96	1.80	1.66

Source: World Population, 2018 (*http://worldpopulationreview.com/*)

Where K (%) is growth rate estimated from reported population data assuming exponential growth as given in Eq. (1):

$$P = P_0 \, Exp\left(\frac{K}{100} \Delta t\right) \quad (1)$$

and P is the population value at time $t + \Delta t$, P_0 is the initial population value at t_0.

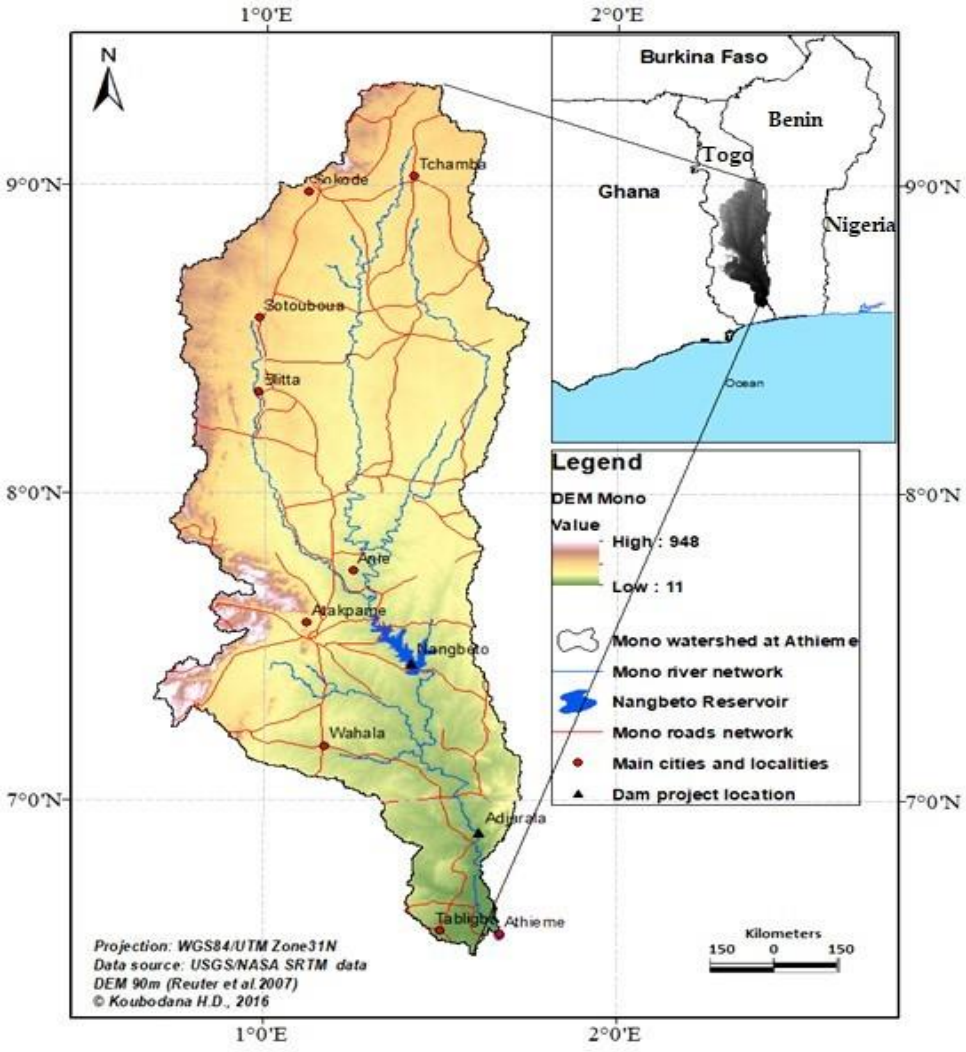

Figure 1: *Location of the Mono River basin in Togo and Benin*

2.2. Data Description

Land use and land cover: In this study, we used three available sources of LULC data for the MRB comprising different temporal and spatial resolutions: the Permanent Interstate Committee for drought control in Sahel (CILSS) (CILSS, 2016) data set developed for West Africa at 2-km spatial resolution, a global map at 300-m resolution offered by the European Space Agency (ESA) in the frame of the project on Climate Change Initiatives (CCI) (Gessner et al., 2012), and the global Globeland30 project land cover map developed by the National Geomatics Center of China (NGCC) with a resolution of 30-m (Eastman, 2006; Mishra and Singh, 2010). The details of the data sets are provided in Table 2.

Table 2: *Land cover datasets description*

Datasets	CILSS	ESA	Globeland30
Spatial resolution	2 km	300 m	30 m
Data available periods	1975, 2000, and 2013	1992 to 2015	2000 and 2010
Coverage	West Africa	Worldwide	Worldwide
Input's images for classification	Google Earth, Landsat, Corona and MODIS	300 m MERIS, 1km SPOT-vegetation, 1km PROBA-V and 1km AVHRR	Landsat TM and ETM+
Classification type	Automated and semi-automated	Automated	Pixel-Object-Knowledge (POK)
Number of LULC type	22	22	10
Website for data availability	*https://eros.usgs.gov/ west Africa/data*	http://maps.elie.ucl.ac.be/CCI/viewer/index.php	http://www.globallandcover.com/

2.3. Data Processing and Methods

2.3.1. Pre-analysis and Harmonization of Land Use and Land Cover Type

After extracting the Mono watershed in CILSS, ESA, and Globeland30 datasets, a maximum of ten LULC types are represented (Table 3). The pre-analysis consists first of reclassifying the ten land cover types into six major LULC types using ArcGIS 10.5 tools. Second, the spatial resolution of the CILSS and ESA maps was resampled to the 30-m resolution of Globeland30 (Thibaut et al., 2011) to be able to superimpose the maps for comparison (Bárdossy and Schmidt, 2009).

Table 3: *LULC categories in the MRB after extraction and reclassification scheme*

No.	Extracted LULC	Description	LULC reclassified
1	Forest	Forests and woody vegetation land (> 75% trees/ha), dense, closed canopy formation of evergreen	Forest
2	Gallery forest and riparian	Corridor of dense permanent vegetation, forest bordering the edges of streams and rivers	
3	Degraded forest	Immature forest, or forest in various stages of regrowth after disturbance	
4	Woodland	Open formations of small to medium height trees, tree cover generally between 50%- 75%	
5	Savanna	Land with trees (< 75% trees/ha) with mixture of shrub and grass undergrowth, with some dominance of grass or shrub	Savanna
6	Wetland and floodplain	Permanent wetlands and swamps	Wetland
7	Agriculture	Cultivated areas with seasonal crops dependent on rainfall.	Cropland
8	Cropland and oil palm	Crop field and fallow land, farms with crops and harvested croplands	
9	Water	Rivers, open water, inland waters and small reservoirs	Water
10	Settlements	Cities and villages, roads, and other buildings	Settlements

The six LULC classes in Table 3 are similar to those proposed by Penman et al. (2003) in the IPCC Guidelines according to the Kyoto Protocol of 2001 and the Good Practices Guidelines for Land Use, Land Use Change and Forestry (GPG-LULUCF).

2.3.2. Accuracy assessment, land use/cover area, and change analysis

According to Sitthi et al. (2016), a LULC accuracy assessment is required in any study using remote sensing data. LULC map accuracy is quantified by creating an error matrix or a confusion matrix,

which compares the classified map with a reference classification or a true map. These matrices can be used as a measure of agreement between model algorithm predictions and the references points (Congalton, 1991). Following the guidelines of the Food and Agriculture Organization (FAO), the tables of accuracy estimates were produced for each of the three data sets. This was followed by confidence intervals for area estimation and comparison of area estimation derived from map data to reference data (FAO-ONU, 2016). Many past studies have estimated the accuracy of the observed LULC map with a modeled one using a Kappa coefficient and overall accuracies (Chen et al., 2015; Franklin and Wulder, 2002; Lunetta et al., 2006; Ren et al., 2018).

Table 4: *Number of reference points for each land cover class for 2010 and 2013*

Number of land cover reference points							
Land cover type	**Forest**	**Savanna**	**Wetland**	**Cropland**	**Water**	**Settlements**	**Total**
Year 2013	23	665	10	289	8	5	1,000
Year 2010	140	527	17	286	13	17	1,000

For accuracy assessment, 1,000 reference points were randomly taken from high-resolution (in meter) satellite images for the years 2010 and 2013 provided by Google Earth Pro (version 7.3). These reference points were distributed proportionally to the size of the six LULC types inside MRB and compared with a 30-m spatial resolution classified map (Table 4).

The accuracy assessment and an error matrix for each category of dataset were generated by following the guidelines of Congalton (1991); Huth et al. (2012) and the method proposed and described by Olofsson et al. (2013). According to this method, an error matrix can be computed by accounting LULC number of pixels. In addition, from this error matrix statistics such as user and producer accuracies are generated for individual LULC category of the data sets, then the overall accuracy and Kappa coefficient are computed from this error matrix (P_{ij}) for each data set.

User's accuracy ($\hat{U}_i$) of class i is the ratio of the correct mapped pixels of a particular class i by the row total pixels (P_{i+}) Eq. (2).

$$\hat{U}_i = \frac{\hat{P}_{ii}}{\hat{P}_{i+}} \tag{2}$$

Producer's accuracy (P_j) of class j is the ratio of the number of correctly classified pixels to class j in the data to be evaluated and is estimated by Eq. (3)

$$\hat{P}_j = \frac{\hat{P}_{jj}}{\hat{P}_{j+}} \tag{3}$$

The overall accuracy ($\hat{O}$) indicates the overall proportion of area correctly classified (P_{ii}). It is the sum of all pixels on the major diagonal in the adjusted error matrix over the total number of pixels in the error matrix (N) as in Eq. (4).

$$\hat{O} = \frac{\sum_{i=1}^{n} \hat{P}_{ii}}{N} \tag{4}$$

The Kappa coefficient (K) is computed based on the error matrix and is the value that shows the consistency of data classification. This value is used to evaluate the accuracy of remote sensing data as following Eq. (5) (Amler et al., 2015; Ren et al., 2018; Sitthi et al., 2016).

$$K = \frac{N \sum_{i=1}^{n} \hat{P}_{ii} - \sum_{i=1}^{n} (\hat{P}_{i+} \times \hat{P}_{j+})}{N^2 - \sum_{i=1}^{n} (\hat{P}_{i+} \times \hat{P}_{j+})} \quad (5)$$

According to, Fitzgerald and Lees (1994), K is considered to be statistically significant at p<0.001 at a level of confidence for the following intervals values:

- Poor if K <40
- Good if 40 ≤ K <75
- Excellent if K ≥ 75

2.3.3. Land use and land cover change scenarios

Developing future LULC scenarios consists of two steps. In the first step, the rate of change has to be estimated, and in the second step the probability for a change into a certain LULC class to take place has to be computed (Verburg and Veldkamp, 2002). The flowchart of Mono land use and land cover modeling is shown in Figure 2.

The spatial trend change analysis was performed for CILSS (1975-2000) and for the periods, 2000-2010 and 2000-2013 (CILSS, ESA and Globeland30). Spatial trends per LULC category were computed as 9th order polynomial and presents positive, no and negative trend area of change (Eastman, 2006; Václavík and Rogan, 2009).

The results are used to compute spatial transition probabilities for every LULC category. In this study, population growth, elevation, and distance to roads were used as drivers for calculating the transitions from forest to savanna, from forest to cropland, from savanna to cropland, and from savanna to forest. Road network and elevation are static drivers while population is a dynamic driver.

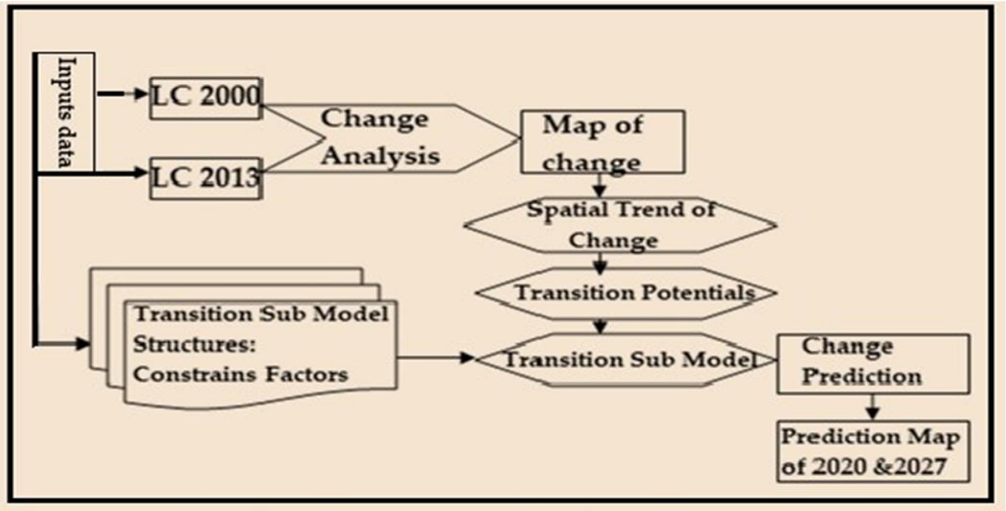

Figure 2: *MRB flowchart for land cover modeling (LC = Land use/cover)*

These transition probabilities are based on a Multi-Layer Perceptron (MLP) neural network (Eastman, 2006). The parameters which are the driving forces of change are assumed to be the same (Eastman, 2006). Many studies have shown that MLP is useful and a good tool for prediction, function approximation and classification (Gardner and Dorling, 1998). We adopted a Markov Chain prediction process and a transition probability to model the future LULC scenarios (Eastman, 2006). The transition probability file is a matrix that records the probability that each LULC category will change to any other category. The quality of the prediction can be evaluated using an observed map not used for

calculating the transition potentials (Eastman, 2006). Computing the rate of change between 1975 and 2000 and comparing the projected LULC of 2013 with the observed one allows validation of CILSS datasets. Afterwards, the prediction of LULC scenarios of CILSS and ESA at a time step of seven years from 2013 to 2027 and for Globeland30 at the step of ten year from 2010 to 2020 was performed.

3. Results

3.1. Accuracy assessment of land use and land cover

The assessment of accuracy of LULC maps was done using the latest available LULC maps of the years 2010 (Globeland30) and 2013 (CILSS and ESA). The percentage of reference points estimated correctly, known as overall accuracy and the Kappa coefficient, were 83% and 68% for CILSS in 2013 product, 69% and 36% using the ESA 2013 data set, and 57%, and 34% using the Globeland30 data set, respectively. The Kappa coefficient from CILSS is considered good but is poor for the ESA and Globeland30 data sets (Chen et al., 2004; Fitzgerald et Lees, 1994). The overall accuracy of CILSS is excellent, good for the ESA and Globeland30 data sets. Detailed producer and user accuracy computed is shown in Table 5.

Table 5: *User and producer accuracy values of each land use and land cover type*

	CILSS 2013		ESA 2013		Globeland30 2010	
	User	Producer	User	Producer	User	Producer
Land cover type	**Accuracy [%]**					
Forest	62.90	95.70	3.90	8.70	37.00	52.90
Savanna	98.30	76.50	78.60	81.10	69.80	55.20
Wetland	81.80	90.00	7.60	50.00	0.00	0.00
Cropland	65.80	95.80	70.80	45.30	56.50	66.80
Water	63.60	97.50	100.00	87.50	88.90	61.50
Settlements	100.00	80.00	80.00	80.00	66.70	11.80

According to Table 5, CILSS dataset shows acceptable results of user and producer accuracies higher than 60%. User and producer accuracies resulting from ESA for forest and wetland are very poor especially for wetland and settlements in Globeland30 data set. Particularly for the LULC categories of forest, savanna, cropland, and water, the accuracies are acceptable with ESA and Globeland30 data sets. In the three data sets, user and producer accuracies for savanna and water are acceptable while forest is good in the CILSS and Globeland30 datasets. We can conclude that globally the reclassification consistence is best from CILSS, ESA to Globeland30 data sets in MRB, whereas some individual LULC type have a best user and producer accuracies according to the data set.

3.2. Land cover area and change area estimation

The analysis of the CILSS data sets LULC type area reveals savanna, cropland and forest as the dominant land cover in the basin (Figure 3). In terms of area percentage coverage, savanna was 75.94% in 1975, 63.75% in 2000 and 50.35% in 2013; cropland was 84.00% in 1975, 25.36% in 2000, and 39.82% in 2013; and forest was 14.87 % in 1975, 9.57% in 2000 and 7.96% in 2013 as shown in Table 6.

LULC change area of savanna and forest decreased whereas settlements and cropland increase between 1975 and 2013 for CILSS data set.

The results are seen to be different for the ESA data set and some were contrary to the CILSS data set. The savanna, surface area was 70.52% in 2000 and 70.70% in 2013. The area of cropland was 20.66% in 2000 and 20.91% in 2013. The forest area decreased from 8.02% in 2000 to 7.51% in 2013.

This means there is an increase of savanna and a reduction of cropland over time. From our knowledge in the field, deforestation is still occurring, resulting in increasing cropland area in the MRB. Table 6 shows that forest decreases at 0.51% from 2000 to 2013 and an increase of savanna from 2000 to 2013 for the ESA dataset. However, the major LULC types in the ESA map are still savanna, cropland and forest, but the change between 2000 and 2013 is positive for savanna, negative for forest, and positive for cropland. Considering the user and the overall accuracy by types (Table 5), it is clear that forest and wetland are not well classified in the ESA data sets (Figure 3 & Table 6).

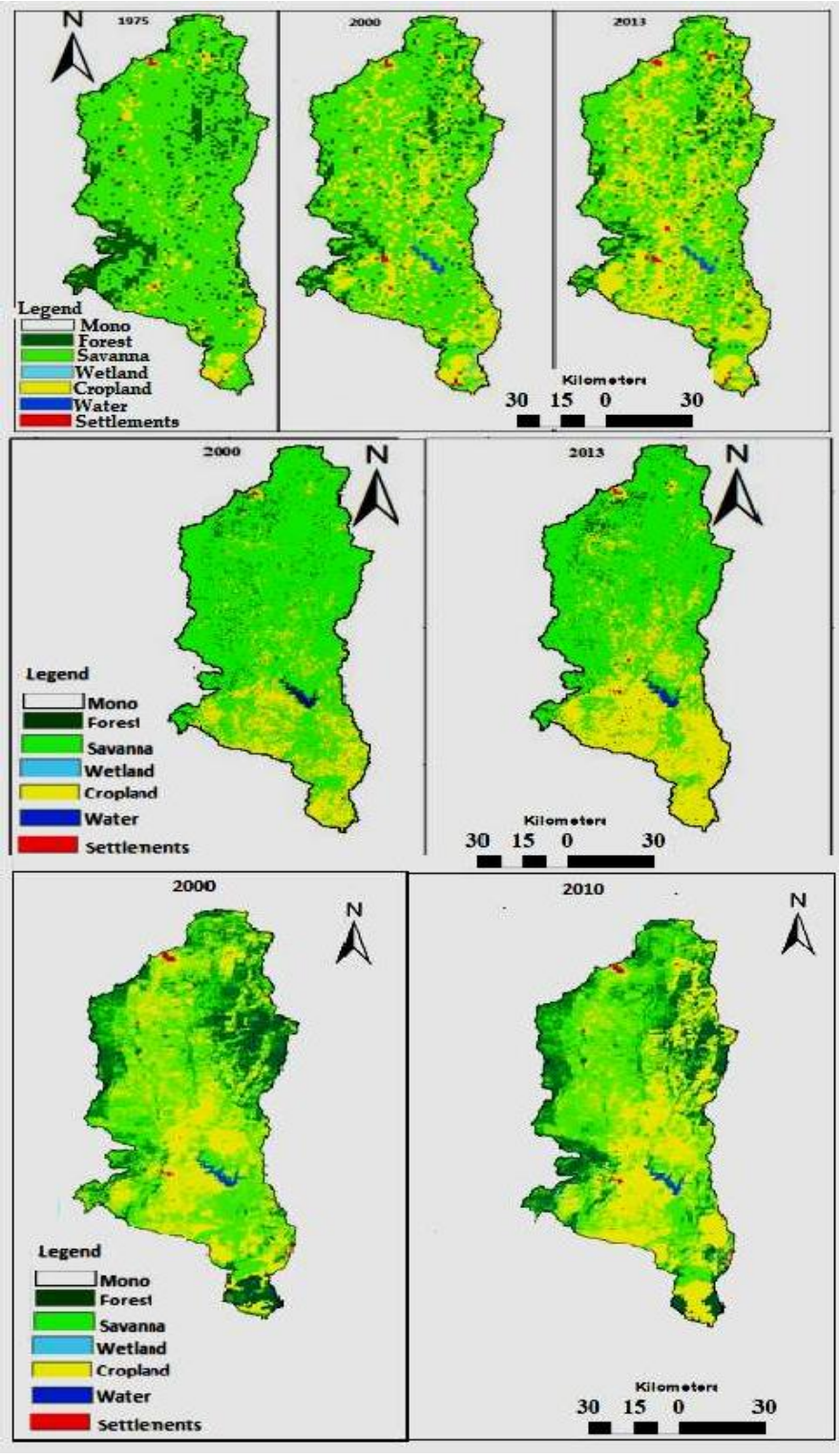

Figure 3: *CILSS (upper), ESA (middle) and Globeland30 (bottom) LULC maps*

The Globeland30 maps for 2000 and 2010 are shown in Figure 3. Forest area was 23.65% in 2000 and 23.96% in 2010. For savanna, it was 44.51% in 2000 and 39.39% in 2010 while cropland was 30.69% in 2000 and 33.68% in 2010. Based on these results, there was an increase of 0.32% area of forest and 3.19% of cropland and a decrease of savanna area of 4.52%.

Table 6: *Land use and land cover area and area change of CILSS, ESA and Globeland30 (GLC)*

	Land cover type area [%]							Land cover type area change [%]				
Year	**1975**		**2000**		**2010**	**2013**		**1975-2000**	**2000-2013**		**2000-2010**	**1975-2013**
Sources	**CILS S**	**CILS S**	**ESA**	**GLC**	**GLC**	**CILS S**	**ESA**	**CILS S**	**CILSS**	**ESA**	**GLC**	**CILS S**
Forest	14.87	9.57	8.02	23.65	23.96	7.96	7.51	-5.31	- 1.61	- 0.51	0.32	-6.91
Savanna	75.94	63.75	70.52	44.51	39.99	50.35	70.70	-12.19	-13.40	0.18	- 4.52	-25.59
Wetland	0.02	0.33	0.05	0.01	1.00	0.16	0.06	0.31	-0.16	0.02	0.99	0.14
Cropland	8.84	25.36	20.66	30.69	33.88	39.82	20.90	16.51	14.50	0.25	3.19	30.97
Water	0.02	0.51	0.68	0.68	0.67	0.49	0.63	0.49	-0.02	-0.06	-0.01	0.47
Settlements	0.31	0.49	0.07	0.48	0.50	1.22	0.19	0.18	0.73	0.12	0.02	0.91
Total	100.00	100.00	100.00	100.00	100.00	100.00	100.00	0.00	0.00	0.00	0.00	0.00

3.3. Land use and land cover data modeling using the Land Change Modeler

3.2.1. Land cover spatial trend of change

The spatial trend of change computed for the CILSS, ESA and Globeland30 data sets is given in Appendix A. CILSS data show a spatial trend between the major LULC during the period of 2000 to 2013 from forest to savanna in the southwest of the basin. The trend in change of forest is more intensive in the southwest and the northeast. These are the locations of the cities of Sokodé, Blitta, Anié and Atakpamé and the road networks as shown in Figure 1. The trend of change from savanna to cropland is high in the center of the basin, where 16.51% of the total area become cropland between 1975 and 2000, 14.46% between 2000 and 2013 and therefore 30.97% from 1975 to 2013 (Table 6). There are some similarities of the spatial trend of the transition forest to savanna between 2000 and 2013 using CILSS and ESA data sets and between 2000-2013 and 2000-2010 using the three data sets for the transition of savanna to cropland (Appendix A).

3.2.2. Quantifications, locations of land use/cover change and driving forces

Land use and land cover modeling requires knowledge about how much change occurs in the land, where it happened and why. Therefore, quantification of historical LULCC allows knowing the past state of LULC. Additionally, drivers involving change are useful for future land projection.

Table 7: *Changes in land use and land cover in the MRB for the three different data sets*

Areal changes [km^2]	**2000 to 2013**		**2000 to 2010**
	CILSS	**ESA**	**Globeland30**
Forest to Savanna	108	72	76.5
Savanna to cropland	252	13.5	9
Water to wetland	36	27	28.8
Forest to cropland	54	180	25
Total change area	450	292.5	139.3

Table 7 shows the main changes in LULC in the study area as derived from CILSS, ESA, and Globeland30 and deduced from LCM analysis. The largest changes are savanna to cropland (252 km^2), forest to savanna (108 km^2), and forest to cropland (54 km^2) using the CILSS data set. The LULCC using ESA and Globeland30 is underestimated compared to CILSS. The LULCC can be

explained by the population growth in the region as from 2000 to 2015, the population in Togo increases from 4.90 to 7.40 million (Table 1).

The hot spot of the change of forest to savanna is located in the southwest of the basin, while forest to cropland change is also important in the northeast. Changes of savanna to cropland are occurring over the entire basin but densely centered in the basin and from the south to the north. The change from forest to savanna with CILLS datasets is located in the south and west of the basin where the rural population likely has access to wood for their domestic needs.

3.2.3. Land use and land cover validation and change predictions

Because of limited data available of the year 1975 of ESA and Globeland30, validation was performed only for the CILSS data set. For that, after assessing LULCC between 1975 and 2000 a LULC map was generated for the year 2013 using the LCM. The estimated map was compared with the observed LULC map. The results of the validation were ranked as acceptable with an accuracy rate higher than 50% (Appendix B).

After analyzing LULC, future LULC was predicted for all data sets by supposing population growth as the main driver.

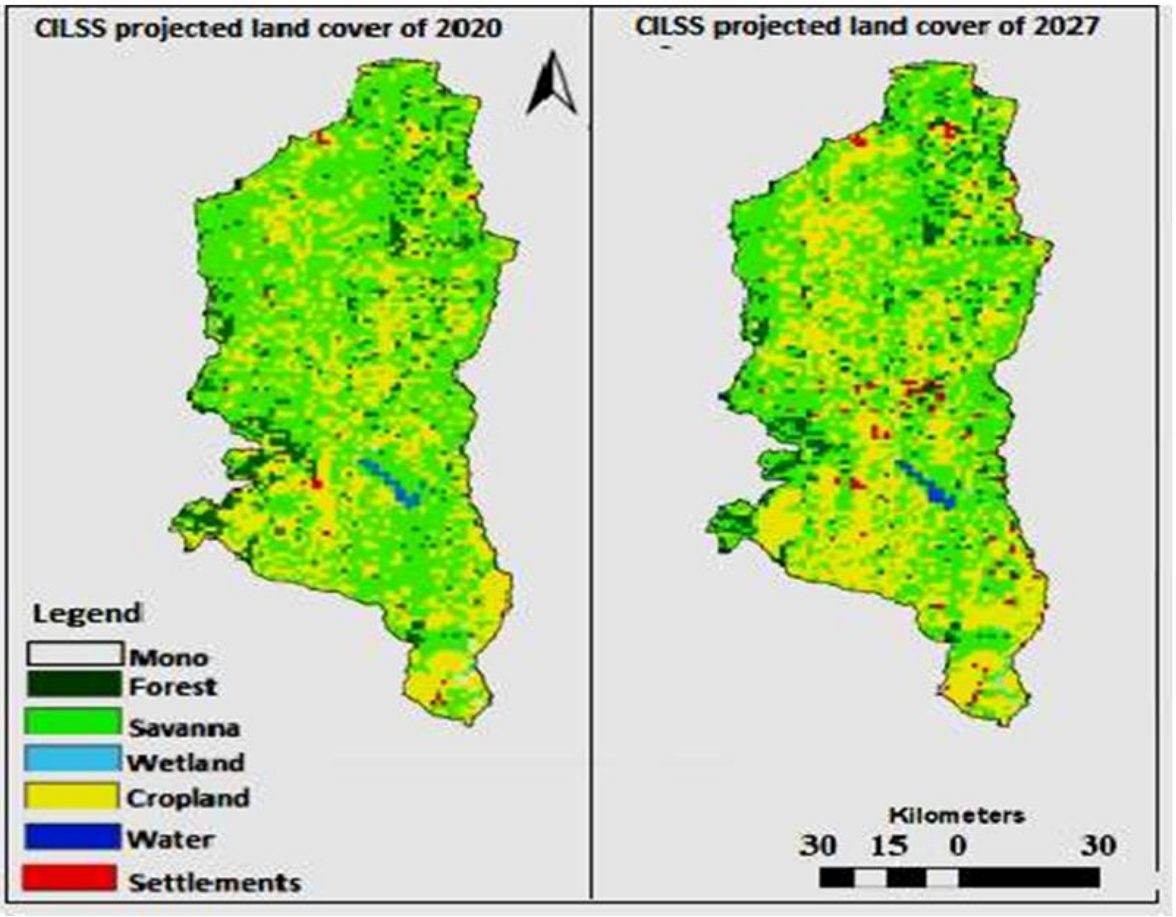

	Land use and land cover area [%]		Change area [%]
Land cover type	**2020**	**2027**	**2020-2027**
Forest	7.56	7.11	-0.45
Savannah	45.13	39.49	-5.64
Wetland	0.07	0.07	0.00
Copland	45.72	50.98	5.26

Water	0.47	0.47	0.00
Settlements	1.05	1.88	0.83
Total	100.00	100.00	0.00

Figure 4: *Projected land use and land cover scenarios and areal changes for 2020 and 2027 with CILSS dataset*

The predicted LULC scenarios for 2020 and 2027 using the CILSS data sets are shown in Figure 4 together with the related statistics. According to this projection, forest and savanna LULC decrease with a change rate of 0.45% for forest and for savanna of 5.64%. By contrast, cropland is constantly increasing with a rate of 5.26% and settlements are increasing at 0.83% between 2020 and 2027. Wetland and water bodies in the area did not change significantly.

Because of weak representation of LULC using ESA and Globeland30 confirmed by the prediction accuracy of less than 50% (Appendix B), the projection was performed only for the year 2020. In Figure 5, CILSS, ESA, and Globeland30, LULC scenarios of 2020 are shown. The projected LULC map of 2020 is almost similar to the earlier LULC map from 2013 and 2010 for ESA and Globeland30, respectively (Figure 2). These similarities can be explained by the low prediction accuracies.

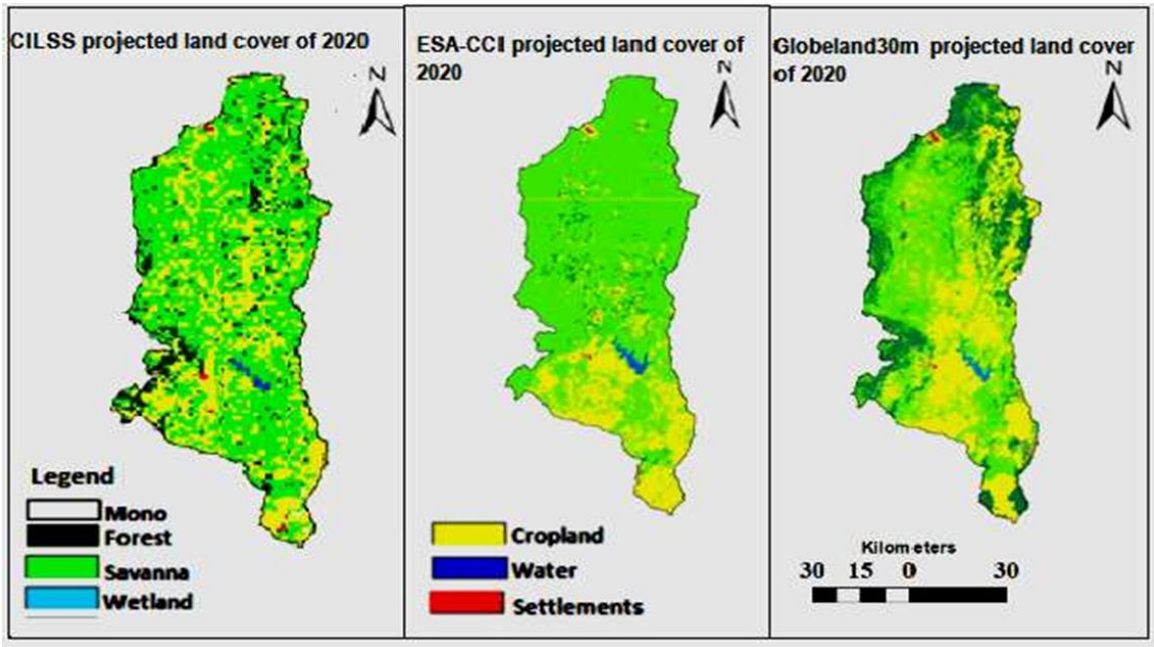

Predicted land use **and** land cover in 2020 area [%]						
Data sets	**Forest**	**Savanna**	**Wetland**	**Cropland**	**Water**	**Settlements**
CILSS	7.56	45.13	0.07	45.72	0.47	1.05
ESA	7.61	70.30	0.07	21.19	0.64	0.20
Globeland30	23.96	39.99	1.00	33.88	0.67	0.50

Figure 5: *Comparison of the projected land cover maps and areal changes for 2020 the CILSS, ESA and Gloeland30 data sets*

The predicted LULC maps in 2020 depend strongly on the accuracy of each LULC source. Results show that the temporal change of LULC in the basin is best reproduced by CILSS. Beyond the CILSS data set, Globeland30 data performs better concerning the spatial representation of some LULC such as forest, savanna, cropland and water LULC types.

Savanna, cropland, and forest are the dominant LULC types in the region. From 1975 to 2027, there is a decrease of forest and savanna followed by an increase of cropland and settlements in the MRB.

4. Discussion

4.1. Accuracy assessment and past land cover change

Although the spatial resolution of the ESA and the Globeland30 data is high, the two data sets do not accurately map some LULC types in the study area, which may be explained by the fact that for CILSS local information are used during the automated and semi-automated classification (CILSS, 2016; Cotillon, 2017). It may be also due to the number of reference points spatial repartition used for the accuracy assessment. Indeed, the selected random points size from Google earth imagery can affect the spatial distribution depending on the resolution of 2-km, 300-m or 30-m (Congalton, 1991; Stehman, 2009). The visual identification of land use or land cover classes is easy when the resolution is high (Huang and Siegert, 2006; Stuckens et al., 2000).

Table 5 shows the difference of user and producer accuracies from CILSS ESA and Globeland30 dataset. CILSS dataset reveals acceptable accuracies of each LULC category. This difference can be explained by the data set spatial resolution and references points.

The finding that savanna and agriculture are the dominant LULC classes in the study area during the study period is in accordance with other studies. For example, Badjana (2015) analyzed LULCC in the Kara River basin, and showed that savanna was dominant. This was also observed by Diwediga et al. (2015) in the Mo River basin, a small tributary of Oti river in central region of Togo. It was also concluded by Koglo et al. (2018) that savanna and forest are the most important LULC type that are being converted by cropland in Kloto, a small district in the south of the MRB.

The results of CILSS LULCC in MRB confirm many analyses performed in Togo and Benin about LULCC mainly caused by deforestation, cropland expansion, and losses of savanna (Akinyemi et al., 2017; Kleemann et al., 2017). The results of Badjana et al. (2017); Koglo et al. (2018) revealed that deforestation and savanna changed to cropland and settlements in south and north of Togo. In Fazao-Malfacassa National Park, in the northern part of the MRB, Atsri et al. (2018) found that forest and savanna are degraded, which could be explained by agriculture expansion, bush fire, timber extraction and linked by population growth. By assessing the land use change process in the Kéran protected area in the northern Togo, Polo-Polo-akpisso et al. (2019) confirmed that savanna and forest have decreased annually at the rate of more than 2%, whereas cropland and settlements have increased in the region.

The results of the current study show that deforestation is increasing over the whole period of analysis. According to Kokou et al. (2005) more than 80% of the rural communities in Togo are using wood for cooking, causing significant losses of forest. Therefore, decision makers need to take measures to reduce forest degradation, sensitizing the local communities concerning the advantages of reforestation, and the negative impacts on the climate due to losses of forests. Measures must be also taken concerning demographic policies.

The increase of the water bodies between 1975 and 2000, can be explained by the building of the Nangbéto dam in 1987 and rainfall variability in this region (Badjana, 2015). As the consequences of climate change and climate variability, reduced precipitation causes a decrease of the water body of the reservoir from 2000 to 2013, which had consequences for hydroelectricity production as mentioned by Houessou (2016). Climate variability, especially the droughts between 1970s and 1980s, negatively affected grassland due to overgrazing. The increase of settlements is also realistic and can be explained by demography in Togo and Benin (see Table 1).

4.2. Land use and land cover scenarios accuracy and assessment

LULC spatial trend direction and location are approximately situated in the locations of the main cities of the basin; therefore, LULC spatial trend can be explained by population activities and growth as

mentioned by Koglo et al. (2018) in the south district of MRB. Because of its fine resolution, the Nangbéto dam area and some protected forests such as Malafacassa (Amoussou et al., 2017; Atsri et al., 2018) are well delimited. The excellent reclassification of these land cover is due to low and high albedo factor of water and forest which plays a role during data collection by satellite's sensors. CILSS LULC scenarios shows positive area change of cropland and settlements; negative area change of forest and savanna can be explained by the same factors cited above.

Difference between future LULC scenarios of the data sets is due to the poor and better Kappa coefficients obtained, which prove the importance of LULC validation. Therefore validation or LULC based on supervised classification are preferable as an input in LULCC scenario studies (Foody, 2002).

LULC scenarios accuracy rate are strongly impacted by the accuracy assessment and LULCC of historical CILSS, ESA and Globeland30 data sets. Furthermore, the low accuracies obtained from the modeling can also be explained by the fact that we were not able to take into account all the drivers as well anthropogenic and natural during the modeling. Others reason are the weakness of LCM software or user manipulation errors (Camacho Olmedo et al., 2015; Mas et al., 2014). The simulation can allow understanding, forecasting, and anticipating the future evolution of environment coverage. Nevertheless it is important to know the validity of LCM outputs based on local expertise (Zoungrana et al., 2015).

5. Conclusion

This work focused on land use and land cover changes assessment and future scenarios in the Mono river basin (MRB) over the period 1975 to 2027 using three different data sets. The results show that the CILSS data set is the most reliable for the MRB with acceptable accuracy assessment efficiencies (higher than 75%). In the MRB, savanna, cropland, and forest are the major land use and land cover classes with decreasing (forest and savanna) and increasing (cropland, settlement) trends. The expansion of agriculture due to population growth occurs at the expense of savanna. In the tropical zone of West Africa, people use wood as an energy source, another cause of deforestation. LULCC must be taken seriously by the authorities and population themselves. It is very important to know the evolution of LULCC in order to develop strategies for planning of an integral water resources management (IWRM) in general.

The study assessed scenarios of future LULC by mapping and analyzing the situation for two time steps (2020 and 2027). The maps obtained from this analysis can be used as inputs in hydrological modeling for assessing the impacts of LULC and climate changes on water yield and surface runoff of in MRB.

Future scenarios of LULC depend significantly on the source of the underlying data set. The high spatial resolutions of Globeland (30 m) and ESA (300 m) are attractive, but the quality is limited to specific land use or land cover categories. The resolution of CILSS is rather coarse and therefore, users often prefer other data sets. Nevertheless, because CILSS data were produced with local knowledge, the quality is convincing and outperforms the others. Using the data sets for scenario analysis results in completely diverging futures; this may significantly affect management strategies. This study shows the importance of validating land cover data sets before scenario analysis.

Author Contributions

Djan'na H. Koubodana, Bernd Diekkrüger and Kristian Näschen designed the study, developed the methodology and wrote the manuscript. Djan'na H. Koubodana conducted the computer analysis; meanwhile Bernd Diekkrüger, Julien Adounkpe and Kossi Atchonouglo supervised the work.

Funding

We would like to thank the German Ministry of Education and Research (BMBF) for their financial support of the Graduated Research Programme of Climate Change and Water Resources at the University of Abomey Calavi, Benin through the West African Science Service Center on Climate Change and Adapted Land use (WASCAL).

Acknowledgments

We are also thankful to the Permanent Interstate Committee for drought control in the Sahel (CILSS), the European Space Agency by its Climate Change Initiative project (ESA-CCI) and the National Geomatics Center of China (NGCC) agencies and institutes for making freely available land cover data that we used in the study.

Conflicts of Interest

The authors declare no conflict of interest.

References

Akinyemi, F.O., Pontius, R.G. and Braimoh, A.K. 2017. Land change dynamics : insights from Intensity Analysis applied to an African emerging city. *Journal of Spatial Science*, 62(1), pp.69–83.

Amler, E., Schmidt, M. and Menz, G. 2015. Definitions and Mapping of East African Wetlands: A Review. *Remote Sensing*, 7(5), pp.5256–5282.

Amoussou, E. 2010. Variabilite pluviometrique et dynamique hydro-sedimentaire du bassin versant du complexe fluvio-lagunaire Mono-Aheme-Couffo (Afrique de l'ouest). These de doctorat de l'Université de Bourgogne - Centre de Recherches de Climatologie (CRC) CNRS – UMR 5210, soutenu le 11 mai 2010.

Amoussou, E., Osseni, A.A., Lange, U. and Preuss, S. 2017. Hydroclimatic variability and flood risk on Naglanou and Akissa forests areas in Mono River Delta (West Africa). *International Journal of Biodiversity and Conservation*, 9(6), pp.212–223.

Anderson, J.R., Hardy, E.E., Roach, J.T. and Witmer, R.E. 1976. A land use and land cover classification system for use with remote sensor data. US Government Printing Office. Vol. 964.

Arsanjani, J.J., Helbich, M., Kainz, W. and Boloorani, D.A. 2013. Integration of logistic regression, Markov chain and cellular automata models to simulate urban expansion. *International Journal of Applied Earth Observations and Geoinformation*, 21, pp.265–275.

Atsri, K.H., Konko, Y., Cuni-Sanchez, A. and Abotsi, K.E. 2018. Changes in the West African forest-savanna mosaic, insights from central Togo. *PLoS ONE*, 13(10), p.10.

Badjana, H.M. 2015. River Basins Assessment and Hydrologic Processes Modeling for Integrated Land and Water Resources Management (ILWRM) in West Africa. PhD Thesis, Graduate Research Program on Climate Change and Water Resources ,University of Abomey Calavi, Benin; defense date: December 11, 2015.

Badjana, H. M., Olofsson, P., Woodcock, C. E., Helmschrot, J., Wala, K. 2017. Mapping and estimating land change between 2001 and 2013 in a heterogeneous landscape in West Africa: Loss of forestlands and capacity building opportunities. *International Journal of Applied Earth Observation and Geoinformation*, 63, pp.15–23.

Bárdossy, A. and Schmidt, F. 2009. GIS approach to scale issues of perimeter-based shape indices for drainage basins. *Hydrological Processes*, 47(6), pp.931–942.

Biondini, M. and Kandus, P. 2006. Transition matrix analysis of land-cover change in the accretion area of the Lower Delta of the Paraná River (Argentina) reveals two succession pathways. *Wetlands*, 26(4), pp.981–991.

Brink, A.B. and Eva, H.D. 2009. Monitoring 25 years of land cover change dynamics in Africa: A sample based remote sensing approach. *Applied Geography*, 29(4), pp.501–512.

Camacho Olmedo, M.T., Pontius, R.G., Paegelow, M. and Mas, J.F. 2015. Comparison of simulation models in terms of quantity and allocation of land change. *Environmental Modelling and Software*, 69, pp.214–221.

Chen, D., Stow, D.A. and Gong, P. 2004. Examining the effect of spatial resolution and texture window size on classification accuracy: an urban environment case. *International Journal of Remote Sensing*, 25(11), pp.2177–2192.

Chen, J., Chen, J., Liao, A., Cao, X., Chen, L., Chen, X., He, C., Han, G., Peng, S., Lu, M., Zhang, W., Tong, X. and Mills, J. 2015. Global land cover mapping at 30 m resolution: A POK-based operational approach. *Journal of Photogrammetry and Remote Sensing*, 103, pp.7–27.

CILSS. 2016. Landscapes of West Africa- A Window on a Changing World. 47914 252nd St, Garretson, SD 57030, United States.

Congalton, R.G. 1991. A review of assessing the accuracy of classifications of remotely sensed data. *Remote Sensing of Environment*, 37(1), pp.35–46.

Cotillon, S. 2017. The landscapes of West Africa - 40 years of change. U.S. Geo- Logical Survey Fact Sheet. p.4.

Diwediga, B., Wala, K., Folega, F., Dourma, M., Woegan, Y.A., Akpagana, K. and Bao, Q. 2015. Biophysical and anthropogenous determinants of landscape patterns and degradation of plant communities in Mo hilly basin (Togo). *Ecological Engineering*, 85, pp.132–143.

Du, J., Qian, L., Rui, H., Zuo, T., Zheng, D., Xu, Y. and Xu, C. 2012. Assessing the effects of urbanization on annual runoff and flood events using an integrated hydrological modeling system for Qinhuai River basin, China. *Journal of Hydrology*, 464–465, pp.127–139.

Eastman, J.R. 2006. The Land Change Modeler for Ecological Sustainability. In: IDRISI Andes Guide to GIS and Image Processing. pp.239–260. Clark Labs Clark University, 950 Main Street Worcester, MA 01610-1477 USA. Retrieved from: https://clarklabs.org/terrset/land-change-modeler/.

Eisfelder, C., Kuenzer, C. and Dech, S. 2012. Derivation of biomass information for semi-arid areas using remote-sensing data. *International Journal of Remote Sensing*, 33(9), pp.2937–2984.

FAO-ONU 2016. Map Accuracy Assessment and Area Estimation: A Practical Guide. Organization of the United Nations Rome, Italia. p. 69. Retrieved from http://www.fao.org/3/a-i5601e.pdf

FAO 2012. FAO Statistical Yearbook 2012 Africa: Food and Agriculture. Food and Agriculture Organization of the United Nations Regional Office for Africa Accra. p. 280. ISBN: 9789251074268.

Fitzgerald, R.W. and Lees, B.G. 1994. Assessing the classification accuracy of multisource remote sensing data. *Remote Sensing of Environment*, 47(3), pp.362–368.

Foody, G.M. 2002. Status of land cover classification accuracy assessment. *Remote Sensing of Environment*, 80(1), pp.185–201.

Franklin, S.E. and Wulder, M.A. 2002. Remote sensing methods in medium spatial resolution satellite data land cover classification of large areas. *Progress in Physical Geography*, 26(2), pp.173–205.

Gardner, M.W. and Dorling, S.R. 1998. Artificial neural networks (the multilayer perceptron) - A review of applications in the atmospheric sciences. *Atmospheric Environment*, 32(14/15), pp.2627–2636.

Gessner, U., Bliefernicht, J., Rahmann, M. and Dech, S. 2012. Land cover maps for regional climate modelling in West Africa – a comparison of datasets. *Advances in Geosciences*, pp.387–397.

Herbst, M., Diekkrüger, B. and Vereecken, H. 2006. Geostatistical co-regionalization of soil hydraulic properties in a micro-scale catchment using terrain attributes. *Geoderma*, 132(1–2), pp.206– 221.

Houessou, S. 2016. Les inondataions et les risques prévisionnels liés aux barrages hydroéléctriques dans la basse vallée du Mono. These de doctorant, Universite d'Abomey Calavi, Benin, Soutenu publiquement le.

Huang, S. and Siegert, F. 2006. Land cover classification optimized to detect areas at risk of desertification in North China based on spot vegetation imagery. *Journal of Arid Environments*, 67(2), pp.308–327.

Huth, J., Kuenzer, C., Wehrmann, T., Gebhardt, S., Tuan, V.Q. and Dech, S. 2012. Land cover and land use classification with TWOPAC: Towards automated processing for pixel- and object-based image classification. *Remote Sens*ing, 4(9), pp.2530–2553.

Kleemann, J., Baysal, G., Bulley, H.N.N. and Fürst, C. 2017. Assessing driving forces of land use and land cover change by a mixed-method approach in north-eastern Ghana, West Africa. *Journal of Environmental Management*, 196, pp.411–442.

Koglo, Y.S., Agyare, W.A., Diwediga, B., Sogbedji, J.M., Adden, A.K. and Gaiser, T. 2018. Remote sensing-based and participatory analysis of forests, agricultural land dynamics, and potential land conservation measures in Kloto District (Togo, West Africa). *Soil Systems*, 2(3), p.49.

Kokou, K., Adjossou, K. and Hamberger, K. 2005. Les Forets Sacrees De L ' Aire Ouatchi Au Sud-Est Modes De Gestion Locale Des Ressources Forestieres. VertigO-La Revue Électronique En Sciences de l'environnement, 6(3).

Koubodana, H.D. 2015. Mecanismes de connexions entre les modes de varaibilités internannuelle equatorial et meridien de l'Atlantique tropical. These de Master, Chaire Internationale en Physique Mathématique et Applications (CIPMA-Chaire UNESCO), Université d'Abomey-Calavi (UAC), Benin, Soutenu en Octobre.

Lambin, E.F., Geist, H.J. and Lepers, E. 2003. Dynamics of land-use and land cover change in tropical regions. *Annual Review of Environment and Resources*, 28(1), pp.205–241.

Lunetta, R.S., Knight, J.F., Ediriwickrema, J., Lyon, J.G. and Dorsey, L. 2006. Land-cover change detection using multi-temporal MODIS NDVI Data. *Remote Sensing of Environment*, 105(2), pp.142–154.

Mas, J.F., Kolb, M., Paegelow, M., Camacho Olmedo, M.T. and Houet, T. 2014. Inductive pattern-based land use/cover change models: A comparison of four software packages. *Environmental Modelling and Software*, 51, pp.94–111.

Milad, M., Ming, Y., Firuz, M. and Hanan, Z. 2017. Improving the capability of an integrated CA-Markov model to simulate spatio-temporal urban growth trends using an Analytical Hierarchy Process and Frequency Ratio. *International Journal of Applied Earth Observations and Geoinformation*, 59, pp.65–78.

Mishra, A.K. and Singh, V.P. 2010. A review of drought concepts. *Journal of Hydrology*, 391(1–2), pp.202–216.

Mishra, V. N., Rai, P. K., Mohan, K. 2014. Prediction of land use changes based on land change modeler (LCM) using remote sensing: a case study of Muzaffarpur (BIHAR), India. *Journal of the Geographical Institute'Jovan Cvijic'SASA*, 64(1), pp.111–127.

Oguntunde, P. G., Friesen, J., Giesen, N. and Savenije, H.H.G. 2006. Hydroclimatology of the Volta River Basin in West Africa: Trends and variability from 1901 to 2002. *Physics and Chemistry of the Earth, Parts A/B/C*, 31(18), pp.1180–1188.

Olofsson, P., Foody, G.M., Stehman, S.V. and Woodcock, C.E. 2013. Making better use of accuracy data in land change studies: Estimating accuracy and area and quantifying uncertainty using stratified estimation. *Remote Sensing of Environment*, 129 (2013), pp.122–131.

PCCP. 2008. Programme PCCP-from Potential Conflict to Cooperation Potential: cas du basin du Mono (Togo-Benin). Lomé-Togo.

Peixoto, M., Costa, A.C., Painho, M. and Bartoschek, T. 2006. A stratified sampling approach to the spatial accuracy assessment of digital cartography: an application to the Portuguese Ecological Reserve. In: M. Caetano, M. Painho (Eds.). *7th International Symposium on Spatial Accuracy Assessment in Natural Resources and Environmental Sciences*. p. 99–108. Lisbon, Portugal. Retrieved from: *http://citeseerx.ist.psu.edu/viewdoc/download?doi=10.1.1.591.6&rep=rep1&type=pdf.*

Penman, J., Gytarsky, M., Hiraishi, T., Krug, T., Kruger, D., Pipatti, R. and Wagner, F. 2003. Good practice guidance for land use, land use change and forestry. 2108 -11, Kamiyamaguchi Hayama, Kanagawa Japan, 240-0115. Institute for Global Environmental Strategies (IGES) for the IPCC. p.590. Retrieved from: *http://www.ipcc-nggip.iges.or.jp.*

Polo-akpisso, A., Wala, K., Soulemane, O., Foléga, F., Akpagana, K. and Tano, Y. 2019. Assessment of habitat change processes within the Oti-Keran-Mandouri Network of Protected Areas in Togo (West Africa) from 1987 to 2013 using decision tree analysis. *Sci.*, 1(1). p.9.

Pontius, R.G., Cornell, J.D. and Hall, C.A.S. 2001. Modeling the spatial pattern of land-use change with GEOMOD2: application and validation for Costa Rica. *Agriculture, Ecosystems and Environment*, 85, pp.191–203.

Pontius, R.G. and Malanson, J. 2014. Comparison of the structure and accuracy of two land change models. *International Journal of Geographical Information Science*, 19(2), pp.243–265.

Pontius, R.G. and Millones, M. 2011. Death to Kappa: Birth of quantity disagreement and allocation disagreement for accuracy assessment. *International Journal of Remote Sensing*, 32(15), pp.4407–4429.

Pontius, R.G. and Neeti, N. 2010. Uncertainty in the difference between maps of future land change scenarios. *Sustainability Science*, 5, pp.39–50.

Pontius, R.G. and Spencer, J. 2005. Uncertainty in extrapolations of predictive land-change models. *Environment and Planning B: Planning and Design*, 32 (2), pp.211–230.

Ren, H., Cai, G., Zhao, G. and Li, Z. 2018. Accuracy assessment of the GlobeLand30 dataset in Jiangxi Province. *Remote Sensing & Spatial Information Sciences*, 42(3), pp.1481–1487.

Rounsevell, M.D.A., Reginster, I., Araujo, M.B., Carter, T.R., Dendoncker, N., Ewert, F., House, J.I., Kankaanpää, S., Leemans, R., Metzger, M.J., Schmit, C., Smith, P. and Tuck, G. 2006. A coherent set of future land use change scenarios for Europe. *Agriculture, Ecosystems and Environment*, 114(1), pp.57–68.

SAWES 2011. Etudes relatives a la promotion de trois (3) nouvelles organisations de bassins transfrontaliers en Afrique de l'ouest Cas du schéma du Bassin du Mono. Aougadougou, Burkina Faso.

Sitthi, A., Nagai, M., Dailey, M. and Ninsawat, S. 2016. Exploring land use and land cover of geotagged social-sensing images using naive bayes classifier. *Sustainability*, 8(9), p.921.

Stehman, S.V. 2009. Sampling designs for accuracy assessment of land cover. *International Journal of Remote Sensing*, 30(20), pp.5243–5272.

Stuckens, J., Coppin, P.R. and Bauer, M.E. 2000. Integrating contextual information with per-pixel classification for improved land cover classification. *Remote Sensing of Environment*, 71(3), pp.282–296.

Sun, B. and Robinson, D. 2018. Comparison of Statistical Approaches for Modelling Land-Use Change. *Land*, 7(4), p.144.

Sutton, P. 1997. Modeling population sensity with night-timed satellite imagery and GIS. *Computers, Environment and Urban Systems*, 21(3/4), pp.227–244.

Thibaut, A., Tchuenté, K., Roujean, J. and Jong, S.M. 2011. Comparison and relative quality assessment of the GLC2000, GLOBCOVER, MODIS and ECOCLIMAP land cover data sets at the African continental scale. *International Journal of Applied Earth Observation and Geoinformation*, 13, pp.207–219.

Václavík, T. and Rogan, J. 2009. Identifying trends in land use/ land cover changes in the context of post-socialist transformation in Central Europe: a case study of the Greater Olomouc Region, Czech Republic. *GI Science & Remote Sensing*, 46(1), pp.54–76.

Veldkamp, A. and Lambin, E.F. 2001. Predicting land-use change. *Agriculture, Ecosystems & Environment*, 85 (1–3), pp.1–6.

Verburg, P.H. and Veldkamp, A. 2002. Modeling the Spatial Dynamics of Regional Land Use: The CLUE- S Model. *Environmental Management*, 30(3), pp.391–405.

Wisser, D., Frolking, S., Douglas, E.M., Fekete, B.M., Schumann, A.H. and Vörösmarty, C.J. 2010. The significance of local water resources captured in small reservoirs for crop production – A global-scale analysis. *Journal of Hydrology*, 384(3–4), pp.264–275.

Zoungrana, B.J., Conrad, C., Amekudzi, L.K., Thiel, M., Da, E.D., Forkuor, G. and Löw, F. 2015. Multi-temporal landsat images and ancillary data for land use/cover change (LULCC) detection in the Southwest of Burkina Faso, West Africa. *Remote Sensing*, 7(9), pp.12076–12102.

World Population. Available from: *http://worldpopulationreview.com/countries/togo-population* (accessed on 25/09/2018).

Appendix A: Spatial trend map of land cover changes

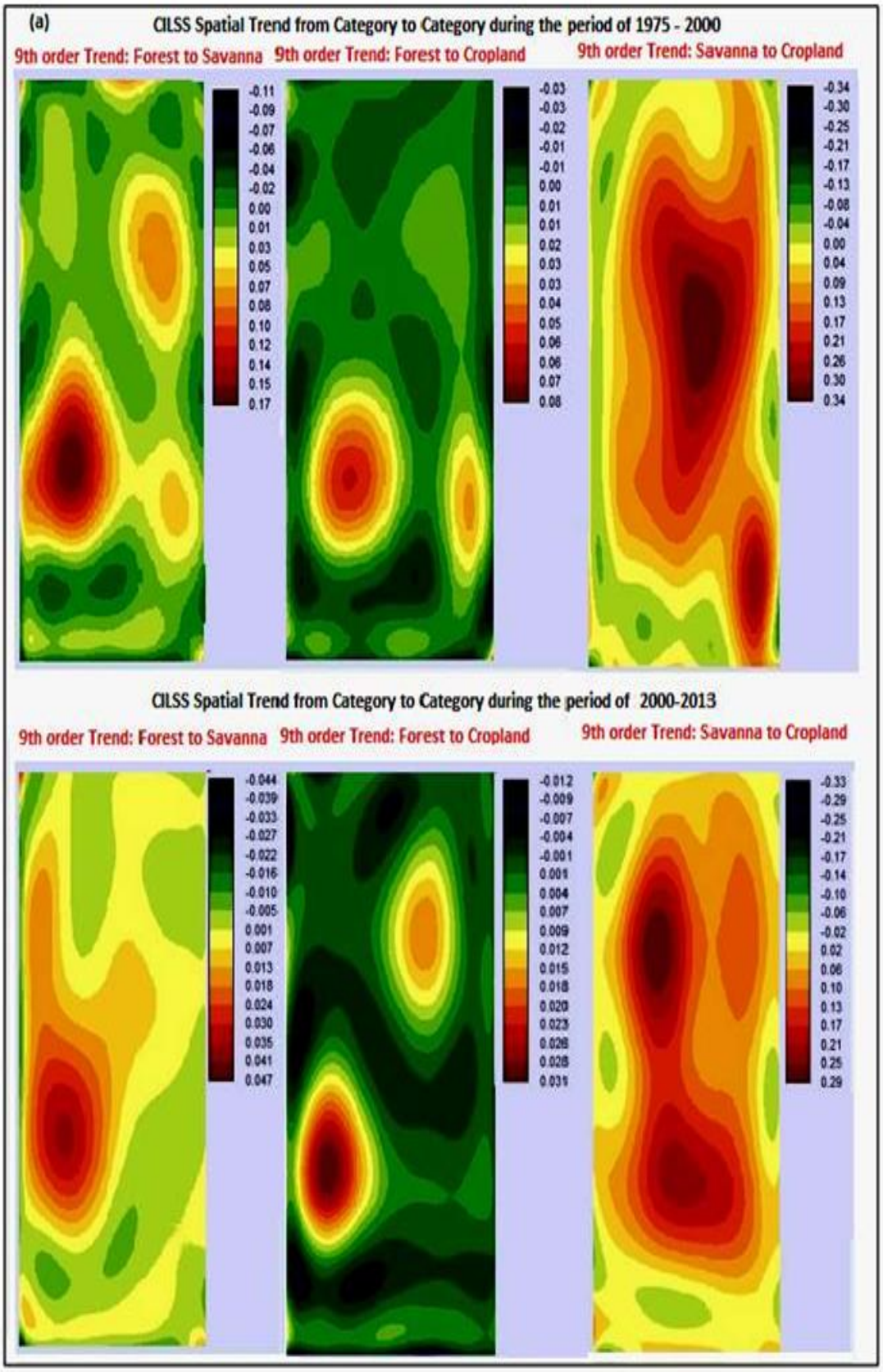

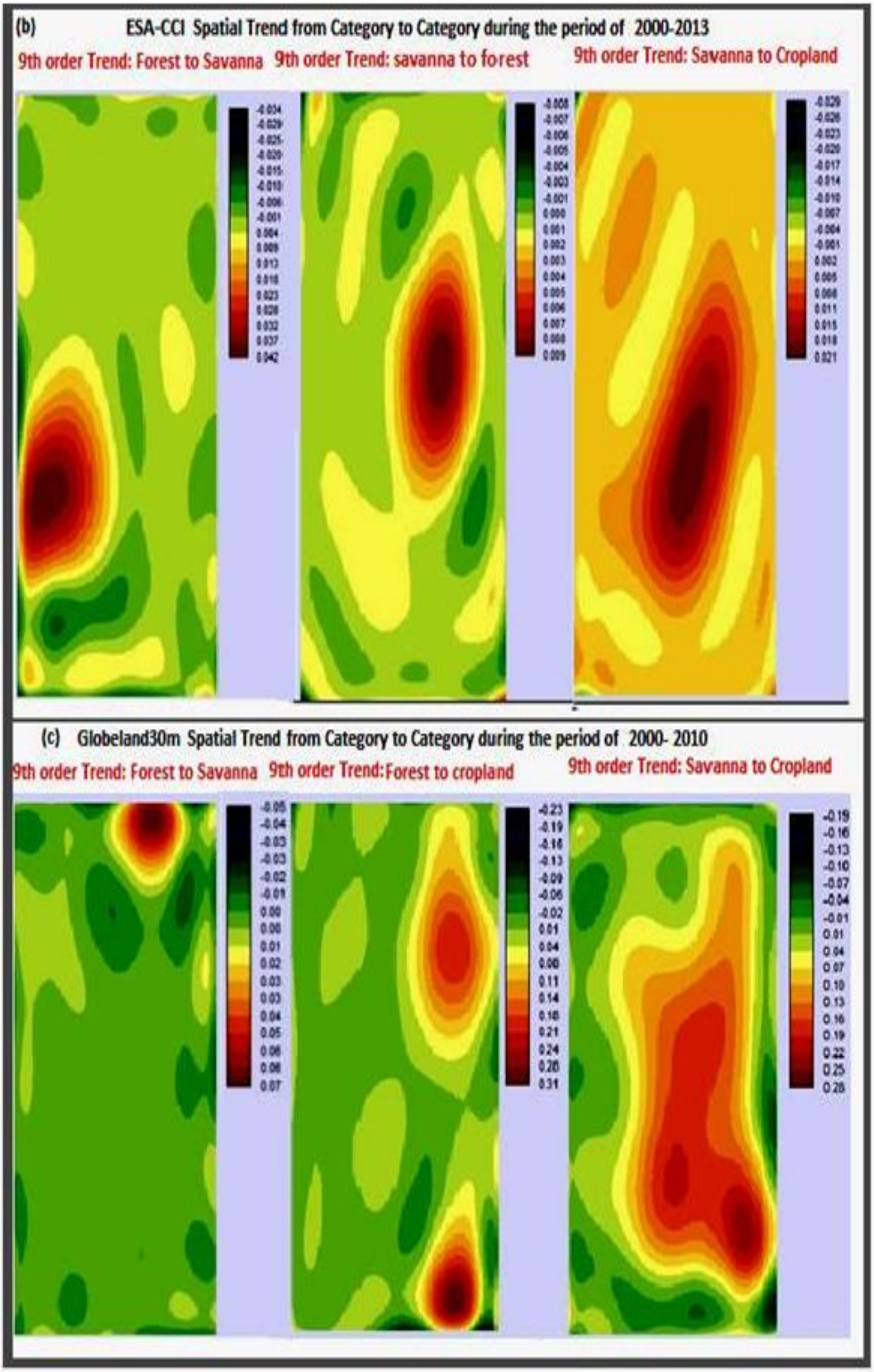

Negative values represent a reverse spatial development for the analyzed trend, whereas increasing positive numbers characterize an increasing intensity for the analyzed trend.

Appendix B: Land Cover Modeler MLP parameters and performance for explaining the change in LULC for CILSS and ESA 2000-2013 as well as for Globeland30 2000-2010/ RMSE: Root Mean Squared Error

	CILSS	ESA	Globeland30
Input layer neurons	2	2	2
Hidden layer neurons	3	2	3
Output layer neurons	6	5	5
Requested samples per class	10,000	10,000	10,000
Final learning rate	0.0001	0.0001	0.0005
Momentum factor	0.50	0.50	0.50
Sigmoid constant	1.00	1.00	1.00
Acceptable RMSE	0.01	0.01	0.01
Iterations	10,00	10,00	10,00
Training RMSE	0.29	0.35	0.40
Testing RMSE	0.29	0.35	0.40
Accuracy rate	50.94%	40.04%	20.13%
Skill measure	0.41	0.24	0.0017

Cloud Publications
International Journal of Advanced Remote Sensing and GIS
2019, Volume 8, Issue 1, pp. 3145-3155
ISSN 2320 – 0243, Crossref: 10.23953/cloud.ijarsg.440

Research Article

To Assess the Impact of Urbanization-Associated Land Use Changes on Actual Evapotranspiration and Water Balance in the Kelani River Basin, Sri Lanka

V.P.I.S. Wijeratne, H.A.C.D. Senavirathna, L. Manawadu

Department of Geography, Faculty of Arts, University of Colombo, Sri Lanka

Correspondence should be addressed to V.P.I.S. Wijeratne, *sandamali@geo.cmb.ac.lk*

Publication Date: 22 November 2019

DOI: https://doi.org/10.23953/cloud.ijarsg.440

Abstract Actual Evapotranspiration (AET) is a major component of the river basin hydrological cycle over land surface and energy balances. More than 60% of input water on land is returned to the atmosphere through evapotranspiration and it greatly influences the water availability on the land surface. Estimation of AET is an essential part in various fields. Thus, this study mainly aims at assessing the impact of urbanization-associated land use changes on actual evapotranspiration and water balance in the Kelani River Basin, Sri Lanka. Thronthwaite equation and land use conditions are mainly considered in this study to estimate AET. Average monthly temperature data has been obtained from NASA MOD1C3 and data has been validated using observed temperature data processed by the Meteorological Department in Sri Lanka. Potential Evapotranspiration (PET) was calculated using monthly average temperature and fractional vegetation cover was calculated using Landsat images (TM, ETM and OLI) to identify the land use and land cover changes from year 2000 to 2018. Both potential evapotranspiration and fractional vegetation cover are used to estimate AET. TRRM data was used to get Digital Elevation Model (DEM) and Landsat images were used to calculate Normalized Differential Vegetation Index (NDVI), Normalized Differential Building Index (NDBI). All the analysis used in this study have been carried out using raster calculator, zonal statistics and pivot tools in ArcGIS 10.1 software. The study revealed that land use and land cover is a major fact to determine AET. Upper catchment of Kelani River has obtained high AET values due to the vegetation cover and the elevation. Lower part of the catchment is associated with the low values due to build - up areas. AET has decreased by 2018 and urbanization is the main reason for it. Rainy seasons reduce the AET since high humidity and reducing AET can be highlighted when considering the temporal changes of AET in Kelani river basin. Evapotranspiration as a major component of water cycle should be considered because it can be a significant fact to reduce precipitation.
Keywords *Evapotranspiration; AET; PET; NDVI; NDBI*

1. Introduction

High population growth rate, rapid urbanization and industrialization in the world increase human production and consumption, which has led to increasing demand for freshwater resources. “It is estimated that by 2050, global water demand would increase by 55% due to different anthropogenic activities such as; manufacturing, thermal electricity generation and domestic water use” (Ubantu,

2016). Due to this reason, water management is a very essential requirement at the present world and it is important to know that major factors of water resource such as; evapotranspiration, rainfall and run-off mainly influence the water resource management in a river basin. Also, evapotranspiration is considered as a major component in the river basin hydrological cycle. It is the combination of two processes named evaporation and transpiration. Evaporation is the process through which water is transferred to the atmosphere from soil & other surfaces and transpiration is from stomata in plants (climate.ncsu.edu, 2019). Moreover, ET plays an important role in the atmospheric process since it controls the water supply from the ocean and earth's surface to the atmosphere. It is an energy-driven process and it is important in the water cycle since it is responsible for 15% of the atmosphere's water vapor (Sanand et al., 2018).

Water demand of crops, soil moisture condition, and water cycle balancing can be considered through estimating ET. Water demand of the crops may help to determine whether or not to irrigate and soil moisture condition helps to farmers to make decisions on farming. As an example, too much water in the soil causes to bog down the farm machinery and too dry soil causes to increase the stress of plants due to lack of available water. So ET can be used as a decision making tool for farming. ET helps to make decisions not only in farming but also in improving the well-being of biodiversity since ET acts a major role in water cycle. In other words clouds can't form without input of water vapors and it will cause lack of precipitation. Precipitation also can be predicted through ET.

There are a numbers of methods to estimate the ET as the (FAO56) Penman-Monteith equation, Thornthwaite equation, Hargreaves equation, Hamon equation, Priestly-Taylor equation, Solar radiation (Rs) based method and Net radiation (Rn) based method (Irmak et al., 2003) but these methods are not always easy to implement and supportive data sources are very limited and expensive. Many river basins in Sri Lanka are ungaged, and it is very difficult to obtain appropriate data at spatial and temporal scale to support any decision making of water management. With the development of technology, remote sensing method has been carried out to find ET and as examples remote sensing and SEBAL Algorithm (Kumar et al., 2014), Soil Plant Atmosphere and Remote Sensing Evapotranspiration (SPARSE) model (Saadi et al., 2018), using color composite (FCC) and Normalized Difference Vegetation Index (NDVI) in ArcGIS environment (Kilic and tarboton, 2012) can be shown. The ET computation by Remote Sensing is mostly based on the energy balance from satellite sensor and it is very effective to give an estimation output over large area.

Land use change is a major factor that influences the river basin hydrological cycle and its major components of rainfall, evapotranspiration and run-off. Land use changes alter the spatial patterns of ET distribution, with significant impact on water balance in a river basin. "Actual evapotranspiration (AET) is the water quantity which is transferred to the atmosphere as water vapor from and evaporating surface under actual conditions; vegetation type, climate, Physiological mechanism and water availability" (Sanand et al., 2018). Assessment of AET is very essential because it can control the exchange of water and heat energy between the atmosphere and earth surface. Also, AET can determine climate drought in arid and semi-arid areas through studying temperature and land use pattern. Further, it is a good tool to identify the crop water requirement and improving any practices of water management at the river basin level is important for future decisions.

Evapotranspiration is a major component of water cycle. Nowadays anthropogenic activities have changed the natural process of Evapotranspiration. Therefore, Evapotranspiration should be considered because it can be a significant fact to reduce precipitation. Water demand of crops, soil water necessity and drought condition can be identified through evapotranspiration and the findings would help to develop the practices for agriculture sector. Moreover, principles can be carried out for anthropogenic activities to balance friendly evapotranspiration process.

The main purpose of this study was to identify the impact of rapid urbanization on AET in a river basin level and GIS and Remote Sensing techniques being used for that purpose. The specific objective of this study are:

- To identify the spatial and temporal variability of Actual Evapotranspiration in Kelani river basin.
- To analyze the spatial and temporal changes in land use at the river basin level.
- To assess the relationship between the evapotranspiration and different types of land use.

2. Literature Review

Evapotranspiration estimation based researches are common conducting in these days. Many researches have documented the impact of reference evapotranspiration and potential evapotranspiration changes on crop water requirement. Several of them focused mainly on water balance effects in a river basin. However, very limited number of studied have been done to analyze the rapid urbanization and its impact on Potential Evapotranspiration.

Alkaeed et al. (2006) have done a research using six reference evapotranspiration (ETo) methods to compare each, based on their daily performances under the given climatic condition in the western region of Fukuoka City, Japan. Penman-Monteith method was considered to be the best method for estimating ETo in which the calculated ETo values correspond to lysimeters and other precise devices where real ETo can best obtained. The performances of the Thorthwaite, Hargreaves, Hamon, Rs-based and Rn-based equations for monthly ETo estimates are significantly correlated with the ETo estimates in Food and Agriculture Organization Penman – Monteith equation (FAO56-PM) method although the Thorthwaite method was found to have highly significant estimates. In this study Thorthwaite method, with the minimum required weather data is used to estimate the potential evapotranspiration.

Kumar et al. (2014) have carried out estimation of ET using MODIS Sensor Data in Udupi District of Karnataka, India. The direct relationship between land use/land cover classes and evapotranspiration is well noticed in the study as in the study carried out here.

Maftei and Barbulescu (2010) implemented an ETo estimation algorithm, the Triangle Method, which is based on the modified Priestly-Taylor equation to estimate the evapotranspiration using remote sensing data and grid computing in Dobrogea, Romania. Their results have shown that the method utilized can derive reasonable estimates for surface temperature (LST) and evapotranspiration (ET). A Web-based client interface was built to make the applications usable to study the geographical distribution of evapotranspiration, consequently water demand in large cultivated areas for irrigation purposes and sustainable water resources management. In this study, remote sensing data has been calculated to find the evapotranspiration although Thornthwaite method was used instead of using Priestly-Taylor equation.

Kilic and Tarboton have conducted a study in 2012, with the purpose of utilizing raw Landsat 5 TM data in order to display a false color composite (FCC) of the Landsat bands from a scene (path 29, Row 32), calculate vegetation index (NDVI) and estimate evapotranspiration (ETo) in the ArcGIS environment. NDVI was calculated to find the AET in this study but FCC was not used.

Sun et al. (2011) have found that synergistic use of the polar-orbiting MODIS data and the geostationary-orbiting SEVIRI data have potential to produce reliable daily ET (actual or reference evapotranspiration) and a measure of drought exclusively from satellite data and weather forecast data. They have applied the methodology over East African highlands, and calculated the daily AET, daily ETo and dryness index for the year 2007. In this study, monthly AET has been calculated for particular months and 2000, 2013 and 2018 has been considered for finding the seasonable variations.

3. Study Area

The study was conducted in the Kelani River basin in Sri Lanka (Figure 1). The Kelani River originates from the Western face of the central highlands located in the Horton Plains National Park and Peak Wilderness Sanctuary. It drains approximately 2,292 square kilometers of land area. It is the second largest river basin and fourth longest river in Sri Lanka. This area is exposed to the south west monsoon and belongs to wet zone in Sri Lanka.

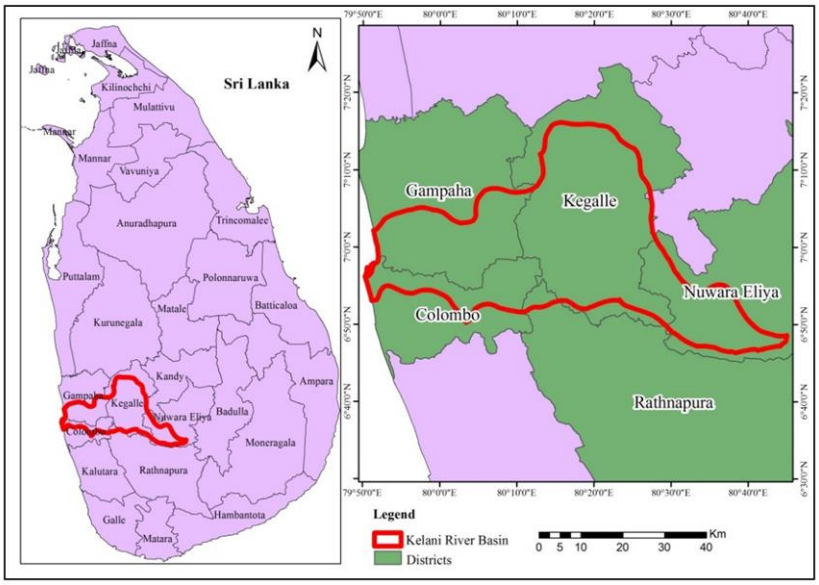

Source: *Prepared by the author based on survey department of Sri Lanka, 2019*

Figure 1: *Study area*

4. Materials and Methods

Seasonal based AET analysis is carried out for the Period of 2000 to 2018. January and May were considered to depute wet and dry seasons in the area.

Data

This study is mainly based on secondary data. MODIS temperature data and Landsat TM, ETM and OLI satellite images (Red, NIR, swir bands) were used. Year 2000, 2013 and 2018 images were downloaded from earth explorer and less than 10% cloud cover were considered for the analysis. Third sub database which is mean monthly temperature included was extracted from MOD1C3 satellite image. TRMM data were used for Digital Elevation Model (DEM) Sunshine hours were calculated using secondary data from timeanddate.com. Observed data set from Metrological Department is used to verify the accuracy of the temperature data.

Calculate Potential Evapotranspiration

Among several equations for measuring evapotranspiration Thornthwaite's equation was used to find the potential evapotranspiration. This equation mainly focused on mean monthly temperature and mean monthly sunshine hour. The main advantage of this method is that only the temperature information is needed beside the sunshine hours.

To calculate Potential Evapotranspiration (PET) using Thornthwaite method, first the Annual Thorthwaite Heat Index (i) calculation is required, using the equation 01:

$$I = \sum_{i=1}^{12} (T_i / 5)^{1.514} \quad \ldots (1)$$

Potential Evapotranspiration (PET) estimation is obtained for each month using the formula below,

$$PET_{\text{non corrected}} = 16 \times (10T_i / I)^a \ldots (2)$$

$$\text{Where } a = (492390 + 17920\, I - 771\, I2 + 0.675\, I3) \times 10\text{-}6 \ldots (3)$$

Obtained values are later corrected according to the real length of the month and the theoretical sunshine hours for the latitude of interest, with the formula:

$$PET = PET_{\text{non corrected}} \times N \times 30 \ldots (4)$$

Where T is the mean monthly temperature (c^0), N is the mean monthly sunshine hour.

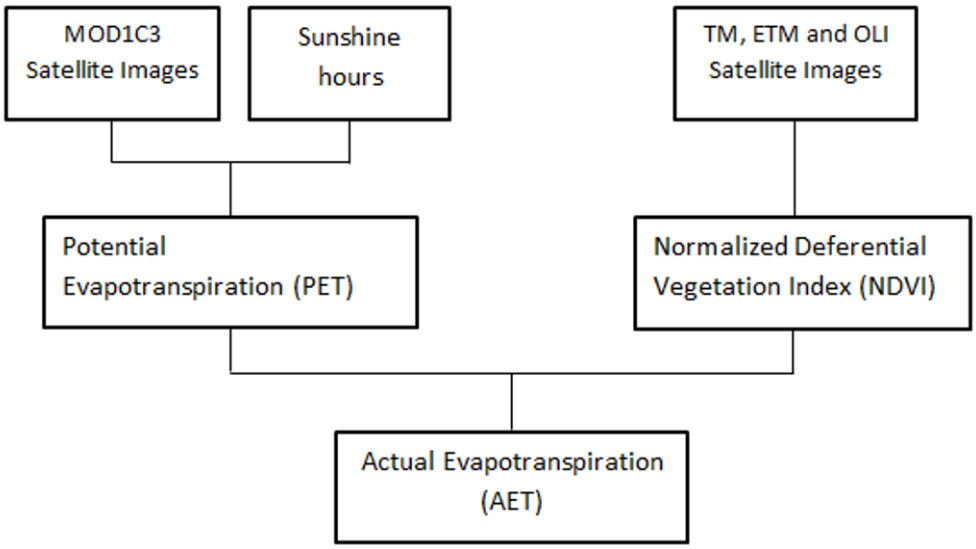

Figure 2: *Methodology for AET*

Fractional Vegetation Cover

The method proposed by Brunsell and Gillies (2003) to obtain the fraction of vegetation cover has been used in this study.

Firstly NDVI was calculated through the below equation using the TM, ETM+ and OLI Landsat Data for year 2000, 2013 and 2018.

$$NDVI = (NIR\text{-}RED) / (NIR) + (RED) \ldots (5)$$

Then, fraction of vegetation cover using the raster calculator was done based on the equation:

$$\text{Square } (("NDVI" - 0.14) / (0.75 - 0.14)) \ldots (6)$$

Estimate Actual Evapotranspiration

Actual Evapotranspiration (AET) was calculated by multiplying fraction of vegetation cover with the potential evapotranspiration. Whole method of calculating AET can be presented as Figure 2:

Calculate Normalized Difference Built-up Index (NDBI)

The Normalized Difference Build-up Index (NDBI) was calculated to identify the impact of urban-associated land use changes on actual evapotranspiration and NDBI was also calculated for above data period using Equation 07.

$$NDBI = (NIR-swir)/(NIR+swir) \ldots (7)$$

ArcGIS environment was used to Calculate above methods and prepare the maps. Spatial analyst methods, raster calculator, pivot tables and zonal statistical tools were used for the analyze data.

5. Results and Discussion

Evapotranspiration was calculated for Kelani river basin and its spatial and temporal variation was significant.

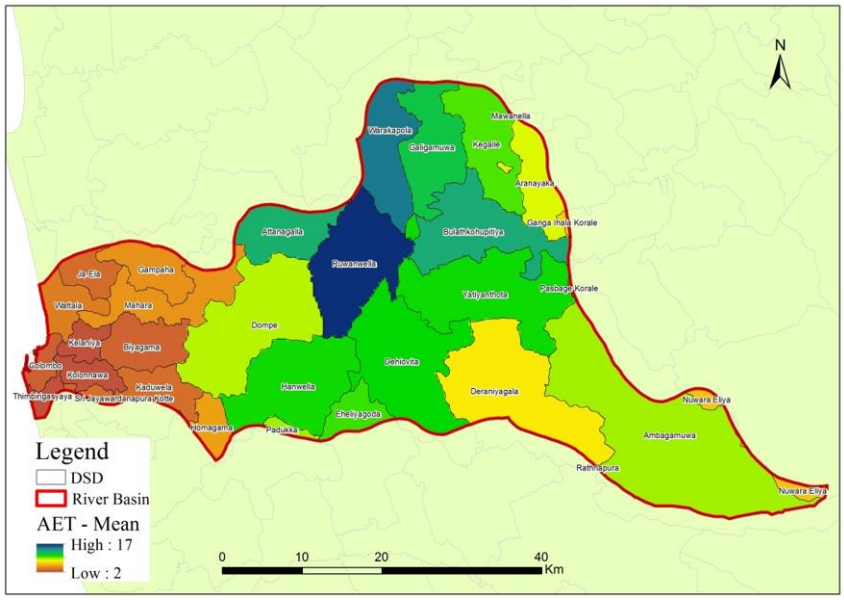

Figure 3: *Mean actual evapotranspiration*

Spatial distribution of the AET shows the significant pattern all over the Kelani river basin. Upper catchment is associated with high AET values while lower catchment is associated with low AET values. Mean AET regarding the Divisional Secretariat Divisions which belong to Kelani river basin shown in Figure 3, clearly reveals its distribution throughout the whole river basin. Figure 4 shows the changes of mean AET in DSD along the Kelani River.

DSDs in lower part and middle parts of the river have obtained low AET values and high AET values respectively although, DSDs which are in upper part of the river have obtained low AET values. Not only the spatial AET but also the temporal AET is shown in the map Figure 5.

Temporal changes have been identified from 2000 to 2018 along January and May. AET has decreased from 2000 to 2018. AET in May is higher than the values in January. This result reveals that

rainy season reduce the AET due to high humidity. The low values of evapotranspiration reported in May are attributed to low temperature and sunshine conditions due to south west monsoon.

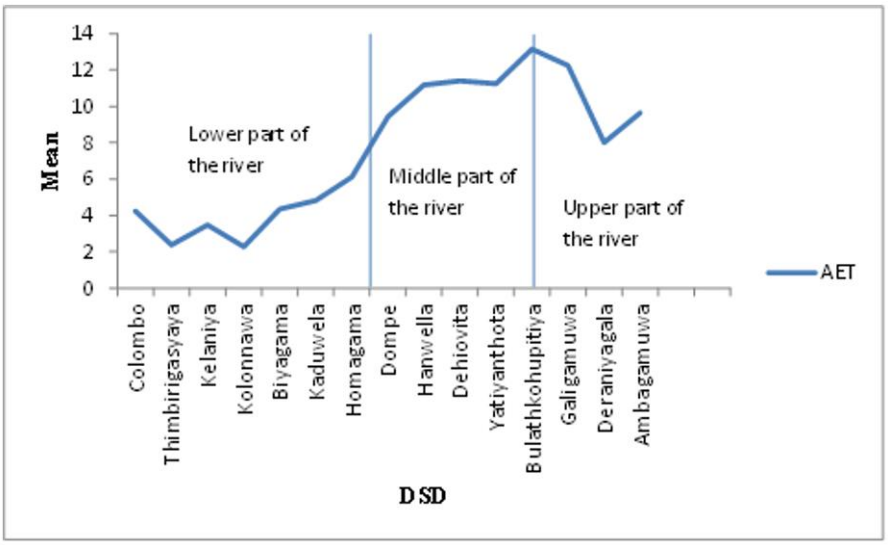

Figure 4: *Mean actual evapotranspiration (mm) of DSD*

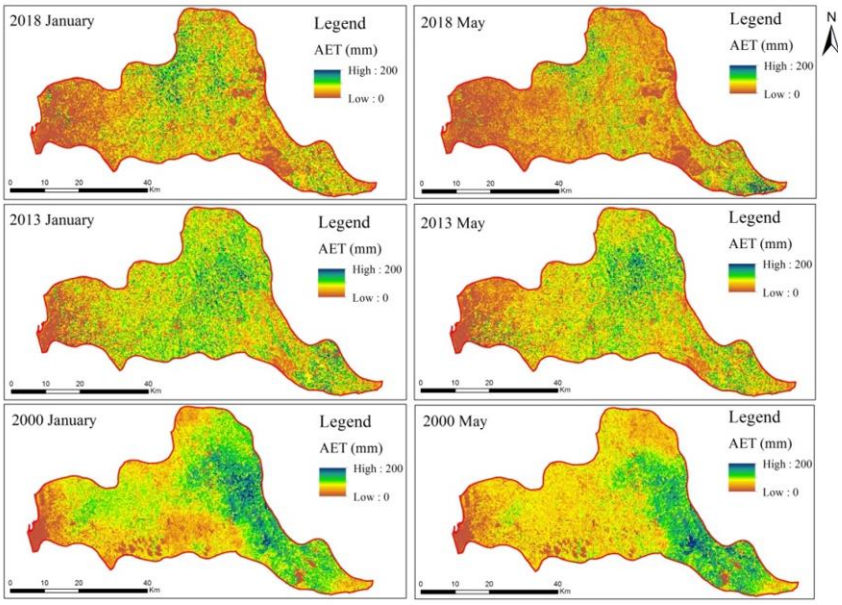

Figure 5: *Actual evapotranspiration*

Affected factors for these variations will be discussed further in this paper. Temperature, Land use, Land cover, Wind and Sunshine are the factors for evapotranspiration. Slope and aspect also play key roles in evapotranspiration as they determine the effectiveness of insolation.

Temperature is the most significant factor for evapotranspiration. It has a positive relation in which the rate of evapotranspiration increases as temperature increases because there is a higher amount of energy availability to convert liquid to water vapor. Therefore, average monthly temperature data has been obtained from NASA MOD1C3 and this data has been validated using observed temperature data processed by the Metrological Department in Sri Lanka. The result showed a validity of more than 80%.

Elevation affect to evapotranspiration due to high canopy layer and effectiveness of insolation. Elevation and AET is shown in Figure 6.

High elevation area has obtained high AET but this situation can be changed with the land use pattern.

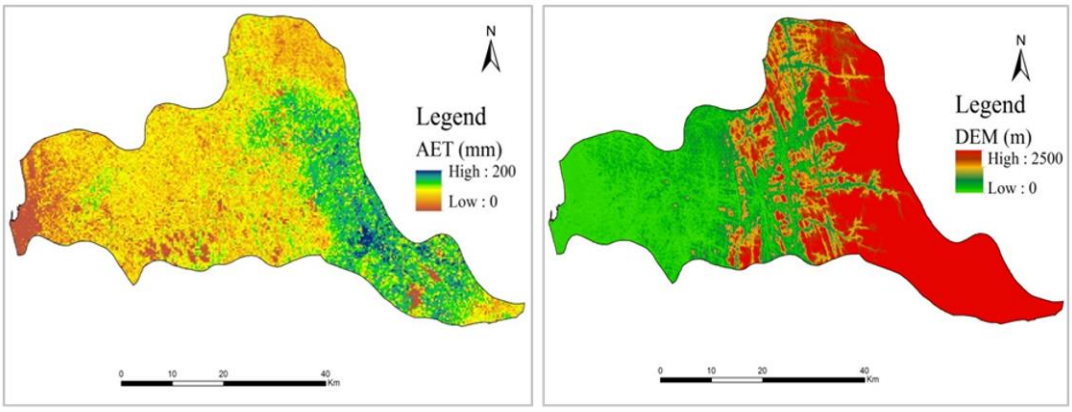

Figure 6: *Actual evapotranspiration and elevation*

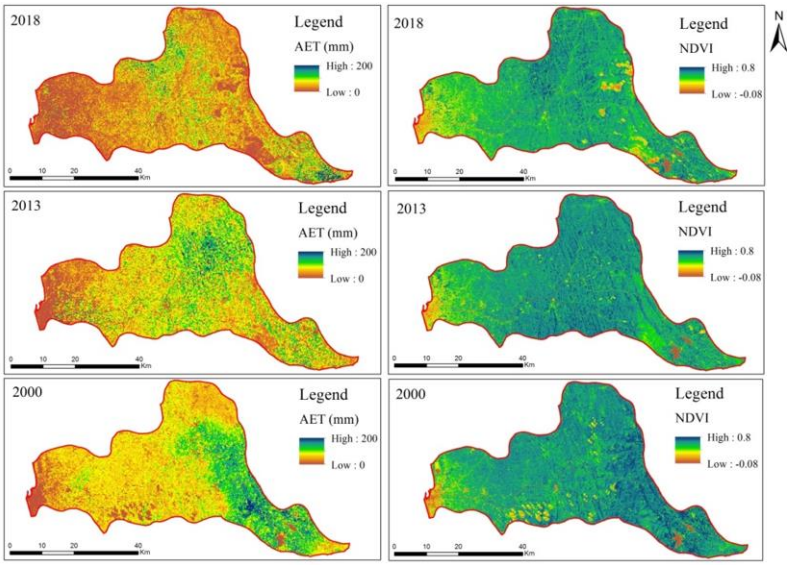

Figure 7: *AET and NDVI*

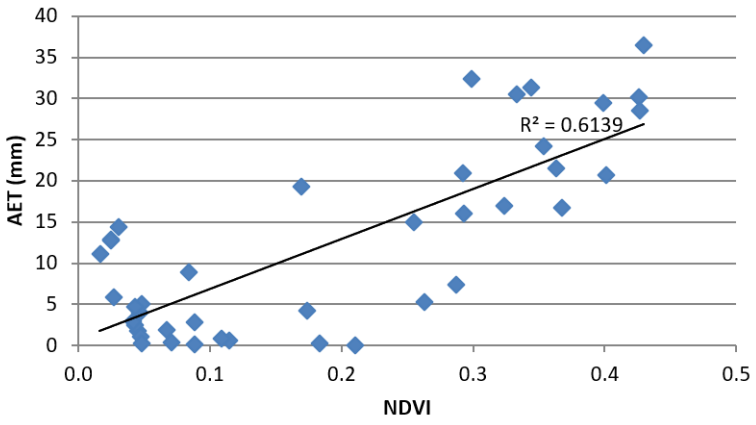

Figure 8: *Correlation between AET and NDVI values*

NDVI and NDBI were calculated to study the relationship between land cover - land use and AET. NDVI helps to reveal how the canopies affect AET while NDBI gives a clear idea of how the buildings affect AET.

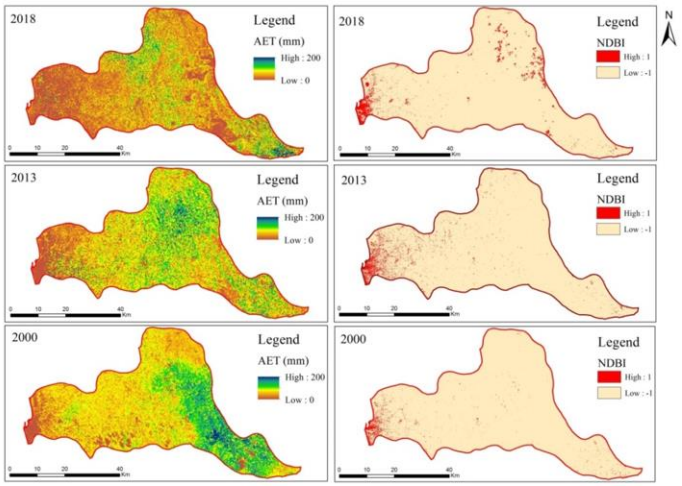

Figure 9: *Actual evapotranspiration*

AET and NDVI are shown in Figure 7 and temporal changes of NDVI can also be identified. Moreover, changes of AET and NDVI resemble throughout the years. When AET decreased, NDVI has also decreased by 2018. It means that there is a correlation between AET and NDVI.

The relationship between NDVI and AET is positive and it is shown in Figure 8. When the NDVI value is high AET value is also high. Low values of NDVI are identified in the areas with low canopy. Nowadays canopy layer is decreasing with the new constructions. Therefore temporally AET has decreased in the built up areas.

Table 1: *The AET values of land use and land cover*

Land Use/Land Cover	AET(mm)
Buit-up areas	2.66
Road	6.71
River (Lower part)	11.27
River (Middle Part)	45.22
River (Upper Part)	79.32
Paddy Fields	26.51
Tea	47.26
Rubber	70.58
Water Bodies	12.46
Open land	19.17
Marsh Land	32.2
Forest	21.63
Forest	36.06
Mountain with forest	85.72

AET is poor in lower catchment of the area as settlements and built-up classes dominate over vegetation cover in this region. Integrating the Table 1, the AET is classified as poor in the built-up areas, moderate in the agricultural lands and plantations, good to very good in upper part of the river. Mountain areas with forests considered in the study show higher evapotranspiration.

Increasing of the built up area and reducing of the canopy cover is the main reason to reduce AET temporally. AET and building distribution is shown in Figure 9. Built up area has increased by 2018 and according to it, AET has decreased. Built-up area has reduced the AET due to rough surface.

6. Conclusion and Recommendation

AET is very important to identify the water necessity of trees and the contribution to water cycle. AET in Kelani river basin was calculated in the study. Spatial and Temporal changes of AET along the Kelani river basin could be clearly identified and affected factors for evapotranspiration were discussed.

When the elevation is high, AET is also high due to high canopy layer and effectiveness of insolation. Land use and land cover are major factors to determine AET. Upper catchment of Kalani River has obtained high AET due to the vegetation cover and the elevation. Lower part of the catchment is associated with the low values due to built up areas. AET has decreased by 2018 and urbanization can be the main reason for it. Reducing AET can be highlighted when considering the temporal changes of AET in Kelani river basin. Rainy seasons reduce the AET since high humidity and temporal changes of AET can be seen in monsoon seasons.

Further researches are needed to identify crop water necessity, cloud analysis, drought index and Soil water requirement through evapotranspiration. Identifying the crop differentials may help to calculate the water necessity.

References

Alkeed, O., Flores, C., Jinno, K. and Tsutsumi, A. 2006. Comparison of several reference evapotranspiration methods for Itoshima Peninsula Area, Fukuoka, Japan. *Memoirs of the Faculty of Engineering, Kyushu University*, 66 (01), pp.1-14.

Kabantu, M. 2016. *Estimation of evapotranspiration and its relationship to land use and water resources in Lufumi catchment, Kinshasa*. M.S. Thesis, Department of Civil Engineering, University of Zimbabwe, p.75.

Kumar, G.D., Purushothaman, B.M., Vinaya, M.S. and Suresh, S. 2014. Estimation of evapotranspiration using MODIS sensor data in Udupi District of Karnataka, India. *International Journal of Advanced Remote Sensing and GIS*, 03 (01), pp.532-543.

Liu, W., Hong, Y., Khan, S.I., Huang, M., Vieux, B., Caliskan, S. and Grout, T. 2010. Actual evapotranspiration estimation for different land use and land cover in urban regions using landsat 5 data. Journal of Applied Remote Sensing, 4(1), p.041873.

Maftei, C. and Barbulescu, A. 2010. Estimation of evapotranspiration using remote sensing data and grid computing: A case study in Dobrogea, Romania. *Theme paper for the International conference on Computers*, p.1.

Matarrese, R., Portoghese, I. and Vurro, M. 2011. *Actual evapotranspiration by use of MODIS data*. International Meeting on Meteorology and Climatology of the Mediterranean.

Sameh, S., Gilles, B., Malik, B., Aurore, B., Émilie, D., Pascal, F., Bernard, M., Vincent, S. and Zohra L.C. 2018. Assessment of actual evapotranspiration over a semiarid heterogeneous land surface by means of coupled low-resolution remote sensing data with an energy balance model: comparison to extra-large aperture scintillometer measurements. *International Journal of Hydrology and Earth System Sciences*, 22, pp.2187-2209.

Sun, Z., Gebremichael, M., Ardo, J. and Bruin, H.A.R.D. 2011. Mapping daily evapotranspiration and dryness index in the East African highlands using MODIS and SEVIRI data. *International Journal of Hydrology and Earth System Sciences*, 15, pp.163-170.

Silva-Fuzzo, D.F. and Rocha, J.V. 2016. Simplified triangle method for estimating evaporative fraction over soybean crops. *Journal of Applied Remote Sensing*, 10(4), p.046027.

Yanfang, X., Zhen, W., Min, H. and Haoxue, A.L. 2011. *Investigation of the impact of surrounding light on monitor' color showing*. International Conference on Environmental, China. pp.499-504.

North California Climate Office, 2019. Evapotranspiration. Available form: *https://climate.ncsu.edu/edu/Evap.*

Timeanddate, 2019. Sunshine. Available form: *https://www.timeanddate.com/.*